



HAL
open science

Highly integrated photovoltaic micro-concentrator for space applications

Anderson Bermudez-Garcia

► **To cite this version:**

Anderson Bermudez-Garcia. Highly integrated photovoltaic micro-concentrator for space applications. Physics [physics]. Université Grenoble Alpes [2020-..], 2022. English. NNT : 2022GRALY040 . tel-04500392

HAL Id: tel-04500392

<https://theses.hal.science/tel-04500392>

Submitted on 12 Mar 2024

HAL is a multi-disciplinary open access archive for the deposit and dissemination of scientific research documents, whether they are published or not. The documents may come from teaching and research institutions in France or abroad, or from public or private research centers.

L'archive ouverte pluridisciplinaire **HAL**, est destinée au dépôt et à la diffusion de documents scientifiques de niveau recherche, publiés ou non, émanant des établissements d'enseignement et de recherche français ou étrangers, des laboratoires publics ou privés.

THÈSE

Pour obtenir le grade de

DOCTEUR DE L'UNIVERSITE GRENOBLE ALPES

Spécialité : **PHYSIQUE DES MATERIAUX**

Arrêté ministériel : 25 mai 2016

Présentée par

Anderson BERMUDEZ-GARCIA

Thèse dirigée par

Olivier RACCURT, Docteur (HDR), Expert senior, CEA,
et encadrée par

Philippe VOARINO, Docteur, Expert senior, CEA

préparée au sein du **Laboratoire d'Innovation pour
les Technologies des Energies Nouvelles (CEA/Liten)**
dans l'**École Doctorale Physique de Grenoble**

**Micro-concentrateur photovoltaïque ultra-
intégré pour applications spatiales**

**Highly integrated photovoltaic micro-
concentrator for space applications**

Thèse soutenue publiquement le « **16 juin 2022** »,
devant le jury composé de :

Monsieur Stéphane COLLIN

Directeur de recherche, CNRS, Rapporteur

Monsieur Hervé PIOMBINI

Ingénieur HDR, DMAT CEA Ripault, Rapporteur

Monsieur César DOMINGUEZ-DOMINGUEZ

Professeur adjoint, IES, Univ. Politécnica de Madrid, Examineur

Madame Anne KAMINSKI-CACHOPO

Professeur des universités, Grenoble INP, Présidente

Monsieur Jean-Louis MONIN

Professeur à l'UGA et directeur du Centre Spatial Universitaire de Grenoble,
Examineur

Monsieur Alexis VOSSIER

Chargé de recherche, CNRS-PROMES, Examineur

Membres invités :

Monsieur Bernard BOULANGER

Ingénieur, Expert, Thales Alenia Space

Monsieur Philippe VOARINO

Ingénieur docteur, Expert senior, CEA



Contents

Acknowledgements	3
Abstract	5
Introduction	9
Context: solar power in outer space	9
Motivation: toward micro-concentrating systems for space applications	14
Outline of the thesis structure	15
1 A brief review of state-of-the-art from Concentrator PhotoVoltaics (CPV) to micro-CPV technologies	17
1.1 Concentrator photovoltaics systems	17
1.2 CPV optics designs for primary optical elements	20
1.2.1 Refractive	20
1.2.2 Reflective	21
1.3 CPV technologies deployed in space missions	23
1.3.1 Proven viability and radiation hardness of CPVs in space	23
1.3.2 Proven reliability of CPVs in space	25
1.3.3 Reflective designs in space: a pursued and compelling approach	27
1.4 Towards micro-CPV systems	29
1.4.1 Overview of micro-CPV systems for terrestrial applications	29
1.4.1.1 Panasonic approach	30
1.4.1.2 Sandia National Laboratories solution	32
1.4.2 Recent proposals of micro-CPV systems for space application	36
1.4.2.1 Air Force Research Laboratory study	36
1.4.2.2 The Pennsylvania State University approach	38
1.5 Discussion and conclusions	40

2	Assessment of specific missions and environments favorable to CPV in space	43
2.1	Environmental factors affecting the conversion efficiency and durability of PVAs	44
2.1.1	Extraterrestrial solar total and spectral irradiance	44
2.1.2	Extreme temperatures and thermal cycling	46
2.1.3	Vacuum	46
2.1.4	Plasmas	47
2.1.5	Space radiation environment	48
2.1.6	Micrometeoroid and orbital debris impact	50
2.2	Specific space environments and description of photovoltaics	52
2.2.1	Earth satellite orbits	54
2.2.1.1	Low Earth Orbit	54
2.2.1.2	Medium Earth Orbit	55
2.2.1.3	Geostationary Earth Orbit	56
2.2.2	Dusty worlds: the Moon and Mars	60
2.2.2.1	Earth's Moon	60
2.2.2.2	Mars	64
2.2.3	High temperature missions: Venus, Mercury and the Sun	66
2.2.3.1	Venus	66
2.2.3.2	Mercury	68
2.2.3.3	Solar Orbiters	70
2.2.4	Low Intensity and Low Temperature (LILT) conditions: Gas Giants	73
2.2.4.1	Jupiter	73
2.2.4.2	Galilean Moons	78
2.2.4.3	Saturn	84
2.2.4.4	Kronian Moons: Two Emerging Worlds	86
2.3	Analysis and discussion	89
2.3.1	High Temperature Missions: Venus, Mercury and the Sun	94
2.3.2	Dusty Worlds: Earth's Moon and Mars	95
2.3.3	High-Radiated Worlds: Earth Orbits and Gas Giants	97
2.4	Conclusions and perspectives	101

3	Optics optimization and integration of a linear compound parabolic concentrator using III-V/Si cells	103
3.1	Description of the baseline design of previous linear CPC	104
3.2	Optical design and optimization of a new generation CPC	105
3.2.1	Receiver optimization	108
3.2.1.1	III-V/Si solar cells	108
3.2.1.2	Target value	109
3.2.1.3	Variables	112
3.2.1.4	Evolution and results of the optimization process	114
3.3	Manufacturing and assembly description	116
3.3.1	Interconnected cells	116
3.3.2	Optics silicone molding and its improvements	117
3.3.2.1	Assembly of the injection mold	117
3.3.2.2	Injection and curing of the silicone optics	118
3.3.2.3	Demolding of optics and final assembly	118
3.3.2.4	Discussion	119
3.4	Performance evaluation of the optimized CPC	120
3.4.1	Electroluminescence	120
3.4.1.1	A brief description of the device measurement	121
3.4.1.2	EL results	122
3.4.2	Current-voltage (I-V) characteristics	123
3.4.2.1	Solar cell simulator: Helios 3030	123
3.4.2.2	Solar module simulator: Helios 3198	124
3.4.2.3	IV characteristics results	125
3.4.3	Comparison between designs and discussion	127
3.5	Conclusions and perspectives	129
4	Optical design of a highly integrated reflector for micro-CPV	131
4.1	Design of a highly integrated micro-CPV	132
4.2	Optical design via raytracing	135
4.2.1	Source modeling and convergence	137
4.2.2	Parabolic reflector	139
4.2.3	Free-form optimized reflector	145

4.2.3.1	Modeled solar source and the target value	145
4.2.3.2	Variables	145
4.2.3.3	Evolution and results of the optimization process	146
4.2.3.4	Analysis of SOE design performance	149
4.2.4	Analysis and conclusions	152
4.3	Optical simulation of a hexagonal truncated parabolic reflector	154
4.3.1	System description	155
4.3.2	Source modeling and convergence	155
4.3.3	Optical losses chain and estimated optical efficiency	158
4.3.3.1	Coverglass	158
4.3.3.2	Solar cell and interconnections shading	162
4.3.3.3	Optics reflectance	163
4.3.3.4	Optical losses summary	165
4.3.4	Irradiance distribution	165
4.3.5	Angular tolerance analysis	166
4.3.6	Mechanical misalignment of the concentrator elements	169
4.3.7	Spectral photocurrent distribution	170
4.3.8	Synthesis and conclusions	172
5	Experimental validation of a highly integrated parabolic reflector	177
5.1	Lamination of double stage composite materials	178
5.2	Molding of polymer optics	182
5.2.1	Manufacturing process of optics inside a honeycomb structure	182
5.2.2	Crosslinking study of polymer silicone	183
5.2.3	Mold design	185
5.2.4	Mold fabrication and characterization	188
5.3	Synthesis and conclusions	194
6	Optical efficiency estimation via topographical characterization by optical microscopy and ray-tracing	195
6.1	Surface topography measurement of optics based on a non-contact technique	197
6.2	Qualification of the application parameters of a matting coating for surface measurements	200

6.2.1	Coating over-thickness and surface area covered vs. number of layers applied.	201
6.2.2	Roughness evolution relative of layers number	204
6.2.3	Temporal evolution of the surface coating during sublimation	208
6.2.4	Analysis and conclusions of method qualification	209
6.3	Recognition, reconstruction and analysis of measured surfaces	211
6.4	Recognition of quadratic surfaces	214
6.4.1	Validation 1: ideal quadratic surface	215
6.4.2	Validation 2: quadratic surface with double curvature	219
6.4.3	Validation 3: scanned well-known surfaces	222
6.4.4	Measurement of one unit of the manufactured mold	226
6.4.5	Measurement of an optical unit molded in silicone	231
6.4.6	Analysis and conclusions of recognition method	235
6.5	Optical efficiency estimation by topographical reconstruction and ray-tracing simulation	237
6.5.1	Reconstruction of an optical unit and the measurement plane . . .	238
6.5.2	Conversion efficiency analysis using raytracing	241
6.5.2.1	Mold's unit estimation	241
6.5.2.2	Molded optics's estimation	246
6.5.3	Analysis and conclusions of recognition method	250
	Conclusion and perspectives	253
	Glossary	257
	Annexes	261
	Annex A: scientific contributions	261
	Annex B: Best Research-Cell Efficiency Chart	263
	Annex C: III-V on Si solar cell manufacturing process	264
	Annex D: Flexural stiffness evaluation of the proposed micro-CPV design by bending tests	265
	Annex E: Some state-of-the-art pick and place machines	267
	Annex F: Mechanical properties tables	268
	Annex G: Measurement of coverglass roughness	269

Annex H: Irradiance maps for angular and mechanical misalignment	270
Annex I: Coating thickness and filled surface evolution for different number of spraying cycles	272
Annex J: Bearing balls precision as defined by the American Bearing Manufac- turers Association (ABMA)	272
Annex K: Structures associated with the point cloud: octree	273
Annex L: Point cloud artifacts and case study approach	273
Annex M: Methods for comparing two models	276
Annex N: Methods for identifying and estimating geometrical model features . .	277
Résumé en français	281
Introduction	281
Chapitre 1 : Etat de l'art des technologies CPV et micro-CPV	283
Chapitre 2 : Évaluation des missions et des environnements spécifiques favorables au CPV dans l'espace	287
Chapitre 3: Optimisation optique et intégration d'un concentrateur parabolique linéaire utilisant des cellules III-V/Si	292
Chapitre 4 : Conception optique d'un réflecteur ultra intégré pour micro-CPV	295
Chapitre 5 : Validation expérimentale d'un réflecteur parabolique hautement intégré	301
Chapitre 6 : Estimation de l'efficacité optique via la caractérisation to- pographique par microscopie optique et tracé de rayons	305
Conclusions et perspectives	315
References	319

to Luz Stella and Cesar Augusto my parents and Salomé my little sister.

Acknowledgements

This thesis was carried out at the *Commissariat à l'Énergie Atomique et aux Énergies Alternatives* - CEA, at the LITEN-INES site.

I would like to start by thanking my supervisor Philippe Voarino and my thesis director Olivier Raccurt. I wish to thank Philippe for having chosen and entrusted me with this thesis and for his continuous support during these three years. And in particular I would like to thank him for his involvement, for welcoming me at INES and guiding me in the world of micro-concentrators for space. I would also like to thank Olivier for pushing me to do research with scientific rigor. I thank you both for your follow-up throughout this thesis, your permanent availability to answer my questions and to overcome all scientific and technical problems.

I also had an excellent thesis jury: Stéphane Collin, Hervé Piombini, César Dominguez-Dominguez, Anne Kaminski-Cachopo, Jean-Louis Monin, Alexis Vossier and Bernard Boulanger, with whom I had the honor to exchange; I thank them for their contributions to this manuscript.

I would like to thank the whole SMPV team for the excellent working atmosphere, for the scientific, friendly and sportive discussions : Fabien, Romain, Julien, Karim, Jean-Baptiste, Tatiana, Baptiste, Ichrak, Carla, Victor, Marion, Marie-Pierre, Jérôme, Nicolas, Thomas, Nouha, Romain, Bertrand, Clément, Aude, Caroline, Martine and the rest of the team. Special thanks to Karim, Romain, Ichrak, Evaa, Caroline and Marion for teaching me how to use a lot of equipment and measurements. I also thank you for your support and advice.

Outside the professional framework, I thank my friends: Julien, Lalou, Thomas, Florian, Sahra, Tinoé, Raoul, Mahindra, Rémi, Arnaud, Lucas, Lucie, Theo, Eloïse, Evan, Joël-Louis, Medeo and Rémy for their unconditional support, making me feel at home, thank you.

Most of all, I thank my wonderful family for their support and encouragement at every stage of my life. To my grandmother Maria-Luz and my aunt Filomena, for always being by my side. To my little sister Salomé, whom I love and hope to inspire to reach her life goals, not only academic, but personal and spiritual.

Dad I thank you for your continuous encouragement, your motivation and for always believing in me. I remember watching you as a little boy building complex textile machines, starting with each of the parts separate and without a single drawing; all the mechanics were in your head. It all started then, you created in me the spirit of a researcher who

wants to understand the mechanics of the universe.

I am very grateful to my mother, for giving me life, and for making me her life goal. I know that enduring 8,846 km of distance after having me in your womb has been particularly challenging for you. Thank you for always motivating me and supporting me in my decisions. Thank you for being the ultimate example of perseverance in pursuing what I want, and, yes, we did it. Thank you for always being by my side, you are my inspiration!

"Last but not least, I wanna thank me for believing in me, for doing all this hard work, for having no days off, I wanna thank me for... for never quitting, I wanna thank me for just being me at all times..." SD.

Abstract

Concentrated PhotoVoltaics (CPV) can reduce the manufacturing cost of space solar generators by reducing the amount of expensive III-V materials. However, based on centimeter-sized cells these CPV systems cannot provide high concentration factors and efficiencies with large angular tolerances while having a compact and lightweight system. In this thesis, we focus on the development of a highly integrated micro-CPV technology using solar cells with a surface area of less than 1 mm^2 . This technology has the potential to meet energy needs while improving electrical power per unit mass (W/kg), and volumetric power density (W/m^3) with passive thermal management and an average concentration factor of less than 100 suns. To precisely define the spatial specifications, an advanced state of the art was conducted to define the environmental constraints according to the different celestial bodies of the solar system. Then, the work consisted in optimizing a linear optical system working by total internal reflection, by integrating III-V multi-junction cells on silicon, with an optical optimization by ray-tracing. Based on the understanding of the issues addressed during these developments, a micro-CPV system with highly integrated optics has been patented. This approach uses a reflective optical system directly molded in a honeycomb structure to form a monolithic, rigid and light-weight grating that can reach $150 \text{ W}/\text{kg}$ under AM0 flux. The objective is to functionalize the constituent elements, using the optics as part of the mechanical support and the honeycomb core is used to stiffen the assembly and keep the optics and the solar micro-cells separated and aligned. While providing a PV concentration of 30X, a theoretical optical efficiency of about 90% and an acceptance angle uni-axial $> 4^\circ$, and bi-axial $> 2.5^\circ$. The optical loss budget was investigated, with an optical efficiency between 82 and 88%. A sensitivity study, to determine the cell location plane and guarantee the optimum angular tolerance criteria, was performed with a peak-to-average ratio of 4.4. Then, optics were molded, and a new optical efficiency estimation method was developed and implemented. This method reconstructs the topography of an optical surface by combining optical microscopy and ray-tracing. An integration quality of 87.4% and 81.2% was achieved for a molding unit and a molded optic, respectively. This research work positions the laboratory as a European pioneer for PV micro-concentration for space solar generators.

Keywords: Concentrator photovoltaics, Optics, Space Applications, Physics, Ray-tracing.

Résumé

L'utilisation de système photovoltaïque (PV) a permis le développement de la conquête spatiale en fournissant une source d'énergie autonome aux engins spatiaux. Les exigences actuelles et futures en termes de réduction de coût, de masse et l'augmentation de performances sont les moteurs de l'innovation en matière d'énergie PV pour le spatial. L'objectif de cette thèse est d'évaluer la pertinence de la micro-concentration pour les applications spatiales par le développement d'une technologie à micro-CPV hautement intégrée utilisant des cellules solaires multi-jonctions (III-V) de surface $< 1 \text{ mm}^2$. Cette technologie a le potentiel de pouvoir répondre aux besoins énergétiques tout en améliorant la puissance électrique par unité de masse (W/kg), et la densité de puissance volumique (W/m^3) avec une gestion thermique passive et un facteur de concentration moyen inférieur à 100 soleils.

Pour définir précisément les spécifications spatiales, un état de l'art a été mené afin d'étudier les contraintes environnementales en fonction des différents corps célestes du système solaire et ainsi identifier les missions spatiales pertinentes pour un système micro-CPV. La deuxième partie de cette thèse est consacrée à l'optimisation optique d'un premier système basé sur une optique linéaire fonctionnant par réflexion totale interne intégrant des cellules multi-jonctions III-V/Si. Ces travaux ont montré les limitations intrinsèques de cette approche. La deuxième partie porte sur une approche alternative basée sur un système micro-CPV avec une optique hautement intégrée. Cette approche utilise un système optique réfléchissant directement moulé dans une structure en nid d'abeille pour former un réseau monolithique, rigide et léger, pouvant atteindre les 150 W/kg sous flux AM0. L'objectif est de fonctionnaliser les éléments constitutifs, en utilisant l'optique comme partie du support mécanique, tout en fournissant une concentration de 30X, une efficacité optique théorique d'environ 90% et un angle d'acceptation uni-axial $> 4^\circ$, et bi-axial $> 2,5^\circ$. Le bilan des pertes optiques a été étudié, avec une efficacité optique comprise entre 82 et 88%. Une étude de sensibilité, pour déterminer le plan de localisation de la cellule et garantir les critères de tolérance angulaire optimum, a été réalisée avec un ratio pic sur moyenne de 4.4. Afin de valider expérimentalement cette conception, des premiers travaux ont été engagés. Des optiques ont été réalisées par moulage, et une nouvelle méthode de caractérisation a été développée et mise en œuvre afin d'estimer l'efficacité optique. Cette méthode est basée sur : (1.) la reconstruction de la topographie d'une surface optique à partir d'imagerie en microscopie optique 3D, (2.) l'utilisation d'un logiciel de tracé de rayons permettant de simuler l'efficacité optique de la surface caractérisée. Les résultats obtenus montrent une performance optique d'intégration de 87,4% pour la surface du moule et 81,2% pour l'optique moulée. Cette performance est proche de la valeur théorique issue de la conception optique et permet ainsi de valider ces étapes de fabrications. Ces travaux de recherche positionnent le laboratoire comme étant un pionnier Européen pour la micro-CPV pour les générateurs solaires spatiaux.

Mots clés: Concentration photovoltaïque, Optique, Applications spatiales, Physique, Tracé de rayons.

Introduction

The conquest of space and today's outer space applications require objects such as satellites, exploration probes and rovers to be equipped with an autonomous power production subsystem. Photovoltaics, discovered shortly before the beginning of space exploration, has been one of its main drivers and remains the main type of power generation system. To better understand what is at stake in this thesis, which is to develop a micro-concentrated photovoltaic system for space applications, it is necessary to go a little deeper into the context and motivation of this thesis. In the following, we will present the structure of the manuscript covering the different aspects discussed throughout this thesis.

Context: solar power in outer space

Throughout history, the discovery and exploration of celestial structures: space exploration, has evolved from the first astronomical observations made by Hans Lippershey and Galileo using telescopes around 1609, to physical exploration with spacecraft. A spacecraft is a vehicle designed to fly in outer space to accomplish a specific mission, from communications, meteorology and Earth observation, to space exploration and colonization. History changed on Oct. 4, 1957, when our planet's first outer space flight, the uncrewed Soviet *Sputnik-1* (Russian for "companion") was launched into low-Earth orbit, with the aim of identifying the density of high atmospheric layers through measurement of its orbital change. Since the first solar-powered satellites *Vanguard-1* and *Sputnik-3* were launched in the spring of 1958, solar cells have become the main source of energy on spacecraft.

The space sector has grown in recent years by the arrival of hundreds of companies grouped under the term of New Space, and worldwide national strategies from space agencies for the planetary sciences. At the same time, escalating launch costs have forced spacecraft engineers to design lighter and more efficient power systems. According to this, space solar power requires technological improvements to achieve advanced performances and thus enhance new mission capabilities.

Man-made satellites are composed of different subsystems, categorized into two groups, the payload and the bus, illustrated in Figure 1 (a) [1]. Payload involves scientific instruments and communications equipment for some commercial spacecraft, while the bus comprises several functional systems such as the data handling system to transmit

commands and information, telemetry sensors to gage the satellite state, thermal control, propulsion and finally the power system. The major components of a power system are power generation, energy storage, and power distribution.

Different power energy sources have been developed to fuel unmanned space probes and human spaceflights in order to provide the highest specific power with sufficient durability during a specific mission environment. Some of them include: PhotoVoltaic Arrays (PVA), Radioisotope Thermoelectric Generator (RTG) and fuel cells. The power system applicability will vary depending on the power levels needs and the duration of use, as shown in Figure 1 (b) published by Patel in 2004 [1]. For the moment, for long missions and needs from 1 kW to 500 kW, photovoltaic solar arrays are the solution.

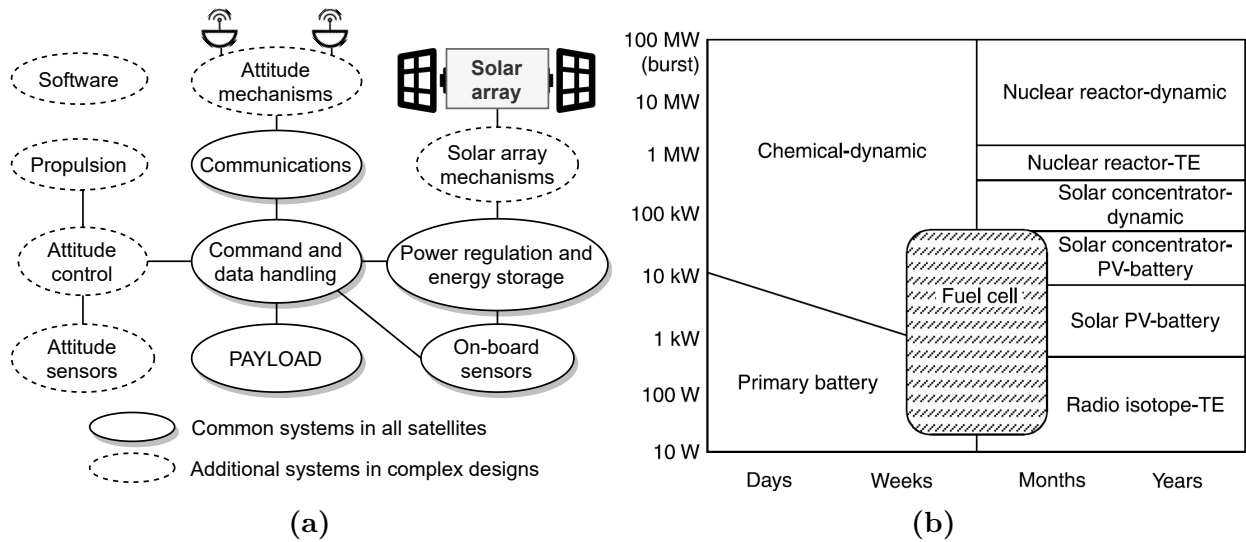


Figure 1: (a) Spacecraft subsystems, (b) Approximate ranges of application of different power sources, based on [1].

Most of the planetary missions led to date used solar cells as their power system, especially for missions close to the Sun and as far as Mars. In contrast, missions to Jupiter and beyond, where the Sun irradiance is lower have been typically powered by RTGs, which transform the heat released by the decay of a suitable radioactive material into electricity by Seebeck effect [2]. Nevertheless, new technological advances are changing this. Nowadays, solar cells with improved efficiency and radiation hardness are used for missions even as far as Jupiter (e.g., *Juno* spacecraft), operating under the combination of LILT conditions [3].

In the present work, we will focus on the power generation subsystem using PVA, which are characterized using different parameters that help to define the performance of a given technology. The specific power is one of the most important factors, it indicates the power per unit array mass (W/kg); other related metrics include specific energy (Wh/kg) and volumetric power density (W/m^3). In other words, surface area, mass and

volume are critical assets, because of the required amount of material and space used, and essentially due to their influence on the cost of take-off.

Constraints on solar array size, weight, and storage volume have encouraged the development of efficient Multi-Junction Solar Cells (MJSC) and lighter substrates materials, while its higher power levels have helped increase spacecraft payload capability and the reduction of mass and size has improved costs. Today, space solar arrays predominantly use Triple-Junction (3J) solar cells, based on III-V materials like Gallium Arsenide (GaAs), Gallium Indium Phosphide (GaInP), and Germanium (Ge). Each junction or “subcell” is optimized to convert a specific portion of the solar spectrum to electrical current, those photons with energy above the bandgap of the subcell material; and they are connected electrically in series. Additionally, subcells in a stack connected in series must be current-matched to maximize efficiency since the junction with lower current will limit the whole stack. MJSC deliver higher efficiency than a single junction does, as they can convert to current higher energy photons (at higher potential) compared to a single junction device with lower bandgap, reducing thermal energy losses.

Actually, space solar cell technologies are focused on increasing solar cell efficiency and enabling operation in specific mission environments. One method consists of redesigning the composition of the solar cells, to select appropriated semiconductor materials, cell architectures and fabrication process to optimize the bandgap of each subcell in the multi-junction stack. However, current cell efficiencies approach its theoretical limits as technologies mature. For a 3J cell that limit is 49% on Earth, and 68% considering an infinite number of junctions, yet, under concentration these limits evolve to 63% and 86%, respectively [4]. In this regard, in 2019, the National Renewable Energy Laboratory (NREL), using six-junction cells at 143X, attained a record for terrestrial applications, reaching a cell efficiency of 47.1% for a spectrum AM1.5D (see Figure 2.1) and a reference temperature of 25°C, as shown in Annex 6.5.3 [5]. Then, in 2021, the same laboratory reached the record cell efficiency (non-concentrated) of 39.5% using 3J MJSC. In the other hand, to date the module record efficiency was achieved in 2016 by the University of New South Wales using a hybrid four-junction (GaInP/GaInAs/Ge; Si) split spectrum submodule (287 cm²) under 365X concentration, for terrestrial applications (outdoor measurement) to obtain a 40.6% efficiency [5, 6].

Current standard PVA for space applications is an assembly of cells protected by coverglass, so-called CIC (Coverglass Interconnected Cell) or Solar Cell Assembly (SCA), which is attached using durable adhesives and bondings agents to a rigid and lightweight structural substrate (aluminum honeycomb core) and carbon-reinforced composites, as shown in Figure 2 [7]. The efficiency of state-of-the-art 3J/4J cells (GaInP/GaAs/Ge layers grown on a Germanium substrate), designed and optimized for Earth orbital missions, vary from the 28% class and end in the advanced cell class of 32%, under

standard test conditions (1 AU, 28°C) [8].

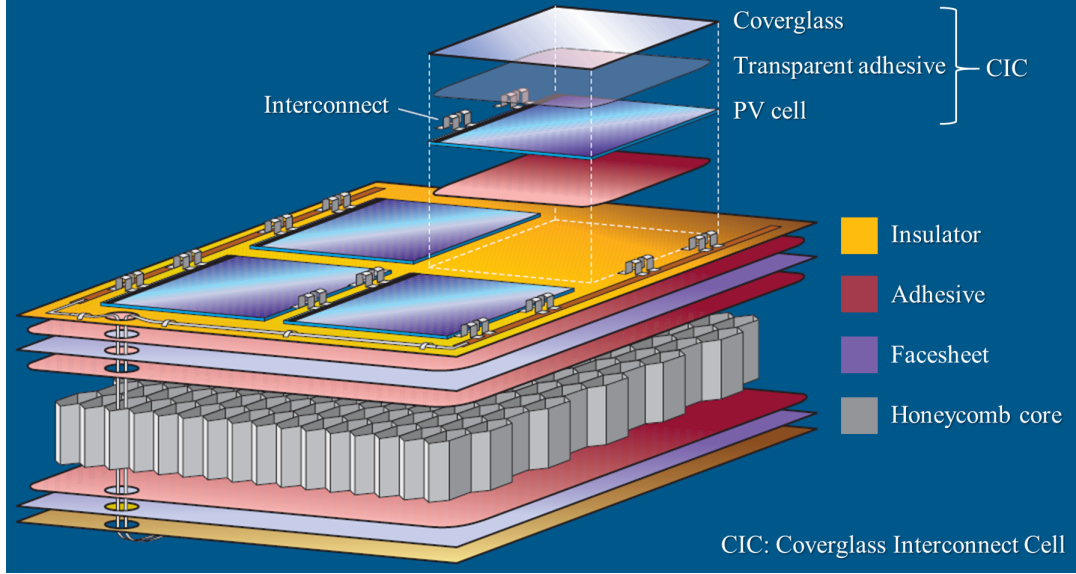


Figure 2: Solar array panel constituents (exploded view), image adapted from Francis *et al.* (2005) [7].

Table 1 shows the current state-of-the-art performance and its expected improvements in the future. The values in the table are approximate, based on today’s literature and European Space Agency (ESA) and National Aeronautics and Space Administration (US) (NASA) strategies [9].

Table 1: Overview of current solar panel metrics for space applications and expected future improvements [9].

Electric Power Generation	Solar Cells Efficiency [%]	Specific Power [W/Kg]	Volumic Power Densities [kW/m ³]
<i>Present – 2020</i> Moving to transition	33	> 50	> 15
<i>2020 – 2025</i> Next generation	36 - 37	> 200	> 60
<i>2025 – 2035</i> High risk, high payoff	> 40	> 200	> 100

Over the past few years, significant advances in solar arrays and blanket technologies let to new concepts that differ substantially from the traditional “standard” design. Enhancing metric improvements towards lower array mass and stowed volumes, higher radiation resistance and high-power array concepts. One solution involves the usage of flexible blanket technology, designed so that significantly larger area of solar cells could be stowed compactly for launch and unfolded or unrolled in space [10–12]; an example of this is the International Space Station (ISS), which uses Silicon solar cells on flexible blankets that

provide a capacity of up to 120 kW. In the other hand, an innovative approach includes the use of CPV arrays, which demonstrated the highest efficiencies ever achieved by any solar technology at the cell, module, and system levels. Most CPVs used in spacecraft use either reflective or refractive elements to focus the sunlight onto a much smaller solar cell area, typically MJSC. In CPV, solar radiation is focused, leading to high heat flux in the system that requires an efficient thermal design, integrating active or passive cooling.

A CPV system, as shown in Figure 3, is, according to the IEC 62108 standard [13], composed of a Primary Optical Element (POE), a possible Secondary Optical Element (SOE) and a high efficiency photovoltaic cell. The cell, SOE, cooling system and connection circuit form the receiver. To ensure that the solar radiation is focused on the receiver, the modules are equipped with solar trackers.

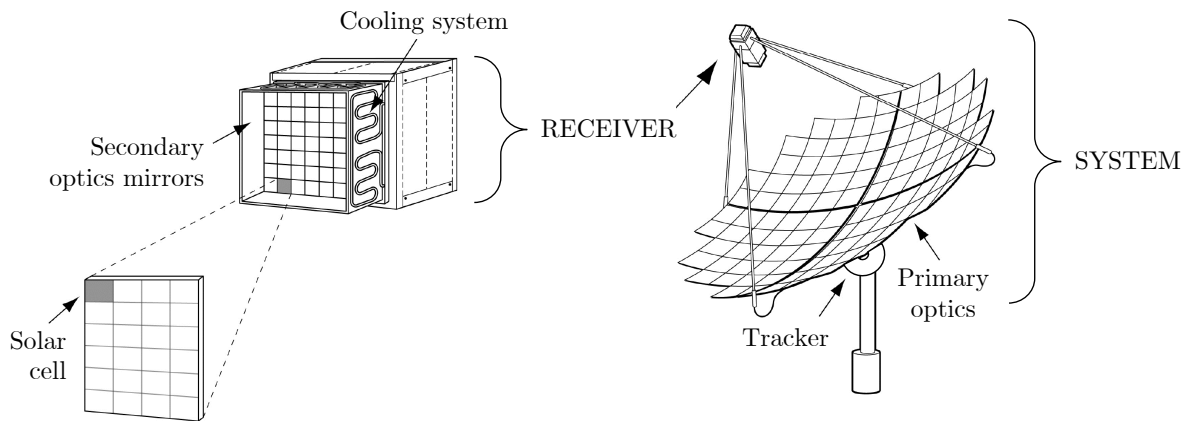


Figure 3: Schematic of point-focus dish CPV [13].

CPV concepts have been successfully used for both space and terrestrial applications. Cost is the first and most obvious advantage it can offer, based on the reduced surface area of the photovoltaic cells compared to current integrated cells in CIC architectures. CPV at concentration ratios of about 100X and even up to 1000X can reduce by several orders of magnitude the main cost driver of current CICs: III-V materials. This is promising because mirrors and lenses are cheaper than the semiconductor photovoltaic cell.

Also, the development of multi-junction cells typically used for space applications is based mainly on materials such as gallium, indium and germanium, whose reserves are limited worldwide. Germanium production is highly concentrated in China (approximately 71%), since it is a by-product of lead-zinc refining and coal ash production. China also manages more than half of the indium refining, having the largest deposits [14]. In addition, the environmental impact for the production of these metals, such as gallium, is severe in terms of the accumulated energy used, human health implications and damage to ecosystems. Most metals have a low recyclability performance. Since these materials are rare, difficult to refine and difficult to commercialize, concentrated photovoltaic systems that

drastically reduce the surface areas used of III-V materials can be considered as a means to reduce the environmental impact of PhotoVoltaic (PV) arrays and mitigate their supply risk.

On the other hand, the implementation of CPVs also allows significantly higher conversion efficiency than cells operating at Air Mass "zero atmospheres" (AM0) conditions, which has a positive impact on the specific power (W/kg) and volumetric power density (W/m³). At the same time, the mass associated with traditional CPV optics may be considered a drawback, but it has a great advantage: improved radiation hardness.

Motivation: toward micro-concentrating systems for space applications

The merit of using CPV in space applications has recently regained attention with a new approach that focuses on leveraging the advantages of microscale photovoltaics (micro-CPV), for a number of reasons. In the past, CPV for space applications using MJSC with areas $> 1 \text{ cm}^2$ have strived to balance high concentration factors with large angular tolerances, while maintaining low mass and compact optics, along with advanced and often massive thermal cooling. Today, the approach we take for CPV in space differs from earlier efforts as the use of microcells ($< 1 \text{ mm}^2$) has the potential to address all of the above issues at once, reducing the Aspect Ratio (AR) (i.e.: thickness divided by aperture width) and mass, while taking advantage of moderate concentration factor ($< 100X$). In addition, by using microconcentration systems, the aperture area of each optical system would be reduced, which would improve heat dissipation, avoiding the use of expensive and massive cooling systems, enhancing passive thermal management in which the interconnection paths are capable of spreading the generated heat. Furthermore, the large number of cells also makes it possible to design CPV modules with a very high voltage and to generally reduce ohmic losses.

Ritou *et al.* demonstrated that one way to optimize the balance between cost and efficiency is the development of the micro-scaled CPV modules (micro-CPV) [15]. Based on a complete analysis of the Cell-to-Module ratio (CTM) loss chain in micro-CPV, the authors address to question: Does micro-scaling of CPV modules improve efficiency? In this regard, optical, mechanical and electrical losses are identified and analyzed according to data reported in the literature. As conclusion it has been demonstrated that the CTM ratio ranges from 71% to 86% for micro-CPV modules while it remains between 65% and 75% for CPV modules. Moreover, the maximum achievable CTM of micro-CPV modules is 93.2%, results that encourage further development of the subject [15].

By contrast, the price of cell size reduction comes at the expense of introducing some manufacturing challenges related to the diminutive cell size and the larger number of units

to be handled. In this regard, the explosive growth of the LED-based lighting industry, which involves intensive development of manufacturing technologies and processes, can be easily adapted to the needs of micro-CPV. Indeed, innovative manufacturing technologies, for example for large displays, enable cost-effective production of units composed of thousands of interconnected semiconductor devices through miniaturization, additive manufacturing, parallelization and self-alignment. This will enable high photovoltaic performance and, at the same time, exploit cost reduction potentials in production.

Outline of the thesis structure

The objective of this thesis is firstly to study the performance advantages of the micro-CPV technology for space applications and secondly to develop a solution that meets the space constraints. This issue raises several scientific questions about optics, materials and their compatibility and stability with respect to the environment, as well as the integration of the assembly into an efficient and lightweight photovoltaic module. In this work, we attempted to answer these questions and present below the articulation of the chapters detailing the scientific approach.

Chapter 1 is dedicated to the state-of-the-art of CPVs, from an introduction to their fundamental concepts and classification, through the different types of optical systems, materials and processes used; covering both terrestrial and space applications. We focused on identifying and discussing the strengths and critical points of traditional CPV systems compared to modern microscale approaches, for space application.

Chapter 2 attempts to answer the question: What kind of mission could be addressed using CPV arrays? First, the environmental factors affecting the conversion efficiency and durability of PVs in space are presented. Then, the environmental conditions and the specific needs for mission concepts to explore the planets of the Solar System and some of its major moons are evaluated. Finally, the spectrum of favorable environments for CPVs is established, highlighting what kind of missions could be addressed by this technology and the challenges that need to be addressed.

During this thesis we explore two different CPV concepts. The first one detailed in *Chapter 3*, is a preliminary study, describing an improved generation of a Compound Parabolic Concentrator (CPC) based on a previous design developed in 2016, to evaluate if it can be improved and adapted to respond to space applications. This includes several aspects, from an optimization of the optical system design through ray-tracing, to the fabrication molding process, along with the integration of low-cost silicon-based (III-V/Si) solar cells.

This first development allowed to highlight the limitations of this approach and led to the definition of a new concept; which is presented in *Chapter 4*, *5* and *6* deal with

the optical design, experimental validation and characterization of this novel micro-CPV concept, respectively, which proposes the use of a highly integrated miniaturized mirror inside a honeycomb core sandwich panel, allowing a significant gain in compactness and mass/power ratio.

Chapter 4 deal with the optical design of a highly integrated reflector in a hexagonal honeycomb cell, which aims to guarantee a homogeneous flux distribution over the cell, a high angular tolerance and to be simple to fabricate. The optical loss chain and the estimation of the short-circuit current density are also presented.

Chapter 5 focuses on the experimental validation of highly integrated optics within a honeycomb structure, using a molding technique, to move from a theoretical concept to a prototype with industrial potential.

Chapter 6 presents a characterization method developed to estimate the optical efficiency of a molded reflector by evaluating and reconstructing its topographical shape using optical microscopy measurements combined with ray-tracing simulations.

Finally, the major contributions of this thesis are summarized, and future research directions are highlighted. A list of my contributions to journal articles and international conferences, as well as patents, resulting from this work are presented in Annexes.

*Alles Gescheite ist schon gedacht worden.
Man muss nur versuchen, es noch einmal zu denken.*

*All intelligent thoughts have already been thought;
what is necessary is only to try to think them again.*

— Johann Wolfgang von Goethe

1

A brief review of state-of-the-art from CPV to micro-CPV technologies

This chapter presents the state-of-the-art of concentrating photovoltaic systems, covering both terrestrial and space applications. The aim is to identify and discuss the strengths and critical points of traditional CPV systems compared to modern microscale approaches, for space applications. This will provide a framework to promote innovative designs, while highlighting the challenges that need to be addressed.

1.1 Concentrator photovoltaics systems

The process of concentrating light is usually described by the Geometrical concentration ratio (C_g). In a physical sense, the concentration ratio is the factor by which the energy flux incident on the aperture area of a primary optical element is optically enhanced at the receiving surface (solar cell), described as follow:

$$C_g = \frac{\text{area of the aperture}}{\text{area of the receiver}} = \frac{A_a}{A_r} \quad (1.1)$$

CPVs use only direct sunlight to operate. The acceptance angle is a characteristic value of the angular tolerance of a module to misalignment. It is measured between the module normal and the incident perpendicular solar rays, and is typically referred to as the maximum full angle by which the module can tilt (with respect to the Sun) while producing 90% of its normalized maximum power output. In this regard, CPVs

integrate a tracking system to operate, since they only use direct light from the Sun. For terrestrial applications the usage of trackers that automatically move photovoltaic panel towards the Sun, as the sun moves across the sky implies additional cost and risk trade-offs in system design. Nevertheless, for outer-space applications, most communication and weather spacecraft already incorporate solar array wings with a high pointing accuracy $< 1^\circ$, satisfying the angular tolerance needed by most concentrating optics [16–18].

Concentrating photovoltaic systems can be classified in several ways, as shown in Figure 1.1. A simple grouping of these different designs is presented below to facilitate comparison from different research areas and applications. Regarding the concentration level these systems can be classified into low (< 10 suns), medium (10 to 100 suns) and high (> 100 suns), depending on the specific solar tracking requirements [19, 20]. In general, the main focusing optical methods are reflective, refractive and luminescent. This brief review of state-of-the-art will focus on reflective and refractive CPV technologies. It is important to note that each type of concentrating photovoltaic system has advantages and disadvantages and it is important to know the application and location in order to choose the most suitable design.

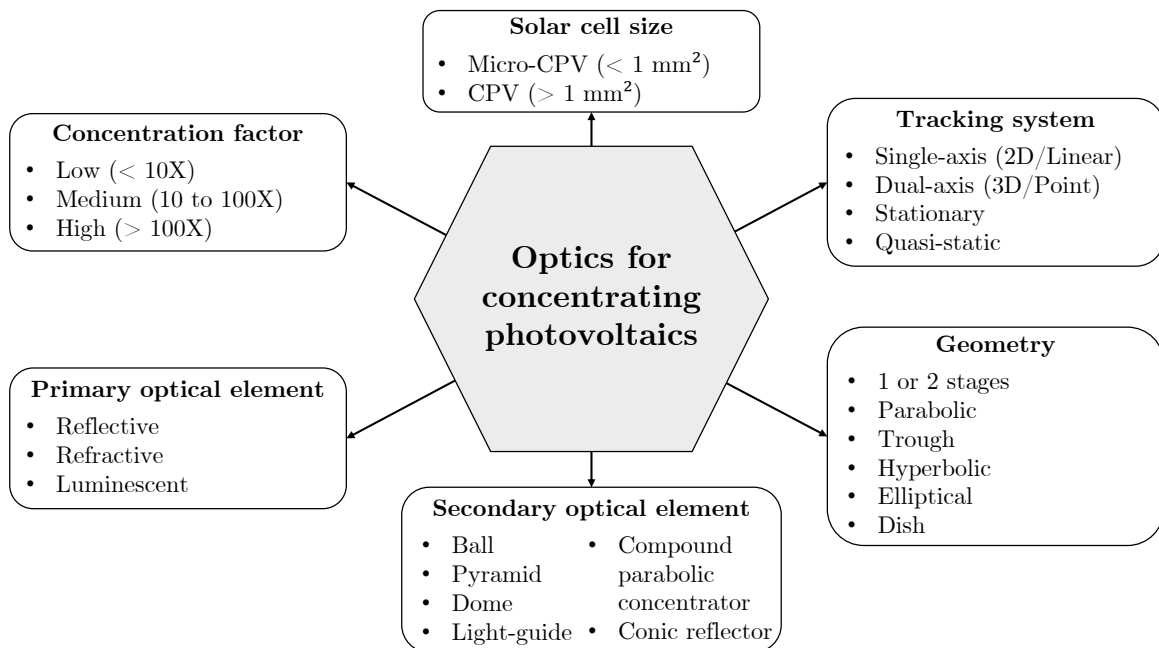


Figure 1.1: Classification chart of optics for concentrating photovoltaics.

In CPVs, in general, the concepts of image formation and phase coherence characteristic of imaging optics are abandoned. Instead, they are replaced by concern for flux density levels and concentration ratios [21]. Indeed, when compared to imaging systems, non-imaging approaches have the merits of wider acceptance angles, higher concentration ratios with less volume and shorter focal length and higher optical efficiency [22]. As

each of the concentrator elements contributes to the formation of flux density in a given area of the receiver. Thus, it is necessary to accumulate the contribution of all elements to estimate the flux density at any given point, considering the local angle of incidence on the receiver surface and the displacement of the target point of each element with respect to its nominal position.

On the other hand, an important parameter to characterize the performance of a CPV is its optical efficiency, which is defined as the efficiency with which the photons of the incoming radiation are transferred to the solar cell. As shown in Equation 1.2, it is the ratio of the Power on the receiver (P_r) to the Power on the aperture area (P_a). The corresponding power output is proportional to the current produced by a solar cell at a corresponding place and time. Thus, the solar power output P_a is proportional to the short-circuit current of the target cell without optics, $I_{SC(\text{without-optics})}(\theta, \alpha)$. And similarly, the power output P_r is proportional to the short-circuit current measured using a given optics system, $I_{SC(\text{with-optics})}(\theta, \alpha)$. Both measured short-circuit currents are normalized to the Direct Normal Irradiance (DNI) at the time of measurement t_1, t_2 . The DNI can be measured in the open air with the pyrheliometer or with the component cells as a spectral sensor. On the other hand, the definition of efficiency is closely related to the concentration factor. The estimated value will be different if we use a large receiver or if, on the contrary, the evaluated output area is too small and part of the light is not captured by it. To take concentration into account, $I_{SC(\text{without-optics})}$ is multiplied by C_g [23, 24].

$$\eta_{\text{optical}} = \frac{P_r}{P_a} = \frac{\frac{I_{SC(\text{with-optics})}}{DNI_{t_1}}}{\frac{I_{SC(\text{without-optics})}}{DNI_{t_2}} C_g} \quad (1.2)$$

A complementary approach to quantify the manufacturing quality of a CPV module is the CTM, which is the fraction of the module efficiency with respect to the cell efficiency, presented in the Equation 1.3. This parameter helps, for example, to identify the best compromise between cost and manufacturing accuracy.

$$CTM = \frac{\text{Module Efficiency}}{\text{Cell Efficiency}} \quad (1.3)$$

In the following section, some relevant optical systems are highlighted and discussed, according to the nature of the optics and materials used, their manufacturing methods and finally their efficiencies. A comparison between them is then proposed, providing an overview of the state of the art technology, from an optics point of view, with the final objective of proposing a system that can be adapted to concentrate light on micrometer-scale PV cells for space applications.

1.2 CPV optics designs for primary optical elements

Different types of primary optics are used to focus sunlight onto photovoltaic devices. Single-stage configurations can be achieved through a reflective (mirror) or refractive (lens) optical element; some of these designs are briefly discussed below.

1.2.1 Refractive

Perhaps the most common type of CPV system uses Fresnel lenses, which focus sunlight through a chain of prisms, each of which represents the slope of the lens surface. There are two basic configurations: the linear consists of parallel linear slots with a line as the focus, and the circular involving concentric circular splines having a small circle as the focus; these require a single or dual axis polar tracking system, respectively, to maintain focal alignment. In comparison to conventional lenses, one of the benefits of these devices is that they use relatively less mass, making them lighter; as shown in Figure 1.2 (a). In the other hand, chromatic aberration resulting from refractive effects as light of different wavelengths travels through the lens leads to different focal points for each spectral band; indeed this phenomenon can be undesirable for multijunction cells. This last is illustrated in Figure 1.2 (b), where sunlight rays of different wavelengths are shown in different colors. Xie *et al.* proposed a comprehensive review on the recent development of concentrated solar power applications using Fresnel lenses [22].

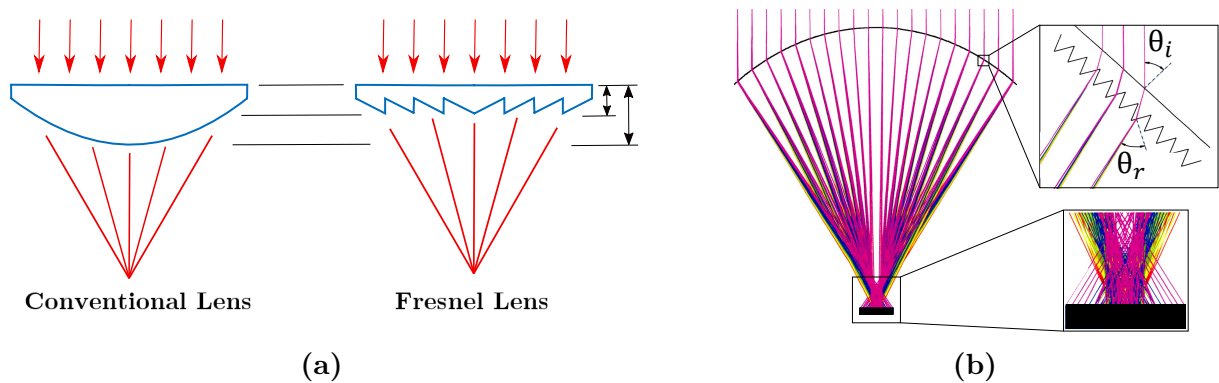


Figure 1.2: (a) Side profile comparison of a conventional plano-convex lens (left) and a flat Fresnel lens (right), (b) Curved Fresnel lens illustrating how light is refracted at different focal points with respect to its wavelength (in colors) adapted from Howell [25], where θ_i is the angle of incidence and θ_r is the angle of refraction.

The fabrication of Fresnel lenses has typically been done using PolyMethylMethAcrylate (PMMA), followed by the use of Polydimethylsiloxane (PDMS), which are currently the preferred choice for bonding to glass and making a Fresnel lens pattern [20]. Also, PolyCarbonate (PC) is sometimes proposed as an alternative to PMMA because of its

significantly higher toughness, preventing mechanical fracture and fatigue. Nevertheless, PC is less scratch resistant [26] and has lower spectral bandwidth and optical transmittance [27] as well as it is subject to more optical scattering, sun-induced photo-oxidation and chromatic aberration [28–31]. In the 70s another technology was proposed, using acrylic or silicone facets stamped on glass however this one is heavier in weight [32, 33]. Lens sources and refractive materials are abundant, but not all have been tested for CPV applications. Various processes are used for manufacturing Fresnel lens facets such as hot stamping, extrusion, casting, lamination, compression molding or thermoplastic injection molding [20, 34].

While the optical transmittance for one face of materials such as PMMA is about 95%, the measured efficiency of Fresnel lenses typically vary between 80 to 85%, due to reflection losses and wavelength-dependent Fresnel transmission coefficients [20, 24]. Indeed, high-temperature treatments such as calcination, which is a method of preparing anti-reflective and anti-fog coatings, cannot be used on PMMA material. To achieve an anti-reflective property on PMMA (refractive index=1.49), one method is to apply lower refractive index coatings. In the other hand, Steiner *et al.* reported a mean efficiency of about 89% with a standard deviation of about 1% using Silicone-on-Glass (SoG) Fresnel lenses with an anti-reflective coating [35].

1.2.2 Reflective

For terrestrial applications the reflective optics are usually flat, parabolic or free-form mirrors. One of the main advantages of mirror-based systems is that they do not suffer from chromatic aberration, since light is reflected off the mirror surface rather than refracted through a dielectric and more importantly they are lighter compared to lenses. Some examples of reflective designs are shown in Figure 1.3, illustrating from left to right, a parabolic trough, Compound Parabolic Concentrator (Compound Parabolic Concentrator (CPC)) and plane receiver with plain reflectors (or V-trough).

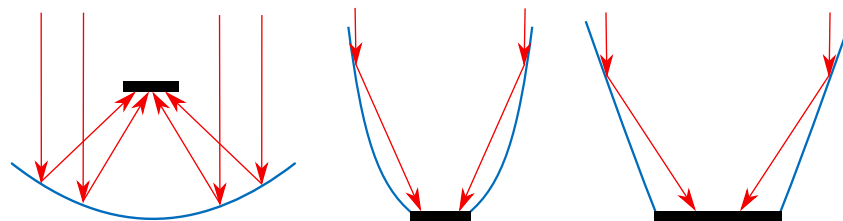


Figure 1.3: Types of concentrating sunlight collectors using reflective surfaces, parabolic trough (left), compound parabolic concentrator (middle) and plane receiver with V-trough reflector (right).

Several approaches are proposed for the construction of CPV reflective systems. These include the application of reflective coatings on the back side of glass (back surface

reflectors, see Figure 1.4 (a), and the deposition of reflective coatings on substrates (front surface reflectors, see Figure 1.4 (b) and (c)). The most common coating materials used as reflective layers in CPVs are silver and aluminum with the best reflectance of 97% and 92% respectively [36, 37]. At the same time glass has been the traditional choice as a superstrate material, while other materials present viable alternatives [38], such as coated aluminum reflectors (Figure 1.4 (b)) and polymer film reflectors (Figure 1.4 (c)) [39].

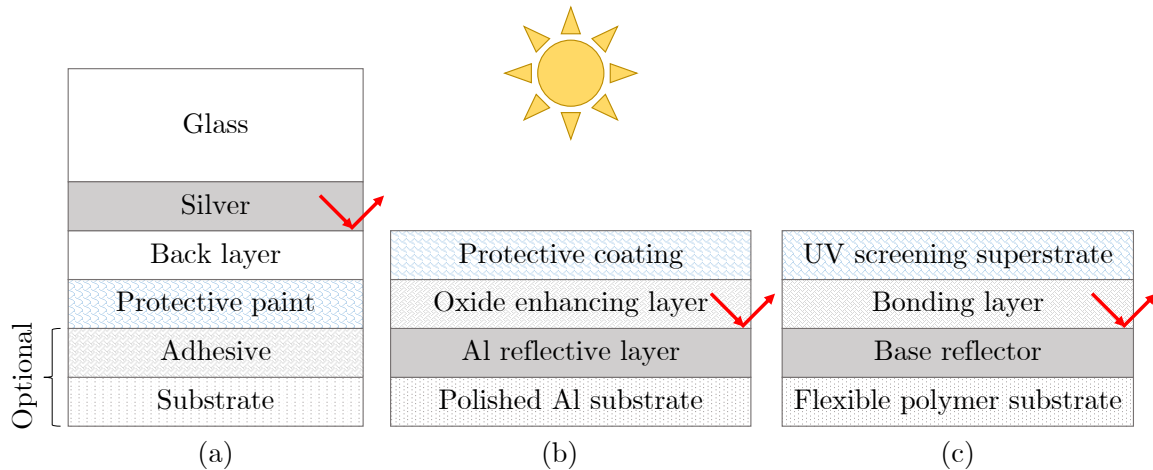


Figure 1.4: Examples of reflector architectures: (a) glass mirror, (b) aluminum reflector and (c) polymer substrate reflector; with red rays depicting reflected sunlight, based on [37, 40].

Among the suitable candidate materials, silver-coated glass and silver-coated polymer films, dominate [37, 40], shown in Figure 1.4 (a) and (c), respectively. Generally, the benefits of using glass include, a higher level of performance than other options, however the use of glass (both thin and thick) may include disadvantages such as weight, brittleness, thermal expansion mismatch between the glass and other layers and its formability [36, 38]. In addition, when using silver in reflectors, protection against the environment is required, which can be achieved by incorporating additional layers of glass, metallic coatings, or polymer stabilizers [41]. In contrast, silver polymer reflectors deal with some of the concerns intrinsic to glass and provide greater design flexibility, lighter weight and the possibility of reduced cost, although with some limitations, such as a life of about 10 years, poor adhesion between the silver and the polymer after exposure to water [40].

Examples of reported silver polymer reflective materials include PolyEthylene Terephthalate (PET) [42], and PMMA [40]. The proposed PMMA architecture was composed by an evaporated Ag reflective layer, a Cu protective layer, and a pressure-sensitive adhesive layer for application to a rigid support structure. Advantages include its excellent environmental stability, excellent optical properties (reflectivity of 94.5%), the durability with test samples that reached 10 years, and the ability to be extruded into a thin, flexible film. The disadvantages are that it has an inherently weak adhesion between the polymer and the silver reflective layer, leading to delamination problems presented

especially after extreme rain conditions. Additionally, Schissel *et al.* [43] demonstrated the environmental durability of silvered-PMMA reflectors which have an un-weathered solar reflectance as high as glass reflectors at 97%. Samples based on PET used a similar architecture with respect to the PMMA and was protected by an optically transparent alumina coating; showing an initial solar-weighted hemispherical reflectance of 95% [42]. Another proposal, ReflecTech, is fabricated from a flexible polymer-based silver film, and is supplied on a roll and developed in conjunction with NREL [40, 44]. This material has a specular reflectance of 94% [44]. Advantages of this material include low cost, light weight (3.6 kg/m²) and flexibility.

1.3 CPV technologies deployed in space missions

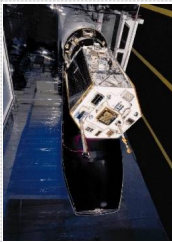
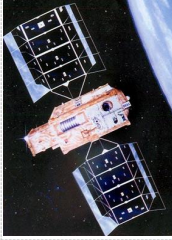
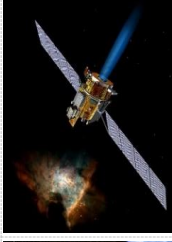
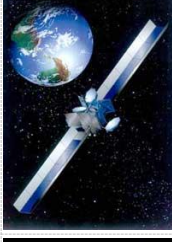
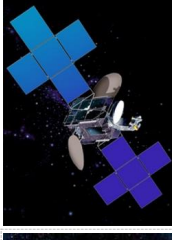
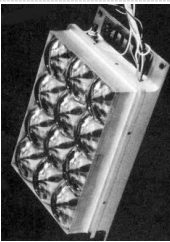
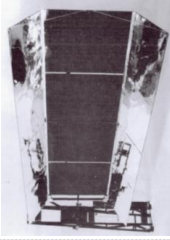

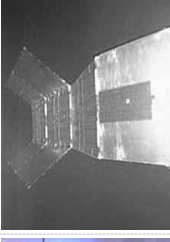

In this section, an overview of the main CPV technologies deployed in space missions is presented, with special attention to the optical systems involved. We introduce this section with a timeline summary of the different assemblies reported deployed in outer space, in order to offer the reader a global and chronological vision, highlighting their main features and metrics. We then analyze in detail each system specifying the advantages and disadvantages and its evolution over time, taking into account the different challenges faced by each technology to leverage its achievements in terms of return on experience.

In space, a number of CPV designs have been established varying in terms of complexity and solar concentration, from low-concentration systems using 2X (i.e., X: concentrating factor) V-trough reflectors, to medium-concentration ratios of about 100X using lenses, mirrors or a combination. A timeline summarizing some of their main characteristics is presented in Table 1.1.

1.3.1 Proven viability and radiation hardness of CPVs in space

The Photovoltaic Array Space Power Diagnostics Plus (PASP+) program was the first satellite with onboard CPV arrays [45]. It comprises 12-advanced PVA, with two concentrators among them: mini-dome lenses and a network of Cassegrainian systems. This mission experiment flew on the Air Force satellite APEX in an elliptical orbit with an apogee of 2552 km, a perigee of 363 km, and an inclination of 70°. The orbit was chosen to put the spacecraft into a wide variety of plasma environments and to receive a high radiation dose that would degrade the PASP+ modules during the life of the flight [45].

Table 1.1: Timeline of deployed concentrating photovoltaics for space applications.

<u>SATELLITE</u>					
Name	APEX (P90-6)	NRO STEX	Deep Space 1	Galaxy XI	SS/L-Cell Saver
Mission	GEO / LEO	LEO	GEO	GEO	-
Year	1994	1998	1998	2000	2004
CPV Space Timeline					
<u>SOLAR ARRAY</u>					
Name	Mini-dome lenses	AstroEdge	SCARLET	BOEING 702	SS/L-CellSaver
Concentration	100X	1.5X	7.5X	1.7X	2X
Optical efficiency	91.5 %	85 %	89 %	90 %	90 %
Solar cell structure	2J (GaAs/GaSb) 4 mm dia.	2J (GaAs/Ge) 34.3 x 60.3 mm ²	(GaInP ₂ /GaAs/Ge) 10 x 40 mm ²	2J (GaAs/Ge) 3J (GaIn ₂ /GaAs/Ge)	3J (GaInP ₂ /GaAs/Ge)
Solar cell efficiency	21.4 %	19 %	22.7 % @7.5X AM0	2J (21 %) 3J (26 %)	-
Specific power(BOL)	75 W/Kg	70 W/Kg	48 W/Kg	60 W/Kg	-
Total Power	-	15 kW 335 W @ 37 VDC (1 W)	2.5 kW @ 100 VDC	7-17 kW @ 101.3 VDC	-
Comments	TRL 9	Deployment failure	3 years missions	Quick degradation TRL 9	TRL 5
References	[45-47]	[57]	[48-50]	[58]	[59,60]

The mini-dome Fresnel system was made by ENTECH and Boeing, using space qualified silicone (Dow Corning 93-500) optics over mechanically stacked MJSC (GaAs//GaSb). Optics have been coated to provide protection against space ultraviolet radiation and atomic oxygen; the flight tested module using 12 elements is shown in Figure 1.5 [45]. The lens had a 40 mm focal length and a $37 \times 37 \text{ mm}^2$ aperture, designed to focus incident light onto a 4 mm diameter cell, which provided a geometric concentration of about 109 suns, which when factoring to the lens optical efficiency operated of 100 suns [46].

PASP+ was subjected to a highly variable radiation flux due to the elliptical nature of the orbit, varying by a factor of ten as the apogee latitude moves around the orbit. Preliminary calculations indicate the 1 MeV equivalent fluence for silicon cells with 6 mil (0.15 mm) covers and 60 mil (1.5 mm) backs is 7.95×10^{13} electrons/cm² after 30 days, and 1.72×10^{14} after 90 days. While *in-situ* measurements demonstrated that CPV presented the smallest degradations induced by space radiation when compared to the other arrays. After 83 days in orbit there was about a 1% drop in Short-circuit current (I_{SC}) and a 2% drop in Maximum power (P_{MAX}) [45], then 7% in the P_{MAX} over one year [47]; these are the smallest degradations of any of the 16 PASP+ modules. The encouraging results of the PASP+ program motivate the development of a new line-focus Fresnel lens concentrator easier to make and more cost-effective than the mini-dome lens CPV; which is presented below.

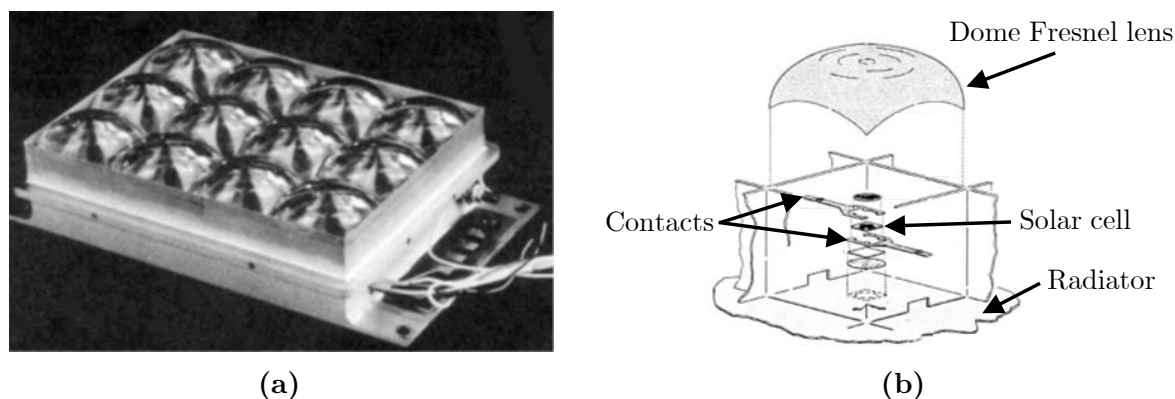


Figure 1.5: Mini-dome lenses CPV by ENTECH and Boeing (a) Flight-tested module, (b) Exploded view of an element showing the main components, image modified from [45].

1.3.2 Proven reliability of CPVs in space

In 1994, ABLE (now Northrop Grumman Innovation Systems) joined the concentrator team and headed the development of a new technological approach: the Solar Concentrator Array with Refractive Linear Element Technology (SCARLET). The baseline design of SCARLET using linear Fresnel lenses on refractive-silicone is presented in Figure 1.6 (a).

Incident light from about 81.8 mm aperture is focused, by more than 1600 precisely formed individual ridges, to a 10 mm wide strip of light in the center of the cell (about 10x40 mm²). In 1998, the first mission to rely upon a solar concentrator was successfully launched. The Deep Space 1 spacecraft using SCARLET has proven the viability of CPVs in space; during its 38-month mission, it powered the instruments and the ion propulsion engine, which propelled the spacecraft throughout its entire journey [48].

The linear Fresnel pattern was molded in a continuous roll process using space-grade silicone (Dow Corning 93-500). Individual lenses are machined and bonded to glass substrates (ceria-doped borosilicate) that have been thermally formed into cylindrical sections. As illustrated in Figure 1.6 (b), SCARLET needs a deployment system to keep a low profile during launch and then it is deployed in space [49]. Additionally, a CPC reflector SOE (Silicone-On-Glass) has been considered as an optional solution to improve the angular tolerance. The average measured optical efficiency of the lenses, without anti-reflection coatings, was about 89%. The effective concentration ratio of 7.14 suns was selected to provide a reasonable pointing error. Wing power is relatively constant (< 5% change) over a range of 1° (alpha - parallel to cell string) and 3° (beta - perpendicular to cell string) [48].

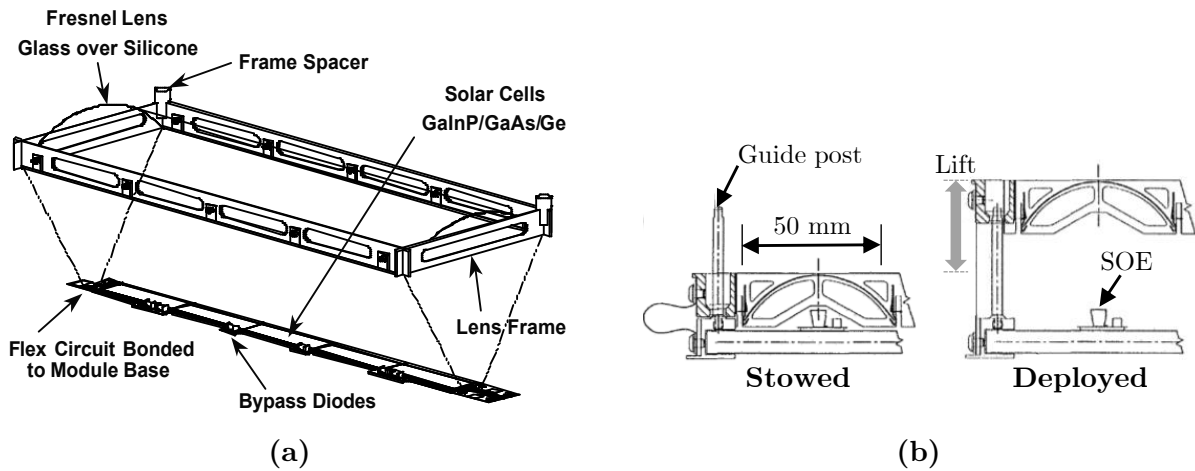


Figure 1.6: (a) Deep Space/SCARLET module design: lens and receiver [16], (b) Lens frame deployment system, image modified from [50].

O'Neill proposed an evolved version of the SCARLET system, the Stretched Lens Array (Stretched Lens Array (SLA)) [51]. The SLA is designed to be folded into a flat package for launch, and then stretched to its deployed configuration on orbit. This new design was intended to eliminate the need for a fragile glass substrate to support the lens, and more importantly, to provide a specific power of 180 W/kg at a much reduced cost compared to conventional planar PV arrays. A demonstration unit of this concentrator is shown in Figure 1.7.

In 2011 a test coupon of the SLA flew on the TacSat-4 mission [52]. Although the test

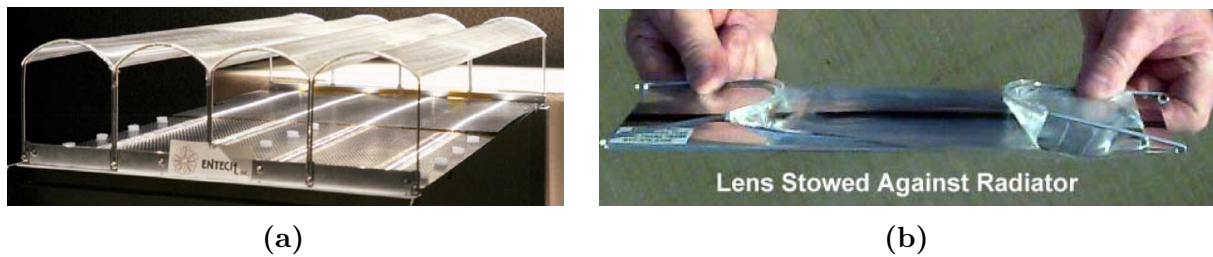


Figure 1.7: SLA module concept (a) mini-module lens demonstrator [51], (b) Lens stowed configuration.

mission evidenced engineering difficulties, in lens failure due to tearing, however the system demonstrated the ability of CPVs to achieve radiation tolerance due to thicker radiation shielding [53]. Then, in 2015, the authors claim that a new approach, using silicone lenses with embedded meshes of either metal or glass or graphene, can avoid this failure mode by reinforcing the weak silicone material, however, this has not yet been demonstrated [54].

1.3.3 Reflective designs in space: a pursued and compelling approach

Reflectors are in fact the most deployed optical systems used for space applications, in particular using V-trough planar reflectors. Some examples of this are: AstroEdge™ array, Orbital-ATK CellSaver [55], DSS FACT (Functional Advanced Concentrator Technology), spacecraft and Hughes 702 designs [56], which provide a concentration of about 2 suns.

AstroEdge™ was the first spacecraft to use a concentrator as its main power source. Launched into orbit aboard the Space Technology Experiment spacecraft (STEX) on October 3, 1998. The experiment payload was intended to demonstrate the deployment and survivability of a new tether design (ATEX), as well as controlled release maneuvers. However, the tether pair inadvertently detached from the STEX spacecraft due to an out-of-limits condition sent by the experiment's tether angle sensor, resulting in a the deployment failure; none of the desired ATEX objectives were achieved [57].

Hughes 702 designs suffered significant degradation caused by contamination problems that would need to be taken into account and mitigated in similar designs, this issue has been analyzed and is now believed to be understood [58]. In this regard, the next-generation of V-trough CPV includes the “CellSaver” system manufactured by Orbital-ATK [58, 59]. In fact, the solar heat load per unit area on a CellSaver panel is reduced compared to a panel with edge reflectors, such as those used on Boeing 702 satellites [60]; illustrated in Figure 1.8. As a result, the CellSaver array and solar cell decrease its operating temperatures to about 75°C, versus panel edge reflectors up to 125°C. This enhancement improves cell efficiency and reduces the outgassing of contaminants from the solar panel reflector that was identified as the cause of the anomalous degradation of Boeing's optical system [60, 61].

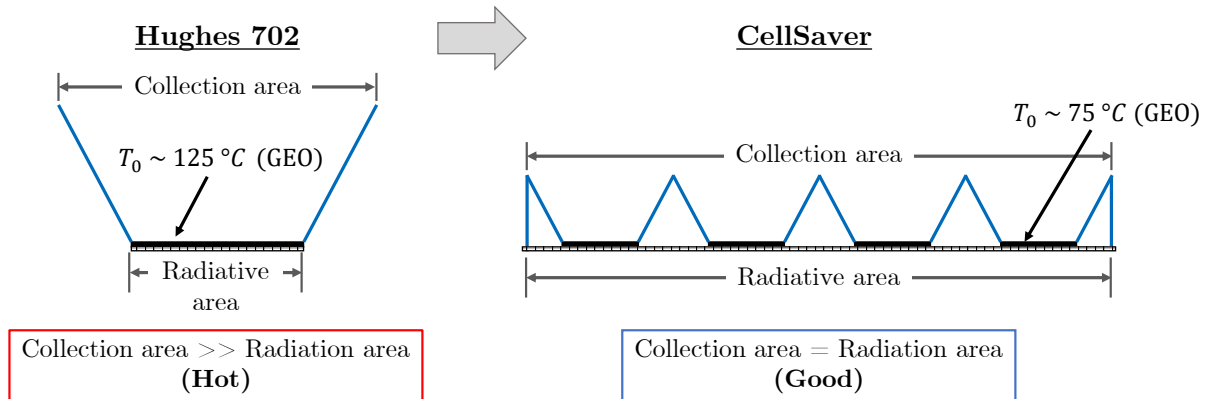


Figure 1.8: Reflective concentrator thermal comparisons, based on Eskenazi *et al.* [60].

CellSavers are fabricated from a single piece of thin ($25\text{ }\mu\text{m}$), high-strength titanium sheet that can be folded with extremely tight radii between panels ($< 0.5\text{ cm}$) without yielding or slipping. In addition, it is extremely stable under exposure to space radiation and thermal cycling, and is lightweight. A vapor-deposited silver coating with a transparent dielectric protective layer provides high reflectance over the entire response range of the $\text{GaInP}_2/\text{GaAs}/\text{Ge}$ 3J cell (350 nm to 1800 nm). CellSaver uses standard solar composites as the structural system and can be folded in small thicknesses ($< 1\text{ cm}$) over long periods of time. When the solar panels unfold in space, CellSavers self-deploy under their own spring energy [60].

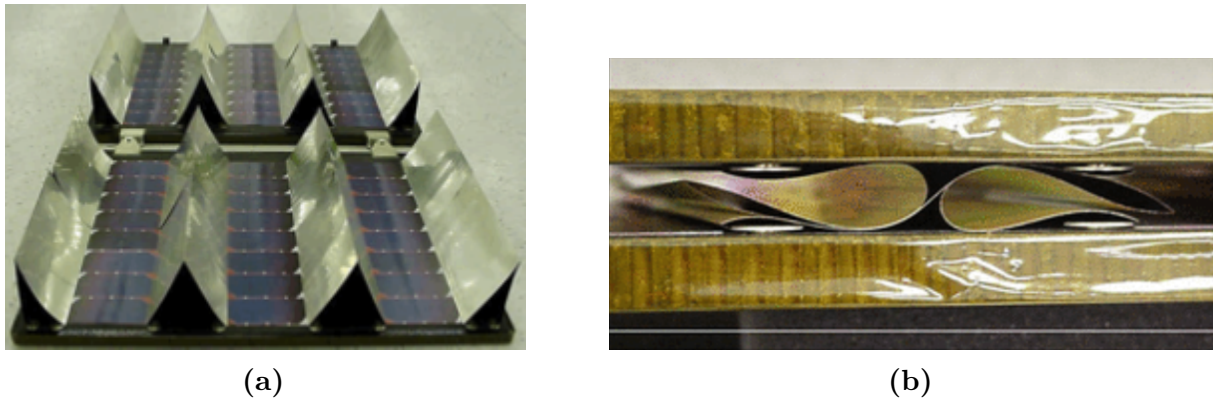


Figure 1.9: (a) CellSaver solar concentrator module design, (b) Stowed CellSaver in a 11 mm gap between the two solar composite panels[55].

In early 2004, a flight experiment to test the CellSaver technology was launched into GEosynchronous Orbit (GEO) on a Space Systems Loral satellite, as shown in the Table 1.1. Eskenazi *et al.* reported encouraging on-orbit test results, including temperature and power measurements for the first 9 months of the successful experiment, which did not show the anomalous early degradation observed in the Boeing arrays experiment [60].

As noted above, from 1994 to 2004 several CPV arrays have been used for space

applications, featuring different optical systems with different Technology Readiness Level (TRL) levels. In this sense, it can be seen that the number of optical systems launched is relatively limited, and has been mostly driven by V-trough reflectors and Fresnel lenses (both point and line focus) which present low and medium concentration factors. On the other hand, these arrays have presented optical efficiencies of around 90% and used high efficiency MJSC; to obtain specific power up to 75 W/Kg.

In terms of space CPV heritage, these systems have been shown to be particularly well suited to address missions with high radiation environments, as well as having great potential to improve MJSC efficiency and reduce cost, with innovative materials and approaches to manufacturing and assembling solar cells and optics. On the other hand, some areas of concern that must be addressed are optics degradation and thermal control of the solar cells, while an improvement in the specific power is required to compete with the conventional CIC solution.

1.4 Towards micro-CPV systems

As highlighted in the introduction, the approach of this thesis is to explore the potential of microscale photovoltaics, which after the recent development of transfer-printed micro-scale multijunction solar cells ($< 1 \text{ mm}^2$) opens the door to a new generation of applications [62]; and more specifically the main focus is to address outer space applications. In fact, scaling to submillimeter dimensions of photovoltaic cells for space CPV systems can improve many of the traditional drawbacks, as discussed in the previous section, including much more compact and low-mass concentrator optics, as well as enhancing passive heat dissipation from the microcells themselves, which simplifies thermal management, heatsink mass; thus high performance and reliability [63].

1.4.1 Overview of micro-CPV systems for terrestrial applications

Since 2015, there has been rapid progress in micro-CPV development, primarily in the United States, as part of Advanced Research Projects Agency-Energy (US) (ARPA-E's) MOSAIC program [64]. The MOSAIC projects, short for Micro-scale Optimized Solar-cell Arrays with Integrated Concentration, seek to exploit new micro-optical concentration techniques to achieve CPV efficiency in a low-profile panel, without increasing manufacturing costs. To this end, \$24 million in innovation funding was earmarked for 11 new solar approaches, in the three main market sectors: residential, commercial and utilities. In Europe, actors such as the French Commission for Atomic and Alternative Energies (CEA) and Franhoufer ISE have also proposed initiatives that are in continuous development, as well as the Institute of Solar Energy of the "Universidad Politécnica de Madrid". In Asia,

Japan's Panasonic Corporation has also committed to the development of micro-CPVs.

For terrestrial applications, the most common and widely adopted optical design concepts for microscale CPV are the plano-convex lens, Fresnel lens, and parabolic mirror. Figure 1.10 illustrates some representative examples of microconcentrator optical designs. (a) Semprius [65, 66], and (c) Pennsylvania University [67] both use plano-convex lenses as primary optics, as well as a SOE that allows them to have the highest concentration ratio of them, 1111X and 743X, respectively. The former uses spherical lenses as SOE and the latter deploys a parabolic mirror. On the other hand, (b) proposed by Panasonic [68] is a single lens directly bonded to the cell, typically used for concentrations below 300X.

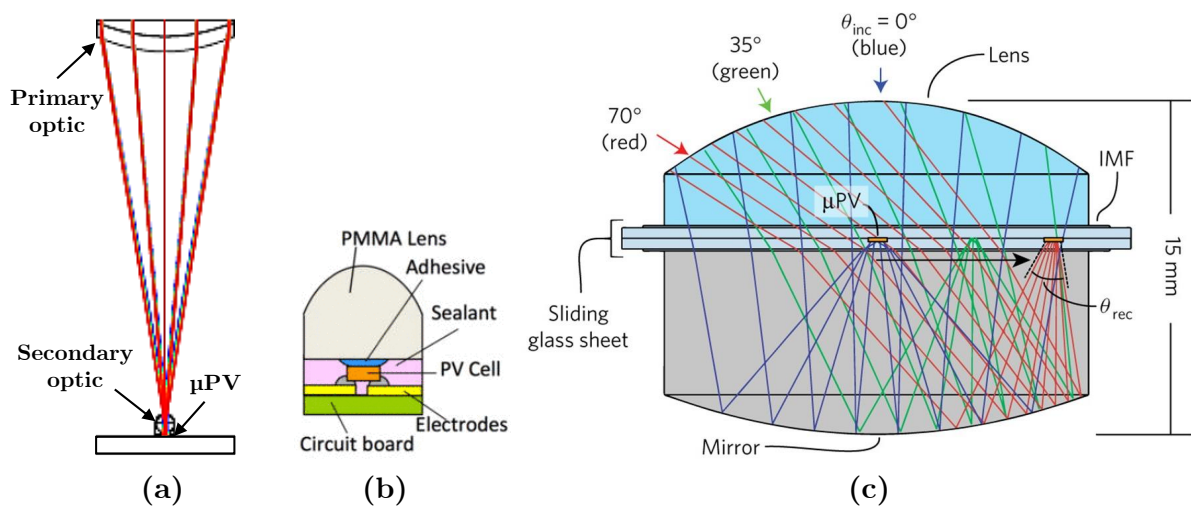


Figure 1.10: Representative micro-CPV modules for terrestrial applications proposed by (a) Semprius using plano-convex (POE) and glass ball (SOE) [69], (b) Panasonic PMMA single lens [68] and (c) Pennsylvania University plano-convex lens (POE) and parabolic mirror (SOE) [67].

Most micro-CPV modules are not yet commercialized and their construction is not standard. Just like the shape of the focusing optics, the mechanical structures and the size are very variable, depending on the roadmap and the technological choices of specific laboratories or companies. Indeed, as the optics and architecture of micro-CPV systems are in constant progress, a temporal evolution of the prototypes proposed by various players has been carried out during this thesis. This has allowed us to have a broader view of why these systems use specific materials, processes, dimensions and designs. Here, we will focus on the optical designs of two developments, first the Panasonic approach, and then the evolution of microscale photovoltaic systems from Sandia National Laboratories.

1.4.1.1 Panasonic approach

In 2014, one of the first Panasonic's proposals was a thin and compact (20 mm thick) CPV concept, in which GaAs-based MJSC were directly attached to a single PMMA lens,

without heat sinks. The authors chose this design, firstly, for its simplicity compared to large lenses that, with high sunlight concentration, require large heat sinks and, secondly, to avoid the chromatic aberrations of Fresnel concentrators that in turn require homogenizers [68]. A prototype module $50 \times 50 \text{ mm}^2$ comprising 25 lens/cell elements, with a geometric concentration factor of 400X presented a 34.7% efficiency under on-Sun measurement. Later, in order to study the non-uniform irradiation in MJSC subcells, and optimize the optics focusing length, a glass substrate with different thickness was added, as shown in Figure 1.11 (I') [70, 71]. The module archived a conversion efficiency of 37.1%. However, the initial design was not intended to be changed. It is worthy to say that for this study the solar cell size was increased from 0.25 mm^2 to 0.67 mm^2 , leading to a reduction on the geometrical concentration factor from 400X to 150X.

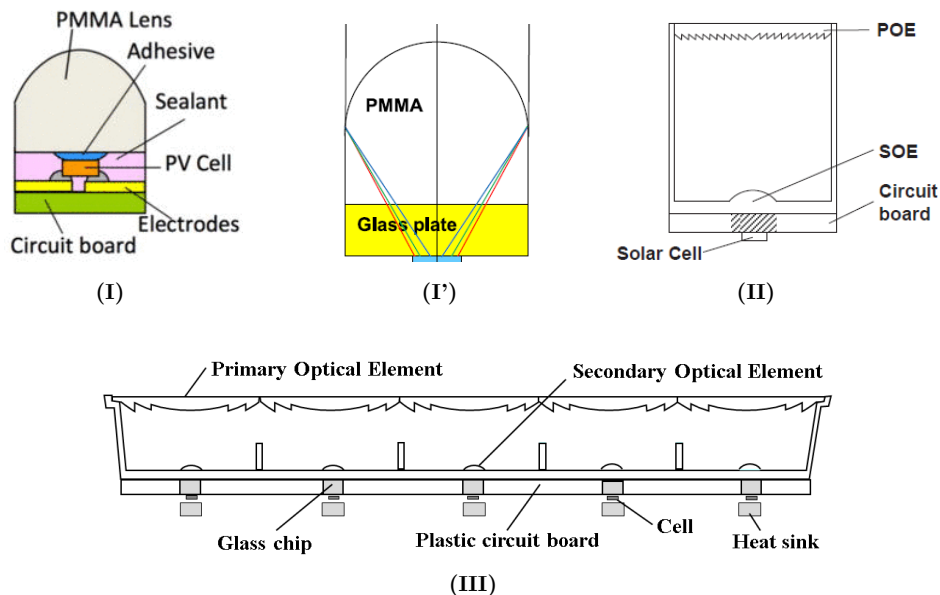


Figure 1.11: Panasonic micro-CPV technology/prototypes evolution [68, 70, 72, 73].

In 2017, Hayashi *et al.* from Panasonic, proposed a completely different optical design compared to the previous one, which used a POE based on 22-circles Fresnel lens and a dome-shaped lens as SOE, both elements made of PMMA injection molding as in their previous design, because the material was thought to be light and reasonable in cost [72]. The optical axis of these POE and SOE optical elements can be easily aligned by simple mechanical adjustment of the POE to the SOE, as each optic is specially designed to be manufactured to an accuracy of a few micrometers. The optical axis of these optics can be easily aligned by simple mechanical adjustment of the POE to the SOE, as each optic is accurate to within a few micrometers. As a result, the module's optical system can be assembled by a simple, low-cost manufacturing process. A prototype module $120 \times 120 \times 30 \text{ mm}^3$ achieved an efficiency of 30.4% [72].

Then in 2018, Panasonic redesigned its precedent design, in this one the Fresnel lens has a smaller size ($< 5 \text{ cm}^2$) to reduce the module thickness, and it changed from a 22-circle lens to 3-circle Fresnel-type lens to reduce the optical loss [73]. The sizes of each lens of the POE and solar cell are $22 \times 22 \text{ mm}^2$ and 1 mm^2 , respectively, leading to a concentration ratio of about 500X. In addition, plastic circuit boards were adopted for 24% weight reduction and minimizing the influence of thermal expansion difference. And in turn, small glass plates were inserted into the plastic substrates to avoid Ultraviolet (UV) degradation. The energy conversion efficiency of a $120 \times 120 \times 30 \text{ mm}^3$ was 31.5% [73].

The evolution of Panasonic's modules described above are illustrated in Figure 1.11 and some of their key metrics and enhancements are summarized in Table 1.2.

Table 1.2: Panasonic micro-CPV technology/metrics evolution.

Prototype /Year	Concentration (suns)	Module Efficiency (%)	Module Size (mm^3)	Optical Design/Improvements	Cell Surface (mm^2)	DNI (W/m^2)	Ref.
I 2014	400X	34.7	50x50x20	<ul style="list-style-type: none"> PMMA lens Simplicity & avoid chromatic aberrations 	0.5x0.5	735	[68]
I' 2015	150X	37.1	50x50x19	<ul style="list-style-type: none"> PMMA on a glass plate on which the solar cells are mounted 	0.672 (octoedric)	807	[70,71]
II 2017	480X	30.4	120x120x30	<ul style="list-style-type: none"> 22-circles Fresnel lens (POE) and dome lens (SOE), both made by injection molding PMMA Reduced optics materials costs and manufacturing complexity 	0.672 (octoedric)	911	[72]
III 2018	500X	31.5	120x120x30	<ul style="list-style-type: none"> 3-circles Fresnel type to reduce optical loss Plastic circuit boards (24 % weight reduction) and minimizing CTE mismatch Small glass plates were inserted into plastic substrates for avoiding UV degradation 	1.0x1.0	817	[73]

1.4.1.2 Sandia National Laboratories solution

One of the early micro-CPV prototype from Sandia National Lab was composed of three lenses per lens column providing a 36X magnification, and a pointing errors of 8° [74]. The cells were designed to be hexagonal with a vertex to vertex dimension of $720 \mu\text{m}$ and a thickness of $20 \mu\text{m}$ based on single crystal crystalline silicon, and an average cell efficiency of 12.1% measured at one sun Air Mass coefficient, 1.5 atmosphere thickness (Direct) (AM1.5D) spectrum [75]. All of the lenses are aspheric plano-convex elements so the front surface of the lens array is flat for ease of cleaning, and the PV cell is glued

to the third lens, making it an immersion lens; Figure 1.12 (I) is a sketch of the system design concept. The module has a focal length and thickness of 13.3 mm and 20 mm, respectively. Due to the high number of elements the optical transmission is low, about 60%, leading to a module efficiency of 6% [76].

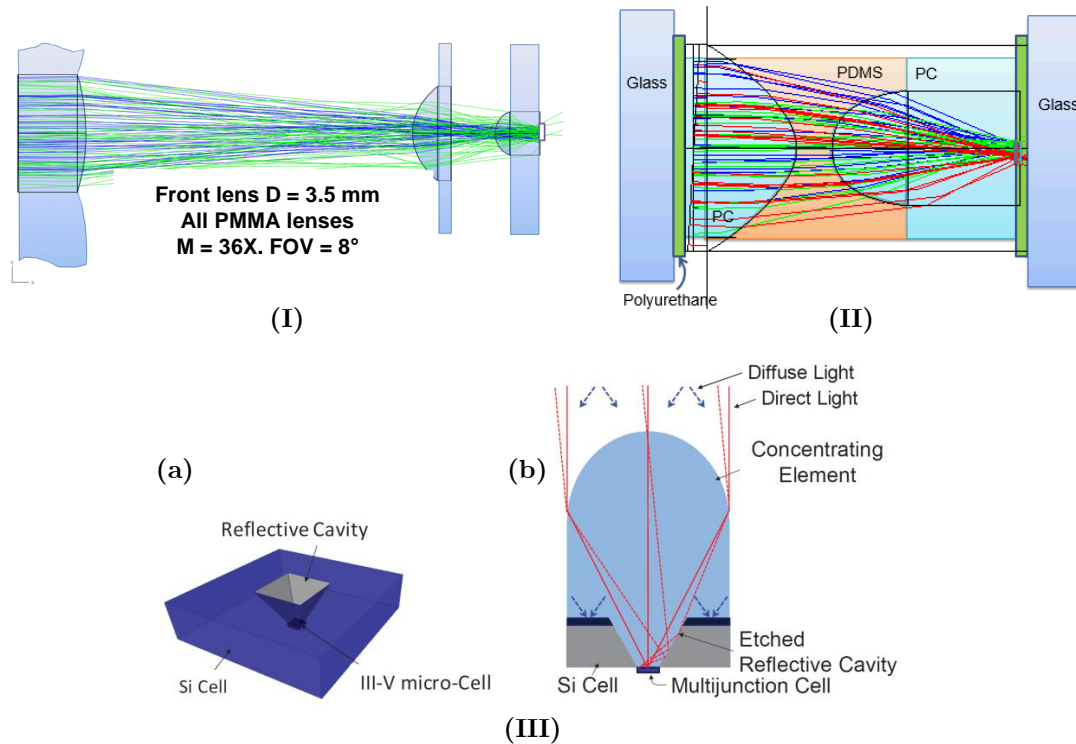


Figure 1.12: Sandia National Laboratories micro-CPV technology/prototypes evolution [74, 77, 78].

Later, a second generation prototype was designed to achieve 100X magnification and optical transmission of about 90% [77], see Figure 1.12 (II). For this, two plano-convex lenses were built in polycarbonate and the gap between them was filled with Sylgard®184 PDMS to minimize Fresnel reflections, prevent moisture ingress and ensure high optical transmission without UV degradation. In addition, the relatively low elastic modulus of PDMS (2.3 MPa) provides an additional advantage in accommodating stresses generated by thermal excursions and Coefficient of Thermal Expansion (CTE) mismatches in the optical assembly. The thickness of the lens sandwich was 5.30 mm, a 65% reduction over the first generation prototype, for a total module area and thickness (15x16 elements) of 40 mm² and 9.96 mm. The prototype displayed an optical efficiency of 84% due to Fresnel and absorption losses, together with a module efficiency of about 20% [76].

Recently, under the MOSAIC program, a novel Wafer-integrated microscale Photo-Voltaic (WPV) concept has been proposed [78], which uses III-V micro-cells integrated with a multi-functional Si platform to take advantage of the high performance of MJSC

and module and system-level benefits of Si flat-plate PV. In the WPV approach, direct sunlight is concentrated on the microcells and diffuse light can be collected by the Si cell. This hybrid concept is shown in Figure 1.12 (III): (a) A Si cell containing V-shaped etched reflective cavities, a tilt angle of 35.3° , with output apertures of $100 \times 100 \mu\text{m}^2$. (b) A prototypical reference module comprising a Si platform, a set of InGaP/GaAs microcells hybrid integrated into the Si platform, an intermediate glass plate, and a set of PDMS aspheric primary lenses (2.5 mm sublens diameter) molded directly on the glass [78]. The WPV characteristics allow for significantly reduced module material, a moderate angular tolerance of 3.7° , and an ultra-compact optical architecture of about 3 mm. The prototype arrays achieve a concentration ratio of 400X which corresponds to a four-fold increase in concentration ratio, and a 70% reduction in thickness compared to the previously presented prototype [78].

In addition to the schematic designs illustrating the evolution of Sandia Labs' micro-CPV concepts presented in Figure 1.12, Table 1.3 provides a summary of the most relevant features and improvements of these concepts mainly linked to the design of the optical systems involved.

Table 1.3: Sandia National Laboratories micro-CPV technology/metrics evolution.

Prototype/ Year	Concentration (suns)	Module Efficiency (%)	Optical Efficiency (%)	Module Thickness (mm)	Optical Design/ Improvements	Acceptance Angle ($^\circ$)	Ref.
I 2013	50X	6	60	20	<ul style="list-style-type: none"> • 3 lens • Air gap 	8	[74-76]
II 2014	100X	20	90	10	<ul style="list-style-type: none"> • 2 immersed lens (no air gap) • Diffuse/direct collection. 	4.5	[76,77]
III 2018	400X	-	-	3	<ul style="list-style-type: none"> • PDMS aspheric primary lens • Si V-shaped reflective cavities • Diffuse/direct collection 	3.7	[78]

Since the primary goal of concentrator systems is to provide strong cost leverage for expensive high-efficiency MJSCs by replacing cheap plastic optics, ground-based systems have focused primarily on creating high-concentration CPVs. This is demonstrated by examples from Panasonic and Sandia National Labs, for which the concentration factor of their proposed concepts over time has evolved to achieve higher concentration ratios. On the other hand, another common aspect is to go in search of more efficient optical systems, using the least amount of material and elements possible to avoid optical losses. Or, alternatively, try to mutualize the functions of the elements.

Additionally, as the price reduction is paid for by the system manufacturability, these systems have proposed from the beginning synergistic methods with technologies from the

fields of optoelectronics, microelectronics, and display fabrication to considerably reduce costs. Applying their legacy experiences and breakthroughs in the fields of miniaturization, self-alignment (e.g. capillary forces), additive manufacturing and parallelization.

In the case of Panasonic, the simplicity and compactness of the system was privileged at first; and chromatic-aberrations free (Fresnel lens). However, they then sought to reduce the amount of optics material at the price of increasing its complexity and size (33% thicker). On the other hand, the concentration factor was increased and the module efficiency decreased by more than 4%. Further, they have tried to decrease the optical losses by optimizing the optical shape and materials while keeping the previous design and achieved an increase of the concentration factor and the module efficiency of 20X and 1% respectively.

Sandia's first prototype evolved from a thick and complex system using three optical elements with a large acceptance angle (8°) and air gap, to hybrid embedded systems using only two optical elements and a reduced angular tolerance. A first evolution that allowed to halve the thickness and to increase the concentration and optical efficiency of the module by 50% and 30% respectively; at the price of decreasing its angular tolerance of more than 43%. Finally, the size of the PV cell was drastically reduced, which represented an increase from 100X to 400X the concentration (400X), which again represented a decrease in the acceptance angle of about 18%.

The following is a summary of the most relevant micro-CPV systems developed for terrestrial applications, describing their main characteristics; shown in Table 1.4.

Table 1.4: Current micro-CPV prototypes and modules for terrestrial applications.

Year	Name	Company/ Institute	Concentration AM1.5D (Suns)	Module	Cell to Module Ratio (%)	Cell Charac.	No. Cells	Ref.
				η (%) Size		Type Size		
2014	Illinois 4J	Semprius	1111X	36.5% 20x20x60 mm ³	83.1	3J + Ge 0.6x0.6 mm ²	1	[79]
2016	μ -X	CEA	275X	29.7% 60x60x41,8 mm ³	79.8	3J 0.9x0.9 mm ²	16	[80]
2016	Commercial	Semprius	1111X	34.90% 60 mm thick	85.1	3J 0.6x0.6 mm ²	660	[82]
2017	Chloralkali generator	Insolight, EPFL, NY Univ.	180X	36.4% 20x20 mm ² f# 6 mm	86.7	3J 0.6x0.6 mm ²	7	[81]
2017	Planar micro- tracking	Semprius, Penn. Univ	743X	30% 20 mm diametre 15 mm thick	71.4	3J 0.65x0.65 mm ²	1	[83]
2017	μ -X	CEA	1000X	33.40% 19x19x72 mm ³	78.8	3J 0.6x0.6 mm ²	1	[84]
2018	Light plastic integrated micro-CPV	Panasonic	500X	31.50% 120x120x30 mm ³	76.3	4J 1.0x1.0 mm ²	25	[73]

These systems concentrate sunlight at levels higher than 180X onto principally three-junction cells, and present module efficiencies from 29.7% to 36.5%, measured at AM1.5D, 25°C and an irradiance of 1000 W/m² [73, 79–84]. The average cell to module ratio is about 80% and high as 86.7%. And the maturity of the technologies, based on the TRL, during the acquisition phase of the modules of these programs ranges from 4 to 9, technology validated in laboratory to real system tested in operational environment, respectively.

1.4.2 Recent proposals of micro-CPV systems for space application

Recently two studies on microconcentrating concepts for space applications are being developed. The first one by the Air Force Research Laboratory in US using a lens array and on the other hand a proposal by the Pennsylvania University using a reflective mirror. These studies will be briefly presented below.

1.4.2.1 Air Force Research Laboratory study

In 2016, the Naval Research Laboratory in collaboration with Semprius, presented initial concepts, experiments and prototyping activities in the development of microlens arrays made of glass and/or silicone. They focused on addressing the potential and challenges associated with the use of microlens arrays using microtransfer printing for terrestrial PV, and not on the performance of a particular optical design but on a family of designs.

A first approach similar to Semprius' terrestrial module previously shown in Figure 1.10 (a) [68], is built from 1 or 2 ply carbon fiber attached to a silicone on glass lens array, for a module thickness 10 mm, no further information was provided for this architecture [63].

Another design approach seeks to integrate the CPV on a standard CIC using silicon (Figure 1.13) (a) and (e), aiming to take advantage of microtransfer printing the cells directly on a non-native substrate, such as glass or a silicon wafer. Four "families" of CPV-CIC designs are distinguished, regarding the materials chosen for the lens assembly and the "filler" medium between the lens and the cell, illustrated in Figure 1.13 (d). While using active silicon cell has the advantage of lower mass it may introduce challenges for CTE matching. Printing to glass adds the mass of the glass, but offers more design flexibility.

Those using silicone as filler (silicone only and glass-on-silicone) have the benefit of mechanical robustness and do not require external mechanical elements to hold the lens assembly above the CPV cells. One solution to reduce mass is to reduce the overall thickness (Z_T) of these designs (see Figure 1.13) (d), however, this in turn requires decreasing the lens apertures (i.e., the pitch) to scales < 1 mm which poses a manufacturing challenge [63]. Designs that leave an air gap (or void) between the lens assembly and the cell assembly can be much lighter, but require additional support structures. Options for such supports is

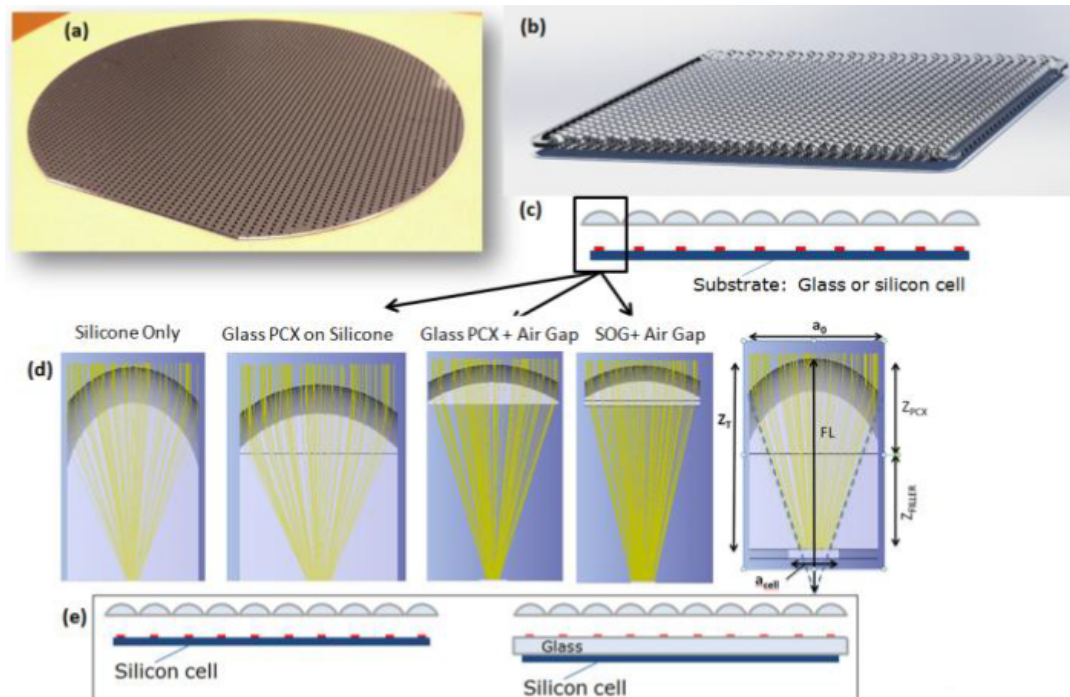


Figure 1.13: CPV-CIC concept. Cells printed directly to glass or silicon substrate (a) with microlens array positioned directly above cell array (b,c). Four different design families are shown (d) with two options for integration of large area silicon cell (e). [63]

under ongoing research, but may include springs, shape memory alloys or even interstitial silicone supports. In addition, designs based on optics that expose the silicone directly to the space environment ("silicone only" and "SoG + AirGap") degrade rapidly by direct exposure to UV radiation and atomic oxygen, requiring protective layers as the use of UV-reflective dielectric coating (UVR) [63].

Specific power was analyzed as a function of designs belonging to these CPV-CIC families for various design parameters, such as focal length, overall length (Z_T), lens size (a_0) and relative lens sag (a_0/a_{0max}), as shown in Figure 1.14 [63]. The model accounts only for the mass of each design and its relative losses from reflection, as well as efficiency estimates based on a semi-empirical cell model which provided the voltage benefits of concentration for 4J, 5J and 6J cells, however it does not take into account the cell mass, thin-film metallization interconnects and the more importantly the mass related structural system. Results for two of these families (glass lens + air gap and SoG lens + air gap), include an optimal lens pitch near 1.5 mm which represents the balance between reducing mass via a reduction of (a_0) and overall lens volume, and the optical losses which are incurred as (a_0) is driven toward zero. Furthermore, the highest specific power (> 500 W/kg) is realized when the relative lens sag is smallest ($a_0/a_{0max} = 15\%$).

Further investigation on this architecture proposition include capability demonstration of microtransfer printing onto 500 μm glass and a radiation degradation modeling that

encourage the usage of CPV for LILT environments.

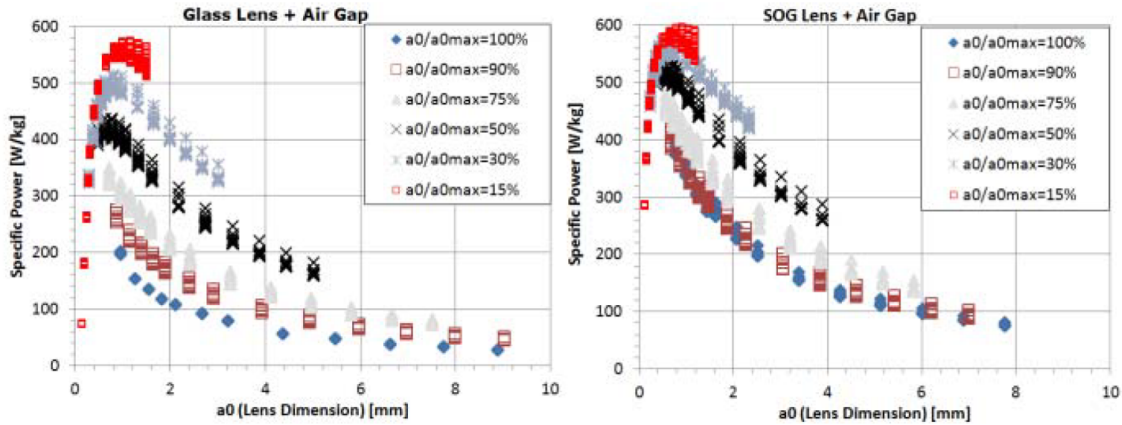


Figure 1.14: Specific power estimates for two selected CPV-CIC families across design space [63].

1.4.2.2 The Pennsylvania State University approach

In 2019, Ruud *et al.* proposed an ultracompact, low-mass micro-CPV for space based on monolithic integration [85]. They demonstrated that a simple reflecting parabolic concentrator provides the best combination of specific power, angular acceptance, and overall fabrication simplicity (shown in Figure 1.15 (a) and (b)), deriving basic limits on compactness as a function of geometric concentration ratio and angular acceptance.

Figure 1.16 (blue curves), shows the impact of edge thickness (ER) variation on a simple paraboloid, which must be finite to form an optical concentrator in practice. The simulation is performed assuming axisymmetric concentrators, a solar disc half-angle of 0.27° , neglecting all losses related to absorption and reflection, and dispersionless $n'=1.5$. Each curve displays a specific power maximum that derives from the trade-off between the loss of optical efficiency due to cell shading at low CR and the increase in mass at high CR. It is noted that as ER increases, the maximum broadens and shifts to higher concentration levels, suggesting an optimal CR range of approximately 8-30X for practical paraboloid-based micro-CPV systems.

On the other hand, the dashed horizontal (red line) denotes a comparative optimal concentrator based on an ellipsoidal lens with the microcell embedded in its second focal point, which does not suffer from cell shading losses, nor spherical aberration. This suggests that the minimum aspect ratio is $AR=1.1$ when $n'=1.5$; which is more than four times larger than the minimum of the paraboloidal concentrator ($AR=0.25$). This difference is fundamentally linked to the limited refractive power of the n to n' index discontinuity, which among others is the main reason why refractive designs applied to micro-CPV underperform their reflective counterparts in space applications.

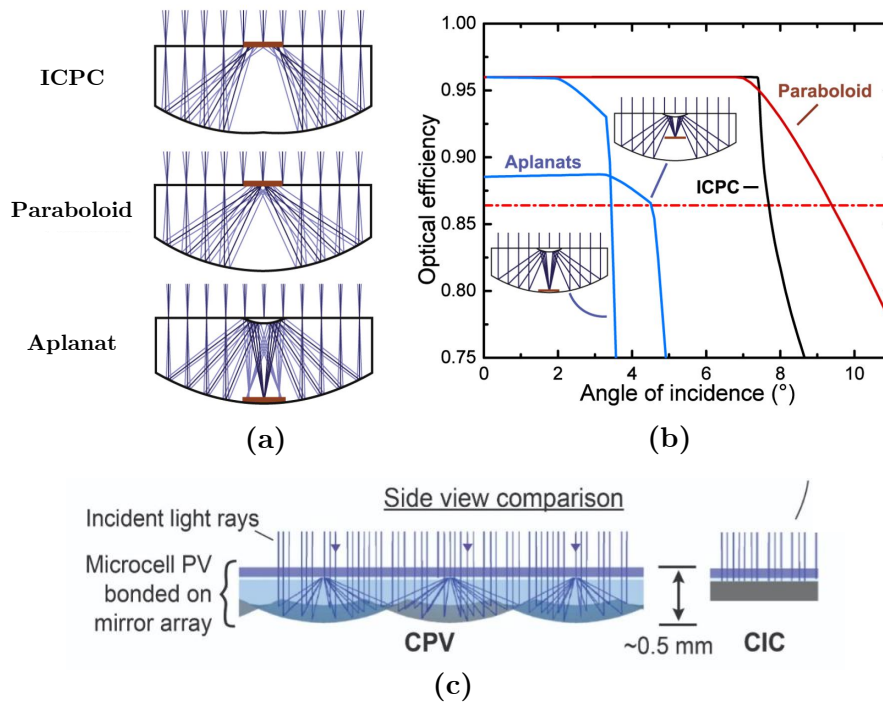


Figure 1.15: (a) Ray tracing diagrams of Inverted Compound Parabolic Concentrator (ICPC), the simple parabola and aplanatic concentrator designs. (b) Simulated optical efficiency as a function of solar incidence angle for the three concentrator designs, for Concentration Ratio (CR) = 25X, shading loss, and $AR = 0.39$ (c) Side view comparison between the mirror based μ CPV and a CIC architecture [85].

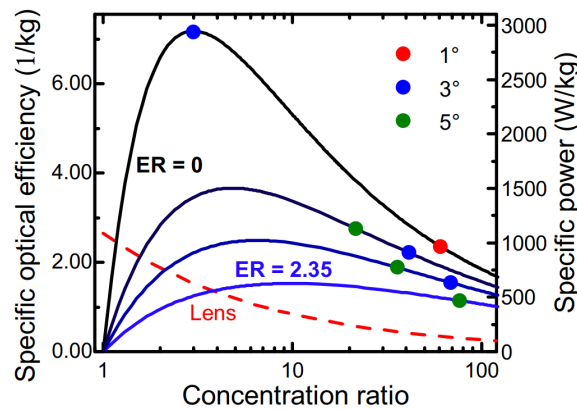


Figure 1.16: Semi-log plot of simulated specific optical efficiency for a simple parabolic concentrator (solid lines) with different rim thicknesses specified by the ratio, ER, of rim thickness to receiver diameter. The colored dots mark different acceptance angles on each curve. The dashed red line is the result for an ellipsoidal refractive concentrator described in the text, as are the assumptions. The right axis rescales the data to the specific power assuming a fixed 30% efficiency of the microcell and the solar flux AM0 of 1366 W/m^2 [85].

A prototype module was constructed, based on an array of twelve $650 \mu\text{m}^2$ 3J (InGaP/GaAs/InGaAsNSb) cells. It uses a $500 \mu\text{m}$ thick cover glass (Corning Eagle XG) on which the cells were printed and interconnected and which also provides protection

against charged particle radiation. The optical system to provide a geometric concentration ratio of 18.4X, this is based on hexagonal shaped paraboloidal mirrors that were molded in glass (Schott B-270) and coated with Ag that provides an average reflectivity of about 96% in the solar spectrum; to obtain a 1.7 mm thick module. The system achieves a ground energy conversion efficiency of $25.8 \pm 0.2\%$, an angular tolerance of $\pm 9.5^\circ$, providing a specific power of about 111 W/kg. The net optical efficiency of the system is estimated to be $73 \pm 2\%$, comparing the short-circuit current of the bare cell array with the CPV sample. The main losses in this prototype are cell and contact shading, Fresnel reflections and cusp losses. The former is generated because the hexagonal mirrors produced by glass molding have a cusp loss between adjacent mirrors that decreases the total light gathering area which becomes more significant as the system is miniaturized. On the other hand, the shading of the cells relies on the ratio between the optical aperture and the cell dimensions. In addition to this, a minimum thickness of the edge of the assembly is required to survive the glass molding process; factors that limit the effective area to mass ratio of the optics.

Some associated drawbacks and unresolved issues of this concept include: brittleness, as the system is composed entirely of molded glass, it is prone to be very fragile. Additionally, the system lacks a stiffening structure that can support an array of the required size in satellites, which among others would not have been taken into account in the specific power calculation, or at least has not been reported.

We note that most of the CPV systems developed have been terrestrial and that there are relatively few systems developed at the space level. In addition, no micro-CPV has been launched into space, partly because it is a new technology, although some proposals are being developed.

1.5 Discussion and conclusions

In this chapter a review of CPV systems has been presented, from an introduction to their fundamental concepts and classification, through the different types of optical systems, materials and processes used. We then focused on specific applications and solutions to conclude with the emerging trends focused on space applications.

From this brief review, methods to improve the performance of MJSC can be highlighted, which include:

- (1.) Reduction of light ray path length;
- (2.) Dependence on material architecture and properties;
- (3.) Tailored surface structures.

Regarding the optical systems used, it was seen that Fresnel lens is a solution that decreases the mass linked to the optics with respect to conventional lenses, however they have the problem of inducing chromatic aberrations which decreases for example the

conversion potential of MJSCs, these present an optical efficiency typically between 80 to 85%. One of the major breakthroughs in Fresnel and its application was the discovery of PMMA, although the Fresnel approach was available before this, they only became popular in CPV technology when they became affordable and practical thanks to PMMA. In this respect, it is not surprising that future advances in the development of optics for CPVs will be largely due to the development of new materials.

Reflective systems, on the other hand, have the best optical efficiencies, up to 97%, they also have the benefit of generally using the least amount of material of CPV optics because they do not need to use bulky material, but are based on thin films. However, they must pay attention to ensure durability over time when subjected to environmental factors such as severe rainfall. Currently the best option for generating highly reflective surfaces is vacuum metallization. The architecture of the deposited coatings depends to a large extent on the material and the quality of the surface to which it is adhered to ensure a high quality mirror finish; and it must be optimized to ensure long lifetimes > 10 years [40, 42, 43].

It was shown that there are some significant differences between space and terrestrial concentrator designs. While the price of the materials and associated processes is important in all cases, the mass of the systems in space is a particularly important parameter. Long-term reliability under operating conditions is important for both applications, but is a particularly crucial point in outer space, since once a system is launched into space it cannot benefit from maintenance. In space, the assemblies must be compact and deploy reliably, whereas on the ground the thickness of the system is not considered such a limiting factor and typically no deployment needed. Additionally, there is an intrinsic relationship between the concentration factor, solar cell size and angular tolerance, with a trade-off to be found regarding the target application. In space, the operational requirements of pointing to the sun lead to low concentration ratios, while on the ground the quest to minimize PV area drives the use of high concentration factors. Moreover, it has also been evidenced that, in general, concentrators use MJSCs with the objective of maximizing their conversion performance to the extent of demonstrating the highest efficiencies in photovoltaic systems.

Micro-CPVs for space applications

In the past, CPVs for space applications using multi-junctions solar cells ($> 1 \text{ cm}^2$) have struggled to balance high concentrating factors with large angular tolerances, while keeping a low-mass and compact optics; along with an advanced thermal cooling. Currently, micro-concentrator photovoltaic systems using μ -cells ($< 1 \text{ mm}^2$) have the potential to address all these issues at once, reducing the optical profile and mass, and improving a passive thermal management, while having a moderate concentration factor ($< 100X$). In addition, innovative manufacturing technologies, e.g. for large-area displays, enable cost-effective production of units consisting of thousands of interconnected semiconductor

devices by miniaturization, additive manufacturing, parallelization and self-alignment. This shall enable high PV performance while exploiting cost reduction potentials in production at the same time.

In this chapter, two promising micro-CPV concepts for space have been evaluated, a refractive one proposed by US Naval Research Laboratory (NRL) and a reflective one developed by Penn State University have been considered. The specific power and volumetric power density of these modules have been studied for different aperture sizes of the optics [63, 85], and here a comparative study has served as a basis for the choice and conception of a new micro-CPV proposal discussed in Section 4. On the one hand, the refractive approach using a set of glass lenses has shown the need to use optics with very small apertures ($1 \times 1 \text{ mm}^2$) to guarantee a compact and lightweight system. Optics that in combination with $170 \times 170 \text{ }\mu\text{m}^2$ aperture cells, provide a concentration of about 35X. The use of such small lenses, however, is compromised by lower optical efficiency due to manufacturing issues, in which a "cusp" region resulting from the surface tension of the glass as it cools in the mold makes it difficult to focus light from the cusp region that extends for about $50 \text{ }\mu\text{m}$ along the perimeter of each lenslet. Another challenge is the need to include additional support structures in designs that leave an air gap (or vacuum) between the lens assembly and the cell array.

It was also shown that there is a lot of potential with a parabolic reflective concentrator at Penn University, in which modules are formed by printing microcells on a thin sheet of glass, which is then bonded to an array of reflective lenses. One of the main advantages of using reflectors is that they allow the cells to operate near the thermodynamic limit of concentration, while the optics have a much lower AR , which can be as low as 0.25. With this design, the mass can reach a new minimum, while increasing the angular acceptance for a given concentration ratio. For comparison, if we consider a cell aperture of say $170 \times 170 \text{ }\mu\text{m}^2$ operating at a concentration of about 35X (as in the case of NRL), the total thickness of a practical concentrator can be as low as 0.5 mm, which is comparable to the thickness of those of current glass-integrated space photovoltaic cells, while the angular acceptance can be about $\pm 5^\circ$. Some practical challenges of this type of module also need to be addressed, such as effective heat dissipation from the cells, since they are embedded in a glass with low thermal conductivity ($> 13 \text{ W/mK}$). This problem is of great importance as was shown in the design of "Boeing 702 satellites" in Section 1.3.3. In addition, the Penn U module also exhibited limited efficiency due to edge errors due to the submillimeter (about 0.5 mm thick) fabrication of the optics. Regarding this, the fragility of the assembly, which is made of thin glass, should integrate a structure that withstands the mechanical loads. In summary, both systems have great potential, although challenges remain to be addressed before they can be successfully deployed in space, in this regard Chapter 2 will address the environmental factors in space for CPV systems.

"The cosmos is also within us, we're made of star-stuff. We are a way for the cosmos, to know itself."
— Carl Sagan, *Cosmos*

2

Assessment of specific missions and environments favorable to CPV in space

One essential questions that remains open is: What kind of mission could be addressed using CPV arrays ? In this regard, the present chapter aim to assess the environmental conditions and needs of PV systems in space, including mission concepts to reach and study planets in the Solar System and some of its principal moons. Firstly, we address this challenge by reviewing the environmental factors affecting conversion efficiency and durability of PVAs in space, described in Section 2.1. Subsequently, the specific constrains of more than 30 mission concepts to explore 14 celestial bodies are identified in Section 2.2. The most relevant conditions of these missions are described, considering the usage of PVAs. The suitability of some solar cells during past missions will be examined, evaluating their behavior during their lifetime. The feasibility of some proposed PVA technologies will be discussed, comparing multiple designs to estimate their potential advantages and limitations. In Section 2.3, a summary of these specific conditions (described in Section 2.2) is carried out. The requirements to address these mission concepts have several unique needs, based on the destination and mission type (e.g., orbiter, flyby, aerial, lander and rover), solar irradiance levels, expected mission lifetimes, temperature range, as well as several specific characteristics of their own environment as radiation, chemical compounds, gravity, pressure, dust, among others.

Finally, a particular focus will be made to evaluate the progress and perspectives of one particular technology: CPV. In this regard, we conclude establishing the spectrum of favorable environments for concentrators, highlighting what kind of missions could be addressed

by this technology. The results presented in this chapter have recently been published as a review article entitled: "Environments, needs and opportunities for future space-based photovoltaic power generation: A review", published in Applied Energy journal [86]. This paper presents a comprehensive review that can help spacecraft designers in the development of PVA for space applications, to choose appropriate encapsulating materials, solar cell technology, thermal management and other specific physical characteristics to enhance reliable power generation for future mission concepts and needs.

2.1 Environmental factors affecting the conversion efficiency and durability of PVAs in space

The large spectrum of candidate missions to different celestial corps in the Solar System demands specific energy requirements and most importantly a variety of space conditions. In the following section, we present a brief review of the main environmental factors affecting the conversion efficiency and the durability of a PVA in space.

2.1.1 Extraterrestrial solar total and spectral irradiance

Solar irradiance is defined as the power per unit area (W/m^2) within a specific spectral distribution that can be modelled by that of a blackbody at about 5,777 K. In space, only a portion of this radiated power impinges on an object that is at some distance from the Sun. About 99.2% of the Sun's energy is focused on the 200–4,000 nm waveband range [87]. The "solar constant" is the measuring mean solar irradiance at one Astronomical Unit (AU) that is, on or near Earth. Although the term solar constant can lead to misunderstanding since the solar energetic output fluctuates following an 11-year solar cycle and the eccentricity of the elliptical orbit of the Earth implies differences in intensity of solar activity [88]. Historically, several initiatives have been carried out to establish an accurate extraterrestrial spectrum, so called "Air Mass Zero" (AM0), indicating that the sunlight has interacted with zero atmospheres, it is shown in Figure 2.1, and compared with the AM1.5 found on Earth. An examination of the available literature defining an accurate extraterrestrial spectrum shows that there is disagreement among various authors defining the solar constant that varies from 1322 to 1429.5 W/m^2 . Today, the space community uses either 1367 or 1366.1 W/m^2 for the solar constant based on the Wehrli spectrum [89, 90], and the American Society for Testing and Materials AM0 (American Society for Testing and Materials (ASTM) E-490-00) [91].

The modelling of the solar irradiance values, both total and spectral, represents an essential factor in evaluating the behavior of a PV system, whose power and optical properties are spectrally selective, and which will evolve from one planet to another (see

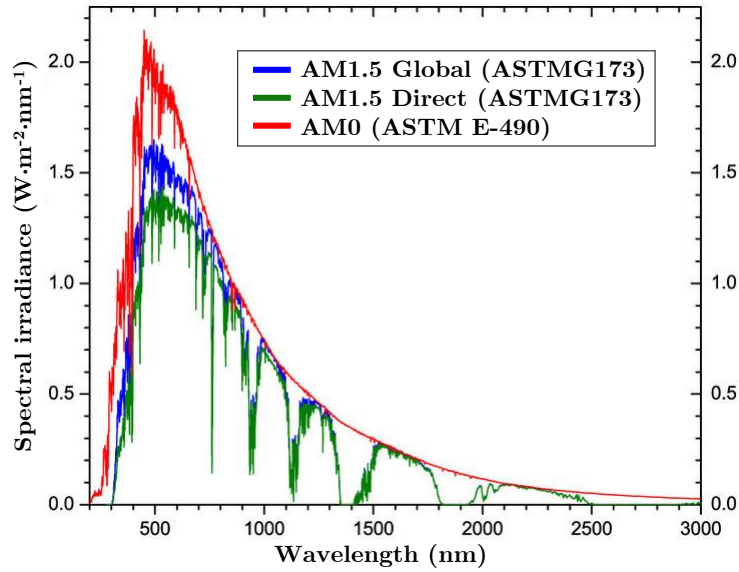


Figure 2.1: Standard solar spectra. Extraterrestrial (AM0), terrestrial Direct (AM1.5D) and Global (AM1.5D), based on data from [92].

Table 2.1). It is possible to calculate the solar intensity received for a body in space by multiplying a reference intensity (AM0) by the inverse square of the distance from the Sun (i.e., Astronomical Units (AU)). As an object moves further away from the Sun, the total sunlight power will now be decreased as it is spread out over a much larger surface area. Table 2.1 shows the distances from the Sun at perihelion (i.e., the point in the orbit of a celestial body nearest to the Sun), at aphelion (i.e., point farthest from the Sun) and the mean distance, as well as the average solar irradiance and the intensity ratio evolution for each planet. On the other hand, variabilities on the spectral distribution for each specific mission type will be described in Section 2.2.

Table 2.1: Average solar irradiance, distances from the Sun, and the intensity ratio evolution for each planet [93].

Planet	Distance from the Sun AU (Astronomical Units)			Mean Solar Irradiance (W/m ²)	Solar Intensity Ratio (Suns)
	Perihelion	Mean	Aphelion		
Mercury	0.31	0.38	0.47	9116.4	6.6738
Venus	0.718	0.72	0.728	2611.0	1.9114
Earth	0.96	1	1.02	1366.1	1.0000
Mars	1.36	1.52	1.67	588.6	0.4309
Jupiter	4.95	5.21	5.45	50.5	0.0370
Saturn	9.02	9.54	10.0	15.0	0.0110
Uranus	18.3	19.18	20.1	3.7	0.0027
Neptune	30.0	30.11	30.3	1.5	0.0011

2.1.2 Extreme temperatures and thermal cycling

Future space missions will operate in locations closer to the Sun, as well as farther from the Sun, so achieving high-efficiency and reliable operation in these temperature regions, higher and lower than standard conditions is a major challenge. In space, spacecraft experience zero gravity and vacuum, which together prevent the natural convection cooling which is normal on Earth; and depend mostly on conduction and radiation cooling. For outer space, however, spacecraft must depend on radiation cooling only. The repetitive cycling of temperatures on spacecraft materials and components stresses systems due to thermal expansion and contraction, which after a while causes the cracking of harnesses, interconnector materials, bus-bars, and also induces series resistance in the solar cell and the interconnector interfaces. Thermal cycle testing is, therefore, a crucial part of any qualification program for spacecraft materials and systems, particularly for PVA systems. Solar cells suffer significant electrical performance loss (e.g. open-circuit voltage) at the high temperatures near the Sun, as for Mercury and Venus orbits. The operating temperature (T) of a solar cell depends on the fourth root of the incident intensity, along with the ratio of solar absorptivity α to thermal emissivity ϵ . According to radiative balance and the Stefan-Boltzmann equation, the equilibrium temperature can be calculated:

$$T = \left[\frac{(\alpha - \eta)I}{(\epsilon_f + \epsilon_r)\sigma} \right]^{1/4} \quad (2.1)$$

where α is the solar absorptivity, η the cell efficiency, I the intensity (W/m^2), σ the Stefan-Boltzmann constant $5.67 \times 10^{-8} \text{ W}/\text{m}^2 \text{ K}^4$, and the subscripts f and r designate the thermal emissivity ϵ from the front and rear sides of the cell, considering radiate waste heat from both sides.

2.1.3 Vacuum

The high vacuum of space (10^{-3} to 10^{-6} Pa) produces outgassing, which is the release of volatiles that were trapped, dissolved, absorbed or frozen in materials. Outgassing molecules can condense onto surfaces affecting spacecraft performance, particularly for sensitive optics, high-voltage devices (i.e., potential cause of arc-induced failure) and for scientific exploration missions. Therefore, a spacecraft designer must compile and control all materials used to develop a specific PVA technology, outgassing and its control measures must be studied in detail. To assess this issue, NASA [94, 95] and ESA [96] used different standards to evaluate, under carefully controlled conditions, outgassed molecules in vacuum. The ECSS-Q-ST-70-02C created by the European Cooperation for Space Standardization (ECSS) [96], and the ASTM E-595 [95], evaluate the mass loss of materials being subjected to 398 K at less than 6.66 mPa (5×10^{-5} torr) for 24 h. The overall mass

loss can be classified into non-condensable and condensable. The latter are characterized herein as being capable of condensing on a collector at a temperature of 298 K. In fact, as a 24 h test-time does not characterize actual outgassing from years of operation, a shorter-time higher test temperature was designated to allow material comparisons with no intent to predict actual outgassing in service. In this regard, the test temperature of 398 K was assumed to be much higher than the expected operating temperature in service, for most missions. Otherwise, if the predicted operating temperatures exceed 338 K to 343 K the test temperature should be increased as well, at least 303 K higher than expected maximum in order to provide material comparisons [95]. On the other hand, the ASTM E-1559 uses three different temperatures employing quartz crystal microbalances, which can provide dynamic data of outgassing in different time and temperature [94]. In order to protect against or remove residual contaminants, some mitigation techniques, such as baking, usage of protective coating or shielding can be applied.

2.1.4 Plasmas

Interplanetary space comprises numerous types of charged particles, varying over a wide energy range. The magnitudes and spectrum of these radiation types vary with location in the Solar System. Those particles below 50 keV are generally regarded as plasma. Such a phenomenon is a critical environment hazard for satellites since spacecraft surface charging, and related Electro-Static Discharge (ESD) can arise [96, 97]. Surface charging is generated when plasma electric charges (from electrons and ions) are able to move and eventually get trapped on material surfaces when they hit them. The accumulated charge (negative or positive) induces the creation of potential gradients between different spacecraft components, a differential charging, resulting in strong local electric fields of thousands or even tens of thousands of volts [98]. Which are known to jeopardize spacecraft and to be responsible for a significant portion of spacecraft anomalies, such as temporary outage and power or function losses [99, 100]. ESD are most likely originated from field effect emission and avalanche process at so-called ‘triple-points’, where metal, dielectric and vacuum are found together [98]. The resulting process can produce the injection of high current electrical transients into the electrical system, inducing transient state changes in electronics large enough to permanently damage material coating or electronic components. Near high potential gradients, plasma released in an ESD can trigger a secondary discharge or even a sustained arc if the potential is maintained e.g. by the solar array. If a surface is maintained at high potential, it draws a current from the plasma, as is the case of exposed PVA interconnects because this leakage current drains power from the array. In addition, the floating potential of the spacecraft can be altered as a result [98].

Threats related to charging, surface and internal, are the result of a complex interaction

between the spacecraft and its plasma environment, and are also influenced by the spacecraft geometry and its material properties [101]. Therefore, the estimated worst-case scenario for one satellite design will likely be different from the worst-case environment for another satellite [102]. A series of studies have addressed the interaction of electrons, which comprise the most damaging species in terms of energy deposition [103, 104], with dielectric materials such as polymers and solar array coverglass [105]. The resulting effects are important to be considered and optimized during the design process. Different reference handbooks and standards provide guidance to many aspects of the space environments. ESA created an assessment of space worst-case charging handbook and two standards to describe the space environment [106], and space charging [98]. NASA proposed a guideline to mitigate charging effects in space [107], a handbook dedicated to Low Earth Orbit (LEO) spacecraft charging design and the respective standard for this specific orbit [108]. Modelling codes include the ESA – Space Environment Information System (SPENVIS) family of codes (available on-line), the NASA Charging Analyzer Program (NASCAP), which is capable of modelling current collection and charging under LEO, GEosynchronous Orbit (GEO), interplanetary, and auroral conditions (exclusive for U.S. citizens). As well as, the Japanese spacecraft charging analysis tool called the Multi-Utility Spacecraft Charging Analysis Tool (MUSCAT) [109]. The formerly cited computer codes for determining potentials on spacecraft surfaces and electric fields in nearby space are certainly useful for solar arrays, but the actual initiation of an arc is extremely difficult to predict. No reliable model for arc initiation exists, so to ensure that arcs will not arise in space tests should be done. International Organization for Standardization (ISO) specifies a set of qualification and characterization test methods to simulate plasma interactions and electrostatic discharges on solar array panels in space [110]. The standard also provides suggested circuit arrangements from laboratories in the United States, Europe, and Japan.

2.1.5 Space radiation environment

The space radiation environment involves a variety of relativistic electrons, protons, and other heavier ions. These particles have energies that range from near-zero up to several hundred million electron volts. They can cause both ionization and displacement damage effects in spacecraft systems, and the effects can be either transient or permanent. Understanding the behavior of solar arrays under radiated environments is extremely important for accurate prediction of the expected mission lifetime, including component selection, material effects and shielding optimization. Solar cells in space suffer a gradual damage of their electrical performances caused mostly by the exposure to energetic electrons and protons, which can induce lattice displacement damage. These particles are found either trapped in radiation belts (e.g., Earth’s Van Allen belts), throughout planetary

magnetospheres or ejected in solar events. Magnetized celestial bodies trap particles of lower energies, typically in the MeV range (i.e., 1 MeV is equivalent to the charge energy of one million electrons falling through one volt in the electric potential field). Earth, Jupiter, Saturn, Uranus and Neptune have strong magnetic fields inducing severe radiation environments in their radiation belts. Mercury has a small magnetosphere, which may lead to transient radiation belts. The other planets (Mars, Venus) have no trapped radiation, and missions to them are only exposed to galactic cosmic rays and solar energetic particles [106].

The mass of the incident particle influences the nature of the dominant mechanism of energy deposition on materials. Massive particles (e.g., heavy ions and protons) deposit huge amounts of ballistic energy (over a relatively short depth), displacing nuclei in the solid, exciting phonons and vibrational transitions sufficient to rupture chemical bonds and create radicals [105]. For much less massive particles such as electrons, they are expected to deposit energy (over a longer trajectory) mainly in the form of electronic excitation; sufficient to similarly induce bonds rupture and a more bond-selective chemical damage. Additionally, UltraViolet (UV) photons have enough energy to dissociate molecular bonds, on some materials (e.g., polyimide-Kapton) causing photo-oxidation reactions [111]. Experimental studies have shown that low mass particles such as He⁺ ions, and low energy ions, induce sufficient energy to break all bonds, through distinct and relatively well defined reactions [112]. Incident particles (e.g., electrons, protons, and photons) can generate secondary electrons to be ejected at the surface and potentially cause a charge imbalance at the penetration depth of the particle. In fact, the particle gets embed itself into the bulk after its kinetic energy is exhausted [113]. The secondary electron emission probability is strongly dependent on the incident energy of the impinging particle [114, 115].

Typically the active regions of a cell are shielded from the incident particle spectrum using coverglass (at the front surface), and by the substrate material and supporting array structure at the back surface, as shown in Figure 2. In fact, each solar cell technology responds differently to radiations depending on the materials used, the thickness, and the type and concentrations of dopants employed. In solar cells, the main effect of radiation damage takes place when incoming particles displace atoms in the semiconductor crystal lattice – called atomic displacement damage [116]. These lattice defects, such as vacancies and interstitials, generate a complex number of defects that act as recombination centers or majority- and minority-carrier trapping centers, which ultimately cause a decrease in the output power of solar cells [117]. Beside the displacement damage, radiation may affect solar cell array materials by several ionization related effects. Electrons and protons with sustained particle bombardments induce defects within oxides – known as total ionizing dose; the unit of dose is the rad, where 1 rad is equivalent to 100 ergs/g. The ionization produces electron–hole pairs that mainly affect insulating materials, like coverglass, which may trap charges and reduce its transmittance. The darkening is caused by the creation of

color centers in glass when ionizing radiation excites an orbital electron to the conduction band, which are trapped by impurity atoms in the oxide to form charged defect complexes [118]. Furthermore, radiation causes several ionization-related effects in organic materials, such as polymers in PVA. These modifications are the consequence of the production of ions, free electrons and radicals, which induce darkening in transparent polymers and crosslinking between main-chain members that can severely change its mechanical properties.

Currently two standard methods for modeling solar cell degradation in space, induced by energetic particles are used: 1) The equivalent fluence method, created by NASA Jet Propulsion Laboratory (JPL) [118, 119], and 2) the displacement damage dose model developed by the NRL [117, 120]. Both methods have the same general approach, they correlate the degradation caused by particles of different energies, i.e., the energy dependence of the cell damage coefficients must be determined. For this, the radiation environment needs to be accurately specified, including the effects of any shielding materials present. Finally, a method is used to convolute the energy dependence of the damage coefficients with the radiation environment for the duration of the mission, in a way that makes comparison with a ground test result possible. This last step is usually accomplished by means of a standard or characteristic degradation curve for a particular cell type. The JPL method approach is the determination of the normal incidence 1 MeV electron fluence, which produces the same level of damage to the cell as a specified space radiation environment [118, 119]. This model uses the concept of relative damage coefficients and it can be implemented through several programs to estimate the radiation dose of a specific mission (e.g. FORTAN programs, and it is included in the ESA – SPENVIS website [121]). In contrast, the NRL method calculates the displacement damage dose for a given mission using the energy dependence of the damage coefficients, and the proton and electron spectra incident on a bare cell [117, 120]. The relative damage coefficients are calculated from the non-ionizing energy loss for protons and electrons traversing the cell material. The NRL approach is generally easier to implement than the JPL method, because it requires far fewer experimental measurements to specify the relative damage coefficients. It can therefore, be used when only limited experimental data is available, as is often the case with new and emerging cell technologies. However, the JPL method has the advantage of familiarity and has been used successfully over a number of years by many workers in the space community. Messenger *et al.* established a detailed comparison of both methods [117].

2.1.6 Micrometeoroid and orbital debris impact

All spacecraft are exposed to risk of damage from micrometeoroid and orbital debris. While micrometeoroids are of natural source mostly created from asteroids or comets, space debris are man-made objects that are remainders of human spaceflight activities.

PVAs are gradually injured when small holes are drilled or large areas of the cell are damaged. Such harm potential must be accounted for in the spacecraft design. Specific models have been created to describe the particle flux relative to a moving spacecraft as a function of mass-density relations, directional collision velocity distributions and flux-mass/diameter relations, and ultimately perform a micrometeoroid and orbital debris risk assessments [122, 123].

Table 2.2 presents a synthesis of the major environmental factors affecting conversion efficiency and durability of PV systems in space and the relative effects. Subsequently, in the following section these factors will be enlarged and specifically studied for a large spectrum of mission concepts to reach different celestial bodies.

Table 2.2: Synthesis of the effects of space environment on the conversion efficiency and durability of solar panels.

Environment Factors	Effects on the conversion efficiency and durability of PV
Solar Irradiance	<ul style="list-style-type: none"> • Power conversion dependence
Temperature	<ul style="list-style-type: none"> • Efficiency degradation • Degradation mechanisms (carrier freeze-out and thermal barriers to conduction) • Thermo-elastic stress cycles (e.g., cracks in solder joints of the interconnects) • Electric resistances
Vacuum	<ul style="list-style-type: none"> • Contamination (degassing) • Pressure differentials (decompression)
Plasmas	<ul style="list-style-type: none"> • Surface charging, electrostatic discharge and dielectric breakdown • Enhanced sputtering and re-attraction of contamination • Increased leakage current
Energetic Particle Radiation	<ul style="list-style-type: none"> • Total ionizing dose effects (electronic degradation) • Displacement damage • Single event effects (upset, latch-up, burnout) • Degradation in optical properties (e.g., coverglass, optics, etc.)
Electrically Neutral Particles	<ul style="list-style-type: none"> • Mechanical effects (aerodynamic drag, physical sputtering) • Chemical effects (ATOX, spacecraft flow)
Ultraviolet & X-Ray Radiation	<ul style="list-style-type: none"> • Degradation of thermo-electric properties • Degradation of optical properties (e.g., coverglass, optics, etc.) • Structural damages
Micrometeoroids & Debris	<ul style="list-style-type: none"> • Damage to cell active area and interconnects • Damage of optical systems caused by hypervelocity impacts (e.g.: coverglass, lenses, mirrors) • Increased cell shunt resistance

2.2 Specific space environments and description of photovoltaics

This section will serve as a baseline for the development of future PV technologies, evaluating the specific environmental conditions of several missions of interest. Reviewing the influence of the space environment on a given solar technology plays a crucial role in determining the system function, reliability and lifetime. The environmental conditions that exists at the Earth's orbits, on the Martian and Lunar dusty surfaces, at the hottest Venus and Mercury, or among the distant Gas Giants, differs radically from one celestial object to another. Different missions can be defined depending on the type of spacecraft (lander, orbiter, flyby, etc.). Indeed, the power required for a specific space mission has unique needs and challenges based on the destination and mission type. The majority of the planetary missions conducted until date used PVA as power system, especially for missions close to the Sun and as far as Mars. Nowadays, it is conceivable even as far as Jupiter, where RTG were typically used. Figure 2.2 shows the status of solar power missions in the Solar System. It presents the approximate relative applicability of PV technologies to target body mission concepts, showing solar power in yellow (i.e., outer rings for orbiters and flybys and inner rings for landers and probes), based on expert opinion developed at JPL-NASA [9]. In this context, solar cells operability is limited at low solar intensities, requiring PV systems with high power capability, as for spacecraft Juno producing more than 14 kW at 1 AU to generate the necessary power > 430 W at Jupiter (5.1 AU).

According to the literature and worldwide national strategies for the planetary sciences, missions from Saturn and beyond become increasingly difficult. As shown in Figure 2.2 and Table 2.1, at the distance of Uranus, the solar intensity has decreased to less than 0.3% of the intensity at Earth orbit, highly demanding PVA systems in terms of mass and area, at the point to become impractical from a cost point of view. With this in mind, concentrating arrays provide an interesting approach for planetary exploration using solar cells at farther distances, such as those of Jupiter and even as far as Saturn. Hence, a comprehensive review was conducted with a focus on suitability in space and environmental damage assessment for PV systems in general, which will be then applied to evaluate the perspectives of one particular technology: CPV.

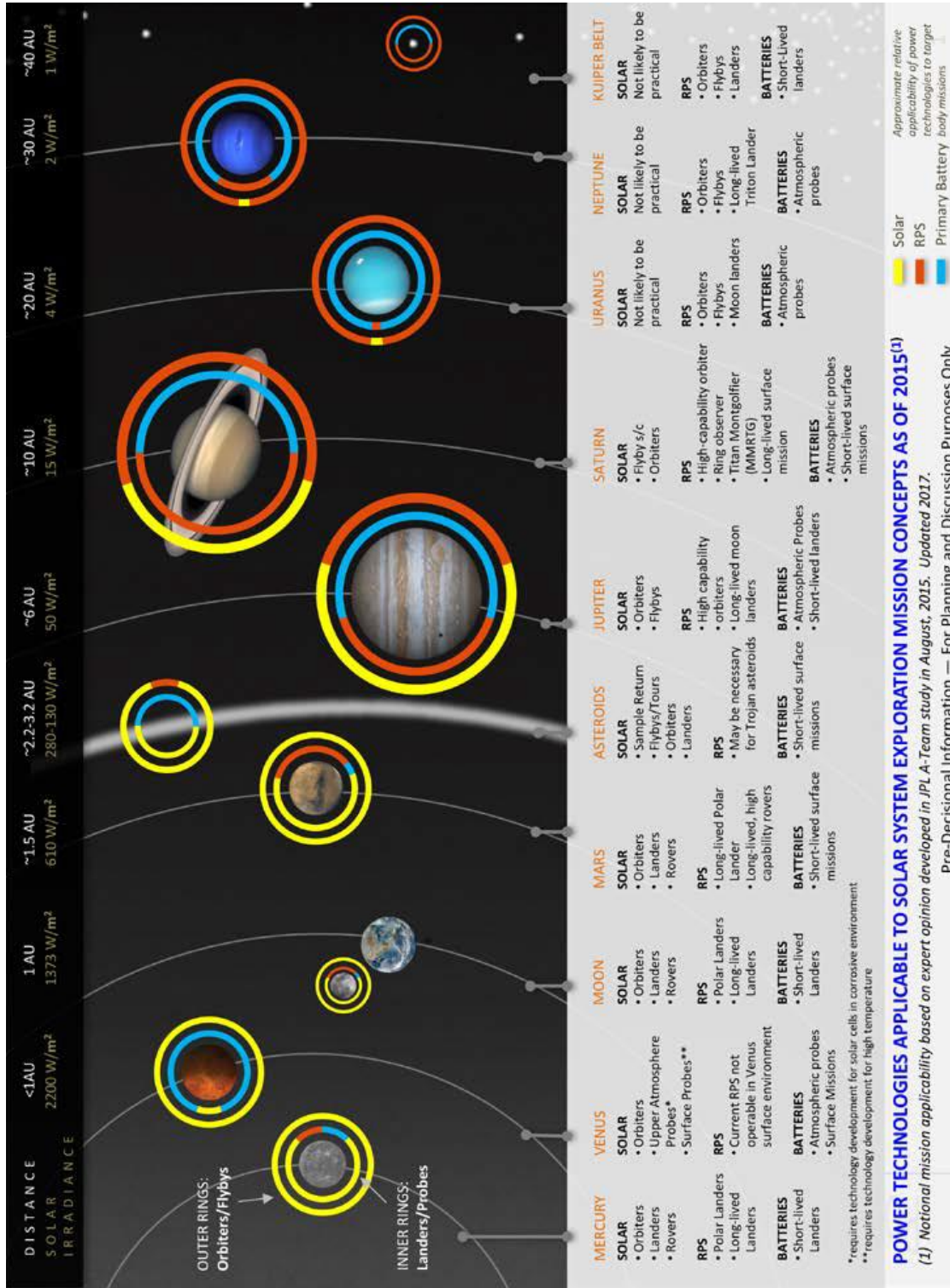


Figure 2.2: Estimated relative applicability of power technologies to target body mission concept showing solar power in yellow (outer rings for orbiters and flybys and inner rings for landers and probes), credits: NASA/JPL [9].

2.2.1 Earth satellite orbits

2.2.1.1 Low Earth Orbit

Earth is the third planet from the Sun and the only astronomical object known to harbor life. The shape of Earth is nearly spherical with a slight flatness at the top. Earth's atmosphere is surrounded by air; it extends up to 160 km above the surface, and beyond it gradually fades into space. Earth artificial satellites are typically located in one of three popular orbital regions: LEO, Medium Earth Orbit (MEO), GEO. Variation with altitude is perhaps the most important parameter for the spacecraft designer on the Earth' orbits. It is not merely a matter of height variation but reflects basic physical processes that differ in the respective regions.

Most of all operational satellites are in LEO, orbiting the Earth from 200 to 2000 km of altitude (e.g., the International Space Station at about 400 km). These satellites are ideally situated for remote sensing as Earth observation and reconnaissance missions, since they have short orbital periods, between 90 minutes and 2 hours. They are characterized by low levels of radiation damage from trapped electrons and protons, and low cost from the point of view of launching and power requirements on board the spacecraft [124]. A spacecraft in LEO experiences a variety of harsh, complex and dynamic environmental conditions, which can evolve with respect to position, local time, season and solar activity [125]. Threats such as ATOMIC OXYGEN (ATOX), UV radiation, thermal cycling, and micrometeoroid/debris impact should be understood for proper selection of PV technologies and materials [126].

The atmosphere at LEO altitudes consists mainly of ATOX ($\sim 80\%$) and Nitrogen molecules ($\sim 80\%$). ATOX is formed when UV radiation (< 243 nm) coming from the Sun photo-dissociates molecular oxygen in the upper atmosphere [125]. Extensive erosion due to ATOX does not exist in the GEO or MEO orbits. In LEO, these neutral oxygen atoms have mean free paths in the order of 10^4 m, resulting in extremely low probabilities of reassociation [126]. As a LEO spacecraft travels at a velocity of about 7.7 km/s, its front surfaces ram with the ATOX species with impingement kinetic energy of approximately 4.5 eV [127]. A nominal range of values for LEO is 10^{14} to 10^{15} atoms / cm^2 s [125]. The ATOX degradation on materials may result in changes in chemical composition and surface morphology (e.g. erosion), changes in optical properties, and formation of particulate and molecular contamination on surfaces. All hydrocarbon based polymers and graphite are easily oxidized. These effects have been widely studied, as well as a variety of solutions as coatings [128].

UV radiation at LEO interacts readily with many materials on spacecraft. The wavelength range of solar UV present in LEO is between 100 to 400 nm, about 8% of the solar constant (~ 110 W/ m^2). Although this is a relatively small amount of energy, it can break polymer bonds such as C-C, C-O and functional groups [129], which may induce

degradation properties of space materials such as adhesion, color, flexibility, hardness, and toughness (e.g., on fluorinated ethylene propylene, Teflon, etc.) [130]. However, others as polyimide Kapton are UV durable [129]. For glasses, UV radiation induces a photochemical reaction that causes a decrease in UV transmittance and color changes (darkening). The UV resistance of each glass is different, for example, some tests shown: excellent resistance - sapphire (alumina), good resistance - fused silica, fair resistance - optical glass, and poor resistance - ultra low expansion glass [126]. In addition, UV radiation affects the thermo-optical properties, leading to decreased efficiency of the thermal control surfaces and strongly affecting mechanical properties. A LEO spacecraft takes 90 min to orbit the Earth. This cyclic fluctuation, from -120 to 393 K, induces thermal stresses on each component producing side effects as microcracking of substrates or coatings, and delamination of coatings produced by different CTE [131]. Furthermore, the presence of micro-particles at LEO is a potential hazard to solar power systems. The average velocity for debris particles ranges from 10 to 13 km/s and is about 19 km/s for micrometeoroids [132]. The impact damage can vary from located cratering due to small particles at high-velocities until the satellites destruction. Another LEO related phenomenon is the surface charging, which is primarily due to ions. It consists of low energy plasma of less than 1 eV with a density ranging from 10^5 to 10^6 particles per cm^3 [1].

2.2.1.2 Medium Earth Orbit

MEO ranges from $2,000$ to $36,000$ km altitude, which yields an orbital period of 12 hours. The most common uses include navigation (e.g. the Global Positioning System: GPS), communication, and geodetic/space environment science at altitudes around $20,000$ km. There are approximately 100 satellites in MEO [133]. One reason explaining the few number of satellites in MEO respect to LEO or GEO is the presence of the Van Allen belts. The radiation belts and plasma in the Earth's magnetosphere pose hazards to spacecraft systems, which restrict design and orbit options with a resultant impact on mission performance and cost [134]. The intense and dynamic electron fluxes (from 0.05 to 10 MeV) of the outer radiation belt cause ionizing dose, non-ionizing energy loss, and internal charging [135, 136]. Additionally, the MEO region is essentially exposed to powerful fluctuations of protons (from 0.1 to 400 MeV) due to the low levels of geomagnetic shielding [134]. For Earth orbits, different standard models have been established describing the energetic particle fluxes around the radiation belts, in order to anticipate the induced degradation, shielding and operations design. The most widely used are the NASA models AP-8 and AE-8 for the trapped protons and electrons in the Earth's radiation belts [136, 137]. Nevertheless, some limitations and deficiencies are well acknowledged, these models for various locations/energies were sometimes too low (resultant in risks from under design) [138], or too high (causing unnecessary costs from overdesign) [139], and no coverage

of the hot and cold plasma populations below 0.1 MeV [140, 141]. Then a significant effort in this area has achieved more accurate and comprehensive models. NASA and the Air Force Research Laboratory have developed the AP-9/AE-9/SPM to address all these issues: covering the full range of energies/locations, expanded further to meet new needs (e.g. to plasma energies in the Standard Plasma Model, or SPM), and incorporating new data sets [142, 143]. In addition, the models can be run in different modes, in terms of how statistical fluctuations due to instrumental uncertainties and space weather are treated. Even though these models are not perfect, more data is required and the range of features is being expanded for future updates [135, 144]. Additionally, some initiatives have provided measurements of great interest for MEO environment, for example, the European Space Agency (ESA) establish the Standard Radiation Environment Monitor (SREM) [145]. Advanced solar cells are being developed to target MEO-type missions or missions with orbit transfer through the Van Allen radiation belt with a cumulative $1 \times 10^{16} \text{e}^{-}/\text{cm}^2$ fluence of equivalent 1 MeV electrons [146]. In parallel, the performance degradation when using shielding coverglass is studied [147].

2.2.1.3 Geostationary Earth Orbit

GEO is a circular orbit 35,786 km above Earth's equator and follows the direction of Earth's rotation. GEO is used for communications and broadcasting [148]. The natural GEO environment comprises a wide spectrum of particle, from electrons and protons to solar ultraviolet (UV) radiation and gamma rays. Although regarding the total energy deposition into a spacecraft, solar charged particles and UV photons are the dominant species interacting with the spacecraft surface [149].

Severe and extreme surface charging had been associated with GEO altitude since 1972, when the ATS-5 GEO satellite became charged to over 12 kV during eclipse and several hundred volts in sunlight [150, 151]. Since then, many guidelines and studies on the radiation effects have been carried out (see Section 2.1). The charging rate in GEO is believed to be determined primarily by the flux of electrons with energy in the order of 30 keV [1]. At LEO, 1% of the atmosphere is ionized while this number increases to 100% ionization in GEO [152]. In fact, ionization in space is highly dependent on altitude. The plasma density in GEO varies from over 100 to 0.1 cm^{-3} and the energy varies from a few eV to tens of keV, depending on local time and geomagnetic conditions [101]. The arcing rate is sensitive to temperature, and most GEO arcing occurs just after coming out of an eclipse.

Fennell *et al.* characterized the worst-case electron flux versus energy, shielding depth, or aggregation time in GEO (daily averaged) and high Earth orbits (10 h averaged) [153]. Moreover, O'Brien *et al.* extended this analysis to include a variety of timescales (hours to days) and energies (90 keV to 4.75 MeV) from L-shell 2 to 8 [154]. They demonstrated that relativistic electron fluxes have a finite upper limit over these three factors. In 2017,

Matéo-Vélez *et al.* analyzed 16 years of Los Alamos National Lab (LANL) data and contrasted them with Polar Orbiting Environmental Satellites (POES) data to determine a new set of severe GEO environments [102]. They compared them with current guidelines for the assessment of worst-case surface charging [106, 108]. Some of their results are: (1) Surface charging are correlated with low energy electron fluxes between 10 and 50 keV, and a high ESD risk when these fluxes exceed $1 \times 10^8 \text{ cm}^{-2} \text{ s}^{-1} \text{ sr}^{-1}$. (2) In sunlight, the LANL spacecraft potential decreased down to -2 kV. In eclipse, high charging levels below -5 kV have been observed during tens of minutes. It is recommended to separate eclipse and non-eclipse charging data and to examine the most severe events for the two cases. (3) A set of extreme LANL environments has been extracted to complete the list of available environments used by guidelines to assess worst-case satellite surface charging in GEO. These events are correlated to the declining phase of the solar cycle, to seasonal effects and to the geomagnetic activity.

Lu *et al.* summarized the characteristics of the Earth’s space environment at each specific altitude [155]. The dominant environmental components and their effects on spacecraft in different orbits (i.e., LEO, MEO, GEO) are investigated, respectively (see Figure 2.3).

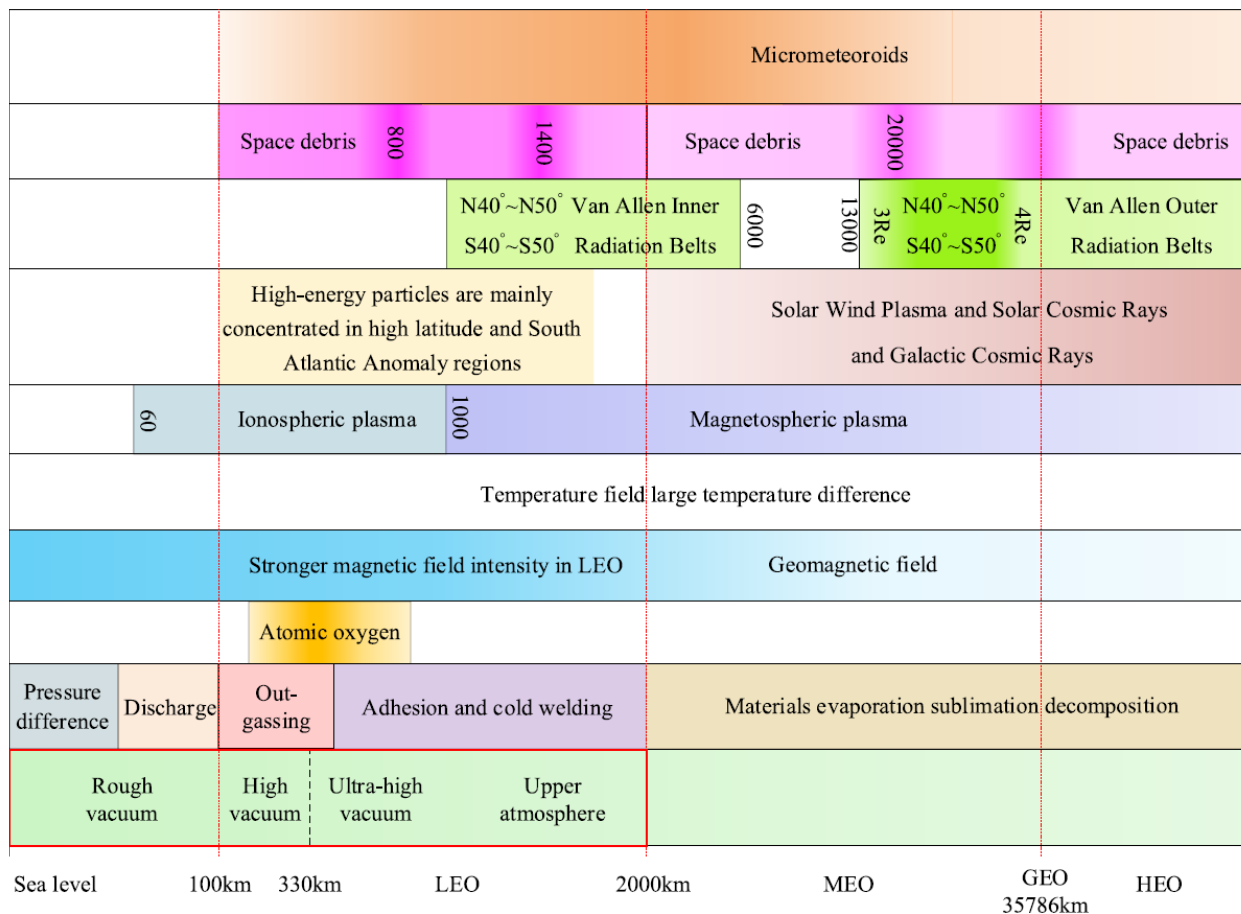


Figure 2.3: Space environmental components in all Earth altitudes [155].

Figure 2.5 illustrates the mean annual electron (> 100 keV) and proton (> 5 MeV) fluxes, experienced by satellites in several orbits, as a function of altitude and maximum latitude [105, 113]. It is based on AE-9 and AP-9 (V1.5) mean radiation belt models, for trapped electrons and protons [156]. EPAM-ACE (Electron, Proton, and Alpha Monitor on the Advanced Composition Explorer) data for untrapped solar wind electrons [134, 157], and the Xapsos model [158] for untrapped protons, with approximate geomagnetic cutoffs in solar proton access based on [159]. Representative orbits are shown as dashed lines for reference. Various satellites are located, ISS in LEO, GPS in MEO and Geostationary Operational Environmental Satellite (GOES) in GEO. In addition, the positions of the Moon and a sun-synchronous orbit are displayed, though, they will be treated later.

Figure 2.4 shows a comparison between the most intense energetic proton and electron spectra, specifically at about 1 MeV, measured within each of the magnetospheres of the five strongly magnetized planets of the Solar System [160, 161]. The radiation belts of Earth, Jupiter, and Uranus possess the most intense measured spectra with energies between 0.1 and 1 MeV. The Earth's data was obtained by the International Sun Earth Explorer mission, and rest by the Voyager spacecraft encounters of the various outer planet magnetospheres; sources and the fitting parameters are provided by the author [162].

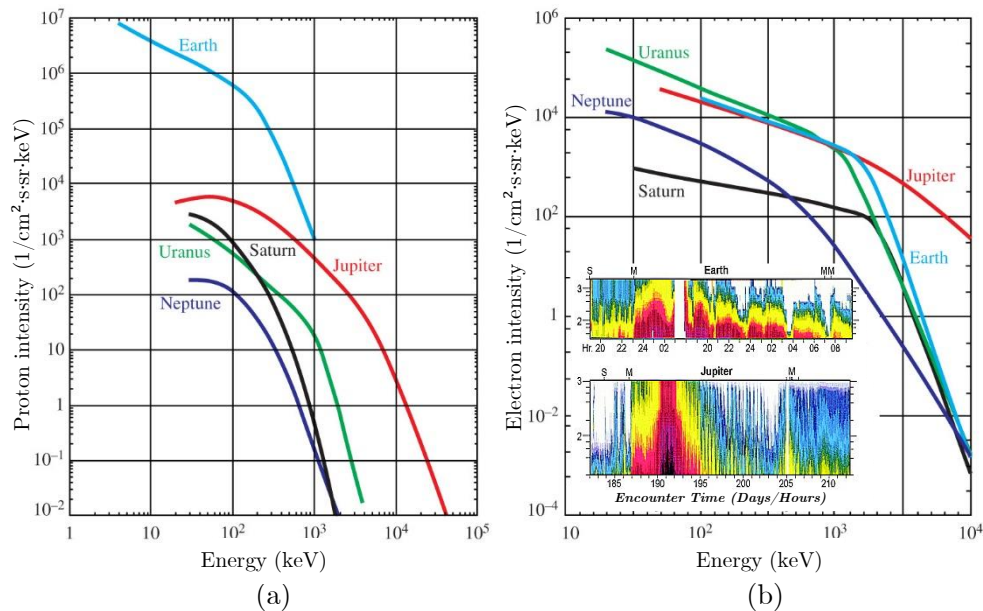
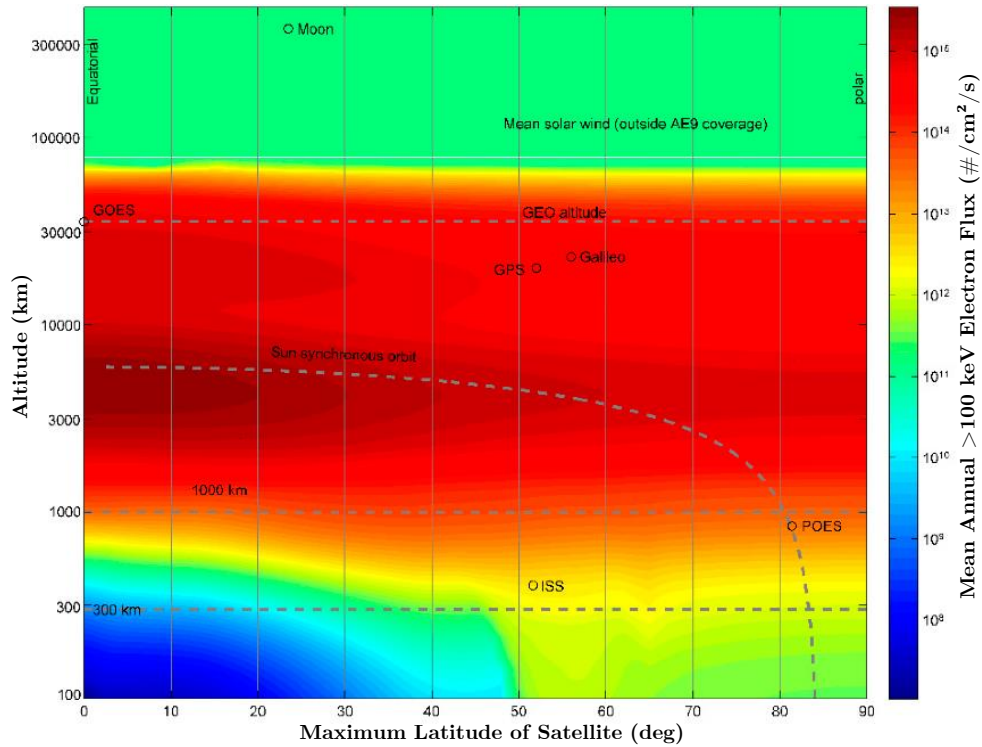


Figure 2.4: The most intense observed spectra of the proton (left; adapted from Mauk) [162, 163] and electron (right; adapted from Mauk Fox [160, 163]) radiation belts of Earth compared to those found in other Solar System magnetospheres. The inset shows the spectrograms of energetic electrons observed at Earth by the International Sun Earth Explorer mission, and Jupiter's data obtained by the Voyager spacecraft encounters, the time scales encompass both inbound and outbound magnetopauses ("M" character above each plot). Energy spans roughly 20 keV to 1 MeV (from Mauk Fox [160]), (In colour).

(a) Mean Electron Flux for Circular Earth Orbits from AE-9 V1.5 (plus ACE EPAM for Solar Wind)



(b) Mean Proton Flux for Circular Earth Orbits from AP-9 V1.5 (plus Xapsos Model for Solar Protons)

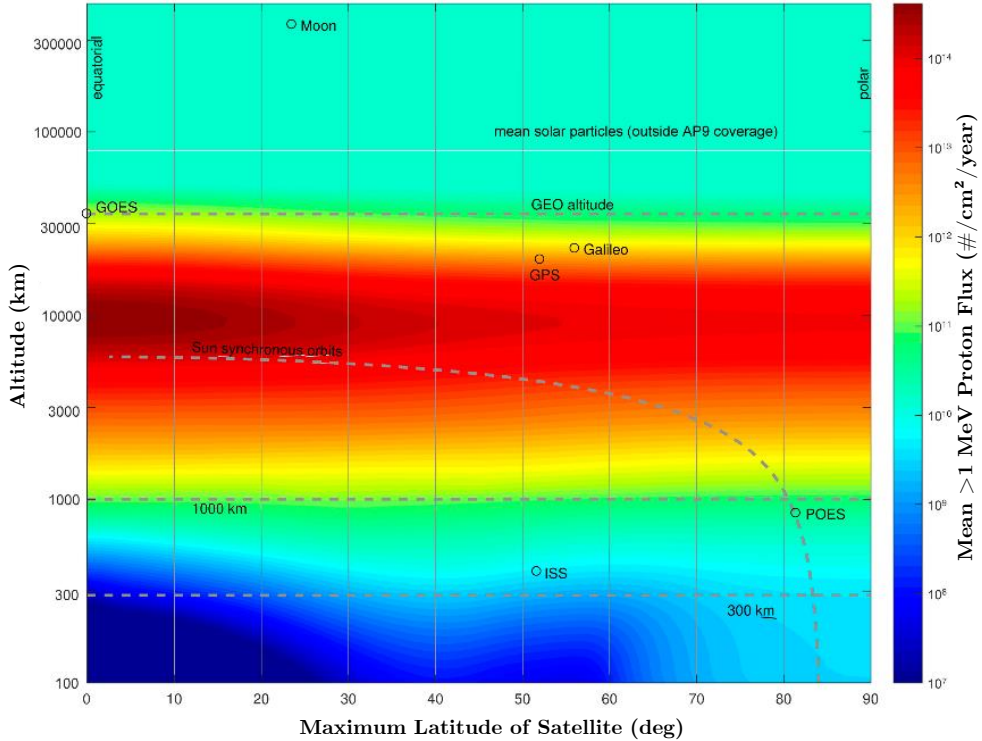


Figure 2.5: Mean annual electron flux > 100 keV electrons (top panel); and mean annual proton flux > 5 MeV protons orbit averaged (bottom panel), experienced by a satellite in a circular GEO as a function of altitude and maximum latitude (inclination for prograde orbits, a supplement of inclination for retrograde orbits). Representative orbits are shown as dashed lines for reference, as are the positions of the moon, International Space Station (ISS), and several other satellites [105, 113].

2.2.2 Dusty worlds: the Moon and Mars

Some celestial bodies in the Universe present common technological challenges associated to similar environmental conditions. This is the case of “dust”, which has been observed by Apollo astronauts on the Earth’s Moon and by several Mars mission such as the Mars Pathfinder and the Mariner-9 missions. Figure 2.6 illustrates these two worlds showing related dust effects, dust glow over the horizon at the Moon as imaged by the Lunar Orbiter, and a global scale dust storm at Mars capture by the Hubble Space Telescope, as will be describe below. Hazards induced by dust particle deposition in planetary exploration can reduce the performance of electronic equipment, including solar panels power loss, obscuration of optical systems, malfunction of mechanical devices, filters, valves and others [164].

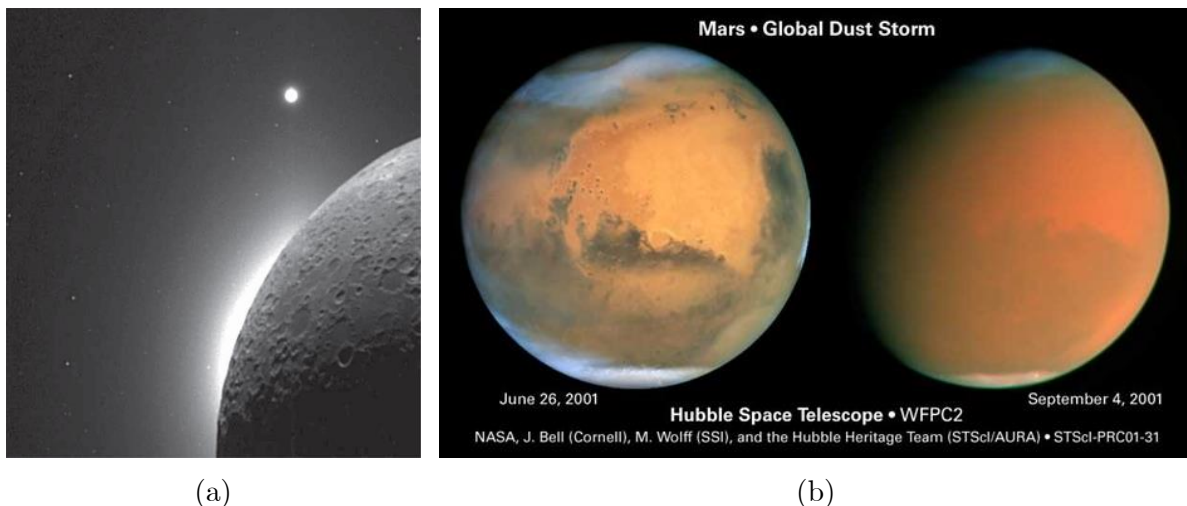


Figure 2.6: (a) Dust glow over the horizon of the Moon as imaged by the lunar orbiter, (b) Hubble images of Mars show the effects of global-scale dust storms on Mars, credit: NASA/JPL [165].

2.2.2.1 Earth’s Moon

The Moon is the only natural satellite that orbits Earth. The lunar surface, being approximately at the same distance from the Sun as the Earth, perceives a solar flux essentially as that in the Earth’s orbit, full-energy spectrum including UV and X-ray components [165]. The Moon has negligible magnetic field and atmosphere, its surface pressure ranges from 10^{-7} during the day and to 10^{-10} Pa at night. This hard vacuum will create problems with outgassing of materials. Incident charged particles can reach its surface without being repelled and trapped in belts and, as consequence solar arrays will degrade more than on Earth. Annually the Moon receives about 10^6 kg of interplanetary micrometeoroids (ranging from 10 nm to about 1 mm in size) at impact speeds of 10–72 km/s [166]; inducing a high rate of mechanical damage on the solar arrays. The temperature on

the surface ranges between 98 K (at night) and 389 K (during day) at the equator [167], nevertheless, temperatures of different areas will vary greatly depending upon whether they are in sunlight or shadow and throughout the year because of varying distance from the Sun.

The Moon perceives many types of ionizing radiation: large fluxes of low-energy solar-wind particles, smaller fluxes of high-energy galactic cosmic rays, and rare but occasionally intense particle fluxes emitted by solar flares or solar cosmic rays. Heiken *et al.* summarized these three major types of radiation as shown in Table 2.3 [168]. Most observations about lunar radiation is a collection of measurements collected by instruments on spacecraft beyond the Earth’s magnetosphere; these observations are representative of what impinges the Moon.

Table 2.3: Summary of the three major types of radiation in the lunar environment [168]

Type	Solar Wind	Solar Cosmic Rays	Galactic Cosmic Rays
Nuclei energies	~ 0.3-3 keV/u *	~ 1 to >100 MeV/u	~ 0.1 to >10GeV/u
Electron energies	~ 1-100 eV	< 0.1 to 1 MeV	~ 0.1 to >10 GeV/u
Flux (protons/cm ² sec)	~ 3 x 10 ⁸	~ 0-10 ⁶ †	2-4

* eV/u = electron volts per nucleon. † Short-term SCR fluxes above 10 MeV; maximum is for the peak of the August 4, 1972 1972 event. Flux above 10 MeV as averaged over ~ 1 m.y. is ~ 100 protons/cm²sec.

The Moon has been the subject of human exploration by actual landing on its surface. Apollo-17 was the final manned Moon mission of NASA’s Apollo program. Under his command, Eugene Cernan reported: “... one of the most aggravating, restricting facets of lunar surface exploration is the dust and its adherence to everything no matter what kind of material, whether it be skin, suit material, metal, no matter what it be and it’s restrictive friction-like action to everything it gets on.” [169]. Figure 2.7 illustrates several dust transport mechanisms on the Moon. Lunar “regolith” designates the surface layer of particles generated by meteoritic impacts and the finest constituent (< 100 μm) is denoted as “dust”. The soil samples collected by Apollo astronauts have been studied in detail and indicated that the major components of lunar surface dust are oxides of silicon (SiO₂ – 42.1%), aluminum (Al₂O₃ – 13.0%), iron (FeO – 17.4%) calcium (CaO – 11.3%), magnesium (MgO – 8.0%) and titanium (TiO₂ – 7.2%) [170–172].

Numerous initiatives investigated the particle size distribution of lunar soil. Carrier *et al.* described and compared the particle size classification of data collected in seven landing sites on the Moon: Apollo 11, 12, 14, 15, 16, 17, and Luna 24. According to measurements, lunar grains ranged from 46 to 110 μm with an average mean particle size of 72 μm, the particle size distribution seems to be very consistent on the Moon to a depth of at least several meters or more [173]. About 20% of the lunar dust has a particle size lower than 70 μm, with a significant fraction of fine and ultrafine particles in the nanometer to 20 μm diameter range [165]. Grain shapes are highly variable, from spherical to very angular forms, though, in general, they are somewhat elongated [168]. Several studies show that a

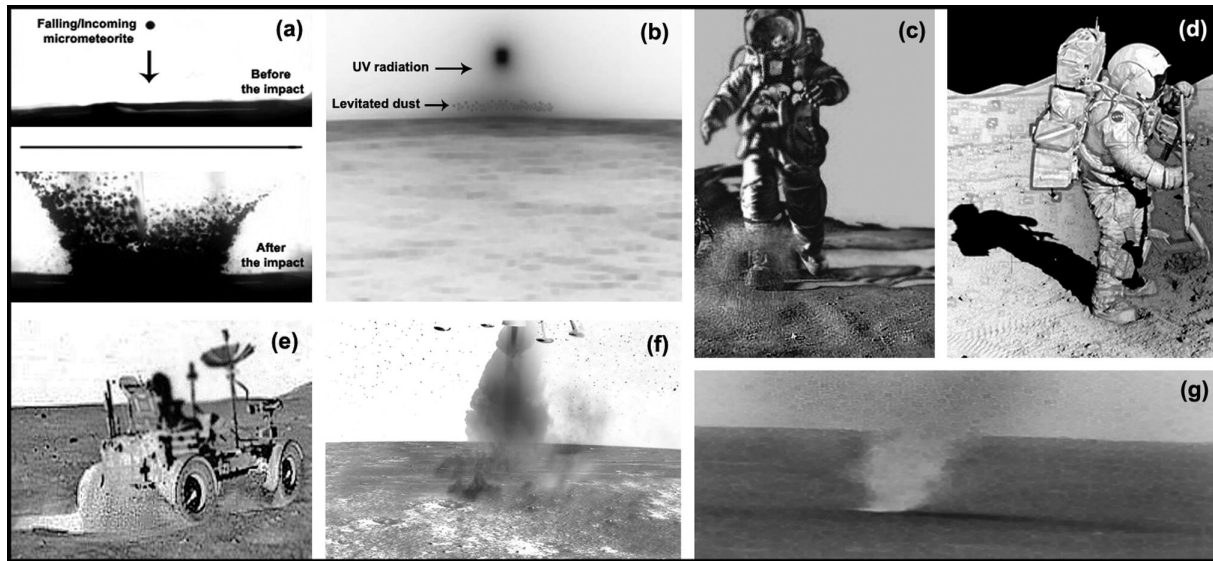


Figure 2.7: Dust transport mechanisms: (a) Lunar meteorite impacts, (b) Lunar electrostatic dust levitation, (c) walking, (d) sampling, (e) traversing with land rovers, (f) landing/launching of spacecraft and (g) Martian devil dust [172]

vapor-deposited coating of iron and nickel has been induced by space weathering on the surfaces of almost every particle of the mature soils, and to a lesser degree for the immature soils [174]. This process is generated by micrometeorite impacts, and/or sputtering due to impacting of high-energy particles, that cause the volatilization of soil grains with the subsequent condensation of this vapor as thin patinas ($< 1 \mu\text{m}$) on soil particles [175].

The Moon is often considered a static environment. However, Apollo astronauts observed that dust on the lunar surface was highly charged and adhered strongly to all surfaces. They noticed that this phenomenon was a real danger for the mission since they found dust particles even into the cabin, which produced throat irritation after inhalation. Furthermore, they indicated the existence of an unexpected glow in the lunar horizon reaching several kilometers of altitudes (ranging from 1 to 100 km) during sunrise and sunset, produced by solar light scattering of ejected dust particles, now called lunar “dust fountains” [176–179], as shown in Figure 2.6 (a) and (c) [165]. In addition, Figure 2.8 (b) shows the Apollo Commander Eugene Cernan sketches (edited) illustrating its observations [165, 179]. Rennilson and Criswell proposed that this horizon glow is induced by particles with diameters of $\sim 10 \mu\text{m}$ levitating a few cm above the surface, and the estimated concentration of particles necessary to explain this phenomenon must to be seven orders of magnitude larger than what is ejected by the impact of micrometeorites [180, 181]. Berg *et al.* 1976 deduced that the sunlight scattering induced by lunar crepuscular rays was probably caused by small dust particles with diameters of about $0.2 \mu\text{m}$ [181, 182]. In fact, estimations about the concentration of particles in the lunar exosphere has not been properly established. In 2008, Renno *et al.* estimated an average particle size of $10 \mu\text{m}$ in

concentration of 50 particles/cm³ [181]. It was also established that lunar dust particle densities ranges from 2.3 to 3.1 g/cm³ [183]. A model based on electrostatic levitation seems to be the most recognized in literature [176–180]. It suggests that, the low electrical conductivity of the regolith allows individual dust grains to retain electrostatic charge. Under sunlight exposure, dust gets positively charged as result of the photon–particle interactions caused by solar UV and X-rays, illustrated in Figure 2.8 (a) and (c), this effect is enhanced by conductivity that can increase with surface temperature, infra-red and UV radiation. While the night side charges negatively, since plasma electron-driven currents dominate at that relatively low temperature [184].

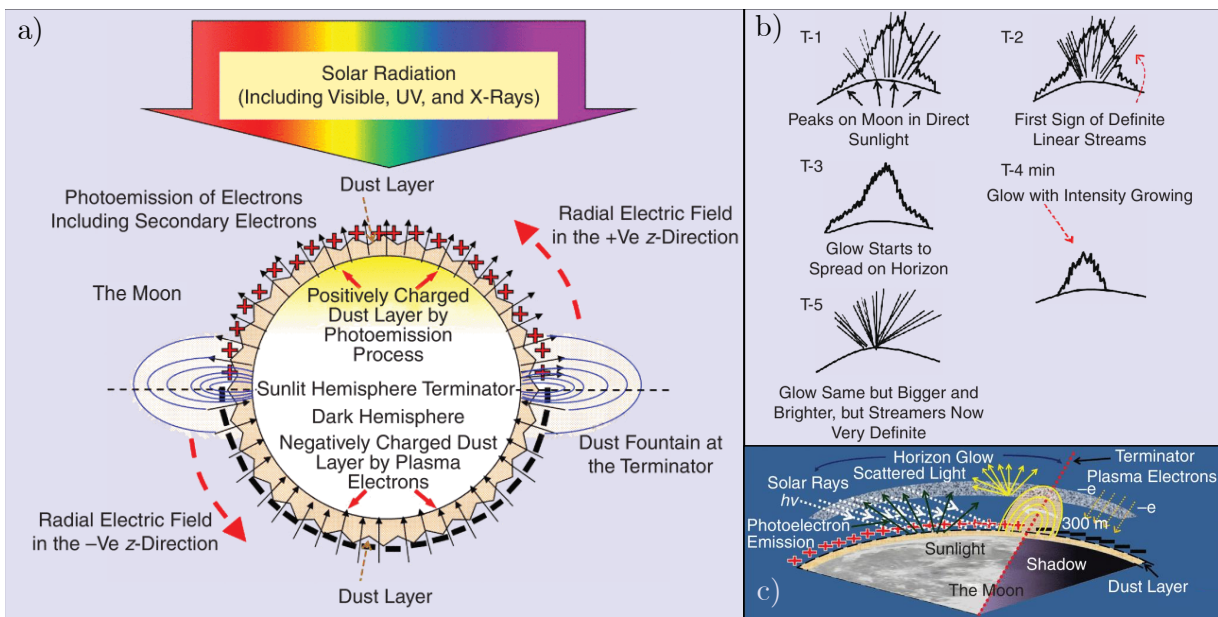


Figure 2.8: (a) Positive photoemission charging of the sun-facing lunar surface and negative solar wind electron charging at the dark regions via solar plasma electrons. The directions of the electric field lines are shown in black arrows. (b) Hand-drawn sketches by Apollo 17 Commander Gene Cernan who noticed dust streamers rising from the lunar surface during sunrise and sunset. (c) Close-up view of lunar surface dust charging by solar radiation and by plasma electrons on a thin section of the lunar surface. Images adapted from Mazumder *et al.* [165]

The sharp gradient in UV flux across the solar terminator (the boundary between day and night) may generate clouds of electrostatically-supported dust and set them into motion as the terminator moves across the Moon. Farrell *et al.*, presented a map of the complex electric fields near the lunar terminator, and developed a dust dynamic model with intense lifting electric field tending to overcome the gravitational force to give rise to vertically directed dust [185]. Even if electrostatic charging is not strong enough to release dust grains from surface adhesion, mechanical impacts from micrometeorites and impact ejecta activity may be sufficient to liberate the already charged particles. Dust accumulation and adhesion to equipment was confirmed by the examination of

several parts from the Surveyor 3 robot lander, including the optical devices. After 945 days on the Moon, the glass-cover of the camera had dust obscuring of about 25% of its surface. Johnson *et al.* proposed another dust disturbance source on the Moon attributable to landing and surface activities [186].

While several researchers have studied the lunar dust charging process, it is only partially understood and no in situ research carried out. Today, the only lunar experiment still in operation that could help us to understand the degradation process of optical devices is the Apollo Cube Corner Retroreflector (CCR) arrays experiment. After more than 50 years, it serves as a reference point in measuring precise ranges between the array and points on the Earth by using the technique of short-pulse laser ranging. The timing of the laser round trip provided evidence supporting Albert Einstein's theory of general relativity [187]. In 2010, Murphy *et al.* indicated that the rate of single photoelectron return is about a factor of ten less than the expected return rate. After evaluating different degradation mechanisms, they suggested that the substantial worsened performance comes from an accumulation of levitated dust on the front surface of the CCR over the decades [188].

2.2.2.2 Mars

The fourth planet from the Sun, Mars - also known as 'the red planet', is a dusty, cold, desert world with a very thin atmosphere. The red planet has the largest dust storms in the Solar System, varying from small area events, to gigantic storms that cover the entire planet at speeds of over 160 km/h. In 1971, the Mariner 9, the first spacecraft to orbit Mars, was unable to image the surface of the planet at all because the entire surface was obscured by a global dust storm [189]. Mars is one of the most explored bodies in our Solar System. Several types of missions as orbiters, rovers, flybys and landers have been committed to understand the evolution of Mars, most of which are powered using solar panels.

The spectrally integrated solar flux at the top of the Martian atmosphere (at a mean distance of 1.52 AU) is about 590 W/m², 43% of the amount of Earth sunlight. Moreover, suspended atmospheric dust, and dust storms scatter and absorb solar wavelength radiation, making it blue-deficient, and enhanced in red and IR compared to the orbital AM0 spectrum [190]. In addition, sunlight can be partly obscured by ground fog, dust hazes, CO₂ and water clouds. The magnitude of atmospheric dust can be quantified by the optical opacity, defined-as the optical depth τ ("tau"), which can fluctuate from less than 0.4 to values greater than 4, relative to the season, the hour of the day, the latitude, and the presence of dust storms [191, 192]. In the course of a clear Martial day of relatively low scattered sunlight e.g., $\tau = 0.4$ a 30% of the total sunlight is indirect [193]. In contrast, for a high optical depth the majority of the total sunlight reaching the surface is indirect [190, 194]. This is evidenced during prominent dust storms, which can reach a peak opacity $\tau > 6$, size area bigger than 106 km² and extend over 100 days. These storms are estimated

to happen with a yearly probability between 30% to 80% [195, 196]. Moreover, local dust storms with <1 spread out over areas $< 10^6$ km². They can last a few days and arise with 5% probability in Mars equatorial regions. Following dust storm activity, dust particles precipitate and accumulate onto surfaces, which prevent the transmission of light to PVAs, ultimately affecting its efficiency [197].

All of the Martian rovers and landers have experience sand and dust deposition. Mars environment represents a particular problem for solar cells. The Mars Pathfinder (1997) and Mars Exploration Rover missions (Spirit and Opportunity, sent in 2003) suffer a dust obscuration of solar arrays; both missions helped to characterizing the dust transport mechanisms on Mars. Newman *et al.* established a general circulation model of the Martian atmosphere. The scheme combines dust lifting, advection by model winds, atmospheric mixing, and gravitational sedimentation to determine dust fluxes and velocity vectors spatially and temporally. Wind stress lifting is predicted to peak during southern summer, largely between latitudes 15° and 35°S, with maxima in regions of strong slope winds or thermal contrast flows [138]. Based on the optical obscuration measurements (i.e., by the materials adherence experiments) on the solar array Sojourner Rover, Landis *et al.* estimated a dust deposition rate of about 0.28% during a Martian day, which represents a degradation in solar panel performance between 22% to 89%, over the course of two years [194, 198]. Moreover, dust deposition on optical devices that are typically exposed to direct high energetic solar radiation will not be detached easily. The particle size distribution and particle density for Martian dust have not been investigated thoroughly [172].

The planet has low variable temperatures, ranging from 293 to 133 K [199, 200]. This wide-ranging temperature is generated by its thin atmosphere, which cannot store much solar heat, the low atmospheric pressure, and the low thermal inertia of Martian soil. Delgado-Bonal *et al.* proposed a simplified equation to determine the operating temperature of a solar cell under Mars environmental conditions, considering convection, radiation losses and wind variations [201]. The combination of LILT produce anomalous behavior and degradation of solar cells, consequently, the selection of PV technology should take into account this phenomenon. By the fact that their consequences are moderate on Mars but are a much more treating problem at greater distances i.e., Gas Giants, LILT effects will be presented on more detail in the Section 2.2.4. Mars has not trapped radiation belts and its atmosphere is thick enough to provide effective shielding from meteors and solar protons/electrons radiation. The Martial radiation environment comprises UV radiation. Moreover, galactic cosmic radiation are not attenuated by the Mars atmosphere but the accumulated dose in solar cells is negligible [197]. Additional considerations should be taken into account to appropriately select an array technology for Mars, stresses induced during landing and the gravitational force, flexing or vibration of the arrays due to wind.

2.2.3 High temperature missions: Venus, Mercury and the Sun

Near-Sun missions have been typically solar powered. Missions where the solar intensity and temperature increase considerably, encounter a quite different challenge for PV systems, since operating under High Intensity and High Temperature (HIHT) conditions dramatically drive the behavior of solar cells. Due to the closeness to the Sun, spacecraft has been typically solar powered. They are by far the hottest places in the Solar System and understanding how a solar cell behaves in such environments is essential to future explorations. Besides the reversible loss of theoretical performance with temperature, solar powered systems encounters irreversible harms that eventually leads to the complete array damage. Including ohmic contact degradation, coverglass delamination, structural degradation and dopant diffusion [194]. Mercury has high thermal radiation and high gravity environments. Venus has a much more complex and dynamic atmosphere including variation on temperature and pressure relative to the altitude, and corrosive sulfuric acid clouds. Despite the hostile environment found by near-Sun missions, there is significant interest in developing future missions to these places.

2.2.3.1 Venus

Venus has one of the most hostile and changing environments in our Solar System. It has a mean surface temperature of 735 K [202]. It has often been described as Earth's sister because of their similar size and bulk composition. It is fundamentally different from Earth in other aspects. Venus spins slowly in the opposite direction most planets do. Its thick atmosphere mainly composed of carbon dioxide ($\text{CO}_2 \sim 96.5\%$) and nitrogen ($\text{N}_2 \sim 3.5\%$), the densest of the four terrestrial planets. It is provided by a minor quantity of noble gases (e.g., He, Ne, Ar, Kr, Xe) and reactive gases (e.g., SO_2 , H_2O , CO , H_2S) [203, 204]. The atmospheric pressure at its surface is about 92 times that of Earth. Figure 2.9 (a) represents a diagram of the mean vertical temperature profile in Venus's atmosphere, showing the major processes at work, and the approximate locations of the main cloud layers [205, 206].

The Venus orbit perceives slightly less than twice the intensity at Earth orbit ($2,662 \pm 6 \text{ W/m}^2$). Because of its high albedo, Venus absorbs on average merely $157 \pm 6 \text{ W/m}^2$, which is much more less than the deposited on Earth ($\sim 240 \text{ W/m}^2$), even if Venus is 30% closer to the Sun [207]. An opaque layer of highly reflective clouds of aqueous sulfuric acid shrouds Venus from about 45 to 70 km attitude. Spectrophotometers on-board numerous probes have measured the solar radiation field inside the Venusian atmosphere, Figure 2.9 (b) shows the data collected by *Venera-13* [207]. At altitudes below 65 km from the surface, the collected measurements provided a data set describing the spectral and angular distribution of solar scattered light in the range of 0.4 to 1.2 μm . As depth, an object enters in the atmosphere of Venus the solar intensity that this perceives decrease as the

spectral absorption of clouds (near-infrared and blue-end) due to the high concentrations of CO₂ and H₂O increase. These clouds reflect and scatter about 90% of the sunlight at the top of the atmosphere, preventing its surface from being seen from space in visible light. And only about 2.5% ($\sim 17 \text{ W/m}^2$) is absorbed at the ground, all this supporting ground-based near-infrared observations [207].

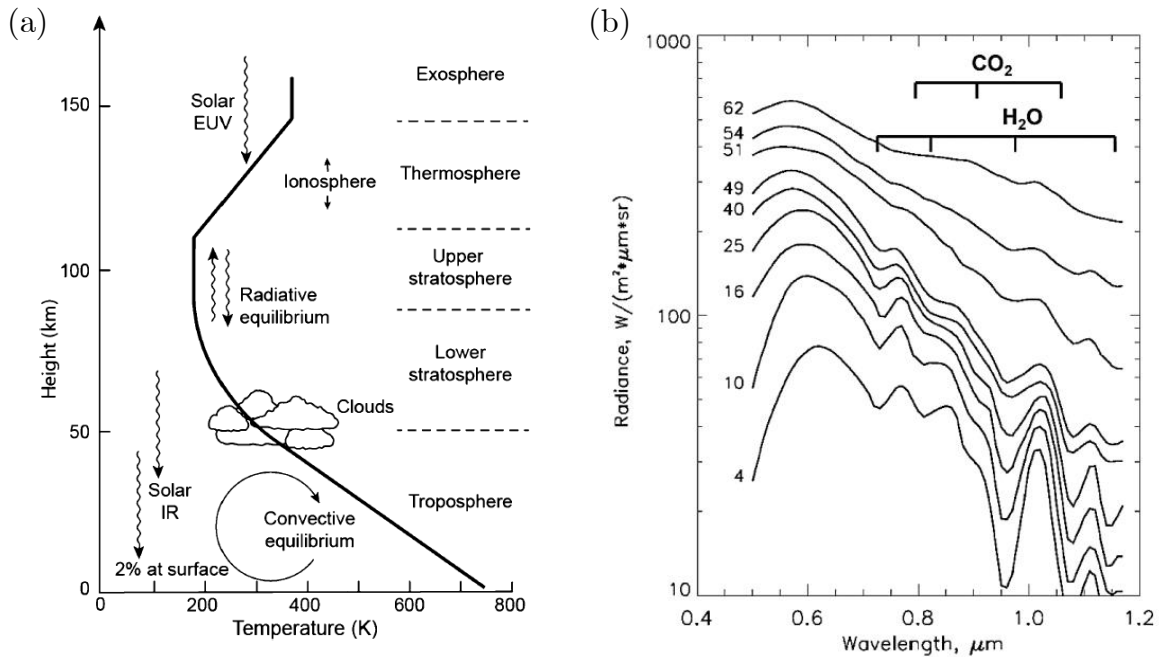


Figure 2.9: (a) Mean vertical temperature profile in Venus’s atmosphere [205, 206]. (b) Spectra of the downward scattered solar radiation measured by the *Venera-13* descent probe. Lines are labelled with probe altitude, in km (at right) [207].

Recently, Taylor *et al.* conducted a brief overview of the Venusian environment and all spacecraft missions, successful and unsuccessful, with relevant information [205]. Cutts *et al.* provided additional information, summarizing several mission characteristics (e.g., temperature, pressure, mass, mission altitude, etc.) and their impact on spacecraft subsystems [203]. Proposed missions include landers, high- and low-altitude balloons, orbiters and microprobes. While short-lived missions could be designed using batteries, long-lived *in-situ* missions require external or internal power sources, such as solar panels or Radioisotope Power Systems (RPS). At high altitudes above the clouds (~ 60 to 65 km from the surface), balloons, airplanes and hybrid vehicles can be used to study the Venus atmosphere and in a restricted manner its surface. There the environmental conditions are similar to Earth (0.01 to 0.1 MPa, and 223 to 203 K), which simplify technological considerations, and state-of-practice solar arrays can be implemented, assuming that a proper encapsulation system is used against the acidic environment [203, 208]. At lower levels, from medium to low-altitude Venus aerial missions should

include technical improvements: high temperature (from 473 to 623 K) and variable pressure, low intensity (50-300 W/m²), corrosive environment and need to be optimized to operate under a downward-scattered solar spectrum, shown in Figure 2.9 (b) [207]. Encapsulation against corrosion by sulfuric acid must be integrated; for example, both glass and Teflon encapsulation are robust against sulfuric acid [209].

Recently, Landis *et al.* proposed a simplified model of photovoltaic performance in the Venus environment, for both the surface and the atmospheric probes (at altitudes from the surface up to 60 km) [209]. The study combined the temperature and intensity dependence of the open-circuit voltage and the temperature dependence of the bandgap and spectral response of the cell as a function of altitude. Different solar cell technologies (e.g., 3J- GaInP₂/GaAs/Ge, 2J- GaInP₂/GaAs/ and 1J- GaAs) were analyzed in order to establish which type of solar cell is most efficient for operation at Venus. Some conclusions are: (a) Outer the atmosphere, 3J has the highest efficiency, nevertheless, the Ge subcell cuts off at temperatures from 473 to 523 K and, the top GaInP₂ subcell becomes blue-light limited at the Venus surface. (b) Against expectations, the 2J and 3J cells outperform (in a very similar manner) the single-junction GaAs at lowest altitudes. The GaInP₂ junction experiences a shift of bandgap induced by the temperature, allowing the subcells to perform until the surface. However, it becomes the current-limiting junction very near the surface and the higher voltage of the GaInP₂ junction slightly outweighs the restriction of current. (c) The bottom Ge junction on 3J cells shuts down at about 30 km above the surface, and yet above this altitude the performance of 3J exceeds the achieved by the 2J and the single-junction GaAs cell). Finally, as the performance of 3J and 2J cells were identical below the 30 km no performance reason exists for choosing one instead of the other. Grandidier *et al.* established the promising performance of 2J GaInP/GaAs under high temperature, no degradation in IV response was measured after brief exposure to a temperature of 738 K [208].

2.2.3.2 Mercury

The smallest planet in our Solar System and nearest to the Sun has a significant and apparently global magnetic field, strong enough to deflect the solar wind around the planet, creating a magnetosphere. It is thought that this magnetic field is generated by a dynamo effect [210]. Provided by almost no atmosphere to retain heat, Mercury has surface temperatures that vary diurnally more than on any other planet in the Solar System, fluctuating from 100 K at night to 700 K during the day across the equatorial regions [211]; while Polar Regions are constantly below 366 K. It is the least explored inner planet in the Solar System, until date the only missions that have made close observations were the Mariner-10 and MESSENGER (i.e., MErcury Surface, Space ENvironment, GEOchemistry, and Ranging) missions, both have been solar powered. Solar power arrays for Mercury

are designed to guarantee a severe operational environment, mainly characterized by high temperatures and high light intensity (up to 11 solar constants, or 15 kW/m^2), due to the vicinity of planet Mercury to the Sun. To mitigate these extreme boundary conditions the solar arrays are typically rotated to a position off-pointed. Even so, they can produce enough energy to power the spacecraft and the solar electric propulsion, while it helps to slow down the degradation of the solar cells, which naturally occurs over time. Additionally, optical solar reflectors are included to balance the temperature of the array [212].

Mariner-10 collected information about the Mercurian atmosphere, from airglow to measurement of gases (e.g., H, He, and O) made by the on board UV spectrometer [213, 214]. Furthermore, data allowed probed that Mercury is exospheric down to the surface, since it has an upper limit for the gas density of about 10^6 cm^{-3} [176], already predicted in 1970 by Banks *et al.* [177]. Launch in 2004, the MESSENGER spacecraft was designed to study the characteristics and environment of Mercury from orbit [215]. The solar array was composed of two deployed single-panel wings ($1.5 \times 1.65 \text{ m}^2$ each). The custom-settled panels were 67% mirrors (called optical solar reflectors) and 33% using 3J solar cells ($3 \times 4 \text{ cm}^2$), 0.14 mm thick, with a minimum efficiency of 28% [216]. The coverglass on each cell is 0.15 mm thick cerium-doped microsheet, with magnesium fluoride anti-reflective coating, it is bonded to the cells with standard DC-93500 transparent adhesive. The panel substrates are 18 mm thick aluminum honeycomb with composite facesheets. To decrease the thermal panel absorbance, each panel has two rows of mirrors for every row of cells; the small mirrors reflect the Sun's energy and keep the panel cooler. In addition, thermal control is achieved by tilting the panels from normal incidence, to assure a normal surface operating temperature of about 423 K. Radiation damage is expected to be predominantly caused by solar flare protons. The estimated total dosage with 0.15 mm microsheet coverglass is 4×10^{14} equivalent 1-MeV/cm² electrons. To demonstrate the survivability and validate the thermal analysis, panels were tested in vacuum over a temperature range from 143 to 543 K thermal cycling from 143 to 423 K in nitrogen environment, using a 353 to 373 K/min rate to mimic the thermal shocks expected at Mercury eclipse exit. They were tested at 11-suns intensity illumination [216]. In addition, tests to evaluate high-intensity UV degradation in vacuum were conducted, CICs were exposed to 5-suns UV radiation at 423 K, for 4,200 hours. The UV degradation was asymptotic and less than 4% [215].

In October 2018, a third mission to Mercury was launched, BepiColombo, a joint mission between the ESA and the Japan Aerospace Exploration Agency (JAXA), expected to arrive in late 2025. BepiColombo was designed to complement the findings of MESSENGER [217]. During the development, JAXA researchers evaluate the durability of 3J (InGaP/GaAs/Ge from Sharp Corp.) with an efficiency of 28.3% at Beginning-of-life (BOL). Several test were performed on a number of different CIC samples, operating under extreme HIHT conditions from 2.2 to 9 suns and 366 to 503 K for an expected life of one Earth year.

HIHT tests indicated that coverglass transparency do not degrade, however, a significant degradation on the transmittance of DC-93500 adhesive, due to UV exposure at high temperature was measured. Thus, AR0213 coverglass from JDSU with a thickness of 300 μm was used, which have longer cut-on wavelength, estimating a decrease in P_{MAX} on a 17.3%. Results indicate that a change in the coverglass thickness from 100 to 300 μm reduces the radiation degradation from 15.9% to 11.0% [218]. Stall *et al.* developed a model for the UV degradation experienced in the MESSENGER (about 10 years) mission. Based on this model, most of the degradation resulted from UV induced degradation and high temperatures [219]. Silicone coloring must be consider, especially when using bulky optics. Additionally, the cosmic radiation fluence was calculated for the solar proton spectrum around Mercury, equivalent to 10-MeV protons.

2.2.3.3 Solar Orbiters

The Sun, is a nearly perfect sphere of hot plasma, with internal convective motion that generates a magnetic field via a dynamo process. Accounting for about 99.86% of the total mass of the Solar System, it is composed mostly of hydrogen ($\sim 73\%$), the rest is mostly helium ($\sim 25\%$), with much smaller quantities of heavier elements, including oxygen, carbon, iron and neon [220]. The Sun has a variable environment that includes solar flares, coronal mass ejections of charged particles and the solar wind. It is then important to have a better understanding of how the Sun interacts with spacecraft systems. Whereas the Sun is not physically explorable with current technology, several solar observation probes have been designed and launched to operate in heliocentric orbit or at one of the Earth–Sun Lagrangian points (i.e., point at which the gravitational pull from both is equal); most of them have been solar powered. For missions in the Sun vicinity, the solar intensity rises to 100 suns at 0.1 AU, until 2,500 suns at 0.02 AU, thus, the relative temperature reached at these places can be a threat for spacecraft component and will generate loses in the power generation capability due to loss in the power generation. Therefore, the development and implementation of thermal shielding is required to enable the majority of the spacecraft systems and instruments to operate in a typical space thermal environment. As it will be shown, several technological solutions are implemented to limit the spacecraft temperature, including array tilting, mirrors on the surface to reduce absorptivity and increase emissivity, specific array shapes, silvered coverglass, louvers and so on [221].

The plasma environment near-Sun is expected to be severe, due to the solar wind that is increasing in density when approaching the Sun, which in combination with energetic charged particles produce an intense radiation environment causing both spacecraft charging effects and radiation damage in materials and electronics. Furthermore, the combination of high concentration of solar wind particles and the elevated UV-flux damages spacecraft materials. Inducing changes in the thermo-optical properties of the materials.

For that reason, during the thermal design, conservative values of the properties should be used, such as for the absorption and emissivity. To minimize the effect of this environment the use of organic materials must be avoided [222]. Brandhorst *et al.* shown that solar cells with high band gap behave better for near-Sun missions [223], as shown in Figure 2.10, for distances superior to 0.5 AU, the effective output power has no substantial effect. However, for distances between 0.5 and 0.1 AU a significant improvement can be achieved. In contrast, for missions closer than 0.1 AU solar cells become impractical. For all cases, it was assumed that the cell temperature is limited to 1273 K.

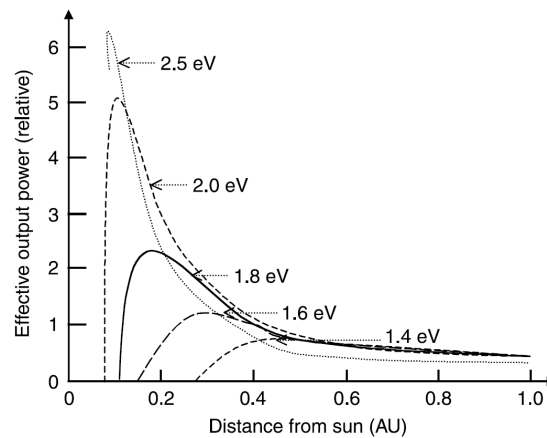


Figure 2.10: The distance from the sun versus power output of PV cells of various band gaps [1, 223].

A brief review detailing some solar probes made until date, using solar cells, will be presented. The aim is to analyse missions with different orbits, PV concepts and strategies to enhance the usage of PV for solar exploration, having a better understanding of the environmental conditions and the needs for future PV developments. The first long term mission designed to study the Sun from interplanetary space were NASA's Pioneers 6 to 9, launched during the 1960's into heliocentric orbit. These probes orbited at a distance similar to that of Earth, studying the positive ions (cations) and electrons in the solar wind, the interplanetary electron density (radio propagation experiment), solar and galactic cosmic rays, and the interplanetary magnetic field [224]. Spacecraft were spin-stabilized 0.94 m diameter by 0.81 m tall cylinders using solar panels mounted around the body with an average efficiency of 10.5% (AM0) operating between 0.8 and 1.2 AU. Each cell is 1 x 2 cm² covered by a 0.15 mm coverglass for radiation protection.

In the 1970s, Helios 1 and 2 probes collected significant data about the processes that cause the solar wind and the acceleration of the particles that make up the interplanetary medium, cosmic rays and cosmic dust between Earth and Sun. The major technical challenge for designers was to manage the heat issue, when the spacecraft Helios has a perihelion of 0.3 AU from the Sun (into heliocentric orbit); it perceives about 11 suns or

22.4 kW/m². Under these conditions, the probe can reach temperature of about 643 K however, the solar cells are not allowed to exceed 438 K and the central compartment of instruments must be maintained at much lower temperatures between 263 and 293 K [225]. This means that 96% of the heat received from the Sun must be rejected from the body of the probe. The Helios's PVA consisted on solar cells attached to two truncated cones, giving the assembly the appearance of a diabolo. In order to keep the solar panels at a temperature below 438 K 50% of the surface were covered with so-called "second surface mirrors" made of fused quartz, with a silver film on the inner face; reflecting part of the incident sunlight while dissipating the excess heat. In fact, the conical shape of the PVA was one of the methods taken to reduce the flow of heat. By tilting array with respect to sunlight arriving perpendicularly to the axis of the probe, a greater proportion of the solar radiation is reflected.

The Solar and Heliospheric Observatory (SOHO), is a project of international collaboration between ESA and NASA to study the Sun, observing all the way from its internal structure (i.e, helioseismology) out to the solar corona and the solar wind [226][188]. The SOHO solar array is composed by two solar wings, of two panels each. The solar cells used are back surface reflection silicon based, with dimensions of 37.8 x 63.8 mm² and a thickness of 210 μm. It uses a CMX coverglass 100 μm thick and silver cell interconnections 20 μm thick. During the mission, the array was expected to have a maximum cell temperature of 328 K. At the begin-of-life, SOHO's PVA had an efficiency of 13.2%, generating 1400 W power, and it expected a power margin end-of-life of 10%, with a predicted radiation 5×10^{13} MeV/cm², additionally, a loss factor of 0.92 was assumed to consider UV/micrometeorite losses, cell mismatch, and calibration error [227]. Brekke *et al.* studied the space weather on SOHO and estimated a 13.8% degradation due to proton events after 80 months in space. For an annual average degradation of 2.01%, well within the 4% per year requirement [228]. Rumler *et al.* estimated the predicted decrease of the working point current to 73% of the initial value for a radiation of 1×10^{15} MeV [227].

Launched in 2018, the Parker Solar Probe mission will be the first spacecraft to fly into the low solar corona. During the 7-year nominal mission, seven Venus gravity assist maneuvers and 24 heliocentric orbits, it will assess the structure and dynamics of the sun's coronal plasma and magnetic field, the energy flow that heats the solar corona and impels the solar wind, and the mechanisms that accelerate energetic particles [221]. Surfaces of the spacecraft exposed to the Sun will experience about 475 suns (649 kWm⁻²), at minimum perihelion (0.0459 AU). Therefore, the thermal system uses louvers, surface treatment, blanketing, and heaters. It integrates a hexagonal shield, mounted on the sun-facing side of the spacecraft, made of a carbon-carbon composite/carbon foam sandwich, and an alumina coating, designed to withstand temperatures outside the spacecraft of about 1643 K. Each of the two solar array wings has a primary and secondary section with a

fixed cant angle between the two sections, for a total area of 1.54 m². A primary array is used when the mission is outside 0.25 AU, otherwise, it is retracted behind the shadow shield during the close approach to the Sun; it uses cells similar to those used during the MESSENGER mission to Mercury. A much smaller angled-secondary-array powers the spacecraft through closest approach; it uses pumped-water through channels in a titanium platen to maintain operating temperature of the array and instrumentation.

2.2.4 LILT conditions: Gas Giants

2.2.4.1 Jupiter

As the most massive world in our Solar System, Jupiter is 11 times wider and 300 times more massive than Earth. Its mean distance from the Sun is about 5 AU, so it receives $\sim 3.7\%$ AM0 (50W/m²), running into LILT conditions. Jupiter is orbited by about 80 known moons, including the four large Galilean moons Io, Europa, Ganymede and Callisto [229]. Unlike the icy rings of Saturn, Jupiter's rings are composed largely of dust particles, likely kicked up as micrometeoroids smash into the planet's four small inner moons. The composition of Jupiter is similar to that of the Sun - mostly hydrogen (about 86%) and helium, its deep atmosphere probably contains hundreds of layer of cloud, each with a different composition. However, only the top three layers have actually been observed, containing trace amounts of methane, water vapor, ammonia, and silicon-based compounds [230]. Deep in the atmosphere, an increase in temperature and pressure compress the hydrogen gas into a liquid that behaves like an electrical conductor [231]. It is believed that a dense core of heavy elements may exist in this extreme environment. Jupiter's enormous magnetic field, nearly 20,000 times as powerful as Earth's field, which combined with the fast rotation of the planet, rotation period ~ 9 h 55 min, create an exceptional magnetosphere. The Jovian magnetosphere has a tadpole shape (shown in Figure 2.11); it traps swarms of charged particles - electrons and ions, creating a hazard for visiting spacecraft. Solar cell arrays near to this gas giant will encounter a combination of high-radiated milieu and LILT conditions. In the past, missions to outer planets have been typically powered using RTG since they can function in environments with limited or no sunlight [232]; including the Pioneer and Voyager programs, Galileo, Cassini and Ulysses missions. In fact, most of them were flyby missions, except for Galileo and Cassini, which were the first mission to orbit around Jupiter and Saturn, respectively. Nowadays, solar arrays have been successfully demonstrated in outer planet exploration. The Juno spacecraft, developed by NASA, was the first solar-powered spacecraft to travel as far as the orbit of the Jovian planet (5 AU) [233]. Inserted into orbit around the gas giant in July 2016, Juno has been measuring the planet's environment with dedicated particle and fields instruments, illustrated in Figure 2.11 [233]. In addition, ESA is also developing a

solar-powered Jupiter mission, JUPiter ICy moons Explorer (JUICE), slated to launch in 2022 [234, 235]. A major technical challenge for solar-powered outer planet missions involves the operation under LILT conditions. The increased distance to the Sun results in reduced incoming sunlight that naturally decreases the photo-generated power, while the low temperature usually improves the voltage. These LILT conditions produces anomalous effects and degradations that are partially understood and can vary from one solar cell technology to another [56, 236]. Initial solar cells under LILT conditions demonstrated sensibility to electrical shunts (current leakage), rear contact Schottky barrier formation, and suffered from the so-called “flat spot” or “broken knee”. Figure 2.12 illustrates I-V characteristics of these degradations, as well as a solar cell under normal behavior [237]. Shunting caused by p-n defects could become a very noteworthy fraction of the cell current output at low intensities; they can be measured under room temperature and reduced by improving the manufacturing process.

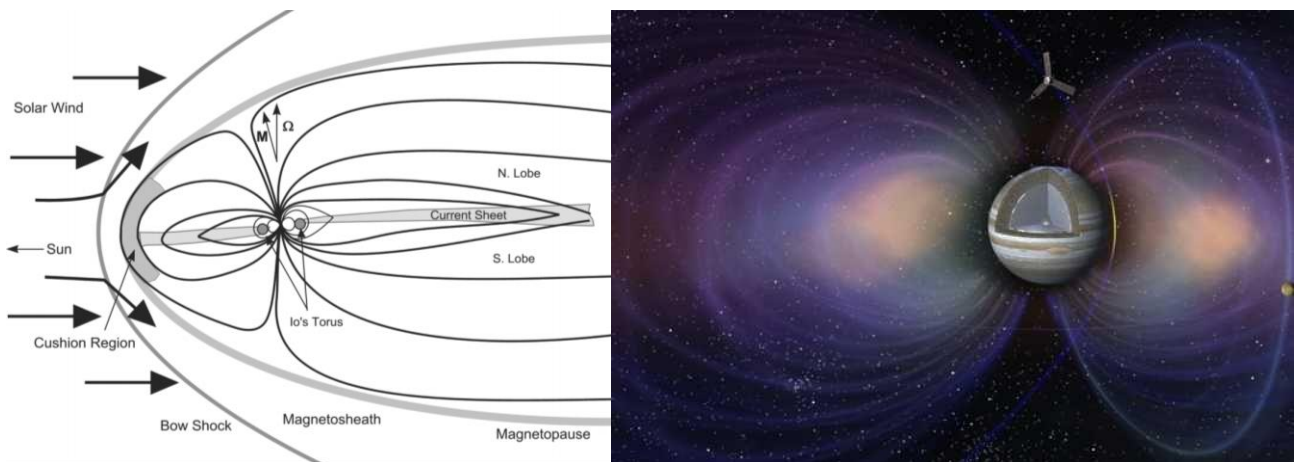


Figure 2.11: Jupiter’s magnetosphere schema showing the noon-midnight meridian (left), by Khurana *et al.* [238]; Illustration of NASA’s Juno spacecraft taking an orbit over Jupiter’s poles, ducking under the radiation belts, and skimming over the clouds (right), published by Bolton *et al.* [233].

In 1981, Weizer V.G *et al.* identified the flat spot degradation mechanism that typically generate a truncation of the maximum power knee in I-V characteristic, it was suggested to be due to a resistive metal-semiconductor-like interface junction between the front side metallization and the top sub-cell; attributable to localized metallurgical interactions [239]. The effects of thermal treatment, crystallographic orientation, junction depth, and metallization were established. Furthermore, experimental data indicates the effectiveness of a TiN diffusion barrier in preventing the vacancy formation at the free surface of the contact metallization. This phenomenon was initially observed in silicon, however, it has also been observed in state-of-the-art high efficiency MJSC. Flat spot unpredictably appears and causes a drop of the cell electrical performances (i.e., Fill Factor (FF)) at low

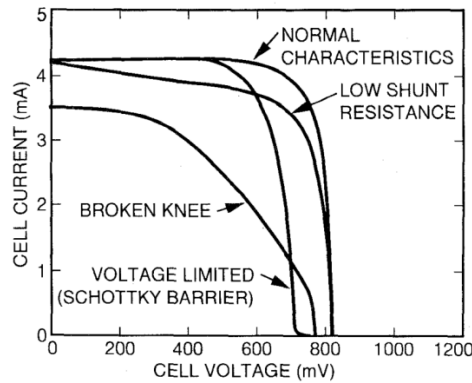


Figure 2.12: Examples of LILT degradations, published by Stella *et al.* [237].

temperatures (below 193 K), and its effects are only detectable at low temperatures [240].

Nowadays technological improvements reduce and prevent these undesirable degradations. A substantial number of ground-based studies have been already performed mostly to space-qualified solar cells under Jupiter conditions, at 5.2 to 5.5 AU irradiances and 133 K to 123 K temperatures. In particular, UTJ cells from Boeing Spectrolab Inc., which is the current state-of-practice solar cell for LILT conditions, powering the Juno spacecraft [3]. UTJ lattice-matched 3J cells demonstrated BOL average efficiencies of $\sim 28\%$ under standard test conditions of 1 AU 301 K and $\sim 30\%$ at Jupiter conditions. Other related technologies include, ZTJ from SolAero Technologies Corp., which is baselined for the planned Europa Clipper mission [241]; and 3G28-LILT from Azur Space, which is baselined for the upcoming JUICE mission [234, 235]. Furthermore, these architectures were recently tested for the Saturn environment (9.5 AU and 108 K), demonstrating promising results [242, 243].

The huge and complex Jovian magnetosphere was first inferred from observations of radio emissions at the end of the 1950s and was directly observed by the Pioneer 10 spacecraft in 1973 [244]. The Magnetosphere of Jupiter is usually categorized into three major regions [238]: (1) the inner magnetosphere found at < 10 Radius of Jupiter (RJ) (where $1 \text{ RJ} = 71,492 \text{ km}$) where the principal magnetic field is induced by the Jovian internal sources. Outside of this region, the magnetic field lines are stretched in the radial direction by the effects of an azimuthal current sheet in the equatorial plane. (2) The middle magnetosphere is situated between 10-40 RJ and is the region where the equatorial currents flow. Lastly, (3) the outer magnetosphere ($> 40 \text{ RJ}$) region where the magnetic field has a large southward component and changes in the solar wind pressure can cause big temporal and/or spatial variations in magnitude and direction. Electrical currents in the Jupiter's outer core, composed of liquid metallic hydrogen, induce the internal magnetic field at the planet. Jupiter's fast rotation and volcanic material from Io's moon eruptions encourage the magnetic field to push against the solar wind even further, giving to the magnetosphere colossal dimensions [230]. The large amounts of sulfur dioxide gas emitted by Io into space,

forms a large torus (located between the radial distances of ~ 5.2 and ~ 10 RJ), which by magnetic field forces rotates with the same angular velocity and direction as the planet [238], see Figure 2.12. As consequence, the torus loads the magnetic field with plasma (~ 1 ton/s), stretching it into a magnetodisk structure that contributes shaping the Jovian magnetosphere, which finally traps and accelerates particles producing intense belts of radiation, similar to Earth's Van Allen belts. In contrast, the Earth's magnetosphere is shaped by the solar wind and it is thousands of times weaker than at Jupiter.

The radiation belts within this giant is one of the most harmful regions in our Solar System, trapping charged particles of extreme energies and fluxes. It generates synchrotron radiation from highly relativistic electrons spiraling in Jupiter's magnetic field, with energies up to tens of MeV [245, 246]; which can be seen remotely using radio telescopes and provide us a global picture of the most intense part of the belts [247]. Additionally, ultra-relativistic protons (i.e., ~ 100 GeV) can be trapped near the planet, above 50 times higher in energy than at Earth [247, 248]. At the inner radiation belts, Jupiter contains electrons with energies higher than 50 MeV [249, 250]. Several initiatives have emerged in order to establish trapped particle models applied to Jupiter, for protons (e.g., *Salammbô* [251], D&G83 [252], JOREM/JOSE), electrons (e.g., *Salammbô*, D&G83, JOREM/JOSE, GIRE) and heavy ions (e.g. JPL-HIC, JOREM/JOSE). They use various energy ranges at different coordinates, even though, the description of these models is out of the scope of this review. (*Office National d'Etudes et de Recherches Aéronautiques*) (ONERA) researchers developed a three-dimensional model called: *Salammbô*, that will allow us to illustrate the omnidirectional integral electron fluxes, it predicts the existence of particles exceeding the 100 MeV; as shown in Figure 2.13 [251].

Recently, ESA researchers have performed an extensive qualification status of the solar cells to be used in the JUICE mission, under LILT conditions, in order to determine reliable BOL and End-of-life (EOL) performances [234]. On its cruise to Jupiter the satellite will make a flyby near Venus, so it will be exposed to both, hot temperatures and high sun illumination, as well as very cold temperatures and low sun illumination; from 413 to 123 K and < 53 K during Jupiter eclipse. Three principal activities were carried out: (1) a qualification test program in line with ECSS-E-ST-20-08 [253], using different solar cell variants AZUR SPACE Solar Power GmbH, 80 and 140 μm thick. (2) Test the vulnerability of the PVA against potential degradation because of primary discharges when a nonconductive coverglass is used [254]. Finally, (3) the coupon test campaign to estimate the thermal cycling survival of PVA. The electrical elements were checked during the cycling for continuity and an insulation check (cells vs. substrate). In general, the test demonstrates a significant confidence in most of the electrical elements [234].

Flat spot unpredictably appears and causes a drop of the cell electrical performances (i.e., fill factor) at low temperatures (below 193 K). Furthermore, it was demonstrated

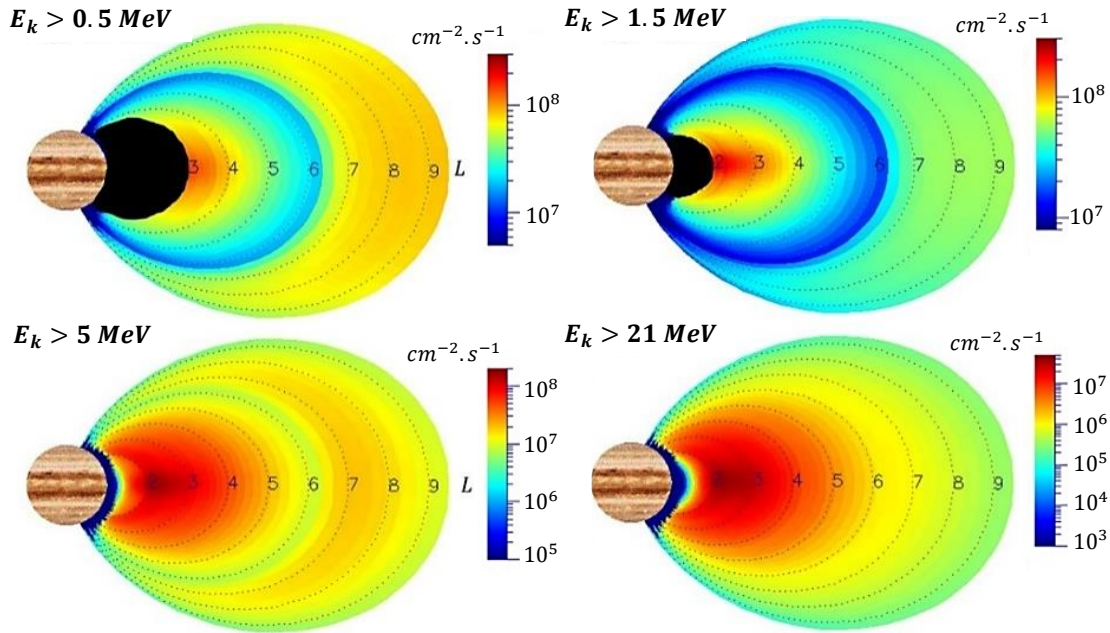


Figure 2.13: Omnidirectional integral electron fluxes predicted by the *Salammbô* model in a magnetic meridian plan. The black areas show where *Salammbô* cannot predict fluxes, because of the minimum in the energy grid [251].

that some standard cell designs for space applications did not show any flat spot effect [240]. Khorenko *et al.* addressed the subject establishing a test procedure for defining the EOL of 3G28 (80 μm thick) state-of-the-art cells from AZUR SPACE, with 33.5% efficiency at BOL [235]. By *in-situ* IV measurements (at 3.7% AM0), it was demonstrated that cells degradation after irradiation ($3e^{15} \text{ cm}^{-2} \text{ 1 MeV}$ electrons) at low temperature (123 K) is stronger for P_{MAX} cell, than it is for the I_{SC} and Open-circuit voltage (V_{OC}) values. They evidenced a strong recovery effect, of about 6% within short time (± 10 min) after irradiations at the same low temperature, show in Figure 2.14.

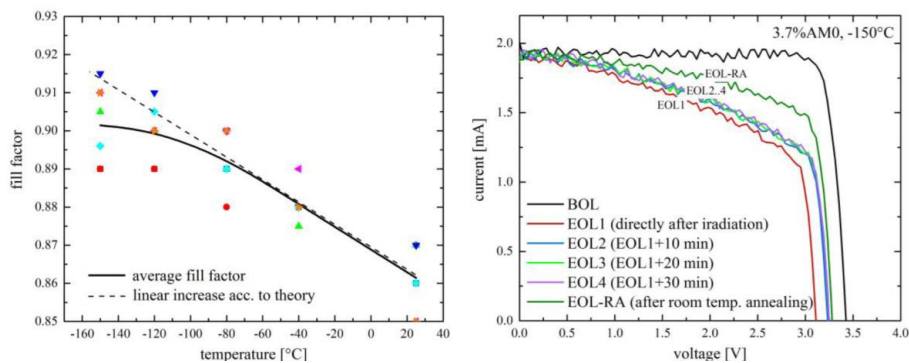


Figure 2.14: Temperature dependence of the fill factor at 3.7 AM0 (left). BOL/EOL IV characteristics recorded directly after irradiation and after keeping the cell at LILT conditions for different time (right), by Khorenko *et al.* [235].

Furthermore, an enhancement of 12% was measured after the cell annealing at room

temperature conditions, as expected. In addition, as the absolute value of the P_{MAX} recovery depends on the irradiation fluence and particle type, they evaluated the recovery for different electron ($5e^{14}\text{cm}^{-2}$, $1e^{15}\text{cm}^{-2}$, $2e^{15}\text{cm}^{-2}$) and proton ($1e^{11}\text{cm}^{-2}$, $2e^{11}\text{cm}^{-2}$, $4e^{11}\text{cm}^{-2}$) fluences. Under the same environmental conditions Park *et al.* demonstrate that the significant degradation of P_{MAX} (respect to I_{SC} and V_{OC}) was induced by the existence of an apparent “shunt effect”. They provided a physical explanation to this phenomenon, and established that it is directly related to an increase of the dark current after the irradiation, induced by a tunneling carriers taking place in the top and bottom sub-cells [212]. It was concluded that *in-situ* measurements of solar cells are necessary to determine a realistic prediction of EOL at LILT, by establishing the remaining factors for electron and proton irradiation. Finally, the corresponding annealing coefficients should be defined for avoiding expensive and time-consuming irradiation tests at low temperature. Nowadays solar cells minimized the degradation induced by LILT conditions [255, 256].

2.2.4.2 Galilean Moons

Jupiter is orbited by a quartet of planet-sized worlds, the Galilean moons, in order of increasing distance from Jupiter we find – the volcanic Io covered by frozen sulfur dioxide, the icy Europa and rock-ice Ganymede and Callisto, which makes the Jovian system a miniature Solar System in its own right; they are illustrated in Figure 2.15 [257]. Several spacecraft have flown close to the Jupiter moons, most of them have been RTG powered. During 8 years in the Jovian system, Galileo spacecraft gathered a large amount of information, finding evidence for thin atmospheres on three of them, as well as the possibility of liquid water beneath the surfaces of Europa, Ganymede, and Callisto. It also discovered a magnetic field around Ganymede.

Volcanic moon: Io

Io is the most geologically active object in the Solar System, having hundreds of active volcanos, some of which blast lava 400 km out into space [241, 258]. Volcanic eruptions create effusion of lava, long distance lava flows (tens to hundreds of kilometers), lava lakes, fire fountains, as well as explosives plumes of sulfur (upward as high as 300 km) [259]. Io has a very thin atmosphere made up mostly of sulfur dioxide SO_2 , with minor constituents including sulfur monoxide (SO), sodium chloride (NaCl), and atomic sulfur (S) and oxygen (O) [260]. The maximum atmospheric pressure varieties from 0.03 to 0.3 mPa, but fluctuates significantly with respect to the volcanic activity, time of day, latitude, and surface frost abundance [261, 262]. Io’s atmospheric temperature ranges based on altitude, with temperature on the surface and low altitudes averaging 110 K with a minimum of 90 K and a maximum of 130 K [263]. The hottest areas, covered by

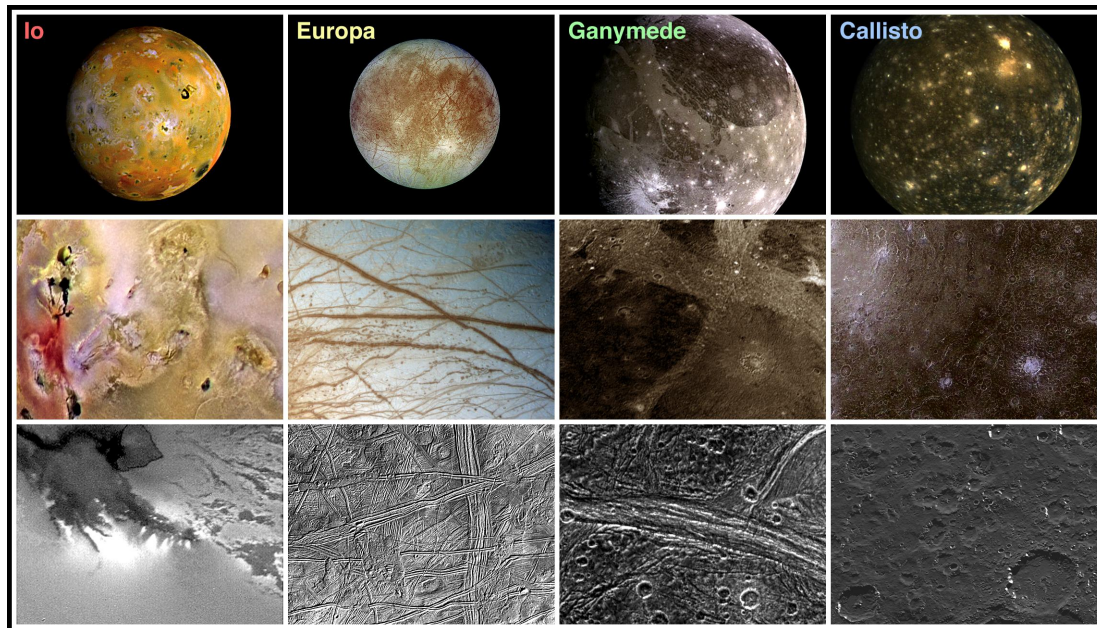


Figure 2.15: Galilean moons mosaic, including images taken by NASA’s spacecraft (i.e., Galileo and Voyager’s mission). From left to right, Io, Europa, Ganymede, and Callisto moons. The top row displays the relative sizes of the moons in global views at relatively low resolution (10 km per picture element – pixel). Surfaces are affected by tectonic or volcanic changes in the moons’ interiors or by exterior deposition. Middle row images (1,000 x 750 km²). Regional features include volcanic caldera fields on Io, tidally-induced cracks thousands of kilometers long on Europa, bright grooved regions on Ganymede, and enormous impact basins on Callisto caused by impacts with primitive comets or asteroids. Bottom row views (100 x 75 km²) show Io’s volcanic plume vents, Europa’s abundant ridges, Ganymede’s fractured, grooved terrain, and Callisto’s heavily eroded and mantled craters. Credit: NASA/JPL/DLR [257].

lava flows, reach elevated temperatures up to about 1973 K thus the average temperature at these places is about 300 K due to the tenuous atmosphere density which does not keep the heat of the Sun and volcanoes. As soon as the gases are expelled from volcanoes, these gases freeze and condense [261, 264].

While Io orbits Jupiter always pointing the same side toward the giant planet, the large moons Europa and Ganymede disturb Io’s orbit into an irregularly elliptical one. Consequently, in its widely changing distances from Jupiter, Io is subjected to tremendous tidal forces, which produce an incredible amount of heat within Io, keeping much of its subsurface crust in liquid form [260]. This process constantly renews the surface of Io and fill any impact craters with molten lava lakes and spreading smooth new floodplains of liquid rock. The surface composition of Io is not yet completely clear, some theories advocate that it is largely molten sulfur and its compounds (which would explain its colorful appearance) or silicate rock (that could better account the apparent temperatures, too hot to be sulfur) [265]. Photometric and colorimetric observations established that Io is the reddest object in the solar system and has a marked color variation with orbital

phase angle [266]. Data from the Galileo spacecraft indicates that Io is provided by its own magnetic field since it has molten iron or iron sulfide core. Near Io, the Jovian magnetic field strength is 1,835 nT. During the Io flyby, the Galileo magnetometer measured a drop of 695 nT in the wake of Io [267].

Icy Galilean Satellites: Europa, Ganymede, and Callisto

The outer Galilean moons, referred to as the “Icy Galilean Satellites” present quantities of water ice on their surfaces, spectroscopically detectable, making them unique places with respect to terrestrial planets that have exteriors mostly covered by silicate [268]. Europa’s surface seems to be almost pure water ice, with an apparent minor signature of sulfur on the trailing hemisphere measured in the UV spectrum [269]. Ice abundance estimations have been established for the surface of Ganymede suggesting a weight percentage range from around 33% to 90%, depending on whether a segregated [270] or a mixture of the ice and other components, respectively [271]. In the same way for Callisto, estimations suggest an ice weight percentage on the surface layers vary from 4% for a segregated surface [269], and up to 90% for an intimate mixture of the ice with dark materials [270]. However, these worlds have different internal composition structures, appearances and interact differently with the Jovian planet, making their environments quite different.

Europa moon has the smoothest identified surface in the Solar System, revealing crisscrossed by long, linear fractures, and a fresh surface with very few impact craters, as shown in Figure 2.15. Evidence indicates that a liquid water ocean underneath the unknown thickness of icy surface that remains liquid by tidal heating [272], which could provide an environment suitable for life due its interaction with a volcanic seafloor. Moreover, the density amount of small (< 3 km diameter) craters on Callisto is less than on Ganymede, the contrary for larger (> 10 km diameter) craters [273]. Regarding this unexpected difference on the craters size between the two moons, it looks as if the formation of small craters on Callisto are by some erosional process. Some authors suggest that this erosion process is driven by sublimation of CO_2 , while others propose ammonia ice [274].

A strong intrinsic magnetic field was measured within Ganymede (750 nT), in addition, data from three Galileo flybys shows that Callisto has a distinct magnetic field signature that responds inductively to Jupiter’s time-varying magnetic field, the same phenomena was observed for Europa [275]. The Earth-orbiting Hubble Space Telescope detected atomic oxygen airglow in the UV spectra, for Ganymede and Europa, suggesting the presence of a tenuous atmosphere with a molecular oxygen column density of 10^{14} to 10^{15} cm^{-2} and scale height of a few hundred kilometers or less [276]. A while later, scientists using the Hubble collected evidence supporting that Europa poses plume eruptions, first detecting the chemical elements hydrogen and oxygen, constituents of water (H_2O) in plume-like configurations in Europa’s atmosphere, and then they snapped photos of finger-

like projections that appeared in silhouette as the moon passed in front of Jupiter [277]. Ground-based observations detected an even more vague sodium atmosphere outspreading at 25 radii of Europa, indicating that material is escaping from Europa's atmosphere [274]. In fact, dissimilarities between Voyager and Galileo plasma and reflectance data, and the many years of International Ultraviolet Explorer reflectance data, all suggest that short-term variability is happening in some form on the icy satellite surfaces and in their atmospheres. Incident particle radiation at the Galilean satellites modifies the surface chemically (radiolysis), by physical damage (amorphization) and by the ejection of atoms and molecules (sputtering or desorption). Radiation damage, sputtering and radiolysis are closely related. Johnson *et al.* described the effects caused by incident particle radiation (energetic ions and electrons) on the Galilean moons, and their intimate dependence with the Jovian magnetosphere [278]. Considering the plasma (i.e., ions and electrons below about 10 keV) and the energetic particles (i.e., > 10 keV), it was shown quantitatively how a number of spectral characteristics of the surfaces of the Galilean satellites are likely determined by radiolysis and photolysis processes of satellite materials that alter the volatility of the surfaces and affects the composition of their atmospheres. At Jupiter, the plasma almost co-rotates with the planet, constantly overtaking the Galilean satellites in their orbital motion. In consequence, cold plasma ions and electrons that compose the plasma bulk run especially on the hemisphere trailing the satellite's motion [278]. Energetic electrons, which represent the majority of the incident energy from irradiation (e.g., $> 75\%$ [279, 280]), but are lower in density, bombard the satellite in more complicated ways by making the access of electrons to a given surface location dependant on particle energy, along with the background electromagnetic fields. In that context, high energetic electrons, which have small gyroradii and travel rapidly along the magnetic field compared with the co-rotation speed of the plasma, principally bombard the equatorial, trailing hemisphere [281]. In contrast, energetic protons and other ions, instead, are expected to bombard the surface much more uniformly due to their comparatively slow bounce times in Jupiter's magnetic field and large gyration radii relative to the size of the moons [282]. Thus, the common finding of "bull's-eye" patterns, as illustrated for the surface of Europa in Figure 2.16. Showing that the majority of electrons are of sufficiently low energy to be carried by Jupiter's magnetic field, and are deposited on the trailing hemisphere, whereas the more energetic electrons (> 20 MeV) experience a net retrograde motion resulting in deposition on the leading hemisphere [280, 281].

Cooper *et al.* established the incident energy fluxes and direct irradiation effects of energetic ions and electrons in the magnetospheric radiation environments near Europa, Ganymede, and Callisto [279]. They used Galileo Orbiter measurements of energetic ions (20 keV to 100 MeV) and electrons (20–700 keV) in Jupiter's magnetosphere [283], in conjunction with the JPL electron model (< 40 MeV), to calculate irradiation effects

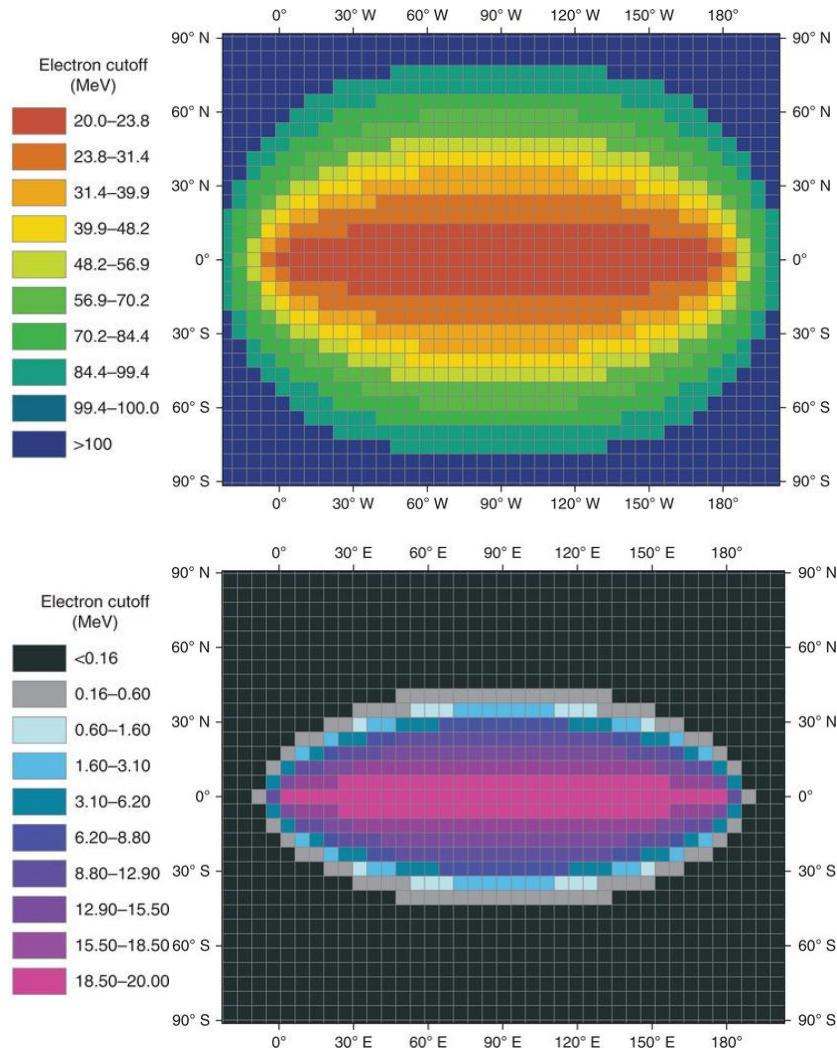


Figure 2.16: Energetic electron bombardment patterns for the surface of Europa. At the leading hemisphere, the cut-off energy represents the lowest energy electrons capable of accessing a region on the surface (above). At the trailing hemisphere, the cut-off energy represents the highest energy electrons (below) [280].

dependent on penetration depth, implantation of stopping particles, and local erosion by ion sputtering. Figure 2.17 shows the ion and electron flux spectra acquired near the orbits of each satellite, including measurements for three ion species, H^+ , On^+ , Sn^+ (n^+ refers to the unmeasured charge states) and electron components. The electron spectra are shown both from Energetic Particles Detector (EPD) and from the model spectrum (DG-83) [252]. The model electron spectrum, and the EPD ion spectra, are used for dosage calculations. (a) Europa during the Galileo Orbiter’s E4 encounter. (b) Ganymede during the Galileo Orbiter’s G2 encounter. (c) Callisto from the Galileo Orbiter’s C3 encounter. For more detail information regarding specific assumptions, fittings, sampling times and locations can be found in the manuscript that we strongly suggest [279].

Spencer J. R. investigated the temperature distribution of the three icy Galilean moons,

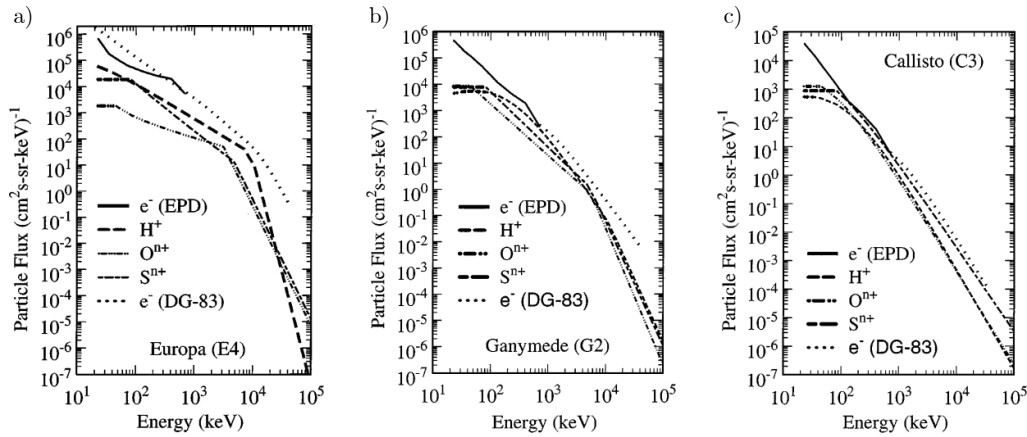


Figure 2.17: Particle flux spectra collected by the EPD on-board Galileo spacecraft to measure the magnetospheric environment at the orbits of Europa, Ganymede, and Callisto [283], published by Cooper *et al.* [279].

as they were saw by the spacecraft Voyager 1 and 2 (resume in Table 2.4). Results shown a strong anti-correlation between albedo and temperature, in fact the magnitude of the temperature variations is consistent with the variation in absorbed sunlight, assuming that surface thermal inertia is constant with albedo [268]. The global distribution of effective temperature was established for each icy satellite, not a trivial issue, since different factors should be taken into account. One of them is the local temperature can fluctuate following: a) Albedo variations, high-albedo regions will be colder than dark regions at all times of day. b) Thermal inertia variations (high thermal inertia materials (e.g. rocks) will tend to be colder during the day than low thermal inertia materials (e.g. dust), with the reverse being true at night. c) Topography, a shadowed region will be cooler than those tilted towards the Sun. More detailed information can be found on the Spencer's dissertation manuscript [268].

Table 2.4: Equatorial Effective Temperature Distributions [268].

Equatorial Effective Temperature Distributions (K)						
Satellite	S/C	Max.	(Time)	Sunset	Midnight	Sunrise
Europa	V2	-	-	91	-	-
Ganymede	V1	140	(210)	107	94	-
Ganymede	V2	147	(190)	105	94	-
Callisto	V1	156	(190)	< 89	80	-
Callisto	V2	158	(180)	-	-	75

V1: Voyager 1, V2: Voyager 2

The maximum daytime temperatures on Ganymede and Callisto are about 147 and 158 K respectively. Night-time temperatures are warmest on Ganymede in the early part of the night than Europa or Callisto. Orton *et al.* studied the thermal infrared measurements (Galileo's spacecraft) [263]. Results have shown a maximum brightness

temperature of about 152 K found shortly after noon in the equatorial portions of “Galileo Regio” at Ganymede, comparable to that measured by Voyager (397 K) [263, 268], which drops from 90 to 94 K at night [284].

2.2.4.3 Saturn

Saturn is the sixth planet from the Sun and the second largest in the Solar System, after Jupiter. The planet’s most famous feature is its prominent icy rings. The Kronian system is composed by more than 80 known moons, including Enceladus with cryovolcanoes that jet water vapour, and Titan, one of the most Earth-like worlds with a dense atmosphere. Saturn takes about 29 Earth years to orbit the Sun (a Saturnian year), and Saturn’s axis of rotation is tilted as Earth’s, resulting in seasons. Similar to Jupiter, Saturn is made mostly of hydrogen and helium. Saturn has a pale yellow hue due to ammonia crystals in its upper atmosphere [285]. Moses *et al.* estimated that Saturn is currently collecting a global average of 10^{-16} g cm⁻² s⁻¹ of exogenic material (i.e., micrometeoroidal material flux) [286]. Wind speeds on Saturn can reach 1,800 km/h, higher than on Jupiter. Currents in the liquid metallic-hydrogen layer are thought to generate the Saturn’s planetary magnetic field (one-twentieth of Jupiter’s), which is weaker than the Earth’s, but has a magnetic moment 580 times that of Earth due to Saturn’s larger dimension [287]. The size of Saturn’s magnetosphere increases and decreases based on solar wind pressure, generally 21–27 Saturn radii (1 Saturn radius = 60,268 km) at the shortest point between Saturn and the Sun.

Until now, all missions to Saturn and its moons have been powered by a RTG systems, including Pioneer 11 and Voyagers 1 and 2. These missions helped to show that Saturn’s plasma consists of hydrogen, water-group, and/or nitrogen ions. Then, the Cassini spacecraft launched in 1997, measured in depth the Kronian system thanks to the 13 years mission, becoming the first human-made object to orbit Saturn in 2004. After the mission, the understanding of neutrals, plasma, and their interactions became even more complex, it was found that the primary source of water group ions is electron impact or photo-ionization of the E-ring material and the neutral cloud produced by the Enceladus plumes [288]. The extremely wide E-ring is a diffuse disk of microscopic icy or dusty material distributed between the orbits of Mimas and Titan moons. Figure 2.18 shows the average equatorial plasma/electron temperatures and densities as a function of radial distance from Saturn for light ions (“H+”), water group ions (“W+”) the core electron population (“e”), and the hotter electron population (“hot e”) [288].

The scientific community views solar power as a potential source to fuel spacecraft [9]. In comparison to Jupiter, the charged-particle radiation environment at the Kronian system is relatively benign, with typical mission concepts having total-dose requirements on the order of only 2×10^{14} 1 MeV e⁻/cm² [243]. Nevertheless, at Saturn the LILT

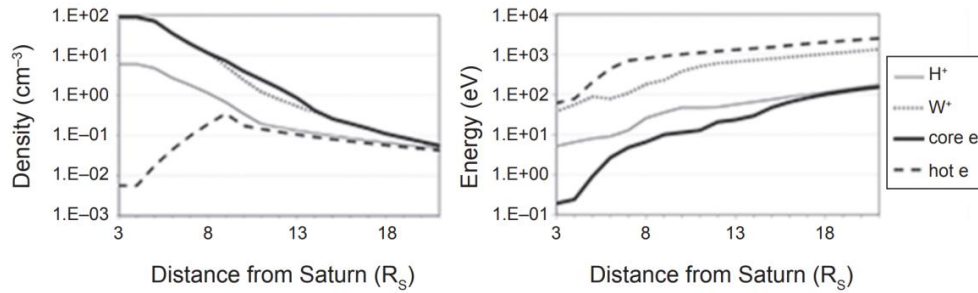


Figure 2.18: Average equatorial plasma/electron temperatures (eV) and densities (cm^{-3}) as a function of radial distance from Saturn (R_S) for light ions (“ H^+ ”), water group ions (“ W^+ ”) the core electron population (“ e^- ”), and the hotter electron population (“hot e^- ”), from Smith *et al.* [288].

conditions represent a factor of three lower in irradiance, as well as lower temperatures, about 15 W/m^2 (at 9.5 AU) and 108 K. Therefore, an appropriate PVA for Saturn missions must to be especially immune to LILT degradation effects covered in Section 2.2.4.

In 2017, Boca *et al.* characterized three solar cells technologies under Saturn LILT laboratory conditions [242]. Clearly, the expected power production at Saturn would be very low due to the incident irradiance, 1.1% of that near Earth. However, these 3J cell technologies are found to have viable efficiencies at Saturn, in the range of ~ 30 to 34%, which was higher than their 1 AU 301 K efficiency. Besides, the investigation showed that brief exposures to 423 K have no measurable effect on later power production at LILT. This means that Venus fly-bys gravity assist (often included), which induce off-nominal conditions, pose minimal risk to the performance of the cells at Saturn. An additional result was that Low Intensity and Room Temperature (LIRT) screening yields for Saturn are comparable to those for Jupiter missions, based on a relatively small sample size (36 cells in total). Meaning that their illuminated I-V curves had fill factors of > 0.77 under 5.5 and 9.5 AU 301 K test conditions. Furthermore, telemetry from the Juno spacecraft, acquired during a Jupiter orbit insertion maneuver, which represents Saturn-like environmental conditions of temperature and irradiance, was used to provide an independent validation of the ground test data. It was then concluded that solar cell technologies are viable for use in flight missions to Saturn-system destinations. Nonetheless, it should be noted that the PVA efficiency is expected to be slightly lower than the efficiency of single bare cells being tested in the lab, because of numerous losses, from voltage and current mismatch, coverglass reflectance and darkening, micrometeoroids, contamination, thermal cycling, and charged-particle radiation. Researchers assumed that these account for an aggregate 94% loss factor in the case under consideration. Recently, promising results were found using CIC samples based on upright metamorphic 3J – UMM3 design from Spectrolab. For UMM3, the efficiency at 9.5 AU 108 K BOL was $35.4\% \pm 1.2\%$, which is a performance improvement over all SoP-architecture cells that we have evaluated under Saturn conditions [243].

2.2.4.4 Kronian Moons: Two Emerging Worlds

After the Cassini-Huygens mission, two emerging worlds have gained importance, Titan and Enceladus moons, revealing Titan’s organically rich environment and Enceladus’ active cryovolcanism. Titan and Enceladus are identified as highly relevant science themes in the roadmaps of space agencies as ESA and NASA [289, 290]. In the last decade, the exploration of ocean worlds in the Solar System has exhibited a ‘boom’ with the selection of ESA’s JUICE and NASA’s Europa Clipper missions to the Galilean moons. This fact is evidenced by the recent selection of the Dragonfly mission as part of the NASA’s New Frontiers program, to explore Titan using a mobile robotic rotorcraft lander [291]. Studying these ocean worlds will expand our present knowledge about the Solar System, its formation, evolution and likelihood that other habitable environments exist outside the Earth’s biosphere.

Enceladus moon

The brightest world in the Solar System, Enceladus, is a small icy moon of about 500 km in diameter, orbiting at about 4 Saturn radii [292]. This ocean world is mostly covered by fresh and clean ice, making it the most reflective surface body in the Solar System, reflecting $\sim 80\%$ of the sunlight that it intercepts. As a result, its surface temperature varies from about 50 K at night to 80 K during the day (at low latitudes) [293]. Cassini revealed that it is the only known icy world in the Solar System with ongoing deep-seated geological activity [294]. At Enceladus’s South Pole, four fissures (so-called “tiger stripes”) expel geyser-like jets water vapour, other volatiles, and ice particles from the underground ocean [295]; as shown in Figure 2.19. These cryovolcanoes are powered by internal tidal flexing [292], and the following water-rich plumes are thought to be the long-suspected source of particles making up Saturn’s E- ring [296], and also the neutral torus of Saturn [297]. Moreover, they are the dominant source for neutrals and plasma in Saturn’s magnetosphere, even in the outer magnetosphere near Titan, where ionization products from Enceladus (primarily O+) are the dominant heavy species. Figure 2.19 (b) shows the current understanding of Saturn’s primary particle source rates, illustrating how Enceladus is a dominant magnetospheric source; compiled in 2018 by Smith *et al.* [288].

At Enceladus, the gas plumes are principally water vapor, plus about 5% CO₂, 1% CH₄, 1% NH₃, and minor amounts of many heavier hydrocarbons and organic molecules, with vent production rates ~ 200 kg/s [292, 296]. The plumes particles contain about 1% of salt (mainly NaCl), overall particle flux is ~ 50 kg/s; with an estimated median radius of the equivalent-volume sphere of about 3.1 μm and a total mass of particles in the plume of $(1.45 \pm 0.5) \times 10^5$ kg [298]. It is likely that most of the gas escapes Enceladus, however, only a small portion of ejected particles material (about 5 – 10% by mass) are launched fast

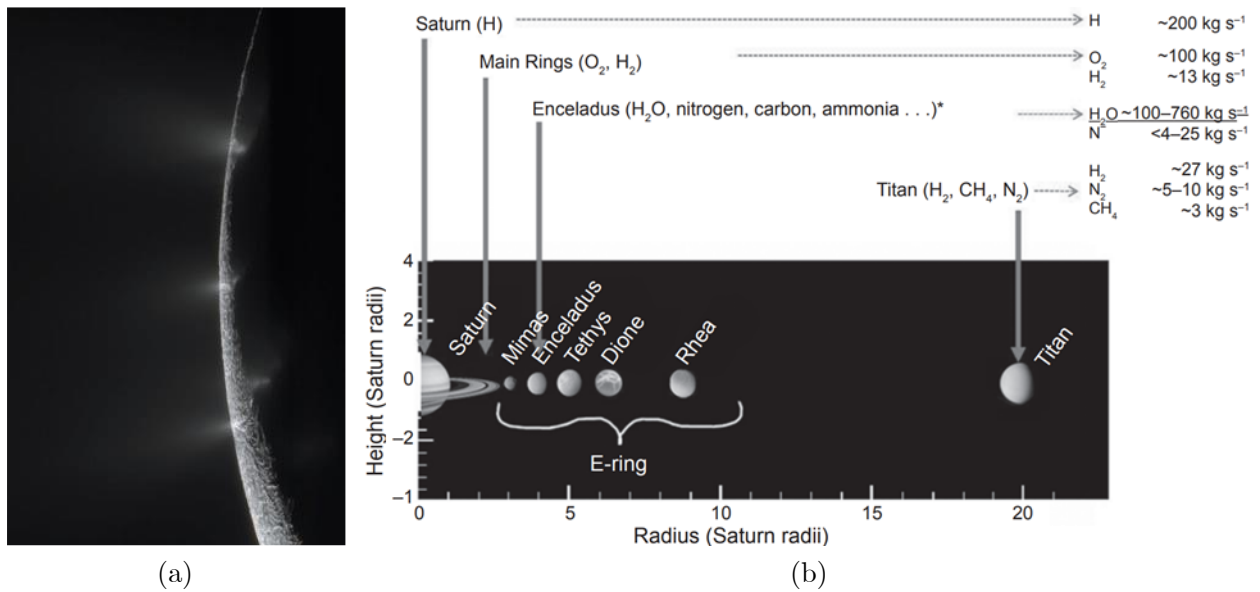


Figure 2.19: (a) The particle plume jets of Enceladus, from the tiger stripes (from below) Cairo, Baghdad, and Damascus, rising into sunlight, taken on August 13, 2010 by the Cassini cameras. Credit: NASA/JPL/Space Science Institute. (b) Current estimates of Saturn’s primary magnetospheric particle source rates, published by Smith *et al.* [288].

enough to exceed the escape speed at Enceladus (240 m/s) and populate the E-ring (these particles have an average lifetime of ~ 8 years in the ring [298]). Thus, most of the icy grains (the larger and more salt-rich ones) fall back and redeposit onto the surface, estimations suggest that the deposition rate is 0.5 mm/year close to the vents, and $10 \mu\text{m}/\text{year}$ at certain regions north of the equator assuming compact ice deposition (density $\approx 0.9 \text{ g/cm}^3$) [299, 300]. Due to interactions with Saturn’s gravity, the plumes’ deposits are broad below 45°S , splitting into two patterns centered at $\sim 45^\circ\text{W}$ and $\sim 225^\circ\text{W}$, respectively. Generally, expelled water molecules can interact with electrons, ions, and solar photons or simply return to the surface of Enceladus. Smith *et al.* summarized some of these processes and its influence on the local and global magnetospheric environment [288].

Krupp *et al.* studied the data from 14 flybys of Cassini at Enceladus (2005–2010), and summarized the results of energetic electron measurements in the energy range 27 keV to 21 MeV taken as low as 25 km above the surface [301]. It was found that that the spacecraft was connected to the plume material along field lines prior entering the high-density region of the plume. In addition, there are regions along the spacecraft trajectories where the electron intensity drops partially in the so called “ramp-like” depletion features followed by full intensity dropouts in the low-energy electron measurements [301]. Farrell *et al.* demonstrated that the “dusty” environment surrounding Enceladus has a profound effect on the local plasma environment, comprising the absorption of electrons entering at the outer edge of the moon-surrounding dust envelop, and a substantial slowing of the originally co-rotating plasma at this dust interaction region [302].

Titan moon

Saturn's largest moon, Titan, with a radius of 2,575 km is the second biggest moon in the Solar System after Ganymede, and the only one with a dense atmosphere. To complete a full orbit around Saturn, Titan takes 15 days and 22 hours. Cassini performed 127 close flybys of Titan, and discovered that it has clouds, rain, lakes and rivers of liquid hydrocarbons, as well as a subsurface ocean of salty water. While in 2005, the Huygens probe detached from Cassini became the first probe to land in the outer solar system.

Titan consists principally of ice and rocky material; its interior may still be hot enough for a liquid layer composed of water and ammonia between the ice crust and deeper ice layers made of high-pressure forms of ice [303]. The presence of ammonia allows water to remain liquid even at a temperature as low as 176 K as it creates forms a eutectic mixture with water. It is the only world besides Earth that has standing bodies of liquid, including seasonal weather patterns with wind and rain [304]. Considering its liquids (both surface and subsurface) and robust nitrogen atmosphere, Titan's methane cycle is analogous to Earth's water cycle, at the much lower temperature of about 93 K

The lack of an intrinsic magnetic field at Titan leads to a direct interaction of the plasma environment with its ionized atmosphere [305]. Titan orbits Saturn at an average distance of 20 radii. Therefore, it spends most of its time in Saturn's partially corotating magnetospheric flow, which is not static in response to variations in the solar wind dynamic pressure. The variability of Titan's magnetic environment implies that the moon is sometimes inside the magnetosphere of Saturn, and at times outside of it, making it fully exposed to the solar wind [306]. Titan's atmosphere is primarily composed of nitrogen ($\sim 97\%$), methane ($\sim 2.7\%$), and hydrogen ($\sim 0.2\%$) with minor amounts of other gases and carbon-rich compounds [307].

Solar UV radiation, high-energy particles accelerated in Saturn's magnetic field, solar wind, and galactic cosmic rays split apart these molecules and lead to the formation of a variety of organic chemicals (constituents based on carbon and hydrogen), and often include nitrogen, oxygen and other elements important to life on Earth. The Solar UV tends to rule the energy input at lower altitudes $\sim 1,200$ km and extend down to about 400 km, while the plasma interaction from Saturn's magnetosphere and solar wind are more relevant at higher altitudes $\sim 1,400$ km [308]. At the same time, heavy ion plasma (O^+) ~ 5 keV and energetic ions (H^+) ~ 30 keV or higher from Saturn's magnetosphere can penetrate below 950 km.

Cosmic rays with energies > 1 GeV can penetrate much deeper into Titan's atmosphere with most of its energy deposited ~ 70 km altitude. Some of these recombined compounds produce a kind of smog- a thick, golden, hazy atmosphere that completely obscures Titan's surface and that makes the moon's surface difficult to view from space. These haze layers are found in scattered solar photons from 510 km, but aerosols are widely spread and

measured in extinction from 1,000 km downward, diffusively separated to 400 km.

Sittler *et al.* summarized various energy sources found at the upper atmosphere of Titan, which were measured by Cassini spacecraft or modelled, as presented in Table 2.5 [308]. These estimates ignore the insulating effect of Titan’s induced magnetosphere against, for example, magnetospheric electron access to Titan’s ionosphere. The table does show that charged particle energy inputs can dominate all other energy input processes including solar UV.

Table 2.5: Titan upper atmosphere energy sources [301, 308, 309].

Energy Source	Energy Flux (erg/cm ² /s) ^e	Global Input (Watts) ^d	Comments
Plasma protons	1.6e-4	3.4e7	Magnetized
Plasma electrons	1.6e-4	3.4e7	Magnetized
Plasma heavy ions	1.5e-3	3.2e8	Unmagnetized
Energetic ions	5.0e-4 to 1.0e-2	1.05e8 to 2.0e9	27 < E _p < 255 keV ^a
Energetic electrons	2.0e-4	4.0e7	28 < E _e < 533 keV ^{a,b}
UV airglow	1.6e-3	3.5e8	Altitude ~ 1,300 km ^c
UV ionization	1.6e-4	3.4e7	Altitude ~ 1,300 km ^c
Galactic cosmic rays	1.6e-4 to 2.7e-3	3.2e7 to 5.4e8	Integrated flux
Dust	1.8e-3	1.8e8	Interplanetary dust
Ohmic heating	-	-	Not yet known

^a Model by Ledvina *et al.* [309] show some magnetic channeling of 50 keV protons. If heavy ions (O+) unmagnetized. Expect energetic electrons to be more magnetized than protons.
^b Energetic electron energy flux derived from Krupp *et al.* [301].
^c For T0 encounter at 90° phase angle UV absorption peaked at 1,325 km, while for TB encounter at 0° phase angle absorption peaked at 1,095 km altitude.
^d Exobase at r ~ 4,000 km and 4π area ~ 2e¹⁸ cm² .
^e Note that 1 eV = 1.6 e-12 erg = 1.6 e-19 J

Enceladus and Titan are certain to make them two of the most scientifically interesting destinations for pursued exploration as a potential habitat for life [310]. As Titan and Enceladus hold the prospect of hosting biosignatures, it is imperative that future missions will require planetary protection. In addition, an Enceladus orbiter is a further level up in complexity and cost to study the south polar plumes, because the moon has a very small gravity and is very close to Saturn, polar orbits would be unstable [311]. Making the plumes difficult to measure. Lunine *et al.* summarized target mission concepts and some considerations for future exploration of Enceladus and other Saturnian moons [311].

2.3 Analysis and discussion

We have reviewed the nature of the specific requirements that must be addressed for the successful application of PV generation in space. In this regard, Table 2.6 and Table 2.7 summarize the principal environmental conditions for space exploration of several celestial bodies in the Solar System (described in Section 2.2), affecting the

conversion efficiency and durability of solar power generation, according to the literature and worldwide national strategies for the planetary sciences. The requirements to address these mission concepts have several unique needs, based on the destination and mission type, solar irradiance levels, expected mission lifetimes, temperature range, as well as several specific characteristics of their own environment as radiation, chemical compounds, gravity, pressure, dust, among others.

Table 2.6: Synthesis of environmental conditions (part 1).

Celestial object	Mission Type	Solar Irradiance (W/m ²)		Mission Life (years)	Temperature Range (K)	Environment	Ref		
		A*	P						
Sun	SOHO Orbiter L1	13,660 0.01 (AU)	1,394 0.99 (AU)	> 10	-	<ul style="list-style-type: none"> • Extreme HIHT conditions • Solar wind, flares and corona ejections • Charged particles 	[220-228]		
	Parker Orbiter HC	2,563 0.73 (AU)	649,000 0.046 (AU)	> 7	1,643	<ul style="list-style-type: none"> • Proton 1x10¹⁵MeV/cm² (SOHO 8-years) • Dust • High UV-flux 			
Mercury	Orbiters	6,271	14,448	> 10	143 to 543	<ul style="list-style-type: none"> • Almost no atmosphere • Extreme HIHT conditions • Magnetosphere • Protons solar flares radiation 4x10¹⁴MeV/cm² • High UV-flux • High gravity environment 	[213-219]		
	Lander				80 to 380 85°N, 0°W			100 to 699 0°N, 0°W	
Venus	Orbiters	2,576	2,646	> 10	103 to 523	<ul style="list-style-type: none"> • No magnetic field • Variable temperature and pressure • HIHT and LIHT conditions • Sulfuric acid clouds < 65km • Extreme LIHT conditions • Corrosive super-critical CO₂ • High pressure (9.2 MPa) • Volcanic plains ~ 40 % of the surface 	[202-209]		
	Aerial > 50km	> 250		> 4	350 to 573				
	Aerial < 50km	50-300			473 to 623				
	Lander	<5		<0.5	738				
Earth's Moon	Orbiters 50km	1,323	1414	> 10	74 to 340	<ul style="list-style-type: none"> • Negligible magnetic field and atmosphere • Micrometeoroid (10 nm to 1 mm diameter; and speed of 10-72 km/s) • Solar wind and flares • Galactic cosmic rays 	[163-171]		
	Landers			> 10	98 to 348			<ul style="list-style-type: none"> • Dust adhesion and transport • Possible solar spectrum scattering induced by "dust fountains" 	
Earth	LEO Orbiter (320-2000km)	1,322	1,413	3 to 10	153 to 393	<ul style="list-style-type: none"> • Atomic Oxygen 10¹⁵ atoms/cm²s • UV radiation • Thermal cycling • Micrometeoroid & debris impact • Protons radiation from solar events • Plasma - spacecraft Charging 	[125-132]		
	MEO Orbiter (2000-35786 km)			10 to 15	93 to 393			<ul style="list-style-type: none"> • Electron and protons radiation induced by Van Allen belts 1x10¹⁶MeV/cm² • Solar events • Plasma • UV radiation • Thermal cycling • Micrometeoroid & debris impact 	[134, 136, 137, 143]
	GEO Orbiter >35786km			> 15	93 to 393			<ul style="list-style-type: none"> • Solar Flare Protons • Electron, protons and UV radiation • Plasma - spacecraft charging • Thermal Cycling • Micrometeoroid & debris impact 	[149-154]
Mars	Orbiter	491.7	715.9	> 15	251 to 191	<ul style="list-style-type: none"> • Atmosphere (95 % CO₂, 3 % N) • UV radiation • Atomic Oxygen • Dusty environment (huge and long storms) • Moderate LILT conditions • Solar spectrum scattering (from dust, CO₂ and water ice clouds) • UV radiation • Thermal Cycling • Winds (50 m/s at 5 m from the surface and 3 m/s on it) 	[189-201]		
	Landers Rovers			> 5	133 to 293				
	Aerial vehicles			> 5					

Distances: Aphelion (A), Perihelion (P). Sun-Earth First Lagrangian point (L1); Heliocentric (HC); High Irradiance High Temperature (HIHT); Low Intensity Low Temperature (LILT), Low Intensity High Temperature (LIHT); UltraViolet (UV)

Table 2.7: Synthesis of environmental conditions (part 2).

Celestial object	Mission Type	Solar Irradiance (W/m^2)		Mission Life (years)	Temperature Range (K)	Environment	Ref		
		A*	P						
Jupiter	Flyby/Orbiter	45.9	55.7	>15 CR: 3–6 SP: #flybys	93	<ul style="list-style-type: none"> LILT conditions High energetic particles Electrons fluence $3 \times 10^{15} \text{ MeV}/\text{cm}^2$ Proton fluence $2 \times 10^{11} \text{ MeV}/\text{cm}^2$ 	[230-240]		
Europa moon	Flyby/Orbiter			>13 CR: 3–6	93	<ul style="list-style-type: none"> LILT conditions Intrinsic magnetic field High energetic particles $6 \times 10^{15} \text{ MeV}/\text{cm}^2$ Energy flux $8 \times 10^{10} \text{ keV}(\text{cm}^{-2} \text{ s})^{-1}$ Atomic oxygen airglow 	82 to 132	<ul style="list-style-type: none"> High energetic particles $e^- 5 \times 10^{15} \text{ MeV}/\text{cm}^2$ Almost pure water ice on its surface and liquid ocean underneath Recent complex resurfacing 	[9, 268-273, 277, 280]
	Lander			Days to years	123	<ul style="list-style-type: none"> LILT conditions No substantial atmosphere High energetic particles Intrinsic magnetic field, shielding energetic ion $< 10 \text{ MeV}$ and electron at the equatorial Energy flux $2 \times 10^8 \text{ keV}(\text{cm}^{-2} \text{ s})^{-1}$ equator & $5 \times 10^9 \text{ keV}(\text{cm}^{-2} \text{ s})^{-1}$ polar cap Atomic oxygen airglow 			
Ganymede moon	Flyby/Orbiter			>13 CR: 3–6			93	<ul style="list-style-type: none"> LILT conditions Water ice mixture on its surface Probable subsurface ocean 	94 to 147
	Lander			Days to years	93	<ul style="list-style-type: none"> LILT conditions SO₂ is a strong absorber in the UV Plasma (Io torus) Volcanism plumes (intense tidally) High energetic particles Energy flux $1 \times 10^9 \text{ keV}(\text{cm}^{-2} \text{ s})^{-1}$ 	[258-267]		
Callisto moon	Flyby/Orbiter			>13 CR: 3–6				93	<ul style="list-style-type: none"> LILT conditions High mountains Thin atmosphere mostly of SO₂
	Lander			Hours to years	108	<ul style="list-style-type: none"> LILT conditions Stratosphere 98.4 % N₂ and CH₄ Energetic particles $2 \times 10^{14} \text{ MeV}/\text{cm}^2$ 	[303-310]		
Io moon	Flyby/Orbiter			>13 CR: 3–6				93	<ul style="list-style-type: none"> LILT conditions Active & complex hydrocarbon hydrologic cycle Atmospheric pressure (0.15 MPa) Lakes, methane abundance Haze attenuation of blue-light relative to red-light
	Lander			Days to years	93	<ul style="list-style-type: none"> LILT conditions Hydrothermal activity (water vapor/ice jets) Possible scattering induced by water vapors Intense recent tectonism 			
Saturn	Flyby/Orbiter			>14 CR: 7–8			108	<ul style="list-style-type: none"> LILT conditions Energetic particles $2 \times 10^{14} \text{ MeV}/\text{cm}^2$ 	50 to 150
	Lander	Days to years	93	<ul style="list-style-type: none"> LILT conditions Hydrothermal activity (water vapor/ice jets) Possible scattering induced by water vapors Intense recent tectonism 					
Titan moon	Flyby/Orbiter	>14 CR: 7–8			108	<ul style="list-style-type: none"> LILT conditions Energetic particles $2 \times 10^{14} \text{ MeV}/\text{cm}^2$ 	50 to 150	<ul style="list-style-type: none"> LILT conditions Hydrothermal activity (water vapor/ice jets) Possible scattering induced by water vapors Intense recent tectonism 	[292-302]
	Lander	Days to years	93	<ul style="list-style-type: none"> LILT conditions Hydrothermal activity (water vapor/ice jets) Possible scattering induced by water vapors Intense recent tectonism 					
Enceladus moon	Flyby/Orbiter	>14 CR: 7–8			108	<ul style="list-style-type: none"> LILT conditions Energetic particles $2 \times 10^{14} \text{ MeV}/\text{cm}^2$ 	50 to 150	<ul style="list-style-type: none"> LILT conditions Hydrothermal activity (water vapor/ice jets) Possible scattering induced by water vapors Intense recent tectonism 	[292-302]
	Lander	Days to years	93	<ul style="list-style-type: none"> LILT conditions Hydrothermal activity (water vapor/ice jets) Possible scattering induced by water vapors Intense recent tectonism 					

Distances: Aphelion (A), Perihelion (P). Cruise (CR), Science Phase (SP); High Irradiance High Temperature (HIHT); Low Intensity Low Temperature (LILT), Low Intensity High Temperature (LIHT); UltraViolet (UV)

Case study: Concentrator PhotoVoltaics

Future spacecraft will require higher-powered photovoltaic subsystems in order to achieve more ambitious missions. As we have already highlighted in the introduction, in space applications, constraints on solar array size, mass, and storage volume have encouraged the development of efficient MJSC. While their higher power levels have helped increase spacecraft payload capability, MJSC for space are composed of expensive III-V semiconductor materials (e.g., Ge, Ga). New generation solar arrays architectures are being proposed and studied; one of these approaches is CPV systems. This section will use the formerly assessed space conditions that could be applied in general for any PVA system, to evaluate the suitability of CPVs for each specific environment.

The key interest of concentrators is to rely on the usage of these high-efficiency MJSC while reducing the cells' area by orders of magnitude, then reducing the cost. In addition, the use of CPV also enables significantly higher conversion efficiency than cells operating under AM0 conditions. In CPVs, the supplementary mass related with the optical system and mechanical support structures could be seen as a drawback, however, it comes with a major advantage: improved radiation hardness, for instance, in Earth orbits and around the Jovian system. Furthermore, advanced approaches designs including microscale ($< 1 \text{ mm}^2$) photovoltaics have the potential to extremely reduce the optical profile, thus lowering mass, while having moderate concentration factor ($< 50X$). Moreover, other advantages of using micro-cells include passive thermal dissipation, which avoid heat sinks and reduce mass through the mitigation of CTE mismatch effects between cell and substrate, due to small dimensions. Nowadays, micro-CPV propositions suggest that high power levels per unit mass (W/Kg) can be achieved, realistically exceeding 350 W/kg (at incident AM0) and serve as a drop-in replacement for existing CIC technology at a substantially lower cost.

In order to establish what kind of missions could be addressed using CPV's it is necessary to sort favorable environments; this is done in the following Table 2.8. Missions are sorted by concept type: orbiters (e.g., LEO, MEO, and GEO), flybys, aerial, landers and rovers. The lifetimes of these missions include four categories: short missions (< 6 months), two classes of mid-lifetime (0.5 to 2 years, 2 to 10 years) and missions longer than 10 years, which corresponds to almost all space missions already performed. Solar irradiance is classified into five ranges, from high-intensities close to the Sun ($> 3000 \text{ W/m}^2$) to extremely low levels ($< 15 \text{ W/m}^2$) at long distances from the Sun. These low amounts of sunlight are also found in scattered environments (e.g., dusty and cloudy surroundings), which also create difficulties for the usage of CPV systems needing direct light from the Sun; this scattering is ranked into high, moderate and clear. Temperature is also an important factor. During usage, this parameter varies more than 373 K for PVAs, and cycles are unique to each mission. Therefore, to simplify, we consider only the minimum

and maximum temperature sorted in four ranges. In addition, the wide spectrum of chemical compounds at each celestial body makes it necessary to distinguish some elements that could deteriorate and corrode used materials, therefore these environments are classed following the pH (acidic, neutral and basic). Finally, radiation of high energetic particles is one of the main conditions that degrade solar cells in space; it is an essential parameter to predict the EOL performances of a PVA. Here again, to simplify we only focus on electron fluence at 1 MeV/cm². These parameters will then be used to select the most viable environments regarding its influence on CPV systems.

Table 2.8: Ranges of parameters extracted from the data of Table 2.6 and Table 2.7

Missions Types	Missions Life (year)	Solar Irradiance (W/m ²)	Scattering	Temperature (K)		pH	Electron Radiation (1 MeV/cm ²)
				Minimum	Maximum		
Orbiter	< 0.5	< 15		< 153	< 273		
Flyby	0.5 to 2	15 to 50	Clear	153 to 123	273 to 413	Acidic	Low < 1e10
Aerial	2 to 10	50 to 1000	Moderate	123 to 223	413 to 523	Neutral	Moderate 1e10 to 1e14
Lander	> 10	1000 to 3000	High	> 223	> 523	Basic	High ≥ 1e15
Rover		> 3000					

2.3.1 High Temperature Missions: Venus, Mercury and the Sun

In this context, near-Sun missions, where the solar intensity and temperature increase significantly, encounter a key challenge for PV systems in general. These temperatures affect performance by decreasing cell bandgaps, and increasing bandgap-to-voltage offsets, dramatically reducing solar cell efficiency. Besides the reversible loss of performance with temperature, irreversible harm jeopardizes the survival of the hardware; this eventually leads to the complete array damage, including ohmic contact degradation [312, 313], coverglass delamination, structural degradation and dopant diffusion [194]. To mitigate these extreme boundary conditions, solar arrays are typically rotated to a position off-pointed. Optical solar mirrors reflect-back incoming light from the Sun, and active-cooling systems are used to control the array temperature. In this regard, CPV systems do not seem to be adapted to such environments; since they need direct exposure to the Sun, they use reflector and optics to focus sunlight, not to reject it, and they tend to elevate the already excessive illumination intensities and temperatures. For this reason, missions with temperatures higher than 523 K and solar irradiances exceeding 3000 W/m² will be excluded, as high temperatures decrease array efficiencies and deteriorate materials. Undoubtedly, PVA for use on the surface of Venus must be encapsulated for operation in the high-temperature, corrosive environment. Landers and deep probes using current technology will have a lifetime limited to a few hours of operation due to this environment. For example, existing adhesives used to attach coverglass to solar array have operating range not optimized to such temperature condition, even though other types of advanced adhesives have been demonstrated at this temperature. It is necessary to anticipate that

technological development should be taken into account to guarantee that the hypervelocity entry of these missions will tolerate the peak heat flux and must consider mass fraction dedicated to the thermal protection system. One approach to improve the thermal management suggests the usage of phase change materials, first used during the *Venera* program and introduced as an efficient heat sink [278]. This technology has not often been used, most often because of mass consideration. However, improved materials and innovative design could change it, particularly with regard to micro/nano-satellites, which are particularly demanding in power saving. Current heritage carbon-phenolic family of materials can tolerate 1 kW/cm^2 [203]. An alternative solution to solar powered landing probes can be implemented, dynamic Stirling Radioisotope Generator (SRG) power system have demonstrated 38% conversion efficiency operating at 1,123 K hot-end, 363 K cold-end temperatures. They could provide both electric power and active thermal control to the spacecraft [314].

2.3.2 Dusty Worlds: Earth's Moon and Mars

CPVs only use direct light from the Sun to operate. One implication of this in selecting a reliable PV technology is that concentrators that generally require collimated light to function will be less effective than planar technologies which accept light from a wide-range of angles. High-scattered environments filter light, decreasing the available solar intensity and inducing spectral variations, which produce mismatches between the electrical currents generated by the series-connected junctions of spectrally "tuned" MJSC, which are typically used in aerospace and by CPVs. This reduction in performance is evidenced in PVA in general, and becomes a more dramatic factor in CPV systems that rely on direct light.

In addition, another concern is that some of these environments with levitated particles, induce the deposition of material onto optics (e.g., coverglass, lenses, mirrors), which over time can prevent the transmission of light on solar cells if they are not removed, thus making photovoltaic generation impossible. Therefore, it is necessary to differentiate highly scattered/polluted environments, found down in the atmospheres of Venus and Titan, and during Martial storms, from moderate and temporal scattering generated across the Moon terminator. While the former impede the implementation of CPVs and in general constrains PVAs, the latter presents not such a dramatic effect on PV systems, which can be reversed using appropriate dust mitigation technologies. In this sense, even if the substantial population of levitated dust during Martial storms could be considered as a temporal phenomenon in relation with the intrinsic "weather", localization and dust nature, their huge size and long duration make the functionality of CPVs intermittent and more affected at highest dust loadings when efficiency is most critical. In consideration of this, high-scattered environments must be avoided as these environments are not the best suited

to be address by CPVs. Whereas the moderate levitated dust at the Moon could potentially be address by CPVs enhanced with future developments in dust cleaning methods.

Under the Venus clouds, the low solar intensity has a double influence on the efficiency, decreasing the cell performance directly, but also making the cell more sensitive to temperature. The solar cell bandgap declines with temperature, moving the response toward longer wavelengths. At the surface, the sunlight gets scattered and tends to be blue-deficient, and in fact the spectral response shift due to increased temperature tends to somewhat compensate for the blue-deficient spectrum [209]. Understanding the dynamic of the lunar dust is a critical step to enable future robotic and human exploration activities on its surface, which today is partially understood. In the future, lunar bases, rovers and landers could take advantage of using CPVs, improving the conversion efficiency and potentially reducing costs. However, they must integrate a dust-removal system and optimized materials to adjust the incident spectrum on solar cells, considering the population of temporal levitated dust present in the terminator region of the Moon. In terms of degradation, it was already demonstrated that optical devices could endure long-term (> 50 years) operating on the Moon [188].

Some of the crucial factor in selecting the most effective dust mitigation technology are: the environment, dust transport mechanism, type of surface materials, area of the surface, energy consumption and surface functionality. A variety of methods of dust-removal has been proposed, such as natural means (e.g., wind, gravitation, etc.) [315, 316], mechanical means (e.g., brushing, blowing, vibrating and ultrasonic driving) [317], electrostatic means and fluidal methods are feasible options for dust removal only in the pressurized Martian environment [318, 319]. Afshar-Mohajer *et al.* executed an extensive review of earlier developed dust mitigation technologies for Lunar and Martian worlds, considering the advantages and limitations of these technologies for both environments and the dust transport mechanisms [172]. In general, the suggested mitigation technologies for protecting solar panels and optical surfaces is the Electrodynamical Dust Shield (EDS) made of transparent electrodes, as shown in [320, 321]. For orbital missions both Mars and the Moon could benefit from CPV systems without major issues, with a proper selection of materials and qualification programs. Missions to Mars in particular could improve the reduction of sunlight caused by its increased distance from the Sun, using CPV, and enhance the implementation of solar electric propulsion.

It is clear from the previous considerations that missions exhibiting extreme temperatures and highly scattered environments should be avoided, since these environments are not the most suitable for CPV systems. Thus, using the synthesis of environmental conditions presented in Table 2.6 and Table 2.7, we will apply some filters as follows: all type of missions, all lifetime, with clear irradiance, with not too high temperature (> 523 K). In this regard, Table 2.9 summarizes the resulting places and mission concepts

with viable environmental conditions to be powered by CPVs. We can notice that for these sorted environments, worlds with chemical corrosive constituents, such as Venus (having sulfuric acid clouds) and Titan (with CH₄), are no longer a concern, as they have already been filtered. It is also possible to appreciate that almost all missions that CPV technologies could address are long missions with harsh environments, requiring them to be resistant to radiation. Moreover, we can distinguish two sorts of missions: on one hand, missions around the Earth/Moon/Mars with medium solar irradiances and moderate temperatures, and on the other hand, LILT missions toward the gas giants. Furthermore, Table 2.10 assesses the potential worlds to be powered by CPVs. In this table the main specific constraints found at each of these mission concepts are summarized and their potential impact (high and moderate) on CPVs is highlighted.

2.3.3 High-Radiated Worlds: Earth Orbits and Gas Giants

CPVs provide inherent protection of the active PV cells against energetic charged particles, strongly evidenced for spacecraft in Earth orbits, and at far distances exploring the Gas Giants. This shielding can be met for example using a refractive approach (e.g., Fresnel and dome lenses) that stops energetic particles in the bulk of the optics, acting as a coverglass with an added functionality value. The Earth orbital environment presents threats such as radiation damage from the trapped electrons and protons, UV radiation, plasma, thermal cycling, micrometeoroid/debris impact, and ATOX in LEO. In this context, the major challenge for CPV systems is to reduce the degradation of optical surfaces, and the formation of particulate and molecular contamination on surfaces, including reflective and refractive optics. Maintenance has also been considered for each environment conditions. For earth orbits, PVA maintenance done by human in LEO is feasible while the same task becomes impossible at GEO due to high radiation level. So maintenance has to be most of the time done by remote-controlled robot. In this regard, the expected life of CPV also depends on specific designs. For example, set the solar cells behind a metallic part which could play the role of reflector, like the system described in [322], which can substantially increase the lifetime of the system compared to classical planar solar panels. Moreover, appropriate materials should be chosen to guarantee their resistance to stresses caused by thermal expansion and contraction following qualification programs. The ATOX degradation in LEO may result in changes in chemical composition and surface morphology (e.g. erosion). All hydrocarbon based polymers and graphite are easily oxidized. These effects have been widely studied, in addition to the study of a variety of solutions, such as coatings [128]. For example, a thin ($\sim 1000\text{\AA}$) *protective layer of SiO₂* can be applied on the top (e.g., silver or aluminum mirrors) of reflective CPVs [323], and on sensitive polymers for lenses and composite materials [125].

For LILT conditions, the reduced incoming sunlight naturally decreases the photo-generated power of any PVA, which also makes that anomalous defects, as shunting, become a very noteworthy fraction of the cell current output at low intensities. In this context, the implementation of solar concentrated systems improves several characteristics of LILT missions: increasing the effective irradiance and performing as if they were closer to the Sun, also mitigating the combination of LILT-type degradation effects such as shunting. Usually elevated cell temperatures are to be eluded, however, under the extremely low temperatures of deep space cell heating is desirable to activate the tunnel junctions, which can be adversely affected at low temperatures. In addition, heating can decrease the probability that thermionic barriers in the cells will inhibit current flow; and perhaps induce an annealing effect on cells, helping them to recover after degradation from high energetic particles. In the future, several of these missions could use solar energy to power its systems and/or combine it with other energy sources (e.g., radioisotope power sources and batteries) to fuel different parts of a mission concept. Additionally, the high-density-power supply by CPV arrays can facilitate the fuel of electric propulsion, which can benefit several missions. At LEO, for example, the relatively low altitude orbit of the ISS experiences fairly high levels of atmospheric drag, requiring periodic altitude boosts; indeed, the combination of CPV and electric propulsion already has been demonstrated by the SCARLET spacecraft.

The extreme LILT condition found at the Kronian system embodies a major challenge for solar power systems considering the mass and area requirements. Future mission concepts to reach outer planets call for power capabilities > 400 W, as Juno at Jupiter. Based on assessed cell efficiencies at Saturn, a solar-powered spacecraft would need an array with about 100 m^2 of active area, or equivalently 40 kW at 1 AU [242]. To get some perspective, the International Space Station solar array can generate about 240 kW in direct sunlight, or about 84 to 120 kW average power (cycling between sunlight and shade). In this context, deployable rigid PVA such as Juno's usually have specific powers of $\sim 60 \text{ W/kg}$ at 1 AU that represents a solar array weight $\sim 600 \text{ kg}$ at Saturn, not likely to be practical from a cost point of view. With this in mind, lightweight concentrating arrays provide an interesting approach to expand planetary exploration using solar cells at distances, such as those of Saturn. Since nowadays propositions suggest that high power levels can realistically achieve 350 W/kg at incident AM0, using ultra-compact microcell (micro-CPV). The implementation of solar concentrated systems improve several benefits for several environments (defined in Table 2.9 and Table 2.10). Nonetheless, each of these missions require specific considerations and improvements, summarized in Table 2.6 and Table 2.7, to guarantee reliable adaptability to such a diverse solar system.

Table 2.9: Viable missions to address using CPV systems

World	Missions Types	Missions Life (year)	Solar Irradiance (W/m ²)	Scattering	Temperature (K)		pH	Electron Radiation (1 MeV/cm ²)
					Minimum	Maximum		
E. Moon	Orbiter	>10	1000 to 3000	Clear	70 to 123	273 to 413	Neutral	Moderate
E. Moon	Lander	>10	1000 to 3000	Moderate	70 to 123	273 to 413	Neutral	Moderate
Earth	LEO	[2, 10]	1000 to 3000	Clear	123 to 223	273 to 413	Neutral	High
Earth	MEO/GEO	>10	1000 to 3000	Clear	70 to 123	273 to 413	Neutral	High
Mars	Orbiter	>10	50 to 1000	Clear	123 to 223	<273	Neutral	Moderate
Jupiter	Orbiters	>10	15 to 50	Clear	70 to 123	<273	Neutral	High
Europa	Orbiter/Landers	>10	15 to 50	Clear	70 to 123	<273	Neutral	High
Ganymede	Orbiters	>10	15 to 50	Clear	70 to 123	<273	Neutral	High
Ganymede	Landers	>10	15 to 50	Clear	<70	<273	Neutral	High
Callisto	Orbiter/Landers	>10	15 to 50	Clear	70 to 123	<273	Neutral	High
Io	Orbiters	>10	15 to 50	Clear	70 to 123	<273	Neutral	High
Saturn	Orbiters	>10	15 to 50	Clear	<70	<273	Neutral	High
Titan	Orbiters	>10	15 to 50	Clear	<70	<273	Neutral	Moderate
Enceladus	Orbiters	>10	15 to 50	Clear	<70	<273	Neutral	High

Titan and Enceladus have encouraged several mission concept propositions. A key issue for exploring these two worlds using solar power is that solar cells will experience extreme LILT conditions as that for Saturn at the orbits, which is even more dramatic on their surfaces (i.e., Titan dense atmosphere and levitated ice particles at Enceladus) inducing a reduction of orders of magnitude in solar radiation. Highly challenging solar power systems, considering the mass and area requirements, and disqualifying its usage to study the underneath liquid oceans. In this context, the maximum amount of sunlight reaching Titan is about 15 W/m² (as at Saturn) with a diurnal average value of 4.8 W/m² [324]. Considering the constituents of Titan’s atmosphere, only 10% of this flux reaches the surface, on top of that, atmospheric transmission is wavelength dependant, since the red and near infrared light are transmitted (minus methane absorption), whereas blue light is absorbed. Furthermore, solar power systems inside Titan’s atmosphere must consider seasonal rainfall, transient cloud cover and tholin sediments settling onto the panels. At the surface, the atmospheric pressure is 0.15 MPa (60% higher than on Earth) and the temperature is about 453 K [324].

Due to Titan’s haze layer and its distance to the Sun, lander and penetrator missions cannot be powered by solar panels and so they should rely on other power system technologies such as RTG. However, radiation is moderate, since Saturn has relatively weak radiation belts. The outermost edge of the main radiation belt is situated at 3.5 Saturn radii, which is below Enceladus’ orbit (4 Saturn radii) and Titan’s orbit (20 Saturn radii). Moreover, Enceladus “sweeps up” energetic particles along its orbit, resulting in a significant reduction in radiation levels in low orbits around it and on the moon’s surface [325]. In the long term, some of these concepts could benefit from using lightweight PVA to power a whole mission (e.g., as orbiters), or to combine it with other sources (e.g., RTG’s and batteries) to be used at different mission stages.

Table 2.10: Assessment of potential worlds to be powered by CPVs and its specific constrains.

ASSESSMENT OF POTENTIAL WORLDS TO BE POWERED BY CPVs AND ITS SPECIFIC CONSTRAINS																
Mean Distance (AU)	~1				1.67				5.5				10			
Solar Flux (W/m ²)	1,366				589				51				15			
WORLD	EARTH				MOON		MARS	JUPITER	IO	EUROPA	EUROPA	GANYMEDE	CALLISTO	SATURN	ENCELADUS	TITAN
	L	M	E	O	O/F	L/R	O/F	O/F	O/F	O/F	L/R	O/F	L/R	O/F	L/R	O/F
MISSION	●	●	●	●	○	○	○	○	○	○	○	○	○	○	○	○
CONDITION	○	○	○	○	○	○	○	○	○	○	○	○	○	○	○	○
Atomic Oxygen	○	○	○	○	○	○	○	○	○	○	○	○	○	○	○	○
Dust	○	○	○	○	○	○	○	○	○	○	○	○	○	○	○	○
Extreme Temperatures	○	○	○	○	○	○	○	○	○	○	○	○	○	○	○	○
Harsh Radiation e- p+	○	○	○	○	○	○	○	○	○	○	○	○	○	○	○	○
Micrometeoroid	○	○	○	○	○	○	○	○	○	○	○	○	○	○	○	○
Plasma	○	○	○	○	○	○	○	○	○	○	○	○	○	○	○	○
Thermal Cycling	○	○	○	○	○	○	○	○	○	○	○	○	○	○	○	○
UV Radiation	○	○	○	○	○	○	○	○	○	○	○	○	○	○	○	○

Convention: ● High impact ○ Moderate impact on Concentrator PhotoVoltaics (CPV). AU : Astronomical Unit (~150 x10⁹m). Low Earth Orbit (LEO), Medium Earth Orbit (MEO), and GEosynchronous Orbit (GEO). O: Orbiter, F: Flyby, L: Lander, R: Rover. e-: electrons, p+: protons.

2.4 Conclusions and perspectives

This paper has presented a comprehensive review that can help spacecraft designers during the development of photovoltaic assemblies for space applications, to choose appropriate encapsulating materials, solar cell technology, thermal management, and other specific constraints to enhance current solar cells technologies to future mission concepts and needs. The major findings from the assessment of future challenges for solar-powered missions are:

1. Variation with altitude is perhaps the most important parameter for the spacecraft designer on the Earth's orbits, because there are basic differences in the physical processes that occur in the respective regions. Energetic particles radiation is higher in medium and geostationary Earth orbits compared to low Earth orbit. While low Earth orbit has extensive erosion due to atomic oxygen, severe surface charging had been associated with geostationary Earth orbit. Ultra-violet radiation, thermal cycling, and micrometeoroid/debris impact are presented in all Earth's orbits, in different levels.
2. Surface mission concepts to Earth's Moon and Mars require solar arrays with dust mitigation capability. While the Moon surface perceives a full-energy spectrum Air Mass as at Earth's orbits, suspended atmospheric dust modifies the solar spectrum and reduces intensity on the Martian surface, making it blue-deficient, and enhanced in red and infrared, thus solar cells must be "tuned" to the Mars spectrum.
3. Near-Sun missions, where the solar intensity and temperature increase considerably, induce reversible loss of theoretical performance with temperature, and irreversible damage leading to ohmic contact degradation, coverglass delamination, structural degradation and dopant diffusion. Mercury has high thermal radiation and high gravity environments. Venus has a much more complex and dynamic atmosphere including variation on temperature and pressure relative to the altitude, and corrosive sulfuric acid clouds.
4. Missions to explore the Jovian and Saturnian systems require high power photovoltaic systems capable of functioning efficiently in low irradiance and low temperature conditions, and high radiation environments.

Capabilities and limitations of concentrated photovoltaics as a solar power system in space

In general, concentrator photovoltaics have the potential to increase the cell theoretical efficiency limit compared to standard (non-concentrated) solar panels, considering that

the current approach towards cell efficiency is reaching its theoretical limits as the technologies mature. In fact, concentrators have already been used in space and their high-density-power can facilitate the employment of other technologies such as electric propulsion systems. In addition to the Table 2.10, which summarizes potential worlds to be powered by concentrator photovoltaics, some of the advantages and limitations that have been highlighted include:

1. Concentrator photovoltaics provide inherent protection of the active photovoltaic cells against high fluxes of high energetic charged particles, found at the Earth's orbits and around the Jovian and the Kronian systems.
2. At long distances, up to five astronomical units, low irradiation and low temperature degradation effects can be mitigated using concentrator photovoltaics, increasing the effective irradiance and performing as if they were closer to the Sun. Even if these systems have already been flight-tested in Earth orbits, further investigation should be done to evaluate the behavior and degradation process of these technologies under the combination of low irradiance and low temperature conditions and high-radiated environments. This is perhaps one of the most adapted environments for concentrator photovoltaics, and its development could enhance the application of photovoltaic at remote distances as far as Jupiter, Saturn, and their moons; and maybe in the far future even further.
3. Concentrator photovoltaics performance is degraded at dusty environments since particulate matter scatters sunlight and deposits onto optics, which disable the transmission of light on solar cells. Highly scattered environments, as Venus, Titan and the stormy weather of Mars make it impractical for concentrators, for aerials and landers mission concepts. In the other hand, the Earth's moon requires dust mitigation capability, even if dust deposition is less dramatic than Mars it is not negligible.
4. In concentrator photovoltaics, solar radiation is focused, leading to high heat flux that tends to deteriorate its life and efficiency for missions with temperatures higher than 523 K and solar irradiances exceeding 3000 W/m².

As our understanding of the universe evolves, with new ground-based observations and as spacecraft gather new information, it is important to consider that the information summarized in this paper is subject to the evidence and used sources currently available. Accordingly, in the future, new data will help to improve the already established needs, as well as the integration of other potentially interesting celestial bodies on the Solar System roadmap to be explored by solar power systems. This concludes the published review, and will be followed by a first concept of CPV addressed during the thesis.

3

Optics optimization and integration of a linear compound parabolic concentrator using III-V/Si cells

Since 2016, the CEA has been investigating an innovative, low cost and robust CPV system composed by a dielectric CPC that attains a concentration factor of approximately 7.6X [326, 327], described in Section 3.1. This approach concentrates light thanks to the optical principle of Total Internal Reflection (TIR). The early stage work of this system has been supported by the *Centre National d'Etudes Spatiales* (CNES) and developed in a framework R&T with Thales Alenia and Space and Thales Research and Technology. This chapter describes an improved generation based on this previous CPC design, with the aim of evaluating whether it can be improved and adapted to respond to space applications. For this purpose, a detailed optimization of several aspects has been carried out, from the optical system design using ray-tracing via TracePro® (Section 3.2), to the manufacturing molding process (Section 3.3), along with the integration of low-cost silicon-based (III-V/Si) solar cells. In this way, proposing the world's first space concentrator prototype using III-V/Si cells for space applications.

3.1 Description of the baseline design of previous linear CPC

The module proposes to directly integrate and mold the optics on the solar cells. The aim is to avoid alignment procedures during solar arrays deployment in space, as it is more robust and less risky to assess the best alignment on the ground before launch. Solar cells are embedded in a low outgassing silicone optic, Dow Corning® 93-500 [328]. The module is composed by twelve MJSC, each with an active size of $1.5 \times 13 \text{ mm}^2$. Cells were manufactured by Azur Space and have been specially designed for space, with an optimized anti-reflective coating matched to the refractive index of the bi-component silicone and a metallization adapted to the low concentration. In fact, the CPC optics may have several functions, increasing performances by focusing incoming solar flux while providing mechanical support and protection to cells from space radiation (e.g., electrons, protons).

For demonstrator purposes, the area of the module is chosen to be as close as the half of the surface of a standard Solar Cell Assembly (SCA) either $43 \times 45.2 \text{ mm}^2$, and it is 15 mm thick comprising the optics and the glass. Figure 3.1 outlines the proposed design with some of its dimensions and a close-up front view of the lower part of a single optic, showing the cavity lodging three interconnected cells laterally disposed.

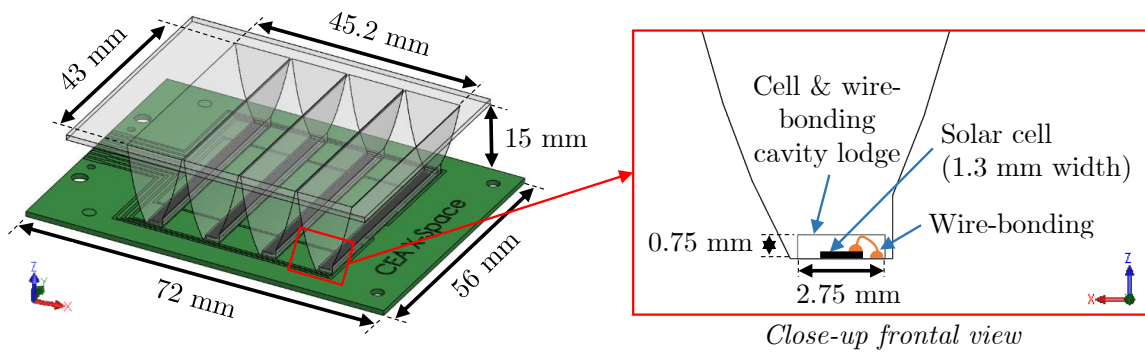


Figure 3.1: Schematic of baseline prototype module illustrating some dimensions (left), close-up front view of the lower part of a single optic, showing the cavity lodging cell and wire-bonding.

Moreover, an angular study has been carried out and an acceptance angle (i.e., maximum angular tolerance to provide 90% of the maximum optical efficiency) of $\theta = \pm 3^\circ$ for the lateral axis and $\alpha = \pm 23.5^\circ$ for the longitudinal are guaranteed, shown in Figure 3.2, which means that for a GEO mission a single-axis tracker is sufficient to track the Sun taking into account the seasonal angle. While the theoretical optical efficiency was 75%, the experimental was about 68% [327].

Regarding the manufacturing process, Figure 3.3 illustrates three of the main issues encountered, including (a) air bubbles trapped in optics, (b) adhesion issues between

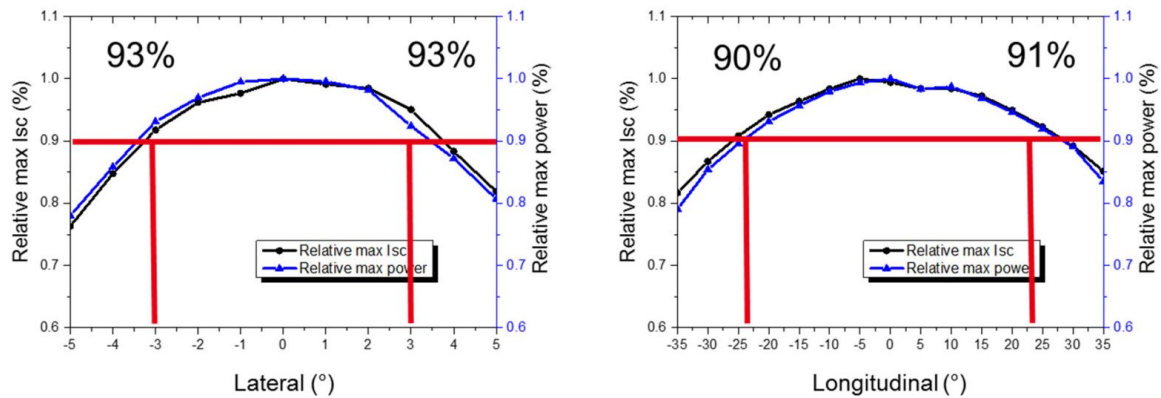


Figure 3.2: Normalized Maximum short circuit current (I_{sc}) and maximum power versus: the lateral between -5° and $+5^\circ$ (left), and the longitudinal between 35° and $+35^\circ$ (right) [327].

coverglass and optics and (c) unwell defined bottom edges, problems that lead to a decrease in the optical efficiency of the CPV system.

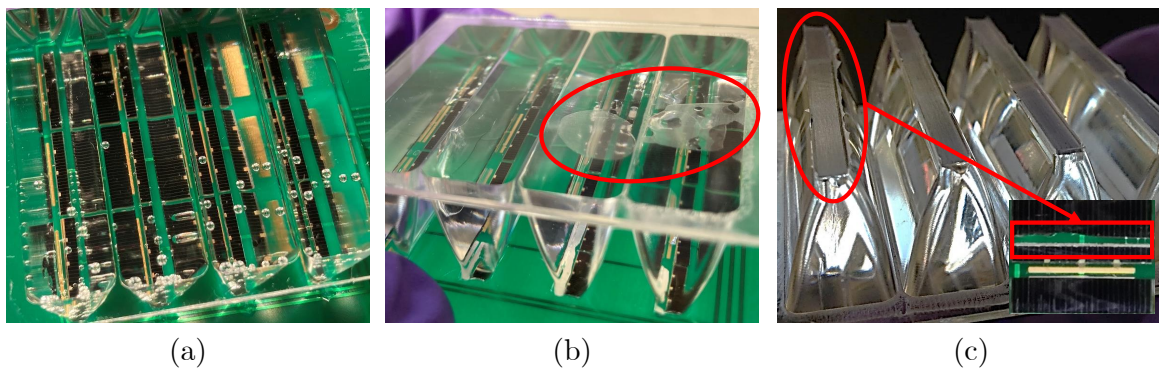


Figure 3.3: Issues encountered with the previous generation CPC prototype: (a) air bubbles trapped in optics, (b) adhesion issues between coverglass and optics and (c) unwell defined bottom edges.

3.2 Optical design and optimization of a new generation CPC

Non-imaging optics is used in the design and optimization of CPVs, that branch of optics this deals with the optimal transfer of light radiation between a source and a target. In contrast to traditional imaging optics, the underlying principles do not attempt to form an image of the source; they seek instead to optimize the optical system for optimal radiative transfer from a source to a target.

As mentioned above, the theoretical optical efficiency of the previous system was about 75%, which is not in line with current state-of-the-art efficiencies of over 90%, as shown in Chapter 1. This is largely attributed to the fact that the cavity housing the cells

was oversized, in order to make room for the interconnecting wires, causing some of the concentrated flow not to reach onto the cell. Thus, in this work, to improve the optical efficiency we proposed to optimize the optical design in order to maximize the rays reaching the cell by redesigning the receiver surface; maintaining a maximum acceptance angle.

To do this, a ray-tracing optimization model via TracePro® has been done, through the Nelder-Mead, or downhill simplex algorithm, commonly applied numerical method used to establish the minimum or maximum of an objective function in a multidimensional space [329]. For this purpose, taking into account a source AM0 and material properties such as refractive index, an initial raw shape is designed in TracePro's "Interactive Optimizer", which will then be varied to find the best local solution. In addition, the edge ray principle has been used to minimize computational time by estimating initial parabolic shapes previously improved.

Edge Ray Principle

The edge ray principle is an important theory in the tailoring method. In 1994, Davies tested and verified the edge ray principle using geometrical optics [330]. In the same year, Ries and Rabl verified the edge ray principle in phase space for the design of a CPC, which established a basis for the tailoring method [331]. In simple terms, the edge ray principle states that if the light rays coming from the edges of the source (consider the two extreme angles $-\theta_i$ and $+\theta_i$ in Figure 3.4) are redirected to the edges of the receiver, this will ensure that all light rays coming from the interior points of the source will hit the receiver. There is no condition for image formation, the only objective is to transfer the light from the source to the target. From the diagram, it is easy to see that each ray with an intermediate angle of incidence necessarily reaches the receiver, even though the parabolas are valid for both angles $-\theta_i$ and $+\theta_i$.

Actual CPC design consists of two symmetrical parabolas filled with a dielectric material, which will increase the acceptance angle of the system. This particular concentrator has an acceptance angle inside the dielectric θ_a and a CPC acceptance angle θ_i . The maximum values $\theta_{a(max)}$ and $\theta_{i(max)}$ to respect a Total Internal Reflection (TIR) are shown in Figure 3.4. If the dielectric has refractive index η , the CPC is, of course, designed with an acceptance angle within the dielectric, according to the law of refraction. Then it is easy to demonstrate that the condition for TIR to occur at all points is defined by the expressions in Equation 3.1, plotted in Figure 3.5.

$$\sin \theta_a < 1 - \left(\frac{2}{n^2}\right) \text{ or } \sin \theta_i < n - \left(\frac{2}{n}\right) \quad (3.1)$$

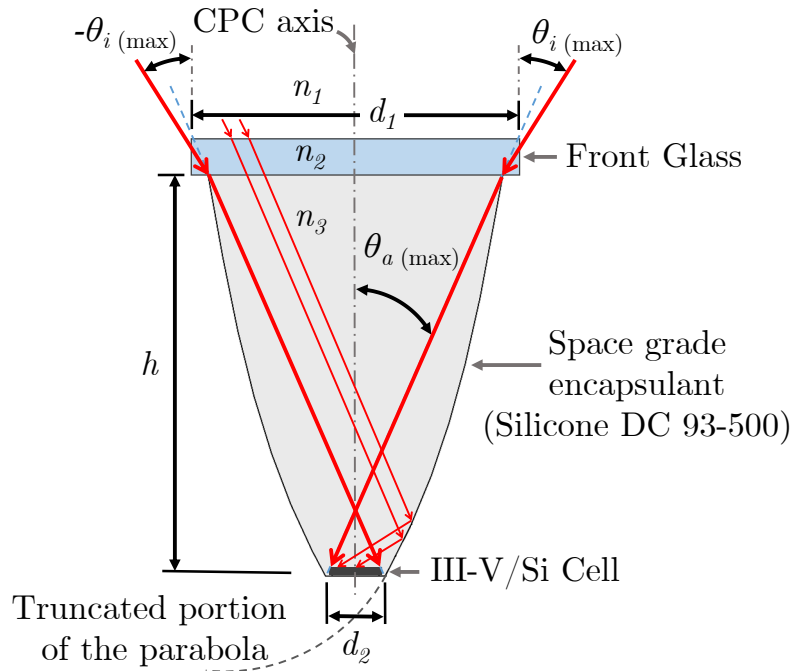


Figure 3.4: Baseline optical design, where θ_i is the CPC acceptance angle, θ_a is the dielectric acceptance angle, d_1 is the optics aperture, d_2 is the receivers, h is the height and n_n is the refractive index of each material.

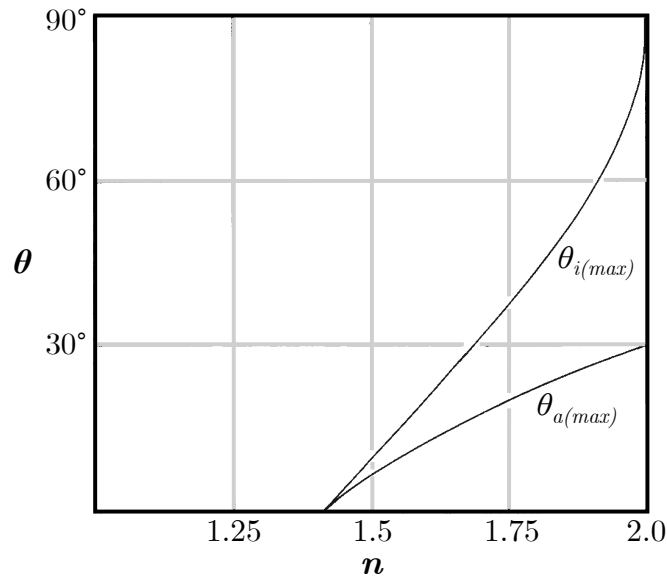


Figure 3.5: Maximum collection angles for a dielectric-filled CPC with TIR, as a function of refractive index.

The aim is to maximize the sunlight flux onto the receiver (solar cell) while keeping a maximum acceptance angle. In this regard, a first approach consists on optimizing the system with an incident sunlight $\theta = 0^\circ$ and then to use a tilt configuration for a $\theta = 3^\circ$; thus be able to guarantee a minimum acceptance angle of $\alpha = 3^\circ$.

3.2.1 Receiver optimization

A major improvement relative to the previous CPC design is the enhancement of the receiver surface. Last version was composed of one large rectangular cavity that lodged three cells and its gold wire interconnections, all in the shaped internal walls of each optics. Meaning that a part of the incident flux was lost at the interface between the bottom of the walls and the PCB's (see Figure 3.6). This is the reason why the new proposition suggests the use of three rectangular cavities per optics, which will host each cell and its interconnection wires independently, maximizing the incident sunlight flux onto solar cells.

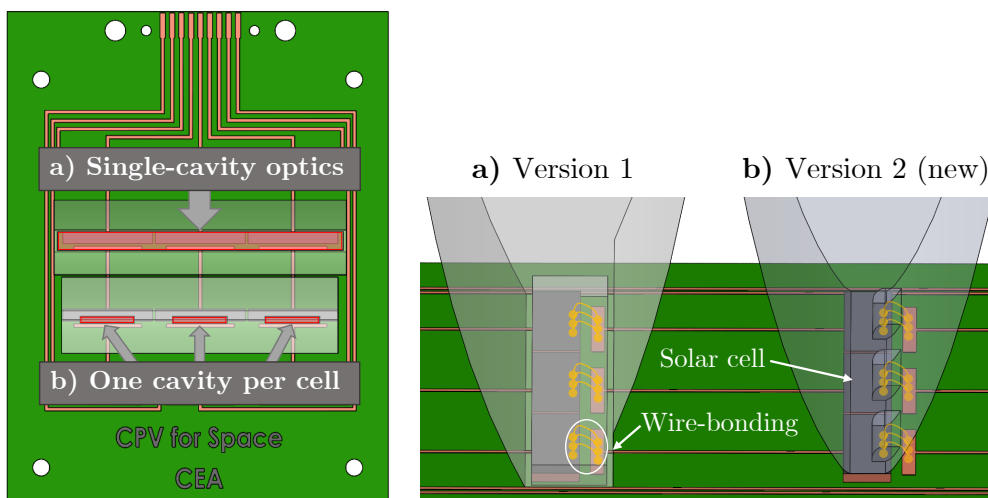


Figure 3.6: CPC Computer-Aided Design (CAD) model: (a) version 1 (7.6X), and (b) version 2 (8.6X).

3.2.1.1 III-V/Si solar cells

Furthermore, this new architecture combines the high conversion efficiencies of CPVs with a low-priced Silicon based (III-V/Si) solar cells that is expected to significantly reduce cost by concentrating sunlight then decreasing cell material, and in particular using III-V/Si 3J cells will allow the usage of Silicon, which is an abundant, twice less dense and low-cost material than the typically used Germanium.

For decades, space community has mainly employed MJSCs based on III-V materials, in part due to their higher radiation resistance and capacity to well-behave in harsh environments compared to other technologies. In contrast, modern III-V solar module prices often surpass \$150/W, which represents 400X the current prices respect to other technologies as c-Si solar and Cadmium Telluride (CdTe) modules (\$0.30–\$0.50/W) [332]. In 2018, the NREL carried out a techno-economic analysis and cost reduction roadmap for III-V solar cells, this study reveals that achieving the cost reductions would involve significant R&D as well as a scale-up of manufacturing [332]. The high cost of Germanium

substrates represents one of the major impacts on the production of III-V cells, replacing it would cut costs. In fact, this is a rare, largely used and expensive material (\$130/6-inch substrate), which amounts to about 30% of cell cost. In parallel, PV energy for terrestrial applications has grown strongly in recent years thanks to a significant cost reduction of photovoltaics based on Silicon wafers. This improvement is in contrast with the achieved efficiencies that reach its theoretical limits [333]; thus, new solar technology proposals have been developed to enhance the cells/modules efficiency at moderate cost.

Two terminal 3J III-V/Si cells used in this study are composed by GaInP (1.90 eV)/ GaAs (1.42 eV)/ Si (1.12 eV), and were fabricated according to the manufacturing process briefly described in Appendix C.

3.2.1.2 Target value

In order to define the target function it is necessary to establish what is the maximum number of watts that can be transmitted by the optical system. In this regard a first step is to defined the solar source, more particularly the AM0 spectrum (ASTM E-490) was modeled. For practical reasons, to save computational time, the optimization process was at first focused on the spectral response of three wavelengths ($\lambda = 0.3, 0.75$ and $1.2 \mu\text{m}$) along the characteristic absorption of the used 3J solar cell, as it is shown in the subcells EQE measurements in Figure 3.7. Moreover, ten thousand rays were used in order to have accurate and fast optimization process, wavelengths composing the modeled source are shown in Table 3.1, specifying the relative weight and the related flux.

Table 3.1: Modeled solar source using three wavelengths ($\lambda = 0.3, 0.75$ and $1.2 \mu\text{m}$).

Wavelength(μm)	Weight	Flux (W)	# Rays
0.3	0.20376	0.0412493	20376
0.75	0.570707	0.115535	57071
1.2	0.225533	0.0456572	22553
Totals		0.2024415	100000

The solar source has been modeled slightly bigger than the optics aperture area (145.6 mm^2) to guarantee that this area is completely covered taking into account the 0.27° of the Sun, achieving an incident ideal perpendicular flux of about 0.1824 W , shown in Figure 3.8. Then, as light travels from the source it will cross several optical interfaces, which induce some losses, to finally arrive and be absorbed by the solar cell.

The refractive indices, $n(\lambda)$, used for silicone and low-Fe coverglass have been previously defined by McIntosh *et al.* [334] (see Table 3.2), using a least-squares fit of the Schott dispersion formula of empirical data to the first three terms, see Equation 3.2, where the uncertainty represents a 95% confidence interval over the range, 300–1600 nm. Schott's

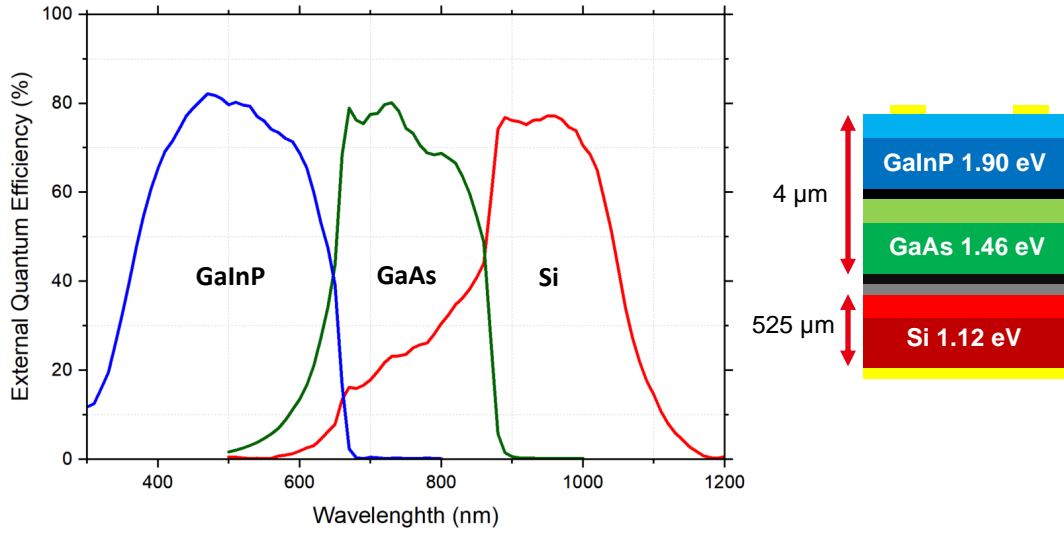


Figure 3.7: External Quantum Efficiency (EQE) measurements of each cell junction (left), and a schema of each sub-cell showing each band-gap and their thicknesses (right).

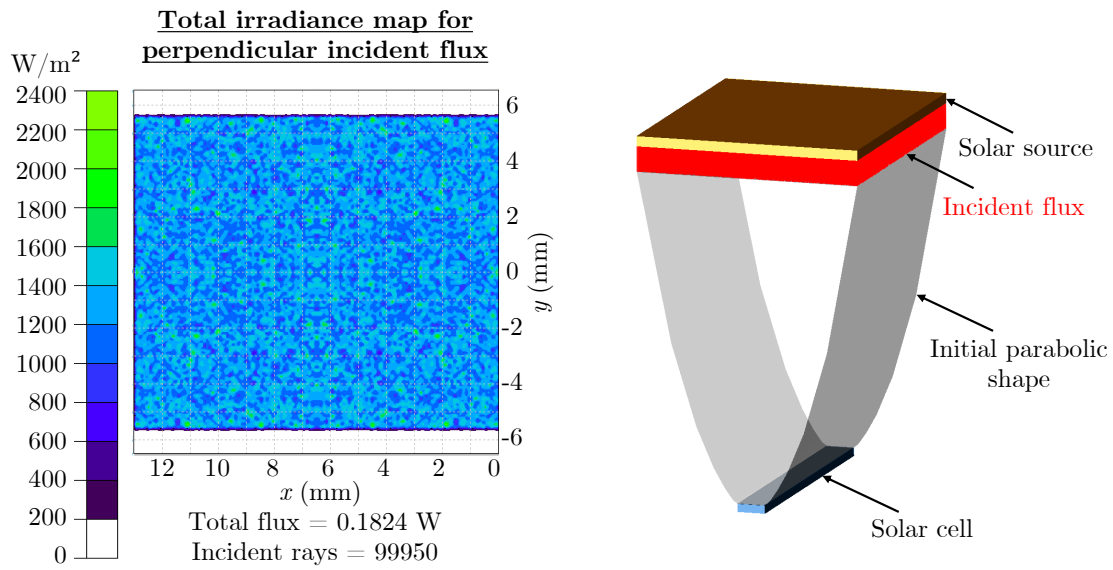


Figure 3.8: Total irradiance map for a perpendicular incident flux in a single unit optic (left), schematic baseline of ray-tracing for incident flux on the top of optics (right).

formula offers a reasonable compromise between simplicity and accuracy, where accuracy can be assessed by the chi-squared (χ^2) shown in the Table 3.2 and Figure 3.9 [334].

$$n(\lambda) = a + b\lambda^2 + c\lambda^{-2} + \dots \tag{3.2}$$

Table 3.2: Least-squares fit of the Schott dispersion formula to empirical data for silicone and low-Fe glass materials [334].

Material	a	b (nm ⁻²)	c (nm ²)	χ^2
Silicone	1.3985 ± 0.0003	-3.8 ± 0.2 × 10 ⁻⁹	38.6 ± 0.5 × 10 ²	8 × 10 ⁻⁶
Low-Fe Glass	1.5048 ± 0.0003	-3.0 ± 0.2 × 10 ⁻⁹	21.1 ± 0.6 × 10 ²	1 × 10 ⁻⁶

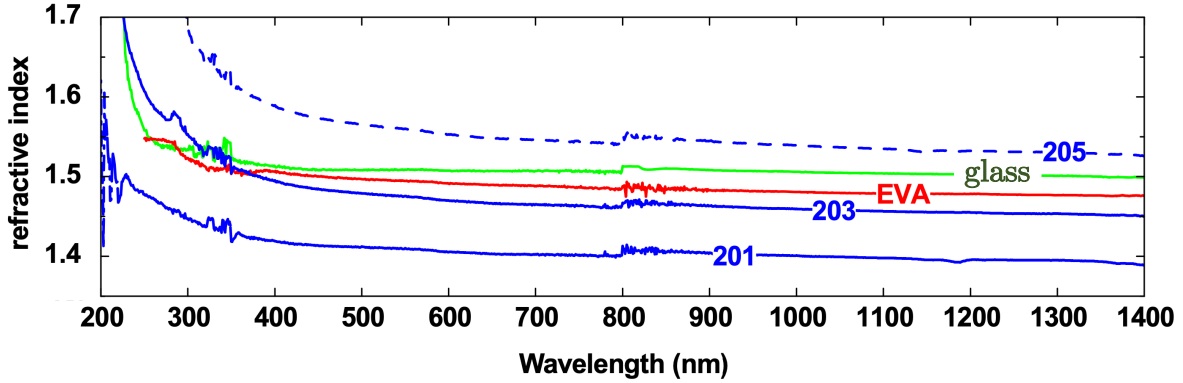


Figure 3.9: Refractive index as a function of wavelength for DC 93-500 (201), other two similar silicones 203 and 205, EVA, and low-iron glass [334].

Fresnel losses

Considering the different refractive indexes of the module materials, we can easily calculate the Fresnel losses at each interface, as shown in Table 3.3 estimated for $\lambda = 0.5461 \mu\text{m}$. For the case of normal incidence and unpolarised light the reflectance is expressed by Equation 3.3. We can appreciate that reflection from the front of the module (vacuum/glass interface) is governed by the refractive index of coverglass 4.14%, while in comparison the Fresnel losses between the glass and the silicone are negligible since they have similar refractive indexes; accounting for a total Fresnel reflection loss of 4.25%.

$$R = \left| \frac{n_1 - n_2}{n_1 + n_2} \right|^2 \quad (3.3)$$

Table 3.3: Refractive indexes and Fresnel losses for materials at $\lambda = 0.5461 \mu\text{m}$.

	Material/ Environment	n	Fresnel loss (%)
n_1	Vacuum	1.0	4.14
n_2	Glass	1.51102	
n_3	DC 93-500 silicone	1.41240	0.11
Total			4.25

Absorption losses

According to the Lambert-Beer law, the intensity of light passing through a transparent medium decreases exponentially as a function of the distance traveled and the properties of the medium it passes through; as expressed by the equation:

$$I(x) = I_0 e^{-\alpha x} \quad (3.4)$$

I_0 is the initial intensity of incident light, $I(x)$ is the intensity of the light after attenuation due to its penetration at distance x into the material, and α is the absorption coefficient. This latter is wavelength dependent and is usually indicated for a material by the manufacturer or in the literature. For example, the absorption coefficient is $\alpha = 0.0074 \text{ mm}^{-1}$ for low-iron glass [334], and $\alpha = 0.0013 \text{ mm}^{-1}$ for transparent silicone [335], at wavelengths greater than 400 nm. For example, in our case considering a 0.9 mm thick coverglass these losses are 0.7%, while for silicone about 12 mm thick this is about 1.5%.

Finally, taking into account the incident total flux on the aperture, shown in Figure 3.8, as well as the Fresnel losses in Table 3.3, and the losses by absorption; a total loss of about 6% can be estimated. It is then possible to calculate the theoretical maximum flux concentrated by an optic on a cell, which is about 0.172 W, this is the maximum flux achievable by TIR at the receiver interface, our target value for the optimization process that follows.

3.2.1.3 Variables

Variables are the parameters that can change during the optimization process, which may include the position of the control point in one, two or three dimensions, the curvature, the conic constant, the angle of rotation, among others [336]. When a variable is defined, the range of the variable is specified, which sets its possible values and allows the variable to "move" during the optimization process; controlling or limiting the size of the optical element. Variables can be defined as absolute, relative or pick-ups. Absolute variables are defined based on the absolute or global coordinates of the variable's range of motion. When the location of the original variable is changed, the range will remain fixed. Relative variables are defined in relation to the current location of a variable, so if the variable moves, the variable's range will move with it. Pick-ups define the position and movement of a variable as a function of the value of another variable [336]. For example, a variable can be defined as a pick-up to maintain a constant thickness in a material or a specific spacing between two components.

Relative and absolute variables have been used for the optimization process, the latter are used to define the cell size width (1.3 mm) and the aperture area width (11.2 mm), which in Figure 3.10 are the lower and upper points (in orange), respectively. On the other

hand, relative variables have been used to drive the shape of the optics to be as efficient as possible following the TIR, which are the points between the defined absolute points, illustrated in green on the right of each model in Figure 3.10. In addition, as the optics are intended to have symmetric behavior, a symmetry axis has been defined in the ZY-plane, red line in the middle of CPC optics, as shown in Figure 3.10, yet the contribution of both parabolic sections is considered in the computation of the maximized flux. Since the optimization process under study deals with a 2D optical system, two-dimensional relative variables have been used in which the Z-axis interval has been set to zero while the Y-axis interval represents the optimization trajectory, defined as Σ_y , as illustrated in Figure 3.10 (Model #3). This will allow the whole optimization process to be more faster, since the value of the variable will travel in only one dimension and not in a three-dimensional space that would require a larger number of iterations to find a solution.

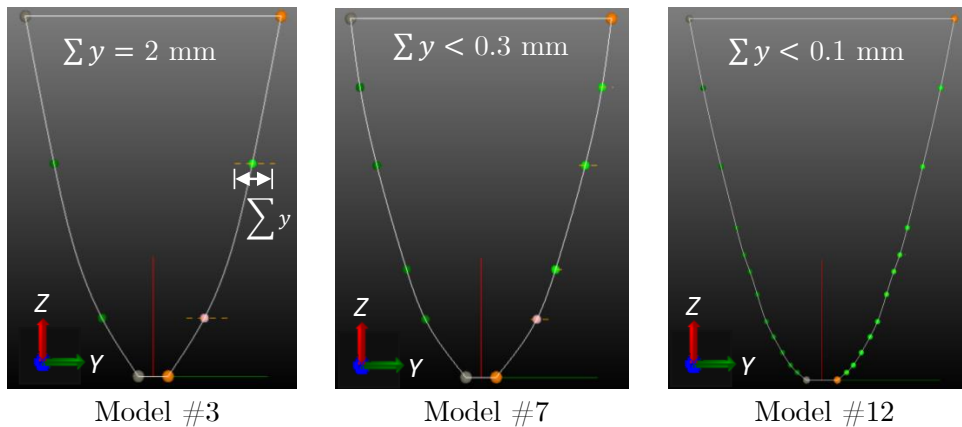


Figure 3.10: Evolution of optimization models exemplifying three stages of the iterative process, Model #3 using 2 variable points and Model #12 using 11 points.

First, a parabolic primitive shape is defined and discretized in a reduced number of variable points (e.g., two, as shown in Figure 3.10 (Model #3)) in order to optimize its angle. For this, it will follow multiple operations until it is found that the error of the objective function does not decrease locally for the defined Σ_y ; this process is repeated multiple times for the same configuration of parameters to ensure that a better solution does not exist. Subsequently, following an iterative process in which the number of variable points are increased (e.g.: until 11 as shown in Figure 3.10 (Model #12)) while its Σ_y are decreased, once the total flux transmitted to the receiver is maximized, via the local optimizer Nelder-Mead method. Through this iterative process it is possible to benefit of using a fast local optimizer while having an accurate and refined solution.

3.2.1.4 Evolution and results of the optimization process

After following the process described previously, some of the results are presented below. The same three stages of the process are shown in Figure 3.11 to illustrate the evolution of the models, on the left is shown the total irradiance map for incident flux on solar cell for these model stages, while on the right side is shown an example of how the rays are concentrated by a CPC, more specifically for model #12 via raytracing modeling (showing only 1% of traced rays). In relation to these results, Table 3.4 shows the metrics relative to the models, showing how for the same target value, the total fluxes increase while the error decreases progressively as the shape is optimized.

Figure 3.12 illustrates as an example the trend plot of the error function versus the number of iterations of model #12, followed by the local optimizer Nelder-Mead. This method uses a specific polytope called simplex, which is a geometric object with “flat” sides ($n+1$ vertices in n dimensions) that using diverse operations such as reflection, expansion, contraction and shrink will adapt itself to the local landscape to establish an optimized solution closest to a starting point. At the beginning this model has an error source of about 13%, then the first oscillations of the relative variables lead to an increase of the error up to more than 40%, after 50 iterations the model returns to the initial error value to continue decreasing and reach a best value of about 0.5% error, which represents the best overall value and the closest to the target value.

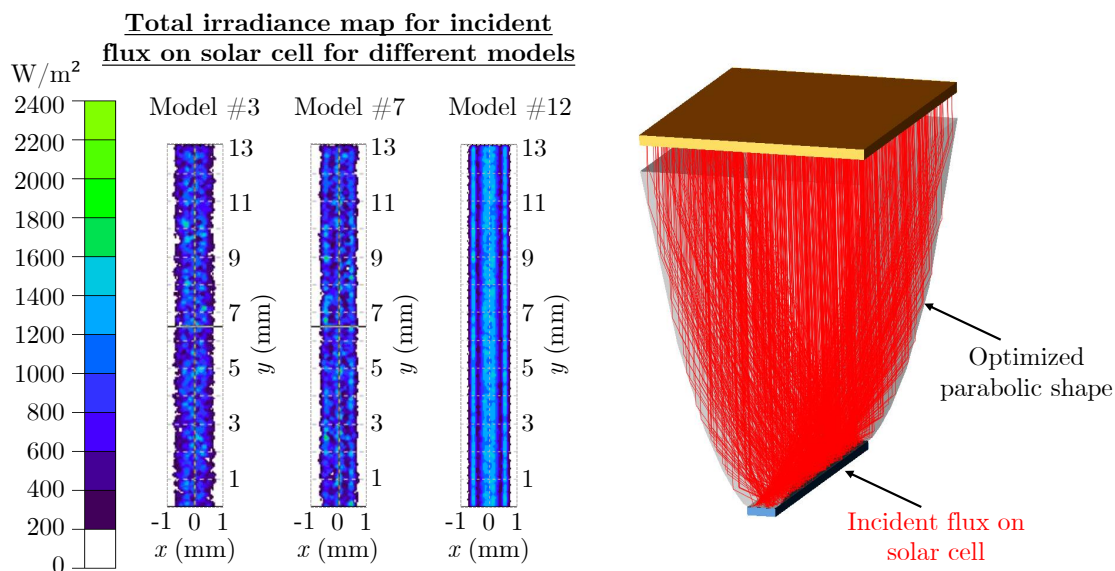


Figure 3.11: Total irradiance map for incident flux on solar cell for three different model stages of the iterative process (left). Raytracing model illustrating concentrated flux via the optimized parabolic shape of Model 12 (showing only 1% of traced rays).

Table 3.5 makes a comparison between versions, between the first design (version 1) and the optimized one (version 2). As the receiver area was reduced about 59.3%, a

Table 3.4: Optimized model metrics for three different stages of the iterative process, for models #3, #7 and #12.

Model \ Metric	#3	#7	#12
Target value (W)	0.172	0.172	0.172
Total flow (W)	0.1133	0.12467	0.17121
Error (%)	34.13	27.52	0.46
No. Incident rays	9641	10576	96647

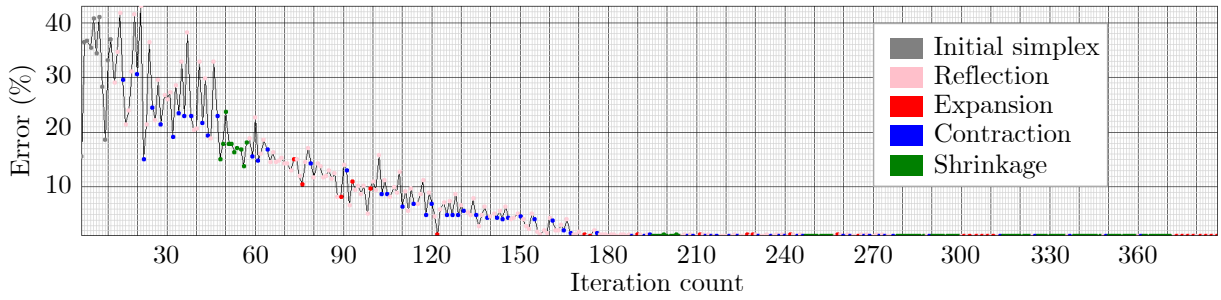


Figure 3.12: Example of trend graph for the iterative process followed by the Nelder-Mead local optimizer for model #12, illustrating the evolution of the error function vs. the number of iterations.

mass redistribution was carried out in order to increase the design efficiency by rising the effective concentrating factor from 7.6X to 8.6X about 13.2%, and a theoretical gain of the optical efficiency of 25.3%.

Table 3.5: Metrics comparison between different versions.

Model \ Metric	Version 1 (a)	Version 2 (b)	Ratio (%)
Receiver surface area per cell (mm ²)	43.2	17.6	-59.3
Concentration (X factor)	7.6	8.6	+13.2
Theoretical optical efficiency (%)	75.0	94.0	+25.3

Once we have defined the theoretical improvement of the optimized model it is necessary to validate the results experimentally, with real prototypes, for this purpose the following part describes the proposed manufacturing process which in turn integrates some improvements.

3.3 Manufacturing and assembly description

The fabrication of the proposed prototype can be divided into two main assemblies which are fabricated separately and then bonded together, one comprising the interconnected cells on a PCB and the other involving the optics molded on the coverglass. The manufacturing steps and methods followed in the constitution of both will be described below.

3.3.1 Interconnected cells

In the first place, cells are bonded on a PCB using Silver paste with a precision of $\pm 50 \mu\text{m}$ and a wire-bonding technique to interconnect the front side to the paths. Specifically, a ball-bonding process was performed, using $25 \mu\text{m}$ gold wire and a combination of heat, pressure, and ultrasonic energy to make a weld at each end of the wire. This PCB was designed to be enough robust to the molding but also to have access to different behaviors of the electrical architecture of the prototype. As shown in Figure 3.13, the three cell contacts are bonded using three wires, such redundancy will guaranteed a reliable interconnection.

It is important to notice that the PCB was designed in such a way that the three strings S1, S2 and S3 could be connected on either parallel or series, so diverse electrical behaviours can be determined, as shown in Figure 3.13. Copper tracks design and a DB9 connector allow measuring each string individually as well as the cells C1, C2, and C3. The four MJSCs are bounded along vertical direction to carry out measurements in order to quantify the edge effect of the optics.

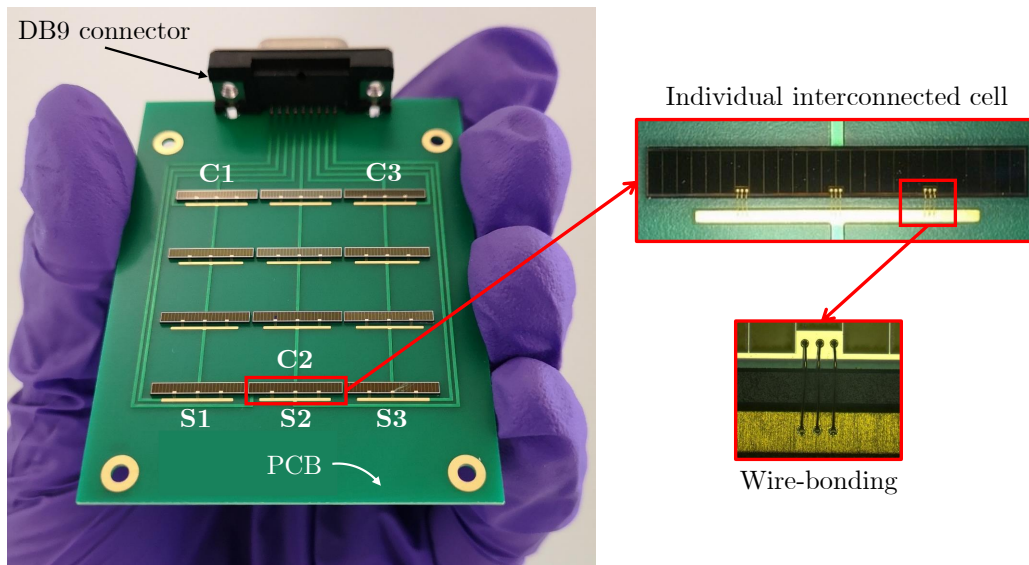


Figure 3.13: Interconnected cells on PCB, showing three strings (S1, S2, S3), and 12-cells with three of them measurable individually (C1, C2, C3) thanks to the electrical DB9 connector. C2 is enlarged on the right side to show its details.

3.3.2 Optics silicone molding and its improvements

In the present prototype architecture optics are "self-supporting". The silicone optics hold together the glass and the structure as a whole. The manufacturing process of the optics can be divided into three main steps, the assembly of the injection mold, the injection and curing of the silicone and finally the demolding and assembly. Each of these steps is briefly presented below and at the end we discuss some of the proposed improvements included in an attempt to solve some of the problems encountered with the previous generation CPC prototype.

3.3.2.1 Assembly of the injection mold

The first step is to prepare the surface of the pre-cut coverglass by performing: (i) a pre-cleaning with isopropanol and compressed air to remove dirt and organic materials. Then, (ii) a plasma treatment is applied during 3 minutes to improve the adhesion on surfaces, this plasma (N_2) pre-treatment cleans and functionalizes the surfaces to activate the adhesion bonds by increasing the surface energy. (iii) A primer coat (Dowsil™ 1200 OS) is then applied over the coverglass to improve the adhesion of the Room Temperature Vulcanizing (RTV) and heat cure silicones. Next, the coverglass is assembled between the top clamping plate and the CPC cavity using four screws, to ensure that there is no leakage between the mold and the glass, as illustrated in Figure 3.14 (left). The silicone injection plate is then assembled with the rest of the assembly Figure 3.14 (right).

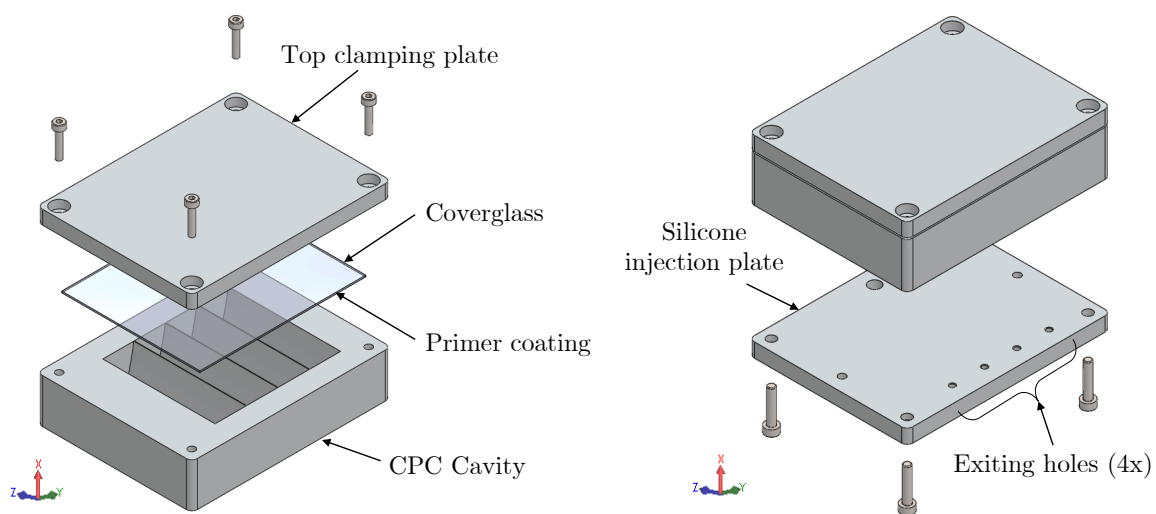


Figure 3.14: Diagram illustrating injection mold assembly. Coverglass is assembled between the top clamping plate and the CPC cavity (left). Silicone injection plate assembly (right).

3.3.2.2 Injection and curing of the silicone optics

Once the mold assembly is completed, the CPCs are molded onto the glass using Dow Corning® 93-500 bicomponent silicone; previously mixed using a universal mixer for 5 minutes. The silicone is injected using a Tygon hose that is connected to the injection cavity shown in Figure 3.15 (1) (on the left) using a pneumatic connection. The silicone flows vertically upwards through the pressure of the syringe filling the optics cavities until it reaches the top of the mold and slightly leaks out of the four outlet cavities, see Figure 3.15 (3). Then the complete system is put under vacuum (0.1 mbar) for 30 minutes to remove all remaining bubbles, the air evacuation is done through these last holes. This stage is completed by reticulation of the silicone, for this the system can be heated for 15 minutes at 150°C or it can be reticulated at room temperature for 24 hours.

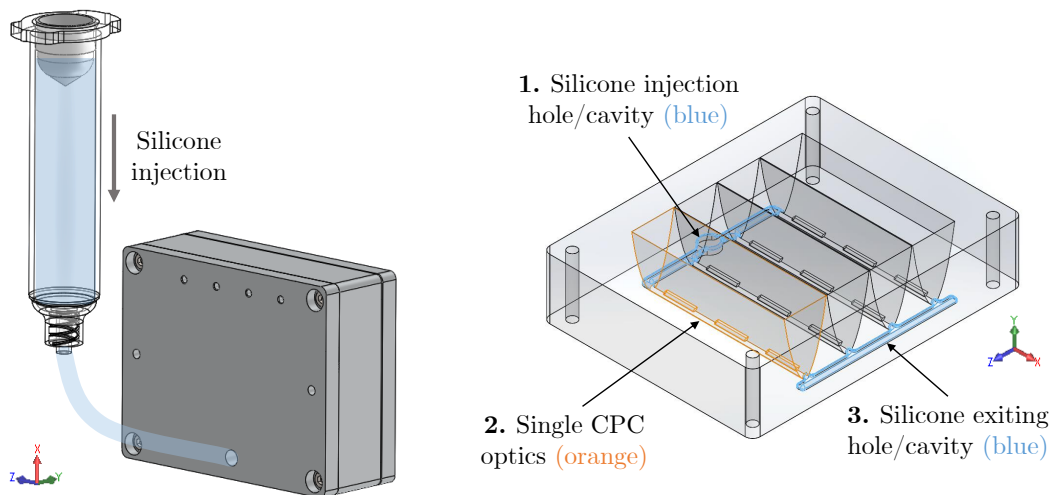


Figure 3.15: Diagram illustrating: silicone injection assembly with a syringe and a Tygon hose (left); the silicone injection and exit cavity (1.) and (2.), respectively (in blue), as well as a single CPC optic (in orange).

3.3.2.3 Demolding of optics and final assembly

Once the optics have cross-linked (and cooled if heated), they must be demolded. The first step is to remove the silicone injection plate in Figure 3.14 (left). Then an extraction counter-mold is used which uses channels designed to inject air into the lower part of the optics and release them, illustrated in Figure 3.16. To inject the air hermetically into the mold, a clean pneumatic connector (of the same type as for injecting silicone) is used with a Tygon hose to "blow" it into the mold using a compressed-air blower.

Then, the interface cells/optics are treated with a layer of "primer" silicone, typically used to assure a reliable adherence. Finally, the hosting-cavities (cell/wiring) are filled using the same Dow Corning silicone and the optics/PCB assembly mechanically bonded.

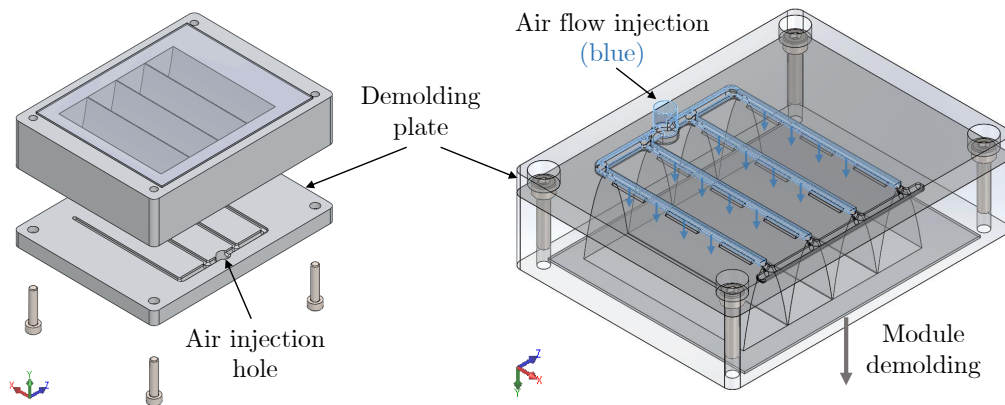
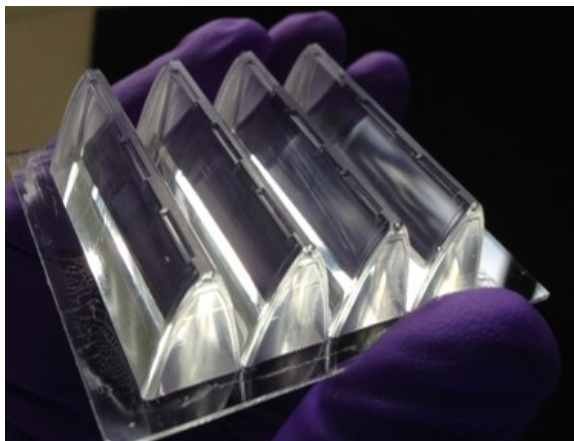
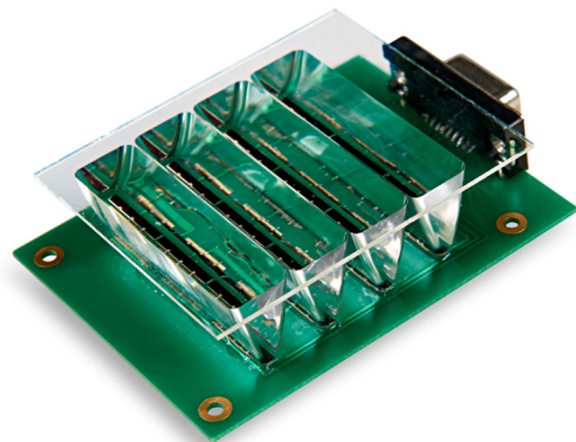


Figure 3.16: The top clamping plate and the silicone injection plate are replaced by the air injection plate (left). Diagram illustrating the injected air flow (in blue) used to demold the optics.

The final prototype module is composed of four line-focus optics, molded on a 900 μm borosilicate front glass. Each linear CPC focus light onto three cells laterally disposed. This design proposes a direct molded (optics/cells) integration that eludes alignment procedures in space, so increasing module reliability. A photo of the final prototype is presented in Figure 3.17 (b).



(a)



(b)

Figure 3.17: (a) CPC optics after demolding; and (b) New generation CPC prototype photography.

3.3.2.4 Discussion

As mentioned above, during the molding process of the previous prototype, the presence of bubbles was occasionally observed. The main associated cause was the creation of a turbulent silicone injection flow, so a new distribution of the molding channels has been developed and integrated in this work. This new design prevents silicone backflow and

sharp-edged molding through the injection channels. Additionally, the silicone injection plate is provided with four injection exit holes, one for each optic, rather than the central one in the previous version, which allows for a more efficient evacuation of air bubbles during the silicone injection and vacuum process.

Another problem was the lack of bonding between the coverglass and the optics, so a meticulous procedure has been adopted in which the coverglass is carefully cleaned and the inner surface in contact with the silicone of the optics has been previously activated, a novelty with respect to the precedent generation is the use of plasma which in combination with the primer, helped to eliminate debonding and the creation of a thin layer of air between the elements.

Finally, one of the main modifications brought to this new generation is the redesign of the cavity linking the optics and the PV cell, which previously used a single large cavity that required the use of thin walls (0.23 mm thick) which at the end of the shaping process were often not well defined and on the one hand, they contributed to generate errors in the shape of the optics and on the other hand did not fulfill the function of keeping the optics at the focal height for which they had been designed. In contrast, the new version eliminates the thin walls and instead proposes a flat lower contact surface.

The improvements mentioned above are expected to increase the optical efficiency of the CPV and reduce the costs associated with optics production, helping to ensure good quality parts and a reliable process. Figure 3.17 shows a picture of the current optics as well as a fully integrated prototype. The next section addresses the opto-electrical characterization of this new generation of CPCs for space, and will allow us to study the extent to which the enhancements will improve performance.

3.4 Performance evaluation of the optimized CPC

As a first step, we investigated the ElectroLuminescence (EL) spectral signal of III-V cells on Si. This was used as it is a fast and non-destructive method to detect cell defects, such as absence of fractures, cracks and localized defects by semiconductor effect; it has been done before and after wire-bonding interconnection. We then evaluated the I-V characteristics of the cells, without optics (@AM0, 8.6X) and after integrating the molded optics (@AM0, 1X), in order to estimate the optical efficiency of the assembly.

3.4.1 Electroluminescence

EL can be considered as the counterpart of the photovoltaic effect: a fraction of the injected carriers is radiatively recombined, resulting in a photon flux that can escape from the semiconductor material. The analysis of this EL signal can be spectral, spatial

and/or temporal, and it provides valuable information about the semiconductor device such as defect mapping, minority carrier lifetimes [337, 338] and various resistances like shunt/series/sheet [339–341].

3.4.1.1 A brief description of the device measurement

The EL test bench, used in this investigation, consists of three main parts: the imaging/detector system, the sample positioning and the bias supply. An overview of the EL experimental arrangement is depicted in Figure 3.18. In principle, each tested sample is forward biased with the use of a Keithley 2602B power supply, at variable amplitude, depending on the technology of the tested sample and the junction (sub-cell) to be measured.

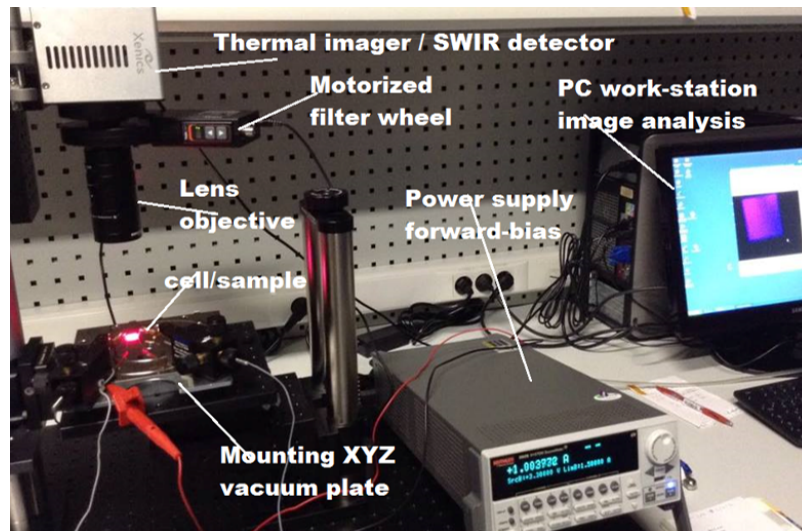


Figure 3.18: Overview of the employed electroluminescence test bench.

The produced light emission, due to radiative recombination of carriers, is detected and measured by a short wave infrared (SWIR) imager. A RAPTOR 640-CL with an acquisition range of 400 to 1700 nm, using 640x512 pixels of $15 \times 15 \mu\text{m}^2$, and the detector is InGaAs. The quantum response of the camera is shown in Figure 3.19.

The imager system further includes: *i*) two interchangeable lens objectives, which allow adjusting the aperture, the magnification and the focus for optimized display of the measured samples, and *ii*) a Thorlabs motorized filter wheel, which allows individual EL imaging for each cell junction (sub-cell), with proper selection of 25 mm optical filters.

The electroluminescence signal is emitted for each sub-cell at the wavelength corresponding to the bandgap from the TOP to the BOTTOM, respectively: GaInP (1.90 eV) at 660 nm, GaAs (1.46 eV) at 890 nm and Si (1.1 eV) at 1150nm.

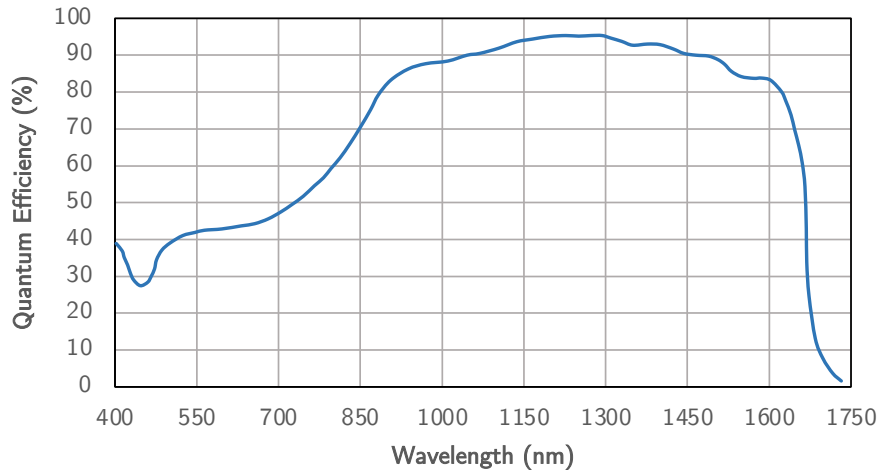


Figure 3.19: Quantum response of the RAPTOR 640-CL camera (InGaAs photodiode array).

3.4.1.2 EL results

Initially, the EL response of each individual cell was checked to select those without defects to be integrated into modules. Figure 3.20 shows: (a) one cell with a homogeneous response over the whole cell surface (i.e., red dashed box) and (b) one cell with defects, showing a light peak at the top, while the rest is dark. Then, EL tests were performed after the wire-bonding process to evaluate possible errors introduced during soldering. Figure 3.20 (c) shows the example of the four cells of a string which perform well.



Figure 3.20: Electroluminescence response of a single III-V/Si solar cell ($1.5 \times 13 \text{ mm}^3$, see red-dashed-line) with: (a) homogeneous radiative emission indicating the absence of fractures (red dotted box represents the cell surface); (b) with a point peak of luminosity on the cell, and the rest shaded, indicating the existence of defects in the semiconductor structure. (c) EL of an interconnected string after wire-bonding.

3.4.2 Current-voltage (I-V) characteristics

Electrical characterizations of a CPV using III-V/Si cells for space applications were carried out. The prototype was characterized under solar simulators to evaluate its electrical performances. Two different devices are typically used, one for measuring cells behaviour before lenses integration (Helios 3030 - cell) and the other one for the assembled module (Helios 3030 - module). Both of them use a collimated Xe lamp source to match AM0 spectrum (1366 W/m^2) at 28°C . In this way, a comparison between these two characterisations helps to determine the module optical efficiency, and the CTM ratio.

3.4.2.1 Solar cell simulator: Helios 3030

A first equipment used during the indoor characterization of the solar cells at INES is the Helios 3030 Solar Simulator, it is shown in Figure 3.21. This simulator is capable of irradiating concentrator devices with light that is similar to that of the Sun so as to allow optical and electrical measurements that are predictive of the in-sun performance. Its main features are:

(i) Selectable irradiance levels (from 1X to 1500X), the concentration varies with the movement of the lamp on the motorized rail and a collimator for high concentration.

(ii) Selectable spectral distribution (ranging from red-rich to blue-rich spectra, through the reference spectrum AM1.5D and AM0). The spectrum and light intensity are controlled by reference cells called isotypes (i.e.: isotypes are MJSCs with a single electrically active junction, for which the current produced by each junction in the cell can be measured directly).

(iii) No collimated light (angular size of the light source).

(iv) Temperature controlled chuck.

The system follows a multi-flash IV measurement method, such that only one (IV) point is measured for each flash pulse. As a result, there is no need for a light pulse with a stable plateau. Furthermore, the variation of the irradiance throughout the light pulse can be used to perform analysis as a function of the irradiance, e.g. extract the IV curve for several irradiance levels simultaneously. However, the spectrum of the light varies with the irradiance as well. Therefore, every level of irradiance intensity is linked to a particular spectral content. Using spectral or neutral filters, different spectra can also be obtained at the same irradiance level, or different irradiance under the same spectrum. This allows covering the whole range of spectral conditions actually found under real operation. The solar simulator for indoor cell measurements has been adjusted to have AM0 spectrum by balanced the short circuit current of the top sub-cell with the short circuit current of the mid sub-cell of a 3J obtained by the convolution of the AM0 with the External Quantum Efficiency (EQE) of these sub-cells. This method can be controlled with a complete

measure of the spectrum from 350 nm to 1800 nm thanks to spectrometers adapted to flash measurements. A precise characterization of the thermal response of the device can also be carried out thanks to a chuck which can be regulated at a temperature upper to 60°C.

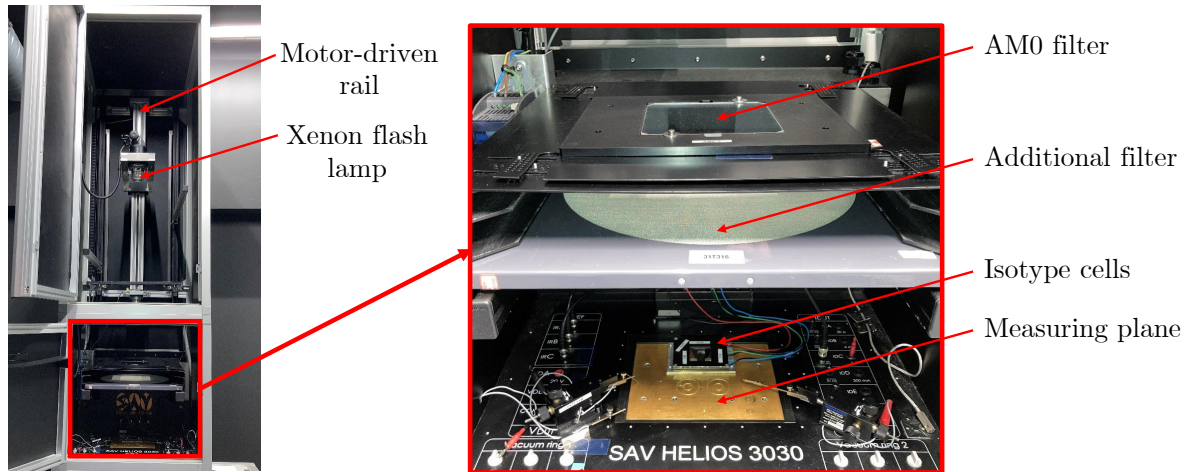


Figure 3.21: Helios 3030 solar simulator for cell IV characteristics.

3.4.2.2 Solar module simulator: Helios 3198

The second solar simulator, HELIOS 3198, with a highly collimated, large-area beam (2 meters in diameter) shown in Figure 3.22, is used for the measurement of CPV modules. Unlike the former, the collimating mirror does not increase the concentration, but provides an aperture angle of $\pm 0.4^\circ$ to the incident beams in the measurement plane. This aperture angle delimits the light cone which contains 90% of the power emitted by the sun under standard operating conditions, this is used in the design of the concentration optics and is provided with an AM0 filter as for the cell simulator. On the one hand, the spectrum and intensity of the light are controlled by a single reference module in the module simulator.

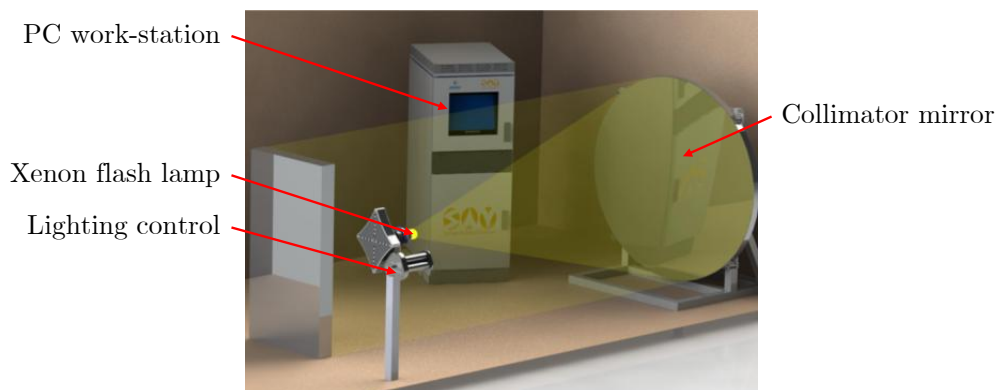


Figure 3.22: Diagram illustrating the Helios 3198 solar simulator for module IV characteristics [342].

3.4.2.3 IV characteristics results

The results of the IV characteristics of both designs (version 1 and 2) are presented below, in order to compare them and quantify the performance improvement between versions, and especially to see if this corresponds to what is expected from the optical simulation. On one side, the world's first space CPV prototype using III-V/Si cells for space applications was based on the previous optical design, without optimization. Prototype for which we obtained an optical efficiency of 68% considering a single cell, representing an relative loss of 9.3% with respect to a theoretical efficiency of 75% [343].

Then, as presented in this chapter, work has been done to increase the theoretical efficiency and an efficient parabolic shape of 94% has been established, providing an expected (theoretical) relative gain of about 25.3% with respect to the previous model. The results below compare the new optimized design with respect to this primordial state, it should be noted that both generations of prototypes use cells from the same manufacturing batch. Thus, we expect the cells to have the same characteristics, and in this case, the differences should be attributed to optical design or module manufacturing differences.

Single cell measurements

To quantify efficiency, a module with only the central string equipped with cells was fabricated to limit cell usage during these early tests. The printed circuit board allows measurement of the complete string or a single cell (see Figure 3.23). These results are presented below.

Figure 3.24 shows three different curves, the IV characteristics of a cell without optics measured at 8.6X, which is the ideal, the theoretical IV response from TracePro, 94% efficient with respect to the ideal, and finally the IV with optics measured with an AM0 spectrum (1366 W/m² and 28°C). Then, the optical efficiency has been calculated, it represents the ratio between the I_{SC} 's of the module with optics @AM0 and without optics @8.6X, in this case optics are 80.4% efficient.

Table 3.6 shows the IV characteristics of the PCB-3, Power at the Maximum Power Point (P_{MPP}), I_{SC} , V_{OC} and the FF . We can distinguish two type of losses, identified in Figure 3.24. Losses attributable to the optical system itself (1), from Fresnel losses, about 4%, and an additional 2% induced during the optical optimization to ensure a high angular tolerance. In addition, (2) associated to the assembly and fabrication processes. In fact, the system is susceptible of misalignment between optics and cells, additionally, the roughness of the parabolic shape during machining (mold) by visual inspection seems not to be as good as the earlier design (average roughness, $R_a < 150$ nm), which transferred some irregularities to the molded optics.

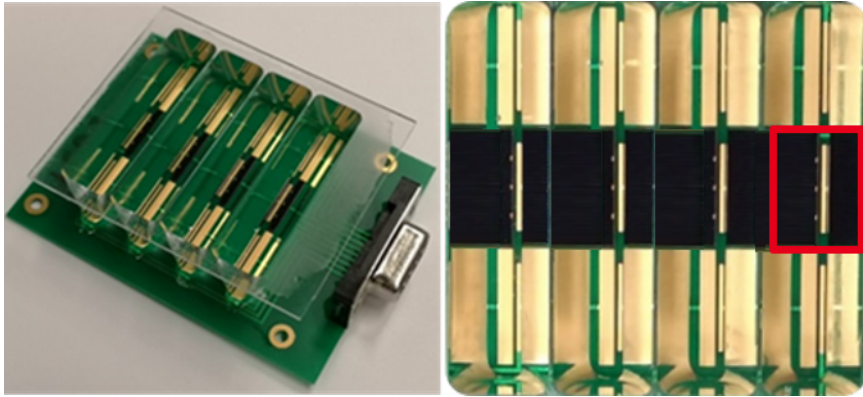


Figure 3.23: Photograph of a prototype: a close-up of the solar cell alignment (left) and top view of the final assembled module illustrating the measured cell (right).

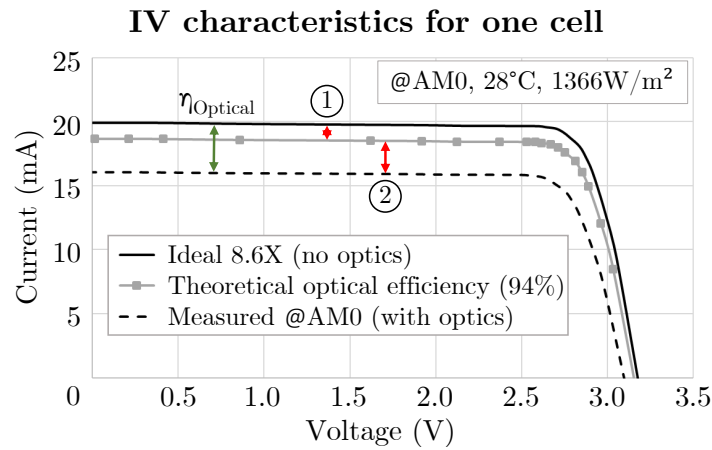


Figure 3.24: IV characteristics for a cell measured with an AM0 spectrum at 28°C: without optics (ideal) measured at 8,6X (solid line); response from TracePro 94% efficient respect to the ideal (solid line with markers), and with optics measured with an AM0 spectrum (dashed line).

Table 3.6: IV characteristics for the one cell.

Measure	IV for one cell before integration	IV for one cell with optics
P _{mpp} [mW]	52.7	41.1
I _{sc} [mA]	19.9	16.0
V _{oc} [V]	3.18	3.10
FF [%]	83.2	82.7

String measurements

The same process has been done for a string, shown in Figure 3.25, comprising four cells. Its electrical performances are illustrated in Figure 3.26 and Table 3.7, before and after optics integration. An optical efficiency of 79.4% has been reached. It is slightly lower with respect to the cell measurements since in one string the cell with the lowest I_{SC} will limited the whole string.

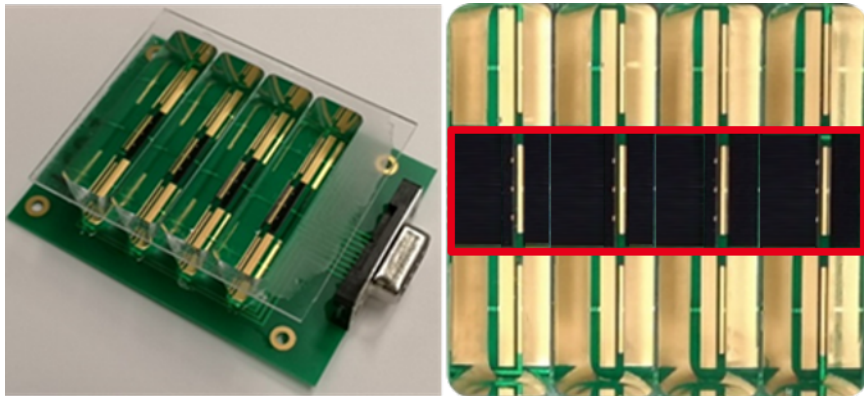


Figure 3.25: Photograph of a prototype: a close-up of the solar cell alignment (left) and top view of the final assembled module illustrating the measured string (right).

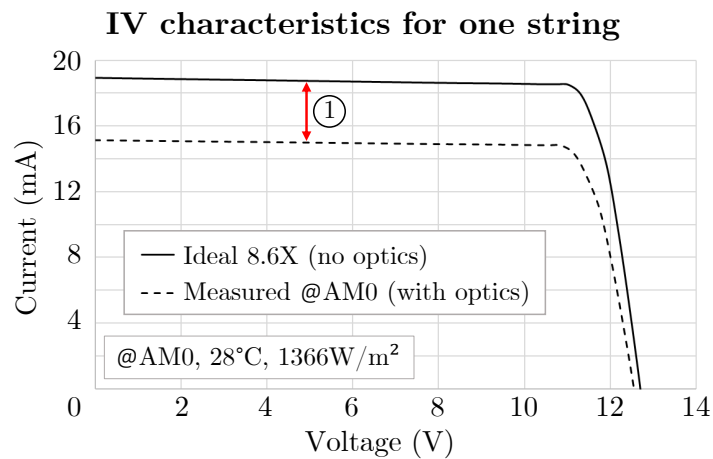


Figure 3.26: Photograph of a prototype: a close-up of the solar cell alignment (left) and top view of the final assembled module illustrating the measured cell (right).

Table 3.7: IV characteristics for one string.

Measure	IV for one string before integration	IV for one string with optics
$\overline{P_{mpp}}$ [mW]	204.4	145.8
$\overline{I_{sc}}$ [mA]	18.9	15.0
$\overline{V_{oc}}$ [V]	12.7	12.5
\overline{FF} [%]	84.9	78.2

3.4.3 Comparison between designs and discussion

If we compare the present results with the previous design, it is possible to appreciate that the receiver area has been reduced to the minimum, see Figure 3.27 (left), the red area represents the associated surface losses, which are eliminated in the new module. Finally, improving the optical performance of about 18%.

As a matter of fact, we can appreciate that there is a difference between the IV performances for all modules before and after integration. It is mainly attributed to the

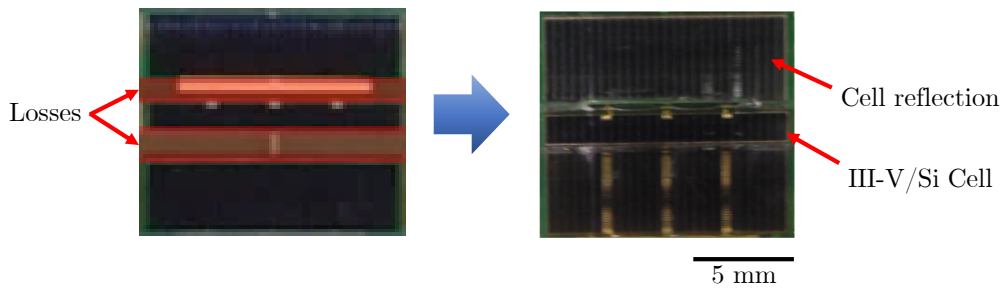


Figure 3.27: Photographs showing a close-up top view of an integrated solar cell: previous version with associated losses in red (left); and the current module illustrating the PV cell used and how it is reflected on the CPC walls (right).

IV characteristics: a comparison between versions using one cell

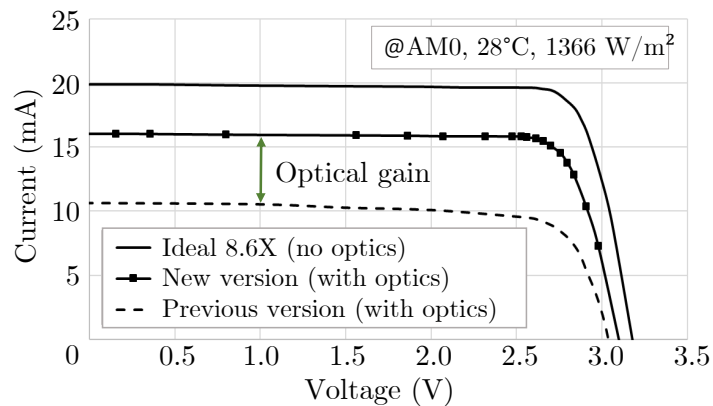


Figure 3.28: Performances comparison between versions using one cell vs the ideal IV characteristics without optics integration.

Table 3.8: IV characteristics for the one cell.

Metric \ Model	Version 1 (a)	Version 2 (b)	Ratio (%)
Receiver surface area per cell (mm ²)	43.2	17.6	-59.3
Concentration (X factor)	7.6	8.6	+13.2
Theoretical optical efficiency (%)	75.0	94.0	+25.3
Experimental optical efficiency (%)	68.0	80.4	+18.2

alignment during the assembly between the optics and the interconnected cells on the printed circuit board, which is done mechanically for the moment. However, alignment is not the only reason that can explain this behavior, the roughness of the silicone lenses, shaped by the machining grooves of the mold, can induce aberrations and chromaticity change. Even a spectral mismatch between the two solar simulators (cell and module),

could produce different input radiances affecting the I_{sc} and V_{oc} parameters, in response to a discrepancy of the estimated concentration used to characterize the cells and the one achieved with the lenses. These are some of the avenues of research to improve the understanding of all the associated phenomena.

For the time being, solar cells are attached on a PCB to initially validate the concept; afterward a support using space-based materials will be implemented. Estimates suggest that some optimization improvements as the use of more efficient MJSC could be performed to achieve high specific power 150 W/kg.

3.5 Conclusions and perspectives

This chapter has described a comparative characterization between the CPV theoretical efficiencies, optical and electrical, and its relative experimental performances, helping to determine the viability of such a system after multilevel optimization. It has taken into account the optical efficiency, the manufacturing and integration process between the cells and its optics. An enhanced prototype of space concentrator using III-V/Si cells has been established. Future work should integrate a study exploring the prospective cost reductions that may result from this proposition, understand how low the costs of III-V solar cells and in general the whole array might be able to go in the future, and whether these could be competitive in space solar markets.

The proposed CPV surface receiver has been optimized, maximizing the sunlight flux on solar cells. At the same time, this optimization process increases the theoretical optical efficiency of 25.3% respect to the previous design and allows a mass redistribution that enhances its concentration factor. Moreover, measurements shown that an experimental increase of the 18.2% has been achieved. It has been determined that the current CPC system, after being optimized achieves a measured optical efficiency of about 80% and a concentration factor of 8.6X, leading to a specific power of about 20 W/kg. Which is not in accordance with the current metrics expected for solar panels that are in quest of specific powers > 100 W/kg in order to overcome the CICs. The fundamental reason for the excessive mass used is the optical system, which represents about 90% of the total weight of the prototype, which is one of the main disadvantages of most filled systems and uses the volume to focus the sun's rays. This has also been shown in the state of the art of Chapter 1, in refractive optics, showing that typical lenses (plano-convex) are not the most advantageous solution for space applications with respect to mass, or that otherwise these systems must drastically reduce the scale of the lenses to reduce profile and low mass, or else must be designed in the form of patterned layers (e.g. Fresnel) involving other technological challenges such as deployment in space.

In this sense, as discussed also in Chapter 1, one of the solutions that showed promise

for powering satellites is the use of micro-CPVs using μ -cells with the potential to address all these issues at once, reducing the optical profile and mass, along with improving passive thermal management, with moderate concentrations ($< 100X$). The following chapter presents the optical design and validation of a new micro-CPV integration concept that aims to increase the array specific power to > 100 W/kg using a network of millimeter-scale reflective parabolas.

Everything is theoretically impossible until it is done.

— Robert A. Heinlein

4

Optical design of a highly integrated reflector for micro-CPV

This chapter presents the optical design of a novel concept of micro-CPV, which proposes the use of a highly integrated miniaturized mirror. This approach is developed with the objective of significantly increasing the specific and volumetric powers (i.e., W/kg, W/m³), of PVAs in space, at the same time reducing the recurring cost of the standard CIC solar array while maintaining a high specific stiffness. In addition, it takes into account the array structure and avoids deployment (i.e., between optics and cells) in space, decreasing the associated risk and complexity. The desired cost reduction is obtained as a result of using highly efficient and very small (< 1 mm²) MJSCs together with low cost optics, which provide a low/medium concentration factor. As a novelty, this new concept is directly integrated inside a honeycomb core sandwich panel, made of aluminum, widely used in the aerospace industry, for its high bending stiffness and flexural strength with low mass.

The first part of this chapter is devoted to the description of the highly integrated micro-CPV concept, as well as its mechanical structure and its potential advantages; see Section 4.1. Second, a study has been carried out comparing two ideal reflector systems: a parabolic one and an optimized free-form; see Section 4.2. In this regard, we searched for the most homogeneous flux distribution achievable over the cell, which could guarantee a given angular tolerance. Third, the modeling and optical simulation of the chosen reflector integrated into a hexagonal honeycomb cell; see Section 4.3. The optical loss chain was studied, as well as the concentrated flux distribution and the angular tolerance. Finally, an estimation of the short-circuit current density based on EQE measurements was made.

4.1 Design of a highly integrated micro-CPV

Looking at the various CPV proposals for space and terrestrial applications (Chapter 1), it can be seen that concentrators require mechanical supports to ensure the rigidity and stability of the assembly. For space, some studies do not take this structure into account, which leads to an underestimation of the mass and thus the real specific power of the solar array. More importantly, optical systems with an air gap (or vacuum) between the cells and the optics must also ensure a structure that keeps them aligned, which implies additional mass.

Honeycomb core is used in a wide range of aerospace applications, wherever lightweight, high strength-to-weight, dampening and dimensional accuracy are critical characteristics. Typically, a honeycomb sandwich panel is formed by bonding two high stiffness thin face sheets with a low density honeycomb core which has lower strength and stiffness, as shown in Figure 4.1 displaying some of its key dimensions. In this respect it is possible to obtain various properties and performance by varying the core, face sheet thickness and material, in particular a high strength-to-weight ratio [344]. Similarly, various types of core shapes and materials have been used for the construction of sandwich structures [345].

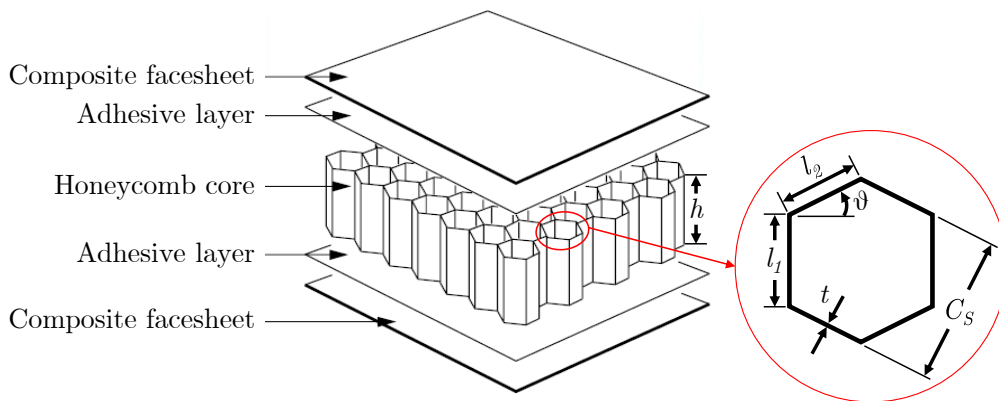


Figure 4.1: The honeycomb sandwich panel is composed of two thin composite facesheets bonded to the core by an adhesive layer (left); and a close-up view of a honeycomb unit showing its principals dimensions. Where C_S is the cell size, l_1 and l_2 are the characteristic lengths of the hexagon, t is the foil thickness, while θ represents the angle between the horizontal plane and l_2 .

In this work, we propose to integrate concentrating systems in a honeycomb core-based architecture. This novel idea, which has been patented [346], relates to a CPV comprising optical elements and a honeycomb structure, each optical element being arranged in one of the cells of the honeycomb core. The invention includes a monolithic structure that functionalizes the constituent elements, on the one hand using the optics as part of the mechanical support, and on the other hand, the honeycomb core is used to stiffen the assembly and keep the optics and the solar micro-cells separated and aligned.

Furthermore, we propose to pursue a reflective optical system design (i.e.: simple paraboloid), as this system has been shown to provide the best combination of specific power and angular acceptance potential, based on the discussion presented in Section 1.5, comparing studies related to reflectors by Pennsylvania State University [85] and for the refractive counterpart by the NRL [63]. For this, the use of a honeycomb core consisting of a thin aluminum panel in the form of hexagonal (quasi-regular) cells perpendicular to the faces is proposed. This core is stiffened at the bottom by a Carbon Fibres Reinforced Plastic (CFRP), while at the top there is a coverglass in which the PV micro-cells and interconnections are located. Finally, inside the core are integrated the reflective optical elements that will concentrate the sunlight upwards on the network of interconnected cells, also these optical elements have the potential to reinforce the assembly and increase its stiffness if filled. In addition, the packing density is maximized using hexagonal unit cells. Figure 4.2 illustrates the applicability of the idea, showing the CAD design of a mini-module, which will be composed of a set of 30 unitary optics and cells: (a) exploded view of the elements, (a') close-up view of one integrated unit, (b) isometric view. This mini-module corresponds to a half-cell surface area of a standard 3J for space applications (i.e. 40x40 mm²) [8].

On the other hand, since the stiffness required by an array depends on the size of the panel wings and the architecture of the frame used to support it, in some cases a single stage of composite materials as described above is not sufficient to provide the required stiffness. Therefore a second composite stage can be envisaged, as shown in Figure 4.2 (c). In this a first honeycomb core structure at the bottom (of height h_2) is formed by two face sheets bonded to both sides of the honeycomb, using an epoxy-based adhesive. Meanwhile, a second (upper) honeycomb is bonded to the lower one (of height h_1) using the same adhesive. These two composite stages can be laminated at the same time or separately, as will be presented later in the experimental validation in Chapter 5.

While the mechanical sizing of a composite sandwich to support a solar panel in space is somehow specific to each application, we can in the first instance make a comparative analysis between a standard panel (i.e., used in a CIC structure) and the double-layer architecture of the proposed system, in order to investigate the advantages of the new proposition in terms of mechanical strength and mass. To compare specimens with different geometries we defined the target metric, D_n (N·mm), i.e. the bending stiffness divided by the width (b) of the sample, while the specific bending stiffness D_ρ , is D_n divided by the areal density of the samples (N·m³/kg). First, we have estimated the stiffness of a single layer standard panel, for which its typical thickness vary from 20 to 30 mm. Then, we compared the target values with those measured for the double stage panel proposed in this work, using different architectures (i.e., 12 configurations in which the dimensions of the elements were varied), described in Annex D, refer to [347].

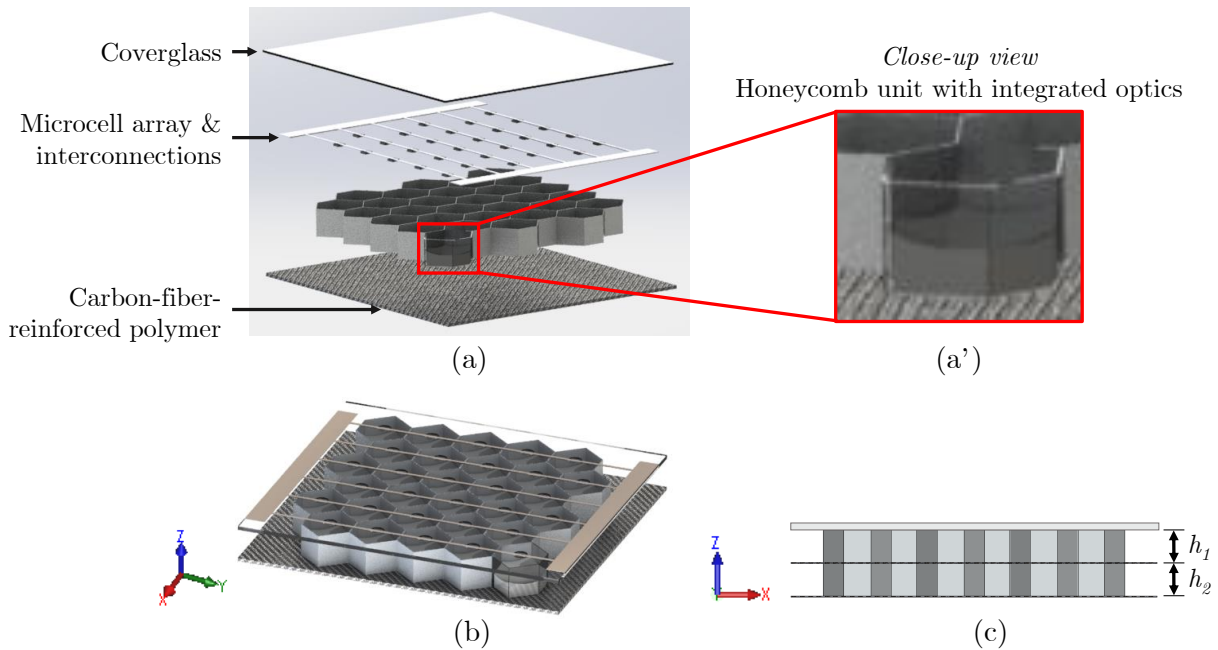


Figure 4.2: Schematic of the micro-CPV mini-module under study, which integrates 30 interconnected micro-cells. (a) Exploded view of the elements that make up the mini-module which has a surface area of about $40 \times 40 \text{ mm}^2$, (a') close-up view of one integrated unit, (b) isometric view showing and (c) a double reinforced layer architecture, where h_1 and h_2 are the layer heights.

Based on a standard CIC composite sandwich, about 20 mm thick, this provides a maximum stiffness of the panel $D_n = 5.6 \times 10^6 \text{ N}\cdot\text{mm}$ and a $D_\rho = 1.6 \times 10^3 \text{ N}\cdot\text{m}^3/\text{kg}$, as a benchmark, for further details refer to Annex C and [348]. In this regard, 7 out of 12 double-layer structures were shown to have a stiffness above the requirement (e.g., configurations 6 through 12), while 3 of these do so while reducing the mass of the assembly (e.g., configuration 6 through 8), up to 46% for architecture 6 and a stiffness 3.5% higher than the target (see Figure A4). Additionally, the current proposal also implies an improvement in compactness (W/m^3), which is evident if a single-stage system ($< 5 \text{ mm}$ thick) is used, but which is true even when using a dual-stage system as in the case of architecture 6 (i.e. 14 mm thick), providing a 43% reduction over the standard 20 mm. The latter is due in part to the use of a (light) carbon interlayer which substantially increases the specific stiffness of the assembly.

In summary, the integration of optics in a honeycomb structure can bring several benefits, including a reduction of the overall mass of the array to achieve high power levels per unit mass, realistically exceeding $150 \text{ W}/\text{kg}$ (for an AM0 spectrum), which allows replacing the existing CIC technology (currently between $50\text{--}80 \text{ W}/\text{kg}$), eventually at a much lower cost (i.e., mainly by reducing the surface area of III-V materials). The choice of the specific material used, as well as the mass associated with the proposed system will be described in Chapter 5, which deals with the experimental validation of the system.

Another potential advantage of this architecture includes a better thermal management of the array, in which the aluminum honeycomb can play the role of a heat sink, since the radiation surface is increased (with respect to non-walled systems), knowing that the thermal conductivity of aluminum is high (> 140 W/mK), compared for example to that of glass (> 13 W/mK). Thus, the solar heat load per unit area can be reduced by lowering its operating temperature, potentially reducing the emission of pollutants from the solar panel reflector that can cause degradation of the optical system, however this advantage still needs to be further studied to prove it.

In addition, the architecture presented allows the use of techniques such as direct molding within the honeycomb, ultimately minimizing the number of fabrication steps required to build an optics network and potentially reducing the associated costs. Finally, the structural features of the assembly include a monolithic structure that avoids a deployment in space, between the optics network and cells. While functionalizing the constituents, since the honeycomb core is used to stiffen the array and keep the optics and solar cells separate and allied.

4.2 Optical design via raytracing

In order to establish the design of the reflective system to be integrated in the honeycomb core, the first step has been to describe the fixed and variable parameters, as well as the criteria that guide the required performance of the optical assembly.

First, some of the fixed parameters of the optical design include:

(i.) The use of an AM0 solar spectrum, since the system is intended to be deployed in space. More particularly, we consider a satellite solar array located at a distance of 1 AU, i.e. for LEO to GEO Earth orbits (1366.1 W/m²), as described in Chapter 2.

(ii.) The geometry of the final integrated optics has a truncated quasi-hexagonal shape, in response to the form of the honeycomb core used. The latter does not have a perfectly hexagonal shape due to associated manufacturing errors.

(iii.) A silver reflective coating will be used given its high specular reflectivity, ranging from 95% to 97%. (iv.) We intend to use solar micro-cells about 800×800 μm^2 .

Then, if we move on to the approach of the requested performances of the system under development, we established certain criteria to satisfy, as follows:

(a.) A CPV system for space applications must provide a minimum acceptance angle to accommodate potential errors induced by phenomena such as mechanical vibrations, thermal distortions as well as tracking errors. While most communication and meteorological spacecraft already incorporate solar panel wings with high pointing accuracy $< 1^\circ$ [16–18], in this work, a minimum acceptance angle of $\pm 4^\circ$ was set for a uni-axial deviation, and for a bi-axial deviation of $\pm 2.5^\circ$, or more.

(*b.*) The concentration factor provided by the optical system must range from 10X to 100X, in order to guarantee an acceptance angle (i.e., uni-axial) of at least $\pm 4^\circ$, as demonstrated in [85]. (*c.*) At the same time, the integrated system must ensure a minimum mechanical misalignment tolerance of the constituent elements resulting from its assembly, to provide at least 90% of the ideal flow. In this regard, the lateral accuracy of alignment of the micro-cell network, using state-of-the-art techniques such as pick and place can vary between ± 3 and ± 50 μm , see Annex 6.5.3.

(*d.*) Finally, concentrating optics tend to produce an irradiance distribution that is most of the time not uniform, neither spatially nor spectrally, this flux in-homogeneity can increase the series resistances that decrease the performance of the photovoltaic cells [349]. The series resistance effects can be evidenced as a decrease in the FF and the Short-circuit current density (J_{SC}) [350]. In this regard, care must be taken to ensure a high level of uniformity of the spot concentrated on the cell.

Accordingly, in view of the parameters set and the criteria defined above, we have made a preliminary estimate of the dimensions of the hexagonal shape of the panel to be used, in response to the micro-cell area and the concentration factor range, parameters (*iv.*) and (*b.*), respectively. In this regard, we sought to use a standard honeycomb panel size (see C_s in Figure 4.1) in the aerospace sector, manufactured by companies such as Hexcel [351], which have been qualified to withstand the aggressive environment encountered in space for years. The most commonly used panel unit sizes include: small 1/8" (3.2 mm), medium 3/16" (4.8 mm) and large 3/8" (9.5 mm), which have internal areas of a unit cell of about 8 mm², 17.9 mm² and 71.5 mm², respectively. Thus considering a 0.64 mm² solar cell and a desired moderate concentration $< 100X$ we have chosen to use a medium cell size of 3/16" (i.e. 17.9 mm²), in order to achieve a concentration factor of about between 25X and 30X. While the small size would generate a very low concentration of 12.5X, the large size would exceed the criterion (*b.*) 112X, limiting the desired acceptance angle.

As mentioned, in the design of CPV arrays the irradiance distribution in the plane of the receiver is critical, since losses due to series resistance scale as the square of the current density in the solar cell, eventually becoming the dominant factor for cell efficiency with increasing current. In this respect, reflective optical systems tend to produce essentially spatial differences in the light profile, rather than spectral variations due to the non-presence of chromatic aberration (e.g., in the case of refractive systems). We therefore concentrate on studying these non-uniformities, which imply that some areas of the cell are illuminated with higher levels of irradiance than others, resulting in an increase in the effective series resistance and, therefore, a decrease in the FF . And for this, we use the Peak-to-Average Ratio (PAR), defined as the relationship between the maximum and average irradiance, used to estimate the degree of non-uniformity of a given light distribution [350].

Thus, in order to design the reflective optical system that presents the optimum

compromise between angular tolerance and homogeneous flux distribution, criteria (a.) and (d.) respectively, a preliminary study has been carried out in which two ideal reflector systems have been compared: a parabolic one and a reflector with an optimized free-form shape. Both were designed with the same concentration factor (26X), using a perfect reflective surface and an AM0 solar source. First, for the parabolic system (Section 4.2.2), different focal planes (i.e. receiver plane defocused around the $-z$ axis) were studied to estimate the best compromise between a highly homogeneous spatial distribution of the flux over the cell (i.e., lower PAR) and the desired acceptance angle. Second, a free-form shape (Section 4.2.3), which has been optimized to obtain a uniformly distributed flux over a percentage of the cell surface, equivalent to the best compromise found for the parabolic system. The latter is studied as an alternative to the parabolic system, with the potential to be less sensitive to shape deformations. Then, both designs have been analyzed and compared following performance criteria, acceptance angles, evaluation of various SOE designs for the free-form (to improve the Acceptance Angle (AA) and the flow uniformity), as well as their misalignment tolerances.

4.2.1 Source modeling and convergence

The first step in the optical design was to define the AM0 solar source. The spectral distribution of the modeled source is based on the Wehrli spectrum [89, 90], which represents the ideal extraterrestrial solar disk of about 1366.1 W/m^2 (i.e., for Earth's orbits) and a solar angular distribution, mean solar angle of about 0.27° . In the source definition, for this first study, we have considered three wavelengths (i.e., 0.3, 0.555 and $1.7 \mu\text{m}$), which cover the spectral range of state-of-the-art lattice matched 3J solar cells [8], by assigning a weighting representing that of the AM0 spectrum. We have designed a 5 mm diameter source, to ensure full coverage of the reflector aperture, 4.6 mm diameter (located at 3.5 mm from the source), even for angular deviations up to 15° .

Convergence analysis based on the incident flux on the optics aperture surface has been performed for different number of traced rays from 100 to 100 million, as shown in Table 4.1. This gives the flux deviation with respect to the numbers of rays traced and perceived, as well as the computation time required. It can be seen that when 100 rays are traced the associated error is 3.8%, this in turn tends to decrease as the number of rays is increased, until stagnating when using from one million to 10 million rays for a deviation of 0.1%. Further, when the number of rays was increased to 100 million, the limit of the computer memory used was reached. Therefore, we have used one million rays since it is the best accuracy found (0.1% error), with respect to the computational cost of the calculation (11 seconds), which is 16 times lower than for 10 million rays, for the same achieved accuracy.

In this regard, Table 4.2 shows the modelled solar source, using three wavelengths

Table 4.1: Convergence analysis of an AM0 solar source 5 mm diameter, based on the flux incident on the optics aperture surface 4.6 mm diameter.

No. of rays traced	Flux (W)	No. of rays on the optics aperture	Flux (W/m ²)	Deviation from ideal AM0 (%)	Computational time (s)
100	0.021838	83	1314.0	3.8	1
1,000	0.022585	842	1359.0	0.5	2
10,000	0.022894	8535	1377.6	0.8	2
100,000	0.022819	85073	1373.1	0.5	3
1,000,000	0.022684	850447	1364.9	0.1	11
10,000,000	0.022681	8503202	1364.8	0.1	180
100,000,000	Computer runs out of memory				

(0.3, 0.555 and 1.7 μm) and one million rays, indicating the total flux emitted (about 0.0268 W), as well as the flux and ray number weighting done by TracePro® for each wavelength. The incident flux map on the aperture of the optical system is shown in the Figure 4.3, composed by 850,447 incident rays, it accounts a total flux of about 0.0227 W and an average flux of 1365 W/m². This means that 15% of the total flux and the rays traced from the source do not reach the aperture of the optical system.

Table 4.2: Modeling of a solar source AM0, 5 mm of diameter, using three wavelengths (0.3, 0.555 and 1.7 μm) and one-million rays.

Wavelength (μm)	Weight	Flux (W)	# Rays
0.3	0.176853	0.00474377	176,853
0.555	0.742	0.0199144	742,429
1.7	0.0807184	0.00216513	80,718
	Totals	0.0268233	1,000,000

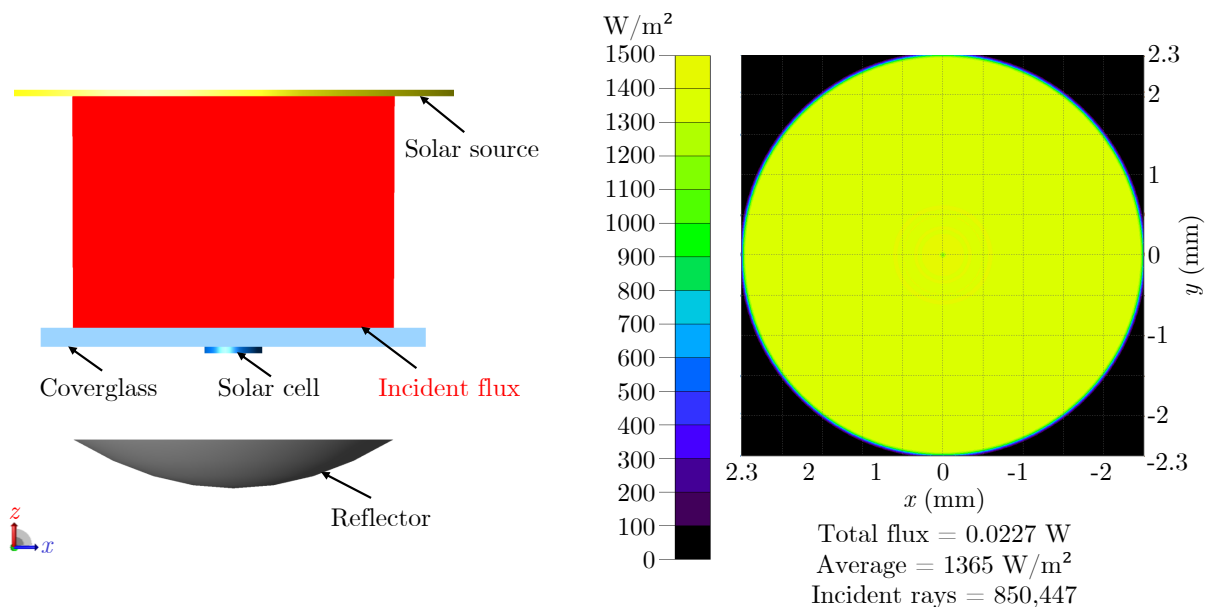


Figure 4.3: Irradiance map of the total flux at the aperture of the optical system.

4.2.2 Parabolic reflector

The first system considered is a parabolic dish. In a cartesian coordinate system, the design of a symmetrical paraboloid dish parallel to the y -axis is presented in Figure 4.4, and its dimensions are related by the equation:

$$4fz = x^2 \quad (4.1)$$

This parabola is U-shaped (upward opening), for which f is the focal distance and x and z the spatial coordinates. In Figure 4.4 the rim angle θ_R is the angle between the axis and a line from the focus to the physical edge of the concentrator. Together, the focal length and rim angle of a parabolic concentrator completely define its cross-sectional geometry. The rim angle of a parabola or paraboloid is given by:

$$\tan \theta_R = \frac{4fW/2}{4f^2 - (W/2)^2} = \frac{W/2}{f - Z_R} \quad (4.2)$$

where W is the width and z_R is the depth of the parabola at the rim.

Then, in order to design a micro-CPV with a concentration factor of 26X, this first ideal approach involves the use of circular cells with a diameter of 0.9 mm (i.e., 0.64 mm²) and a radial parabolic receiver with a diameter of 4.6 mm (i.e., 16.62 mm²).

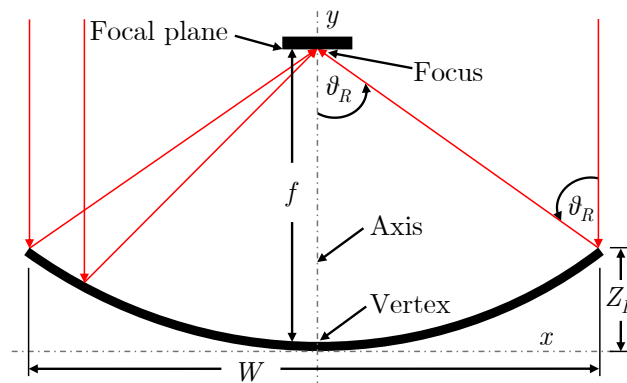


Figure 4.4: Part of a parabola, with various features and some ray traced (red). The complete parabola has no endpoints. In this orientation, it extends infinitely to the left, right, and upward.

Ruud *et al.* showed that there is an inherent trade-off between concentration ratio and compactness [85], which becomes more acute with increasing acceptance half-angle. Thus, the decrease of the concentration ratio with a high AR (equivalent to the total height of the optical system divided by its optical aperture), occurs when the angle subtended by the receiver is limited by the height of the concentrator and not by the width of the entrance aperture, this limiting AR occurs between 0.48 and 0.5 for concentration factors $< 200X$.

Based on this, for a defined aperture of 4.6 mm and an $AR = 0.49$ (i.e. range average) we have calculated the maximum concentrator thickness of 2.25 mm, which guarantees

full angular acceptance from the edge of the entrance aperture. In our case this maximum height is used as the focal length of the parabolic design, a configuration equivalent to a highly focused spot. This configuration represents the maximum distance between the optics and the receiver of the configurations of interest in this work, since we consider that a tight bond between the coverglass and the honeycomb is assured, while the height of the cell bonding paste is an uncertainty at the moment, which can vary from about 50 μm using a pick-and-place method, to 160 μm using self-aligning methods by capillary forces (according to preliminary tests done in the lab). Thus, later we are interested in studying receiver planes (shorter than the focal length along the $-z$ axis) that will tend to decrease the cell/reflector distance and the AR (i.e. there will be no limitation in the AA achieved by the AR). Thus the equation governing this design can be described by:

$$z = \frac{x^2}{4f} = 0.111x^2 \quad (4.3)$$

Next, the optical design of a micro-CPV unit was performed using TracePro® software. For this, some basic elements were taken into account, such as the coverglass, the micro-cell, and the previously described parabola, as well as different receptor planes of the cell size (900 μm diameter) located every 50 μm from the focal, shown in Figure 4.5.

The effect of the receiver position on the spatial distribution of light on the solar cells of a parabolic dish is then analyzed using ray-tracing. For this, the solar source described above was used, using one million rays at normal incidence, the reflection of the mirror was considered perfect, while the 0.5 mm coverglass was assumed to be made of borosilicate with low iron content, described in Table 3.2 of Chapter 3.

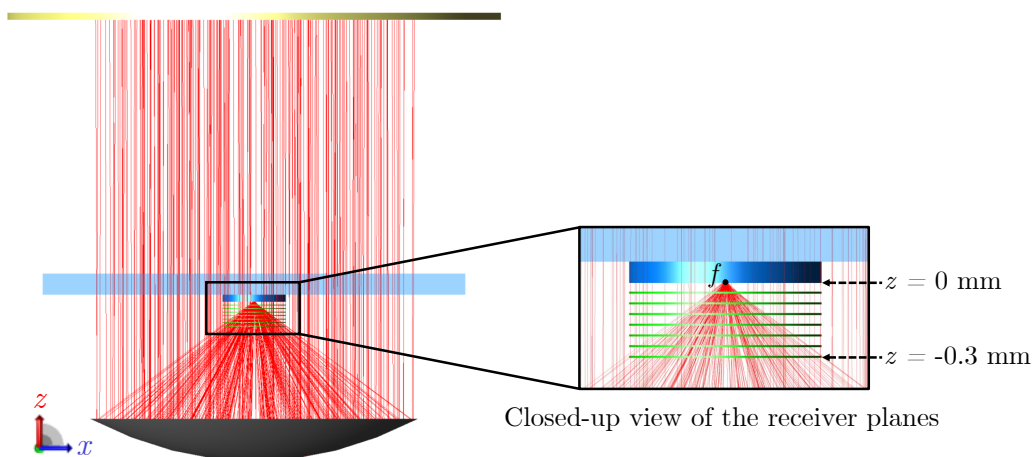


Figure 4.5: Parabolic design with different receiver planes localized each 50 μm along the z -axis from the focal point.

Then, based on the normalized to peak irradiance maps shown in Figure 4.6, the PAR of each of the positions has been calculated considering the surface of the cell, which is

0.9 mm in diameter. For each of the distributions the PAR has been plotted, as well as the percentage of effective area it represents with respect to the total cell size, see Figure 4.33. These simulated light distributions can be considered close to the actual irradiance distribution on the solar cells. However, it should also be considered that (ideal) ray-tracing simulations of CPVs may predict extremely high concentration peaks that do not occur in practice. This is mainly because some factors, such as scattering due to surface roughness, imperfections (e.g., manufacturing and assembly processes), dust, among others, that generate implicit scattering which are not usually taken into account; as discussed in [352]. This is evidenced in the focal plane ($z = 0$) of the optical system, in which the flux on the receiver is highly concentrated at a point (close to a Dirac delta distribution) equivalent to 0.2% of the cell surface, which generates a $\text{PAR} = 1,342$. This configuration, as expected, would make the use of a solar cell impractical. Then, as the distance along z is increased, the PAR decreases monolithically to 2.2 for a plane located at 0.35 mm from the focal, while the effective irradiance surface increases to a maximum of 97.8%. It is also possible to see on the irradiance maps the shading effects generated by the receiver at the entrance of the flux to the optical system, which appears in black at the center of the maps and tends to grow for more distant planes.

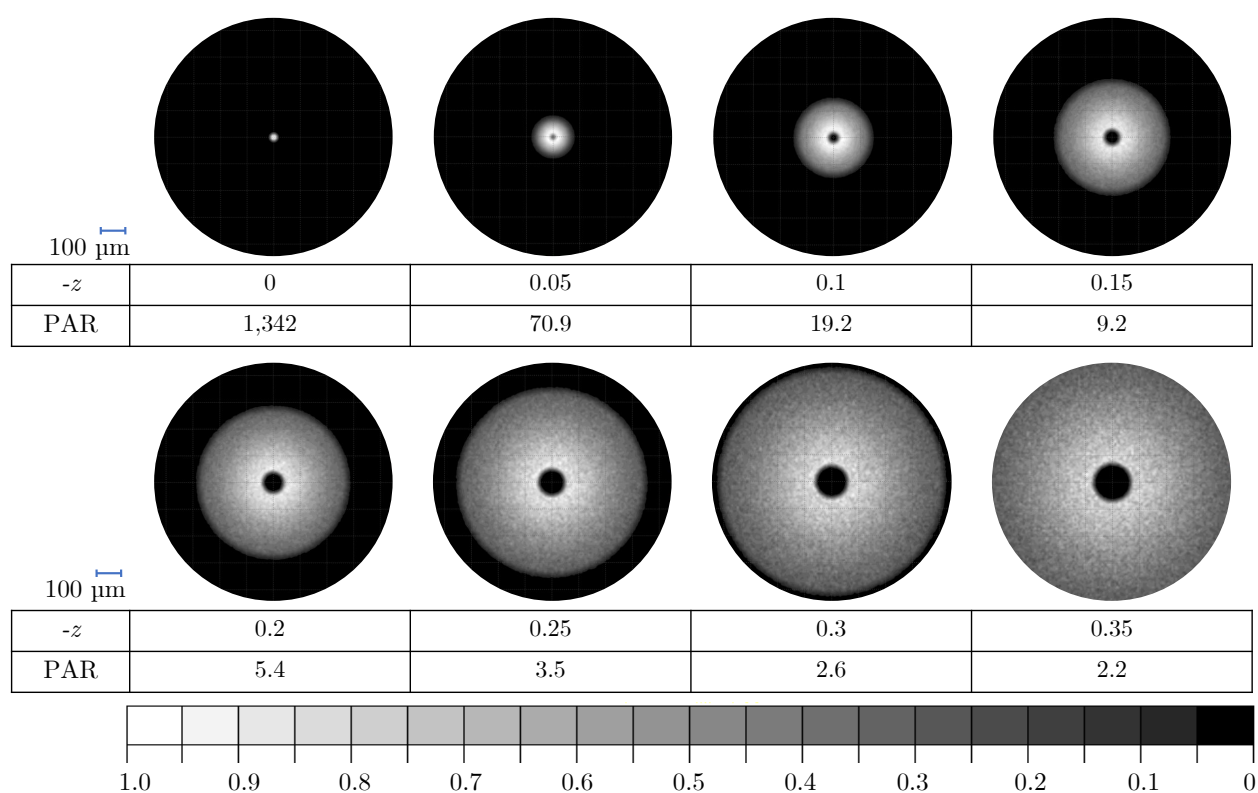


Figure 4.6: Normalized to peak irradiance maps for different detector positions following the z -axis (900 μm of diameter) and its associated Peak-to-Average Ratio (PAR).

To quantify the different non-uniformity profiles, Herrero *et al.* [350] characterized the

non-uniform light patterns produced by optical systems and reproduced them in CPV cells to obtain the FF under different non-uniformity profiles in which the percentage variation of the FF versus the PAR of the MJSC is calculated. Based on these results, if considering for example a PAR ranging between 2.2 and 5.4 as in our study (position 0.35 and 0.2 mm from the focal point), a loss in FF between 1% and 3% respectively can be estimated.

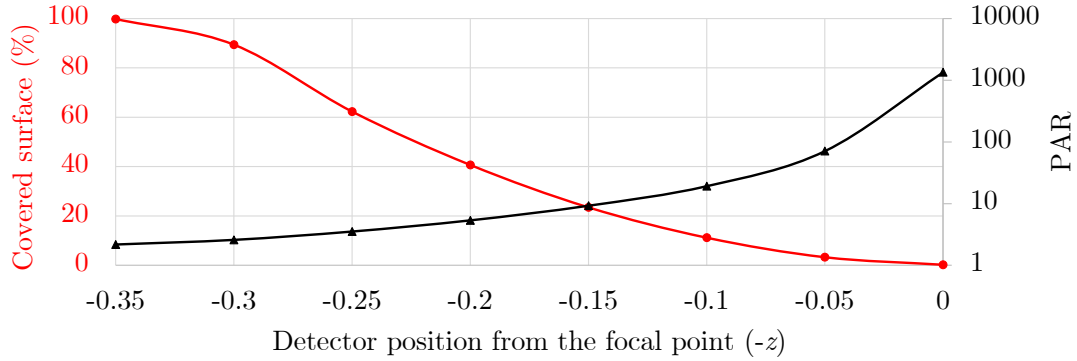


Figure 4.7: Evolution of the PAR and the covered surface percentage for different detector in a defocused position.

Subsequently, we have studied the evolution of the acceptance angle, both uni-axial AA_y° (around the y -axis) and bi-axial AA_{xy}° (around the x and y -axis), for various planes corresponding to deviations with respect to the z -axis, every 0.025 mm with respect to the focal, from $z = 0$ to $z = -0.3$ mm. Only a uni-axial deviation was considered since the system has a radial symmetry, while the bi-axial deflection (AA_{xy}) was evaluated, considered as the worst case scenario in which both axis are deflected at the same angle simultaneously.

From an uni-axial deviation around the y -axis, it can be seen that between the 0 and -0.05 mm positions the angular tolerance remains constant, around 6.5° , see Figure 4.8 (a). Then, it tends to decrease as the gap increases, until it reaches a minimum of 3° for a deviation of -0.3 mm (i.e. spot covering the entire receiver surface). It is also observed that, considering the minimum angular tolerance criterion for a uni-axial deflection this must be $> 4^\circ$, which is reached for a plane located for a z -position between 0 and 0.225 mm.

For the bi-axial offset, a decrease in the acceptance angle can also be observed as the detector moves away from the focal point, since in the range considered, a greater distance means a larger spot, which in turn implies that it will have less freedom to move over the cell in the presence of an angular deviation. Thus, the acceptance angle evolves from about 4.5° for z values between 0 and -0.1 mm to a minimum of 1.8° for a plane at 0.3 mm. While the range that guarantees an $AA_{xy}^\circ > 2.5^\circ$ is found between $z = 0$ to $z = -0.25$ mm.

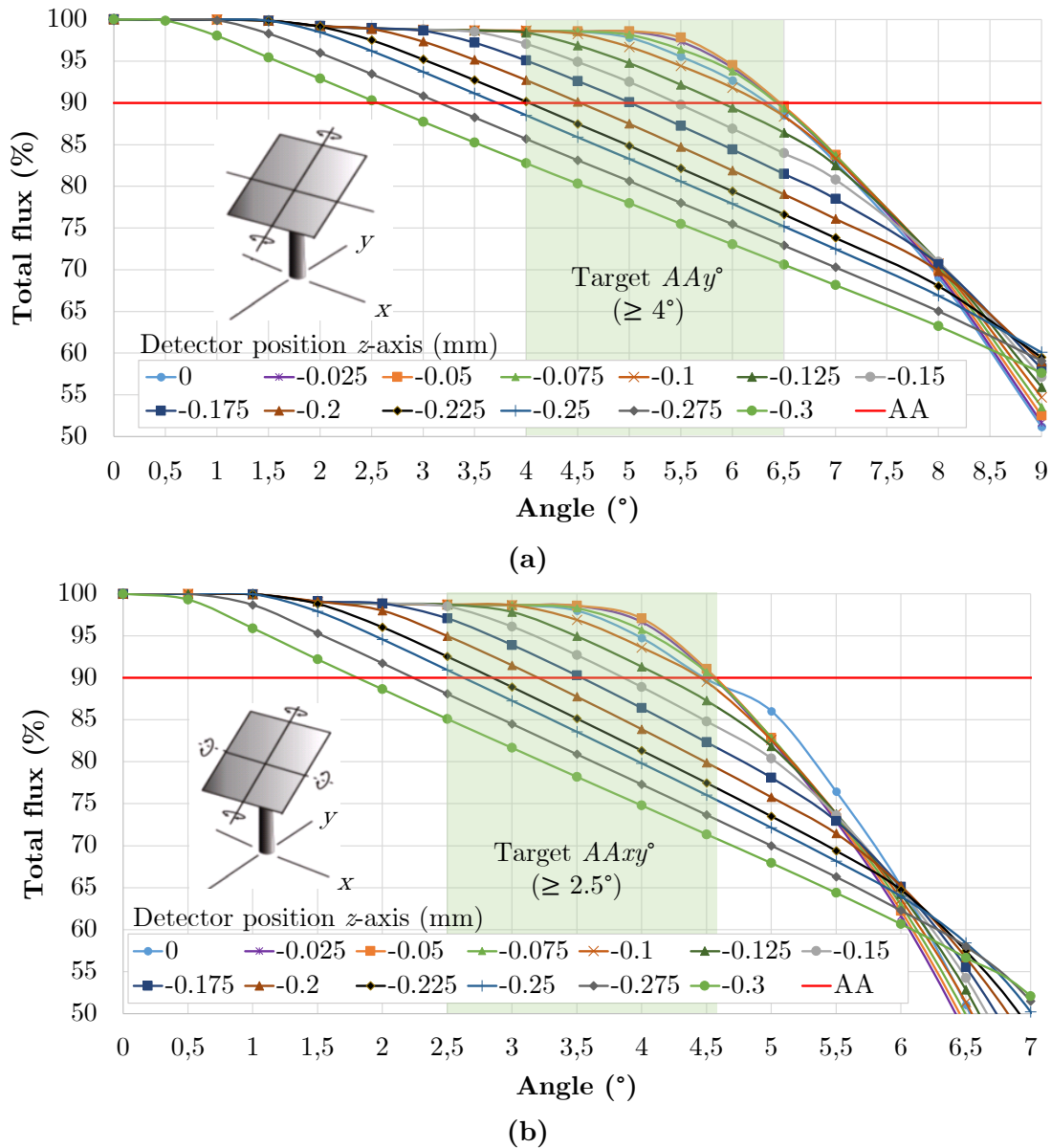


Figure 4.8: Acceptance angle study for different detectors placed each 25 μm ($-z$) position (in colors), for a deviation: (a) uni-axial around the y -axis and (b) bi-axial around the x,y -axis, simultaneously.

From this it can be concluded that from the parabolic system considered, the receiver plane that guarantees the desired angular tolerance with the most homogeneous flow distribution is $z = -0.225$ mm, see Figure 4.9. Which in turn presents a PAR of 4.4, and a flux distributed over 60% of the solar cell surface. The latter is then considered as the reference architecture that can best satisfy the defined design criteria. Figure 4.10 shows the irradiance maps of an ideal parabolic reflector at the chosen plane for a: (a) normal flux, (b) uni-axial deviation around y -axis (4°); and (c) bi-axial deviation xy -axis (2.5°).

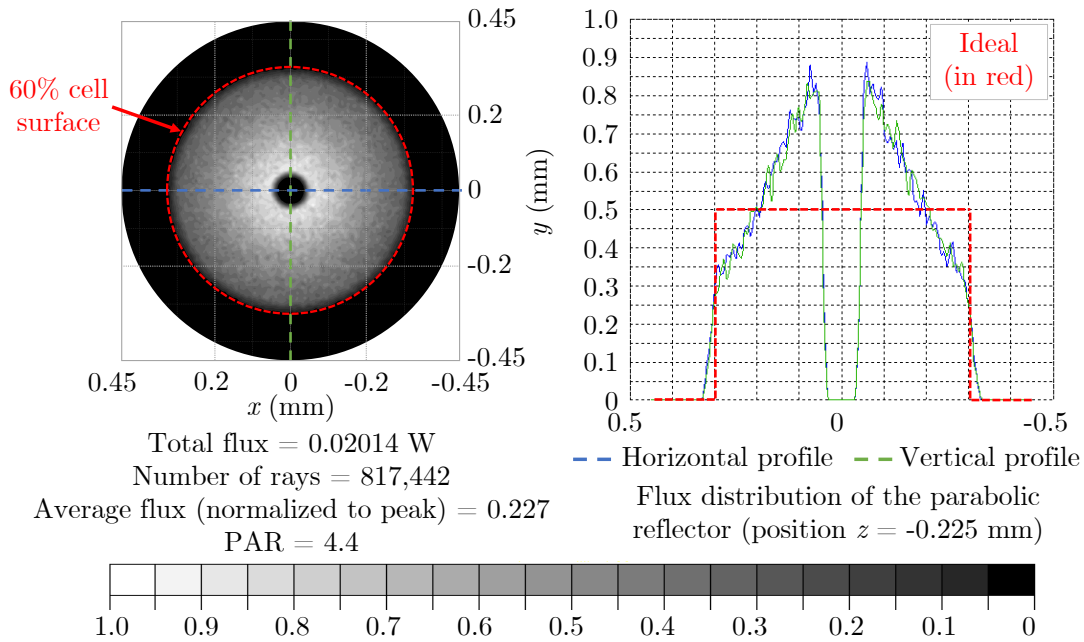


Figure 4.9: Maps and irradiance profiles normalized to the peak of a parabola with a detector at $z=-0.225$ mm from the focus. Showing the total flux and number of perceived rays, as well as the average peak-normalized flux and relative PAR.

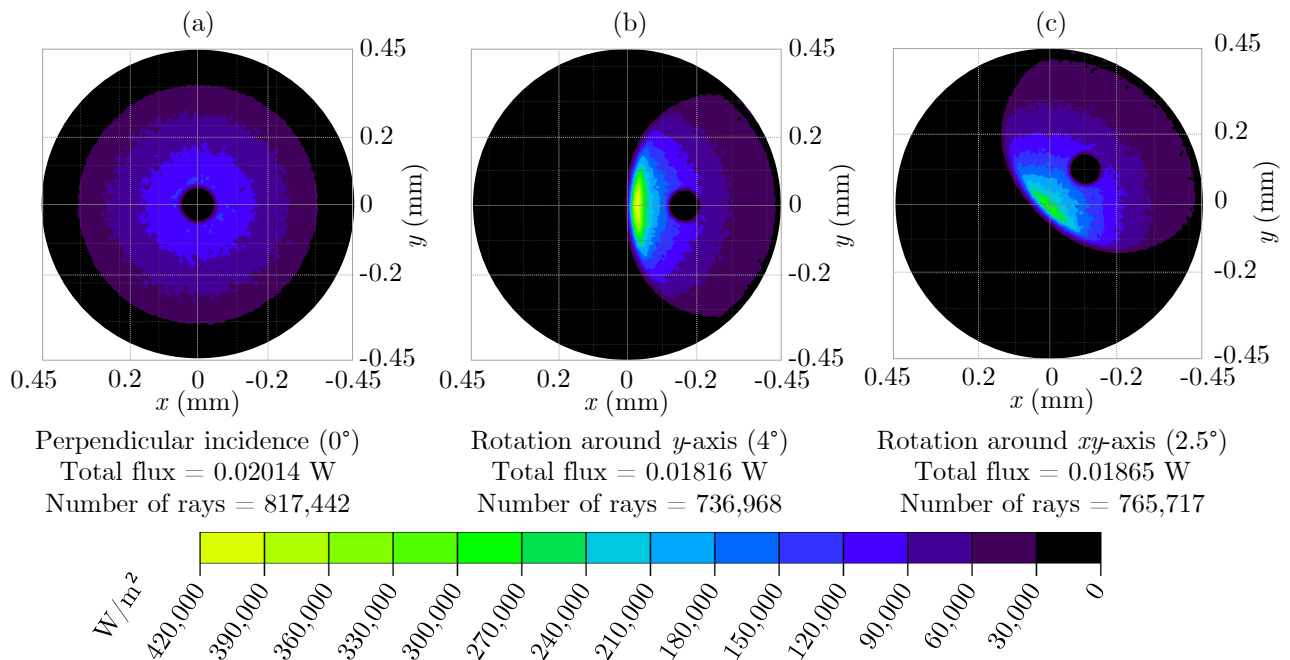


Figure 4.10: Irradiance map for a detector placed at $z = -0.225$ mm from the focal point, using an ideal parabola, for a perpendicular or normal incident flux and the relative acceptance angles (uni-axial and bi-axial).

4.2.3 Free-form optimized reflector

The subsequent research consisted in the study of a free-form reflector, with the objective of finding the optical design with the best flux uniformity over the receiver, on a percentage of the cell surface equivalent to that of the parabolic mirror. For this purpose, two objective functions have been established, the first is to maximize the incident flux on the cell, and the second is to establish that the flux profile is over 60% of the receiver surface, distributed as homogeneously as possible.

4.2.3.1 Modeled solar source and the target value

As we intend to use TracePro's interactive optimizer, we use the AM0 source that we have just defined with three wavelengths (Section 4.2.1), but in this case we have traced 100,000 rays instead of one million in order to minimize the computation time during the optimizations. Thus, 85,073 rays are incident on the aperture of the optical system, as shown in Figure 4.11. We also note that the total incident aperture flux is 0.02282 W (i.e.: lossless) and averages about 1373.1 W/m², the difference of 0.5% of the average perceived flux with respect to an ideal AM0 irradiance, is linked to the use of a source with a non-optimal convergence.

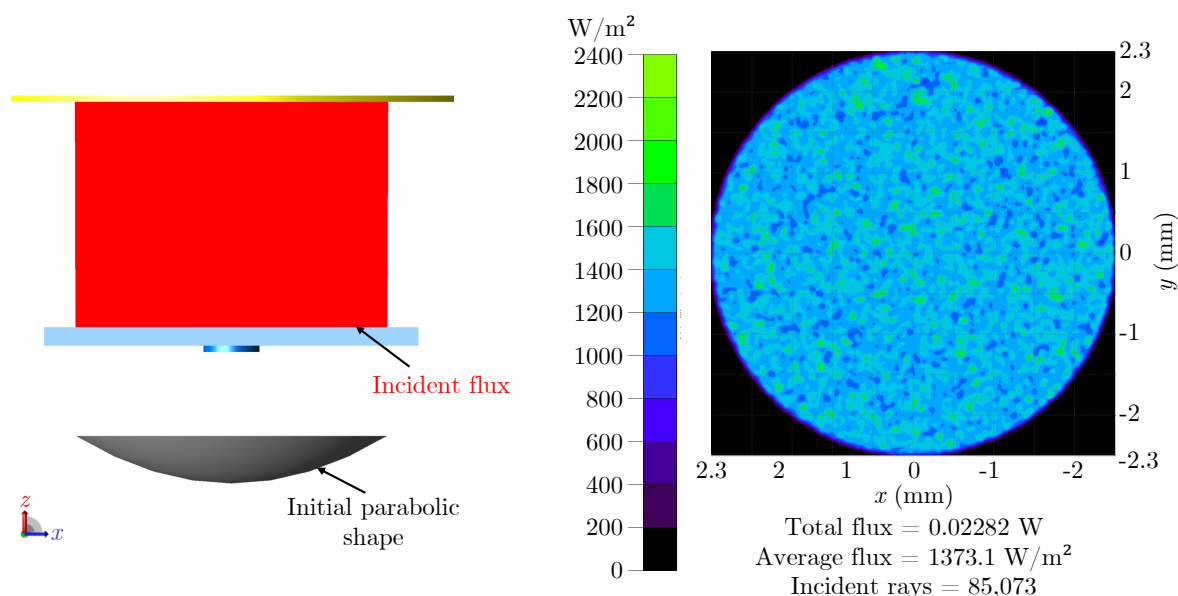


Figure 4.11: Defined solar source for the optimization process of a free-form reflector.

4.2.3.2 Variables

During the process of optimizing the free-form reflector, a methodology similar to that described in Section 3.2.1 (i.e., for designing the CPC system) has been followed. An

initial parabolic shape is designed using two variable points $\Sigma_z = 0.4$ mm, and an axis of symmetry; as shown in Figure 4.12 (Model 1). After minimizing the error of the objective functions (i.e.; flux and uniformity), we proceed to increase the number of variable points (e.g.: up to 4 as shown in Figure 4.12 (Model #2)) while decreasing their $\Sigma_z (< 0.1$ mm); thus refining the shape of the free-form reflector.

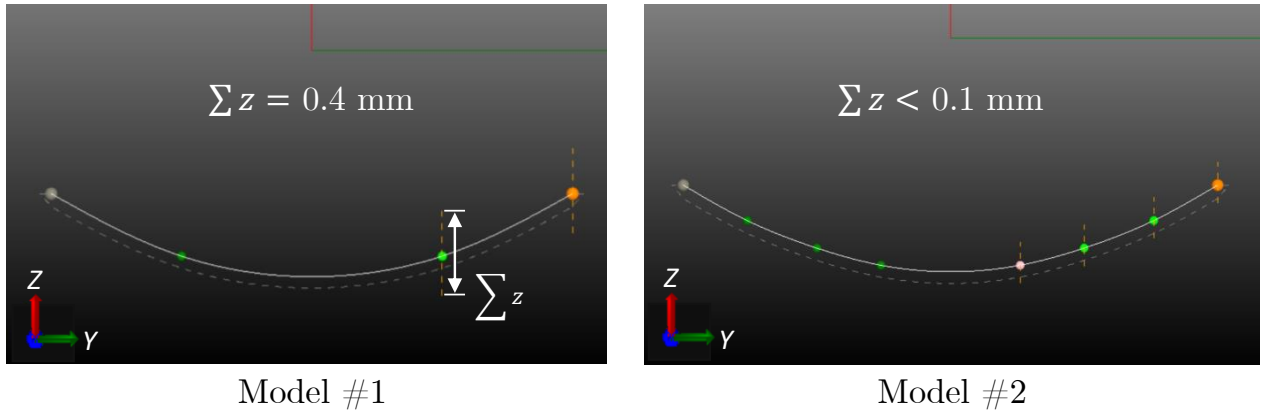


Figure 4.12: Optimization models of the free-form reflector. The dotted curve corresponds to the thickness of the reflector, arbitrarily defined in this case as 0.01 mm.

4.2.3.3 Evolution and results of the optimization process

Figure 4.13 (a) illustrates the trend plot of the error function versus the number of iterations of the Model #2, followed by the spot uniformity operand via the local optimizer Nelder-Mead. At the beginning this model has an error source of about 35%, then the first oscillations fluctuate and reach up to $> 90\%$ error, after 20 to 35 it stagnates at 48% error and then reaches a minimum value of about 20% error. On the other hand, Figure 4.13 (b) illustrates the operator that maximizes the flow over the cell, which up to about iteration 45 fluctuates like the uniformity operator, but this in turn stabilizes at iteration 60, near which the operator finds its minimum error (i.e., near zero).

The result is shown in Figure 4.14 (a), where the optimized free-form focus sunlight onto 60% (at $z = -0.225$ mm) the surface of a circular micro-solar cell (dashed-circle in red). Then, in order to analyze the radiation profile obtained by the free-form in a more precise way, we have used the source described in Figure 4.3), which is defined by one million rays and has an associated error of 0.1% respect to the ideal AM0 source. From this it can be seen that the increase in the number of traced rays homogenizes the flux distribution slightly, while the total flux perceived by the receptor remains almost constant, with a variation of 0.06%.

Figure 4.15 shows the peak-normalized irradiance maps, as well as the horizontal (blue) and vertical (green) irradiance profiles of the free-form reflector, showing the target operator

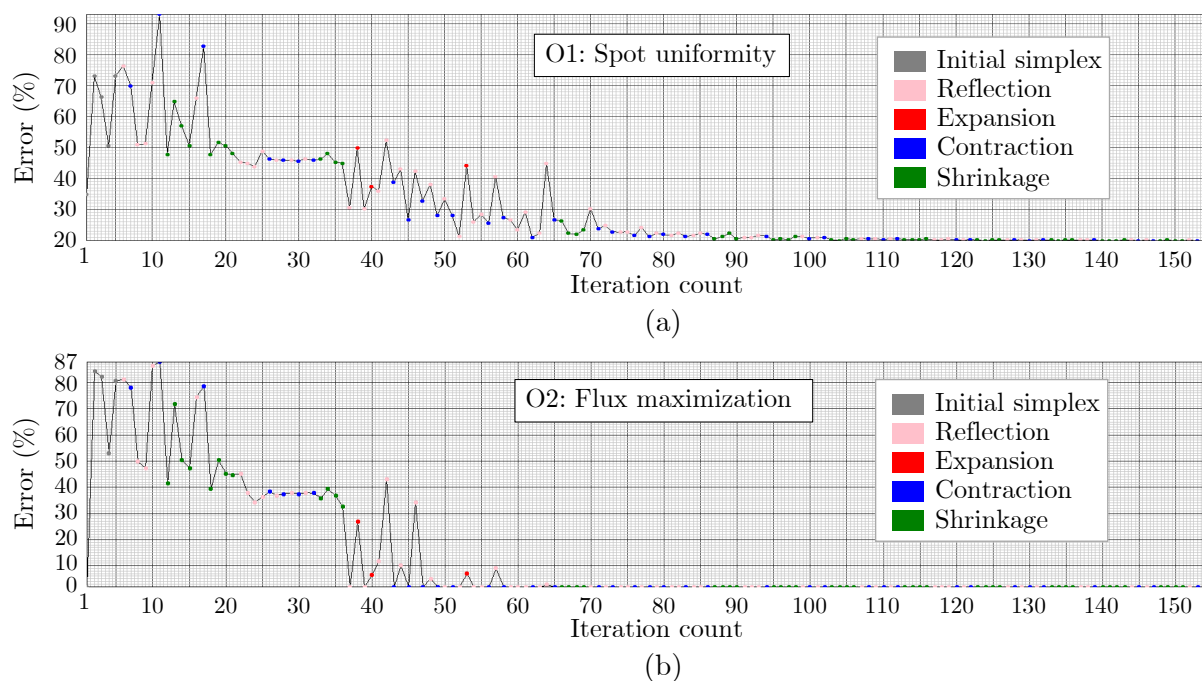


Figure 4.13: Error function free-form optimization process (Model #2) for the operand: (a) spot uniformity and (b) flux maximization.

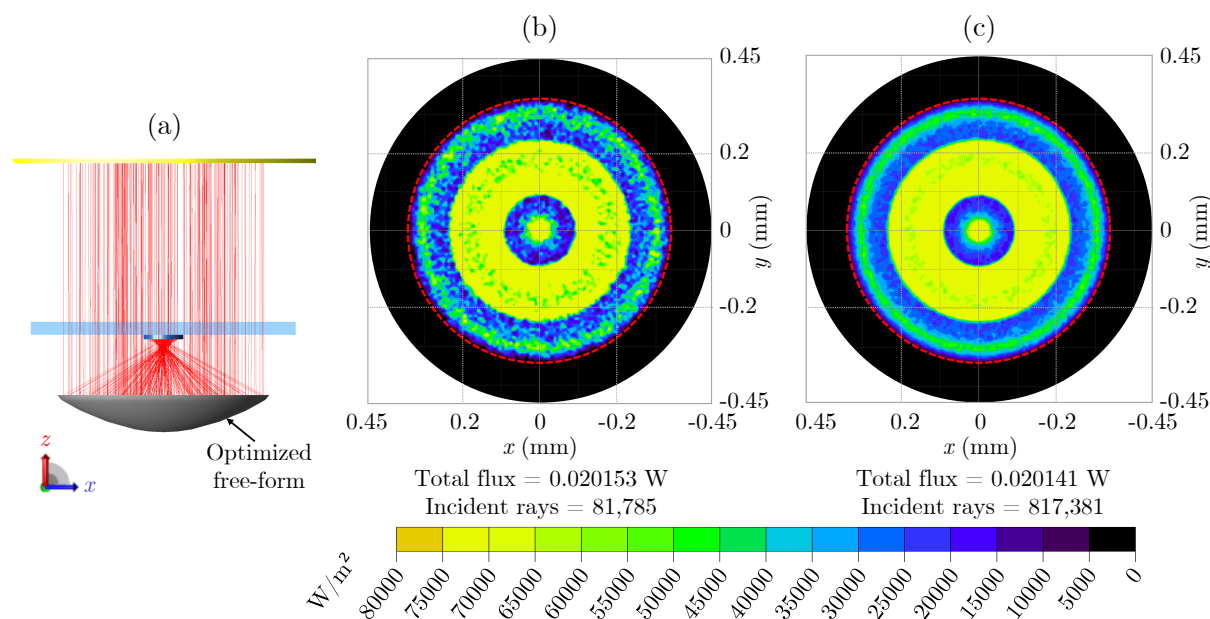


Figure 4.14: (a) Ray-tracing for the optimized free-form reflector Model #2 (using 1,000 rays for visualization), (b) irradiance map of the optimized free-form using the solar source defined for the optimization process (i.e., 100,000 rays traced), (c) irradiance map using one million ray traced.

for the 60% uniformity (in red). From this, we can see that the total perceived fluxes of the free-form reflector is 0.02014 W, as for the parabola. Thus, it can be verified that the optimized free-form design maximized the total flux satisfactorily as well as the parabolic

reflector. In turn, the free-form reflector presents some inhomogeneous flux peaks (see Figure 4.15 below) which increase the PAR to 6.7, calculated on the surface of the cell, which is 0.9 mm in diameter. This is evidenced in Figure 4.13, in which the uniformity operator found a solution close to the objective function, with a final associated error of about 20%.

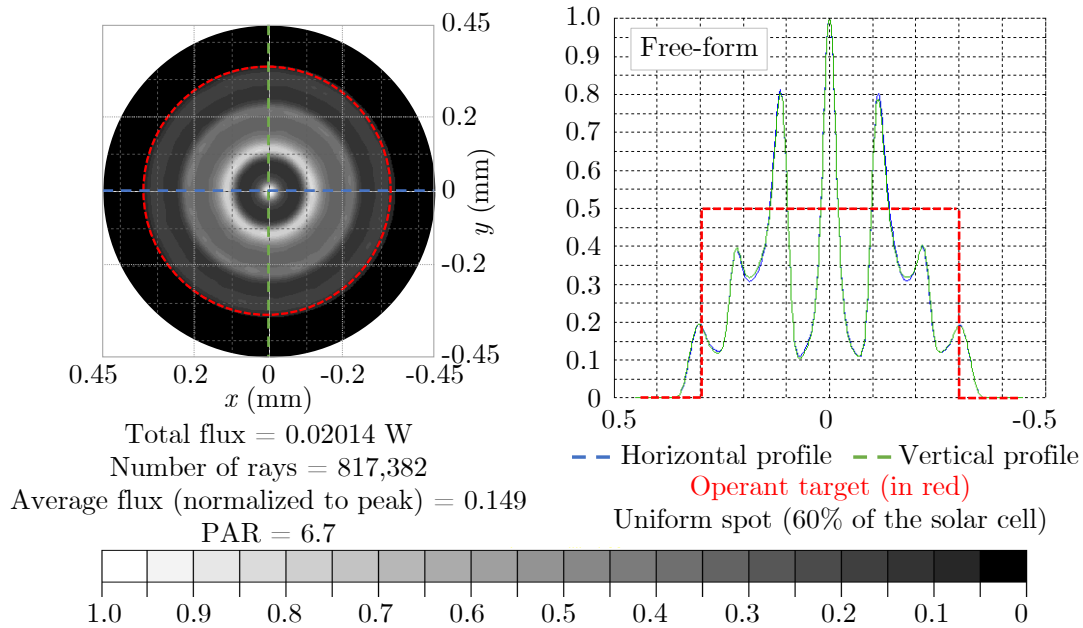


Figure 4.15: Maps and irradiance profiles normalized to the peak of the free-form. Showing the total flux and number of perceived rays, as well as the average peak-normalized flux and relative PAR. Target of the free-form uniformity operation (in red), which seeks an average flux over 60% of the cell surface.

After having studied the optimized free-form design for a perpendicular solar flux, we evaluated its response to angular deviations. For this purpose, we have evaluated the total flux on the cell after simulating a deviation of the solar source every 0.25° , both a uni-axial deviation with respect to the y -axis (y°) and a bi-axial deviation (x° , y°) have been studied; the latter represents the worst-case scenario in which both axes have the same maximum deviation. Figure 4.16 shows the comparative results, total flux percentage vs. angular offset, solid line for uni-axial deflection and dashed line for bi-axial deflection, while the horizontal line (in red) represents the acceptance angle (i.e., 90% of the maximum flow). It can be seen that the free-form design does not satisfy the minimum angular tolerance criterion. On the one hand, for a uni-axial deflection, an $AA_y = 3^\circ$ was found instead of 4° , i.e. 33% lower than expected. On the other hand, for a bi-axial deviation it was 2° instead of 2.5° , i.e. 25% less than expected.

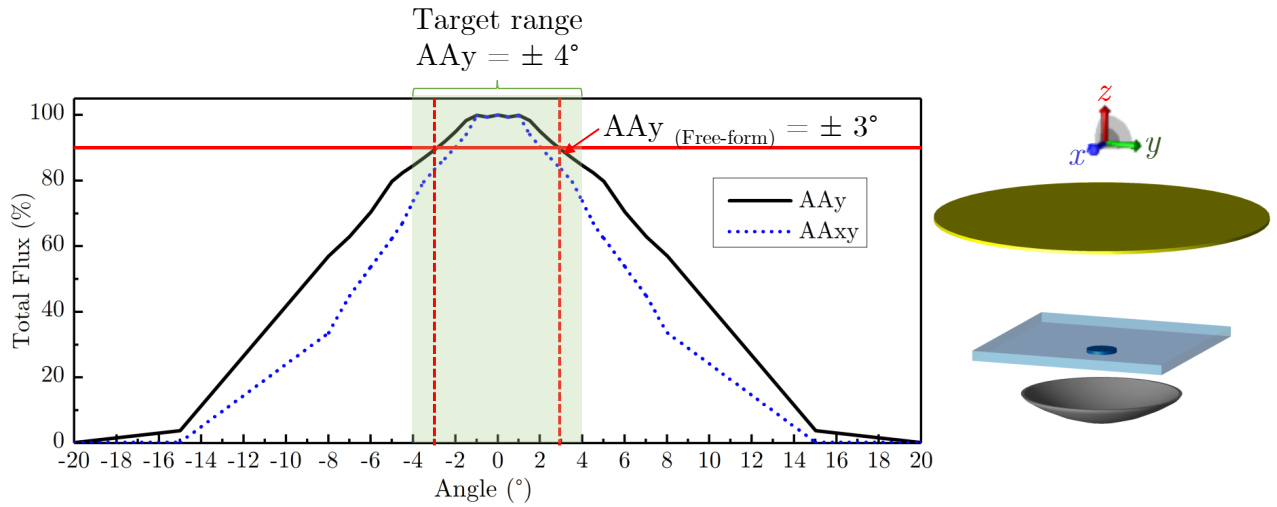


Figure 4.16: Acceptance angle of the free-form reflector for an uni-axial (AA_y) and a bi-axial (AA_{xy}) angular deviation.

4.2.3.4 Analysis of SOE design performance

Other research explores the use of SOE, with the objective of improving the flux distribution in the receiver and increasing the angular tolerance of the free-form reflector design to ensure compliance with the defined design criteria. Typically, the parameters (e.g., geometry and dimensions) of the SOE of a CPV unit are usually adapted according to the design details of the POE, the performance requirements and the size of the solar cell. With this in mind, we have focused on studying refractive SOEs with different shapes, more particularly two SOE designs have been studied, including: (a) a hemisphere (or half-sphere), and b) a free-form SOE optimized, both of which have been externally sized with the same radius as the solar cell, to avoid shading of the light entering the optical system. In this study, we have not considered SILO (for SInGLE Optical surface) as SOE, which remains a good solution, treated by other authors [353, 354]. During the modeling of these SOEs we have considered them to be made of a low-Fe glass, a material given previously in Table 3.2.

As mentioned above, in order to increase the angular tolerance of the free-form reflector, a free-form SOE has been optimized. For this, we have used three solar sources simultaneously, with angles of 0° , 5° and 10° (around the y -axis), and we have used an operator that sought to maximize the total perceived flux. Initially a dome shape was defined as shown in Figure 4.17 (a), and as the considered optical system has a radial symmetry, it was defined in the zy -plane, red line in the center of the SOE. Relative and absolute variables have been used in the optimization process, the latter to define the radius, which is equal to 0.45 mm, that of the solar cell (point D in Figure 4.17).

On the other hand, relative variables were used, one-dimensional for the central point A and two-dimensional for B and C. Initially point A was located at 0.5 mm, around the z -axis, and an optimization distance $\Sigma_z = 0.2$ mm was defined. While for B and

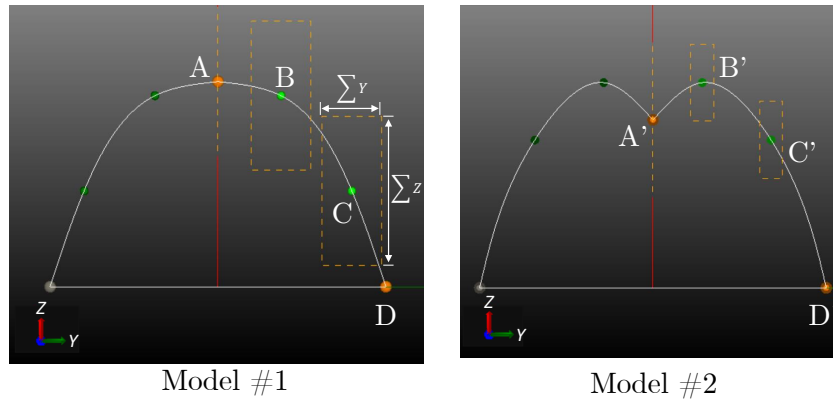


Figure 4.17: Optimization models of the free-form SOE.

C a $\Sigma_Z = 0.2$ mm and a $\Sigma_Y = 0.08$ were defined. Subsequently, following an iterative process, the mobility range of the control points (or optimization space) was reduced, to about a half, to refine the solution. Figure 4.17 (b) illustrates the final optimized model, in which A', B', C' correspond to the optimal positions.

First, we studied how the homogeneity of the flux evolves of the free-form reflector for a normal incidence using the SOEs described, see Figure 4.18: (a) the hemispheric shape and (b) the free-form optimized SOE. While the results are shown in Figure 4.19. On the one hand, the semi-sphere presented a spot concentrated in a narrower zone, over 18% of the cell surface, three times less than without SOE. This leads to an increase in PAR of 46%, from 6.7 without SOE to 12.5 with the half-sphere SOE. On the other hand, the free-form SOE showed a slight increase in spot area, from 60% without SOE to 63%, while the homogeneity of the distribution increased considerably, evidenced by a decrease in PAR of about 20%, from 6.7 to 5.6, with and without free-form SOE, respectively. However, as expected, the addition of an optical surface implies additional losses (about 4%), on the total flux perceived by the receiver.

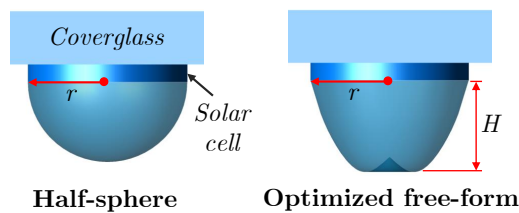


Figure 4.18: Secondary Optical Elements (SOE) designs used in this study, the half-sphere with $r=0.45$ mm, while the free-form with $r=0.45$ mm and $H=0.53$ mm.

Then, we evaluated the angular response and both of them have presented an increase in their acceptance angles, as it can be seen in Figure 4.20. The free-form reflector had a considerably higher increase, for a uni-axial deviation (AA_y), it evolves from 3° without SOE to 7.2° and 8.2° , using a half-sphere and a free-form SOEs, respectively. While for a bi-axial (AA_{xy}) offset it goes from 2° without SOE, to 5.1° and 5.7° , using

a half-sphere and a free-form SOEs, respectively.

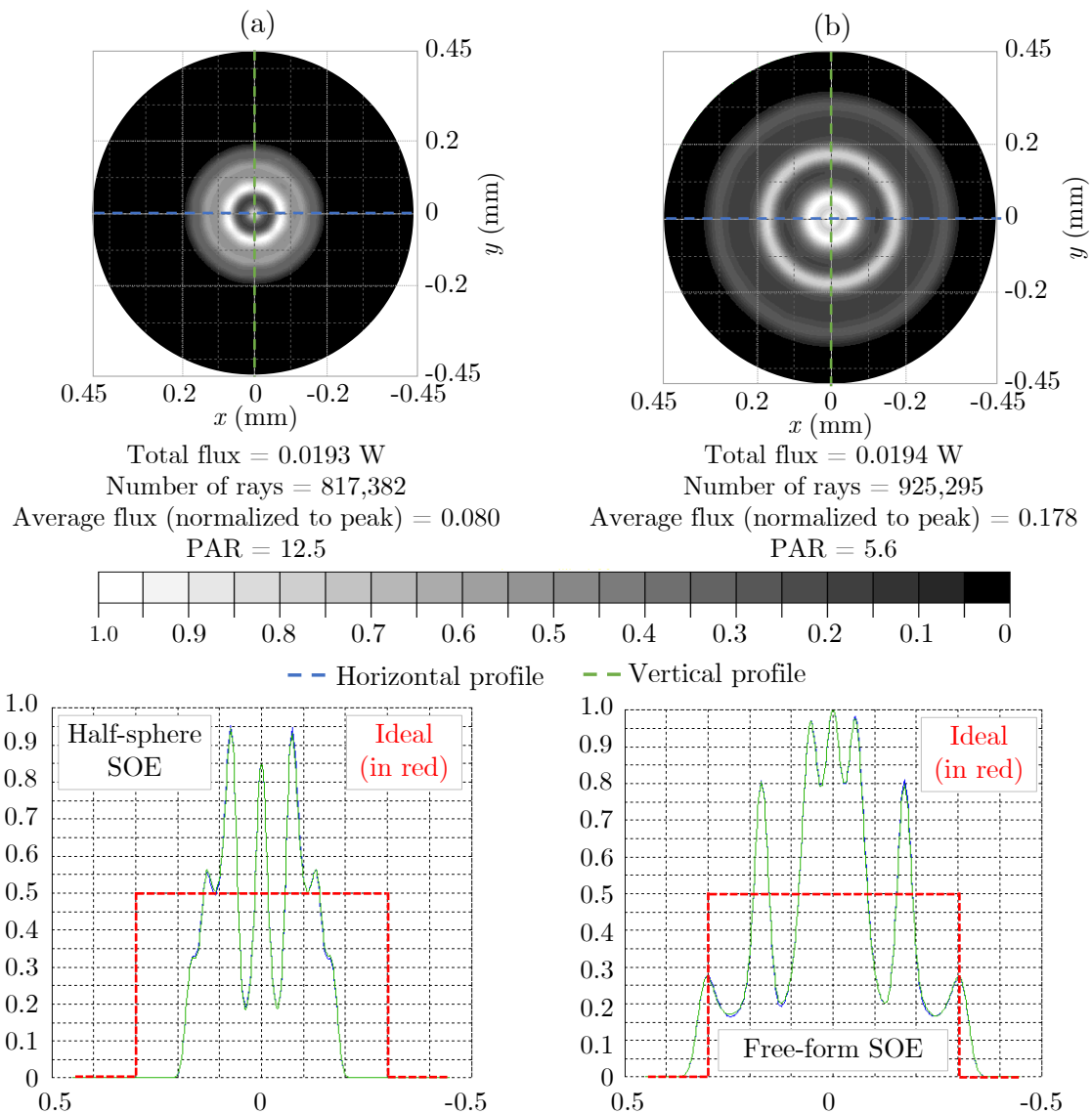


Figure 4.19: Maps and irradiance profiles normalized to the peak of a free-form reflector with a: (a) half-sphere SOE and (b) free-form SOE.

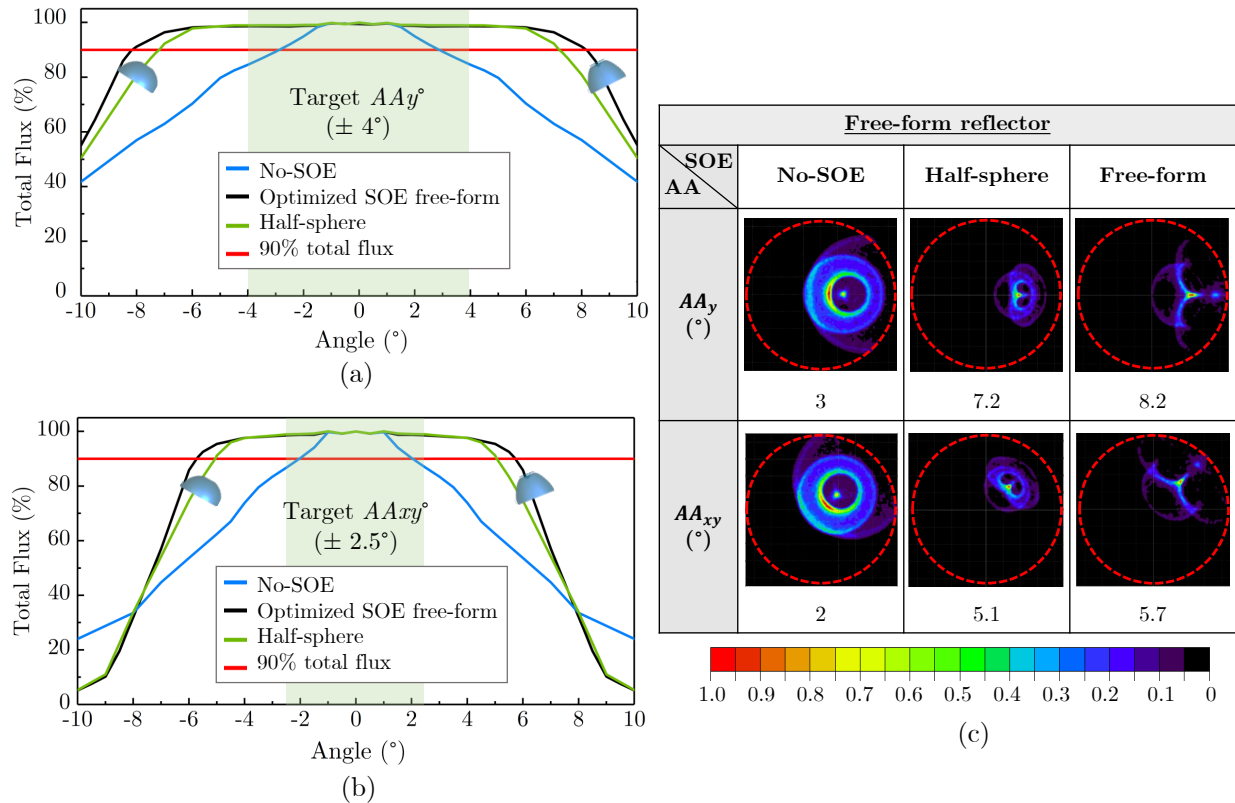


Figure 4.20: Acceptance angle improvement of a free-form reflector, using SOEs (a half-sphere and an optimized radial free-form), horizontal red-line for the 90% of the total flux, and the green-zone indicates the target zone: a) uni-axial, b) bi-axial deviation, c) relative irradiance maps.

4.2.4 Analysis and conclusions

In order to design and integrate an optical reflector into a honeycomb unit, we have analyzed the potential of two reflector families, a parabolic and a free-form design optimized for uniform flux and high angular tolerance, desired in the development of a micro-CPV for space applications. To this end, we began by studying the parabolic system, establishing that the plane with the best homogeneity of concentrated flux ($PAR = 4.4$), which guarantees a target angular variation uni-axial ($AA_y = 4^\circ$), and bi-axial ($AA_{xy} = 2.5^\circ$), is achieved for a plane located at $z = -0.225$ mm (i.e., with respect to the focal), generating a spot spread over 60% of the cell.

Subsequently, a free-form reflector was optimized in order to improve the angular tolerance and flux uniformity of a spot of equivalent size to that of the parabola for a plane $z = -0.225$ mm. Moreover, this system is considered as an alternative to the parabolic system which tends to be sensitive to shape deformations. In this regard, it was observed that the optimized free-form has an acceptance angle that does not correspond to the design specifications, with $AA_y = 3^\circ$ and $AA_{xy} = 2^\circ$. Thus, SOEs were used to

improve the angular tolerance and uniformity of the assembly, using a hemisphere and an optimized radial free-form, which substantially improved the angular tolerance, using a hemisphere SOE of $AA_y = 7.2^\circ$ and $AA_{xy} = 5.1$, and up to $AA_y = 8.2^\circ$ and $AA_{xy} = 5.7^\circ$, for an optimized free-form SOE. The latter also resulted in a 20% improvement in flux homogeneity, reducing the PAR from 6.7 to 5.6. While the semi-sphere produced a 46% increase in PAR. However, when comparing the uniformity of the free-form reflector and SOE with that of the parabolic reflector (for a plane $z=-0.255$ mm), the former is still 21% inferior to the parabola, see Figure 4.21.

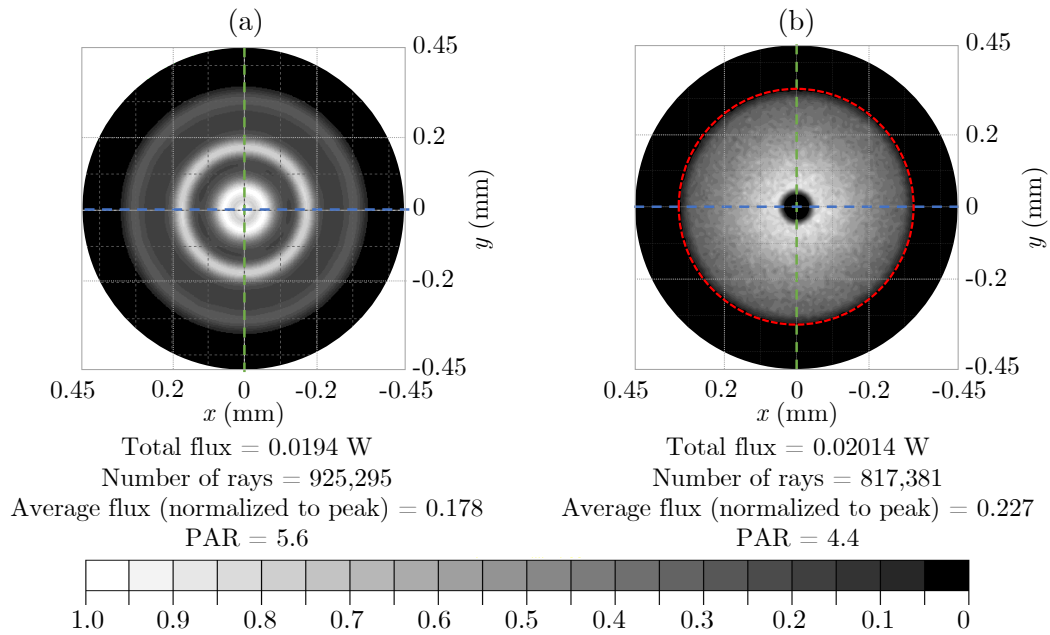


Figure 4.21: Irradiance maps normalized to the peak of : (a) a free-form reflector with a free-form SOE and (b) a parabola with a detector at $z=-0.225$ mm from the focus. Showing the total flux and number of perceived rays, as well as the average peak-normalized flux and relative PAR.

As a complement to the angular and uniformity study described above, a misalignment sensitivity study of both systems, has been carried out in order to estimate the system tolerance to dimensional errors due to manufacturing. In this, a displacement between the cell and the reflector around the z -axis (i.e., $x=y=0$) and the y -axis (i.e., $x=z=0$) was considered. Then to estimate the impact on the total flux received on the cell it was determined as a basis that the total flux maintained should be greater than or equal to 90% of the maximum flux (i.e., with respect to a perfectly well aligned system), as in the case of the AA. Figure 4.22 shows the result of this analysis.

According to the z -axis the parabolic reflector has a tolerance of ± 0.28 for a $\Sigma_z = 0.56$ mm, while the free-form of -0.05 to $+0.35$ for a $\Sigma_z = 0.4$ mm. While with respect to the y -axis this is ± 0.4 mm for the parabola ($\Sigma_y = 0.8$ mm), and ± 0.2 mm

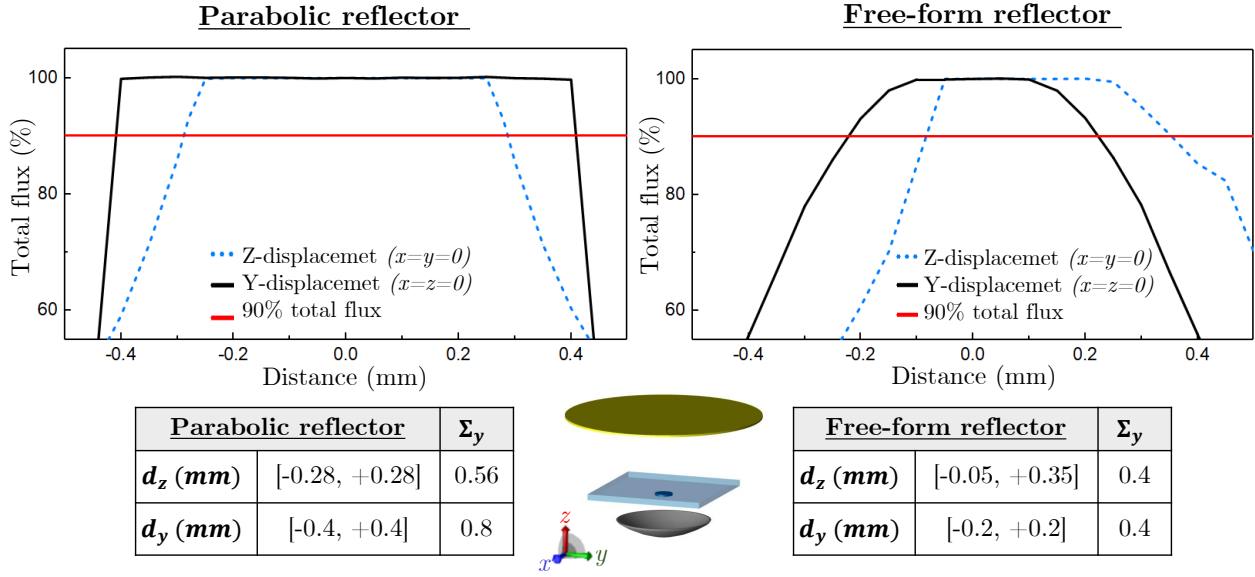


Figure 4.22: Misalignment sensitivity study for a parabolic reflector vs. a free-form.

for the free-form ($\Sigma_y = 0.4$ mm). From which it can be seen that the parabolic reflector has a 30% higher Σ_z tolerance for the z -axis and 50% for the y -axis; which is also more symmetrical than its free-form counterpart.

It can be concluded that the free-form reflector can largely guarantee the minimum angular tolerance criteria established when using a SOE. Meanwhile, the parabolic reflector proved to be an efficient solution in terms of flux homogeneity in relation to the desired angular and mechanical tolerance, and overall in terms of manufacturing simplicity. For this reason, we have chosen to pursue the latter design in order to validate the concept of a highly integrated reflector in a honeycomb. For this purpose, the simulation of a parabolic unit disposed inside a hexagonal unit is presented below, and then the experimental validation will be presented in Chapter 4.

4.3 Optical simulation of a hexagonal truncated parabolic reflector

This section deals with the optical simulation of a parabolic reflector integrated in a honeycomb core unit, which has a hexagonal shape. This honeycomb core serves as a structural spacer between the optics and the cells, ensuring that they remain aligned when the final composite sandwich is assembled, which is used in the assembly because of its high mechanical strength to mass ratio. Thus, the objective here is to evaluate the impact on the optical performance of this hexagonal shape, compared to previous work done on an idealized radially symmetric parabola. This can be divided into the following steps. First, a description of the truncated optical system and each of the elements and materials

considered is given. Then we are interested in studying the convergence of the incident flux over the hexagonal optical aperture; using an AM0 solar source which has been modeled for its entire spectral range. Once the Monte Carlo ray-tracing method has been applied to establish the initial set of incident rays (i.e., over the aperture of the optical system) that minimize the error with respect to an ideal source, we move on to a performance analysis of the optical system. First, a study of the set of optical losses is proposed to estimate the array optical efficiency, taking into account scattering, specular reflection, absorption, as well as refraction of light through the aperture for a normal incidence. Then an investigation of both angular tolerance and misalignment of the internal elements of a micro-CPV unit is carried out in order to estimate the distribution and intensity of the radiation flux reaching the micrometer photogenerator used.

4.3.1 System description

The first component in the optical pathway, the front coverglass, acts as a mechanical support for the network of interconnected micro-cells, and also helps to shield the internal components from the energetic particle environment in outer space. On the other hand, the solar cells used are rectangular 3J (885x685 μm^2), 200 μm thick, i.e. about 0.6 mm^2 surface, which are currently available. These cells are interconnected with each other using metallic paths, which intended to be about 100 μm wide and 120 μm thick.

Since the truncated hexagonal shape of the reflectors is intrinsically linked to the shape of the hexagons of the honeycomb system, a characterization campaign was carried out to establish the dimensions of an unit. For this purpose, a honeycomb core of reference CR-III® 5.7 3/16 5052, 3 mm thick, manufactured by Hexcel [351], was chosen. CR-III - signifies that the honeycomb is treated with a corrosion-resistant coating, 5.7 - is the density in pounds per cubic foot, 3/16 - is the cell size in fractions of an inch, 5052 - is the aluminum alloy used, its specific dimensions are shown in Figure 4.23, while its mechanical properties can be seen in Annex C.

Finally, the parabolic reflector is made of space silicone and has a silver coating, which is 200-300 nm thick. Figure 4.24 shows the raytracing model via TracePro® for an unit of the system under study.

4.3.2 Source modeling and convergence

By considering the full spectrum from 0.1 to 50 μm , we have defined a 14 mm diameter solar source. It takes into account a solar angular distribution, half solar angle of 0.27° .

After defining the spectral distribution and the intensity of the source, it is necessary to evaluate the convergence of the flux incident on the surface of the hexagonal optics aperture. Considering the dimensions of Figure 4.23 and a mechanical tolerance of 0.15

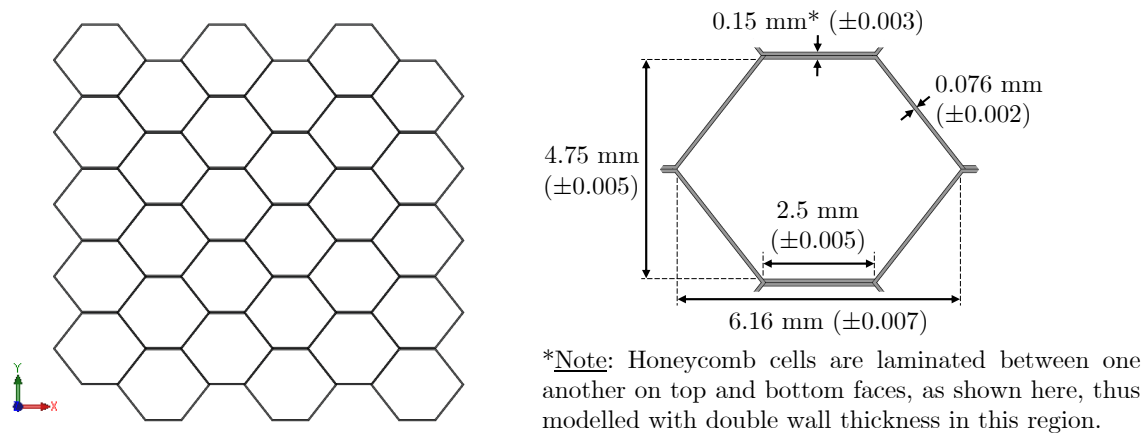


Figure 4.23: Honeycomb unit dimensions.

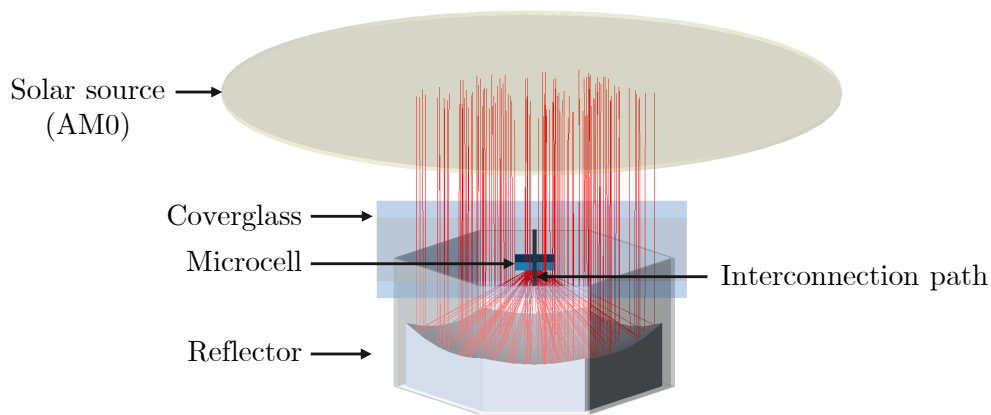


Figure 4.24: Optical design model using TracePro®, representing the main elements involved and considered during the ray-tracing analysis.

mm towards the inside of the hexagon that will allow the insertion of the mold in the hexagonal cavity network, the useful surface is $\approx 17.92 \text{ mm}^2$.

The latter, in order to find a balance between accuracy and computational time, and to ensure that the parameters used will allow us to obtain reliable results in the simulations that follow in this section. For this, a first study consisted in evaluating the influence of the number of rays traced, and Table 4.3 shows the result, showing the relative fluxes, their deviation with respect to an AM0 flux (i.e., a theoretical value 1366.1 W/m^2); also the calculation time is specified. It can be observed that the incident flux deviation starts at 12.6% for one hundred rays and decreases to 0.5% with ten thousand rays, then fluctuates non-monotonically until it reaches 0.6% for ten million. From this it can be concluded that the number of rays is not the only parameter involved in the convergence of the source.

Further investigation revealed that TracePro® does in fact use pseudo-random numbers for a variety of tasks, for example, to establish the directions of scattered rays or the starting locations of a random surface source. Whenever a random number is needed, a random number generator is used to obtain the random number. The random number generator

Table 4.3: Convergence analysis based on the flux incident on the hexagonal optics aperture surface $\approx 17.92 \text{ mm}^2$, using an AM0 solar source (14 mm of diameter) modeled from 0.1 to 50 μm and various number of rays, using a random seed of 1.

# Rays	Flux (W)	Flux (W/m^2)	Deviation from ideal AM0 (%)	Computational time (s)
100	0.027560	1537.8	12.6	2
1,000	0.022421	1251.0	8.4	3
10,000	0.024597	1372.4	0.5	3
100,000	0.024701	1378.3	0.9	6
1'000,000	0.024593	1372.2	0.5	39
10'000,000	0.024619	1373.7	0.6	95

requires a seed, or initial value, to get it started generating a sequence of pseudorandom numbers. If the seed is the same for two successive simulations, the same sequence of random numbers is generated. Since that sequence can be an advantage or a disadvantage, TracePro® allows to set that seed value. In our case, the configuration used (circular source and quasi-hexagonal aperture) evidences the need to make a convergence study in which, both, the number of rays and the seed value used are taken into account, to ensure a more accurate input flux with a deviation $< \pm 0.1\%$, at least. Results are represented in Figure 4.25.

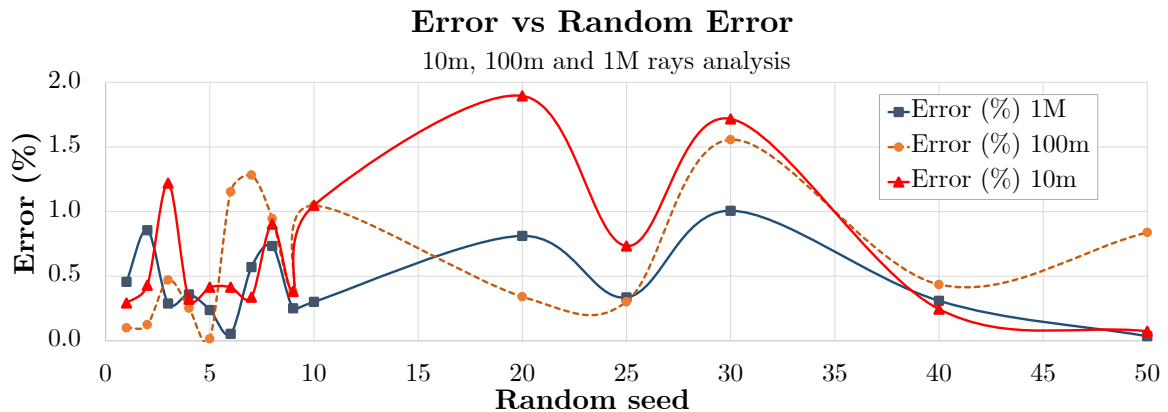


Figure 4.25: Convergence study varying the random seed and the number of rays traced.

From this, three statements can be derived:

(1.) Changing the random seed, and keeping the number of rays the same, results in a new ray set.

(2.) Changing the number of rays, and keeping the random seed the same, also results in a new ray set.

(3.) If the number of rays were fixed, and raytraces performed with different random seeds, it is expected that those results form a normal distribution. In addition, it is observed from the set considered that:

(i.) Using ten thousand rays a minimum error of 0.074% is found for a random seed of 50.

(ii.) When considering one hundred thousand, and a random seed equal to 5, the

error goes down to 0.03%.

(iii.) Using one million rays and a random seed of 50 the error is minimized to 0.015%. This last parameter setting has been chosen to perform the following performance analysis since it significantly reduces the associated error. Figure 4.26 shows the total irradiance map of a micro-CPV unit for perpendicular incidence over the collector aperture.

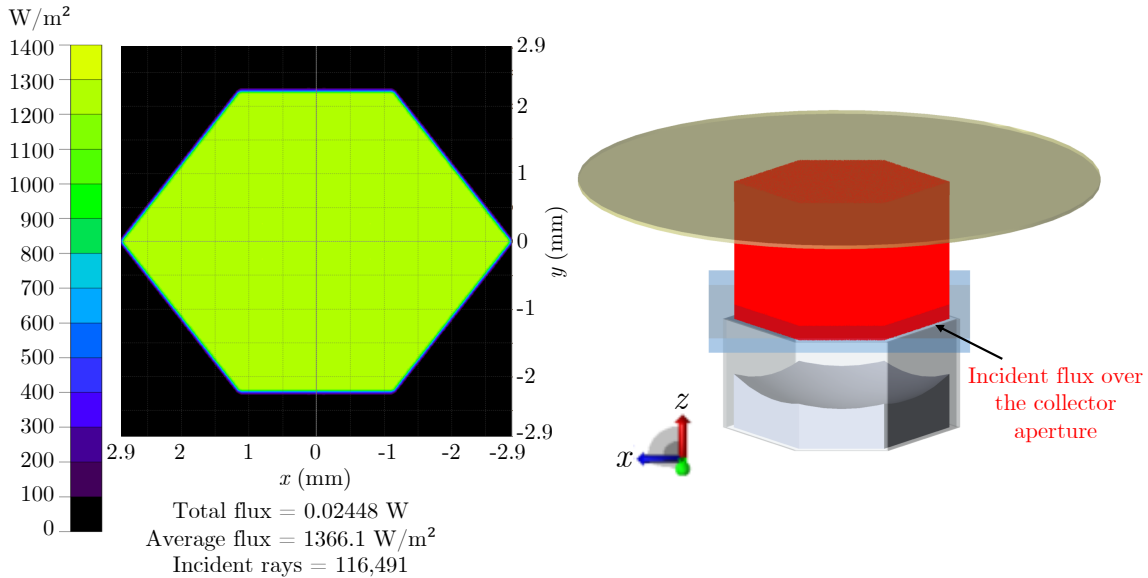


Figure 4.26: Total irradiance map for perpendicular incident flux of one hexagonal unit.

Once this difficulty in the convergence of the simulation (depending on the number of rays and the random seed used) has been encountered, and we have determined the optimum, we present the results of the modeling. To do this we begin with an analysis of the performance of the integrated system, starting with a study of the optical losses to estimate the optical efficiency for a perpendicular solar flux, and then move on to evaluate the angular and mechanical misalignment tolerance of an optical unit.

4.3.3 Optical losses chain and estimated optical efficiency

To estimate the optical losses of the system architecture described above, we propose to track the optical path followed by the light by evaluating its interaction with each of the constituent elements. At the point of intersection with each component, the ray can be reflected, refracted or absorbed. The process continues until the beam is lost from the system, completely absorbed, or intersects with the target detecting the beam.

4.3.3.1 Coverglass

The first optical element is the coverglass, here we will consider reflection (i.e., Fresnel), scattering and absorption losses. The selected material is a low-iron borosilicate glass,

and the optical properties (n, k) considered in this study have been previously defined in Table 3.2 (Section 3.2). A 400 μm thick coverglass has been considered, as a first approach without taking into account Anti-Reflective Coatings (ARC), and then estimating the improvement potential of using an ARC on the development of prototypes.

Fresnel reflection loss

When light is incident on the boundary between two media, in this case the space vacuum and the coverglass, a part of the light is lost in reflection; depending on the refractive indices, n_1 and n_2 , respectively. We have already defined the relationship describing the associated reflectance losses, for the case of normal incidence sunlight, in Equation 3.3. As a first approximation, this last equation is used to calculate numerically η (0.5461 μm), showing a power reflectance loss of about 8.11% taking into account both sides of the borosilicate glass; presented in Table 4.4.

Table 4.4: Fresnel reflection induced by a coverglass, calculated for the case of normal incidence and a η (0.5461 μm).

	Material/ Environment	n	Fresnel loss (%)	Solar Flux (W) for $\lambda=0.5461 \mu\text{m}$
n_1	Vacuum	1.0	4.14	0.02448
n_2	Glass	1.51102		0.02346
n_3	Vacuum	1.0	4.14	0.02249
Total Fresnel losses				8.11%

From Table 4.4 it can be seen that at the vacuum-glass and glass-glass interfaces, for a normal incidence of rays, each of them generates a loss in the order of 4%. It is also true that this can be reduced by adding an anti-reflective coating (ARC) on the coverglass, limiting these losses on average to 2% (i.e., at each interface) over the 0.3 to 1.7 μm spectrum. This can be seen in Figure 4.27, based on [355].

Absorption loss

Then we have evaluated the absorption of a 0.4 mm thick coverglass, considering the absorption coefficient α (i.e., low-Fe glass) and the Equation 3.4, previously defined in Section 3.2.1.2. It is then possible to calculate a 0.24% loss by absorption.

Surface roughness

Further investigation included the estimation of the Bidirectional Scattering Distribution Function (BSDF) to assess scattering properties of the coverglass used. Mathematically, the BSDF is defined as the scattered radiance per unit incident irradiance, or

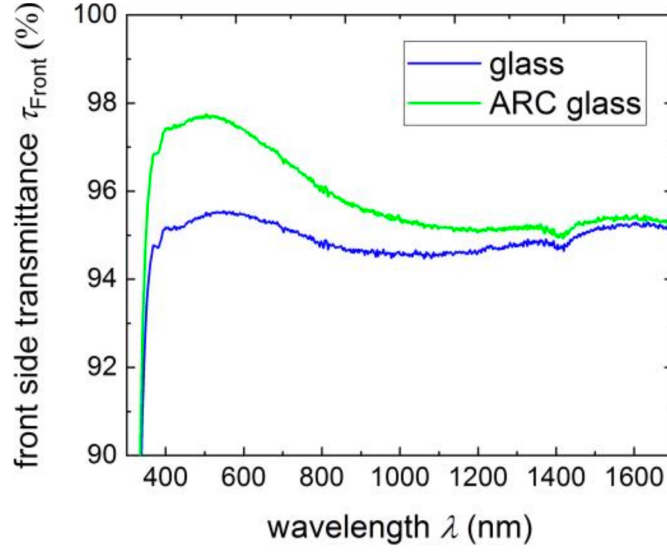


Figure 4.27: The hemispherical spectral transmittance of the glass front side τ_{Front} with and without anti-reflective coating (ARC) [355].

$$\text{BSDF}(\theta_i, \phi_i, \theta_s, \phi_s) = \frac{dL_s(\theta_s, \phi_s)}{dE_i(\theta_i, \phi_i)} \quad (4.4)$$

We note θ_i the angle of incidence of the incoming illumination and θ_s the angle of the specular output direction (reflected or transmitted), while L_s represents the fraction of the specular radiance (reflected or transmitted) with respect to the incident illumination E_i . Because radiance has units $\text{W} \cdot \text{sr}^{-1} \cdot \text{m}^{-2}$ and irradiance has units $\text{W} \cdot \text{m}^{-2}$, the BSDF has units sr^{-1} (inverse steradians).

The Harvey-Shack model [356] and the ABg model are probably the two most popular used to fit collected data. The BSDF model used in TracePro® is a quasi-inverse-power-law model called the ABg model. It is called the ABg model because of the three parameters in the following equation,

$$\text{BSDF} = \frac{A}{B + |\vec{\beta} - \vec{\beta}_0|^g} \quad (4.5)$$

where A, B, and g are parameters that can be used to fit the formula to measured data and β_0 is a projection onto the surface of the unit vector in the specular direction, while β is a projection onto the surface of the unit vector in the scattering direction, and the magnitude of their difference, $|\beta - \beta_0|$, is the argument of the BSDF.

Here we use a tool proposed by TracePro® to estimate the coefficients A, B, and g knowing the RMS roughness and the autocorrelation length, as described in [357], which in turn is based on Stover's book "Optical Scattering: Measurement and Analysis" [358]. Once the ABg parameters are integrated in TracePro, the BSDF estimation differentiates between reflection effects, Bidirectional Reflectance Distribution Function (BRDF), and

transmission effects, or Bidirectional Transmittance Distribution Function (BTDF). This theory is only valid if the RMS roughness is much smaller than one wavelength. The guideline for the RMS roughness/wavelength ratio is 0.02 or less to provide reliable BSDF predictions [357]. Prediction accuracy will be "degraded" if larger values of RMS roughness are used. When the integrated BSDF approaches or exceeds one, it is a sure sign that the RMS value is too large for the theory to be accurate.

For this purpose, coverglass roughness measurements have been made, using a Bruker Dektak XT contact profilometer, and relaying the ISO 4287 standard for the filtering type, shown in Annex 6.5.3. The Figure 4.28 shows the roughness, waviness and total measured profiles of a measurement. While Table 4.5 describes the amplitude parameters for the measured roughness according to the standard, both for a single measurement (Glass #3), as well as the mean values for a 6-measurement campaign.

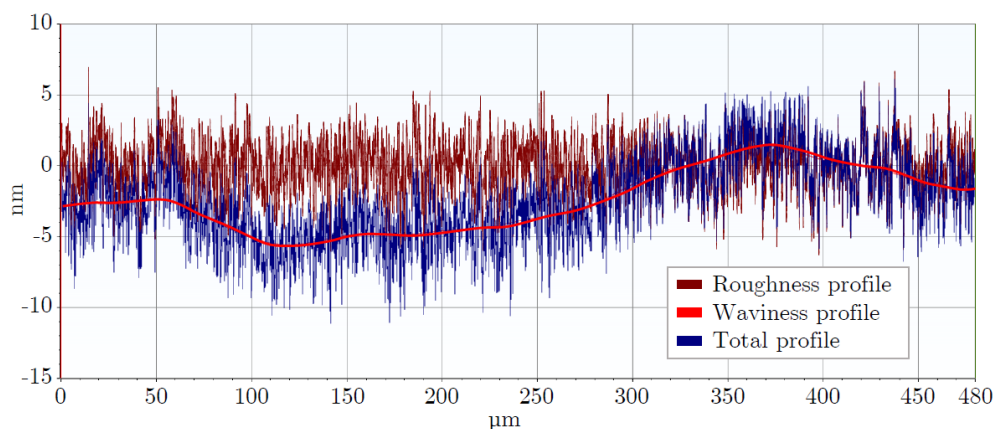


Figure 4.28: Coverglass roughness, waviness and total measured profile of one test.

Table 4.5: Coverglass roughness results.

Amplitude parameters – Roughness profile (ISO 4287)				
Label/ Measure	Units	Value (Glass #3)	Average (6 meas.)	Description
Ra	nm	1.4	1.3	Arithmetic mean deviation of the assessed profile
Rq	nm	1.8	1.7	Root Mean Square (RMS) deviation of the assessed profile
Rz	nm	11.8	10.9	Maximum height of the profile

A mean Rq (or RMS) = 1.7 nm was then found, which in turn was integrated into the ABg model. The coefficients relative to three wavelengths (0.3, 0.555 and 1.7 μm) have been calculated as a first approximation [357, 358], presented in Table 4.6. Once these coefficients were calculated, they were entered into TracePro® and the BTDF and BRDF estimates are presented in Table 4.7. For each of these wavelengths, the index of the absorption, reflection and total and specular transmission coefficients are shown. In

addition, the ratio between the BRDF and specular reflection and the BRDF and specular transmission were calculated, showing that their impact is low, for example for this last it was about 0.3% for a $\lambda = 0.3 \mu\text{m}$ and $< 0.1\%$ for a $\lambda = 0.555 \mu\text{m}$.

Table 4.6: ABg coefficients based coverglass roughness RMS.

ABg coefficients for TracePro			
Wavelength (μm)	0.3	0.555	1.7
Coefficient			
A	1.92E-07	1.05E-07	3.45E-08
B	1.09E-10	6.89E-10	1.98E-08
g	3	3	3

Table 4.7: Coverglass roughness RMS-ABg.

$\lambda(\mu\text{m})$	BRDF	BTDF	n	R	T	R specular	T specular	Flux
0.3	0.003046	0.003046	1.5217	0.043	0.957	0.0398	0.954	1.0
0.555	0.000899	0.000899	1.5108	0.041	0.959	0.0405	0.958	1.0
1.7	9.7E-05	9.7E-05	1.5019	0.040	0.960	0.0401	0.960	1.0

In view of the low roughness of the coverglass, which generates a very low estimated scattering, it was disregarded from the loss chain under consideration.

4.3.3.2 Solar cell and interconnections shading

After interacting with the coverglass, the solar flux that has been transmitted through the second glass interface travels on its path to the parabolic reflector. However, part of it is shaded by the micro-cell and its interconnections. Figure 4.29 illustrates a top view of these elements with their dimensions. The solar cell and interconnections have areas of about 0.61 and 0.35 mm^2 , respectively. These represent 3.4% for the cell and 1.9% for the interconnections, with respect to the aperture area of 17.92 mm^2 , for a total of 5.3% shading.

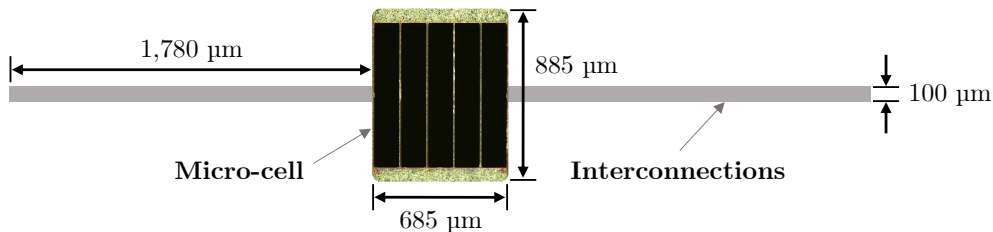


Figure 4.29: Top view of cell and interconnections showing its dimensions.

Considering shading effect, it is also possible to calculate the effective concentration of the designed micro-CPV. Considering the ratio of aperture area to cell area, for an effective concentration factor of 30X.

4.3.3.3 Optics reflectance

To determine the optical properties of a silver coating using DC 93-500 silicone as a substrate, a series of depositions were carried out at the laboratory, and glass was also used as a comparison substrate. For both architectures three samples were tested, and glass substrates 50x50 mm² and 1 mm thick were used. The reference sample consisted in applying the coating directly on the glass, while the specimen of interest used the same type of glass as support and a homogeneous layer of silicone was applied (300 μm thick), which was degassed and cross-linked (at 150°C). The latter was prepared one month before the application of the coating to ensure the stability of the silicone. Then, after having previously cleaned and prepared the surface of the substrates with plasma, we proceeded to apply the plating using a physical vapor deposition technique, using equipment from Vinci technologies. The deposit had a thickness of 200 nm using the quartz balance of the evaporator, this was measured (5 times) with a profilometer for a thickness of 196 nm ±3. A pressure of 5.7×10^{-7} mbar was used, which was maintained for 12 hours before applying the coating to guarantee silicone degassing. Coated samples are shown in Figure 4.30 (a') and (b'), for the glass and silicone on glass substrates, respectively.

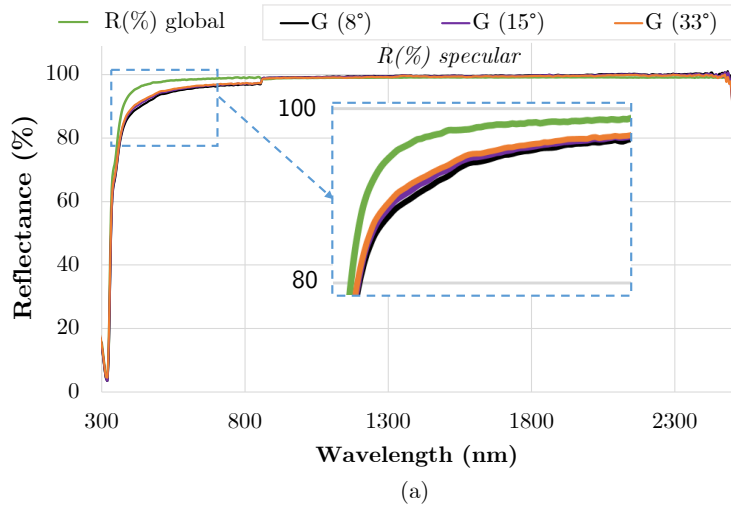
These were in turn characterized, starting with transmission measurements at 8° (being the instrument minimum) to evaluate the degree of opacity of the silver coatings, and then moving on to specular reflectance at 8°, 15°, 33°. The latter being the maximum angle of reflection/incidence of a ray, half of θ_R (i.e., rim, see Figure 4.4), which based on Equation 4.2 and taking into account $f = 2.25$ mm, $W = 5.8$ mm and $Z_R = 0.926$ mm results in Equation 4.6 and 4.7. Transmittance and reflectance measurements were made using an ARTA (Absolute Reflectance Transmittance Analyzer) instrument in the range of 250 nm to 2500 nm, in 5 nm steps. Then, using the same range and step, global reflection measurements were performed using a Perkin Elmer Lambda 950, equipped with an integrating sphere.

$$\theta_R = \tan^{-1} \left(\frac{\frac{4fW}{2}}{\left(4f^2 - \left(\frac{W}{2}\right)^2\right)} \right) = \tan^{-1} \left(\frac{\frac{W}{2}}{f - Z_R} \right) = 65.37^\circ \quad (4.6)$$

$$\theta_{MAX, INCIDENCE} = \frac{\theta_R}{2} \approx 33^\circ \quad (4.7)$$

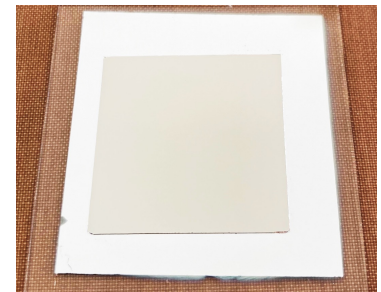
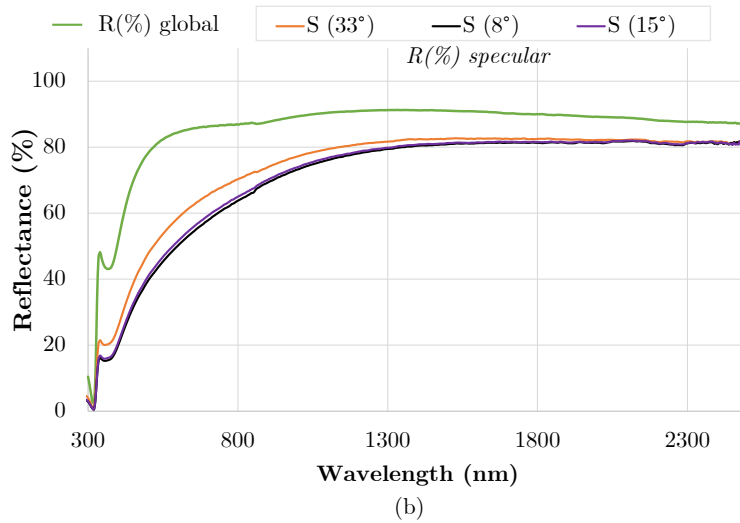
While transmittance measurements showed that the deposits were well opaque, total reflectance measurements ranged from 96.3% to 98% for the glass substrate, and from 70% to 88% for the silicone. On the one hand, the results showed a high specular reflectivity for the coatings made on glass substrates, about 97%, while those made on silicon were about 70%, see Figure 4.30 (a) and (b). Also, it is possible to appreciate that there is a small jump in the measurements made, around 860 nm, this is due to a

measurement artifact when changing the detector. For the Ag coated on silicone, the specular reflectance is characteristic of scattering. Moreover as the reflectance is lower than on glass, the Ag thickness and the coating deposition parameters must be optimized to obtain state-of-the-art characteristics.



Ag on glass

(a')



Ag on silicone DC 93-500

(b')

Figure 4.30: (a) Measured spectra of the master mirror silvered on glass (or G), compared to (b) the spectrum of a silvered on 93-500 silicone (or S), showing the total reflectance $R(\%)$, and the specular measured (at 8° , 15° and 33°).

Given the low performance of the non-optimized coating, which has not been provided with adequate adhesion or protective coatings, it was decided to include during the performance analysis the reflective characteristics equivalent to a state-of-the-art polymer-based silver coating [42, 44], such as those described in Section 1.2.2. Furthermore, scattering due to the actual surface properties, which are not known at the moment, is not taken into account in these simulations. For this purpose, a mirror with a specular

reflectance of 94.8%, an absorbance of 5% and 0.2% of scattering was defined.

4.3.3.4 Optical losses summary

Section 4.3 described the predominant optical losses in the system through the three main elements (coverglass, cell and interconnections and mirror), which generate reflection, absorption and scattering losses. Figure 4.31 represents these three optical phenomena that occur in the loss chain between the cell and the module, for which an optical efficiency of about 82% is found; which considering anti-reflection coating on both sides of the coverglass could be increased to 86%. Another way to increase the optical performance of the integrated system is to decrease the shadowing generated by the interconnection lines which can improve the overall optical performance by as much as 2% to 88%.

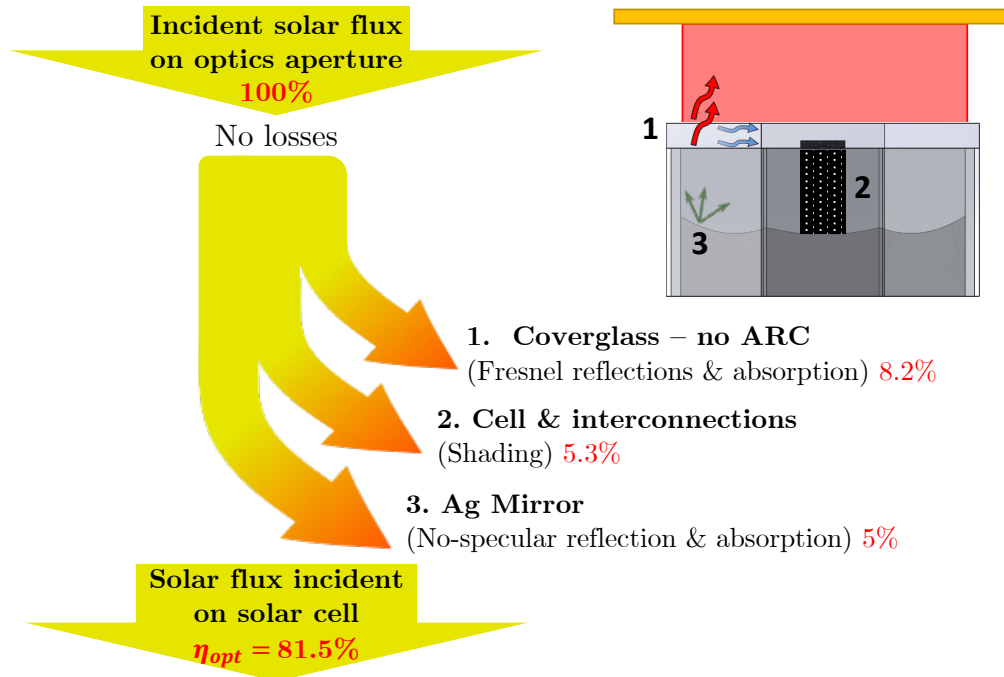


Figure 4.31: Representation of main optical power losses along the constituent elements.

4.3.4 Irradiance distribution

Subsequently, the effect of the receiver position on the flux distribution over the cells of the integrated system was analyzed by ray-tracing, for different receiver planes located every 25 μm from the focal point, taking into account the elements and materials previously described. Then, from the normalized-to-peak irradiance maps shown (see Figure 4.32), the PAR for each of the positions was calculated and plotted, as well as the percentage of effective area it represents with respect to the total cell size, see Figure 4.33.

From this, it can be seen that for the focal plane ($z = 0$) the flux on the receiver is highly concentrated at a point, equivalent to 0.2% of the cell surface, which generates a $\text{PAR} = 1,010$. This configuration, as expected, would make the use of a solar cell impractical. Then, as the z gap is increased the PAR decreases monolithically until 3.3 for a plane located at -0.25 mm from the focal, while the effective irradiance surface increases to a maximum of 73%. It is also possible to see on the irradiance maps the shading effects generated by the square receiver at the entrance of the flux to the optical system, which appears in black at the center of the maps and tends to grow for more distant planes.

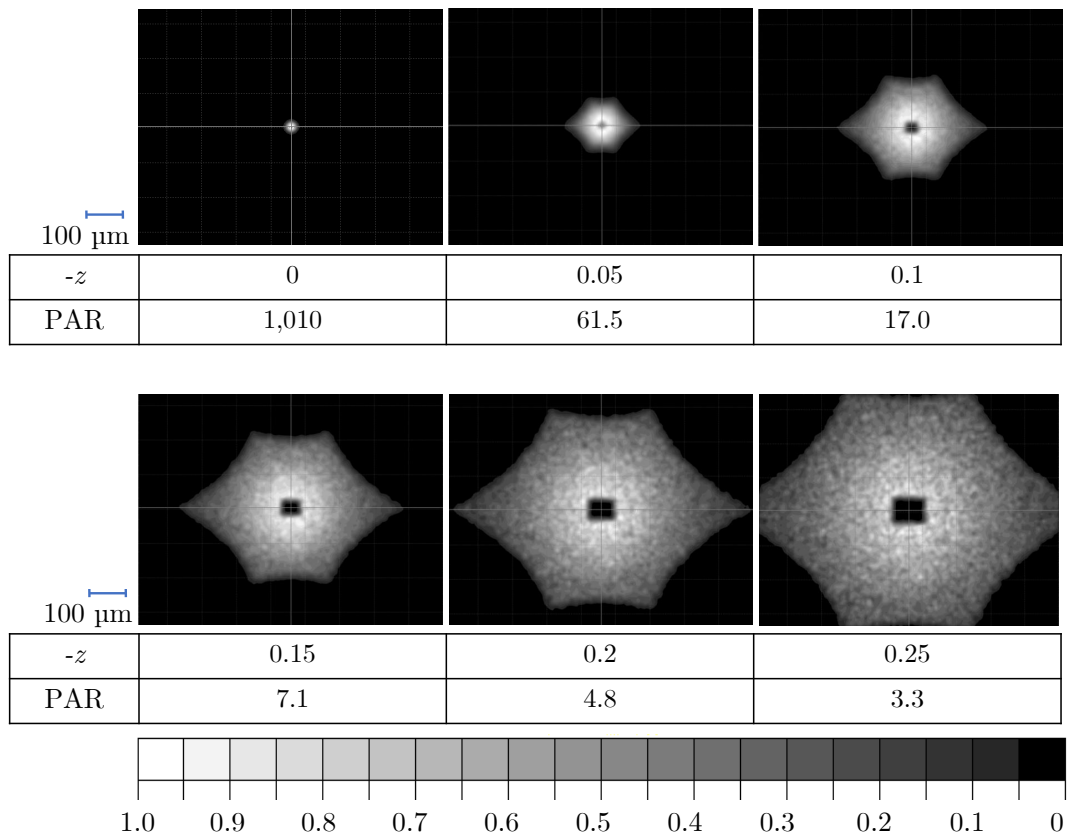


Figure 4.32: Normalized to peak irradiance maps for different detector positions ($885 \times 685 \mu\text{m}^2$) and its associated Peak-to-Average Ratio (PAR).

4.3.5 Angular tolerance analysis

To evaluate the angular tolerance of the integrated parabolic reflector, ray-tracing simulations were performed, in which the solar source was rotated around each of the axes (each 0.5°), either a uni-axial deviation, for the x -axis was denoted (AA_x), for the y -axis (AA_y). In addition, a bi-axial deflection was also evaluated (AA_{xy}) considered as the worst case scenario. In order to establish the best compromise between flux homogeneity and

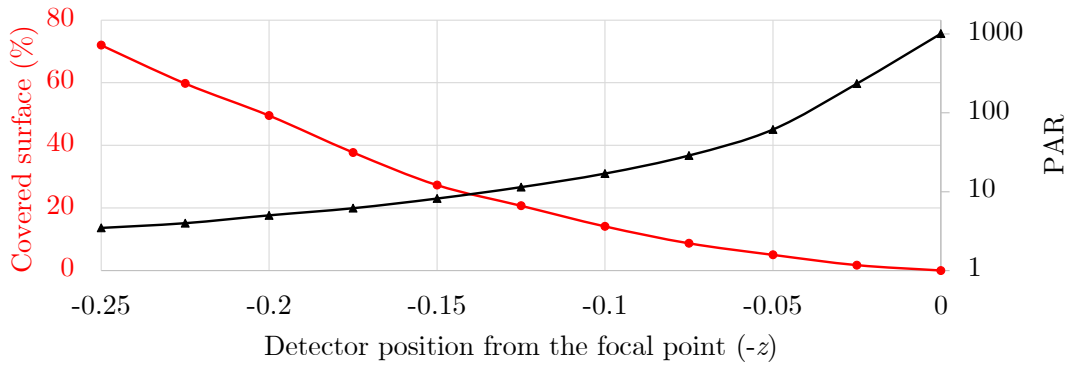


Figure 4.33: Evolution of the PAR and the covered surface percentage for different detector in a defocused position of a integrated parabolic mirror with a constant total irradiance.

the angular acceptance, we consider various planes corresponding to defocused planes with respect to the z -axis, every 0.025 mm with respect to the focal, from $z = 0$ to $z = -0.25$ mm. The results are shown in Figure 4.34 showing how the total flux perceived by the cell evolves for each deviation, a horizontal line (in red) shows the 90% of the total flux (i.e., equivalent to the angle of acceptance at the intersection with each curve), while the target range is show in green.

For an uni-axial deviation around the y -axis, it can be seen that the angular tolerance remains constant, around 5.8° , between the 0 and -0.05 mm z -positions, see Figure 4.34 (a). Then, it tends to decrease as the z gap increases, until it reaches a minimum of 3.8° for a deviation of -0.25 mm. One can also see that around the x -axis the AA has a maximum of 5.1° between 0° and -0.05 mm, see Figure 4.34 (b). Then it decreases until 2.5° for $z = -0.25$ mm.

The reduction of the angular acceptance of the uni-axial deviation of x with respect to y is mainly due to the non-symmetric dimensions of the receiver, which is 29% shorter with respect to x than y . For the bi-axial offset, shown in Figure 4.34 (c), a decrease in the AA can also be observed as the detector moves away from the focal point, it evolves from about 4.5° for z values between 0 and -0.075 mm to a minimum of 1.8° for a plane at -0.25 mm.

In this regard, considering the minimum angular tolerance criterion for a uni-axial deflection that must be $> 4^\circ$, it is found from the focal plane to z positions at -0.225 mm and -0.15 mm, for the y and x axis, respectively. While the range that guarantees an $AA_{xy} > 2.5^\circ$ is found from the focus to $z = -0.2$ mm. Thus, in terms of angular tolerance, the limiting axis is x , for a detection plane at -0.15 mm. Considering this, Figure 4.35 shows the irradiance maps of the integrated system for a detector at $z = -0.15$ mm from the focal plane: (a) for an irradiance normal to the optical aperture; as well as the acceptance angles: (b) around the y -axis (5.5°), (c) around the x -axis (4°) and (d) for a bi-axial xy deviation (3.4°).

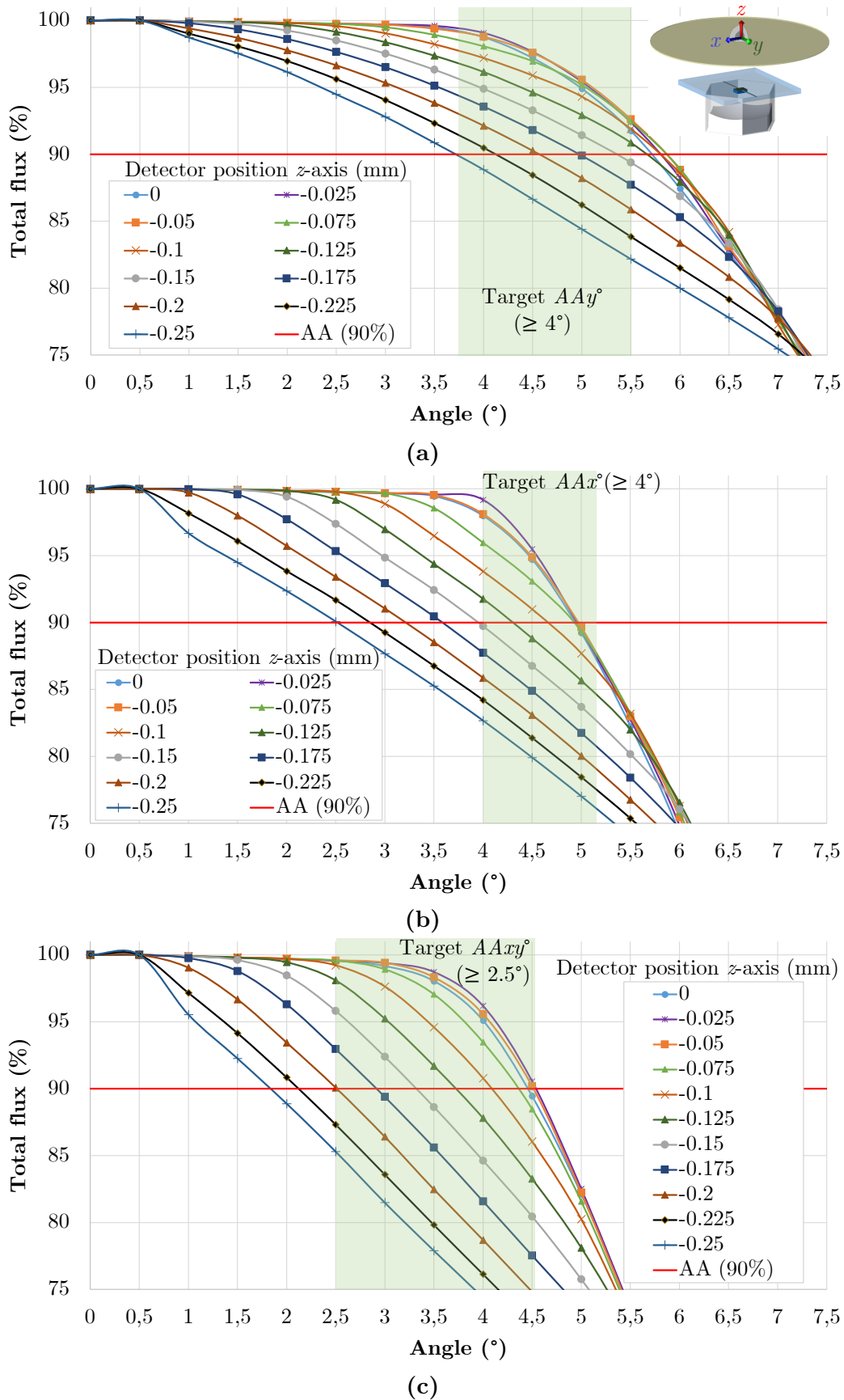


Figure 4.34: Acceptance angle study for different detectors placed each 25 μm ($-z$) position (in colors), for a deviation: (a) uni-axial around y -axis, and uni-axial around x -axis (b), while (c) for a bi-axial following x,y -axis.

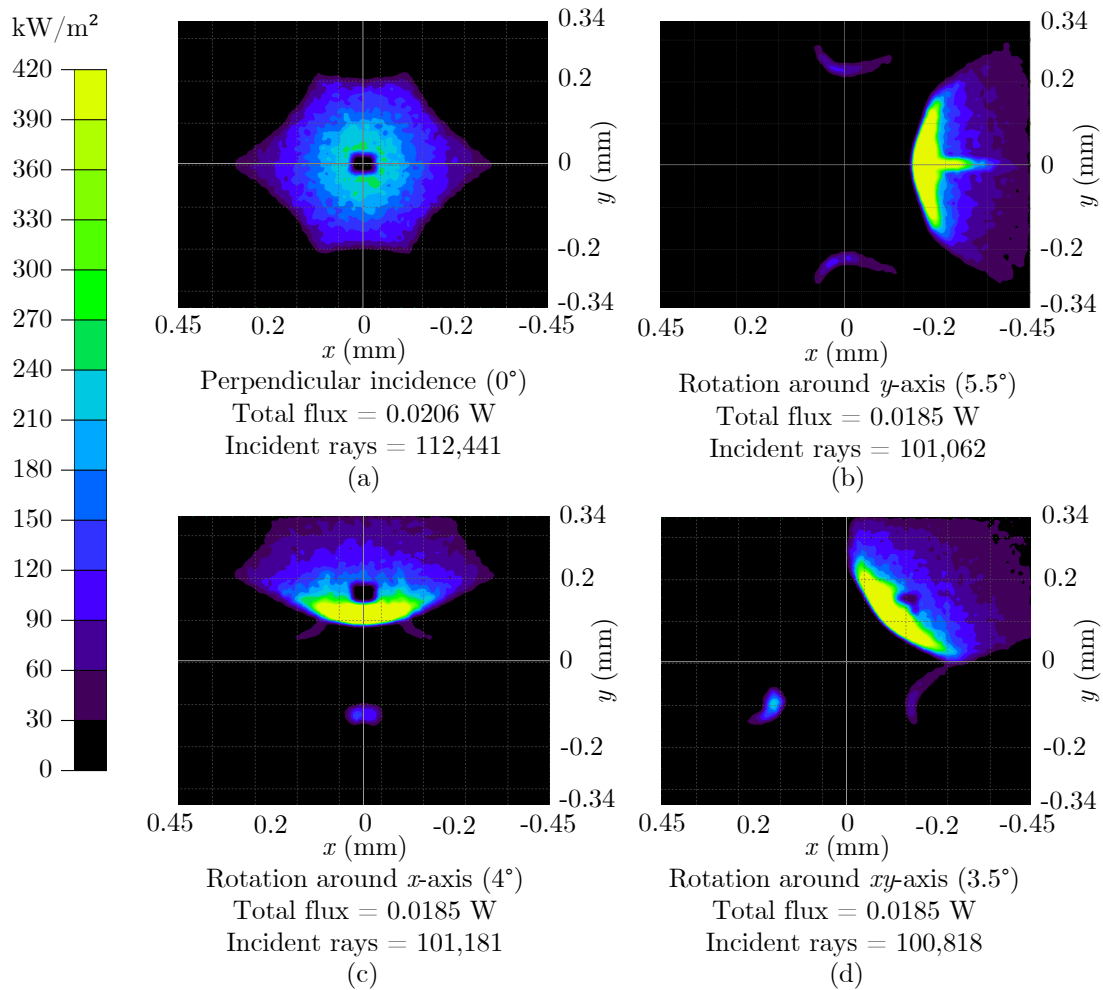


Figure 4.35: Irradiance map for a detector placed at $z = -0.15$ mm from the focal point, using an integrated parabola.

4.3.6 Mechanical misalignment of the concentrator elements

Once the angular tolerance of the system has been established, we proceed to study the mechanical misalignment tolerance of the constituent elements, which must be sufficiently accurate to limit the losses in the module. The objective of these simulations is to quantify the power losses due to optical alignment errors, and subsequently, the tolerances of the mounting parts by means of ray-tracing simulations. For this purpose, the same requirement parameter as for the angular tolerance has been taken as a reference, i.e. that 90% of the flux for perpendicular incidence is preserved. Here, we have considered the optical estimation for perpendicular incidence described in the previous section, as a starting point, using the same parameters such as, the light source that reproduces the angular aperture and the solar spectrum, the refractive indices and absorption losses of the glass and the reflection of the mirror.

In this section, we try to quantify more particularly the influence of the mobilities between the focusing optics and the receiver cell, with respect to translations around the x , y and z -axes; while rotation between elements have not been taken into account.

We have studied the misalignment response for a cell that has been offset from the focal point of 50 μm , since this position guaranteed the maximum acceptance angle for all axis (since they do not vary from the focal to 50 μm), while avoiding having a very focused spot, which is undesirable for the performance of a solar cell. The results are shown in Figure 4.36, and the irradiance maps evolution in Annex 6.5.3. From this it can be seen at first glance that the translations around the x and y axes are symmetric. A tolerance of approximately ± 0.4 mm and ± 0.3 mm, around the x -axis and y -axis respectively, was found, this difference as in the case of the acceptance angle is due to the use of a rectangular cell, where there is a larger displacement length around the x -axis. On the other hand, around the z -axis there is a non-symmetrical response varying between -0.25 and 0.35 mm.

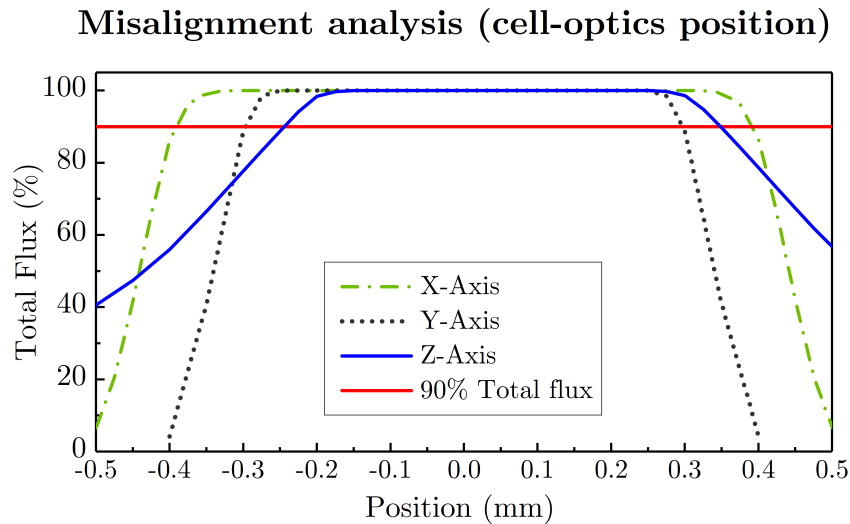


Figure 4.36: Alignment tolerance between cell and optics.

4.3.7 Spectral photocurrent distribution

After having estimated the optical losses of the system, we were also interested in estimating the photocurrent at each subcell and its spatial distribution, to get a better view of the optical performance of the system. For this purpose, we relied on EQE measurements (see Equation 4.8), we used data from the Azur Space MJSC data-sheet to estimate the short-circuit current density (J_{SC}) at given wavelength, every 10 nm (spectral irradiance of the AM0 spectrum at a solar intensity of 1 sun). These were then integrated over the wavelength range from 300 to 1800 nm, spread over the three different spectral beaches corresponding to each absorption band of each sub-cell (i.e., 300-660 nm, 660-900 nm

and 900-1800 nm), by means of Equation 4.9. Where q is the elementary charge, c is the speed of light and h is the Planck's constant. Then each of these photocurrents were integrated as emitting sources via TracePro, see Figure 4.37.

$$EQE = \frac{\text{electrons/sec}}{\text{photons/sec}} = \frac{(\text{current})/(\text{charge of one electron})}{(\text{total power of photons})/(\text{energy of one photon})} \quad (4.8)$$

$$J_{sc} = \int_{\lambda_1}^{\lambda_2} \frac{q\lambda}{hc} EQE(\lambda) AM0(\lambda) d\lambda \quad (4.9)$$

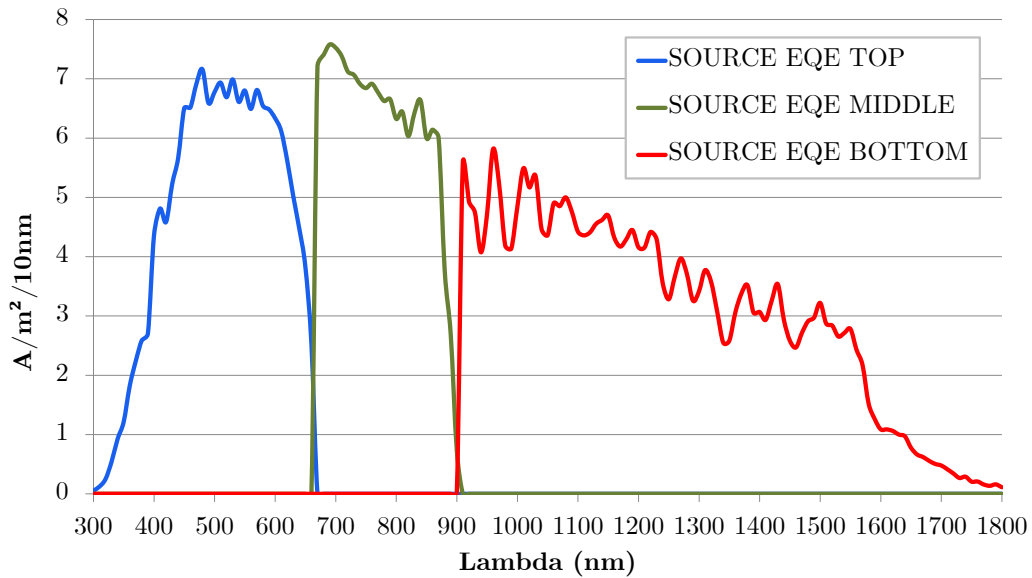


Figure 4.37: Solar sources based on estimations of the photocurrent at each subcells using a AM0 spectrum, TOP (GaInP), MIDDLE (GaAs) and BOTTOM (Ge).

Furthermore, Figure 4.38 shows a map of the estimated short-circuit current distribution, for each of the subcells of the 3J cell, more particularly for a cell located at $z=-0.05$ mm (Best AA with higher uniformity) above, and $z=-0.15$ mm (Best uniformity in accordance with minimum AA criteria) below. In addition, at the top of each junction the associated J_{SC} in mA is shown. From this, it can be seen that the limiting subcell is the middle one with a current of about 2.26 mA. While the higher intensity for $z=-0.05$ mm is one order of magnitude higher than for the $z=-0.15$ mm.

Then, to quantify the spectral variations measured between the first two subcells, the Spectral Matching Ratio (SMR) is introduced:

$$SMR = \frac{J_{SC}^{TOP}}{J_{SC}^{MID}} \quad (4.10)$$

If the subcells receive the AM0 spectrum, the SMR is equal to 1; if the intensity is

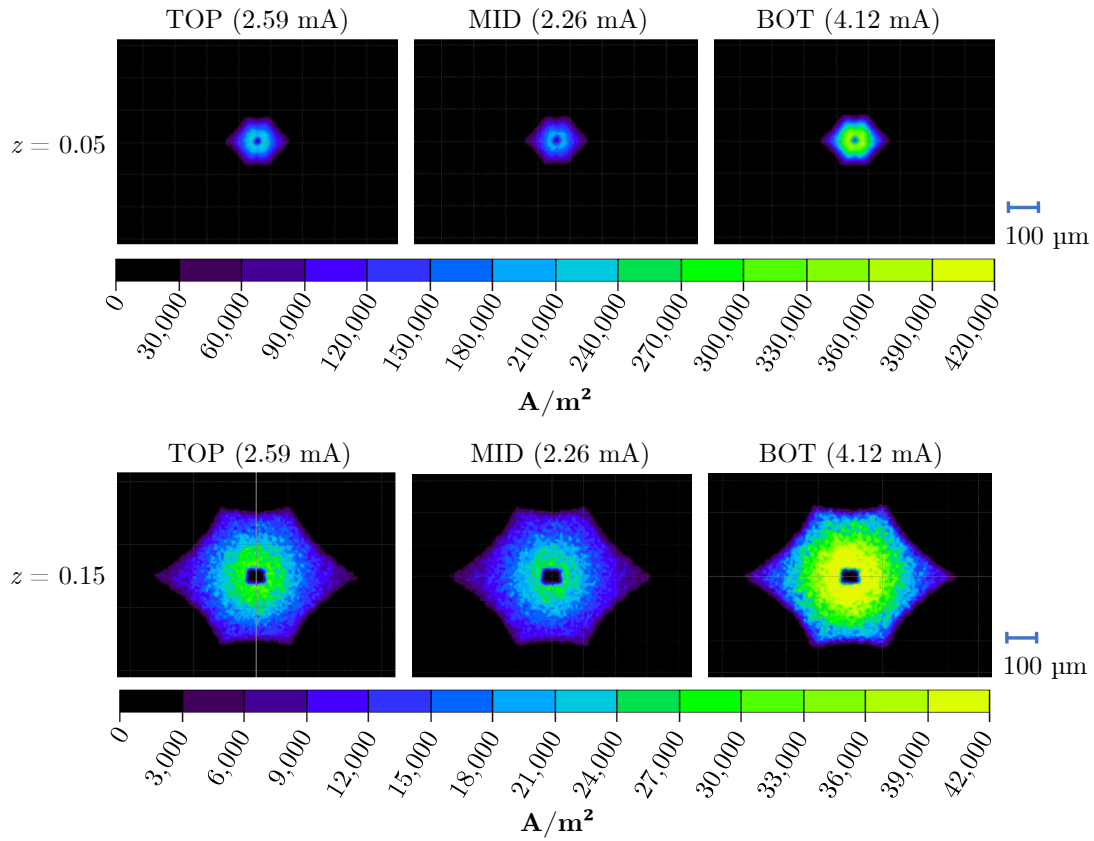


Figure 4.38: Photo-current mapping of each sub-junction TOP (GaInP), MID (GaAs) and BOT (Ge), using EQE spectral response and an AM0 spectrum.

higher in the top spectral band than in the middle, the SMR is greater than 1. In this regard, as the SMR is equal to 1.15, there is a mismatch of 13%.

4.3.8 Synthesis and conclusions

In this chapter we presented the optical design of a new micro-CPV concept, more particularly a miniaturized parabolic mirror highly integrated in a honeycomb using a molding technique. Aiming to: (i.) Significantly reduce the recurring cost of the standard CIC solar array using micrometer cells ($<1\text{mm}$). (ii.) Increase the specific power up to 150 W/kg (at incident AM0), compared to an existing standard CIC technology, currently between $50\text{--}80\text{ W/kg}$. (iii.) Provide a compact architecture between $4\text{--}15\text{ mm}$ thickness, compared to $20\text{--}30\text{ mm}$ of the standard system, and thus increase the volumetric power (W/m^3). (iv.) Reduce the number of manufacturing steps to produce optics by molding a complete assembly in a single step. (v.) Include a monolithic structure that avoids deployment in space, between the optical lattice and the cells where the honeycomb provides rigidity and keeps the optics and solar cells separate and allied.

Optical design by raytracing

In order to establish a reflector system adapted for micro-CPV in space (using cells of about 0.6 mm²), design criteria were established, such as: a uni-axial and bi-axial acceptance angle of $> 4^\circ$ and $> 2.5^\circ$, respectively, a concentration between 25X and 30X, a misalignment tolerance $> 50 \mu\text{m}$, and the best possible flux uniformity. For this, a comparative study of two idealized (radially symmetric) systems was performed, using a parabola with different defocusing planes and an optimized free-form. Both with a distributed flux in 60% of the cell.

From this it was concluded that for the considered parabolic system, the receiving plane that guarantees the desired angular tolerance with the most homogeneous flux distribution (PAR = 4.4) is $z = -0.225 \text{ mm}$, with a $AA_y = 4^\circ$ and $AA_{xy} = 3^\circ$.

Subsequently, a free-form reflector was optimized to improve the angular tolerance and flux uniformity of a spot of size equivalent to that of the parabola for the plane $z = -0.225 \text{ mm}$. It was observed that the optimized reflector free-form has an acceptance angle that does not match the design specifications, with $AA_y = 3^\circ$ and $AA_{xy} = 2^\circ$. Thus, SOEs were used to improve its angular tolerance and the uniformity of the array, using a hemisphere and an optimized radial free-form. These substantially improved the angular tolerance, particularly the free-form SOE, for $AA_y = 8.2^\circ$ and $AA_{xy} = 5.7^\circ$. The latter also resulted in a 20% improvement in flow homogeneity, reducing the PAR from 6.7 to 5.6, with respect to it without SOE.

Although the free-form reflector can largely guarantee the minimum angular tolerance criteria established when using an SOE, it presents a spot with a PAR about 21% higher than the parabola, and more importantly it implies a higher complexity in manufacturing. The parabolic reflector, therefore, proved to be an efficient solution in terms of flux homogeneity, as well as in terms of manufacturing simplicity. For this reason, the latter design was chosen to validate the concept of a highly integrated reflector in a honeycomb.

Optical simulation of a hexagonal truncated parabolic reflector

Then we moved from studying idealized systems to propose an optical simulation of a parabolic reflector integrated in a honeycomb. First, we described the truncated optical system and each of the elements and materials considered. Then we studied the convergence of the incident flux on the hexagonal optical aperture of an AM0 (circular) solar source, modeled for its entire spectral range, 1366.1 W/m² and an average solar angle of about 0.27°. In our case, the configuration used (circular source and quasi-hexagonal aperture) showed the need to perform a convergence study taking into account both the number of rays and the value of the seed used to ensure a more accurate input flux with a deviation $< 0.1\%$, at least. From the sets considered it was found that using one million rays and a random

seed of 50 the error is minimized to 0.015%. This last parameter setting was chosen to perform the following performance analysis, as it significantly reduces the associated error.

Furthermore, the first silver coatings (i.e., not optimized) were made on silicone DC 93-500, which were compared to samples made on glass. Then the specular and total reflectance of the samples were measured, as well as the transmission to verify opaque coatings. From this we observed a specular reflectance around 97% for the glass substrates, while those made on silicon were around 70%, both in the range of 250 nm to 2500 nm. These results open the door for further research to improve the coating deposition technique on the polymer used.

Then, the predominant optical losses of the micro-CPV under development were studied, considering reflection, absorption and scattering losses. This presented an estimated optical efficiency of around 82%, which considering an ARC on both sides of the coverglass could be increased up to 86%. Another way to increase the optical performance of the integrated system is to decrease the shadowing generated by the interconnection lines which can improve the overall optical performance by as much as 2% to 88%.

Simulated performance of the system

Ray-tracing simulations were performed to evaluate the performance of the system. We started by evaluating the angular tolerance of the integrated parabolic reflector. In this sense, considering the minimum angular tolerance criterion for a uniaxial deviation that must be $> 4^\circ$, it is found from the focal plane to z positions at -0.225 mm and -0.15 mm, for the y and x axes, respectively. While the range that guarantees a $AA_{xy}^\circ > 2.5^\circ$ is from the focus to $z = -0.2$ mm. Thus, in terms of angular tolerance, the limiting axis is x , for a detection plane at -0.15 mm, which in turn has a $PAR = 7.1$. It should be said that the simulated light distributions (PAR) are to some extent overdimensioned with extremely high concentration peaks that do not occur in practice. This is mainly due to some factors, such as scattering due to surface roughness, imperfections (e.g. manufacturing and assembly processes), among others, which generate an implicit scattering that has not been taken into account.

Furthermore, if we compare the receiving plane (according to z) that guarantees the desired angular tolerance with the most homogeneous flux distribution it decreased by 1.5 times, from $z = -0.225$ mm to $z = -0.15$ mm from a parabolic (ideal) system to an integrated one. Linked to this, the associated PAR increased by 38%, from 4.4 to 7.1 from a parabolic system before and after integration, respectively. Estimates implying an increase due to series resistance losses ($> 2\%$), which will have to be studied further using real systems.

Then, regarding the misalignment analysis, a tolerance of approximately ± 0.4 mm and ± 0.3 mm was found, around the x and y axis respectively. On the other hand, around the z -axis there is a non-symmetric response varying between -0.25 and 0.35 mm. Mechanical

tolerances also meet the initial minimum specifications (50 μm).

Finally, we estimated the short-circuit current density (J_{SC}) of each junction, based on EQE measurements, from which it could be observed that the middle subcell is the limiting one with a current of approximately 2.26 mA. In addition, a $\text{SMR} = 1.15$ was found. In complement to this, the experimental validation (prototyping) of the micro-CPV proposed is presented in the following chapter.

Everything is theoretically impossible until it is done.

— Robert A. Heinlein

5

Experimental validation of a highly integrated parabolic reflector

Once the integrated optical unit has been designed and its theoretical optical performance estimated, we move on to the experimental validation. The manufacturing of the proposed micro-CPV array can be divided into two main subassemblies, on the one hand there is the fabrication of the composite structure and the optics formed inside it, while on the other hand there are the interconnected cells on the coverglass. Then, these two parts must be carefully assembled in compliance with the mechanical tolerances described above to ensure maximum rated performance.

In this chapter, we focus especially on the development of highly integrated optics within a honeycomb structure, which can be formed by various techniques such as molding, thermoforming, forging, stamping or machining, within the panel. More specifically, we focus on a molding technique, to make the transition from a theoretical concept to a prototype with industrial potential. This technique has been chosen mainly because it is a promising low-cost technology that allows the fabrication of a complete optical assembly (in this case the parabolic dish array) in a single injection molding. Moreover, it is a technique available in the laboratory, which has been developed over the years. The overall process for prototyping highly integrated honeycomb mirrors can be divided into three main stages, starting with the fabrication of the composite structure (see Section 5.1), through the formation of the optics (Section 5.2), and ending with the metallization of the reflective surface.

5.1 Lamination of double stage composite materials

For prototyping we aim to develop mini-modules of about 40x40 mm² (i.e. half of a space solar cell), for this purpose samples of 200x200 mm² were made first, which were then cut and prepared to the required size. The composite stack (200x200 mm² total surface area) was cured using a 3S PV laminator (model S1815E). The 3S laminator allows the processing of PV modules by the classical hot lamination process, capable of processing modules with dimensions up to 1700x1200 mm² and a thickness of 20 mm (thicker module are possible if the membrane frame is modified), and temperatures between 30-175°C. The laminator is compatible with materials of different nature, such as: front-sheet of glass or polymer, encapsulated by Ethylene-Vinyl Acetate (EVA), Poly Vinyl Butyral (PVB), Thermoplastic PolyUrethane (TPU) or alternative resins, back-sheet of metal, polymer, glass, ceramic, composite material among others.

As previously mentioned, the composite stack can be composed of either one or two stages of composites depending on the stiffness needed, the Figure 5.1 shows a dual-stage setup. Typically, each stage is composed of a core honeycomb that is bonded with a CFRP prepreg by means of an epoxy adhesive film. During lamination, the stack is placed between two outer sheets of PolyTetraFluoroEthylene (PTFE) (or Teflon), whose structure is supported between two 3 mm thick glass plates. This configuration is intended to ensure a stable structure during lamination with the use of glass/stack, and PTFE is used to prevent adhesion between the latter.

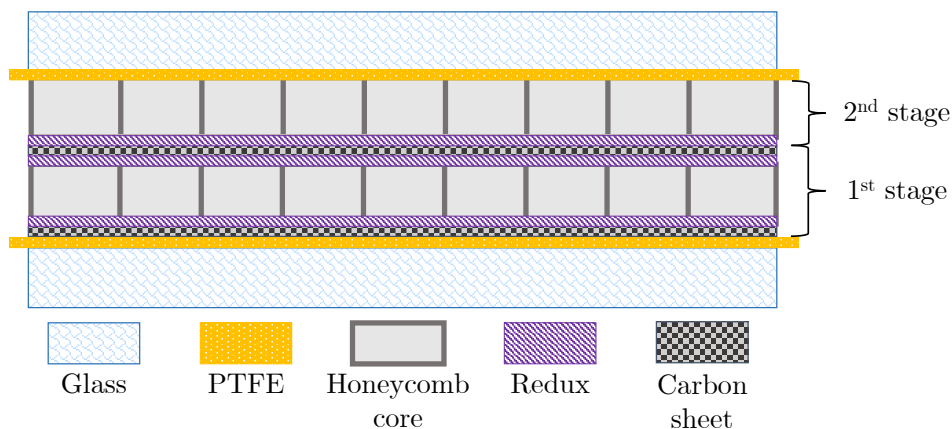


Figure 5.1: Lamination stack structure.

During prototyping, with the exception of the honeycomb core (CR-III® 5.7 3/16 5052), the materials used are not space qualified, a Hexbond 312UL-100 epoxy adhesive film was used instead of e.g. M18 (for space), since the latter is 15 times more expensive. The CFRP prepreps used are made of light fabrics (90 g/m² and 116 g/m²) made of high modulus carbon fiber balanced 50/50, TeXtreme 86 PW HS40 WD/20:4320:43-1000 fibres.

The laminator consists of two vacuum chambers, separated by a flexible membrane, which can be independently evacuated or vented to degas the laminates and perform selective stratification with adjustable pressure. In addition, this membrane, by controlling the relative chamber pressures, can exert a controlled force on the laminates during the process. The laminator is equipped with a pin lifting system to lift the laminates by pneumatic means from the heating plate before and after lamination. In the lower part of the lower chamber there is a heating plate that allows the laminates to be heated quickly and homogeneously with a maximum temperature deviation over the entire heating surface of 2°C . Finally, the cooling system allows the heat transfer oil to cool down quickly when switching from a high-temperature to a low-temperature process. Figure 5.2 shows a schematic drawing depicting the different stages of the lamination process: (1) The stack is heated under vacuum to 150°C , while initially resting on a set of pins; the gas from the still solid epoxy sheets is thus evacuated into the vacuum. (2) The pins are lowered and a pressure of about 1 atm is applied to the PV module that comes in direct contact with the heating plate, this for 20 minutes; (3) After the lamination process, the PV module is removed and allowed to cool to room temperature.

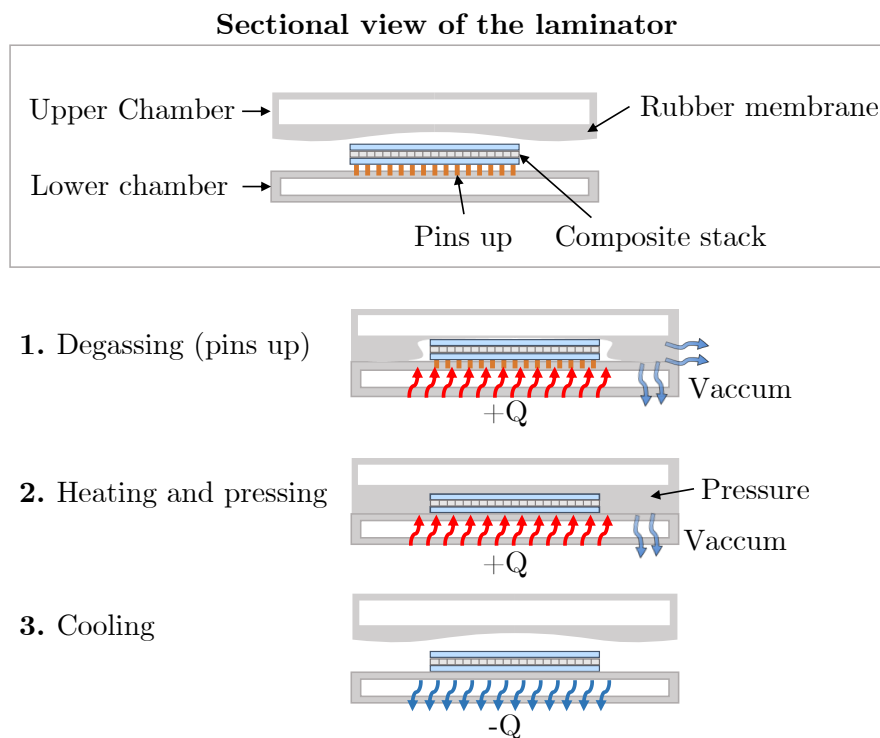


Figure 5.2: The different stages of the lamination process: (1) The stack is heated ($+Q$) under vacuum; (2) The pins are lowered and pressure is applied to the stack which comes into direct contact with the heating plate; (3) After the lamination process, the laminated is removed and allowed to cool ($-Q$) to room temperature.

The first laminations developed using the described method and configuration showed

good adhesion upon visual inspection, however the upper stage that serves as a pocket for the creation of the optics suffered significant deformations around the sample. Only 32% of the surface shows regular pockets with potential to be used for grinding optics, if the surface is divided into samples of the size of a mini-module, i.e. 8/25, as shown in the Figure 5.3.

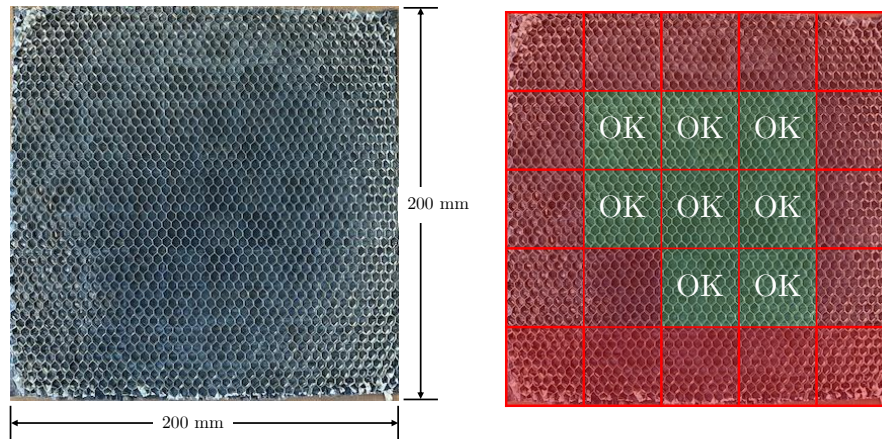


Figure 5.3: First lamination of a double-layer composite, showing in green the areas of mini-modules with regular hexagons, while in red those deformed ones not usable for molding optics inside.

To improve the number of useful mini-modules, it was proposed to use a system of fixed wedges, which would allow the upper membrane to avoid the concentration of pressure along the upper edges of the system and would also avoid the movement of the assembly during the lamination process, which is believed to be linked to the origin of the deformations. Figure 5.4 shows the process followed: (a) The stack with its different overlapping layers; (b) the wedge system at the edges, fixed using high temperature resistant tape; (c) Positioning of the top PTFE sheet and glass; (d) Previous assembly ready to enter the S3 Laminator; (e) Final laminated module, in which the total surface is usable for the creation of mini-modules.

After being laminated, the 200x200 mm² samples must be cut to generate 40x40 mm² mini-modules. For this purpose, the protocol shown in Figure 5.5 was followed:

(a) First, a protective layer was placed on the top of the module; (b) The mini-modules were sliced using a diamond wire cutter, typically used to cut silicon wafers. To ensure accurate cutting, a rotational speed of 2000 turns/min, a cutting speed of 5 mm/min and a wire tension of 1.3 bars were used, and water was used as a cooling method;

(c) Image showing the 5 transverse and longitudinal cuts to form 25 mini-modules from the 200x200 mm² samples;

(d) These were then cleaned using an ultrasonic bath for 20 min, in sweep mode, using iso-propanol to remove any residue from the cutting process;

(e) And finally dried in an oven, at 60°C for 3 min to evaporate the remaining potential

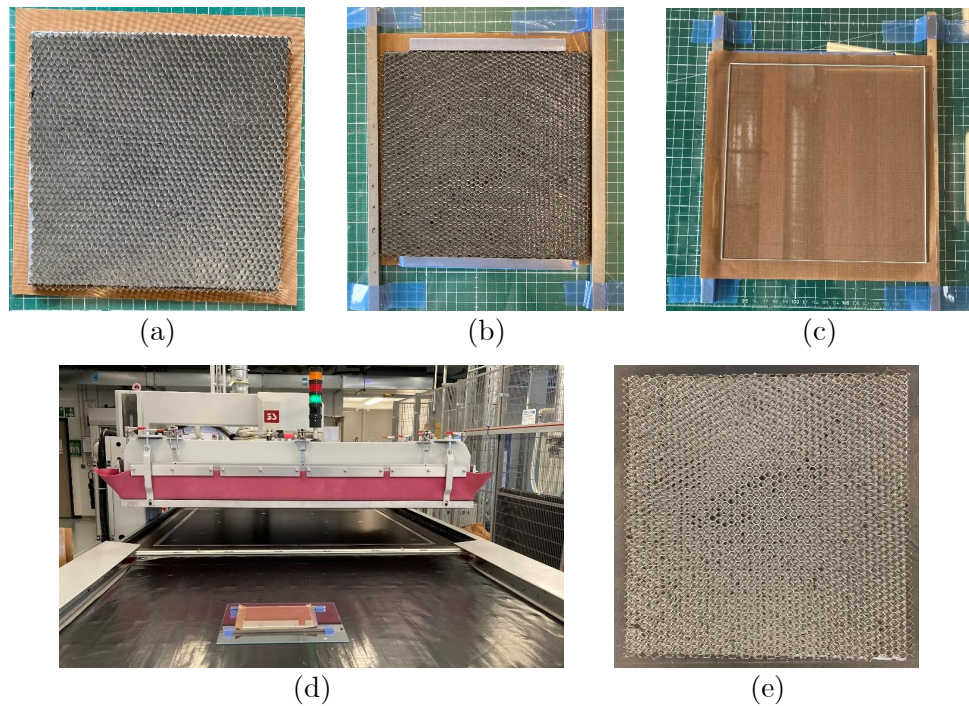


Figure 5.4: Improved lamination process: (a) Stack of composite materials; (b) Installation of wedges around the module, these are glued onto the bottom glass using a high temperature resistant tape; (c) System ready for lamination; (d) System over the laminator; (e) Laminated module.

liquids.

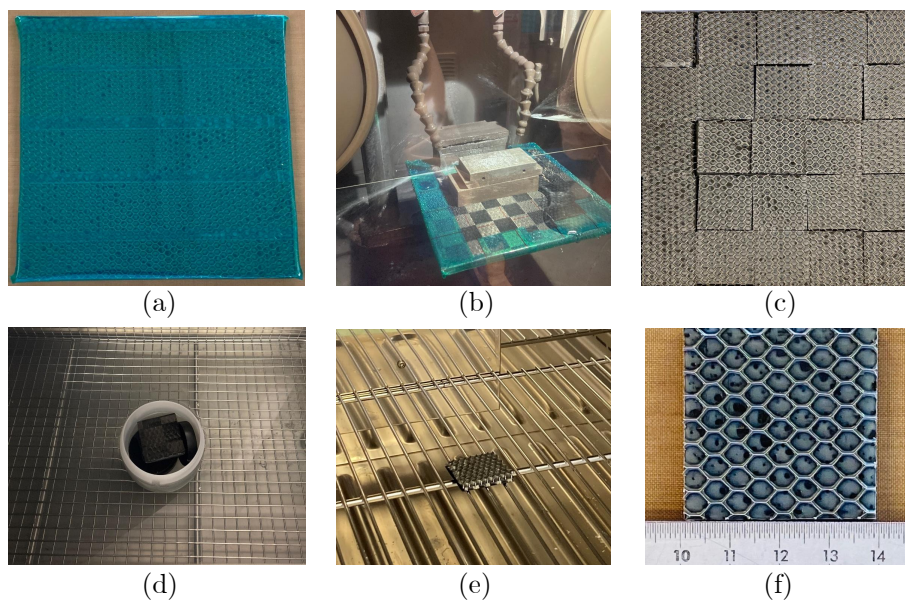


Figure 5.5: Preparation mini-module after lamination: (a) Protective tape on; (b) Cutting process of the laminated sample into mini-modules; (c) 25 mini-modules cut; (d) Cleaning of a module with ultrasound and iso-propanol; (e) Mini-module laminated and cleaned.

5.2 Molding of polymer optics

Once we have described the procedure followed to laminate the composite stack, we will describe the proposed technique for the fabrication of the parabolic reflectors molded with polymers. To do so, we will begin by describing the design, fabrication and characterization of the mold, with the objective of obtaining the dimensional and surface characteristics that will subsequently be reproduced by the optics. We will then move into the analysis to estimate the W/kg that could be achieved by the proposed micro-CPV, and we will end the chapter by presenting a synthesis and conclusions.

To fabricate the first prototypes of highly integrated mirrors in a honeycomb, using a polymer injection molding method, we used a space-grade silicone polymer, Dow Corning® (DC) 93-500, which has very low out-gassing properties (TML= 0.30%, RML= 0.28%, CVCM= 0.03%, according to the standard ECSS-Q-70-02) [328]. This silicone has been used as an adhesive for spacecraft solar cells and has been proposed for use in Fresnel lens [359], and CPC optics [343], in solar concentrator for space power applications. DC 93-500 provides robust environmental protection for modules against thermal shock and extreme temperatures (-80 to 200°C), radiation and mechanical vibration [328]. Afterwards, the injected parts are coated with a reflective film made of materials such as aluminum or silver.

5.2.1 Manufacturing process of optics inside a honeycomb structure

The process proposed in this thesis for molding optics using polymers can be divided into five stages: (1.) It starts by preparing the surfaces involved, the mold is cleaned using an ultrasonic and iso-propanol bath and dried with compressed air. While the composite stack is pre-treated to clean and improve the adhesion on surfaces using a plasma treatment (N_2) during 3 minutes and a primer coat (Dowsil™ 1200 OS) is then applied over the CFRP and aluminum honeycomb bottom walls; the latter is allowed to dry for 30-40 min at room temperature. (2.) Once the primer is dry, the polymer is injected into a confined geometry that will shape the optics; (3.) Once the molding material has been introduced, the assembly is placed in a vacuum chamber at 0.01 mbars, for at least 20 min or until all the bubbles present have been removed. (4.) The ensemble is then heated in an oven at 150°C for 10 min. Further research on the study of the crosslinking parameters (time and temperature) of the Dow Corning 93-500 silicone used during prototyping can be found as follow. (5.) Finally, the mold is extracted using compressed air and, if necessary, extraction screws.

5.2.2 Crosslinking study of polymer silicone

With the aim of understanding the crosslinking kinetics of the bi-component silicone DC 93-500 at different temperatures, and thus to establish the temperature and time relationship necessary to obtain a complete crosslinking of the silicone, eventually as an Arrhenius law, DSC (Differential Scanning Calorimeter) analysis was performed. Another important aspect that we seek to evaluate with the DSC tests is to know the handling time available for the preparation of the molding before the silicone starts to cross-link. The principle of DSC is based on measuring the heat flow, as a function of temperature, to maintain a sample and a reference (empty capsule) at the same temperature. The results are graphs called thermograms (heat flow, in W/g, as a function of temperature). This allows us to track physical phenomena in polymeric materials:

1. Endothermic phenomena: melting, T_g (glass transition temperature).
2. Exothermic phenomena: crystallization, polymerization/cross-linking reaction, degradation reaction.

The thermal crosslinking of the DC 93-500 silicone was investigated with a TA Instruments (Q2000 DSC) device available in the laboratory. The tests are performed in the temperature range from -80°C (minimum temperature achievable with the RCS refrigeration unit) to 250°C , using approximately 10 mg samples from the molten state. The rate of temperature rise/fall was $10^{\circ}\text{C}/\text{min}$.

The methodology was as follows: (1.) First we performed a temperature ramp to estimate the reaction peaks and their enthalpy over the entire temperature range (-80 to 250°C). (2.) Then, the same test was performed using the same mixture but one hour later, considered sufficient time for the preparation of the molding. On the other hand, this is intended to ensure that the same mixture can be used during different DSC tests and thus avoid uncertainty errors associated with the use of different mixtures of the bi-component silicone (i.e. 1/10 ratio between the components). (3.) Once the temperature associated with the reaction peak of the first step ramp was known, thermograms were performed with various samples at different temperatures and the time needed for an estimated 100% conversion was established. (4.) From these data (time/temperature pairs), it is intended to verify if the crosslinking cure rate follows an Arrhenius law or otherwise to determine the temperature/time combination necessary to obtain a complete crosslinking of the silicone.

Starting with the temperature ramp, three consecutive cycles were studied to evaluate potential variations between them, the result is presented in Figure 5.6. From this it can be seen that after the reaction peak centered at about 90°C , the material is stable over the entire temperature range (-80 , 250°C). The enthalpy of reaction was also calculated to be about 25 J/g.

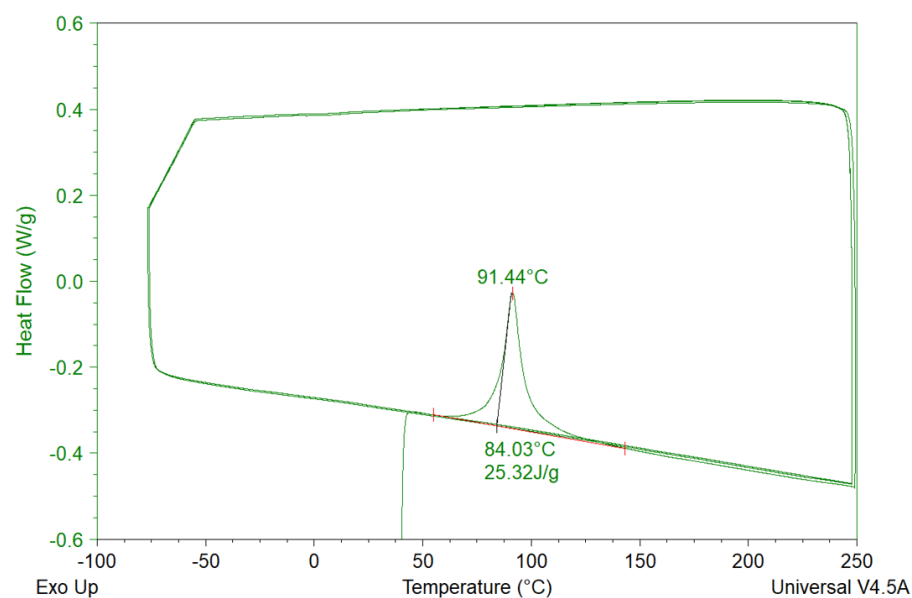


Figure 5.6: DSC test following temperature ramps between -80, 250°C, for 3 consecutive cycles, test done just after mixing the DC 93-500 silicone.

We then performed the same study but in this case one hour after mixing the two silicone components, also limiting the temperature range between 40 and 200°C since, as we had seen in the previous test, outside these limits there were no reactions in the system. The results are shown in Figure 5.7, in which the enthalpy of reaction remained around 25 J/g, confirming that the material had not evolved after one hour.

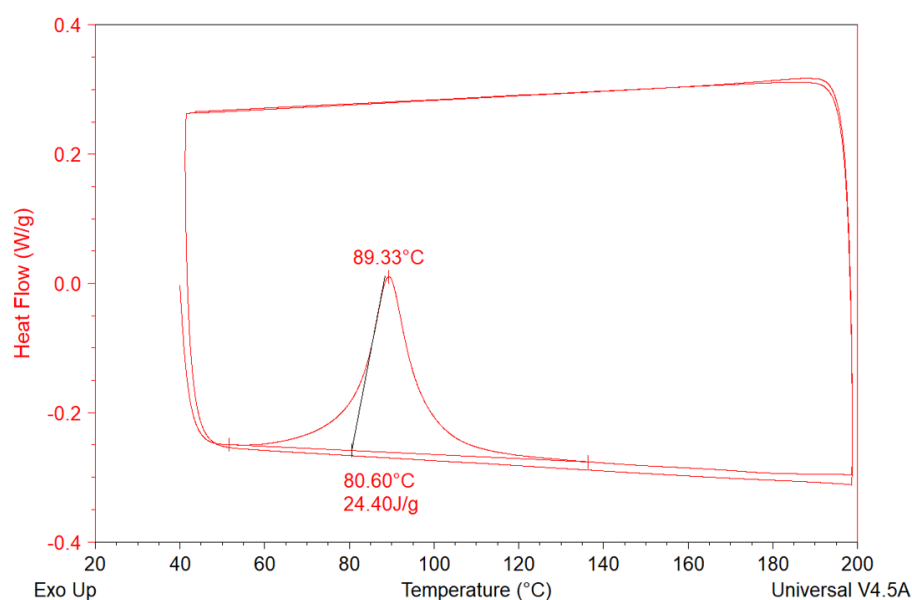


Figure 5.7: DSC test following temperature ramps between -80, 250°C, for three consecutive cycles, test done one hour after mixing the DC 93-500 silicone.

The polymerization of the mixtures from the molten state was also studied under

isothermal conditions at various temperatures (90, 130, 150 and 180°C). Figure 5.8 shows the isothermal DSC curves, showing good reproducibility of tests 2 to 2 (same isotherm temperature), slight shift at 150°C after introduction of the sample into the oven. A particular behavior is appreciated at 90°C, with high reaction enthalpy, corresponding to the maximum peak in the temperature ramp thermograms. This could be explained by a crosslinking optimum near this temperature, while on the one hand at lower temperatures the reaction takes longer to start, on the other hand at higher temperatures, the already formed three-dimensional network starts to interfere with the rest of the crosslinking reaction. For the manufacturing process of the optics, we chose to use a crosslinking temperature of 150°C, which is sufficiently high to exceed the operating temperature and thus ensure crosslinking and degassing of the components.

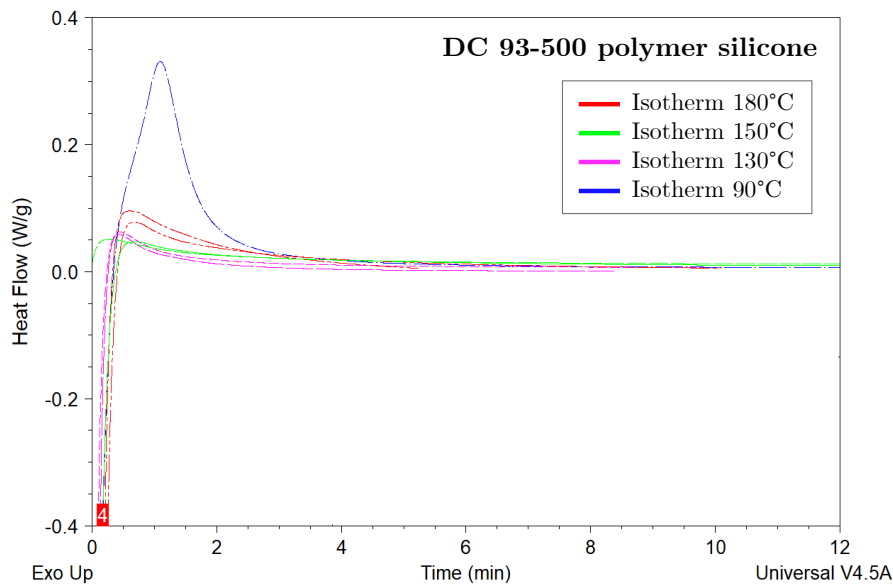


Figure 5.8: DSC test following temperature isotherms at 90, 130, 150 and 180°C, test done within one hour after mixing the DC 93-500 silicone.

5.2.3 Mold design

As mentioned in the previous section, we propose to realize 40x40 mm² mini-modules, which would be formed by 6 strings (connected in series), each of which would be confirmed by 5 cells (connected in parallel), to finally form a module of 30 units (cells/reflectors). In order to design a mold that allows the formation of parabolic surfaces inside a honeycomb network (i.e. a laminated composite structure), it is necessary to design cavities in the mold that have the same shape of the network to allow the parabolic shape to enter inside, as shown in Figure 5.9. In addition, it is necessary to take into account a mechanical tolerance t_m to make a smooth insertion, and to consider possible small variations in

the shape of the honeycomb core. On the other hand, the depth of these cavities will determine the height rim Z_R of the parabola.

Figure 5.9 (right) shows some of the relevant dimensions involved in designing the mold from a honeycomb unit. In the present design, a t_m between the edge of the honeycomb and the mold of about 0.1 mm, based on prototypes made with 3D printers; an injection hole diameter of $\phi=0.8$ mm, to allow the polymer to pass inside and limit losses in the molded reflector; and a slight fillet (r_f) on the edges of the mold hexagon of 0.25 mm was considered, to avoid friction with the hexagonal edges and for being the minimum machinable radius. Also, taking into account the optical design of the Section 4.3, which considers the truncation of a parabola with a hexagonal shape with slightly different cross-sectional lengths (x and y axis), two different heights have been formed between the base of the edge and the Z_R (of 0.93 mm). The shorter height h_1 of 1.52 mm (corresponding to the shorter length of the hexagon, y -axis) and a longer height h_2 of 1.75 mm (the longer length of the hexagon, x -axis).

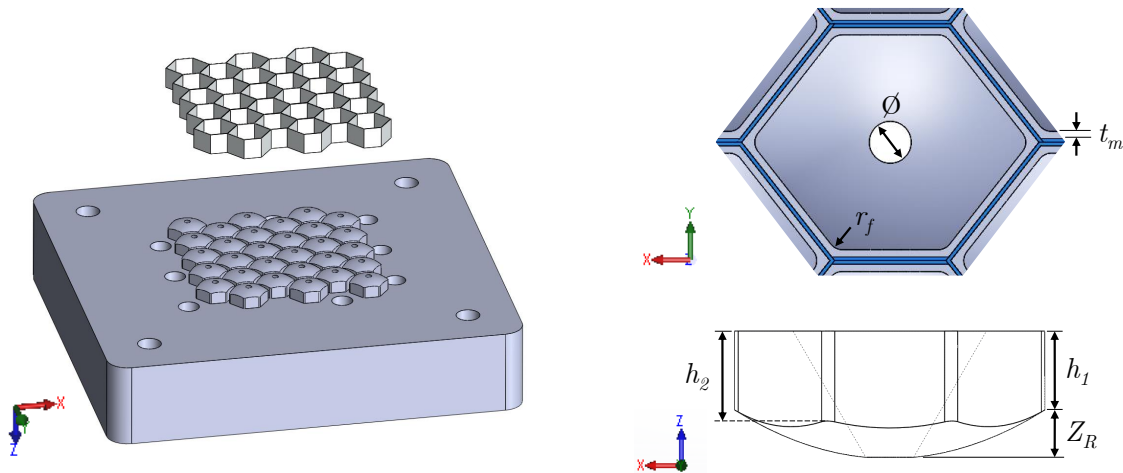


Figure 5.9: Mold design, showing close upper and frontal views of an hexagonal mold unit using the CAD software, featuring some of its dimensions: Z_R the height of the edge (or rim), the shorter and longer lengths of the hexagon h_1 and h_2 and the mechanical tolerance t_m .

Then, to ensure that the system is hermetic during polymer injection, a bottom clamping plate was designed to allow the composite structure to be attached to the mold using four mounting socket cap screws, as shown in Figure 5.10. In addition, the mold has a rectangular cavity that houses the polymer during molding, which has a height of 8 mm to contain the material when it is subjected to vacuum (i.e., which increases its volume) to extract potential bubbles. Figure 5.10 (right) shows (in blue), above one of the injection cavities and below the silicone injected into the honeycomb. On the other hand, 8 holes distributed around the network of injection cavities have been designed to demold the prototype, these must be closed using 8 sealing socket cap screws during molding.

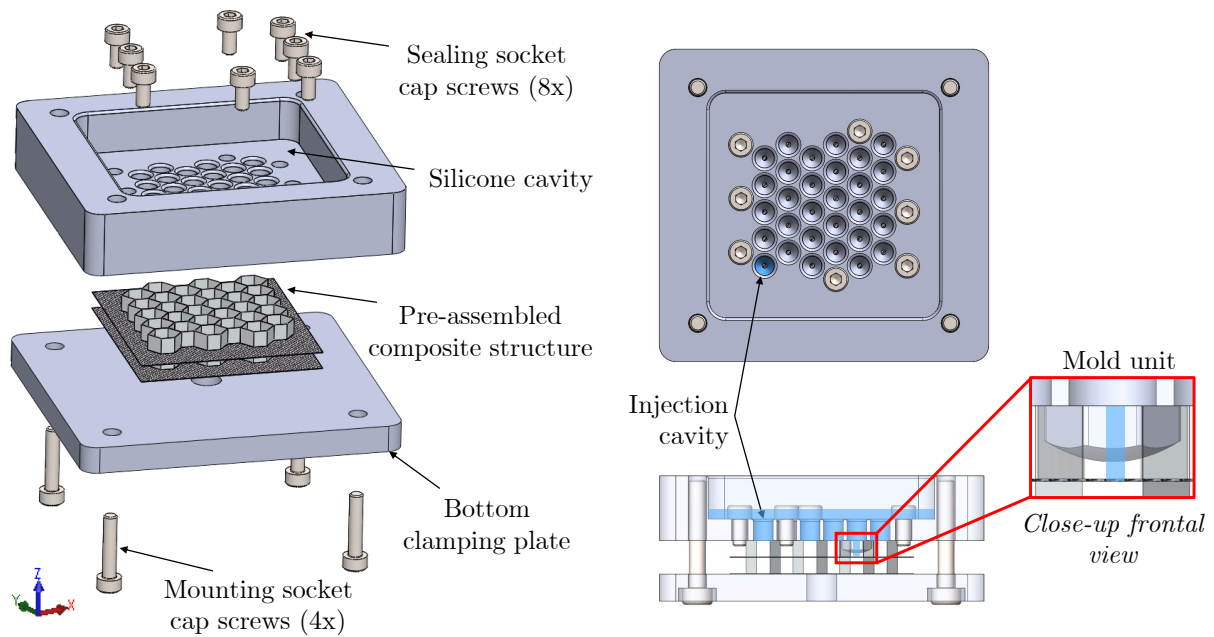


Figure 5.10: Laminated mono-module assembled in the mold, showing : a exploded view of each element used (left), the topside displaying the silicone injection channels (right above), and a close-up view of a silicone injected mold unit.

Once the cross-linking is finished and the system is at room temperature, the 8 sealing socket cap screws are removed as well as the bottom clamping plate. The latter is placed at the top of the mold as shown in Figure 5.11, in fact this plate has a double functionality, allowing to hold the assembly during molding but also provides an airtight chamber in which air pressure is injected to demold the prototype. Moreover, the 8 air injection holes (in purple) in Figure 5.11 are arranged over empty airtight cavities that allow the flow of compressed air to generate sufficient pressure to extract the assembly. Normally, the air is sufficient for extraction, however in cases where it is not effective, the 8 air injection holes can be used to insert screws and use the CFRP as a support to finish the demolding.

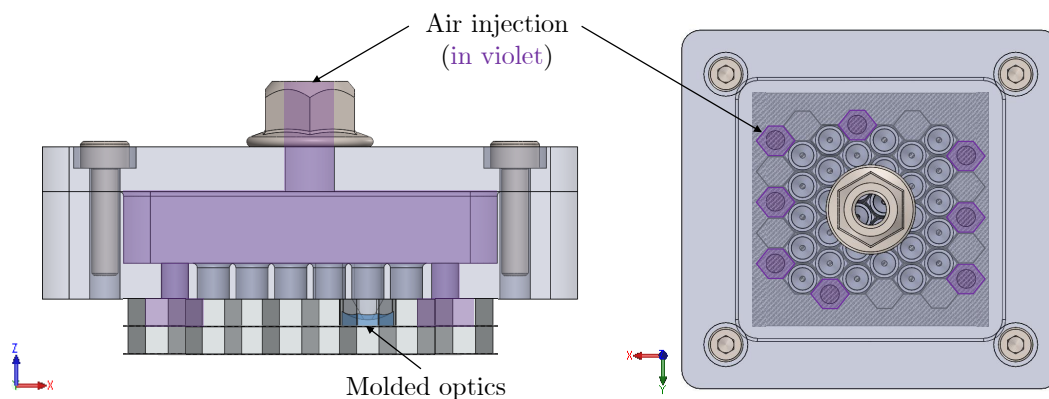


Figure 5.11: Mold design using SolidWorks.

5.2.4 Mold fabrication and characterization

After designing the different elements of the mold, we move on to its manufacture. The specifications of the mold under development include: (1.) A roughness of the parabola $Ra < 150$ nm, mirror quality, must be guaranteed. (2.) While for the rest of the surfaces this can be $Ra < 1.6$ μm , considered as a regular-good quality, knowing that the minimum roughness through ultra precision machining using CNC machines varies between 0.001 to 0.01 μm Ra . (3.) The material used is stainless steel - 1.2083 Electro-Slag-Remelting (ESR), which was chosen for its good corrosion resistance, very low inclusion content, excellent polishability in hardened condition and high surface finish. Key features for molding optical parts, including injection-molded thermosetting grades.

On the other hand, the mold fabrication process included the following steps: (1.) First, the cavities in which the honeycomb would be housed were machined by Electrical Discharge Machining (EDM). (2.) Then a CNC milling machine was used using a cutting tool with a diamond tip, more specifically a 5-axis Rödgers TEC (RXP601DSH) CNC, equipped with an air bearing spindle for better surface finish was used. (3.) Finally, the optical surfaces were hand polished afterwards to achieve the required optical quality. Figure 5.12 shows a photograph of the final manufactured mold, showing a close-up view of 7 units in which the mirror-like surface finish can be seen at a glance.

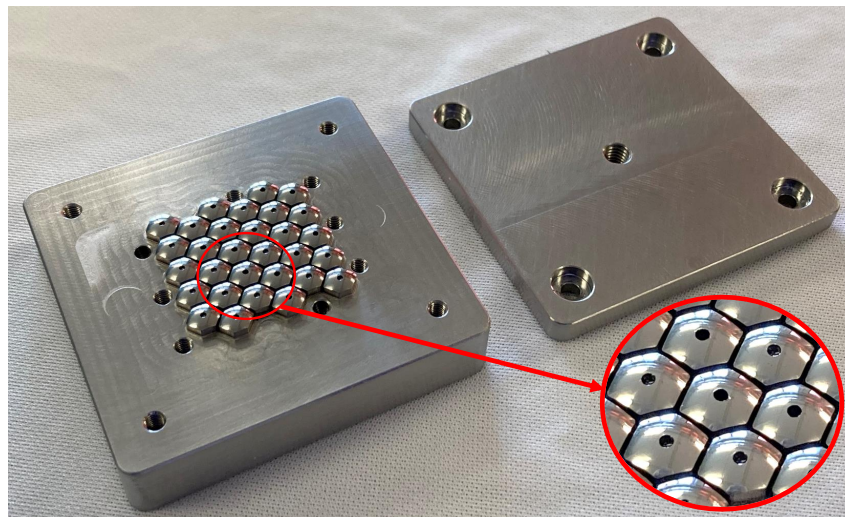


Figure 5.12: Photograph of the final manufactured mold, showing a close-up view of 7 units.

Figure 5.13 depicts the nomenclature used to identify each mold unit, from the top view of the mold where the silicone cavity is visible. For this purpose, letters from A to F have been used to define the columns and numbers from 1 to 5 for the rows.

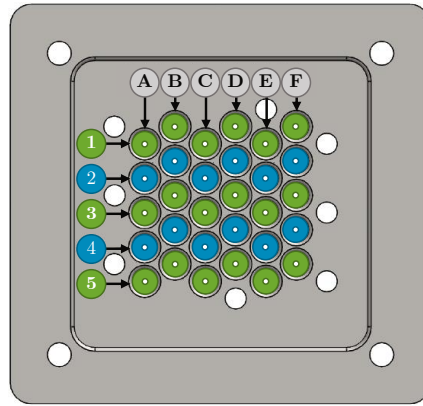
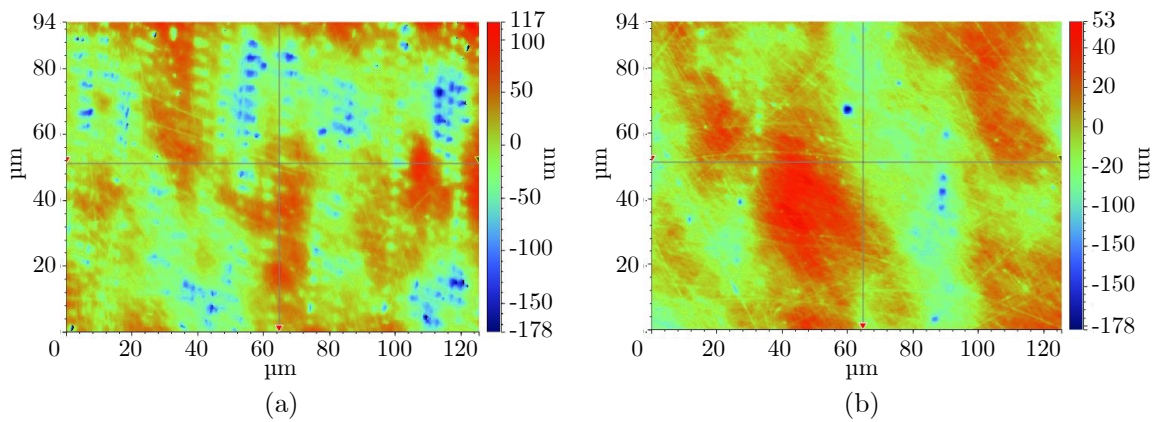


Figure 5.13: Nomenclature of the mold units.

Mold roughness

To ensure compliance with the specified requirements ($Ra < 150\text{nm}$) the manufacturer determined the polished surface finish by measuring the roughness of the mold using a Bruker Contour GT K white light interferometer. From this set of measurements (at least 6 measures), here two of them are presented in Figure 5.14.



Label	Value (a)	Value (b)	Units	Nomenclature
Sa	27.016	12.699	nm	Arithmetical mean height of the surface
Sp	116.956	53.238	nm	Maximum height of the peaks
Sq	34.099	15.863	nm	Root Mean Square (RMS) height of the surface
Sv	-177.577	-101.96	nm	Maximum height of the valleys
Sz	294.533	155.198	nm	Maximum height of the surface

Figure 5.14: Mold roughness characterization.

On the left, measurement (a) presents one of the highest roughnesses measured on the parabolas, based on the parameter Sa (arithmetic mean height of the surface) which is the extension of Ra (arithmetic mean height of a line) to a surface. It expresses, in absolute value, the difference in height of each point with respect to the arithmetic mean of the surface. This parameter is generally used to evaluate surface roughness. For (a) a

value $Sa = 27$ nm was found. On the other hand, measurement (b) displays one of the lowest roughness values obtained with a value of $Sa = 12.7$ nm. From these measurements, made at different locations on the mold, it can be seen that the roughness of the mold is in accordance with the defined specifications, i.e. $Ra < 150$ nm.

Characterization of mold dimensions

To verify the final mold dimensions, optical microscopy measurements were performed using a VHX-600 KEYENCE digital microscope. Figure 5.15 (left) shows some of the characteristic dimensions of a mold unit, while an example of a measuring unit is illustrated on the right. Each measurement was repeated at least three times on each unit to make the study reliable.

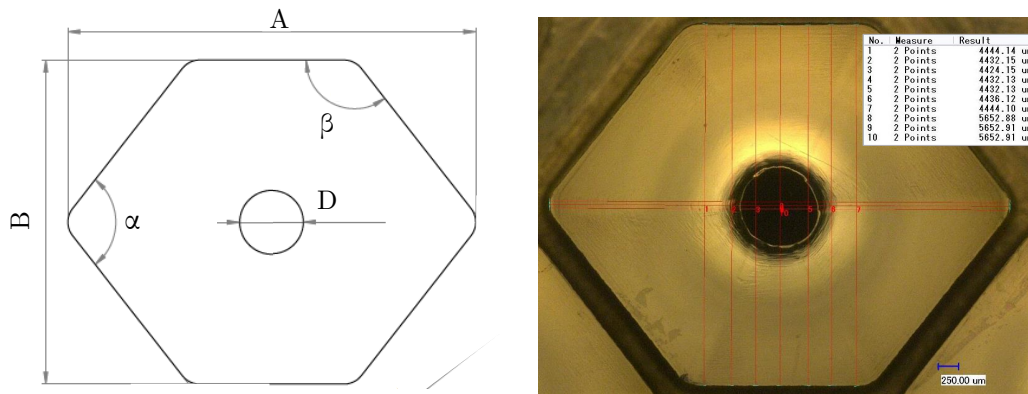


Figure 5.15: Characterization of mold dimensions

Table 5.1 shows the results obtained, indicating the design dimensions, the average measurements and their relative standard deviation and error respect to the design ideal measurements. From this it can be seen that the angular dimensions α and β are the most accurate with an associated error of about 0.3 and 0.2%, respectively. Followed by planar dimensions (B) with an error of 0.3%, while (A) is about 0.5%. Finally, the diameter (D) of the injection hole was the part with the most important error of about 20%, this is partly due to the fact that the hole does not have a well defined circular shape and during the measurements we have considered the external radius comprising the machined part. It can be concluded that the dimensions of the mold units respect the mechanical tolerance specified during design, with the exception of the injection diameter which on average is 1.2 times larger than expected.

Characterization of mold surface defects

A rather exhaustive analysis was carried out to measure the manufacturing surface defects of each of the mold units. These errors can be classified into two categories, on the

Table 5.1: Characterization of mold dimensions.

Dimensions	A (mm)	B (mm)	D (mm)	α (°)	β (°)
Ideal conception	5.50 ± 0.1	4.45 ± 0.1	0.80 ± 0.1	103.7 ± 0.5	128.1 ± 0.5
Measured average	5.47	4.44	0.96	103.4	128.4
Standard deviation	0.028	0.009	0.12	0.15	0.13
Difference (%)	-0.5	-0.3	+20.3	-0.3	-0.2

one hand permanent defects such as machining tool marks, corrosion and scratches, while on the other hand there are removable defects such as chemical contaminants such as oils, silicone, etc. An example illustrating the defect identification process for mold unit B1 is shown in Figure 5.16.

On the one hand, machining marks are remnants of the CNC machining process that have not been completely polished. These marks are mainly located on the edges of the hexagons (see Figure 5.16 (3)) where a kind of cavity is formed (i.e. intersection of the minimum height of the units), which is difficult to access during polishing.

On the other hand, the pitting corrosion seen on the edges of the units as seen in Figure 5.16 (5), is suspected to be due to the EDM technique that was used to generate the cavities where the honeycomb is housed. Indeed, the roughening EDM machining conditions (i.e. > 12 A) are related to differences in the structure and chemical composition of the white layer which affect pitting corrosion resistance, as demonstrated by Sidhom *et al* [360]. While these hypotheses must be supported by electrochemical and SEM metallographic tests, here, pitting corrosion was initially calculated separately, but will later be summed into a single metric with the permanent defects.

Finally, the scratch marks as shown in Figure 5.16 (7) are mainly related to mold handling from the time of manufacture to the moment of receipt and measurement. Once the manufacturing errors were spatially identified, the percentage of defects was calculated in relation to the effective surface of the projection on the hexagonal plane of observation, as shown in Figure 5.17. Taking into account the projected area of a unit's hexagon (i.e. the aperture area of an optical system unit), which is about 17.92 mm^2 and subtracting the area of the injection hole (0.64 mm^2) to calculate an effective surface area of 17.28 mm^2 .

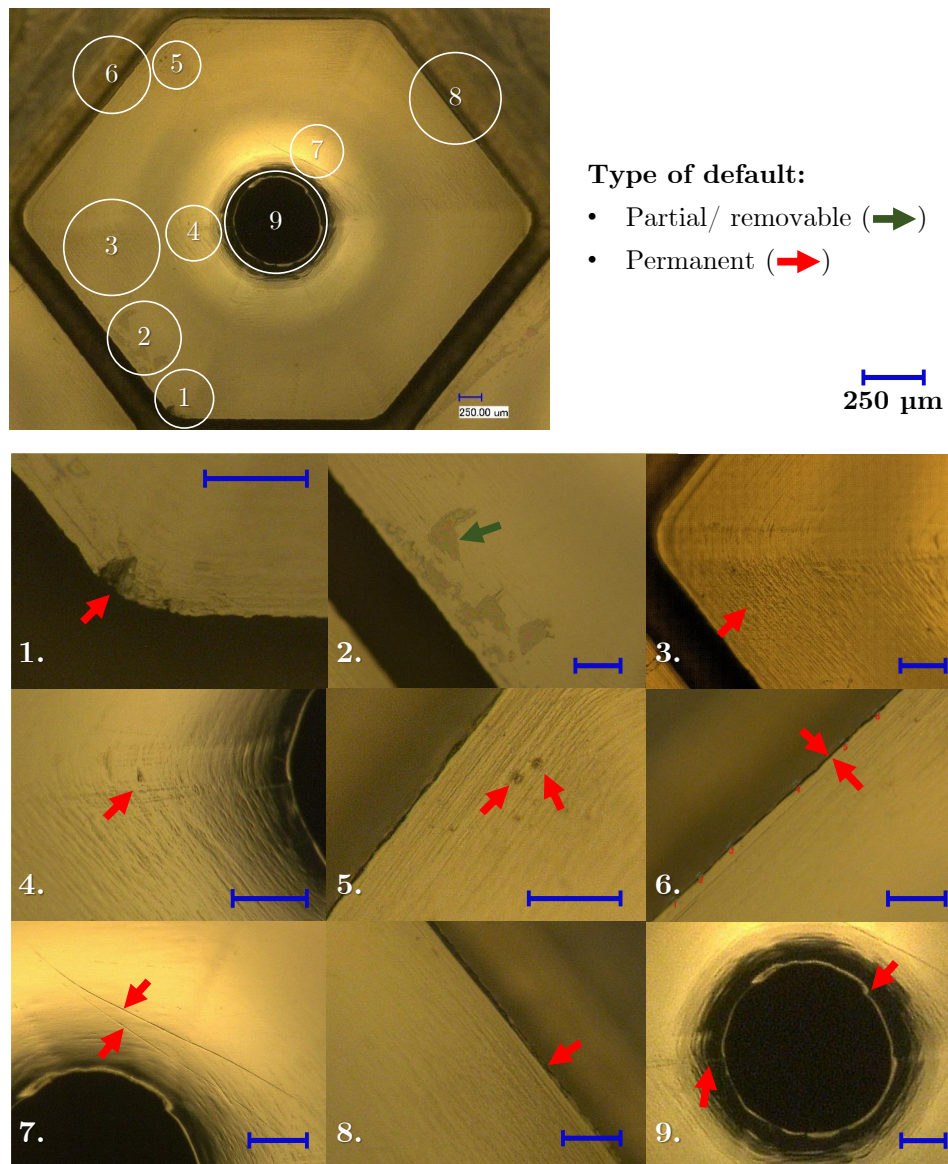


Figure 5.16: Default identification of mold unit B1 (above), and detailed view of identified defects (below); via optical microscopy.

A summary of these results is presented in Figure 5.18, in which the defects are presented in terms of surface area (mm^2) and in percentage with respect to the useful surface area to estimate the impact on the total surface area. Within the permanent defects machining tool marks are noticeable in all units defects everywhere, while mechanical scratches in two thirds of the units and corrosion-type spots in only half. It can be observed that the hexagon with the highest percentage of permanent defects (mechanical scratches + corrosion) (D4) with an equivalent of 0.3 mm^2 , i.e. 1.7%, which in the end is still relatively low. On the other hand, regarding the removable chemical compounds pollution, which are present in 36% of the mold units and are as large as 0.35 mm^2 , equivalent to about 2% of the surface.

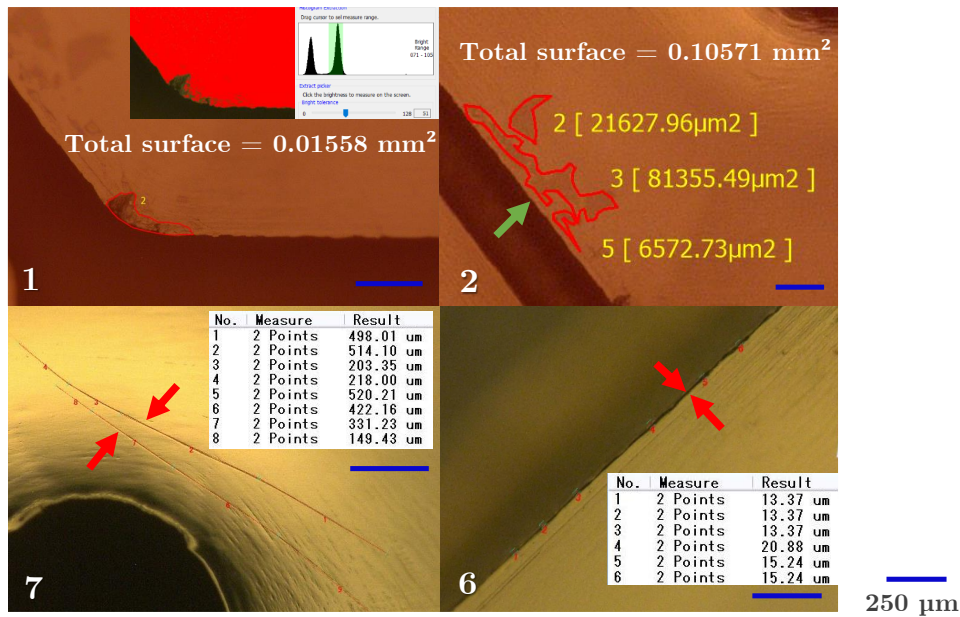


Figure 5.17: Defaults measurement of some the mold's unit B1 defaults.

Mechanical scratches							
	A	B	C	D	E	F	Units
1	0.01	0.03	0.01	0.02	0	0.08	mm ²
	0.03	0.17	0.04	0.09		0.45	%
2	0.17	0.06	0.15	0.17	0	0	mm ²
	0.99	0.33	0.84	1.01		0	%
3	0.15	0.26	0.13	0.09	0	0.114	mm ²
	0.87	1.49	0.74	0.53		0.62	%
4	0	0.01	0.11	0.11	0.05	0	mm ²
		0.05	0.63	0.62		0.26	%
5	0.29	0.15	0	0.01	0.09	0	mm ²
	1.67	0.84		0.07		0.55	%

Corrosion							
	A	B	C	D	E	F	Units
1	0	0	0.01	0.04	0.02	0.14	mm ²
			0.05	0.21		0.11	0.82
2	0	0	0.08	0.02	0	0.1	mm ²
			0.49	0.11		0.60	%
3	0	0	0.04	0.01	0.09	0	mm ²
			0.25	0.08		0.52	%
4	0	0	0.02	0.19	0.03	0	mm ²
			0.13	1.09		0.18	%
5	0.01	0	0.02	0	0.01	0.17	mm ²
	0.03		0.04			0.99	%

Permanent defaults (Mechanical scratches + Corrosion)							
	A	B	C	D	E	F	Units
1	0.01	0.03	0.02	0.05	0.02	0.22	mm ²
	0.03	0.18	0.09	0.29		0.11	1.27
2	0.17	0.06	0.23	0.19	0	0.10	mm ²
	0.99	0.34	1.33	1.12		0.60	%
3	0.15	0.26	0.17	0.11	0.09	0.11	mm ²
	0.87	1.49	0.99	0.61		0.52	0.62
4	0	0.01	0.13	0.30	0.08	0	mm ²
		0.05	0.76	1.71		0.44	%
5	0.29	0.15	0.02	0.01	0.10	0.17	mm ²
	1.70	0.84	0.13	0.07		0.59	0.99

Removable chemical compounds pollution							
	A	B	C	D	E	F	Units
1	0.19	0.11	0.06	0	0.1	0	mm ²
	1.13	0.63	0.37			0.60	%
2	0	0.07	0.18	0.07	0.06	0.08	mm ²
		0.40	1.02			0.41	0.35
3	0	0.35	0.27	0.05	0	0.08	mm ²
		2.04	1.57			0.28	0.46
4	0.03	0.03	0.12	0	0.08	0.15	mm ²
	0.16	0.15	0.69			0.49	0.86
5	0	0	0.1	0	0.14	0.06	mm ²
			0.59			0.83	0.38

Figure 5.18: Mold defaults measurement maps.

5.3 Synthesis and conclusions

In this chapter, we focused on the fabrication method of the integrated optics, in order to move from a theoretical concept to a prototype with industrial potential. This process can be divided into three main stages, (1.) Fabrication of the composite structure; (2.) Formation of the optics; (3.) Metallization of the reflective surface. In the prototyping phase, our objective was to validate the concept with mini-modules of about $40 \times 40 \text{ mm}^2$, i.e. half of a space solar cell.

In this respect, the dual-stage composite lamination method has been improved to maximize the usable surface area, up to its totality, avoiding shape deformations of the stack. On the other hand, the crosslinking of the polymeric silicone was studied in the molding of optics to establish the temperature and time ratio necessary to obtain a complete crosslinking by means of a DSC analysis. It was observed that at 90°C the silicone has a high reaction enthalpy, which corresponds to the maximum peak in the temperature ramp thermograms. This could be explained by a crosslinking optimum (minimum) near this temperature.

Finally, a mold was designed and manufactured to cast 30 units of parabolic reflectors. This was then characterized, starting with roughness and dimensional analysis. Then going through an identification and measurement of the permanent and removable surface errors of each unit, it was observed that the maximum attained surface defects is about 1.7% and 2%, respectively.

Once characterized, the mold was used for prototyping, as can be seen in Figure 5.19, showing the prototyping of the structure and optics of a 30-unit module, illustrating: a) molding process, then, b) molded optics, and finally, c) the module with silver reflective coating.

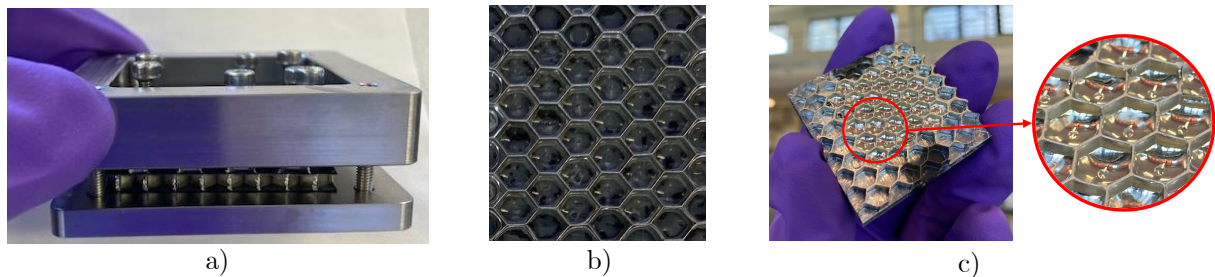


Figure 5.19: Prototyping of a 30-unit module ($40 \times 40 \text{ mm}^2$ enclosure): a) Molding process, b) Molded optics, c) Module with reflective silver coating

In complement to this experimental validation, the following chapter will present a method of characterizing the parabolic surface topography of both the mold and prototypes to estimate the achievable optical performance.

*At the sight of a single bone, of a single piece of bone,
I recognize and reconstruct the portion of the whole
from which it would have been taken. The whole
being to which this fragment belonged appears in my
mind's eye.*

— Geoffroy Saint-Hilaire

6

Optical efficiency estimation via topographical characterization by optical microscopy and ray-tracing

The optical quality of reflective surfaces is an issue of great importance in CPV systems, for both, terrestrial and space applications. Deviations of the optical shapes from their nominal geometry, theoretically perfect, together with irregularities of the optical interfaces, can lead to substantial energy losses in the form of radiation leakage. This is a particularly critical challenge, due to the large dimensions of the panels. The errors associated with the parabolic surface can be sorted into two types: random and non-random [361]. Random errors are truly random in nature, such as: apparent changes in the width of the Sun and scattering effects associated with the optical material used in the reflector. Non-random errors, deterministic in nature, may have a somewhat greater impact on the degradation of parabolic shape performance [362]. They represent gross errors in fabrication/assembly and/or operation, including: errors in reflector profile and misalignment of the receiver with the effective optics focus.

Deviations from the ideal performance are called CPV optical errors, these optical errors have different contributions. Several authors have defined an optical error, which is in fact a lumped parameter that results from different contributions. It is then possible to define the optical error (σ_{opt}), as the addition of several errors in quadrature [361, 363]:

$$\sigma_{opt}^2 = \sigma_{spec}^2 + \sigma_{shape}^2 + \sigma_{canting}^2 \quad (6.1)$$

where σ_{spec} is the specularity error, defined as the standard deviation of the characteristic scattering function of reflectors. The other two contributions, σ_{shape} and $\sigma_{canting}$, for shape and canting errors, respectively, are describe as a single parameter called, σ_{slope} ($\sigma_{slope}^2 = \sigma_{shape}^2 + \sigma_{canting}^2$). These optical errors are illustrated in Figure 6.1: a) Surface scattering produced by surface roughness at the micro- and meso-scale. b) Divergence from the nominal geometry. c) Misalignment between optics and photovoltaic receivers. All of them result in a non-nominal deflection of the reflected beam d).

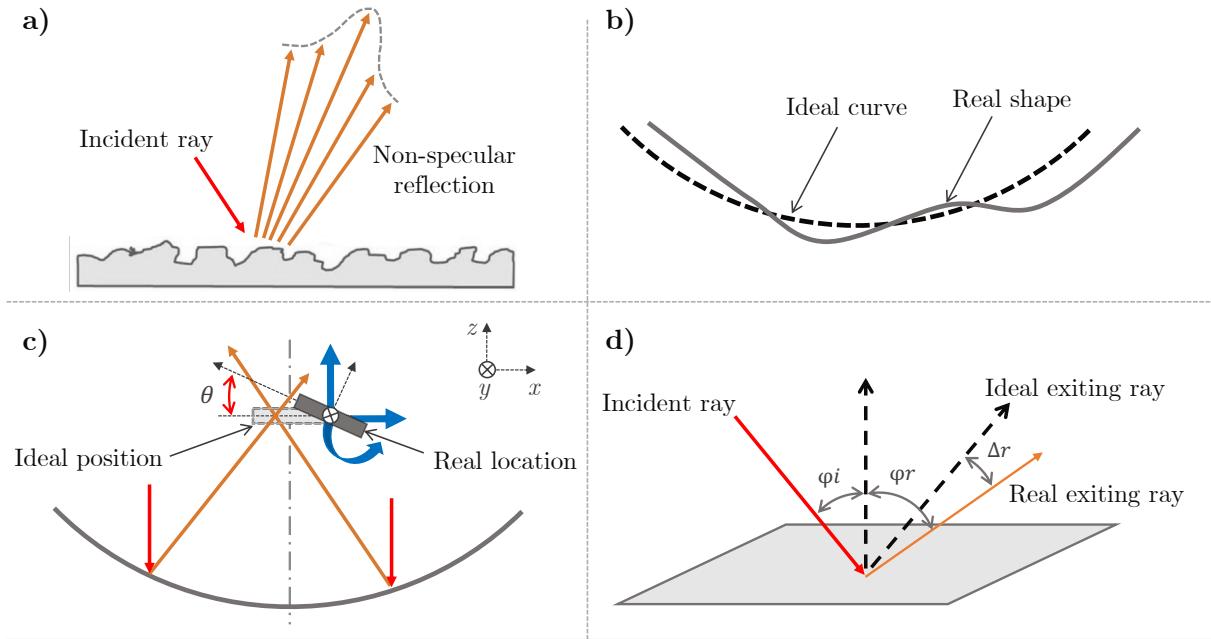


Figure 6.1: Concentrating mirror features causing deviations from ideal reflection: a) Surface roughness; b) Shape errors; c) Elements misalignment; d) Resulting reflected ray deviation.

In order to validate the proposed micro-CPV, highly integrated in a honeycomb, we aim to concentrate on the non-random errors to concentrate on the shape error (σ_{slope}) and quantify the manufacturing defects of the optics compared to the ideal surfaces from the optical design; thus estimating the losses of the real optics compared to simulations. In this chapter we present a characterization method developed to estimate the optical efficiency of a molded reflector by evaluating its topographical shape through optical microscopy measurements combined with ray-tracing simulations. We will start by exposing the characterization of the proposed method which uses a self-evaporating scanning coating to enhance the contrast of the measured surfaces. We are then interested in characterizing the shape of both the mold and the fabricated optics, which is divided into two main parts. First, a recognition of the quadratic shape described by the measured point cloud will be made using a least-squares fit. And second, we made a reconstruction of the shape, which was then used in the estimation of the optical efficiency using ray-tracing. Finally, a correlation analysis between recognition and shape reconstruction is presented.

6.1 Surface topography measurement of optics based on a non-contact technique

For over a century, optical methods have played an essential role in the dimension measurement [364, 365]. These optical measurements have been of dimension, form, surface topography, and even sub-surface damage [366]. The surface quality of an optical component is an evaluation of the surface imperfections, such as scratches and pits, or digs, which may be caused during the manufacturing or handling process. Arancibia-Bulnes *et al.* carried out a complete review of the different techniques that have been developed for the optical characterization of solar concentrating mirrors; they proposed a classification of the techniques based on their underlying principles and common features [363].

Hocken *et al.* investigate a wide variety of instruments that are used for measuring surface topography via optical techniques [365]. These devices can be classified into 14 different categories, ranging from optical profilers, microscopy systems, grazing incidence methods, interferometry methods (burke), holographic methods, speckle methods, confocal microscopy and others. In this study, we are interested in measuring the topography of millimeter-scale optics using an optical profiler. This non-contact technique has been chosen because of the small size of the optics, techniques based on microscopy are well suitable to the acquisition of short-range 3D measurements. While other techniques such as mechanical surface profilometry (i.e., contact type) are not adapted because the surfaces are too curved and too small in size.

The optical 3D shape reconstruction by optical microscopy is a kind of widespread cost-effective technique using optical images as a means of detection and transmitting information. It possesses the advantages of large range, high-speed, high precision (i.e., with sub-micrometer resolution), as well as great system flexibility. In this work, surface analysis and 3D topography mapping were performed using a VHX-600 Keyence digital profiler [367]; which uses a camera with high image resolution (1600 x 1200 on a 13" thin film transistor) and accuracy in micron range. Fixed with a movable control stage, this unit allows for easy navigation as well as image stitching abilities, +/- 90 degrees for oblique imaging. Two magnification lenses could be used (20x-200x) and (100x-1000x). The process of imaging is based on a Depth-From-Defocus (DFD) technique, used to estimate the depth in the scene based on the difference of defocuses in at least 2 images captured at different focal positions, illustrated in Figure 6.2, showing how layers are compiled to provide a 3D image.

Microscopic 3D scanning can be adapted to the measurement and inspection of contoured surfaces and complex geometries. However, there are some limitations, mainly related to the properties of light and its behavior at the measured interface that need to be addressed. In fact, scanned parts have specific requirements depending on the nature of

the material, surface quality, dimensions and arrangement of the elements. Thus, a method for characterizing surface morphologies must take into account all these parameters to ensure accurate and high quality measurements.

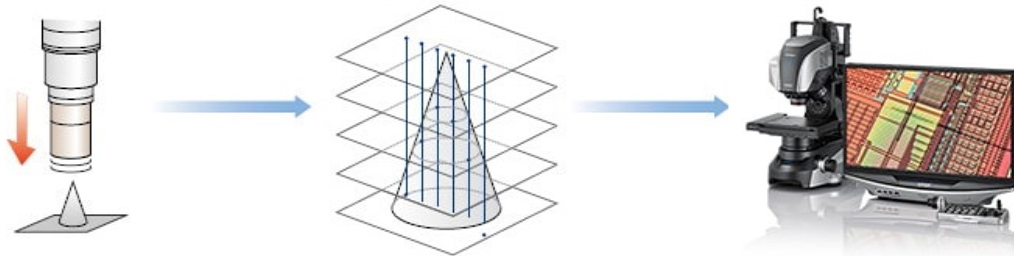


Figure 6.2: Image formation using an optical microscope, where each of the focus layers are compiled to provide 3D image; picture of the device used at right [367].

On the one hand, since we are recording an inclined surface and most of the reflected rays do not enter the microscope, we would have to work with very open objectives in the dark field.

In addition, as we are interested in measuring an optical system after molding, it would have the transparent aspect of the polymer used (as in the case of lenses), so light provided by a lamp in the visible range will pass through the surface instead of reflecting off it. Consequently, for transparent optics in this wavelength range this technique does not work and the scanner cannot correctly capture the surface structure, as shown in Figure 6.3 a) and c). Moreover, in the case where the parts have been coated with a reflective layer, the light beams will be reflected in a focused rather than diffuse manner. This means that the chance of a light beam hitting the scanner reflector is greatly reduced and the scanner will only pick up a fraction of the reflected light beams. In fact, areas with glare cannot provide the level of color contrast information that would help distinguish between a focused or unfocused pixel. Moreover, in the case of focused optics, the light will be concentrated in a small spot, making 3D surface reconstruction impossible, see Figure 6.3 b) and d).

Once we have seen that optical microscopy is not suitable for measuring specularly reflective and transparent surfaces, we have been interested in looking for alternatives to make the surfaces diffuse so that the measurements can be made in such a way that the focal plane corresponds to the surface to be measured for each z -step. In this case, the difficulty lies in finding suitable materials to carry out this deposition. For this we have considered the following criteria:

- i)* The material should be easy to deposit and form a layer that fits the surface.
- ii)* The layer formed must be uniform over the surface, and the roughness must be negligible compared to the shape.
- iii)* The material should be easy to remove and should not leave any residue.

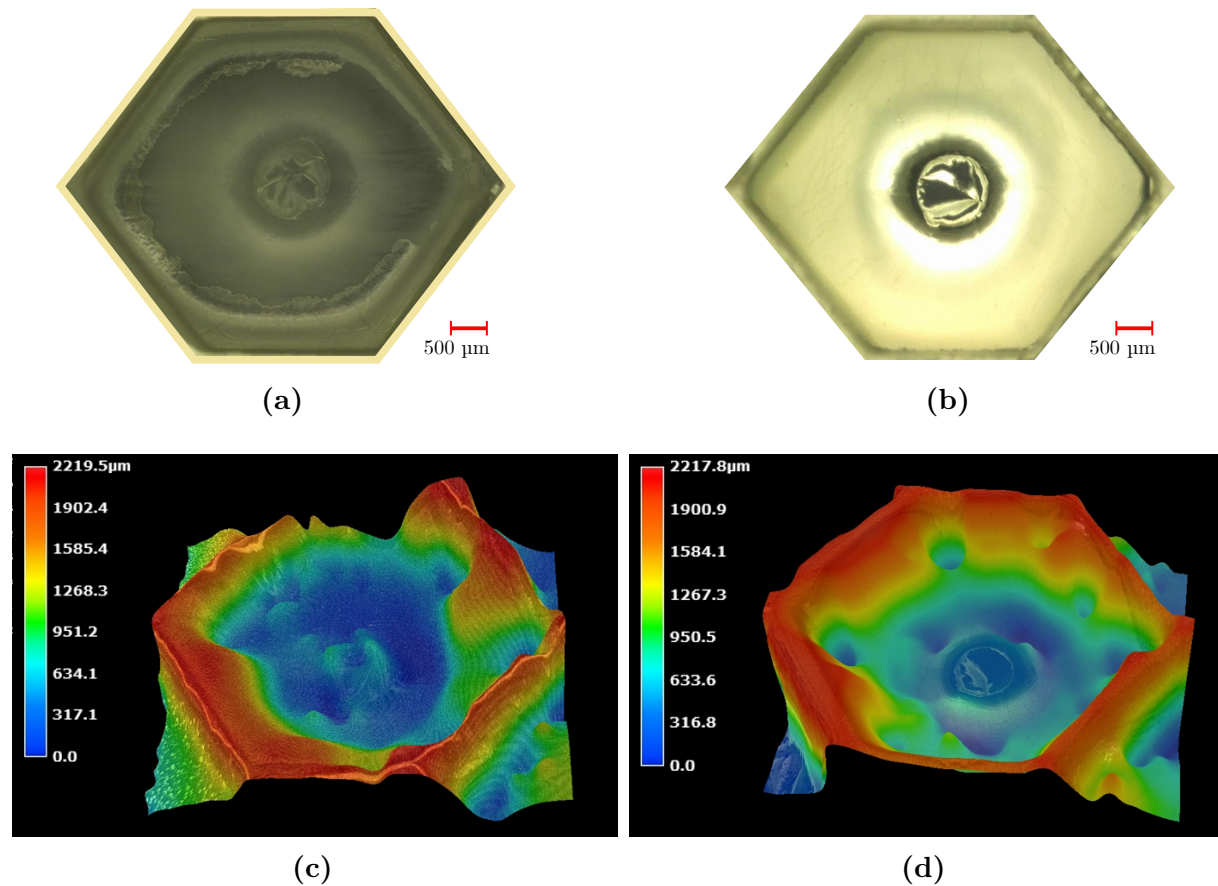


Figure 6.3: Measurements of molded optics showing the lack of contrast of topographic measurements using optical microscopy: (a) and (c) transparent optical unit, before applying a reflective coating; (b) and (d) silver coated optics.

In general, matting coatings used in 3D metrology for contrast enhancement can be classified into the following two groups. First, semi-permanent sprays for which the measurement surface remains white after scanning and needs to be cleaned or removed from the scanned object. Second, evanescent sprays for which the coating evaporates automatically, no cleaning is necessary after scanning and there is no pigment contamination from laboratories, sensors, environments, scanners and users.

This work presents an original approach to overcome the instrumental limitation in generating contrast of measured optical surfaces. More specifically, we propose the use of an AESUB® blue scanning spray [368], a self-fading coating intended to evaporate in a few hours without leaving residues, which means that it is not necessary to clean it after scanning. Although the exact composition of the coating is not communicated, it has 67.36% solvent content, 0% solids and 32.64% propellant content. According to the datasheet, the coating is applied "wet", at a distance of 15 to 20 cm and the recommended ambient temperature is 21°C. The solvent fades in a few seconds while the coating remains on the surface. The degree of whiteness of the coating continues to increase for a couple of seconds.

Furthermore, the manufacturer claims that the thickness of an opaque layer is 8-15 μm , depending on the user's specific application. Therefore, before using the coating, some preliminary measurements were made to qualify and validate the method in terms of accuracy in relation to the parabolic surface to be measured, and to find the adequate working conditions, as presented below.

6.2 Qualification of the application parameters of a matting coating for surface measurements

In order to qualify the use a self-evaporating scanning spray for contrast enhancement of optical microscopy measurements, a series of analyses have been carried out. To do this, the deposition method must first be refined by optimizing the thickness. The layer must be thick enough to cover the entire surface, but not too thick as to mask the surface defects we are trying to characterize. In addition, since the deposit sublimates, the variation linked to material loss should not affect the measurement. Finally, it is also necessary to characterize the roughness of the coating itself as a function of thickness, to verify that it is low compared to the defects of the surface we aim to characterize.

We first present thickness measurements and covered surface as a function of the number of layers deposited. Then, the roughness measurements, and finally the sublimation of the covered surface as a function of time, under the illumination of the microscope during the surface characterization will be presented. For these tests, portions of a polished mono-crystalline silicon wafer, chosen for its low roughness, were used as a reference sample.

Once the coating has been applied, the sampling process to measure the topography of a sample by optical microscopy is carried out as follows: (1.) The acquisition parameters, minimum height Z_{min} (i.e. the lower part of the optics or the wafer in the method characterization), and maximum height Z_{max} corresponding to the maximum height of the feature being measured, are defined using a microscope magnification of 1000X; with the objective of focusing a small area on the Z reference points as precisely as possible. Then we define the number of images in which it is desired to divide the gap between Z_{min} and Z_{max} , this can vary between 1 and 50, with an associated resolution of $(Z_{min}/Z_{max})/50$. (2.) The microscope makes a compilation and automatic recording of the digital images in 3D to be processed in the VHX program. (3.) It must be verified that the reference points have been well chosen and that the registration topography has not been cut off by a choice of Z -heights too small (i.e. a completely flat top and/or bottom surface). If the latter occurs, the procedure must be restarted.

6.2.1 Coating over-thickness and surface area covered vs. number of layers applied.

Measurements have been made to experimentally qualify the evolution of the layer thickness of an AESUB® blue spray for a given number of spray cycles. For this purpose, silicon samples of about 15x15 mm² were prepared, which were partially coated with Kapton tape to generate a step-up effect between the deposited coating and the wafer. The sample preparation process was as follows (1.) Cleaning of the silicon wafer surface with isopropanol; (2.) Drying with compressed air; (3.) Masking with Kapton tape; (4.) Matting of the surface; (5.) Removal of the tape. Figure 6.7 illustrates: (a) Three polished monocrystalline silicon wafer samples (about 15x15 mm²) which have been cut using a diamond tip; (b) Optical microscope image (at 200X magnification), of the masking of a silicon wafer with Kapton tape; (c) Optical microscope image (at 200X magnification) of a coated sample, dark side (right) for the matte coating and bright side (left) of the silicon surface.

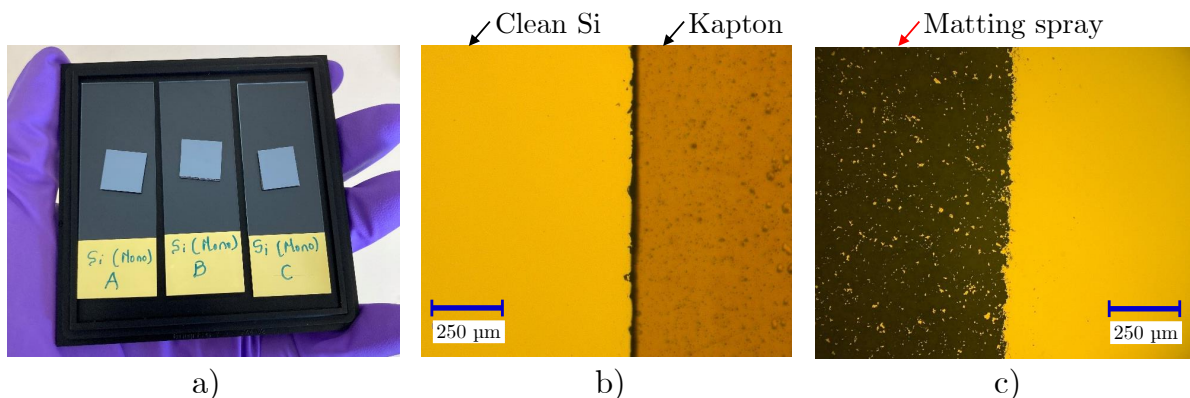


Figure 6.4: Image of: a) Three polished monocrystalline silicon wafer samples (about 15x15 mm²); b) Silicone wafer masking using Kapton tape; c) A coated sample, dark-side for the matte coating and bright-side silicon surface.

Once the coating has been applied and the sampling process finished, as described above, the thickness of the coating is measured using a tool (from the microscope program) that allows to determine the profile by means of lines drawn on the top view of the 3D image. Figure 6.5 shows examples of these measurements for 3, 8 and 13 spray coats applied, a), b), c), respectively. On the left is shown a top view of the coating and in red the location of the profile being measured, while on the right are the measured profiles where the distance A-B represents the thickness of the coating. For these measurements, a lens power of 100X was employed, and a total of 30 images were recorded to reconstruct each profile. During the deposition and measuring, the room temperature was 22°C ± 2°C. For the thinnest thickness shown in Figure 6.5, i.e. 3 layers, some black spots can be observed in the deposit, which suggests that not all the surface is covered and that the minimum

thickness to cover the whole surface has not been reached, which in turn introduces an important roughness in the coating, these two characteristics were characterized as follows.

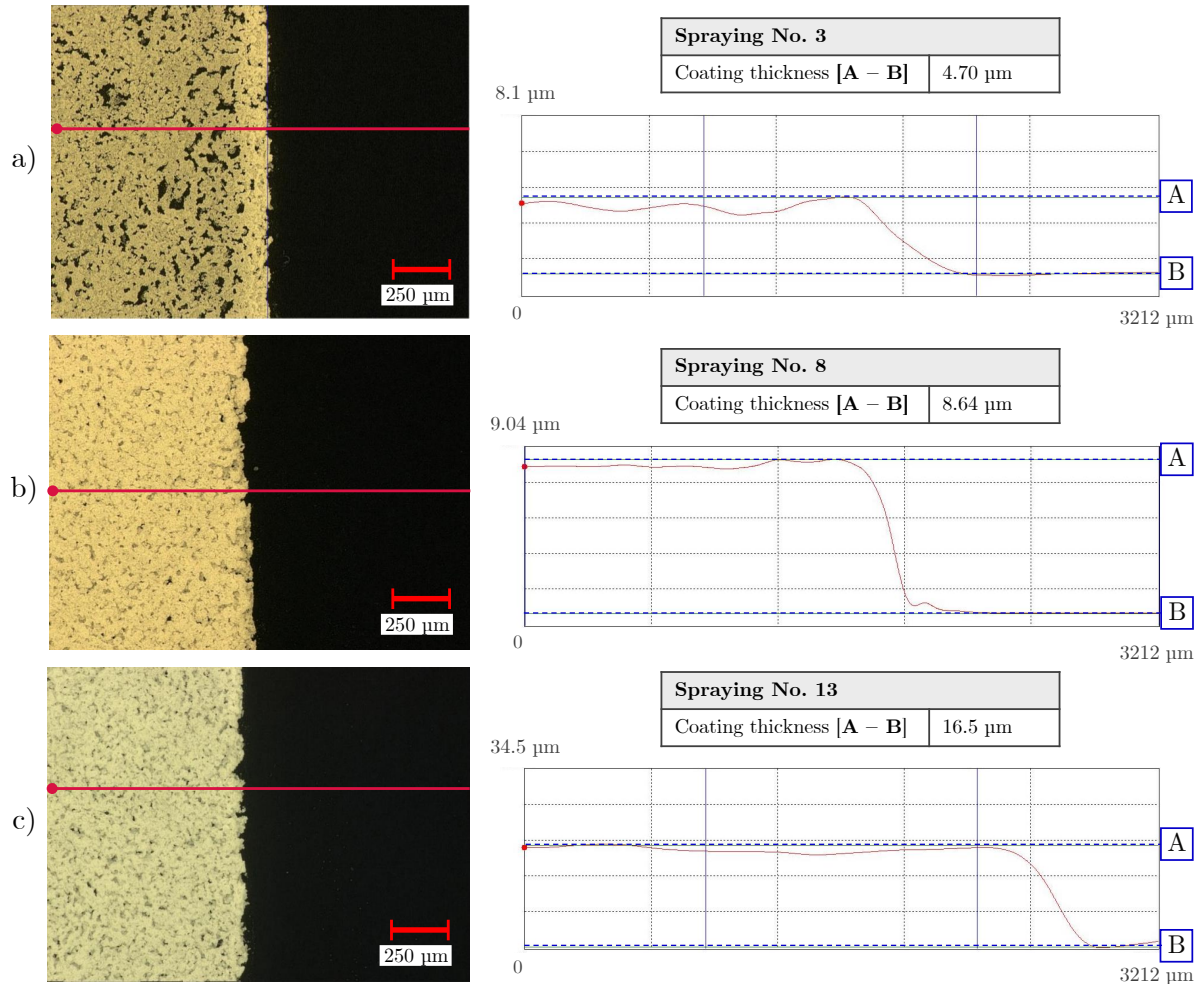


Figure 6.5: Cross-sectional microstructures of the deposited coating on silicon wafer showing the thickness evolution as a function of layers number, coating in clear color, while silicon in black. Deposition and measuring temperature of 25°C. All images have the same magnification (100X).

Next, we were interested in studying the evolution of the percentage of covered surface with respect to the number of spray layers applied. For this purpose, high resolution images (1600 x 1200 pixels minimum) were recorded by microscopy and then analyzed with ImageJ software [369], this procedure was performed at least three times for each number of spray cycles from 1 to 13 cycles. The measurement protocol that will be described below provides an example of how to measure the percentage of clear areas on an uncovered (black) silicon wafer. The images do not need to be calibrated since a percentage is being considered. The white areas are estimated using an intensity threshold. This methodology is shown in Figure 6.6 using for one of the cases in which a spray coating was applied. The procedure was as follows: (a) After having taken the image using the optical microscope, it is imported into ImageJ; (b) It is then converted to gray-scale (8-bit),

to transform the color information of each pixel into a measure of brightness (i.e., varying between 0 and 255); c) Next, the Image Threshold is adjusted, which allows highlighting the pixels of an image that have values within a chosen range, so that the light and low value pixels representing the applied spray become red, but those representing the silicon do not change. In this regard, the silicon wafer is represented by a pixel value from 0 to 74, so the same threshold range has been used for all images (pixel value) from 75 to 255; d) Finally, the latter is converted into a binary image, to then estimate the percentage of area covered with spray (black), with respect to the white one representing the silicon wafer. In this particular case of a measurement after the application of one spray cycle, a coverage percentage of 41.6% was measured.

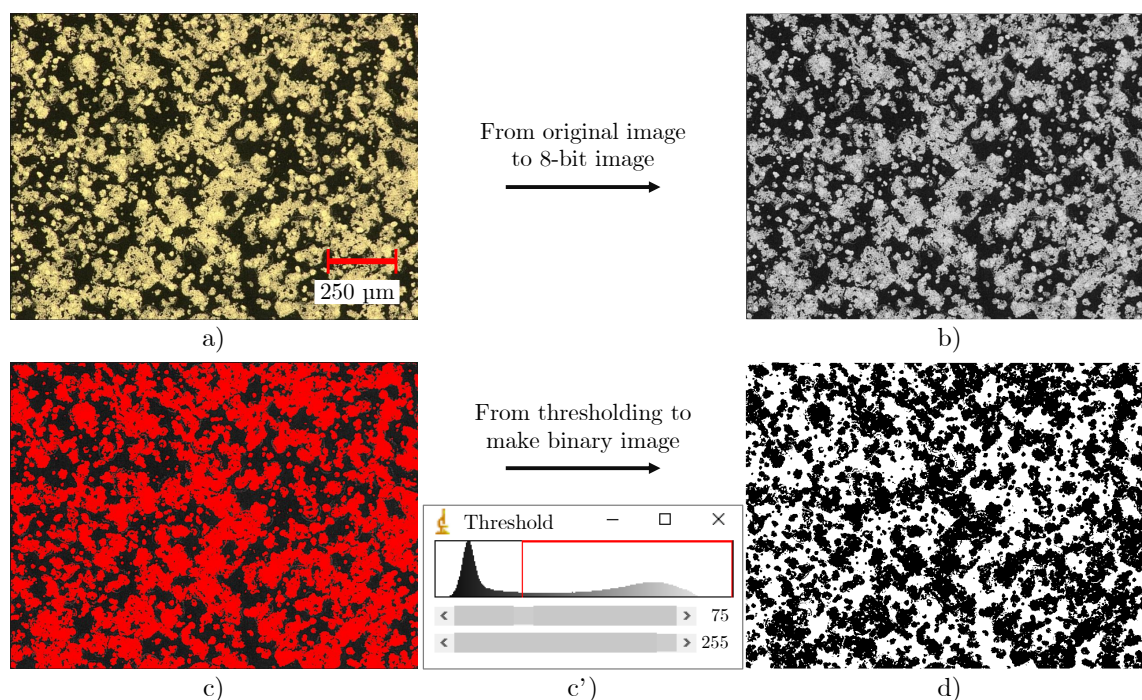


Figure 6.6: Image analysis steps for quantification of the spray coverage area: a) Original image; b) Grayscale image; c) Contour detection by adjusting the threshold; d) Extraction of both surfaces: substrate (white) and spray (black).

Figure 6.7 presents the results of the series of tests carried out on the silicon wafer, applying different layers (cycles) of spray, between 1 and 13; while the data used are compiled in the Annex I. On the one hand, it can be seen that the coating thickness starts at about 1.6 μm ($2\sigma = 0.3 \mu\text{m}$) with a filled surface of about 43% ($2\sigma = 3.1\%$) and evolves monotonically to a maximum thickness of 17 μm ($2\sigma = 0.8 \mu\text{m}$) for a quasi-total coverage, i.e., 99.8% ($2\sigma = 0.1\%$). The average thickness of each spray cycle (i.e. thickness/number of cycles) was also calculated and it was observed that each layer generates on average 1.2 μm of over-thickness. While the reproducibility of this technique, in the thickness measurement, an average standard deviation (i.e. between 1 and 13 coats

applied) of $2\sigma = 0.6 \mu\text{m}$ was observed.

Furthermore, the progression of the covered surface area starts to stagnate from 7 to 9 cycles, with area coverage from 95% ($2\sigma = 1.2\%$) to 96.4% ($2\sigma = 1.5\%$), and thicknesses from $7.6 \mu\text{m}$ ($2\sigma = 0.5 \mu\text{m}$) to $9.5 \mu\text{m}$ ($2\sigma = 0.7 \mu\text{m}$), respectively. Here, with the aim of implementing a method that maximizes the covered surface for the smallest possible thickness (i.e., to measure the shape as accurately as possible), we have adopted the use of 8 spray cycles equivalent to a covered surface of more than 96.5% ($2\sigma = 0.8\%$) and a thickness of $8.8 \mu\text{m}$ ($2\sigma = 0.25 \mu\text{m}$).

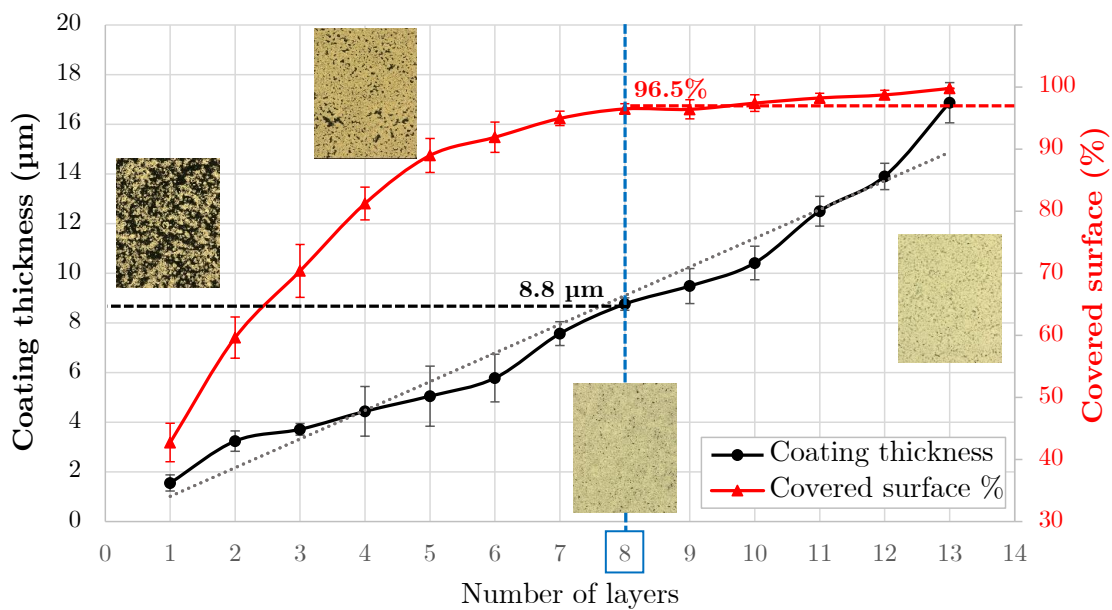


Figure 6.7: Evolution of layer thickness and surface area covered for different number of layers.

6.2.2 Roughness evolution relative of layers number

Other investigations include the study of how the roughness of the applied coating evolves as a function of the number of layers. Firstly, to validate that the deposit does not cause an error in the measurement of the optical surface. In addition, this analysis must allow us to know if the roughness generated by the deposit is low enough to be able to characterize surface defects, shape defects or both. These topography measurements were performed using the polished silicon wafer samples used in this study (as a reference for their low roughness) with matting coating applied.

The first step was then to determine the surface roughness of the bare silicon wafer samples. For this purpose, the Bruker Dektak XT Profilometer described in Chapter 4 was used. Once the roughness of the silicon wafer has been established, we investigate the evolution of the topography with respect to the number of layers of the coating. For

this purpose, 3D images of the top surface of the coating were taken using the Keyence VHX-600 digital microscope described above, with a 1000X magnification lens. In the description of the method presented here, we have considered as a parameter of comparison the maximum height of the measured profiles (equivalent to the Rz), i.e. the absolute vertical distance between the maximum height of the profile peak and the maximum depth of the profile valley along the sampling length, taken as the extreme case since this is the maximum roughness of the coating. We have also considered the root mean square deviation (Rq), which represents the root mean square of $Z(x)$ within the sampling length.

Table 6.1 illustrates the parameters used, from the scan resolution and length, to stylus type. As well as the ISO 4287 filtering type, and cutoffs used λ_c and λ_s , which respectively denote the long and short wave cutoffs.

Table 6.1: Roughness measurement parameters.

Profilometric Measurement Chart		Evaluation Processing and Filtering	
Sample	Silicon wafer #4	Standard	ISO 4287
Profile	Hills & Valleys	Filter Type	Gaussian Regression
Scan Duration	120 s	Short Cutoff (λ_s)	0.8 μm
Scan Length	480 μm	Long Cutoff (λ_c)	80 μm
Scan Resolution	0.0133326 μm	Number Lengths	5
Scan Type	Standard Scan		
Stylus Force	1.44 mg		
Stylus Scan Range	6.5 μm		
Stylus Type	Radius: 2 μm		

Figure 6.8 shows the roughness profile of a measurement, while Table 6.2 describes the amplitude parameters for the measured roughness according to the standard, both for a single measurement (Silicon wafer #4) and the average of 6 different measurements. From this we can see that for the measurement of Silicon wafer #4, a Root-Mean-Square (RMS) roughness (Rq) of 0.7 nm was obtained, while the average was a slightly lower 0.48 nm. On the other hand, it was observed that the maximum height of the profile (Rz), referred to as the maximum roughness (i.e. $Rz = Rp + Rv$), see nomenclature in Figure 6.2, were 4.5 and 3.58 nm, for the measurement of Silicon wafer #4 and the average, respectively.

Once we have characterized the silicon wafer and validated the substrates as references of planarity, with a roughness in the order of nanometers ($Ra < 5$ nm), we have characterized the roughness of the applied deposition various numbers of layers by optical microscopy. It is pertinent to note that the roughness measured with a profilometer is not comparable to the roughness given by a microscope since the spatial frequency range is different. From a top-of-sample perspective, at least 6 horizontal measurements were performed using 4 samples for each number of layers, consisting of three applications of the coating and

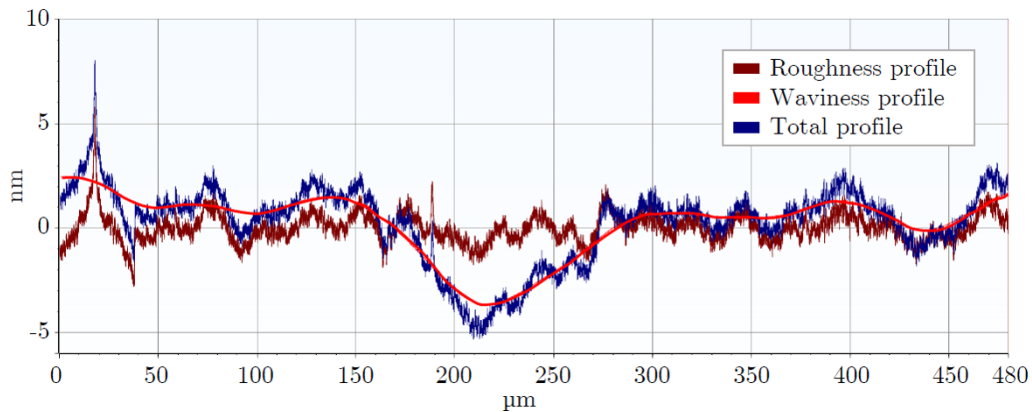


Figure 6.8: Silicon roughness, waviness and total measured profile of one test.

two measurements per application. Figure 6.9 shows three of the measured coatings, considering 3, 8 and 13 layers.

Table 6.2: Silicon roughness results.

Amplitude parameters – Roughness profile (ISO 4287)				
Label/Measure	Units	Value (Silicon wafer #4)	Average (6 meas.)	Description
Ra	nm	0.5	0.48	Arithmetic mean deviation of the assessed profile
Rq	nm	0.7	0.60	Root Mean Square (RMS) deviation of the assessed profile
Rz	nm	4.5	3.58	Maximum height of the profile

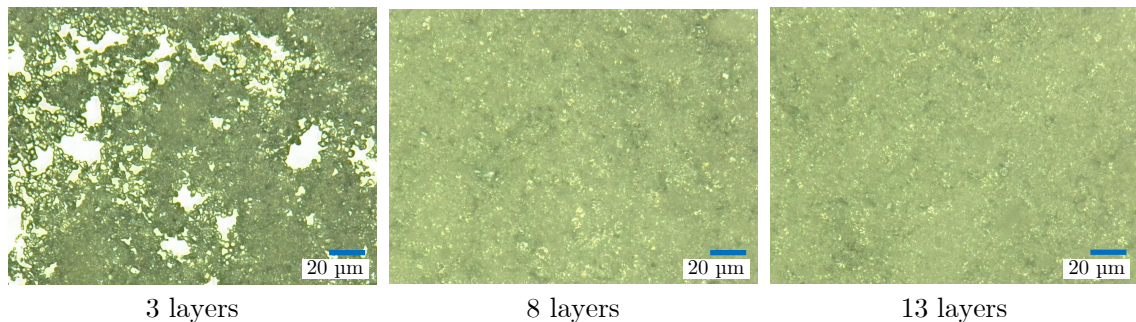


Figure 6.9: Applied spray layers equivalent roughness results.

An example of the measured roughness for each number of layers is shown in Figure 6.10, for which the maximum roughness (Rq) measured in the test campaign is shown. While Table 6.3 presents the maximum (i.e. profiles of Figure 6.10) and average roughness values of the profiles, including the roughness Rq (or RMS), Rz (max. height), the resolution along x and z , and the sampling length. From this it can be observed that the maximum measured Rq roughness decreases monolithically as the number of layers increases, varying from 3400 nm for 3 layers to 1400 nm with 8 layers (i.e. 59% less), to finally 1200 nm (i.e. 14% with respect to the previous one). Then considering the mean values for Rq , it

starts at 3100 nm for 3 layers, and then decreases to 1100 and 700 nm for 8 and 13 layers (i.e. 65% and 34% less), respectively. This allowed us to quantify the standard deviation of the coating height distribution. This is one of the most commonly used parameters as it facilitates statistical handling and allows us to obtain stable results, since it is not significantly influenced by scratches, contamination and measurement noise.

On the other hand, if we consider the average Ra roughness of the coatings, we see that it starts at 1200 nm for 3 layers and decreases by 67% when 8 layers are applied, i.e. to 400 nm. While for 13 layers it is 300 nm, i.e. a decrease of 25% with respect to the 8 layers. Like the Rq , the Ra is used because it provides stable results, without significant influences due to measurement artifacts. It allows us to measure the mean of the average height difference for the average coating surface.

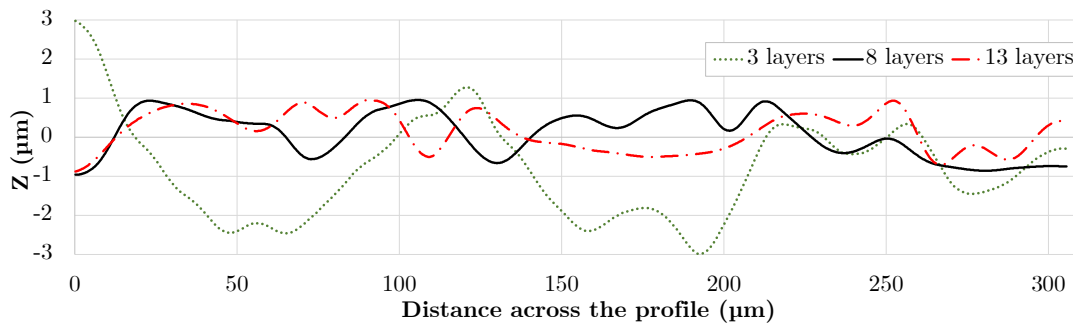


Figure 6.10: Applied spray layers equivalent roughness results.

Table 6.3: Roughness results for different number of layers applied (3, 8 and 13) measured by optical microscopy.

Roughness profile & parameters										
Label/ Measure	Units	3 layers			8 layers			13 layers		
		Highest value	Average	2σ	Highest value	Average	2σ	Highest value	Average	2σ
Rq	nm	3400	3100	700	1400	1100	600	1200	700	900
Ra	nm	1300	1200	200	500	400	200	500	300	500
Rz	nm	5900	4500	1900	1900	1700	500	1800	1100	1300
Resolution-z	nm	100			40			20		
Resolution-x	nm	190								
Sampling length	µm	305.6								

Finally, we see that the roughness Rz of the profiles starts at 4500 nm and decreases to 1700 and 1100 nm from 3 to 13 layers (i.e. a decrease of 62% and 36%), respectively. Although frequently used, the maximum height can be influenced by scratches, contamination and measurement noise because it is based on maximum values. However, it allows us to quantify the maximum measurement deviation, in the form of noise, if we consider that the silicon wafer is well polished and has been cleaned prior to deposition.

6.2.3 Temporal evolution of the surface coating during sublimation

The scanning aerosol used (AESUB® blue) is a self-fading aerosol intended to evaporate in a few hours without leaving residues, and therefore the sublimation time of the components must be taken into account during measurements to ensure reliable measurements. This evaporation time may depend on several factors, as described in Table 6.4.

Table 6.4: Coating scanning-time evolution for different materials.

Parameter	Impact
Temperature	<ul style="list-style-type: none"> ▪ High: shorten sublimation time. ▪ Low: extend sublimation time, even above 4h possible as described by the manufacturer.
Layer thickness	<ul style="list-style-type: none"> ▪ Higher layer thickness extends sublimation time.
Substrate surface structure	<ul style="list-style-type: none"> ▪ Features such as pockets, holes or grooves within the surface structure extend sublimation time.
Material/substrate	<ul style="list-style-type: none"> ▪ Sublimation time also depends on the material.
Airflow ventilation	<ul style="list-style-type: none"> ▪ Shortens sublimation time.

Here we will concentrate on studying the evaporation evolution for three different materials planar architectures, including silicon wafer (about 0.75 mm thick), DC 93-500 silicone (1.2 mm thick) and DC 93-500 silicone on a CFRP substrate (1.2 mm and 0.3 mm thick, respectively). The latter being the structure and materials foreseen for the optics developed in this work. For the sublimation measurements the samples were kept in the same place and we focused on evaluating the evolution of the coverage over the edge of the silicon sample, since preliminary tests showed that sublimation takes place mostly in this area. In this respect, the surface of interest of the substrate has been delimited before treatment. In addition, the planar structures were compared with a molded optics in order to study how the sublimation rate changes when a pocket structure, such as the final optics, is considered.

In this first estimation, the average ambient temperature measured was about 22°C, during the measurements. Nevertheless, the temperature at the sample surface is expected to increase slightly, since the illumination system of the KEYENCE microscope focuses light on a small area; however, the latter has not been taken into account. Similarly, it has been considered that the ventilation in the measuring room remains constant and therefore its effect is negligible. On the other hand, the thickness of the coating used was approximately 8.8 μm ($2\sigma = 0.8 \mu\text{m}$) equivalent to applying 8 layers of spray, considered to be the optimum compromise between filled surface and thickness. The results obtained are shown in Figure 6.11, they include a time evolution starting just after the spray is applied

until 50 minutes later, with a step of every 10 minutes. In this respect, the time elapsing between the application of the deposit and the first image, about 15 seconds, is considered minimal with respect to the total measurement time and is therefore disregarded.

These results were then used to estimate the surface sublimation with respect to the uncovered surface of the substrates, using the image analysis described previously, via ImageJ. Figure 6.12 presents the analysis results, from which it can be seen how the percentage of uncovered surface evolves with time. In addition, a horizontal line (in red) representing 10% sublimation has been drawn, which we will assume here to be the maximum acceptable for accurate measurements. It can be seen that the most important coating sublimation rate is for the DC 93-500 silicone, followed by the silicon wafer and the DC 93-500 silicone on CFRP which have a similar behavior, guaranteeing 90% of the coated surface with respect to the initial one up to 27 minutes.

It could also be seen that in the case of an integrated molded optical unit, the sublimation rate was the lowest. It was observed that this structure after 50 minutes still retains about 97% of the coated surface, see Figure 6.12. This is believed to be due to two main phenomena, on the one hand the pocket effect attenuates the ventilation rate on the surface, while on the other hand the potential thermal gradients generated by the microscope light source are dissipated by conduction thanks to the aluminum honeycomb.

6.2.4 Analysis and conclusions of method qualification

We have qualified the coating method, in which it could be observed that using 8 layers of the spray an optimum compromise between the covered surface and the generated overthickness 96.5% and a thickness of 8.8 μm , respectively, was achieved. Regarding the reproducibility of this technique, in the thickness measurement, an average standard deviation (i.e. between 1 and 13 coats applied) of $2\sigma = 0.6 \mu\text{m}$ was observed, while for the case of 8 coats this was $2\sigma = 0.25 \mu\text{m}$.

In addition, the applied coating induces an increase in roughness, which tends to attenuate as the number of layers increases. Based on the 8 applied layers, the measured root mean square roughness (Rq or the noise equivalent) is 1100 nm with a maximum peak to peak roughness (Rz or the maximal deviation) of 1700 nm. Furthermore, it was shown that the maximum time to perform the measurement and guarantee the 90% of the covered surface depends both on the materials used and their structure. For example, considering flat structures and 8 spray layers, a maximum measurement time of less than 15 minutes was observed for a substrate made only of silicone, whereas if a silicon substrate, or a silicone on CFRP substrate is considered, this increases to close to 30 min.

On the other hand, it was observed that if the structure and materials of the developing optics, i.e. a pocket structure, and silicon on CFRP surrounded by an aluminum honeycomb

6.2. Qualification of the application parameters of a matting coating for surface measurements

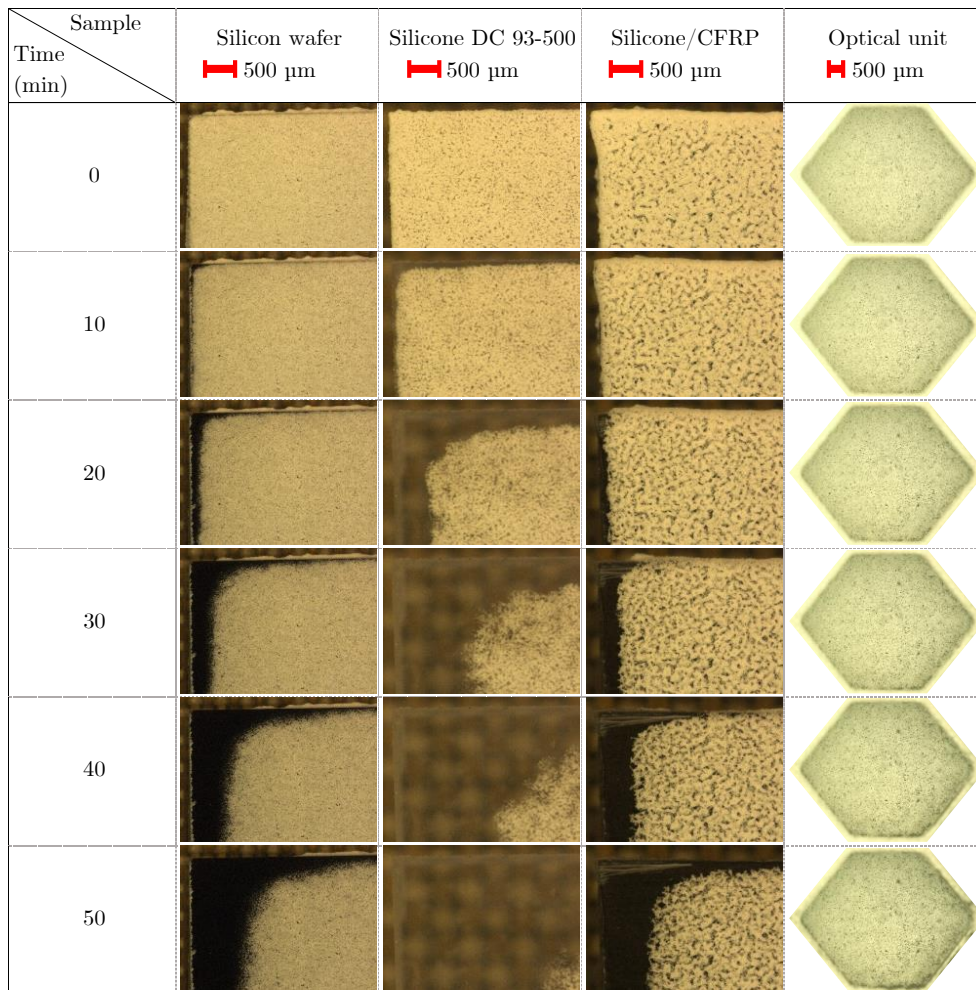


Figure 6.11: Coating scanning-time evolution for different materials, for 8 layers.

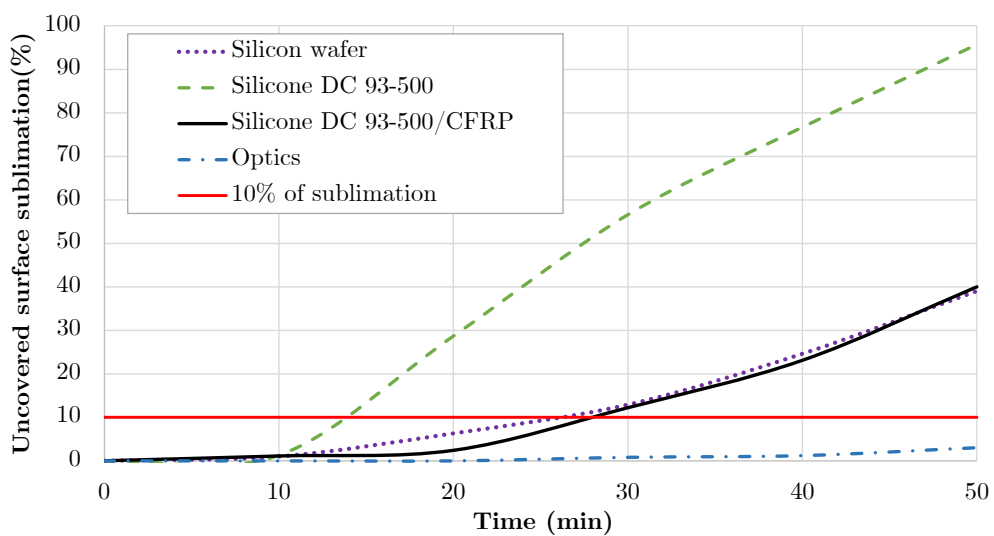


Figure 6.12: Coating scanning-time evolution for different materials.

are used (and 8 layers of spray), the coated surface (> 90% of the total) can be preserved up to more than two hours after application. However, even knowing the latter, it was decided to set a maximum measurement time of 30 min on the fabricated optical units in order to reduce the risk of local sublimation and to guarantee a homogeneous coating. The latter is sufficient for a topographic measurement using the optical microscope, which takes up to 3 min, i.e. 10 times less than the defined maximum time.

Moreover, during the application of the coating used, it is difficult to guarantee the homogeneity of the deposit with the currently employed method, which relies on an aerosol spray for which the application distance and direction can be variable from one layer to the other. The latter is even more crucial when there is a pocket effect in the measured device, since some zones can be shaded at the time of application depending on the angle of inclination.

Finally, there are some limitations of the measuring device used, mainly related to light behavior at the interface of the measured surface, as determined by the reflectivity of the surface, the roughness and the numerical aperture of the lens. These can generate local signal loss and generate for example a maximum detectable slope, resulting in a limited detection providing a poor characterization of the surface.

6.3 Recognition, reconstruction and analysis of measured surfaces

Once we have passed the first phase, which consisted of a qualification of the characterization method, we move on to the next stages in the estimation of the optical efficiency of molded optics. We characterize the surface by an optical method, from which we extract and use the reconstructed topography by means of a point cloud as output data. First, we are interested in making a recognition of the quadratic shape described by the measured point cloud by means of a least-squares fit, with the aim of identifying potential deviations of the assessed surface. Secondly, we want to be able to reconstruct from this point cloud a surface as representative as possible of the real measured surface, and to estimate the error of this reconstruction. This reconstruction is then used in the estimation of the optical efficiency by ray tracing. Finally, a correlation analysis between the obtained measurements (recognition and reconstruction) and the designed nominal shape is proposed.

For data processing we use the open source software CloudCompare [370], dedicated to editing and processing 3D point clouds (and triangular meshes), in order to compare the measurements with a nominal shape, fit an equation that best describes the point cloud, and finally reconstruct the optical surface using a Poisson method. Originally, CloudCompare has been designed to perform a direct comparison between dense 3D

point clouds, which is based on a specific octree structure that allows high performance when performing this kind of tasks [371].

Followed methodology

The overall method followed during the experimental process from sample preparation to data processing is illustrated in the form of a flow chart in Figure 6.13. This starts with i) sample preparation, in which the part is cleaned using iso-propanol and compressed air, followed by the application of the matting coating. Then we move on to ii) the digital acquisition of the data, in which we define the appropriate minimum and maximum heights (Z) of the sample, as well as the number of acquisition images. Up to the iii) pre-processing of the data, it starts by importing and scaling the 3D measurements (in millimeters) in CloudCompare. Then the set of points of interest is segmented and the outliers removed, using algorithms such as RANSAC and/or using polylines cuts with the desired shape.

Before moving on to the recognition and reconstruction of the measured optical surfaces, we will briefly define some of the entities used in point cloud processing. We also mention the measurement artifacts, detection methods, segmentation and comparison of entities used, which are described in detail in the relative annexes.

One of the main entities to define is the concept of point cloud, which is simply a set of unorganized 3D points $\{(x_i, y_i, z_i)\}_{i=1}^m$. Among all the "features" that can be associated to a point cloud (colors, normals, etc.) one has a particularly used in this study: the scalar field. A scalar field is a set of values (one per point - for example, the distance from each point to another entity). As each value is associated with a point (or vertex) it is possible to display those values as colors and of course to segment the cloud relatively to those values (thresholding, local statistical filtering, etc.).

On the one hand, a mesh is a set of triangles. Internally, the triangles are represented by triples of integer indices. These indices are relative to an associated cloud (the vertices of the mesh). Furthermore, primitives are a special type of meshes that are described by simple parameters (radius, height, etc.). However, they are associated with a tessellated representation (i.e. a triangular mesh itself). They can thus be used as standard meshes (for calculating distances, etc.). A polyline is a set of points connected by contiguous segments. The polyline can be closed (i.e. a loop) or not. By default, a polyline is a 3D object. But they can also be 2D entities (in which case they will be displayed as a 2D overlay object and their coordinates will always be in pixels).

Furthermore, point cloud comparison and surface reconstruction methods must handle various types of uncertainties and pose certain requirements on the input. In Annex L we summarize these properties in order to cover the basic principles underlying the surface comparison and reconstruction techniques used in this work. In particular, we

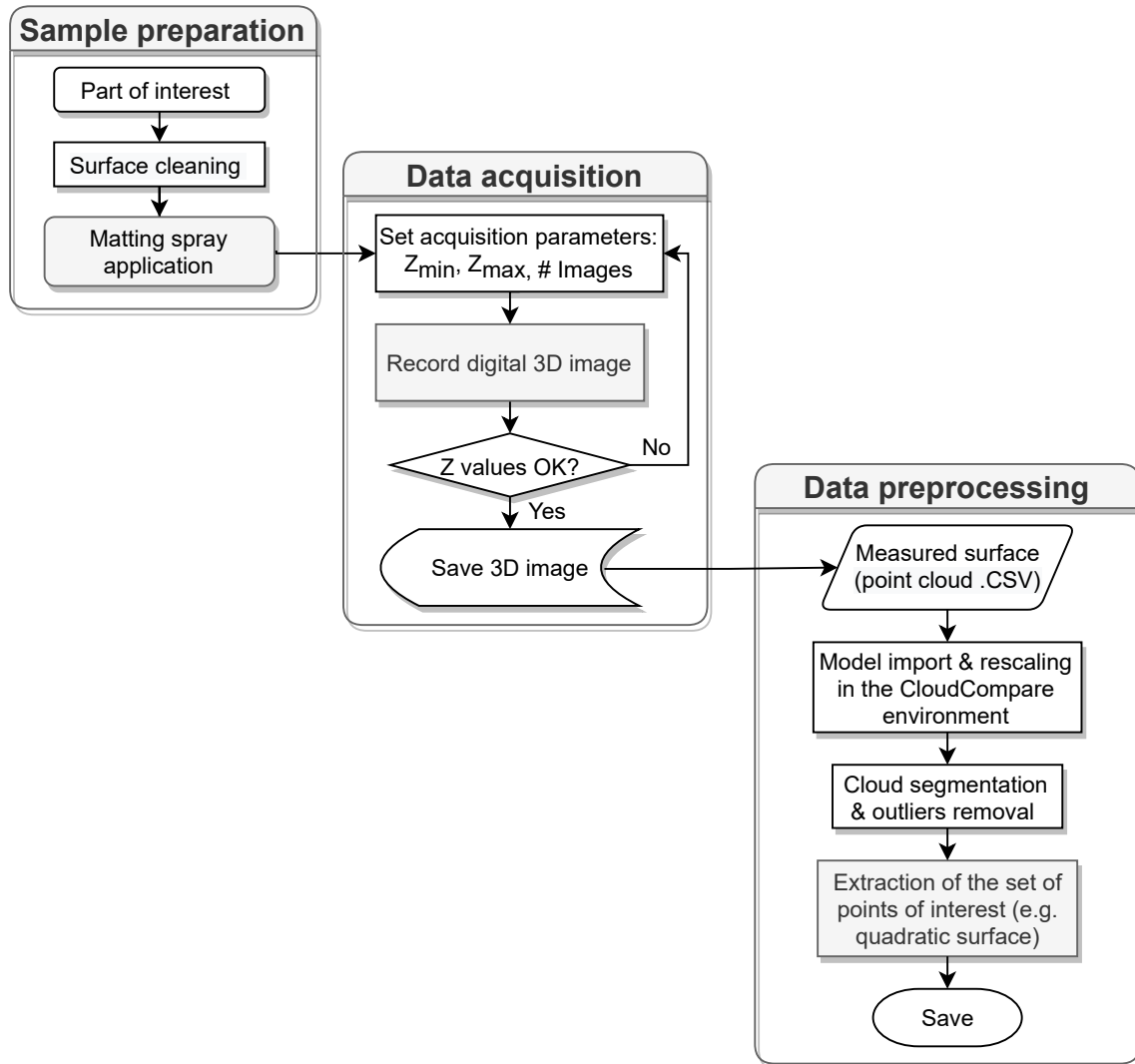


Figure 6.13: Flowchart of the overall process from sample preparation to data processing

will focus on the most recurrent and impactful properties, such as: a) sampling density, b) noise, c) outliers and d) misalignment.

In the context of this research, we have used two different methods to compare the models. We employed a direct cloud-to-cloud comparison (C2C) and cloud-to-mesh or cloud-to-model distance (C2M), both of which are briefly described in Annex M. Moreover, two surface recognition techniques have been used, the least squares fitting approach for the recognition of quadric functions (i.e., the parabolic form of the optics). In addition, the RANdom SAMple Consensus (RANSAC) was used to identify the primitive shapes and to make a segmentation of the point cloud (i.e. into basic shapes) in order to extract the surface of interest. These are briefly described in Annex N.

6.4 Recognition of quadratic surfaces

The first step in the analysis of topographic measurements is the identification or recognition of the shape of interest, described by the acquired point cloud. For this purpose, a methodology has been proposed which is described in Figure 6.14. The process begins with an estimation of the curve by means of the least squares method, effective when the number of outliers is low, which is guaranteed thanks to the preprocessing previously described. Once the curve has been fitted, CloudCompare will generate by default a mesh describing the surface, its equation, as well as its *RMS* deviation. The latter as a measure of the imperfection of the estimator's fit to the data. Then, in order to locally compare the resulting surface with the measured point cloud, we start by maximizing the accuracy of the mesh (i.e. number of faces), which by default is of moderate resolution, and then calculate the Cloud-to-Mesh (C2M) distance between them. It is then possible to calculate the corresponding *RMS* and fit a normal distribution and read the standard deviation for instance. These factors can give a fiability of the relative estimated mesh.

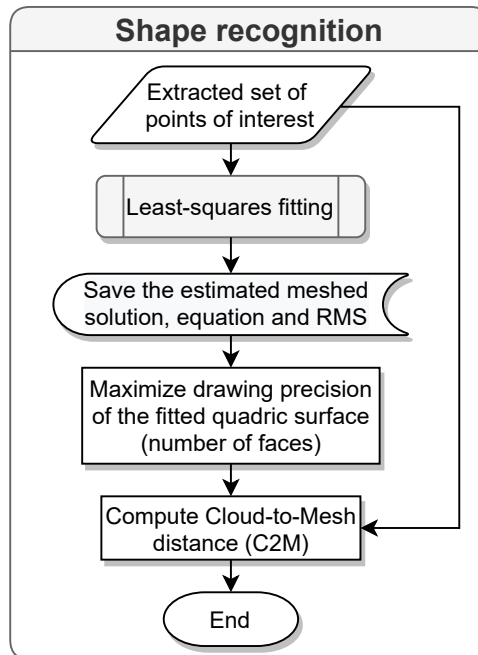


Figure 6.14: Flowchart of the shape recognition process.

To verify the efficiency and accuracy of the proposed recognition method using the least squares method, preliminary tests were performed to recognize known quadratic surfaces. For this purpose, CAD models with known curvature were used and compared with the estimated ones. The ideal shape follows the equation :

$$z = (0.1111)x^2 + (0.1111)y^2 \quad (6.2)$$

Furthermore, the accuracy of the proposed reconstruction method was evaluated experimentally, i.e. using a self-evaporating scanning spray and an optical microscope. For that, tests were performed using controlled shape molded parts (bearing balls), and their geometrical parameters were estimated. These examinations are presented below.

6.4.1 Validation 1: ideal quadratic surface

With the aim of validating the efficiency and estimate the associated error of the least squares method for fitting a parabolic surface, the ideal shape, i.e. the mold's design, was used. For this we relied on the virtual CAD model of a mold unit, which was imported into CloudCompare using the most refined possible meshing parameters generated for this part by SolidWorks using 886,000 triangles. The steps followed to pre-process the data are shown in Figure 6.15: a) Imported CAD model of an ideal hexagonal mold unit; b) Three million sample points were used to represent the whole mesh (i.e., unitary element); c) Then the parabolic surface was extracted using a segmentation process using the RANSAC shape detection algorithm, in which each of the detected features (e.g., planes and curves) are presented with different colors; and d) The segmented parabolic shape was extracted, which is composed by 993,427 points; this is the set of points of interest.

Once the cloud of points of interest was extracted, we fitted a quadratic surface using the least squares method, as shown in Figure 6.16 (a). Then we have increased the refinement (resolution) of the detected mesh from 1,058 faces (by default) to 257,762 faces, i.e. increasing the drawing precision from 24 to 360 (maximum defined in CloudCompare). We then calculated the C2M between this mesh and the point cloud of interest, as can be seen in Figure 6.16 (b), illustrating on the right the distance scalar field in mm. The latter is also presented in the form of a histogram in Figure 6.16 (c), the abscissa shows the distance in mm and the ordinate shows the count of values classified in this case in 256 classes. It can be seen that the correlation between the fitted mesh and the point cloud are in agreement, with the distance field over the entire surface varying between -6×10^{-5} and 2.5×10^{-5} mm, which is almost zero percent compared to the maximum height of the parabola ($Z_{RIM} = 1.5$ mm) under measurement. Furthermore, the fitted surface is described by the equation:

$$\mathbf{z} = -0.3384 + (1.6334e-5)\mathbf{x} + (1.1724e-5)\mathbf{y} - (8.3039e-9)\mathbf{xy} + (0.1111)\mathbf{x}^2 + (0.1111)\mathbf{y}^2 \quad (6.3)$$

It can be seen that it has coefficients other than the quadratic part (i.e. x , y and xy components) that represent displacements and rotations of the quadratic form. To obtain an equation of the form $z = p_1x^2 + p_3y^2 + p_6$, estimating the angular deviation and

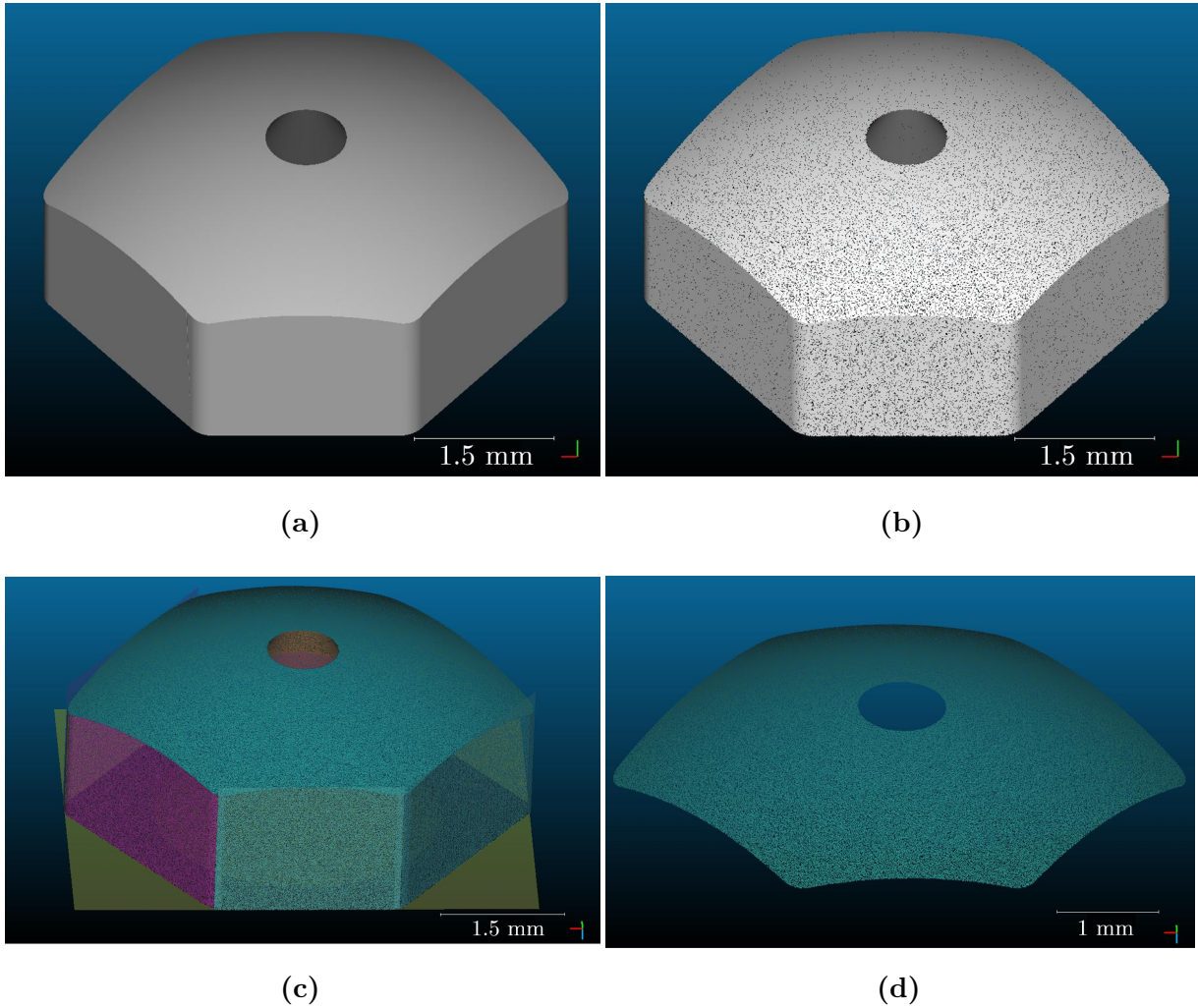


Figure 6.15: Description of data processing: (a) Imported CAD model of an ideal hexagonal mold unit, (b) Sampling points on the mesh (three million points), (c) Segmentation process using the RANSAC shape detection algorithm, and (d) Segmented parabolic shape composed by 993,427 point (millimeters-scale).

the associated error, a basis transformation was implemented using a code in the Python program. In this case, after the matrix transformation the x , y and xy coefficients that were low, 1.6334×10^{-5} , 1.1724×10^{-5} , 8.3039×10^{-9} , respectively, result in a quasi-zero associated error and angle, and the resulting equation is:

$$z = -0.3384 + (0.1111)x^2 + (0.1111)y^2 \quad (6.4)$$

On the other hand, it was evidenced that the algorithm implemented in CloudCompare takes as reference in the adjustment of the quadratic the upper surface of the box containing the points, which implies a displacement of approximately -0.34 mm along the z -axis.

Subsequently, we were interested in studying the robustness of the technique used, decreasing the number of points used in the quadratic shape fitting and evaluating its

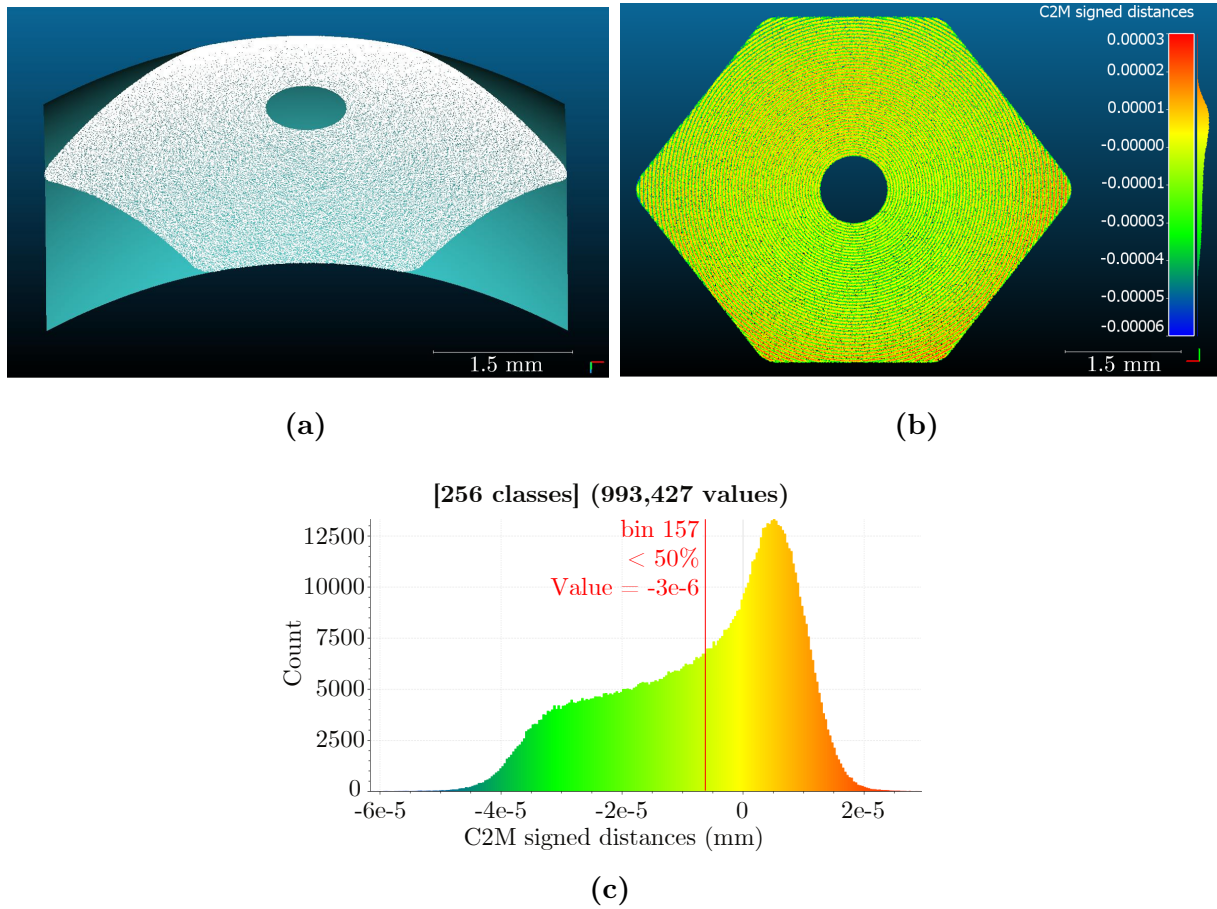


Figure 6.16: (a) Quadratic function fitting of an ideal hexagonal mold unit, (b) Cloud-to-Mesh (C2M) comparison between the point cloud (993,427 point) and the fitted quadratic (scalar distance field in mm), (c) Histogram of C2M comparison (color scaled).

impact on the accuracy of the estimated shape. To do so, we lowered the number of points describing the parabola from 993,427 to 261,315, 26,291 and 2,529 points. A C2M comparison was then made between each of the point sets and the associated mesh (described by the estimated equation). Figure 6.17 (a), (c) and (e) show the results of the C2M comparisons, for each set of data sets, respectively. Also, to study the evolution of the distribution of the measured distances, a histogram of the calculated distances was made and the number of classes have been fixed to 256 classes (bins) to have comparative data, see Figure 6.17 (b), (d) and (f). In addition, a normal distribution (Gaussian or Laplace-Gaussian) was fitted to analyse each set of distances. The general form of the probability density function is given by:

$$f(x) = \frac{1}{\sigma\sqrt{2\pi}} e^{-\frac{1}{2}\left(\frac{x-\mu}{\sigma}\right)^2} \quad (6.5)$$

where μ is the mean or expectation of the distribution (and also its median and mode), while the parameter σ is its standard deviation and the variance of the distribution is σ^2 .

Table 6.5 shows the fitted quadratic equation for each set of points, while Table 6.6 showing the mean distance, standard deviation and computation time required by the C2M method.

Table 6.5: Surface recognition of a quadratic function for various number of data sets.

No. points parabola	Fitted equation (using the least-squares method)
993,427	$z = -0.3384 + (1.6334e-5)x + (1.1724e-5)y - (8.3039e-9)xy + (0.1111)x^2 + (0.1111)y^2$
261,315	$z = -0.3384 + (1.8729e-4)x - (6.7150e-5)y - (8.0393e-9)xy + (0.1111)x^2 + (0.1111)y^2$
26,291	$z = -0.3387 - (4.5143e-5)x - (2.6293e-4)y - (2.9426e-7)xy + (0.1111)x^2 + (0.1111)y^2$
2,529	$z = -0.3256 + (8.4570e-3)x + (6.5817e-4)y - (1.9992e-5)xy + (0.1110)x^2 + (0.1111)y^2$

Table 6.6: Mean distance and standard deviation of C2M distance for a Gaussian fitting (between points and fitted quadratic function) for various number of data sets.

No. points parabola	C2M comparison		
	μ (nm)	σ (nm)	Comp. time(s)
993,427	-6.93	14.6	1.13
261315	-6.85	15.0	0.60
26291	-6.87	32.1	0.41
2529	-6.19	610.0	0.35

These results show that the least squares method can be used in the recognition of an ideal quadratic surface with a single curvature and no outliers, accurately, i.e., with a maximum error distance of 60 nm, see scalar field (in blue) in Figure 6.17 (a), using between 993,427 to 261,315 points. When a lower number of points is considered this error increases to 170 nm and 290 nm using 26,291 and 2,529, Figure 6.17 (c) and (e) respectively. On the other hand, it can be seen that the absolute value of the mean value has a less marked variation ranging between 6.93 nm and 6.19 nm, for 993,427 and 2,529 points, respectively. It could also be seen that the C2M comparison method allows the calculation of a large number of elements in a fast way, varying from 1.13 to 0.35 seconds considering 993,427 and 2,529 points, respectively. In view of the low computational time required to treat a million points, we decided to use the point cloud on this range of elements, which will allow us to take into account in greater detail the surface imperfections when using the method on real objects. Moreover, since the maximum error associated with the use of a million points is 60 nm, and considering that the roughness of the *Rq* method for 8 layers is 1100 nm, this error can be neglected since it is two orders of magnitude lower than the roughness.

Thus, we were able to see the potential of the least squares method in the estimation of the function describing an idealized point cloud with unique curvature. We have observed that the quadratic coefficients of the estimated equation are in agreement with those modeled virtually in the CAD model, besides it was seen that the method is robust when the number of points is decreased (between 993,427 to 2,529 points).

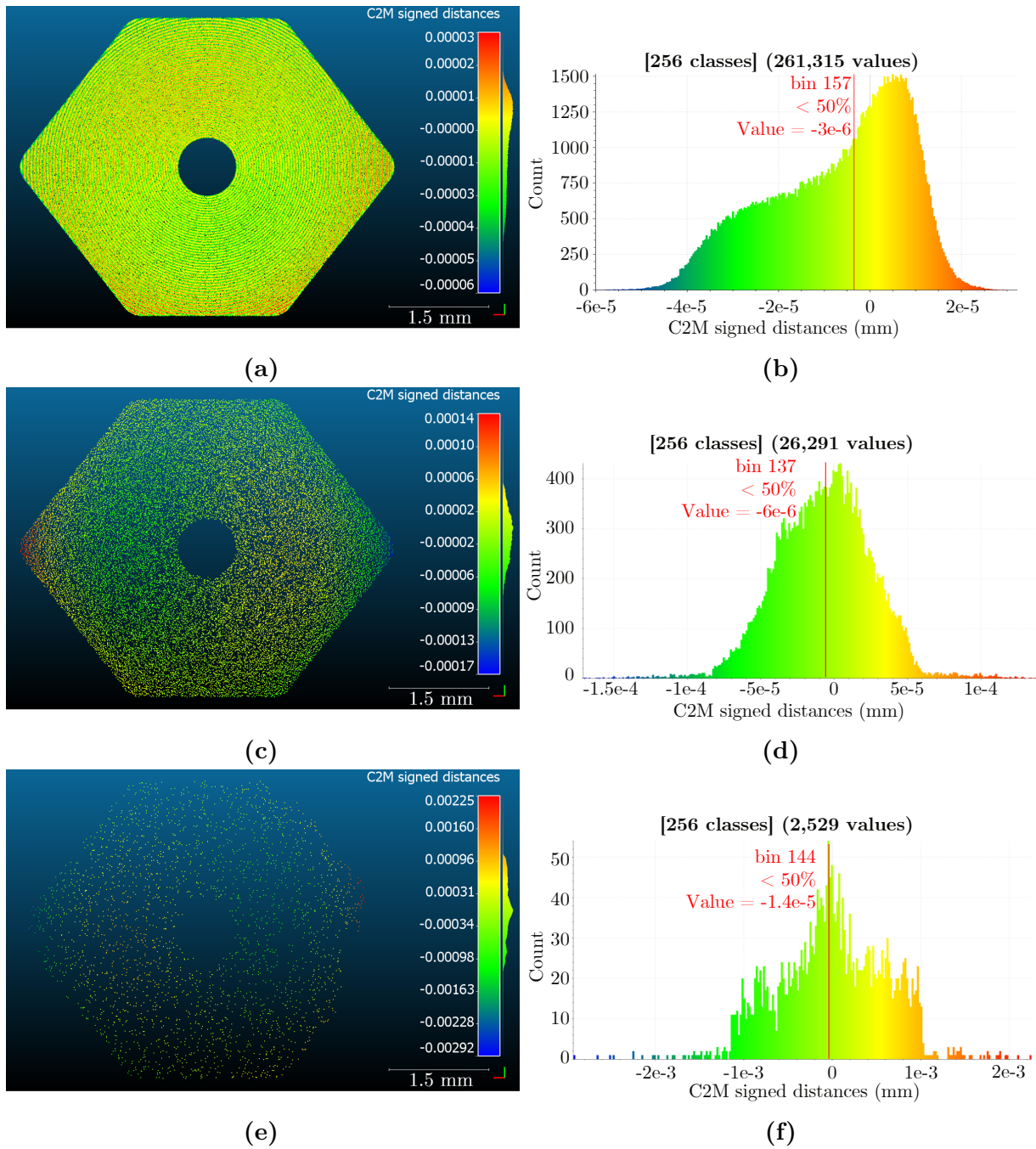


Figure 6.17: C2M comparison between the point cloud model and the fitted quadratic (scalar distance field in mm), using 261,315 points (a), 26,291 points (c) and 2,529 points (e); Histogram of C2M comparison (color scaled), using 261,315 points (b), 26,291 points (d) and 2,529 points (f), the last two with a Gaussian distribution fitting.

6.4.2 Validation 2: quadratic surface with double curvature

Subsequent research consisted of evaluating the efficiency of the method for estimating the parameters of an ideal surface (i.e., virtual CAD model) with double curvature. The idea behind this is to verify the robustness of the method for estimating quadratic surfaces.

More particularly to evaluate if potential shape errors in the manufacture of the mold and the optics, as in the case of a double curvature, can be quantified. In addition, we seek to estimate how the error and computational time associated with the fit evolves in this particular case. The baseline shape of a mold unit was then used and one of the curvatures was modified, for this we consider an abrupt increase of the quadratic coefficient along the x -axis of 30% (i.e. $0.14x^2$), Figure 6.18 a) illustrates the point cloud considered. The modeled shape follows the equation :

$$z = (0.14)x^2 + (0.11)y^2 \quad (6.6)$$

First we estimated the equation describing the point cloud (1,000,021 points) using the least square method. The resulting surface is shown in Figure 6.18 b), which is defined by the equation:

$$z = -0.44 + (1.39e - 6)x - (1.71e - 5)y - (8.89e - 6)xy + (0.14)x^2 + (0.11)y^2 \quad (6.7)$$

Then the first step to analyze it was to do a basis transformation to avoid cross terms, even if these at first sight are low. The fitted equation after the basis transformation becomes the Equation 6.8, which has quadratic coefficients in correspondence to the model equation.

$$z = -0.44 + (0.14)x^2 + (0.11)y^2 \quad (6.8)$$

Then the mesh of the fitted surface was compared with the set of points, and the results are shown in Figure 6.18 c) C2M comparison between the fitted surface (257,762 faces) and the points, with a computational time of 1.21 seconds; d) Histogram of the distances resulting from the C2M comparison.

From these results it can be seen that the distance C2M between the measured point cloud and the fitted surface using the least square method varies between ± 400 nm, with an average value centered on 300 nm. In this respect it is observed that the peaks of the error are concentrated in the central part of the hexagon, forming orange contours in the center, and then two blue lines towards the edges, which are horizontal, i.e. along the x -axis, component for which the quadratic parameter has a higher value (i.e. $14x^2$). Therefore, in the adjustment of an idealized parabolic surface with abrupt double curvature (i.e., 30% of difference between the two axes) the method loss precision and became somehow limited with maximum associated error of 400 nm, corresponding to the maximum deviation between the mesh described by the equation and the points considered. If we compare the fit of an idealized parabolic surface with double curvature and a single curvature on both

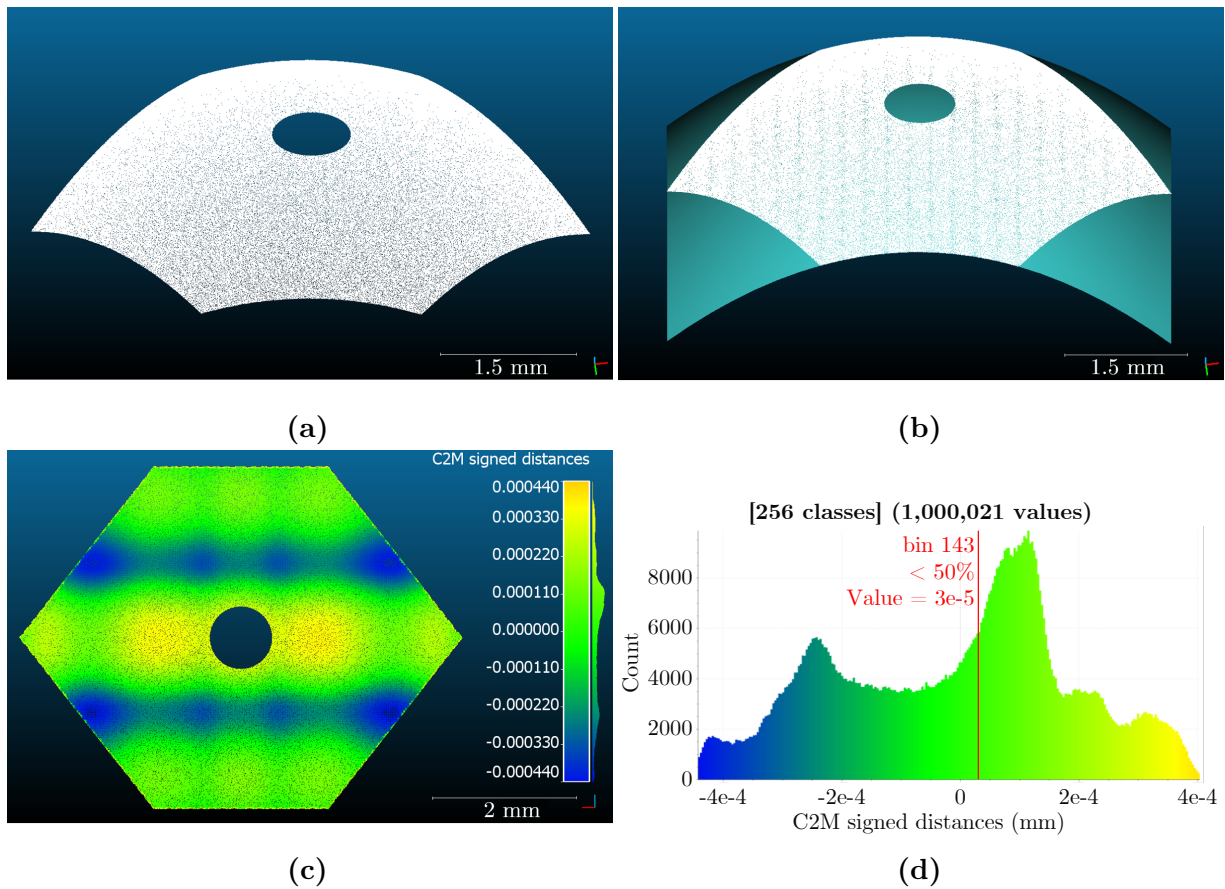


Figure 6.18: (a) Imported CAD model of an hexagonal truncated parabolic dish with double curvature (one million points), (b) Quadratic function fitting, (c) C2M comparison between the point cloud model and the fitted quadratic, and (d) Histogram of C2M comparison.

axes, using approximately one million points in both cases, the maximum error associated with the method undergoes an increase of 85%. This goes from 60 nm to 400 nm, for the single and double curvature, respectively, corresponding to the maximum deviations between the meshes described by the adjusted equation and the points considered. Then if we compare the maximum error of the estimation (i.e. 400 nm) and the limit of the coating method used, 1100 nm (i.e. Rq) we see that this is an order of magnitude lower. In turn, if we consider the time needed for the calculation between a single and a double bend, this is low for both cases, 1.13 and 1.21 seconds, respectively.

On the other hand, if we consider the potential of the method in the estimation of the function describing the idealized point cloud with double curvature, we can appreciate that the quadratic coefficients of the estimated equation are in agreement with those modeled virtually in the CAD model, with a shift of -0.44 mm along the z -axis since the algorithm centers the function on the upper surface of the box containing the points, as in the case of the simple parabola.

6.4.3 Validation 3: scanned well-known surfaces

In order to verify the effectiveness and accuracy of the proposed reconstruction method, using a self-evaporating scanning spray and an optical microscope, preliminary tests were performed to recognize and measure well-known geometries, using a real surface. For this, bearing balls were used, since they are special highly spherical and smooth elements, and their semi-spherical shape have been silicone molded. In fact, ball bearings are graded by number, which sets standards for their precision, as shown in Annex 6.5.3.

For this experimental validation, surface reconstruction was carried out using a bearings ball 5 mm of diameter, made in stainless steel (440C), and a grade of G25 (see Annex J), as defined by the American Bearing Manufacturers Association (ABMA). Therefore, the maximum surface roughness arithmetical average (Ra) and sphericity (i.e., refers to how much the ball deviates from a true spherical form, out of roundness), for these elements is 51 nm and 0.6 nm, respectively. Additionally, it has a nominal ball diameter tolerance of about 2500 nm.

Figure 6.19 illustrates (a) the bearing ball used about 5 mm diameter, (b) the molded shape using DC 93-500 silicone, (c) the sample after spraying of the coating. The diameter of the bearing ball was measured with a micrometer, with an accuracy of 0.01 mm. For this, 10 measurements were made in multiple directions of the ball, and the results showed a diameter of 4.99 ± 0.002 mm, in accordance with the manufacturer specifications. Two hypothesis can be made:

- i.*) The molding process using Dow Corning 93-500 silicone does not undergo shrinkage, as defined by the manufacturer [328], so the cast shape is perfectly formed.
- ii.*) Since the molded shapes (e.g., bearing balls, optics) and the applied coating have associated tolerances, it is necessary to consider the overall tolerance range. In this regard, the approach is based on the worst-case or arithmetic tolerance; the coating is considered to adhere to the molded form and there is not space between the measured surface and the coating.

The approach followed to pre-process and adjust the bearing measurements is shown in Figure 6.20:

- a) Original registered model composed of 1,916,800 points, in which outliers can be observed at the bottom in the shape of an "L";
- b) Subsampled image (15,732 points) for visualization purposes;
- c) Segmentation of the hemispherical shape; and
- d) Recognition of the spherical primitive, using a set of 884,757 points.

After maximizing the number of facets of the fitted sphere to 258,480 facets, the C2M distance between it and the relative point cloud was calculated, as shown in Figure 6.21 (a). On the left is an isometric view of the points (distance scalar field

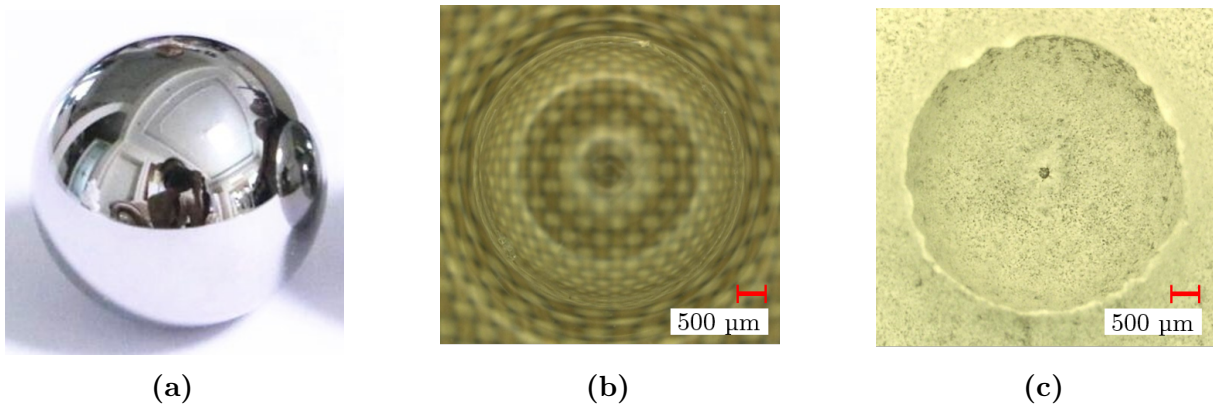


Figure 6.19: (a) Bearing ball (5 mm diameter); Molded shape using DC 93-500 silicone: (b) before coating, (c) After coating using 8 layers.

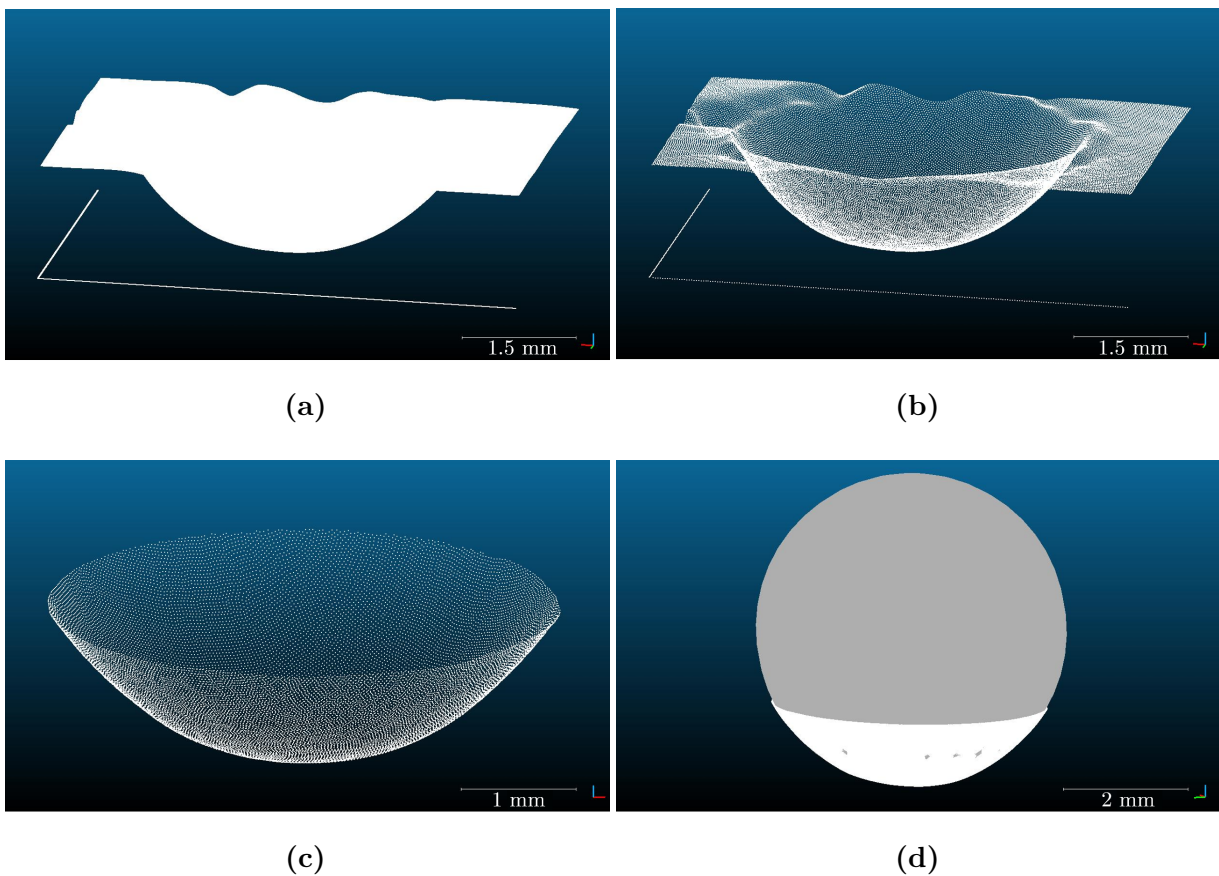


Figure 6.20: Description of data processing: (a) Original recorded model, (b) Sub-sampled image, (c) Segmentation of semi-spherical shape, and (d) Recognition of spherical primitive using RANSAC algorithm.

in mm) while on the right is a top view.

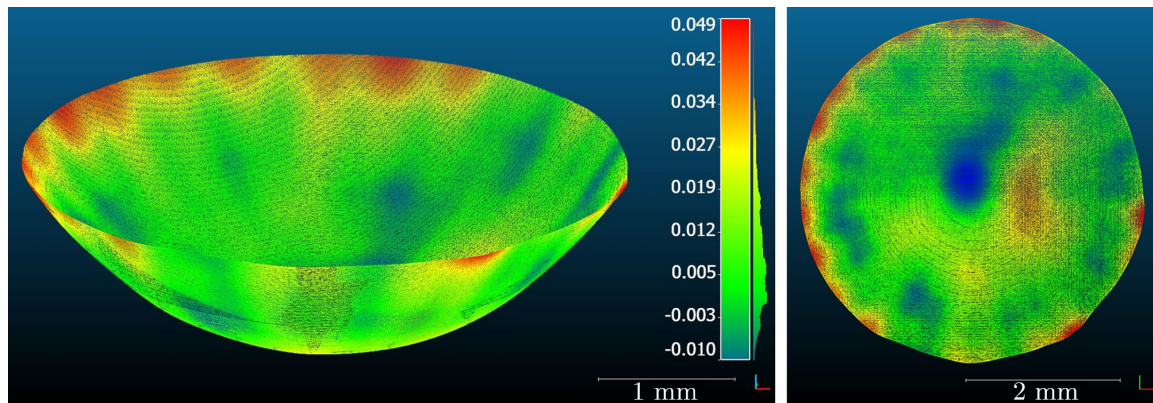
Normal distributions are important in statistics and are often used in the natural sciences to represent real-valued random variables whose distributions are not known. Their importance is due in part to the central limit theorem. This theorem states that,

under certain conditions, the mean of many samples (observations) of a random variable with finite mean and variance is itself a random variable whose distribution converges to a normal distribution as the number of samples increases.

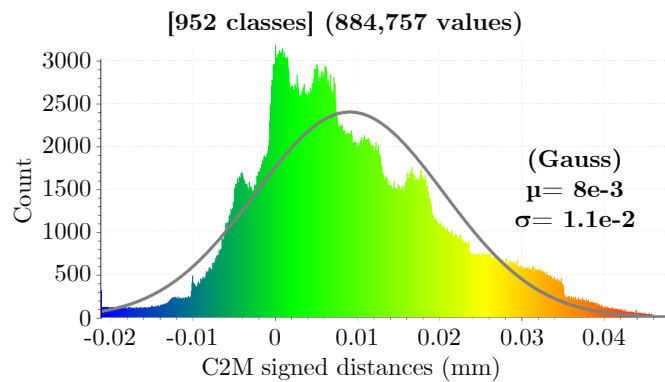
From this if we assume that the distances have a Gaussian distribution, we can estimate a $\mu = 8 \text{ }\mu\text{m}$ and a $\sigma = 11 \text{ }\mu\text{m}$, see Figure 6.21 (b). Moreover, a maximum deviation of $49 \text{ }\mu\text{m}$ (in red) is observed at the top of the hemisphere, which is 25 times greater than the maximum deviation of the coating, i.e. a maximum roughness $Rz = 1900 \text{ nm}$. This maximum deviation which is located at the upper edges of the surface, with respect to the sphere, corresponds to a molding effect corresponding to a portion of the silicone that tends to rise by capillary forces on the sphere, and that once demolded remain solidified. Additionally it can be seen that in the center of the molded half-sphere there is a distortion of the shape, resulting from the molding process, with a deviation of about $10 \text{ }\mu\text{m}$. These effects can be seen in Figure 6.19 (c), where the molded sample can be seen with the spray applied.

Furthermore, the estimated diameter of the fitted molded bearing ball was 2.476 mm , with an average distance between the measured point cloud and the adjusted sphere of $8 \text{ }\mu\text{m}$ and a standard deviation of $11 \text{ }\mu\text{m}$. Which with respect to the measured radius of $2.495 \pm 0.01 \text{ mm}$ (i.e., using a micrometer) represents an error of $19 \text{ }\mu\text{m}$, or 0.8% . Then, if we consider a homogeneous distribution of the matting layer, the 8 layers applied result in an overthickness of about $8.8 \text{ }\mu\text{m}$ ($2\sigma = 0.25 \text{ }\mu\text{m}$), however this does not explain the remaining $10.2 \text{ }\mu\text{m}$ of difference in the estimated diameter. This difference in the fit of the sphere can be associated to the not well defined upper edges of the molded bearing ball, which generate a bias and act as outliers in the shape recognition. Thus, in order to estimate the impact of these edges on the error estimation, we have segmented a part of the height of the semi-sphere point cloud (z -axis), of about 0.3 mm , corresponding to the maximum deviations (see Figure 6.22 in red), going from a height of about 2.49 to 2.19 mm (i.e. 12%), and we have repeated the estimation process.

Regarding this, Figure 6.22 shows (a) the segmented part of the point cloud and (b) the new histogram of the C2M comparison, in which the gray part shows how the maximum deviations decrease after having cut the edges. For this new estimate using $798,406$ points, or 9.8% less than the previous estimate, we find that on the one hand the maximum deviation between the point cloud and the sphere decreased from $49 \text{ }\mu\text{m}$ to $21 \text{ }\mu\text{m}$, or 57.1% , while the mean C2M deviation is $6.4 \text{ }\mu\text{m}$ (20% less), and the standard deviation is $4 \text{ }\mu\text{m}$, for a reduction of 60% .

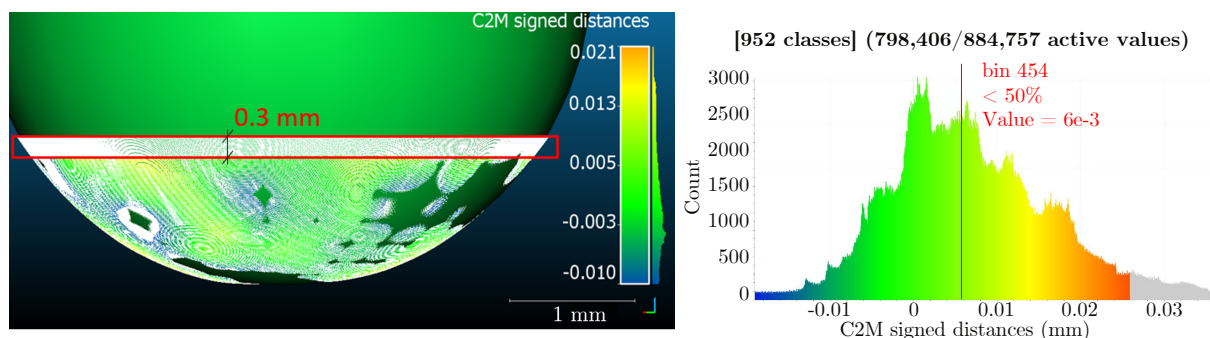


(a)

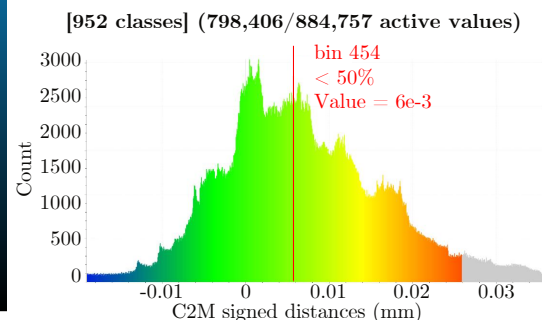


(b)

Figure 6.21: (a) C2M comparison between recognize spherical shape using RANSAC (mesh) and recorded cloud points (scalar distance field in mm), (b) Histogram of C2M comparison (color scaled).



(a)



(b)

Figure 6.22: (a) C2M bearing ball cutted, (b) C2M distance histogram using a segmented point cloud (one million points).

Furthermore, if we consider the new estimate of the sphere radius it is about 4.486 mm, a difference of minus 9.5 μm or 0.4% with respect to the micrometer measurements, which

is in agreement with the estimates of the overthickness generated by the shading layer for 8 applied layers. While the RMS of the C2M comparison (i.e. $4\ \mu\text{m}$) is three times higher than the maximum RMS roughness measured during the method qualification, i.e. $Rq = 1400\ \text{nm}$. This difference between the standard deviations can be attributed to several factors, including in-homogeneous application of the coating, surface errors of the bearing ball, among others. Once we have validated the method, as well as the potential of the least square method to recognize quadratic functions and the estimate the accuracy of using the matting spray, we proceed to evaluate the surface of one unit mold after manufacturing as well as for one molded parabolic surface.

6.4.4 Measurement of one unit of the manufactured mold

The first measurement made in the recognition of a parabolic surface was using the manufactured mold. The same process of sample preparation and pretreatment as previously described was followed. Figure 6.24 a) shows the measured point cloud composed by 1,916,800 points, then b) illustrates the same cloud but with a lower number of points (70,000) with the only objective of showing the reader the underlying shape; c) shows the segmented points of interest (1,117,855 points), also at the top is presented a projection of the contour corresponding to the polyline of the mold unit. Finally, d) shows the mesh fitted using the least squares method.

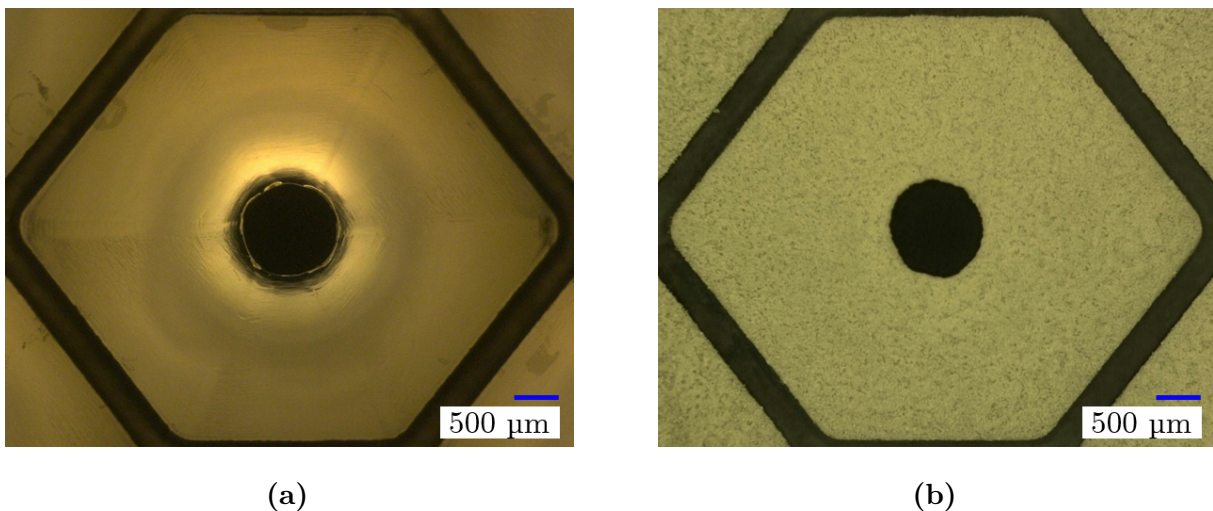


Figure 6.23: (a) Mold-before-spray, (b) Mold-after-spray

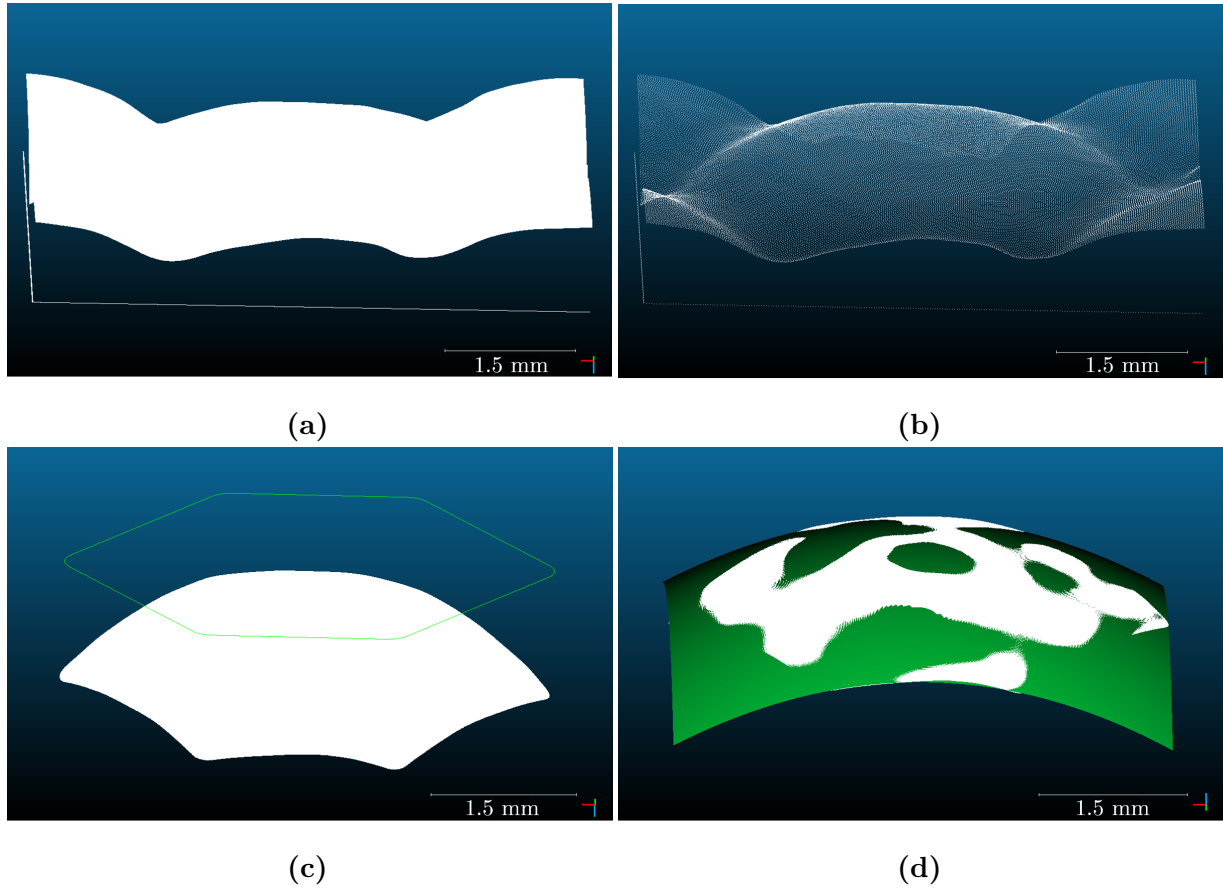


Figure 6.24: (a) Point cloud of registered mold unit (B2) using 1,916,800 points, (b) Sampling points on the mesh (70,000 points) for illustration purpose, (c) Segmentation process using ideal optics contour, and (d) Fitted quadratic.

On the one hand, the shape of the fitting surface is described by:

$$z = 0.3271 + (1.1125e - 3)x - (1.1138e - 3)y - (3.8216e - 4)xy - (0.1117)x^2 - (0.1150)y^2 \quad (6.9)$$

Which after a base transformation results in:

$$z = 0.3271 - (0.1117)x^2 - (0.1150)y^2 \quad (6.10)$$

Once the plane that best describes the measured points was adjusted, the refined estimated mesh (257,762 faces) was used and the C2M distance between it and the set of points was calculated. Figure 6.25 shows the results of the measured distances and the histogram with an adjusted Gaussian distribution.

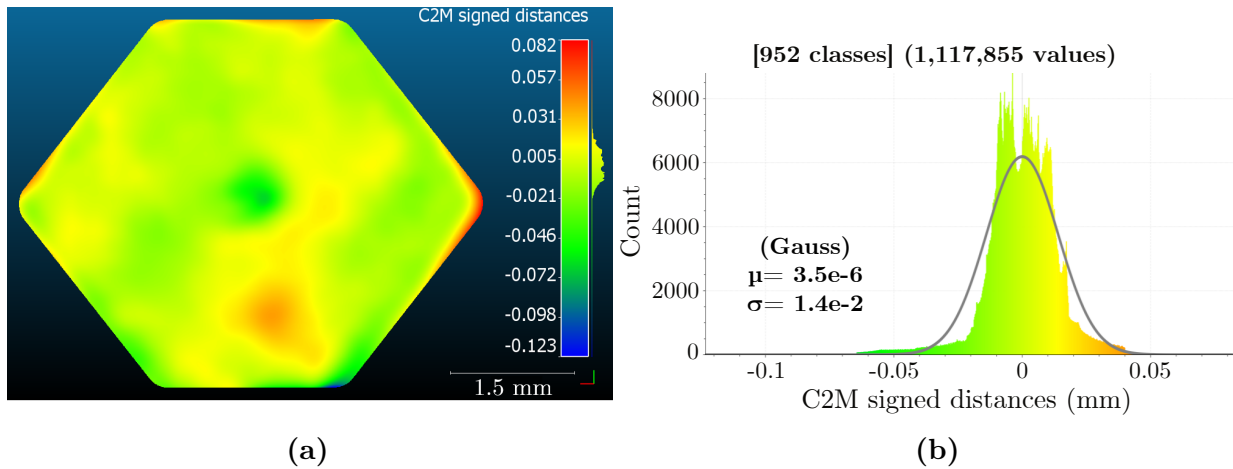


Figure 6.25: (a) C2M comparison between the point cloud model and the fitted quadratic, (b) Histogram of C2M comparison with a Gaussian distribution fitting

It can be seen from the fitted equation that while the coefficient of the quadratic component according to x approaches the nominal form with an error $< 0.5\%$, this is not the case for the y -component which has an associated error of about 3.5% . It can also be seen from the C2M distance estimation that there is a maximum error of 0.123 mm (in blue) corresponding to a displacement as the y -axis (vertical) is located at the lower edge of the point cloud. To investigate the origin of these deviations we first turn to analyze the manufacturing surface defects of this mold unit (i.e. position B2). Figure 6.26 shows some of the most relevant defects found for this mold unit and their location with respect to the unit. Of which we can appreciate a close relationship between the major deviations found in the topographical measurements.

In order to investigate the origin of these deviations we first refer to the analysis of the manufacturing surface defects of this mold unit (i.e. position B2), made after mold reception. Figure 6.26 shows some of the most relevant defects found for this mold unit and their location with respect to the unit. Of which we can appreciate a close relationship between the major deviations found in the topographic measurements. The quantification of both permanent and removable defects were qualified and presented previously in Section 5.2.4. Permanent defects, such as scratches, for this mold unit accounted for 0.06 mm², or 0.34% , of the equivalent top surface projection.

Furthermore, to investigate the percentage of the projected area that limits the fit of the measurement, a sort of low pass filter was applied in which the high distances, which in this case are located at the edges, are progressively cut off. The impact of a 5% contour reduction, which was gradually increased between 100% and 85% of the measurement, was evaluated. Table 6.10 shows the equations fitted with respect to the projected area considered and the number of points remaining. While, the results relating to the calculation of the height function (C2M distance) are shown in Figure 6.27, for different

projected areas: (a) 95%, (c) 90%, (e) 85%; and its respective histograms in (b), (d), (f).

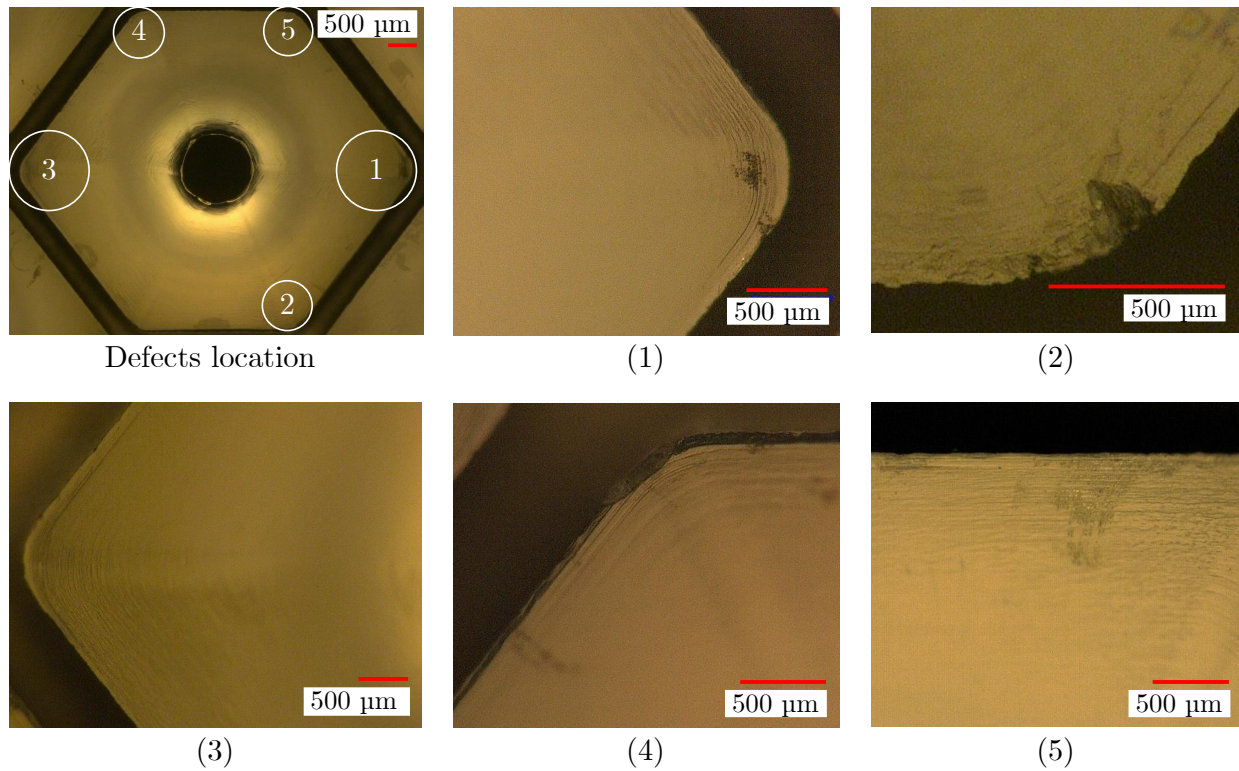


Figure 6.26: B2 unit defaults.

Table 6.7: Surface recognition of one unit mold (B2) using a quadratic function, for various surface percentage of the same data set.

Projected area (%)	No. points parabola	Fitted equation (using the least-squares method)
100	1,117,855	$z = 0.3271 + (1.1383\text{e-}3)x - (1.117\text{e-}3)y - (3.821\text{e-}4)xy - (0.1117)x^2 - (0.1150)y^2$
95	1,008,860	$z = 0.2952 + (1.0026\text{e-}3)x - (0.9156\text{e-}3)y - (3.9010\text{e-}4)xy - (0.1112)x^2 - (0.1131)y^2$
90	905,488	$z = 0.2635 + (0.9024\text{e-}3)x - (0.7611\text{e-}3)y - (2.2796\text{e-}4)xy - (0.1124)x^2 - (0.1125)y^2$
85	807,661	$z = 0.23325 + (0.8193\text{e-}3)x - (0.6372\text{e-}3)y - (5.9252\text{e-}5)xy - (0.1118)x^2 - (0.1114)y^2$

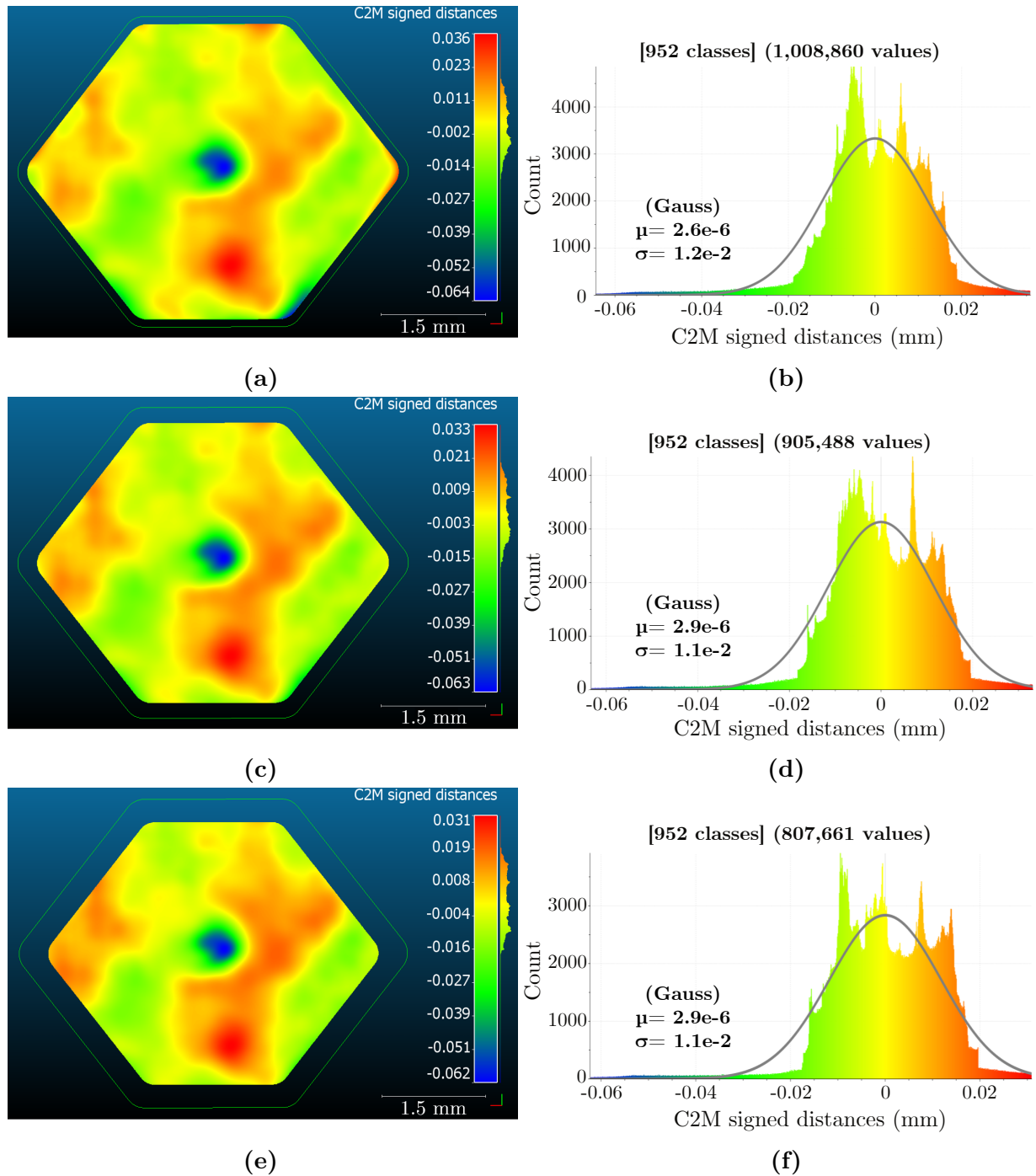


Figure 6.27: C2M comparison between the point cloud measured of one mold's unit (position B2) and the fitted quadratic, for different surfaces segmented at the edges to avoid distortion, considering: 95% (a), 90% (c) y 85% (e) of the surface; and Histogram of C2M comparison with a Gaussian distribution fitting for 95% (b), 90% (d) y 85% (f) of the point cloud model.

From these results it can be perceived that when considering the globality of the surface of the mold unit, the characterization method combined with a least squares adjustment is sensitive when a certain number of points diverge from the predominant shape. This could

Table 6.8: Mean distance and standard deviation of C2M distance, between points and fitted quadratic function of unit mold B2, for various number of data sets.

Projected area (%)	C2M comparison		
	μ (nm)	σ (μm)	Comp. time(s)
100	3.5	14	3.73
95	2.6	12	3.67
90	2.9	11	3.07
85	2.9	11	2.84

be seen in the initial fitted equation (100% of the surface area) in which the quadratic component in y (i.e. 0.1150), went from having an associated error (with respect to the ideal shape i.e. 0.1111) of 5% to 1.8% when the surface area considered was decreased to 95%. The latter continued to decrease to about 1.3% and 0.3% when considering 90% and 85% of the initial surface, respectively. On the other hand, it was observed that the error associated with the x -component remained almost unchanged when considering either 100% or 85% of the surface area for errors $< 0.6\%$. This recognition of the surface allows us to characterize the shape described by the mold.

6.4.5 Measurement of an optical unit molded in silicone

Having recognized the shape of a fabricated mold unit, we set out to investigate the shape of the cast optics resulting from the molding process. For this purpose, the molding procedure described in Chapter 4 was followed, and subsequently a shape recognition of one of the molded optics was made, more precisely the same mold unit previously analyzed (i.e., mold unit B2) was used. Figure 6.28 illustrates a photography of the optical unit under study before and after coating deposition.

Figure 6.29 shows (a) the measured point cloud composed of 1,916,800 points; (b) illustrates the same cloud using 75,000 points for its visualization; (c) shows the segmented points of interest (1,119,759 points), in addition a projection of the contour corresponding to the polyline of the mold unit is presented at the top. Finally, (d) shows the function fitted by the least squares method.

The fitted equation has the following form:

$$z = -0.3352 - (2.7894e-4)x + (1.1974e-4)y - (4.1249e-5)xy + (0.1134)x^2 + (0.1194)y^2 \quad (6.11)$$

Which after a base transformation to eliminate the cross coefficients, results in:

$$z = -0.3352 + (0.1134)x^2 + (0.1194)y^2 \quad (6.12)$$

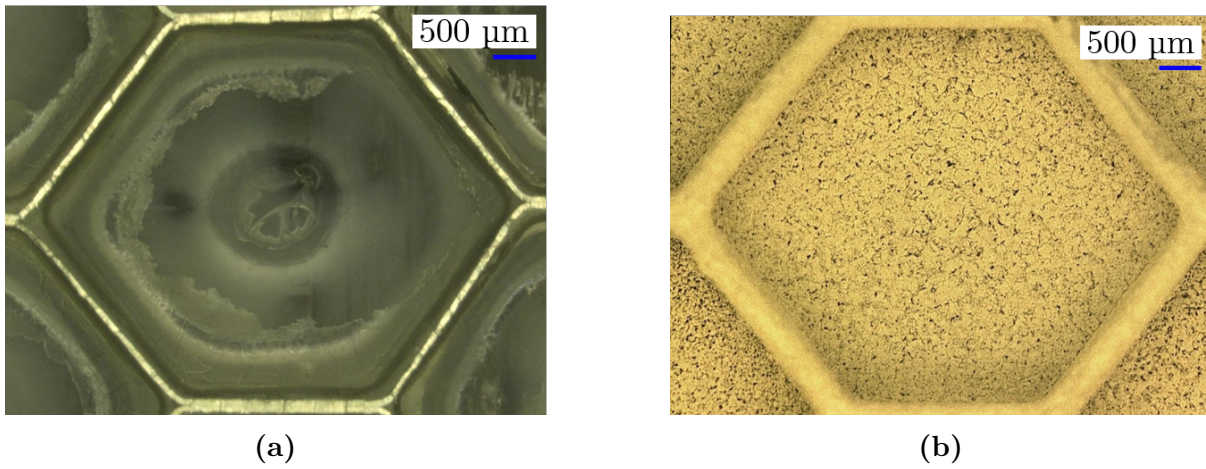


Figure 6.28: Picture of the optical unit under study: (a) before coating deposition, (b) after coating deposition.

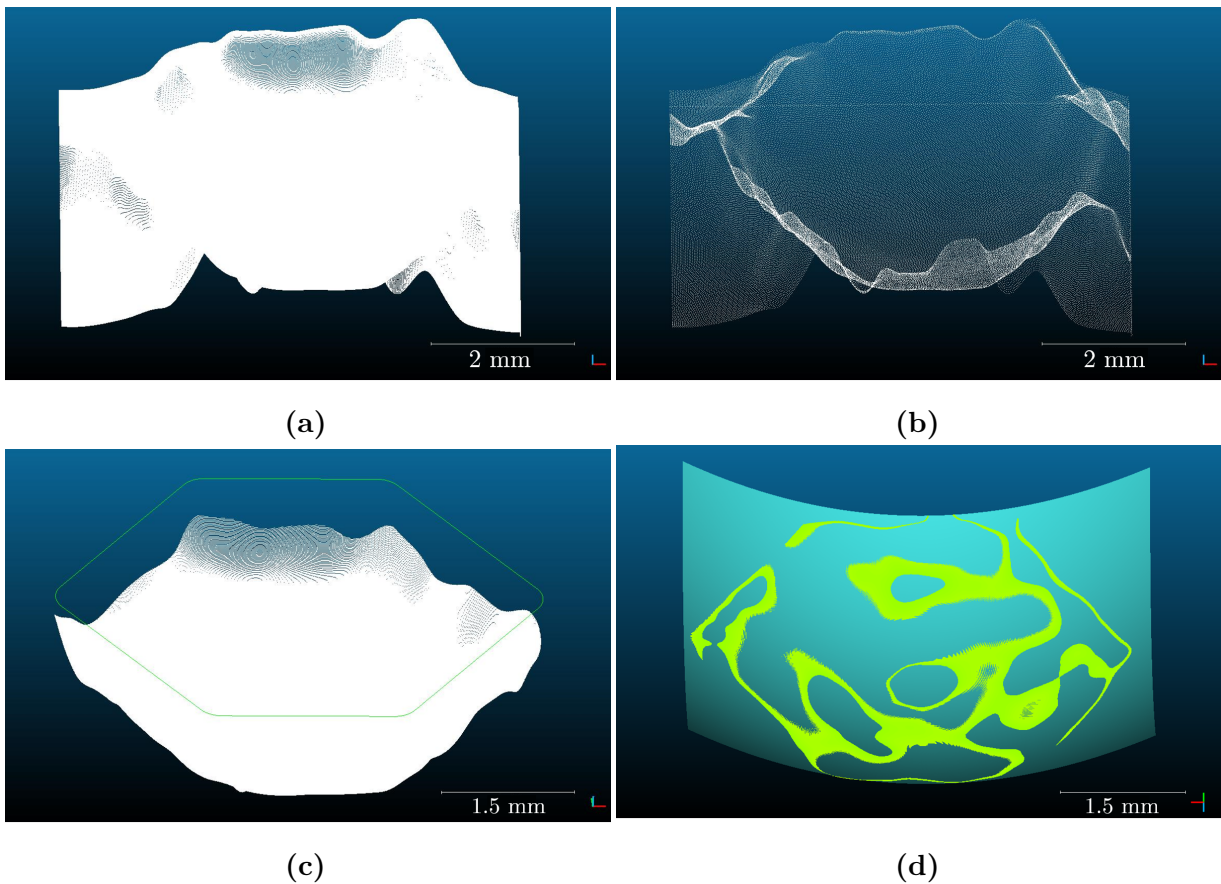


Figure 6.29: (a) Point cloud of registered unit (one-million points), (b) Sampling points on the mesh (70,000 points) for illustration purpose, (c) Segmentation process using ideal optics contour, and (d) Fitted quadratic (in millimeters).

Figure 6.30 shows (a) the calculated C2M distance between the fitted plane and the set of points describing the topography of the optics, and (b) the histogram with a

fitted Gaussian distribution.

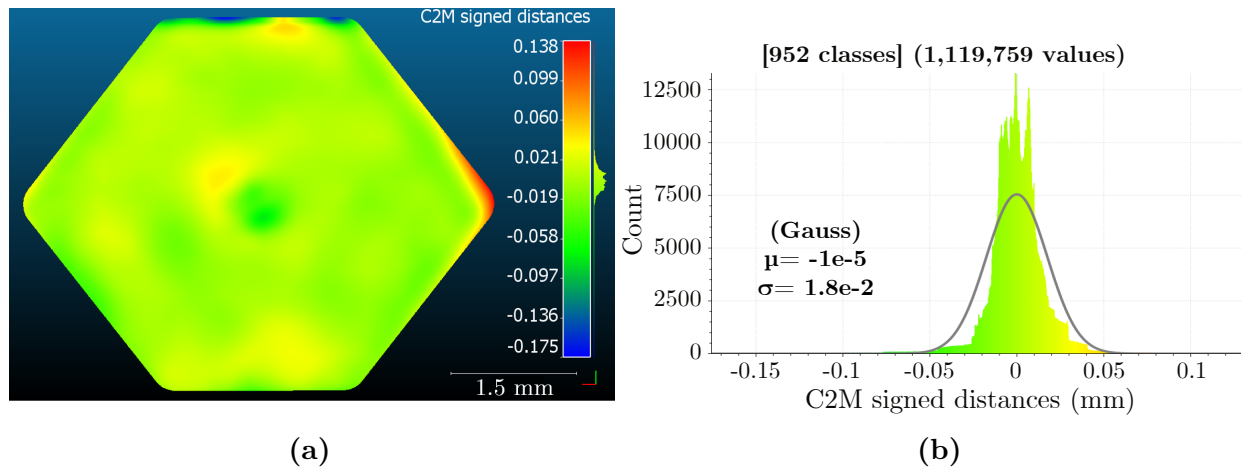


Figure 6.30: (a) C2M comparison between the point cloud measured for one molded optics (position B2) and the fitted quadratic, (b) Histogram of C2M comparison with a Gaussian distribution fitting

On the one hand, it can be observed in the fitted equation that the coefficients of the cross components are in the order of 3×10^{-4} and 4×10^{-5} , in fact, after a base transformation they disappear without producing a change in the rest of the equation. It can also be seen that the quadratic components have an associated percentage error of 2.1% and 7.5%, according to the x and y components respectively. It can also be seen in the estimation of the C2M distance that there is a maximum error of 0.18 mm (in blue), corresponding to a displacement at the top edge of the point cloud based on the projection (top view) in Figure 6.30. To investigate the percentage of the projected area that limits the fit of the measurement and subsequently compare it with the resultant of the fabricated mold. For this purpose a low pass filter was applied in which the high distances and thus segment the edges that generate distortion, progressively every 5% between 100% and 85% of the measurement.

Table 6.9 shows the equations adjusted as a function of the projected surface considered and the number of remaining points varying between 1,119,759 and 809,067, for 100% and 85% of the surface, respectively. While the results related to the calculation of the height function (C2M distance) are shown in Figure 6.37, for different projected areas: (a) 95%, (c) 90%, (e) 85%, where the hexagonal contour represents 100% of the optics; and their respective histograms in (b), (d), (f).

Table 6.9: Surface recognition of one molded optics (mold's position B2) using a quadratic function, for various surface percentage of the same data set.

Projected area (%)	No. points parabola	Fitted equation (using the least-squares method)
100	1,119,759	$z = -0.3352 - (2.7894e-4)x + (1.1974e-4)y - (4.1249e-5)xy + (0.1134)x^2 + (0.1194)y^2$
95	1,010,608	$z = -0.3009 + (2.8617e-5)x + (2.2289e-4)y - (6.4470e-4)xy + (0.1142)x^2 + (0.1165)y^2$
90	907,059	$z = -0.2694 - (8.3278e-4)x + (1.2573e-4)y - (1.0563e-3)xy + (0.1130)x^2 + (0.1135)y^2$
85	809,067	$z = -0.2394 - (6.4616e-5)x + (1.1718e-4)y - (1.2410e-3)xy + (0.1122)x^2 + (0.1129)y^2$

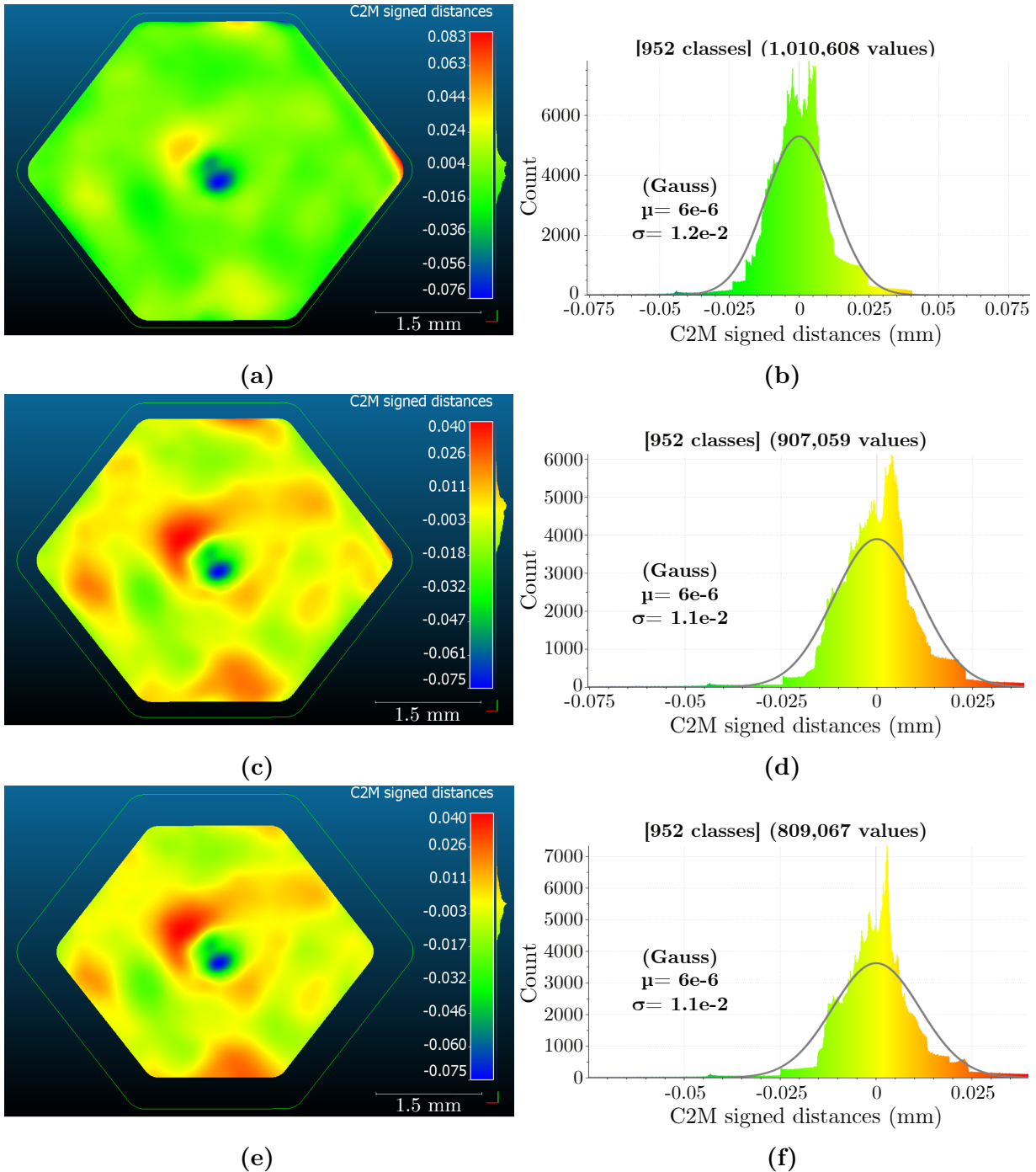


Figure 6.31: C2M comparison between the point cloud measured of one molded optics (mold's position B2) and the fitted quadratic, for different surfaces segmented at the edges to avoid distortion, considering: 95% (a), 90% (c) y 85% (e) of the surface; and Histogram of C2M comparison with a Gaussian distribution fitting for 95% (b), 90% (d) y 85% (f) of the point cloud model.

Table 6.10: Mean distance and standard deviation of C2M distance, between points and fitted quadratic function of unit mold B2, for various number of data sets.

Projected area (%)	C2M comparison		
	μ (nm)	σ (μm)	Comp. time(s)
100	-10	18	3.94
95	-6	12	3.40
90	-6	11	3.12
85	-6	11	2.80

From these results it could be observed that the initial fitted equation (100% of the surface area) that the maximum error associated with the fit is the quadratic component in y (of 0.1194). This decreased from having an associated error (with respect to the ideal form i.e. 0.1111) of 7.5% to 4.9% when the surface area considered was reduced to 95%. The latter continued to decrease to approximately 2.2% and 1.6% when 90% and 85% of the initial surface area were considered, respectively. While the error associated with the x component evolved from 2.1% to 0.1% considering 100% or 85% of the total area, respectively.

6.4.6 Analysis and conclusions of recognition method

During the recognition of quadratic shapes we have been able to validate that the least squares algorithm is a useful method. We have started the validation of the fit using idealized quadratic shapes, i.e. a virtual CAD design of a mold unit. For this we have used different numbers of points describing the surface of interest, which after shape recognition presented standard deviations evolving from 14.6 nm for 993,427 points to 610 nm using 2,529 points. This guarantees a relatively precise fit, two orders of magnitude lower than the RMS roughness of the deposit (1100 nm).

Moreover, to qualify the molding technique (using the DC-93500 silicone that is used to manufacture optics), as well as the accuracy of the topographic recognition we have used the spherical shape of a bearing ball (radius 2.5 mm) as a reference for a real controlled surface and its semi-spherical shape has been molded. Through shape recognition analysis we found that there was a significant shape deviation at the top of the sphere of 49 μm which is 25 times greater than the maximum expected deviation of the coating, i.e. a maximum roughness $Rz = 1900$ nm. This was attributed to the open molding technique used, which did not delimit the top of the shape so as to make it flat and controlled (as in the case of the real mold), which generated an over-thickness of silicone on the sphere by capillarity. Thus, this wavelike overthickness induced a radius underestimation (using the least squares method) of about 10.2 μm difference in radius when considering the 8 spray-applied layers which induced an overthickness of about 8.8 ± 0.25 μm .

This approach was shown to be sensitive to outliers that were concentrated at a height of about 0.3 mm ($< 10\%$ of the total number of points). However, we took advantage

of this apparent shortcoming to filter outliers and estimate from what percentage of the measured point cloud corresponds to the nominal shape of the design. It was observed that once the point cloud was segmented, the radius of the molded sphere could be estimated with a precision of 0.4% (i.e. 4.486 mm). However, when comparing the standard deviation of the new estimation (mesh sphere) and the point cloud, it was observed that the standard deviation of the distance between the two is 4.3 μm or about four times more than expected, if we consider the RMS roughness (Rq) of the applied deposit (i.e. 1100 nm). This difference is believed to be influenced by a non-homogeneous distribution of the coating on a concave surface, which differs in some way from that generated on a flat plane (e.g. in the spray qualification).

Then we have investigated the recognition of the real quadratic surface using a mold unit, and the proposed coating. We saw that maximum perceived deviations of about 0.1 mm occur at the edges of the hexagonal shape which in turn generate an error of up to 3.5% in the estimated quadratic coefficients. Furthermore, it was found that these shape deviations are linked in part to the mold manufacturing defects, in the form of poorly polished surfaces or scratches. In this respect, we considered the edges, which are the main cause of the error, as outliers, and the subsequent segmentation of these as a low-pass filter. In this sense, we found from the mold measurements that the ideal shape can be recognized from 90% (upper projection) and an associated maximum error of 1.3%. While this reaches 0.3% when 85% of the total surface is used.

The same shape recognition procedure was performed for a molded optic using the same mold unit. In this case, considering the total surface area measured, a maximum deviation of 0.18 mm was obtained at the edges and a maximum error of the estimated coefficients of 7.5%, which decreases to 2.2% and 1.6% when considering 90% and 85% of the total surface area, respectively. This difference in the deviations between the mold unit and the optics are the result of a combination of measurement artifacts and spray deposition, as well as errors associated with the shape casting technique.

It is also pertinent to consider that instruments based on vertical scanning methods, such as optical profilers, provide extremely fast and non-contact characterization of the micro-topography of surfaces, with sub-micrometer resolution. However, there are some limitations, mainly related to the properties of light and its behavior at the measured interface. The reflectivity of the material influences the signal response; the maximum detectable slope (typically $< 35^\circ$) is determined by the surface reflectivity, roughness and numerical aperture of the target. Local signal loss, resulting from this limited detection, results in data files containing empty pixels, which ultimately provide poor surface characterization. Having concluded the shape recognition using the least squares method, we will now proceed to reconstruct these shapes, mold and optical units, to estimate their optical efficiency by ray-tracing.

6.5 Optical efficiency estimation by topographical reconstruction and ray-tracing simulation

Further studies consisted in estimating the optical efficiency of fabricated optics through its topographic reconstruction combined with ray-tracing. So far we have considered parametric models as base models in ray-tracing, these parametric geometries as their name says are defined by certain parameters, such as radius, height, thickness, to define a specific contour. On the other hand, in the reconstruction of geometries based on discrete topographic measurements, through a point cloud, the latter must be meshed for subsequent ray-tracing.

The use of meshes in the definition of high precision optical surfaces, such as telescopes, for ray-tracing has been used in the past. Heijmans *et al.* proposed an opto-mechanical study coupled to an analysis of thermo-structural deformations using meshed optics, where the impact of the deformation on the optical performance has been studied [372]. Lauterbach *et al.* proposed the ray-tracing of meshed surfaces for computer graphics applications, using a ray-strips mesh representation to reduce memory overhead of the original model and the hierarchical representation [373].

In this work we propose to reconstruct topographical measurements using a set of points using a Poisson mesh reconstruction method, which allows to fit the scanned data and fill the surface holes for a given sampling density set of points; it is incorporated in the CloudCompare software. Poisson surface reconstruction follows a commonly-used pipeline for surface reconstruction that consists of calculating the implicit surface representation using, e.g., a signed distance function; the algorithm is described in detail in [374]. In this approach, point clouds with oriented normals are required as input. An indicator function whose value is one inside and zero outside the reconstructed one is defined. The gradient of the indicator function is equated to a vector field, constructed from the normal vectors of the point cloud. The Poisson equation is then formed and solved to obtain the indicator function. The watertight surface is reconstructed using the running cube algorithm and stored in an octree. The Poisson algorithm can be applied to closed 3D shapes in a straightforward manner, or it can use the output "density" information to obtain an open mesh, as in our case, and thus reduce the extensions of the output mesh to fit as closely as possible to the input point cloud. In the CloudCompare environment this is done by changing the scalar field value 'min displayed' (in the mesh properties).

The general flowchart of the proposed method is presented in Figure 6.32. The process starts with the segmented point cloud (i.e., surface of interest), which is subsampled to reduce the huge amount of measurement points (more than a million), which otherwise would require extensive computation time and memory; in the meshing, but especially

in the analysis of consecutive ray-tracing. For these we used a subsampling based on the octree level, which as it has been shown in literature guaranteed a high level of detail in the reconstruction of complex surfaces, as curved shapes [375], while it ensures a good relationship between memory usage and speed of extraction of points from the neighborhood. Then once the point normals have been calculated, the Poisson reconstruction is used, which is then imported into SolidWorks in (.PLY) format and re-exported in (.SAT) format used in TracePro for ray-tracing.

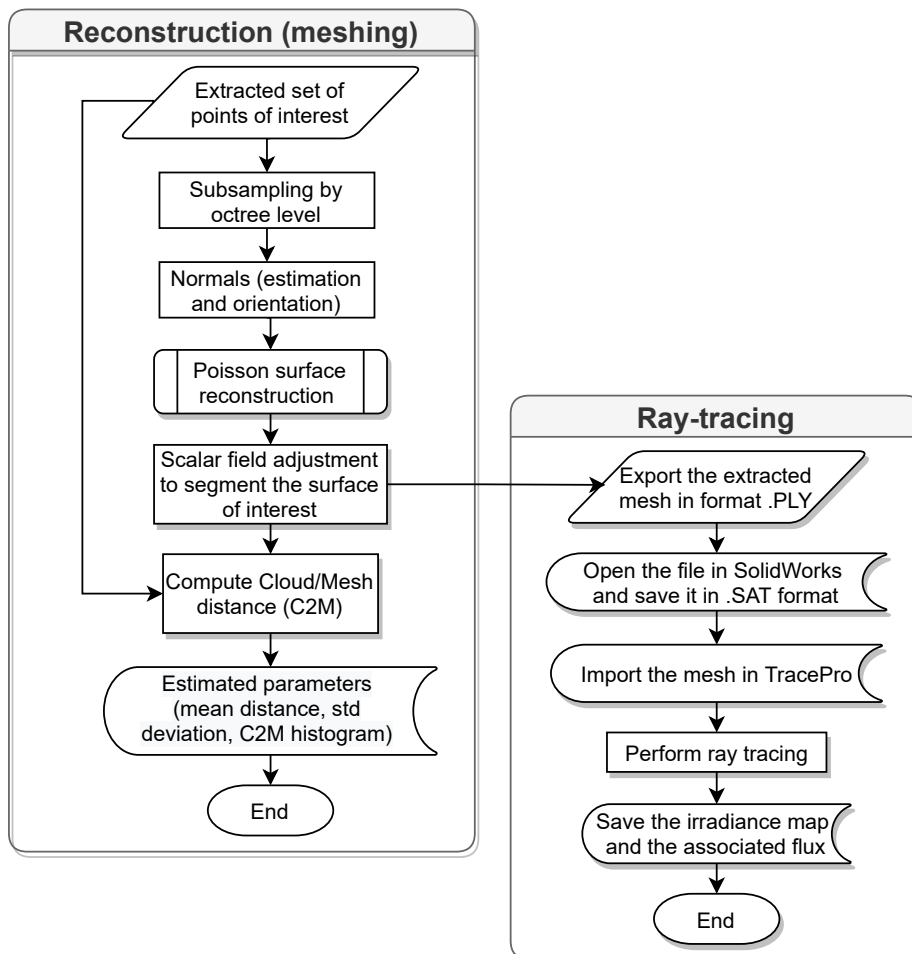


Figure 6.32: Flowchart from the reconstruction process of scanned data to ray-tracing.

6.5.1 Reconstruction of an optical unit and the measurement plane

The first step in the accurate reconstruction of an optical surface consisted in analyzing the number of facets required to mesh a parabolic unit, in relation to the number of traced rays used. For this, the ideal parametric model (i.e., virtual CAD model) was used as a basis, which was then sampled and meshed using a Poisson reconstruction,

with a different refinement (i.e. number of faces). Models composed of 1,000, 5,000, 10,000 and 20,000 facets were studied, knowing that the latter is the closest to TracePro's importable refinement limit of about 25,000 facets.

In relation to this, to study the optical performance of the reconstructed optical surface, we are interested in analyzing the flow and distribution of the reflected rays in an unfocused plane (parallel to the focal plane); both for the parametric model and for the meshes. The position of this plane of interest must maximize the perceived flux (i.e., equal to that of the focal point), as well as the spot size in order to obtain as much detail as possible on the shape and flow distribution. Figure 6.33 shows how the flux evolves with respect to a displacement along the z -axis, using 500,000 rays. It follows that the meshed models with a low number of facets, for example 1,000 and 5,000, tend to shorten the distance to the focal plane that maximizes the flow, which are -0.07 and -0.17 mm (z), respectively, regardless of the number of rays traced. While for the parabolic model as for the meshing using 10,000 and 20,000 facets, this point is -0.19 mm (z), as indicated by the dotted line (in red). In this respect, here we show the graph corresponding to the use of 500,000 rays, however, the same behavior has been observed when moving the measurement plane with respect to the focal plane using 12,000 rays, with a difference of (+) 0.7% in the maximum flux perceived.

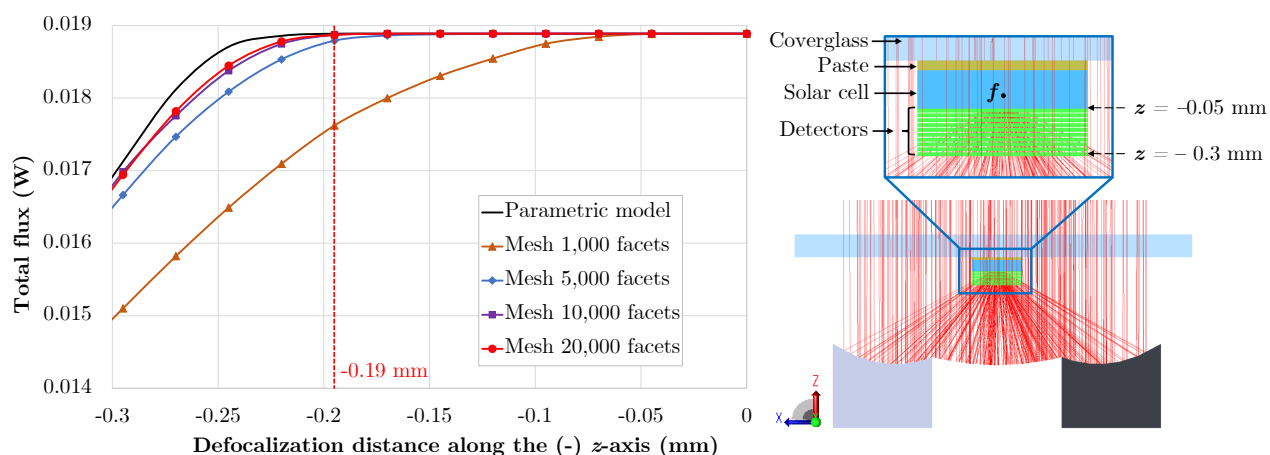


Figure 6.33: Ray-tracing analysis of one unit mold using a parametric model and reconstructed meshes based in the ideal parametric design.

Once we have determined that the optimal distance relative to the focal length to study the spot distribution is -0.19 mm using more than 10,000 facets, we have studied the distribution on a detector placed at this distance. Figure 6.34 shows a comparative ray-tracing analysis for meshes using different number of facets and rays traced (i.e. 12,000 and 500,000). While Table 6.11 shows the associated metrics, as the total flux at this interface, the associated error calculated with respect to the parametric case, the number of incident rays and the associated computation time.

These results show first the focal shape seen in the irradiance map, for the parametric

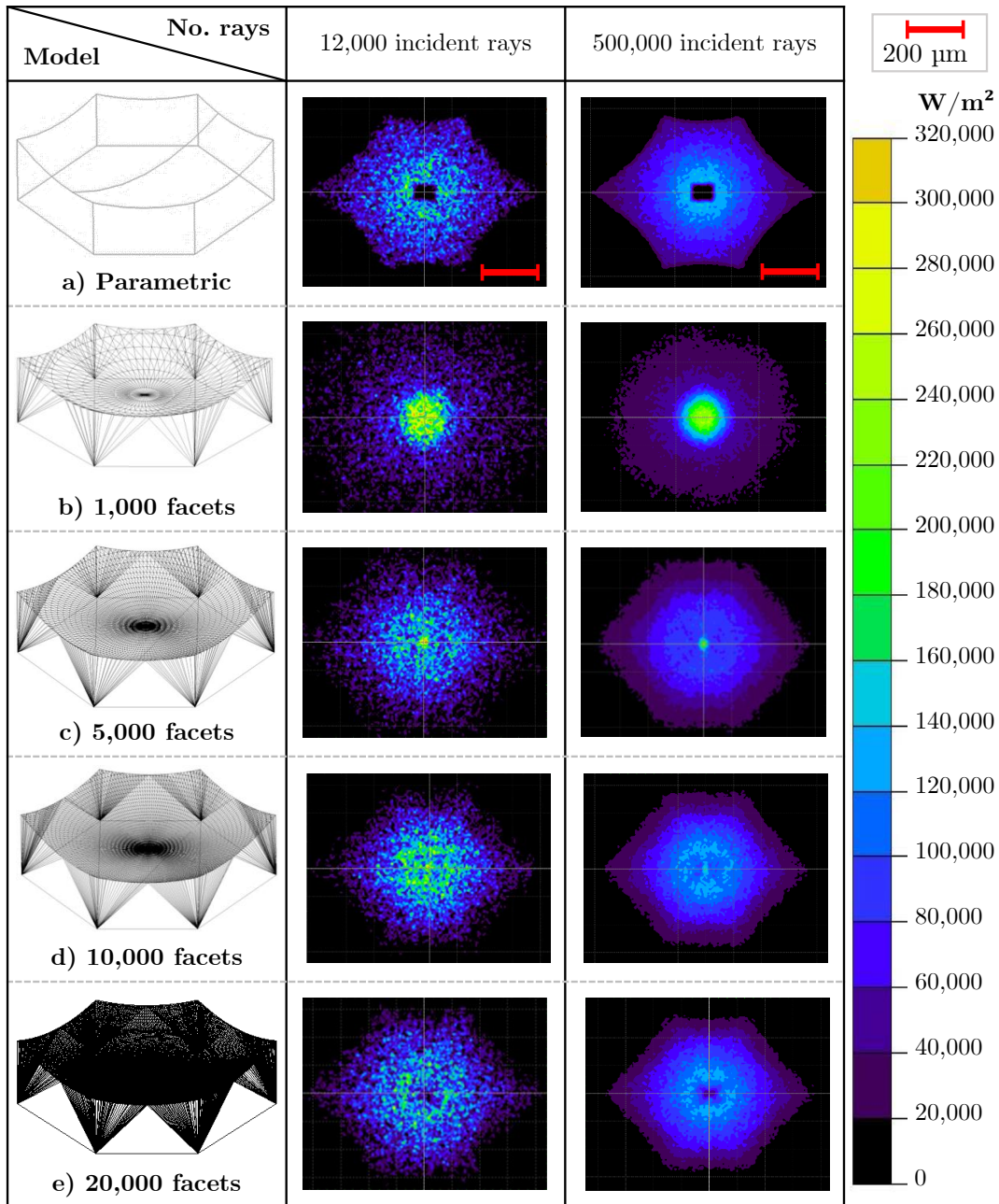


Figure 6.34: Analysis of the number of mesh facets and traced rays (for a plane $z = -0.19$ mm), considering: a) a parametric model, and a mesh composed of b) 1,000 facets; c) 5,000 facets, d) 10,000 facets and e) 20,000 facets.

model, which in our case is the ideal one. Then analyzing the meshed models we see that the spot is highly focused when using 1,000 facets while a part of the flux is not lost, 6.7% and 6.8%, using 12,000 and 500,000 rays, respectively. This is due to a lack of accuracy in the description of the curvature of the parabola, in which the low resolution of the facets plays a flat mirror effect in which the incident rays on the facets are focused either in the direction of the captor forming a narrow spot, or outside of it. Also, as

Table 6.11: Ray-tracing metrics for an ideal meshed parabolic surface using different number of facets and traced rays, for a focal plane at -0.19 mm along the (z -axis).

No. rays on the optics aperture	12,000				500,000			
Model \ Metrics	Flux (W)	Error (%)	Incident rays	Comp. time (s)	Flux (W)	Error (%)	Incident rays	Comp. time (s)
Parametric	0.01889	-	11,356	18	0.01876	-	451,174	209
Mesh 1,000 facets	0.01762	6.7	10,595	42	0.01749	6.8	420,656	220
Mesh 5,000 facets	0.01879	0.5	11,297	867	0.01867	0.5	448,974	4144
Mesh 10,000 facets	0.01887	0.1	11,345	5,036	0.01873	0.1	450,531	10,080
Mesh 20,000 facets	0.01887	0.1	11,345	10,288	0.01876	0.0	451,153	11,495

expected if the number of facets is increased, the spot shape becomes closer and closer to that of the parametric model for each set of launched rays, and the associated flux error decreases as well. In this sense, using 5,000 and 10,000 facets, the spot pattern becomes closer and closer to that of the ideal model and the flux error becomes 0.5% and 0.1%, respectively, for both sets of rays (12,000 and 500,000 rays). Finally, when 20,000 facets and 500,000 rays were used, the best distribution agreement is found and the flux globality is incident. Therefore, in the reconstruction of the topographies of the developed optics we chose to use this last configuration, to guarantee a good resolution of the focal spot distribution and the totality of the flux.

6.5.2 Conversion efficiency analysis using raytracing

In the study of the conversion efficiency of a reconstructed optical surface, we have analyzed two cases using ray tracing via TracePro. First, the shape of a mold unit (i.e. position B2) was studied, in order to validate its shape after fabrication, and secondly the efficiency estimation of an optic molded using this same mold unit was analyzed. Both cases were then compared with the quadratic shape recognition results previously described.

6.5.2.1 Mold's unit estimation

The first step in estimating the efficiency of a measured topography was the use of a unit of the fabricated mold unit B2 (see Figure 6.24), recognized in the previous section. For this we followed the methodology presented in Figure 6.32. We used the set of segmented points, which for the case of the mold has been presented in Figure 6.25. The first step consisted of subsampling the point set. The evolution of the subsampling distribution as a function of the octree level considered, from 1 to 8 is shown in Figure 6.35, while metrics as the number of points and computational time are presented in Table 6.12. In this work, an octree level of 7 is used to obtain 13,414 points. Then, to reconstruct the associated shape underlying the set of points via Poisson reconstruction, one must choose

the desired meshing accuracy by determining either a specific resolution or the depth of the octree. We have used the same octree level of 7, (as used in the subsampling) to obtain a resulting mesh composed of 22,648 facets, as it is the closest of the mentioned limit of 25,000 facets. It has an average surface area of the facets of $840 \mu\text{m}^2$ calculated using CloudCompare, and it is shown in Figure 6.36.

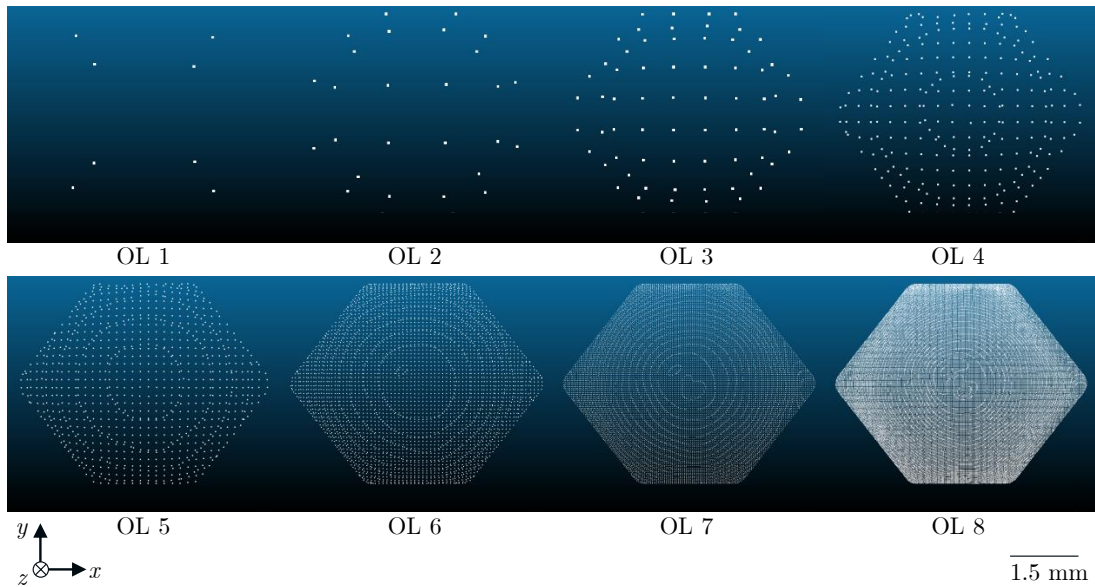


Figure 6.35: Octree-level (OL) evolution from 1 to 8.

Table 6.12: Evolution of the number of point with respect to the octree-level, from 1 to 8.

Octree level	No. of points	Computational time (s)
1	8	0.53
2	28	0.25
3	72	0.25
4	245	0.45
5	898	0.76
6	3,462	0.79
7	13,414	0.46
8	51,507	0.27

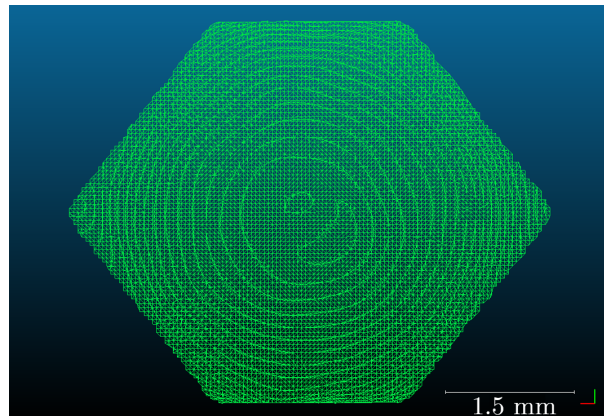


Figure 6.36: Surface reconstruction of one mold's unit (position B2) using a Poisson approach.

Next, to analyze the resulting mesh and the quality of the reconstruction, a number of characteristics have been measured. Starting with the 'density' of the mesh derived from the Poisson reconstruction, which indicates the estimated depth values of the vertices of the isosurface, see Figure 6.37 a) and b). Higher density meshes tend to produce more accurate analysis results, but take longer to analyze. Different areas can be meshed with different densities. Using a higher density mesh on important features usually provides more accurate results in those areas. In this respect the reconstructed mesh has a mean of 7 and a standard deviation of 0.1, which guarantees a homogeneous accuracy over the whole surface and it is in correspondence with the depth of the subsampling and reconstruction octree level equal to 7.

Then we calculate the orientation (i.e. angles) of each of the elements of the mesh, which will finally direct the reflection of sunlight on the micro-cell, see Figure 6.37 c) and d). From this we can observe a progressive evolution from the center of the hexagonal surface to the outside. Measurement artifacts in combination with manufacturing defaults are also observed at the edges of the surface where a maximum of 67° is reached (in red). Similarly, in the center and at certain edges, a minimum angle of about 0.1° (blue) can be seen. The surface has a mean angle of 22° with a standard deviation of 8.9° .

Finally, in order to study the reliability of the Poisson method for reconstructing the initial points of the measurement, we calculated the C2M distance between the rebuilt surface (based on 22,648 triangles) and the whole set of segmented point cloud (using 1,119,735 points). The result of the relative distances of the point cloud (as a scalar field) to the computed mesh is shown in Figure 6.37 e) and f). This difference between the two entities can be considered as the degree of smoothing that the Poisson function introduces to the mesh, with respect to the initial point cloud. In this case it can be observed that the extreme values (i.e. the distances) of (+) 2.4 and (-) 3 μm , in orange and blue respectively, occur either at the ends of the hexagon or in the center of it, places which, as we have

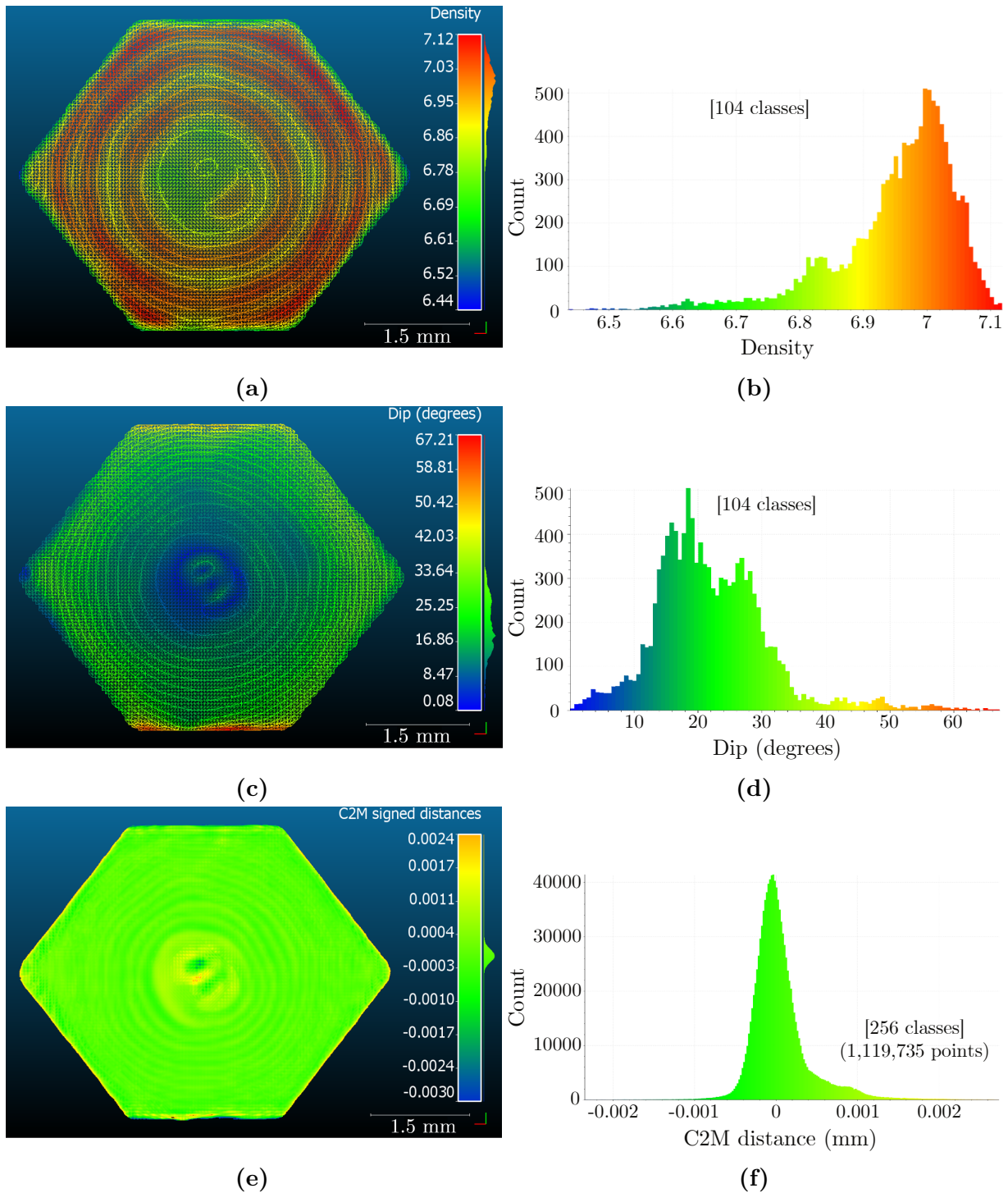


Figure 6.37: Reconstruction analysis of one mold's unit (position B2) using a Poisson approach: (a) and (b) density properties; (c) and (d) angles of the facets; (e) and (f) C2M comparison between the point cloud measured and the associated mesh.

seen, present the greatest difficulty in the measurement and recognition of the surface under study. On the other hand, a mean distance of 10 nm with a standard deviation of 500 nm was calculated. This standard deviation is 2.2 times lower than the average

roughness measured in the application of the 8 coats applied ($Rq= 1100$ nm), during the method qualification. These results shown a reliable reconstruction of the measured points, using the Poisson algorithm, over almost the entire surface in the sub-micrometric order.

After having reconstructed the topography of a unit mold (composed of about 22,648 facets), we have performed ray tracing using an AM0 source, with 500,000 incident rays on the hexagonal optical aperture. The ray tracing is shown in Figure 6.38 from different perspectives of the model, showing the incident rays on the photovoltaic cell (in green). It can be observed that a part the edges of the reconstructed surface does not focus the rays on the cell, from which it is inferred that the surface presents deviations with respect to the nominal shape. This has also been evidenced during the recognition of the quadratic shape with the least squares method, in which the shape of the mold unit (B2) could be recognized when using between 90% and 95% of the set of segmented points.

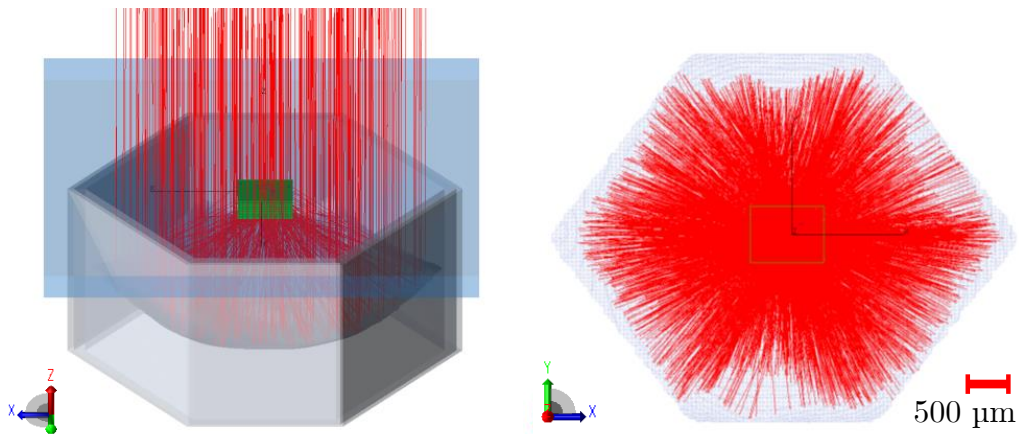


Figure 6.38: Irradiance map of a reconstructed mold's unit (position B2).

On the other hand, microcell-sized ($885 \times 685 \mu\text{m}^2$) detectors were located at 0.05 and 0.19 mm from the focal, the former corresponding to the location of the cell according to the integrated design, while the latter corresponds to the plane that maximizes the spot size and flux, discussed in Section 6.5.1, and the irradiance maps can be seen in Figure 6.38. In these maps, the shape of the ideal expected spot (i.e., of the parametric model) at each of these focal distances can be seen in red dashed lines. The distributions that the generated spot shape approximate to some extent to the expected shapes, knowing that the shape defects notably of the edges influence to some extent the contours of the spot.

Furthermore, it can be observed that if we compare the perceived flux for a plane placed at $z = -0.19$ mm (i.e 0.01639 W) with the parametric ideal (i.e. 0.01876 W) presented in Table 6.11, it corresponds to 87.4%. We can also observe a slight decrease of 0.57% of the latter when approaching the focal, indicating that some of the rays reflected by the reconstructed surface and captured at the $z = -0.19$ mm position do not have the appropriate focusing orientation.

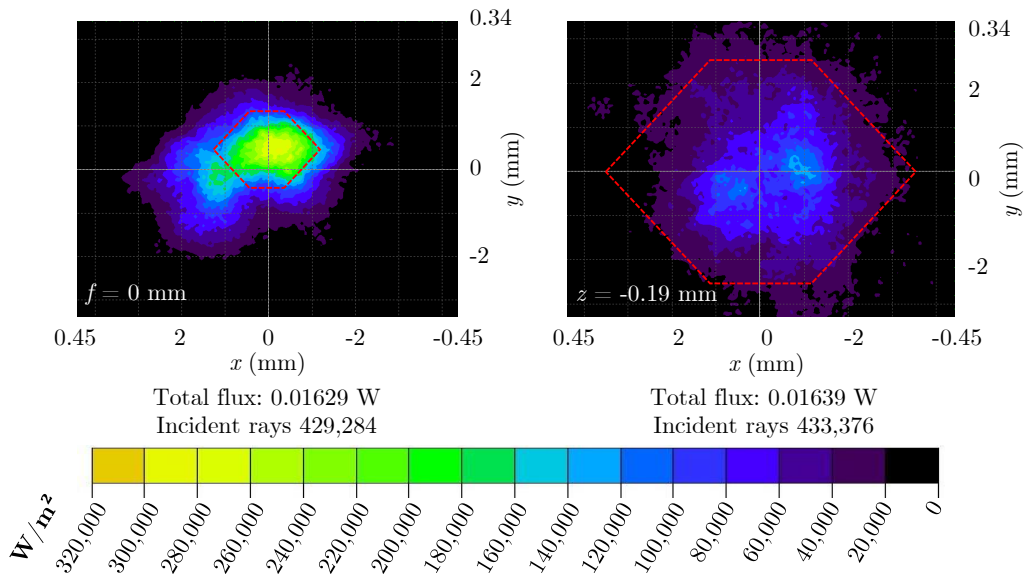


Figure 6.39: Ray-tracing mold map.

6.5.2.2 Molded optics's estimation

The same reconstruction process described for the mold unit was followed for a molded optical unit of the same position (i.e. B2). An octree level of 7 was used for the subsampling which went from 1,119,758 points to retaining 13,464 points (see Table 6.12), which in turn using a Poisson reconstruction produced a reconstructed surface composed of 22,629 facets, see Figure 6.40.

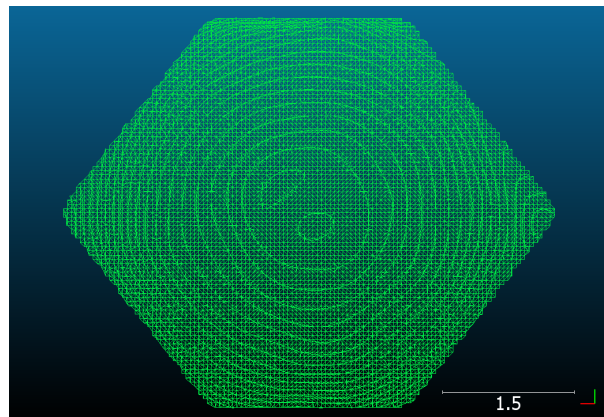


Figure 6.40: Optics Poisson meshing.

Regarding the estimated depth 'density' values of the isosurface this was 6.95 with a standard deviation of 0.12, ensuring a homogeneous level of detail over the entire surface, see Figure 6.41 a) and b). Then considering the distribution of the angles of each element of the surface (i.e. triangle of the mesh), a progressive evolution of its inclination was observed, with a mean of 21.9° with a standard deviation of 9.1° . While at the edges

abrupt variations were observed from 0.2° (in blue) on the right side, to about 65° (in red) at the top of the hexagon, shown in Figure 6.41 c) and d). Finally, to study the reliability of the reconstruction, we calculated the C2M distance between the reconstructed surface (based on 22,629 triangles) and the initial segmented point cloud (using 1,119,758 elements). The result of the relative distances of the point cloud (as a scalar field) to the computed mesh is shown in Figure 6.41 e) and f). This difference between the two entities can be considered as the degree of smoothing that the Poisson function introduces in the mesh, with respect to the initial point cloud.

In this case it can be seen that the extreme values (i.e., distances) of (+) 2.8 and (-) 2.3 μm , in orange and blue respectively, occur either at the ends of the hexagon or at the center of the hexagon, as in the case of the mold unit. A mean distance of 500 nm with a standard deviation of 900 nm was observed, this standard deviation is 1.6 times lower than the average roughness measured in the application of the 8 coats applied ($Rq = 1400$ nm), during the qualification of the coating method; which ensures the reliability of the reconstruction. In addition, a maximum deviation of about 3 μm was observed at specific locations such as in the center of the hexagon, although this is twice the average roughness advocated, this area will not contribute to the ray-tracing calculation, as it is an area opaqued by the cell.

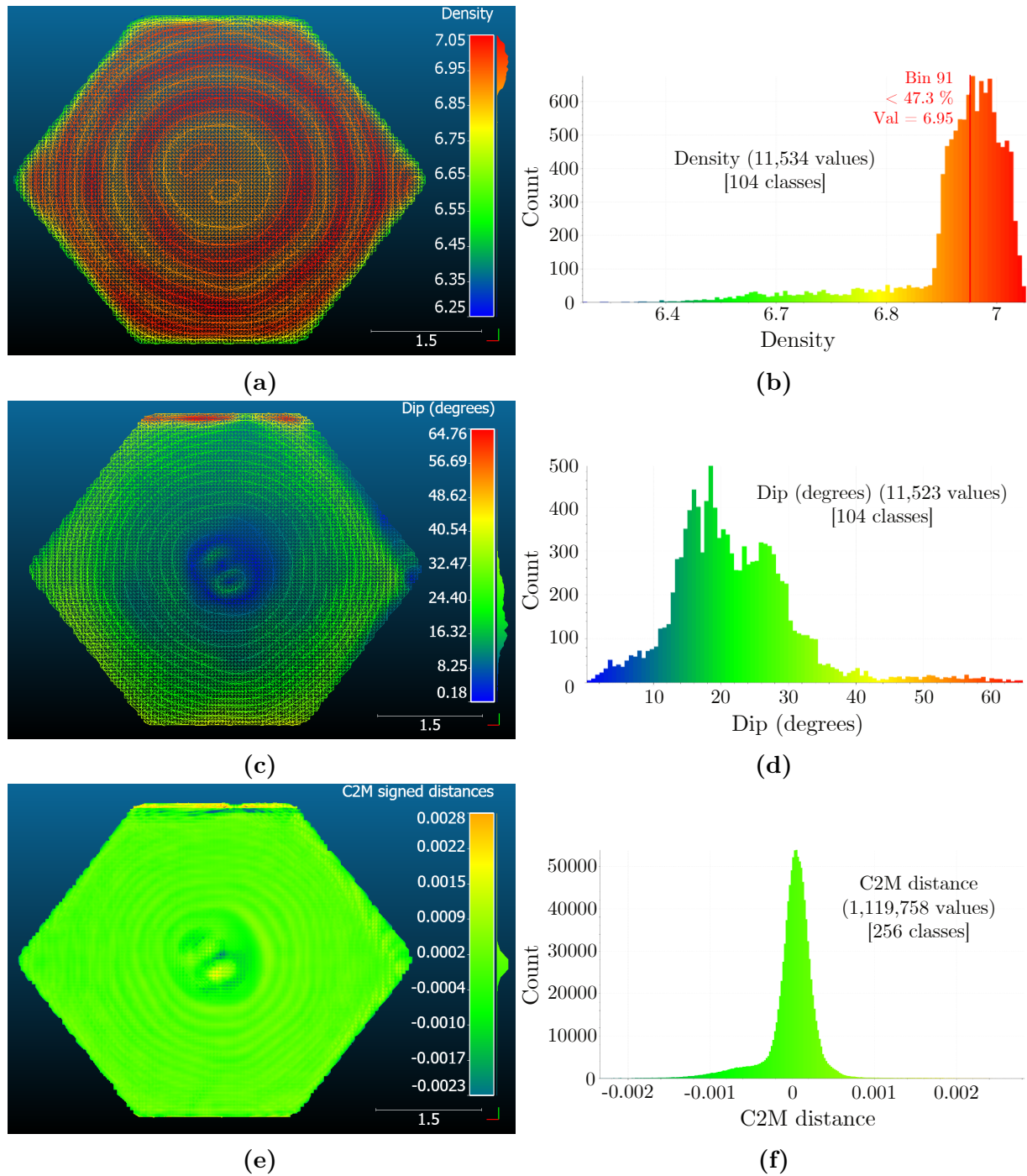


Figure 6.41: Reconstruction analysis of one molded optics (mold's position B2) using a Poisson approach: (a) and (b) density properties; (c) and (d) angles of the facets; (e) and (f) C2M comparison between the point cloud measured and the associated mesh.

We then performed ray tracing using the AM0 source, with 500,000 incident rays on the hexagonal optical aperture, see Figure 6.42. It can be seen from the top view (top-right) that on the edges of the reconstructed surface a portion of the rays are not incident on the cell (i.e., detector); as was evidenced previously in the case of the mold. Also from the

lateral view (right-bottom) it can be clearly noticed how the surface shows irregularities of the shape on the edges of the surface. This has also been evidenced during the recognition of the quadratic shape with the least squares method, where the 3D form of this optical unit could be recognized using 85% to 90% of the segmented point set.

In addition, the irradiance maps can be seen in Figure 6.43, with red dotted line indicating the ideal spot shape (i.e. of the parametric model) at each of these focal distances. In these the generated spot distributions tend to approximate the expected shapes, knowing that shape defects notably at the edges influence the spot contours to some extent. If we compare the flux perceived in the plane at -0.19 mm (z) from the focal with the parametric ideal (i.e. 0.01876 W), it corresponds to 81.2% of the total flux. A slight decrease of 0.64% of the latter can also be observed when approaching -0.05 mm (z) of the focal.

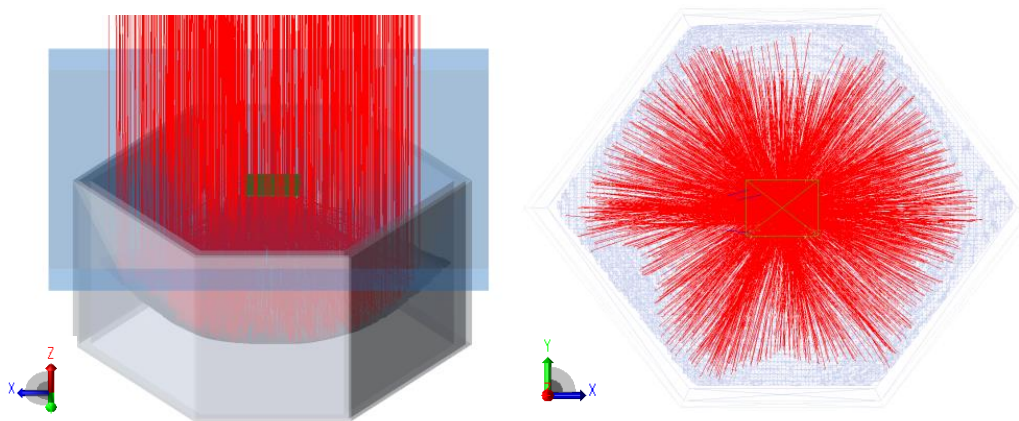


Figure 6.42: Ray-tracing optics.

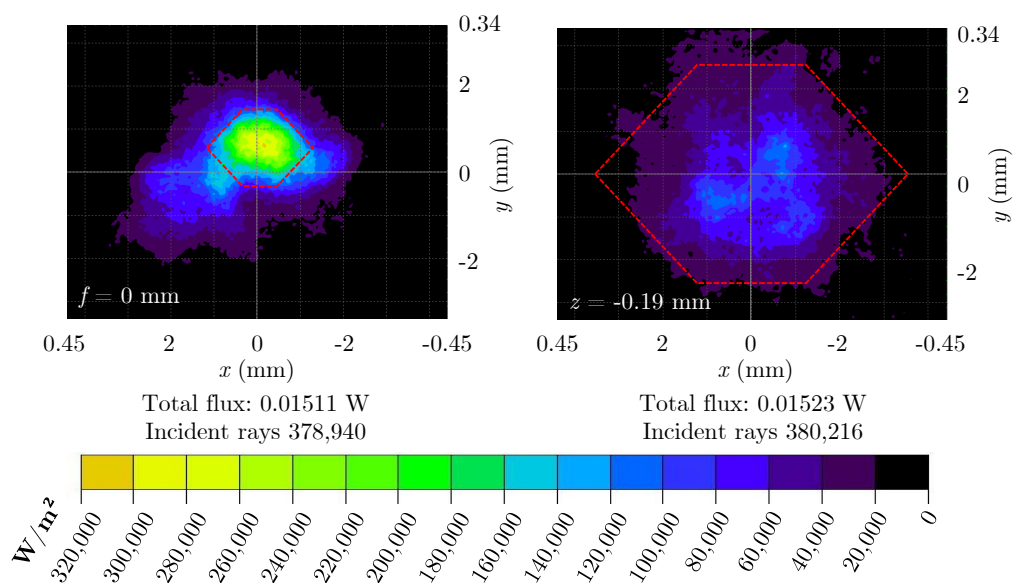


Figure 6.43: Ray-tracing optics map.

6.5.3 Analysis and conclusions of recognition method

In estimating the optical efficiency of the developing optical surface, we first determined the position of the optimal measurement plane with respect to the focal (along the z-axis) to study the spot distribution. Knowing that the optimal distance of interest should maximize the perceived flux as well as the spot size to obtain as much detail as possible of the shape and distribution of the flux. For this, we considered a parametric model and compared it with meshed models using different number of facets considered, between 1,000 and 20,000. It was observed that this plane is located at -0.19 mm from the focal and that using between 10,000 and 20,000 facets, and 500,000 traced rays. In this regard, it is possible to obtain both the flux distribution and the total flux closer to that obtained with the ideal parametric model, with errors of 0.1% and 0%, respectively with 500,000 rays. While the use of a lower number of facets would imply both flux and irradiance distribution losses of, for example, 6.8% and 0.5% of the perceived flux, for 1,000 and 5,000 facets, respectively.

We then proceeded to perform the reconstruction of the mesh using the set of measured points (previously segmented), from a mold unit and a fabricated optic, via Poisson's technique. In the reconstruction of the mold, it was observed that the generated mesh is accurate with respect to the point cloud, with a deviation of the average distance between these entities of 500 nm, that is, 2.2 times less than the precision of the overlay method ($Rq = 1100$ nm). While for the mold this was 900 nm or 1.2 times less.

It was also seen that both reconstructions have a maximum deviation of about 3 μm , located at the edges and the center of the surface, places where the topography has the most abrupt angular changes. In this respect, the spatial distribution of the angles of the triangles used in the meshing were analyzed. It was found that at the edges the maximum angles are reached, both for the mold and for the optics, 67° and 65° respectively. While mostly near the center of the surface the minimum of about 0.1° is observed for both the mold and the optics. It was also evident that the mean of the angles of these surfaces was approximately 22° with a standard deviation of 9° .

Then, a ray-tracing of the reconstructed meshes was performed using an AM0 solar source and 500,000 rays. It was observed that the irregularities seen at the edges, from the reconstruction, of both surfaces, presented difficulties in focusing, as expected. We then moved on to the estimation of the optical efficiency compared to the ray tracing of an ideal parametric model with the same solar source. It was then found that the mold has an optical efficiency of 87.4%, while for the molded optics it was 81.2% (i.e. about 7% less), see Figure 6.44. This difference in efficiency estimation, between the same mold unit and the fabricated optics, is believed to be linked to molding errors such as silicone shrinkage.

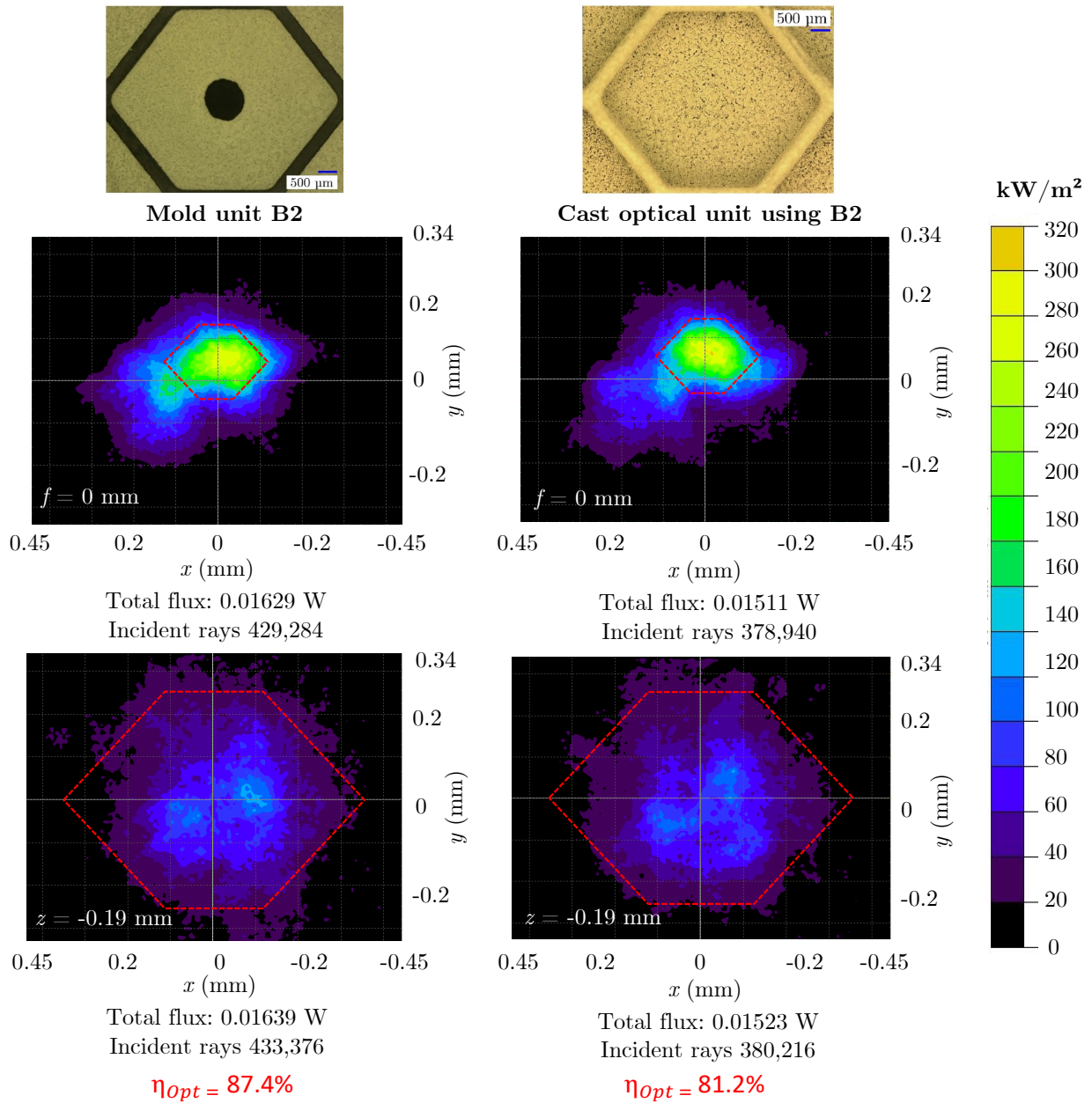


Figure 6.44: Optical efficiency comparison between a mold unit (B2) and its relative molded optical unit.

Thus, in the reconstruction of a quadratic shape it has been shown that using Poisson's method it is possible to obtain reliable meshes. And that the resulting surfaces can be adapted to estimate its optical efficiency via ray-tracing. In turn, in the estimation of the optical efficiency of both surfaces, errors of 12.6% and 18.8% are evidenced, for the mold and the optics, respectively, for which the nature of the associated error comes from different sources. On the other hand, the proposed method, which uses a matting coating to enhance contrast, induces both an over-thickness of 8.8 μm and a roughness Rq of about 1100 nm (i.e., for 8 applied layers), on the surface under study, which induces

biases in the topography measured by optical microscopy.

Therefore, it could be evidenced that the mold presents some manufacturing, polishing and scratching errors, especially located on the edges of the optical unit. The latter, in turn, transmits the surface defects to the molded optics, as seen in Figure 6.44, in which the spots generated by both optical surfaces (mold and optics) tend to have a similar shape, which is somewhat close to the idea (in dotted red line), both for the focal plane $f = 0$ mm and for one located at $z = -0.19$ mm.

Finally, the developed method allows to characterize the shape errors of the optics, as well as surface defects > 10 μm , however it is not useful in the measurement of smaller defects, such as the roughness of the optical surfaces, since the coating used covers these. Consequently, the characterization of the optical performance can only be done on the complete module with measurements under irradiation, using the interconnected cells on the coverglass, which could not be done in this thesis due to lack of time. Therefore, this is among the future work to be developed.

Conclusion and perspectives

In this thesis, we have investigated the relevance and feasibility of new microscale photovoltaic concepts, i.e. micro-CPV, for space applications, in order to study the performance advantages of micro-CPV technology to achieve high optical efficiencies and high specific and volumetric power densities. A number of scientific questions have arisen in this regard, about optics, materials and their compatibility and stability with respect to the environment, as well as the integration of the array into an efficient and lightweight photovoltaic module.

To address some of these questions, a review of the state-of-the-art of CPV systems was first carried out, highlighting some methods to achieve more efficient photovoltaic technologies, including not only new geometries, but also the effect of different materials and tailored structures. It was seen that compared to previous CPV systems for space applications with $> 1 \text{ cm}^2$ solar cells, micro-CPVs ($< 1 \text{ mm}^2$ cells) have the potential to reduce optical profile and mass, providing passive thermal management with medium concentration levels ($< 100X$). Reflective and refractive optical systems were studied, both of which have great potential, although challenges remain to be overcome before they can be successfully deployed in space. To this end, semiconductor technologies were seen to be crucial in micro-CPV development, for miniaturization, additive manufacturing, parallelization and self-alignment of arrays composed of thousands of interconnected semiconductor devices.

We then moved on to assess the specific missions and environments suitable for deploying CPV in space and providing a real advantage over other power sources. Thus, it was found that these systems provide inherent protection to active photovoltaic cells against the high fluxes of high-energy charged particles found in Earth's orbits and around the Jovian and Kronian systems, making CPV well suited to power these missions. At large distances, up to five astronomical units, the effects of low irradiance and low temperature degradation (LILT) can be mitigated using CPV systems by increasing the effective irradiance and operating as if closer to the Sun. This is perhaps one of the most suitable environments for CPV, and its development could improve the application of PV at remote distances as far away as Jupiter, Saturn and their moons; and perhaps in the distant future even beyond. However, CPVs have some limitations and challenges, if used in dusty environments (e.g. Venus, Titan and the stormy climate of Mars), as particles scatter sunlight and deposit

on the optics, which disables light transmission to solar cells; and necessitates the use of dust mitigation technologies that have not been effectively deployed to date. In addition, missions with temperatures above 523 K and solar irradiances above 3000 W/m² tend to limit the lifetime and efficiency of CPVs and thus their applicability.

Having established the spectrum of favorable environments for CPV, highlighting the type of missions that could be addressed with this technology and the challenges to be faced, we moved on to the exploration of two different CPV concepts. A first approach in the design of a CPV involved the re-conception of a CPC based on a previous design, with the objective of evaluating whether it can be improved. For this purpose, a multilevel optimization was performed, from the redesign of the optical system by ray-tracing to maximize the sunlight flux over the receivers, through the fabrication molding process, to the integration of low-cost silicon-based (III-V/Si) solar cells. After being optimized, an increase in optical efficiency of 19% theoretically and 12% experimentally was observed, for a measured optical efficiency of about 80% and a concentration factor that went from 7.6X to 8.6X; leading to a specific power of about 20 W/kg. However, the latter is not in line with current expected metrics for solar panels seeking specific powers > 100 W/kg to overcome CIC, mainly due to the excessive mass used in the optical system, which represents about 90% of the total weight of the prototype.

Then, a new concept based on a miniaturized mirror highly integrated inside a honeycomb core sandwich panel has been proposed, with the objective of increasing the specific and volumetric power of a micro-CPV. While providing a monolithic structure that avoids deployment in space, between the optical network and the cells, decreasing the associated risk and complexity; whereas the honeycomb provides rigidity and keeps the optics and solar cells separated and allied.

Furthermore, to establish an adapted reflector system for micro-CPV in space, in terms of angular and mechanical tolerances and flux uniformity, a comparative study of two idealized systems, a parabola with different defocusing planes and an optimized free-form was performed. In this regard, even if the free-form reflector can largely guarantee the minimum angular tolerance criteria established when using an SOE, it presents a spot with a PAR about 21% higher than the parabola, and more importantly it implies a higher complexity in manufacturing. The parabolic reflector, therefore, proved to be an efficient solution in terms of flux homogeneity, as well as in terms of manufacturing simplicity. For this reason, the latter design was chosen to validate the concept of a highly integrated reflector in a honeycomb.

Once integrated, the predominant optical losses of the micro-CPV were studied, considering reflection, absorption and scattering losses. This presented an estimated optical efficiency of around 82%, which considering an ARC on both sides of the cover glass and optimized interconnection lines could be increased up to 88%. Thus, in terms

of angular tolerance it was found that the optimal detection plane to locate the cell and guarantee the minimum angular tolerance criteria (uniaxial $> 4^\circ$, and bi-axial $> 2.5^\circ$), is located at -0.15 mm along the z -axis, which in turn has an estimated PAR of about 7. Finally, the short-circuit current density (J_{SC}) of each junction was estimated from EQE measurements, from which it could be observed that the central subcell is the limiting one with a current of approximately 2.26 mA. In addition, an $SMR = 1.15$ was found.

To move from a theoretical concept to a validated prototype with industrial potential, we proposed a molding method for the fabrication of optics integrated directly into a honeycomb. First, a one-step, double-layer composite lamination method was developed to maximize the usable surface area to its full extent. Second, the cross-linking of polymer silicone was studied, by DSC analysis to ensure complete cross-linking of the components. Third, a mold was designed and fabricated to cast 30 units of parabolic reflectors, about 40×40 mm², i.e., half of a standard space solar cell. The mold was characterized, from its surface roughness and dimensional analysis, to an identification and measurement of the permanent and removable surface errors of each unit, it was observed that the maximum attained surface defects is about 1.7% and 2%, respectively, to a total of about 4% of the surface. Finally, several pre-industrial mini-modules were fabricated from composite lamination to silver reflective coating.

For characterizing the surface and shape defects of an optical surface (at millimeter scale) and thus estimating its optical efficiency, a characterization method has been developed, which is based on topographic measurements by optical microscopy combined with ray-tracing simulations. First, the proposed method, which uses a self-evaporating scanning coating to enhance the contrast of the measured surfaces, was characterized. Experimentally, it was observed that the use of 8 spray layers is the optimal compromise for a coating thick enough ($8.8 \mu\text{m}$ $2\sigma = 0.25 \mu\text{m}$) to cover most of the surface (96.5% $2\sigma = 0.8\%$), but not too thick to mask the surface defects we are trying to characterize. Then to study the limits of the proposed technique we found that the average roughness Rq generated by the 8 layers is 1100 nm, i.e. the noise associated with the measurement, while the maximum deviation Rz was 1700 nm, on average. We can therefore detect defects of the order of 4-5 μm in size. Finally, a maximum measurement time of 30 min was set to reduce the risk of local sublimation and to ensure a homogeneous coating.

Next, the shape of a mold unit, and an optical unit manufactured with it, was analyzed in two steps. First, a recognition of the topography (quadratic shape) described by the measured point cloud was performed by means of a least squares fit. In addition, a reconstruction of the optical shape was performed using a Poisson algorithm, which is then used in the estimation of the optical efficiency by ray-tracing. The correlation between shape recognition and shape reconstruction showed that in both cases, the edges of the optical unit (between 5% and 15% of the total surface) show deviations from the ideal

shape, corresponding largely to manufacturing errors (e.g. polishing and scratching) on the mold especially located at the edges. These can also be associated to some extent to the over-thickness, roughness and homogeneity of the applied coating, however their respective contributions have not been dissociated.

Finally, a ray-tracing of the reconstructed meshes was performed using an AM0 solar source and it was then found that the mold has an integration quality of 87.4% with respect to the ideal, while for the molded optics it was 81.2%, i.e. 7% less. This difference in quality estimation, between the same mold unit and the fabricated optics, is believed to be linked to molding errors such as silicone shrinkage.

The end of the research work carried out leaves some open questions that could be addressed in future work, such as: (*i.*) To finish the optical part, the parameters and deposition method of the reflective coating used could be optimized to achieve high optical performance, i.e. reflectivity $> 90\%$. It is necessary to be able to study the deposition techniques and their impact in terms of optical performance and also their durability with respect to spatial constraints (chemical stability, mechanical resistance linked to differential expansion during thermal cycling, radiation sensitivity, etc.). (*ii.*) In addition, another way to improve the optical efficiency of this system is to optimize the interconnection lines used to reduce the shading they generate.

(*iii.*) The direct continuation of the work carried out consists in the integration of interconnected cells for the realization of a complete module and to characterize its efficiency. This result could not be achieved due to lack of time during the thesis, but it will allow to complete the study of this solution in terms of performance. Considering the estimated efficiencies of the integrated system, from the optical efficiency, uniformity, angular acceptance and misalignment, these must be confronted with the measurements of the final device integrating the coverglass and the interconnected cells.

(*iv.*) Since the target application of the proposed micro-CPV technology is space applications, a series of qualifications should be carried out to study the different degradation phenomena of the materials used, with respect to the environmental conditions studied in the Chapter 2, such as degassing, thermal cycling, vibration, among others aging studies according to the stress factors encountered in the spatial environment. Finally, the investigation of this type of system in a space environment will allow validation of the design and technological choices.

Glossary

AA Acceptance Angle 137

AR Aspect Ratio 14, 39, 42, 139, 140

CR Concentration Ratio 39

FF Fill Factor 74, 125, 136, 142

I_{SC} Short-circuit current 25, 77, 78, 125, 126

J_{SC} Short-circuit current density 136

P_{MAX} Maximum power 25, 77, 78

P_{MPP} Power at the Maximum Power Point 125

RMS Root-Mean-Square 205, 206, 214

V_{OC} Open-circuit voltage 77, 78, 125

C_g Geometrical concentration ratio 17, 19

P_a Power on the aperture area 19

P_r Power on the receiver 19

3J Triple-Junction 11, 28, 39, 68, 69, 75, 85, 108, 109, 281

AM0 Air Mass "zero atmospheres" 14, 44, 45, 64, 71, 73, 77, 93, 98, 106, 109, 123

AM1.5D Air Mass coefficient, 1.5 atmosphere thickness (Direct) 32, 36, 45, 123

ARPA-E's Advanced Research Projects Agency-Energy (US) 29

ASTM American Society for Testing and Materials 44, 46, 47, 109

ATOX ATomic OXygen 54, 97

AU Astronomical Units 45, 52, 64, 70–73, 75, 85, 98, 135

BOL Beginning-of-life 69, 75–77, 85

- BRDF** Bidirectional Reflectance Distribution Function 160
- BSDF** Bidirectional Scattering Distribution Function 159, 161
- BTDF** Bidirectional Transmittance Distribution Function 161
- C2M** Cloud-to-Mesh 214
- CAD** Computer-Aided Design 108, 133, 214, 215, 218, 238, 295
- CEA** French Commission for Atomic and Alternative Energies 29, 103, 292
- CFRP** Carbon Fibres Reinforced Plastic 133, 178, 182, 187, 266, 295
- CNES** *Centre National d'Etudes Spatiales* 103, 292
- CPC** Compound Parabolic Concentrator 21, 26, 103, 104, 106, 292
- CPV** Concentrator PhotoVoltaics 13, 17, 19, 21, 23, 25, 27, 29, 31, 33, 35, 37, 39, 41, 52, 93, 103, 282, 283, 292
- CTE** Coefficient of Thermal Expansion 33, 36, 55, 93
- CTM** Cell-to-Module ratio 14, 19, 123
- DFD** Depth-From-Defocus 197
- DNI** Direct Normal Irradiance 19
- ECSS** European Cooperation for Space Standardization 46, 76
- EDM** Electrical Discharge Machining 188, 191
- EL** ElectroLuminescence 120
- EOL** End-of-life 76, 77, 94
- EPD** Energetic Particles Detector 82, 83
- ESA** European Space Agency 12, 46, 48, 50, 56, 69, 72, 73, 76, 86
- ESD** Electro-Static Discharge 47, 57
- ESR** Electro-Slag-Remelting 188
- EVA** Ethylene-Vinyl Acetate 178
- GEO** GEosynchronous Orbit 48, 54–59, 93, 97
- HIHT** High Intensity and High Temperature 66, 69, 70

- ISO** International Organization for Standardization 48
- ISS** International Space Station 12, 58, 98
- JAXA** Japan Aerospace Exploration Agency 69
- JPL** Jet Propulsion Laboratory 50, 52, 53, 60, 76, 81, 87
- JUICE** JUPiter ICy moons Explorer 74–76, 86
- LANL** Los Alamos National Lab 57
- LEO** Low Earth Orbit 48, 54–57, 93, 97, 98
- LILT** Low Intensity and Low Temperature 10, 38, 65, 73–78, 84, 85, 97–99
- LIRT** Low Intensity and Room Temperature 85
- MEO** Medium Earth Orbit 54–58, 93
- MJSC** Multi-Junction Solar Cells 11, 13, 14, 25, 29, 33, 74, 104, 108, 116, 129, 142, 292
- MUSCAT** Multi-Utility Spacecraft Charging Analysis Tool 48
- NASA** National Aeronautics and Space Administration (US) 12, 46, 48, 50, 52, 53, 55, 56, 60, 61, 71–74, 79, 86, 87
- NASCAP** NASA Charging Analyzer Program 48
- NREL** National Renewable Energy Laboratory 11, 23, 108
- NRL** US Naval Research Laboratory 42, 50, 133, 286
- ONERA** (*Office National d'Etudes et de Recherches Aéropatiales*) 76
- PAR** Peak-to-Average Ratio 136, 137, 140–142, 165
- PASP+** Photovoltaic Array Space Power Diagnostics Plus 23, 25
- PC** PolyCarbonate 20, 21
- PDMS** Polydimethylsiloxane 20, 33, 34
- PET** PolyEthylene Terephthalate 22, 23
- PMMA** PolyMethylMethAcrylate 20–23, 30, 31, 41
- POE** Primary Optical Element 13, 30–32, 282
- POES** Polar Orbiting Environmental Satellites 57

- PTFE** PolyTetraFluoroEthylene 178
- PV** PhotoVoltaic 14, 19, 26, 32, 34–36, 41–44, 51, 52, 54, 65, 66, 71, 89, 94, 95, 97, 109
- PVA** PhotoVoltaic Arrays 10, 11, 23, 43, 44, 46, 47, 50–52, 65, 72, 76, 85, 93–95, 97–99, 131, 281, 287, 288
- PVB** Poly Vinyl Butyral 178
- RANSAC** RANdom SAmple Consensus 213, 277
- RJ** Radius of Jupiter 75, 76
- RTG** Radioisotope Thermoelectric Generator 10, 52, 73, 78, 84, 99
- SCA** Solar Cell Assembly 11
- SCARLET** Solar Concentrator Array with Refractive Linear Element Technology 25, 26, 98
- SLA** Stretched Lens Array 26, 27
- SOE** Secondary Optical Element 13, 26, 30, 31, 137, 282
- SoG** Silicone-on-Glass 21, 37
- SOHO** Solar and Heliospheric Observatory 72
- SPENVIS** Space Environment Information System 48, 50
- SREM** Standard Radiation Environment Monitor 56
- STEX** Space Technology Experiment spacecraft 27
- TIR** Total Internal Reflection 106, 107, 112
- TPU** Thermoplastic PolyUrethane 178
- TRL** Technology Readiness Level 29, 36
- UV** Ultraviolet 32, 33, 37
- UVR** UV-reflective dielectric coating 37
- WPV** Wafer-integrated microscale PhotoVoltaic 33, 34

Annex A: Scientific contributions

A1: Published journal articles

1. A. Bermudez-Garcia, P. Voarino, and O. Raccurt. “Environments, needs and opportunities for future space photovoltaic power generation: A review”. In: Applied Energy 290 (2021), p. 116757. <https://doi.org/10.1016/j.apenergy.2021.116757>

A2: Patent

Title: "Concentrateur optique à structure alvéolaire"

Registration number: FR201385

Filing date: 21/12/2020

Inventor(s): A. Bermudez-Garcia, P. Voarino, and O. Raccurt

Submitter(s): CEA

A3: Proceedings articles

1. A. Bermudez-Garcia et al., "First space concentrator prototype using III-V/Si cells," 2019 European Space Power Conference (ESPC), 2019, pp. 1-7, Oral presentation and published proceedings IEEE, doi: 10.1109/ESPC.2019.8932066.
2. A. Bermudez-Garcia et al., “Optics Development and Demonstration of Line-Focus Space Concentrator Prototype Using III-V/Si Cells” (EU-PVSEC 2020 oral presentation and published proceedings IEEE).
3. P. Voarino, A. Bermudez-Garcia, A. Chehade, R. Couderc, “Development of an External Quantum Efficiency Method to Characterize Solar Cells with a Micro Spot: Applied to Micro-Concentrated Systems”, doi: 10.4229/EUPVSEC20202020-5BO.15.5. EU-PVSEC 2020 oral presentation and published proceedings IEEE.
4. V. Vareilles, A. Bermudez-Garcia, J. Francois, Y. Veschetti, M. Amara, P. Voarino, F. Chabuel, "First Mechanical Study on Lightweight Microconcentrators Systems

for Space Applications”. In: 2021, published proceedings, pp. 1101–1105. url: www.eupvsec-proceedings.com.

5. V. Vareilles, A. Bermudez-Garcia, J. Francois, Y. Veschetti, M. Amara, P. Voarino, F. Chabuel, "Influence of the thermally induced deflection of a space micro-concentrator photovoltaic array on its optical performances using finite element method", oral presentation accepted (pending proceedings), CPV-18 and TPV-13 Conferences, April 25-27, 2022. Hosted by the University of Miyazaki, Japan.

A4: Posters

1. A. Bermudez-Garcia, P. Voarino, and O. Raccurt. “Micro-concentrator for space applications”. PVSchool2020 at Les Houches (Alps), France, 1-6 March 2020. And attendance to 25 hours of courses (lectures and tutorials).
2. P. Voarino, A. Chehade, A. Bermudez-Garcia, Y. Roujol, F. Chabuel, R. Couderc, "Advanced characterization for micro-concentration systems", Journées Nationales du PhotoVoltaïque (JNPV), 2020, Dourdan, France.

A5: Other participations

1. Oral presentation at the SPECIAL PV Workshop: "Viability of solar power in various space environments" - November 23rd - 24th Space Photovoltaics for Energy Conversion in extra-terrestrial environment

Annex C: III-V on Si solar cell manufacturing process

Two terminal triple junction III-V/Si cells used in this study were fabricated according to the following:

1. N-on-p GaInP/GaAs subcells were grown lattice matched in inverted configuration on 4-inch GaAs substrates at Fraunhofer-ISE, as described in [376].
2. The optimized Si bottom subcells were manufactured separately at the CEA (LETI-LITEN collaboration), by deposition of 100 nm LPCVD n+ poly-Si at the front surface and PECVD p+ poly-Si/SiN at the rear surface [377], on double side polished 4-inch p-type FZ Si substrates.
3. After surface preparation, III-V and Si surfaces were bonded together using Surface-Activated Bonding (SAB) technique [378].
4. GaAs substrate was removed by wet chemical etching. Finally, processing into 1.5 x 13 mm² and 2 x 2 cm² cells was performed by front metallization, mesa etching, SiN/SiO₂ anti-reflective coating deposition, rear metallization [379].

The resulting cells are composed by GaInP (1.90 eV)/ GaAs (1.42 eV)/ Si (1.12 eV), a schema of a cell is shown in Figure A2. Cells exhibited 30.0% and 25.7% power conversion efficiency under AM1.5D and AM0 respectively. IV performance under AM0 reference spectra is carried out at CEA laboratories [379].

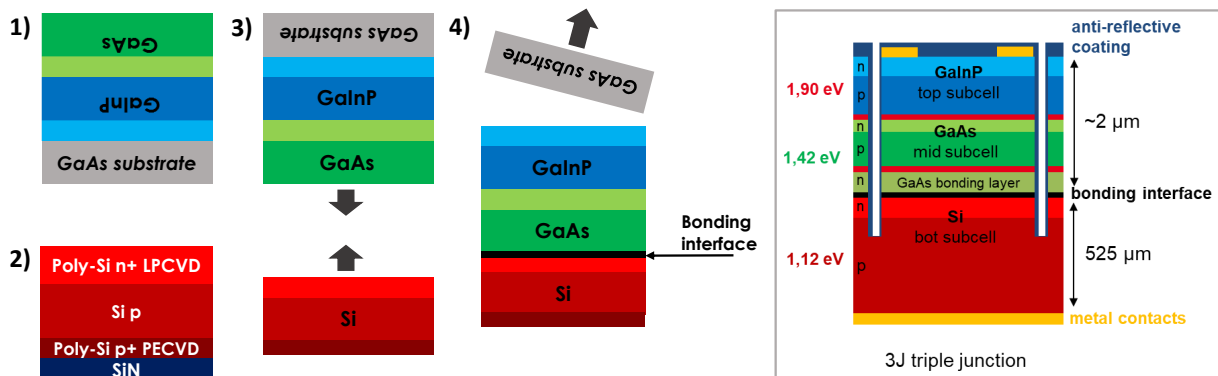


Figure A2: III-V/Si solar cell fabrication process: 1) GaInP/GaAs subcells growing in a lattice matched inverted configuration on a GaAs substrate, 2) Si bottom subcell; 3) GaInP/GaAs and Si bonding; 4) GaAs substrate removal.

Annex D: Flexural stiffness evaluation of the proposed micro-CPV design by bending tests

Considering a sandwich structure and beam theory for a 2D model, the bending stiffness (D) of a symmetric sandwich beam with a shear stiffened core and made of isotropic materials is given by Equation 6.13, as defined by Howard G. Allen [380]. This is composed of three terms, the first one is the bending stiffness of the faces around the central axis of the sandwich, a second one corresponding to the stiffness of the faces around their own central axis and a last one which is the stiffness of the core around the central axis of the sandwich.

$$D = \frac{E_f b t_f d^2}{2} + \frac{E_f b t_f^3}{6} + \frac{E_c b c^3}{12} \quad (6.13)$$

where the elastic modulus of the faces and the core are E_f and E_c , respectively, b is the width of the beam, t_f ; c are the thicknesses of the faces and the core respectively and d is the distance between the central axes of the faces; $d = c + t_f$; see Figure A3.

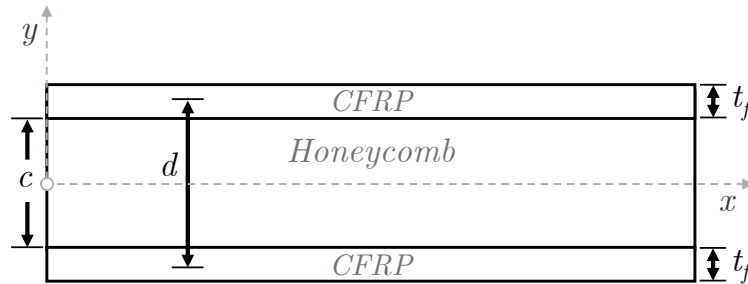


Figure A3: Stiffness of a honeycomb sandwich architecture.

In the stiffness calculation, we have considered that the faces are "thin", therefore we can disregard the second term of Equation 6.13. In addition, we considered the core as "weak" so we can neglect the third term of the equation. To compare specimens with different geometries, we present D_n , the bending stiffness divided by the width (b) of the specimens, while the specific bending stiffness D_ρ , is D_n divided by the areal density of the samples.

Then, based on the resulting expression and the mechanical properties/data of standard panels (about 20 mm thick) reported in the literature [348, 381], we have calculated a target bending stiffness D_n ranging from 4.9 to 5.6×10^6 N·mm. In this regard, we have considered the maximum stiffness of the panel (20 mm thick) as a benchmark of 5.6×10^6 N·mm [348], which has a specific stiffness of 1.6×10^3 N·m³/kg.

Recently, a first mechanical study has been carried out by Vareilles *et al.* [347] using the dual-stage architecture we proposed, in which the influence of several parameters on stiffness, stiffness-to-weight ratio and failure modes is studied. The bending stiffness and failure of 12 different structures (see Table A1) were studied using 4-point bending tests, and the

mass of the different components was determined to identify ways to lighten the structure without decreasing its mechanical properties. More particularly, the size and density of the honeycomb (bottom), the number of CFRP plies and the thickness of the glass were varied.

Table A1: Summary of tested configurations, with a fixed honeycomb thickness of 3 mm.

No. Configuration	Bottom honeycomb		Glass thickness (μm)	No. plies CFRP	Total thickness (mm)
	Cell size (mm)	Thickness (mm)			
1	4.76	10	300	2	14
2	4.76	10	400	2	14
3	4.76	10	500	2	14
4	4.76	10	300	4	14
5	4.76	10	400	4	14
6	4.76	10	500	4	14
7	6.35	20	300	2	24
8	6.35	20	400	2	24
9	6.35	20	500	2	24
10	6.35	20	300	4	24
11	6.35	20	400	4	24
12	6.35	20	500	4	24

Figure A4 shows the results of this study, illustrating the bending stiffness D_n (N·mm) and specific bending stiffness D_ρ (N·m³/kg) of each of the configurations studied. In addition, the horizontal dotted lines show the target values, in green D_ρ and in red D_n .

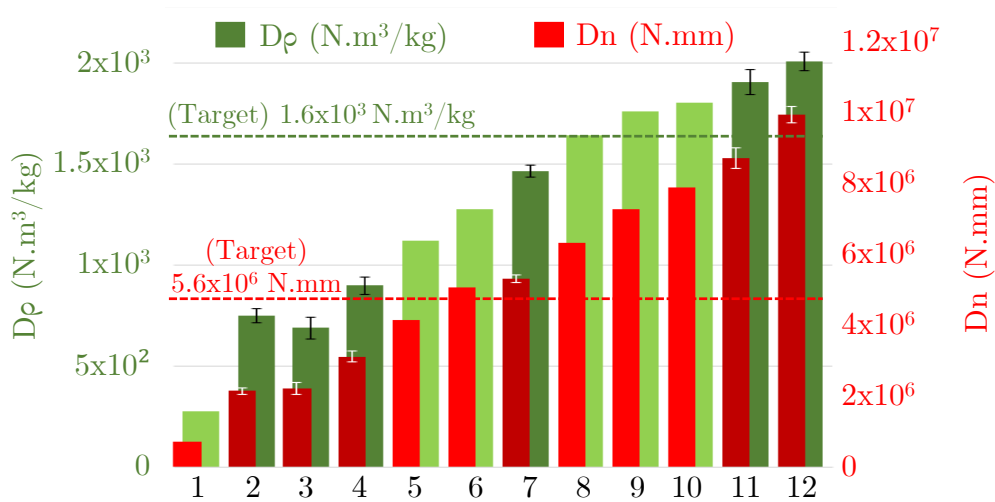


Figure A4: Stiffness measurements of different honeycomb sandwich architectures [347].

It was concluded that configurations with thicker glass (400, 500 μm) and thinner CFRP (2 layers) proved to be more efficient in protecting the cover glass and distributing stress (e.g. structure 2). However, decreasing the glass thickness and increasing the CFRP thickness is a good way to increase the specific stiffness, so a compromise is necessary.

Annex E: Some state-of-the-art pick and place machines

Table A2: Some state-of-the-art pick and place machines showing components per hour assembled and their accuracy in micrometers.

Equipment	Components per hour	Precision (μm)
Datacon 2200 evo advanced	-	3
Neoden 8	16,000	10
Ginkgoem SMT-W1	6,000	10
Ginkgoem SMT-Pi8	10,000	10
Neoden 3V Advanced	3,500 - 5,000	20
Europlacer XPii+ I	13,000	22
Yamaha YRM20	100,000	25
Yamaha YSM40 r	200,000	35
Europlacer Atom 4	78,000	50

Annex F: Mechanical properties tables

Table A3: Mechanical properties: HexWeb® CR III 5052 Hexagonal Aluminum Honeycomb.

Cell Size	Nominal Density pcf	Compressive					Crush Strength psi	Plate Shear					
		Bare		Stabilized				L Direction			W Direction		
		Strength psi		Strength psi		Modulus ksi		Strength psi		Modulus ksi	Strength psi		Modulus ksi
		typ	min	typ	min	typ		typ	min	typ	min	typ	
1/8	3.1	285	200	300	215	75	130	210	155	45.0	130	90	22.0
1/8	4.5	550	375	570	405	150	260	340	285	70.0	220	168	31.0
1/8	6.1	980	650	1020	680	240	450	560	455	98.0	340	272	41.0
1/8	8.1	1500	1000	1560	1100	350	750	800	670	135.0	470	400	54.0
1/8	10.0	2100p	1575p	2250p	1685p	-	-	980p	735p	175.0p	550p	415p	65.0p
1/8	12.0	2700	2100	2900	2200	900	-	1940l	1250l	-	1430l	1000l	-
5/32	2.6	220	150	240	160	55	90	165	120	37.0	100	70	19.0
5/32	3.8	395	285	410	300	110	185	270	215	56.0	165	125	26.4
5/32	5.3	690	490	720	535	195	340	420	370	84.0	270	215	36.0
5/32	6.9	1080	770	1130	800	285	575	590	540	114.0	375	328	46.4
5/32	8.4	1530	1070	1160	1180	370	800	760	690	140.0	475	420	56.0
3/16	2.0	160	90	175	100	34	60	120	80	27.0	70	46	13.3
3/16	3.1	290	200	335	215	75	130	210	155	45.0	125	90	22.0
3/16	4.4	520	360	550	385	145	250	330	280	68.0	215	160	30.0
3/16	5.7	820	560	860	600	220	390	460	410	90.0	300	244	38.5
3/16	6.9	1120	770	1175	800	285	575	590	540	114.0	375	328	46.4
3/16	8.1	1600	1000	1720	1100	350	750	725	670	135.0	480	400	54.0
1/4	1.6	90	60	100	70	20	40	85	60	21.0	50	32	11.0
1/4	2.3	190	120	210	130	45	75	140	100	32.0	85	57	16.2
1/4	3.4	340	240	370	250	90	150	230	180	50.0	140	105	24.0
1/4	4.3	500	350	540	370	140	230	320	265	66.0	200	155	29.8
1/4	5.2	690	500	760	510	190	335	410	360	82.0	265	200	35.4
1/4	6.0	990	630	1100	660	235	430	530	445	96.0	340	265	40.5
3/8	1.0	50	20	55	20	10	25	45	32	12.0	30	20	7.0
3/8	1.6	90	60	95	70	20	40	85	60	21.0	50	32	11.0
3/8	2.3	190	120	200	130	45	75	135	100	32.0	80	57	16.2
3/8	3.0	285	190	310	200	70	120	200	145	43.0	125	85	21.2
3/8	3.7	370	270	410	285	105	180	250	200	55.0	160	115	26.0
3/8	4.2	520	335	560	355	135	220	310	255	65.0	200	150	29.0

Test data obtained at 0.625" thickness. p = preliminary

x = predicted values

l = beam shear for 12.0 pcf products.

maximum block size 48 in. x 60 in., maximum thickness = 1.00 in.

Annex G: Measurement of coverglass roughness

The Bruker Dektak XT contact profilometer has been used to measure the roughness of the coverglass, shown in Figure A5. This profilometer has ISO compatibility of the two-dimensional (2D) profile ISO 4287 and 4288 standards through the Vision64® software, which is used to drive the Dektak-XT® StylusProfiler.

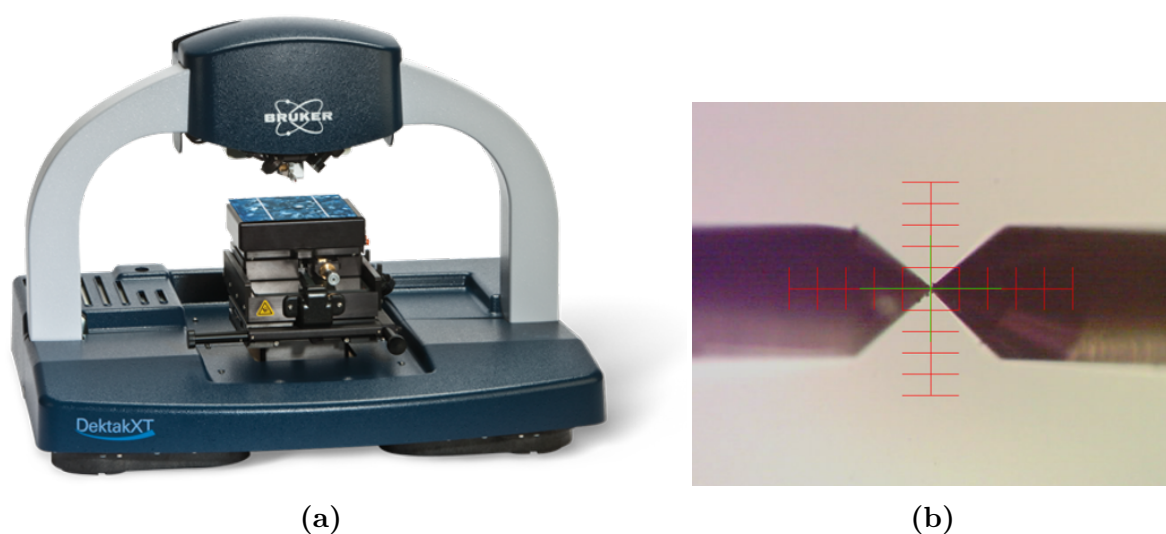


Figure A5: Description of data processing: (a) Picture of the instrument: Bruker Dektak XT Profilometer, (b) Stylus profiler used (2 μm radius).

Figure A4 illustrates the parameters used, from the scan resolution and length, to stylus type. As well as the ISO 4287 filtering type, and cutoffs used λ_c and λ_s , which respectively denote the long and short wave cutoffs.

Table A4: Coverglass roughness parameters.

Profilometric Measurement Chart		Evaluation Processing and Filtering	
Sample	Coverglass #3	Standard	ISO 4287
Profile	Hills & Valleys	Filter Type	Gaussian Regression
Scan Duration	120 s	Short Cutoff (λ_s)	0.8 μm
Scan Length	480 μm	Long Cutoff (λ_c)	0.08 mm
Scan Resolution	0.0133326 μm	Number Lengths	5
Scan Type	Standard Scan		
Stylus Force	1.44 mg		
Stylus Scan Range	6.5 μm		
Stylus Type	Radius: 2 μm		

Annex H: Irradiance maps for angular and mechanical misalignment

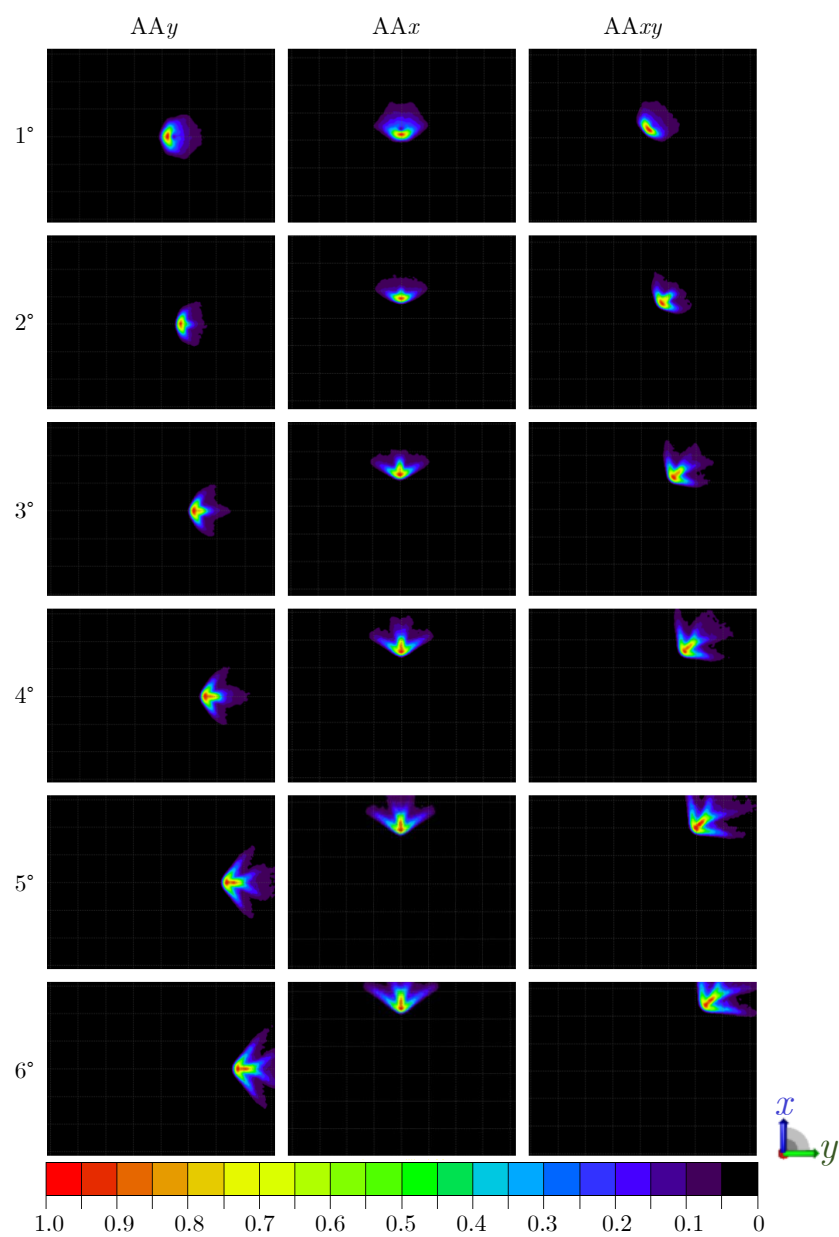
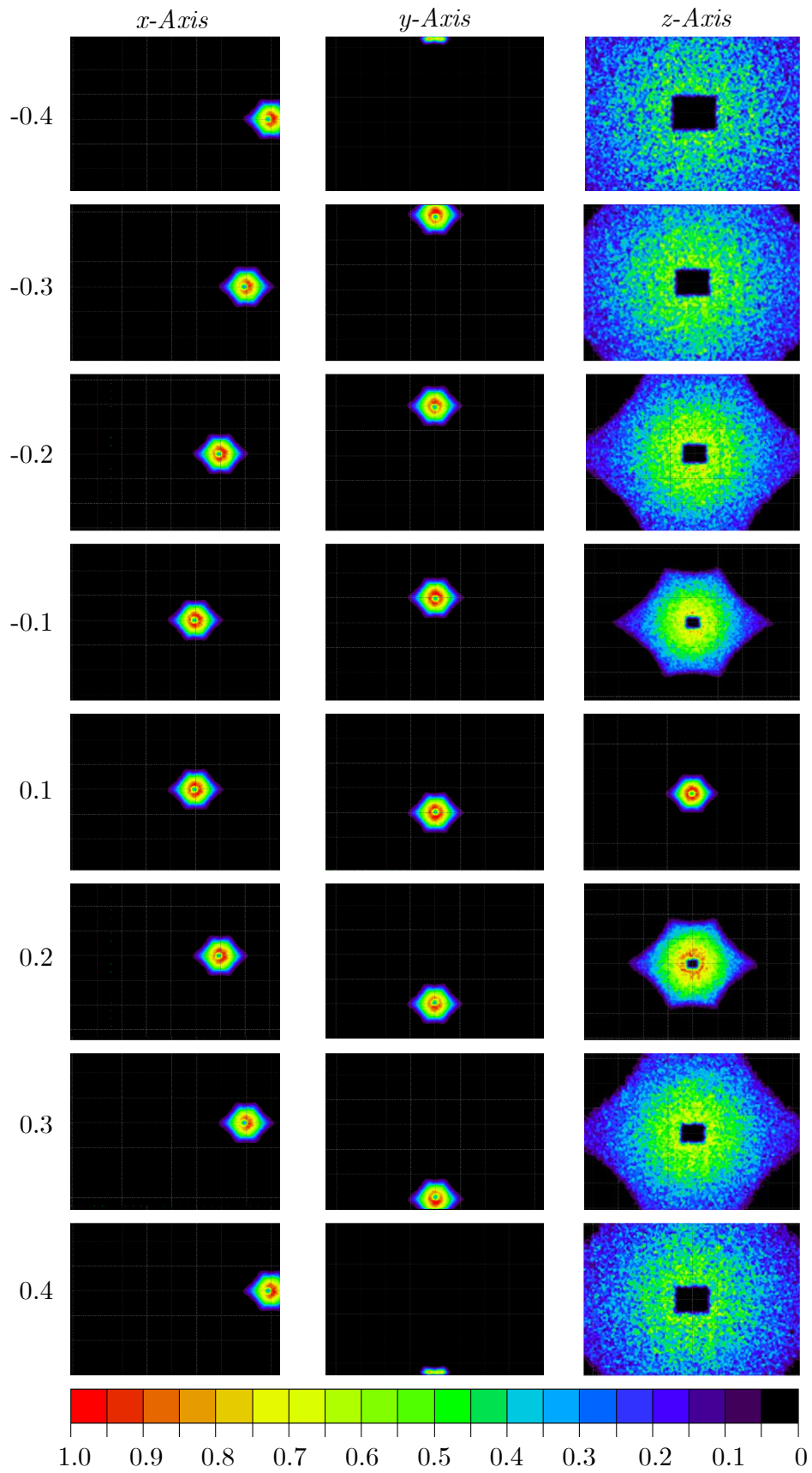


Figure A6: Total irradiance maps for deviated incident flux on solar cell ($885 \times 685 \mu\text{m}^2$) normalized to peak irradiance.

**Figure A7:** Alignment tolerance between cell and optics.

Annex I: Coating thickness and filled surface evolution for different number of spraying cycles

Table A5: Coating thickness and filled surface evolution for different number of spraying cycles.

No. of layers	Thickness measurements (μm)						Covered surface estimation (%)					
	1	2	3	Average	2σ	2 sigma/average	1	2	3	Average	2σ	2 sigma/average
1	1.52	1.73	1.41	1.55	0.33	0.21	44.0	39.2	45.0	42.7	3.1	0.1
2	3.05	3.46	3.21	3.24	0.41	0.13	61.6	55.8	61.5	59.6	3.3	0.1
3	3.61	3.84	3.69	3.71	0.23	0.06	65.5	73.4	72.2	70.4	4.3	0.1
4	4.10	4.20	5.01	4.44	1.00	0.22	82.5	83.0	78.2	81.2	2.6	0.0
5	4.69	5.75	4.71	5.05	1.21	0.24	86.5	88.5	91.9	89.0	2.7	0.0
6	5.60	5.41	6.32	5.78	0.96	0.17	89.3	92.3	94.1	91.9	2.4	0.0
7	7.31	7.60	7.79	7.57	0.48	0.06	93.9	94.7	96.2	94.9	1.2	0.0
8	8.89	8.74	8.64	8.76	0.25	0.03	96.9	97.0	95.5	96.5	0.8	0.0
9	9.43	9.86	9.16	9.48	0.71	0.07	97.7	94.7	96.8	96.4	1.5	0.0
10	10.03	10.52	10.68	10.41	0.68	0.07	98.8	97.3	96.1	97.4	1.4	0.0
11	12.50	12.20	12.80	12.50	0.60	0.05	98.9	98.4	97.4	98.2	0.8	0.0
12	13.70	13.80	14.20	13.90	0.53	0.04	99.0	97.9	99.3	98.7	0.7	0.0
13	16.50	17.30	16.80	16.87	0.81	0.05	99.8	99.7	99.8	99.8	0.1	0.0

Annex J: Bearing balls precision as defined by the American Bearing Manufacturers Association (ABMA)

<i>Grade and Tolerance - Metric (Millimeter)</i>				
ABMA Grade	Sphericity [mm]	Lot diameter variation [mm]	Nominal ball diameter toletance [mm]	Maximum surface roughness (Ra) [μm]
3	0.0008	0.00008	± 0.0008	0.012
5	0.00013	0.00013	± 0.0013	0.02
10	0.00025	0.00025	± 0.0013	0.025
25	0.0006	0.0006	± 0.0025	0.051
50	0.0012	0.0012	± 0.0051	0.076
100	0.0025	0.0025	± 0.0127	0.127
200	0.005	0.005	± 0.025	0.203
1000	0.025	0.025	± 0.127	

Annex K: Structures associated with the point cloud: octree

Originally, CloudCompare has been designed to perform a direct comparison between dense 3D point clouds. It is based on a specific octree structure that allows high performance when performing this kind of tasks, e.g. it took about 10 seconds to calculate the distances of 3 million points to a 14,000 triangle mesh on a laptop with dual core processor [371].

An Octree is a recursive, axis-aligned, spatial partitioning data structure commonly used in computer graphics to optimize collision detection, nearest neighbor search, etc. In the CloudCompare context, Octree is used by most processing algorithms (e.g., distance calculation, spatial operators, etc.). An octree is a tree-like data structure in which each internal node has exactly eight children [382]. The root cell of the octree encloses the entire world. The Octree is constructed by recursively subdividing the space into eight cells until the remaining number of objects in each cell is less than the predefined threshold, or the maximum depth of the tree is reached. Each cell is subdivided by three axis alignment planes, which are usually located at the center of the parent node. Thus, each node can have up to eight children.

Annex L: Point cloud artifacts and case study approach

In the following we summarize these properties in order to cover the basic principles underlying the surface comparison and reconstruction techniques used in this work. In particular we will concentrate on the most recurrent and impacting properties, including: a) sampling density, b) noise, c) outliers and d) misalignment (see Figure A8), which have been discussed in detail by Berger *et al.* [383]. In addition, the tools, algorithms and methods used in this work via CloudCompare will be briefly presented.

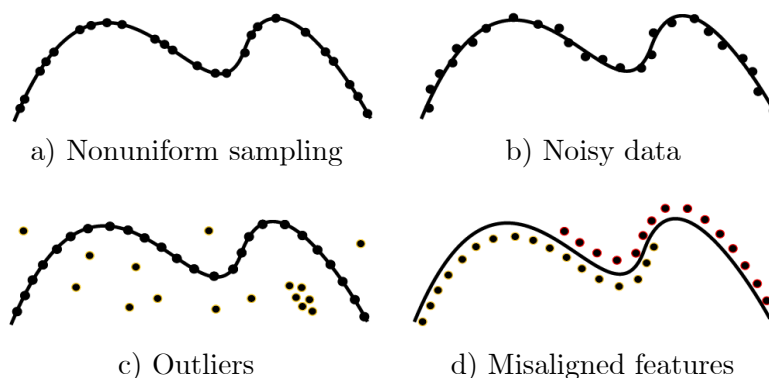


Figure A8: Different forms of point cloud artifacts: a) sampling density, b) noise, c) outliers and d) misalignment. Shown here in the case of a curve in 2D, modified from [383].

Sampling density

The distribution of the sampled points is defined as the sampling density, which is defined by its neighborhood, i.e. the set of points close to a given point that captures the local geometry of the surface. A neighborhood must be large enough to describe the local geometry, but small enough so that local features are preserved. When it is desired to decrease the number of points by "subsampling" a cloud, there are several methods, such as: i) Random, a specified number of points will be chosen randomly; ii) Spatial, a minimum distance between two points will be set, and then points from the original cloud will be chosen so that no point in the output cloud is closer to another point than the specified value. The higher this value, the fewer points will be kept; iii) Octree-based allows to select a level of octree subdivision at which the cloud will be "simplified", so that in each octree cell the point closest to the center of the octree cell is kept.

Noise data

This corresponds to randomly distributed points near the surface, based on a set of scan artifacts (e.g. sensor noise, depth quantization, etc.). Noise is introduced along the viewing path, and can be impacted by surface properties, including the scattering characteristics of the materials. In this regard, surface reconstruction algorithms seek to generate a surface that passes close to the points without conforming too closely to the noise. Some robust algorithms that impose smoothness on the output include Poisson reconstruction [374], as well as methods that employ robust statistics [384].

Outliers

These are points far from the real surface, and are usually due to structural artifacts in the acquisition process. Outliers are randomly distributed in the volume, their density can be variable, and they can occur as a result of false sight correspondences. Unlike noise outliers should not be used to infer the surface. One of the methods implemented in CloudCompare includes the use of a Statistical Outlier Removal (SOR) Filter, which uses point neighborhood statistics to filter out outliers. The algorithm runs through the entire input twice: in the first iteration it calculates the average distance each point has to its k nearest neighbors. Then, the mean and standard deviation of all these distances are calculated to determine a distance threshold. The distance threshold is described by 6.14. In the next iteration, points will be classified as "inlier" or "outlier" if their average distance between neighbors is less than or greater than this threshold, respectively.

$$(\text{max distance} = \text{average distance} + n \text{ Sigma} * \text{std. dev.}) \quad (6.14)$$

Misalignment

Except in the rare case where a scanning instrument is replaced at exactly the same position, the coordinate systems of the two clouds have a systematic error that is a complex function of the method used to reference the two clouds. In scanning scenarios where we are only concerned with the acquisition of a single object it is common for the object to rotate in place with respect to the sensor for each scan; therefore, the amount of misalignment is limited since the initial scan alignment can be estimated from known rotations; refer to Kaick *et al.* [385] for a survey on registration techniques. Three methods were used to roughly or finely align point clouds or meshes are:

- **Match bounding-box centers:** is the simplest method of point cloud registration, this translates all selected entities (point cloud data sets) so that their bounding box centers are mapped to the same location. For this, a 4x4 transformation matrix is used which corresponds to the translation applied between a selected reference entity (point cloud data) and a second entity will be mapped at the center of the reference data. This method is used as the initial alignment method, and is then refined using one of the following two techniques.
- **Iterative Closest Point (ICP):** so far, the only automatic method to register very finely two entities (clouds or meshes). This is one of the most popular methods for cloud data registration, of general purpose, representation-independent, for accurate and computationally efficient registration of three-dimensional shapes, including curves and free-form surfaces [386]. For this purpose the ICP algorithm estimates a rigid transformation between $p_i \in P$, a point in the reference 3D point cloud, and $q_i \in Q$, a point in the target point cloud. Figure XX shows the estimation of the correspondence between the data in the target point cloud P and the aligned ones Q .

The ICP method implements the computation of nearest neighbors and Euclidean distance and estimates the nearest point between p_i and q_i as matching points. To calculate the rotation R and translation t between p_i and q_i the ICP method uses an error function to minimize the sum of squared distances described by Equation 6.15.

$$E(R, t) = \min_{R, t} \sum_i \|p_i - (Rq_i + t)\|^2 \quad (6.15)$$

This method is usually efficient and may be sufficient to align the entities, however in case the associated error has not been minimized as expected the following method is used.

- **Selection of pairs of (equivalent) points or spheres:** is another powerful but simple tool for aligning two entities. It allows to choose several pairs of equivalent points (or spheres of given radius) in each cloud to be registered. Although the process is manual, it can be relatively fast and quite accurate (especially if there are registration spheres in both clouds, as this tool is able to detect their center automatically).

Annex M: Methods for comparing two models

In this work we have used two different methods to compare the models. We employed a direct cloud-to-cloud comparison (C2C) and cloud-to-mesh or cloud-to-model distance (C2M), both of which are briefly described below.

Direct cloud-to-cloud comparison (C2C)

The direct comparison of 3D point clouds is the simplest and fastest method, since it does not require data meshing or the calculation of surface normals [375]. A common way to calculate the distances between two point clouds is the "nearest neighbor distance": for each point of the compared cloud, the nearest point in the reference cloud is found and its Euclidean distance is calculated, see Figure A9 a). The comparison between two sets of points is commonly done by calculating the Hausdorff distance, which consists in calculating for each point p of a cloud S the distance to its nearest point in the other cloud S' :

$$d(p, S') = \min_{p' \in S'} \|p - p'\|_2 \quad (6.16)$$

It is also possible to use a "local modeling strategy" which consists in calculating a local model around the nearest point to approximate the real surface and obtain a better estimate of the "real" distance, either by a height function or by a least squares fit of the nearest neighboring points [375].

Cloud-to-mesh distance or cloud-to-model distance (C2M)

On the other hand, cloud-to-mesh distance calculation is the most common technique in inspection software. In this approach, the topographic change is calculated by the distance between a point cloud and either a reference triangulated model or a theoretical model (see Figure A9 b), some recent reviews include [387, 388]. CloudCompare software calculates the distance from a point cloud to a 3D model (triangular mesh) using a powerful and well-known algorithm developed by P. Cignoni *et al.* [387], and studied in detail by [371]. The distance from a point to a 3D triangular mesh is globally the distance from the point

to the plane of the triangular mesh if its projection on the plane is inside the triangular mesh, and the distance from the point to the nearest artery otherwise.

It is possible to compare two meshes using this approach, for that the reference mesh is preserved in its original state, while the compared mesh is sampled (i.e. mesh converted into a point cloud with specified density), in this way the cloud-mesh comparison can be made. The resulting scalar field's can be viewed in color scale.

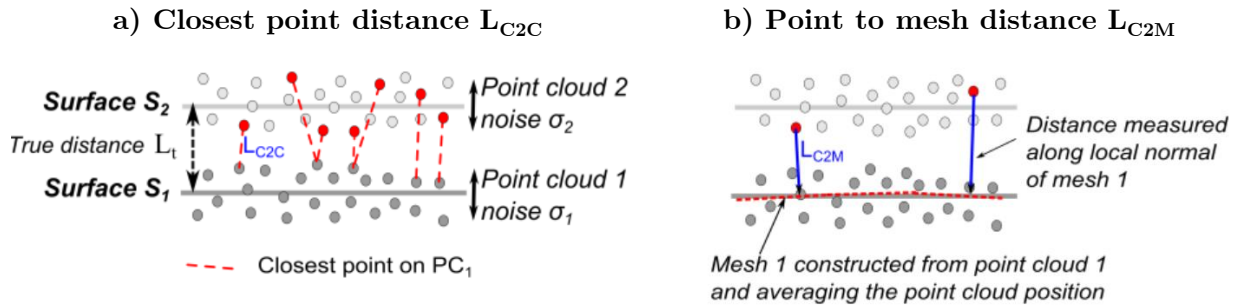


Figure A9: Figure 2: Existing 3D comparison methods (implemented in this work). Given two point clouds PC_1 and PC_2 . Each point cloud is characterized by a roughness (1 and 2 which are not identical a priori) that is a combination of instrument-related noise and surface roughness. In this example we assume that S_1 is the reference surface that has been displaced along the local normal of S_1 by a true distance L_t . A distance is calculated for each point of S_2 . a) Simpler cloud-to-cloud distance L_{C2C} , based on the nearest point distance. For a L_t L_{C2C} depends on the roughness and point density of PC_1 and PC_2 . b) Cloud-to-mesh distance (C2M) L_{C2M} . PC_1 is meshed and the distance between each point of PC_2 and S_1 is calculated along the local normal of S_1 . If the mesh correctly approximates the mean position of S_1 then $L_{C2M} = L_t + \epsilon$ [389].

Annex N: Methods for identifying and estimating geometrical model features

Estimating the parameters of a geometric model is an important problem in various fields, from computer vision and robotics to artificial intelligence. Different approaches have been described for robust estimation of a model from 3D data [371, 389]. In practice, the challenge arises from outlier points, which are observed outside the model from the rest of the data. In this work, two surface recognition techniques have been used, the least squares fitting approach and the RANSAC method, described as follows.

Fitting a paraboloid to 3D points using least-squares minimization

We propose to estimate the equation that best describes the parabolic shape of the optics based on least squares estimation from point correspondences, implemented in

CloudCompare. A technique for processing measuring surface using a a set of samples $\{(x_i, y_i, z_i)\}_{i=1}^m$ and assuming that the true values lie on a paraboloid:

$$z = f(x, y) = p_1x^2 + p_2xy + p_3y^2 + p_4x + p_5y + p_6 = P \cdot Q(x, y) \quad (6.17)$$

where $P = (p_1, p_2, p_3, p_4, p_5, p_6)$ and $Q(x, y) = (x^2, xy, y^2, x, y, 1)$, select P to minimize the sum of squared errors:

$$E(P) = \sum_{i=1}^m (P \cdot Q_i - z_i)^2 \quad (6.18)$$

where $Q_i = Q(x_i, y_i)$. This function is nonnegative and the minimum occurs when the gradient of E is the zero vector,

$$\nabla E = 2 \sum_{i=1}^m (\vec{P} \cdot \vec{Q}_i - z_i) \vec{Q}_i = \vec{0} \quad (6.19)$$

Some algebra converts this to a system of 6 equations in 6 unknowns:

$$\left(\sum_{i=1}^m \vec{Q}_i \vec{Q}_i^t \right) \vec{P} = \sum_{i=1}^m z_i \vec{Q}_i \quad (6.20)$$

Define the 6×6 symmetric matrix $A = \sum_{i=1}^m \vec{Q}_i \vec{Q}_i^t$ and the 6×1 vector $\vec{B} = \sum_{i=1}^m z_i \vec{Q}_i$. The choice for \vec{P} is the solution to the linear system of equations $A\vec{P} = \vec{B}$.

However, this approach is sensitive to outliers, so a few outliers may bias the result. Furthermore, multiple structures (i.e. shapes) may also bias the results since the fitting procedure implicitly assumes that there is only one instance of the model in the data. In these cases it is necessary to use estimation methods that are robust to outliers, such as RANSAC.

RANSAC shape detection algorithm

The RANSAC paradigm is the opposite of conventional recognition techniques, i.e. instead of using as much data as possible to obtain an initial solution and then trying to eliminate invalid data points, RANSAC extracts shapes by randomly drawing minimal sets of data points and constructing corresponding shape primitives (e.g. plans, spheres, cylinders, cones, tori, etc.) [390]. A minimal set is the smallest number of points needed to uniquely define a given type of geometric primitive. The resulting candidate shapes are compared to all points in the data to determine how many points approximate the primitive well (called the shape score) [391]. If there are enough compatible points, RANSAC would employ techniques, such as least squares, to compute an improved parameter estimate once a set of mutually consistent points has been identified. After a given number of

trials, the shape that approximates the largest number of points is extracted and the algorithm continues with the remaining data.

Some desirable attributes of RANSAC are that it is conceptually simple and general, which makes it easy to implement and extensible to a wide range of environments [391], and it can robustly handle data containing more than 50% outliers [392]. Its major shortcoming is the considerable computational demand if no further optimizations are applied.

Résumé en français

Les applications spatiales actuelles exigent que les objets, tels que les satellites, les sondes d'exploration et les rovers soient équipés d'un sous-système autonome de production d'énergie. Depuis 1957, le photovoltaïque reste le principal type de système de production d'énergie. L'enjeu de cette thèse est de développer un système à concentration photovoltaïque (micro-CPV) pour des applications spatiales. Nous résumons ci-dessous les travaux réalisés et les principaux résultats obtenus.

Introduction

Tout d'abord, nous définissons les différents paramètres de performance caractérisant le PVA. La puissance spécifique est l'un des facteurs les plus importants, elle indique la puissance par unité de masse du réseau W/kg ; l'énergie spécifique Wh/kg et la densité de puissance volumétrique W/m^3 sont d'autres métriques utilisées. Le Tableau B1 montre les performances actuelles de l'état de l'art et les améliorations attendues, basées sur la littérature actuelle et les stratégies de l'ESA et de la NASA [9]. Aujourd'hui, les générateurs solaires spatiaux utilisent principalement des cellules solaires 3J, basées sur des matériaux III-V comme l'arséniure de gallium (GaAs), le phosphore d'indium et de gallium (GaInP) et le germanium (Ge). Chaque jonction ou "sous-cellule" est optimisée pour convertir en courant électrique une partie spécifique du spectre solaire.

Table B1: Panorama des métriques actuelles des panneaux solaires pour les applications spatiales et des améliorations futures attendues [9].

Electric Power Generation	Solar Cells Efficiency [%]	Specific Power [W/Kg]	Volumic Power Densities [kW/m³]
<i>Present - 2020</i> Moving to transition	33	> 50	> 15
<i>2020 - 2025</i> Next generation	36 - 37	> 200	> 60
<i>2025 - 2035</i> High risk, high payoff	> 40	> 200	> 100

Les rendements actuels des cellules se rapprochent de leurs limites théoriques à mesure que les technologies atteignent leur maturité. Pour une cellule 3J, cette limite est de

49% sur Terre, et de 68% en considérant un nombre infini de jonctions, mais, sous concentration, ces limites augmentent jusqu'à 63% et 86%, respectivement [4]. Un panneau photovoltaïque à concentration (CPV), est un module solaire photovoltaïque composé d'une série de dispositifs optiques de concentration qui concentre la lumière sur des cellules photovoltaïques parfois refroidies par un dissipateur. Cette approche innovante a permis d'obtenir le rendement cellule le plus élevé jamais atteint : 47.1% sous 143 soleils [5, 6]. Un système CPV, comme le montre la Figure B1, est, selon la norme IEC 62108 [13], composé d'une optique primaire (POE), d'une éventuel optique secondaire (SOE) et d'une cellule photovoltaïque à haut rendement. La cellule, le SOE, le système de refroidissement et le circuit de connexion forment le récepteur. Pour que le rayonnement solaire soit concentré sur le récepteur, les modules sont équipés de suiveurs solaires.

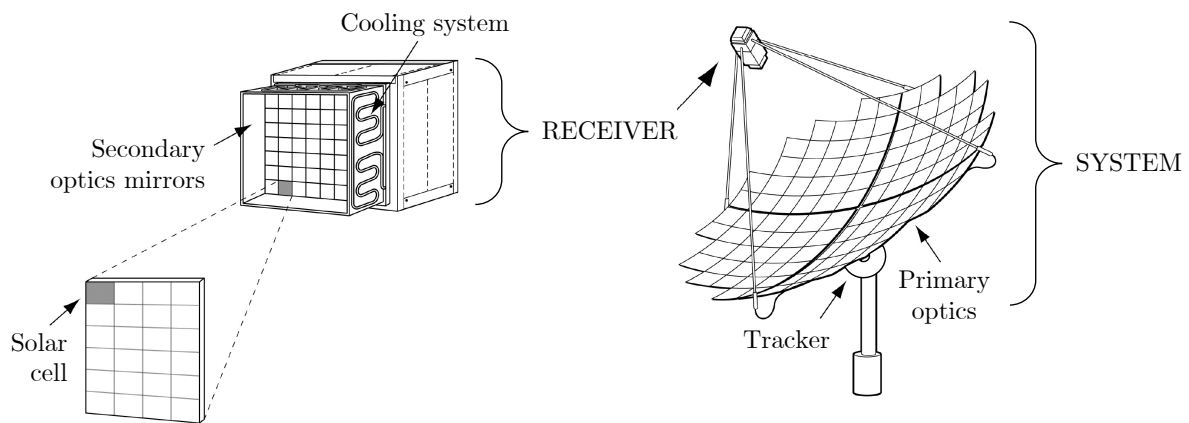


Figure B1: Schéma d'un CPV à focalisation ponctuelle [13].

Le CPV permet de réduire le coût de fabrication des générateurs solaires spatiaux en diminuant la quantité de matériaux III-V coûteux. Cependant, basé sur des cellules de taille centimétrique, ces systèmes CPV ne peuvent pas assurer des facteurs de concentration et des rendements élevés avec de grandes tolérances angulaires tout en étant compact et léger. Les travaux de cette thèse sont axés sur le développement d'une technologie à micro-CPV hautement intégrée utilisant des cellules solaires de surface $< 1 \text{ mm}^2$. Cette approche devrait permettre de répondre aux besoins énergétiques tout en améliorant la puissance électrique par unité de masse (W/kg), et la densité de puissance volumétrique (W/m^3) avec une gestion thermique passive.

Chapitre 1 : Etat de l'art des technologies CPV et micro-CPV

Ce chapitre présente l'état de l'art des systèmes photovoltaïques à concentration, couvrant à la fois les applications terrestres et spatiales. L'objectif est : (1.) d'identifier et de discuter les points forts et les points faibles des systèmes CPV; (2.) de mettre en avant les avantages qu'apporteraient la micro-concentration.

Les systèmes CPV peuvent être classés de plusieurs façons, comme le montre la Figure B2. En termes de concentration, on distingue trois niveaux : faible (< 10 soleils), moyen (10 à 100 soleils) et élevé (> 100 soleils), en fonction des exigences spécifiques du suivi solaire [19, 20]. Différents types d'optiques primaires sont utilisés pour focaliser la lumière du soleil sur les cellules photovoltaïques. Les systèmes optiques peuvent être réalisés au moyen d'éléments optiques réfractifs ou réfléchissants. Les concentrateurs peuvent également intégrer un second élément optique, utilisé pour augmenter l'angle d'acceptance et l'homogénéité du flux sur la cellule, telle qu'une bille ou un dôme. Il est important de noter que chaque type de système CPV présente des avantages et des inconvénients et qu'il est important de connaître l'application et l'environnement afin de choisir la conception la plus appropriée.

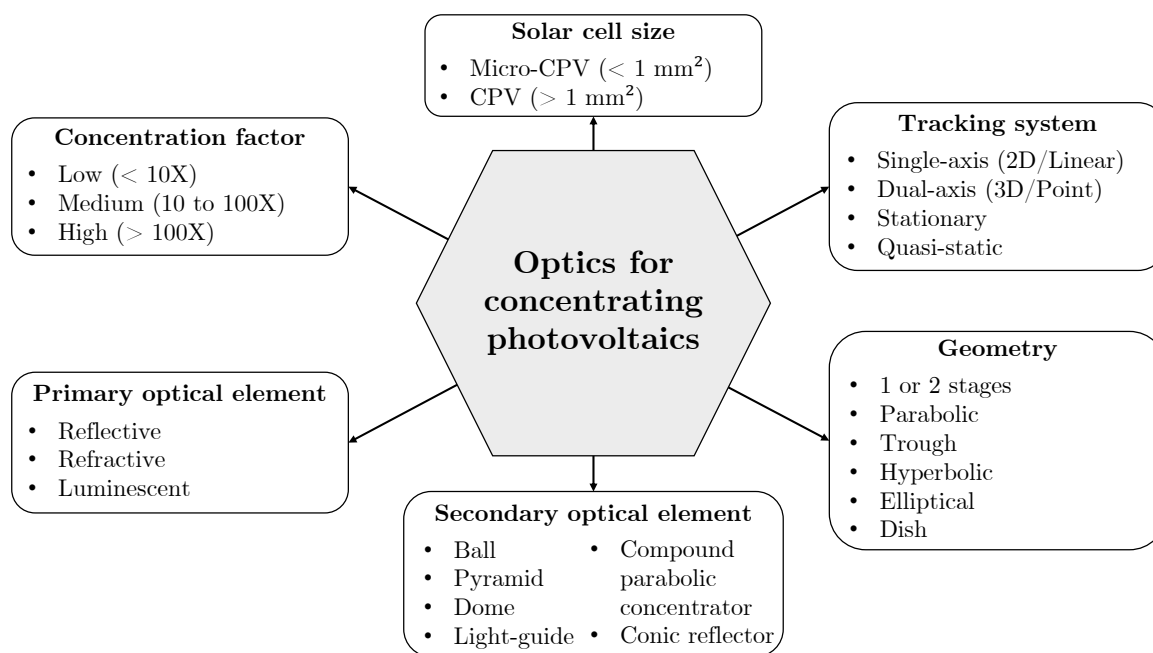


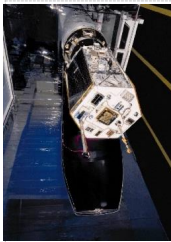
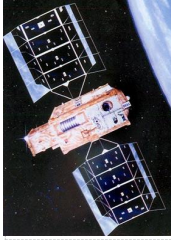
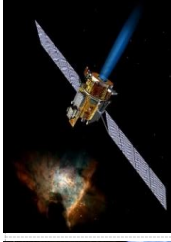
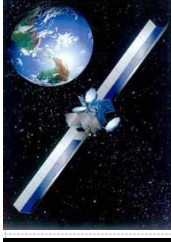
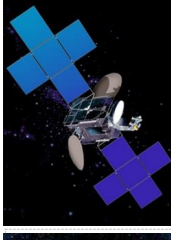
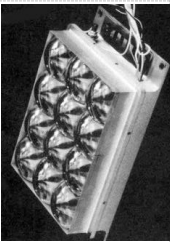
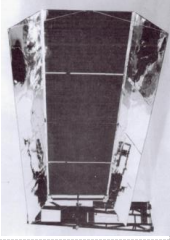

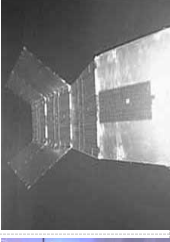

Figure B2: Classification des optiques pour le photovoltaïque à concentration.

Dans la plupart des systèmes CPV, la lentille de Fresnel est une solution plus légère et moins volumineuse pour une même focale comparée aux lentilles conventionnelles. Ces optiques réfractives ont parfois des défauts de forme au niveau des dents avec des aberrations chromatiques qui diminuent le flux lumineux incident sur les cellules solaires multi-jonctions. Le rendement optique de tels systèmes réfractifs est typiquement compris

entre 80 et 85%. Les systèmes réfléchissants, quant à eux, présentent les meilleurs rendements optiques, pouvant atteindre près de 97%. Souvent constitué de plaques ou de films réfléchissants, ils ont également l'avantage d'utiliser généralement moins de matériau.

Il a été démontré qu'il existe des différences significatives entre les conceptions de concentrateurs spatiaux et terrestres. Si le prix des matériaux et des procédés associés est important dans tous les cas, la masse des systèmes dans l'espace est un paramètre particulièrement important. La fiabilité à long terme dans des conditions d'exploitation est essentielle pour les deux applications, mais c'est un point particulièrement crucial dans l'espace, car une fois qu'un système est lancé dans l'espace, il ne peut plus bénéficier de maintenance. Dans l'espace, les ensembles doivent être compacts et se déployer de manière fiable. En outre, il existe une corrélation entre le facteur de concentration, la taille des cellules solaires et la tolérance angulaire, avec un compromis à trouver en fonction de l'application visée. Dans l'espace, les exigences opérationnelles (orbite géostationnaire : $\pm 3^\circ$; $\pm 23,5^\circ$) de suivi du soleil conduisent à des rapports de concentration faibles, tandis qu'au sol, les trackers sont plus précis ($< 1^\circ$) et conduisent à l'utilisation de facteurs de concentration élevés. Un aperçu des principales technologies CPV déployées dans l'espace est présenté sur le Tableau B2. Ces systèmes à concentration ont été lancés dans l'espace entre 1994 et 2004. La concentration des systèmes varie entre 2X et 100X. Les cellules utilisées ont chaque fois été les meilleures cellules du marché. Actuellement, ce sont les cellules multi-jonctions à base de matériaux III-V qui sont intégrées dans les systèmes à concentration.

Table B2: Chronologie du déploiement des systèmes photovoltaïques à concentration pour les applications spatiales.

<u>SATELLITE</u>						
Nom	APEX (P90-6)	NRO STEX	Deep Space 1	Galaxy XI	SS/L-Cell Saver	
Mission	GEO / LEO	LEO	GEO	GEO	-	
Année	1994	1998	1998	2000	2004	
Chronologie spatiale du CPV						
<u>ARRAY SOLAIRE</u>						
Nom	Mini-dome lenses	AstroEdge	SCARLET	BOEING 702	SS/L-CellSaver	
Concentration	100X	1.5X	7.5X	1.7X	2X	
Efficacité optique	91.5 %	85 %	89 %	90 %	90 %	
Structure de la cellule solaire	2J (GaAs/GaSb) 4 mm dia.	2J (GaAs/Ge) 34.3 x 60.3 mm ²	(GaInP ₂ /GaAs/Ge) 10 x 40 mm ²	2J (GaAs/Ge) 3J (GaIn ₂ /GaAs/Ge)	3J (GaInP ₂ /GaAs/Ge)	
Efficacité des cellules solaires	21.4 %	19 %	22.7 % @7.5X AM0	2J (21 %) 3J (26 %)	-	
Puissance spécifique(BOL)	75 W/Kg	70 W/Kg	48 W/Kg	60 W/Kg	-	
Puissance totale	-	15 kW 335 W @ 37 VDC (1 W)	2.5 kW @ 100 VDC	7-17 kW @ 101.3 VDC	-	
Commentaires	TRL 9	Échec du déploiement	3 ans de missions	Dégradation rapide TRL 9	TRL 5	
Références	[45-47]	[57]	[48-50]	[58]	[59,60]	

Actuellement, les systèmes photovoltaïques à micro-concentrateur utilisant des micro-cellules ($< 1 \text{ mm}^2$) permettent d'avoir de meilleurs rendements tout en utilisant moins de matériaux, et en assurant une meilleure gestion thermique. À cet égard, deux concepts récents de micro-CPV ont été étudiés pour l'espace, un concept réfractif proposé par NRL [63], et un autre réfléchissant développé par l'université de Penn State [85]. Le premier concept, pour garantir un système compact et léger utilise des lentilles en verre à très faible ouverture ($1 \times 1 \text{ mm}^2$). En combinant ces optiques avec des cellules de $170 \times 170 \mu\text{m}^2$ d'ouverture la concentration atteint 35X. D'autre part, dans le cas du réflecteur, les modules sont formés par impression de microcellules sur un verre mince. Ce réflecteur est ensuite fixé à un ensemble de lentille. Ce système ultra-compact d'environ 0,5 mm d'épaisseur possède une concentration de 25X.

Les deux systèmes ont un grand potentiel, mais il reste des défis à relever avant qu'ils puissent être déployés avec succès dans l'espace. En effet, l'utilisation d'optiques aussi petites est pénalisée par une efficacité optique réduite en raison de problèmes de fabrication, où une région au niveau du sommet rend difficile la mise au point de la lumière. Dans le cas du système réfractif, il devient nécessaire d'inclure des structures de support supplémentaires laissant un espace d'air (ou vide) entre le réseau de lentilles et le réseau de cellules. Pour le système réflecteur, utilisant du verre mince, la fragilité de l'assemblage peut être critique et doit aussi intégrer une structure qui supporte les charges mécaniques. Ainsi la technologie micro-CPV est un sujet d'actualité qui peut être une solution pour alimenter les systèmes électriques spatiaux.

Chapitre 2 : Évaluation des missions et des environnements spécifiques favorables au CPV dans l'espace

La micro-concentration semble donc être une solution pertinente pour pouvoir assurer la gestion de la puissance d'un satellite. Mais est-ce que toutes les missions spatiales peuvent être pourvues en électricité grâce à la micro-concentration ? À cet égard, le présent chapitre vise à évaluer les conditions environnementales et les besoins des engins spatiaux photovoltaïques.

Tout d'abord, nous étudions les facteurs environnementaux affectant l'efficacité de conversion et la durabilité des PVA dans l'espace, décrits dans la Section 2.1 ; voir le Tableau B3 pour un résumé.

Table B3: Synthèse des effets de l'environnement spatial sur l'efficacité de conversion et la durabilité des panneaux solaires.

Environment Factors	Effects on the conversion efficiency and durability of PV
Solar Irradiance	<ul style="list-style-type: none"> • Power conversion dependence
Temperature	<ul style="list-style-type: none"> • Efficiency degradation • Degradation mechanisms (carrier freeze-out and thermal barriers to conduction) • Thermo-elastic stress cycles (e.g., cracks in solder joints of the interconnects) • Electric resistances
Vacuum	<ul style="list-style-type: none"> • Contamination (degassing) • Pressure differentials (decompression)
Plasmas	<ul style="list-style-type: none"> • Surface charging, electrostatic discharge and dielectric breakdown • Enhanced sputtering and re-attraction of contamination • Increased leakage current
Energetic Particle Radiation	<ul style="list-style-type: none"> • Total ionizing dose effects (electronic degradation) • Displacement damage • Single event effects (upset, latch-up, burnout) • Degradation in optical properties (e.g., coverglass, optics, etc.)
Electrically Neutral Particles	<ul style="list-style-type: none"> • Mechanical effects (aerodynamic drag, physical sputtering) • Chemical effects (ATOX, spacecraft flow)
Ultraviolet & X-Ray Radiation	<ul style="list-style-type: none"> • Degradation of thermo-electric properties • Degradation of optical properties (e.g., coverglass, optics, etc.) • Structural damages
Micrometeoroids & Debris	<ul style="list-style-type: none"> • Damage to cell active area and interconnects • Damage of optical systems caused by hypervelocity impacts (e.g.: coverglass, lenses, mirrors) • Increased cell shunt resistance

Ensuite, les contraintes spécifiques de plus de 30 concepts de mission visant à explorer 14 corps célestes sont identifiées dans la Section 2.2. Les conditions les plus pertinentes de ces missions sont décrites, en tenant compte de l'utilisation des PVAs. L'adéquation

de certaines cellules solaires au cours des missions passées est examinée, en évaluant leur comportement pendant toute la durée de vie de la mission. La faisabilité de certaines technologies PVA proposées est alors discutée, en comparant plusieurs conceptions pour estimer leurs avantages et limites potentiels. Dans la Section 2.3, un résumé de ces conditions spécifiques (décrites dans la Section 2.2) est effectué. Les exigences pour répondre à ces concepts de mission ont plusieurs besoins uniques, basés sur la destination et le type de mission (par exemple, orbiteur, flyby, aérien, atterrisseur et rover), les niveaux d'irradiation solaire, les durées de vie attendues de la mission, la gamme de température, ainsi que plusieurs caractéristiques spécifiques de leur propre environnement comme le rayonnement, les composés chimiques, la gravité, la pression, la poussière, entre autres. Ces paramètres ont donc été classés par plages, comme on peut le voir dans le Tableau B4.

Table B4: Plages de paramètres des conditions environnementales, proposées pour établir l'applicabilité d'une technologie PV dans l'espace.

Missions Types	Missions Life (year)	Solar Irradiance (W/m ²)	Scattering	Temperature (K)		pH	Electron Radiation (1 MeV/cm ²)
				Minimum	Maximum		
Orbiter	< 0.5	< 15	Clear Moderate High	< 153	< 273	Acidic Neutral Basic	Low < 1e10 Moderate 1e10 to 1e14 High ≥ 1e15
Flyby	0.5 to 2	15 to 50		153 to 123	273 to 413		
Aerial	2 to 10	50 to 1000		123 to 223	413 to 523		
Lander	> 10	1000 to 3000		> 223	> 523		
Rover		> 3000					

Enfin, un accent particulier est mis sur l'évaluation du solaire à concentration. À cet égard, nous concluons en établissant la plage des environnements favorables aux concentrateurs, en soulignant le type de missions qui pourraient être abordées par cette technologie. Les résultats présentés dans ce chapitre ont récemment fait l'objet d'un article publié dans *Applied Energy journal* [86].

Cette étude, qui se veut exhaustive, peut aider les concepteurs d'engins spatiaux lors du développement d'assemblages photovoltaïques, à choisir les matériaux d'encapsulation appropriés, la technologie des cellules solaires et les dissipateurs thermiques. Les principaux résultats de cette étude sont résumés ci-dessous :

1. La variation en fonction de l'altitude est le paramètre le plus important pour le concepteur d'engins spatiaux sur les orbites de la Terre, car il existe des différences fondamentales dans les processus physiques qui se produisent dans les régions respectives. Le rayonnement des particules énergétiques est plus élevé sur les orbites terrestres moyennes et géostationnaires que sur l'orbite terrestre basse. Alors que l'orbite terrestre basse présente une érosion importante due à l'oxygène atomique, une charge de surface sévère a été associée à l'orbite terrestre géostationnaire. Le rayonnement ultraviolet, le cycle thermique et l'impact de micrométéorites/débris sont présents sur toutes les orbites terrestres, à différents niveaux.

2. Les concepts de mission de surface vers la Lune et Mars nécessitent des panneaux solaires minimisant l'effet de la poussière. Alors que la surface de la Lune perçoit un spectre énergétique complet de la masse d'air comme sur les orbites terrestres, la poussière atmosphérique en suspension modifie le spectre solaire et réduit l'intensité sur la surface martienne, la rendant déficiente en bleu et renforcée en rouge et en infrarouge. Les cellules solaires doivent donc être "accordées" au spectre martien.
3. Les missions à proximité du Soleil, où l'intensité et la température augmentent considérablement, induisent une perte réversible des performances théoriques avec la température, ainsi que des dommages irréversibles entraînant la dégradation des contacts ohmiques, la délamination du verre de couverture, la dégradation structurelle et la diffusion de dopants. Mercure présente des environnements à fort rayonnement thermique et à forte gravité. Vénus a une atmosphère beaucoup plus complexe et dynamique, avec des variations de température et de pression en fonction de l'altitude, et des nuages corrosifs d'acide sulfurique.
4. Les missions d'exploration des systèmes jovien et saturnien nécessitent des systèmes photovoltaïques de grande puissance capables de fonctionner efficacement dans des conditions de faible irradiation et de basse température, et dans des environnements à fort rayonnement.

En général, les systèmes à concentration ont le potentiel d'augmenter la limite d'efficacité théorique des modules par rapport aux panneaux solaires standard (non concentrés). En fait, les concentrateurs ont déjà été utilisés dans l'espace et leur puissance à haute densité peut faciliter l'emploi d'autres technologies telles que les systèmes de propulsion électrique. En plus du Tableau B5, qui résume les mondes potentiels pouvant être alimentés par des concentrateurs photovoltaïques, certains des avantages et des inconvénients qui ont été mis en évidence :

1. Les systèmes photovoltaïques à concentration offrent une protection inhérente des cellules photovoltaïques actives contre les flux élevés de particules chargées hautement énergétiques, que l'on trouve sur les orbites de la Terre et autour des systèmes joviens et kroniens.
2. A de longues distances, jusqu'à cinq unités astronomiques, les pertes de performances dus à une faible irradiation et à une température basse peuvent être atténués en utilisant des concentrateurs photovoltaïques, qui permettent d'augmenter l'irradiation effective sur la cellule. Même si ces systèmes ont déjà fait l'objet de tests en vol sur des orbites terrestres, il convient de poursuivre les recherches afin d'évaluer le comportement et le processus de dégradation de ces technologies dans des conditions

de faible irradiation et de basse température combinées à des environnements à fort rayonnement. Il s'agit peut-être de l'un des environnements les plus adaptés au photovoltaïque à concentration, et son développement pourrait améliorer l'application du photovoltaïque à des distances aussi éloignées que Jupiter, Saturne et leurs lunes.

3. La performance des concentrateurs photovoltaïques se dégrade dans les environnements poussiéreux (Mars et Lune) car les particules diffusent la lumière du soleil et se déposent sur les optiques, ce qui nuit à la transmission de la lumière sur les cellules solaires. Les environnements très dispersés, comme Vénus, Titan et les tempêtes de Mars, rendent les concentrateurs inadaptés pour les concepts de missions aériennes et terrestres.
4. Dans les concentrateurs photovoltaïques, le rayonnement solaire est focalisé, ce qui entraîne un flux thermique élevé. Cela peut impacter sa durée de vie et son efficacité, en particulier pour les missions dont la température est supérieure à 523 K et l'irradiance solaire dépasse 3000 W/m².

La connaissance des environnements spatiaux et la compréhension des phénomènes physiques associés s'améliorent au fur et à mesure que des nouvelles informations sont recueillies par les différentes missions spatiales.

Table B5: Évaluation des mondes potentiels à alimenter par des CPV et de leurs contraintes spécifiques.

MONDE	~1				1.67	5.5				10			
	1,366				589	51				15			
MISSION	TERRE				MARS	JUPITER	IO	EUROPA	GANYMEDE	CALLISTO	SATURN	ENCELADUS	TITAN
	L	M	G	O	O/F	O/F	O/F	O/F	O/F	O/F	O/F	O/F	O/F
CONDITION	E	E	O	O	L/R	L/R	L/R	L/R	L/R	L/R	L/R	L/R	L/R
	Oxygène atomique	●				○		○		○			○
Poussière				○									
Températures extrêmes	○	○	○	○	○	●	●	●	●	●	●	●	●
Radiation intense e- p+	○	●				●	●	●	●	○	○	○	○
Micrométéorite	●	○	○	○		○				○			
Plasma	○	○	●			●				○			
Cyclage thermique	●	●	●	●	○	○	○	○	○	○	○	○	○
Rayonnement UV	●	●	●	●	●	○	○	○	○	○	○	○	○

Convention: ● Impact élevé ○ Impact modéré sur le Concentrator PhotoVoltaics (CPV). AU : Unité astronomique (~150 x10⁹m). Orbite terrestre basse (LEO), moyenne (MEO), and GEosynchrone (GEO). O : Orbiter, F : Flyby, L : Lander, R : Rover. e- : électrons, p+ : protons.

Chapitre 3 : Optimisation optique et intégration d'un concentrateur parabolique linéaire utilisant des cellules III-V/Si

Depuis 2016, le CEA étudie un système CPV innovant et robuste composé d'un CPC diélectrique qui atteint un facteur de concentration d'environ 7,6X [326, 327], décrit dans la Section 3.1. Ce système concentre la lumière grâce au principe optique de réflexion interne totale (TIR). Les premiers travaux ont été soutenus par le CNES et développés dans un cadre R&T avec Thales Alenia and Space et Thales Research and Technology. La solution consiste à intégrer et mouler directement les optiques sur les cellules solaires. Cette approche permet d'éviter les procédures d'alignement lors du déploiement de panneaux solaires dans l'espace. Cet alignement est inhérent à la technique de fabrication et peut être qualifié avant le lancement. Cela présente un certain avantage en termes de fiabilité. Les cellules solaires sont intégrées dans une optique en silicone à faible dégazage, Dow Corning® 93-500 [328]. La Figure B3 décrit la conception proposée avec ses dimensions et une vue en coupe de la partie inférieure d'une seule optique, montrant la cavité les trois cellules interconnectées disposées latéralement.

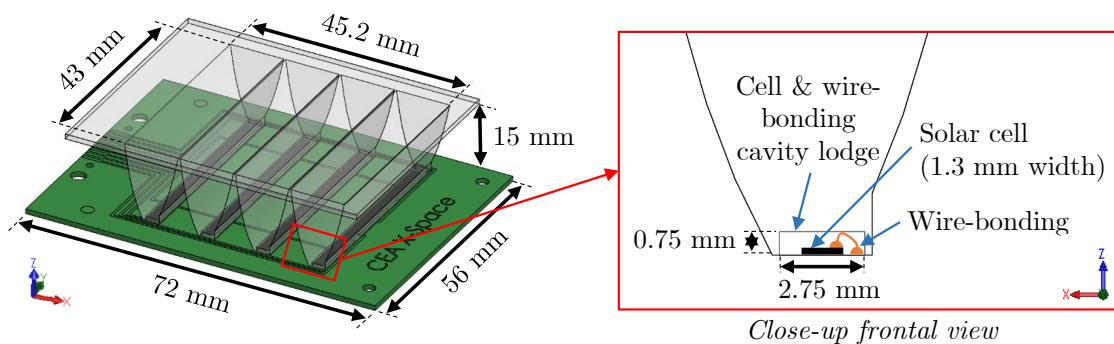


Figure B3: Schéma du prototype CPC (à gauche), vue en coupe de la partie inférieure d'une seule optique, montrant la cavité de logement des cellules et la liaison des fils d'interconnexion.

La surface du module de démonstration a été fixée à $43 \times 45.2 \text{ mm}^2$ ce qui correspond à environ la moitié de la surface d'une cellule solaire standard. Il présente une épaisseur de 15 mm comprenant l'optique et le verre. Il est composé de douze MJSCs, de $1,5 \times 13 \text{ mm}^2$ chacune. Les cellules ont été fabriquées par Azur Space et ont été spécialement conçues pour l'espace, avec un revêtement anti-reflet optimisé adapté à l'indice de réfraction du silicone bi-composant et une métallisation adaptée à la faible concentration. De plus, une étude angulaire a été réalisée et un angle d'acceptance (pour fournir 90% de l'efficacité optique maximale) de $\theta = \pm 3^\circ$ pour l'axe latéral et $\alpha = \pm 23,5^\circ$ pour l'axe longitudinal. Ce qui signifie que pour une mission GEO, un suiveur à un seul axe est suffisant pour suivre le Soleil en tenant compte de l'angle saisonnier. L'efficacité optique théorique était de 75%, alors que l'efficacité mesurée était d'environ 68% [327].

Le travail effectué dans cette thèse et décrit dans ce chapitre porte sur trois améliorations: (1.) une optique avec un meilleur rendement sans augmentation de masse, (2.) un processus de moulage optimisé, (3.) une intégration de cellules II-V/Si moins coûteuses.

Une des évolutions majeures par rapport à la conception précédente du CPC est l'amélioration de la surface du récepteur. La dernière version était composée d'une grande cavité rectangulaire qui logeait trois cellules et ses interconnexions en fil d'or, le tout dans les parois internes profilées de chaque optique. Une partie du flux incident était donc perdue à l'interface entre le bas des parois et les PCB (voir Figure B4). C'est la raison pour laquelle la nouvelle proposition suggère l'utilisation de trois cavités rectangulaires par optique, qui accueille chaque cellule et ses fils d'interconnexion indépendamment, maximisant ainsi le flux de lumière solaire incident sur les cellules solaires.

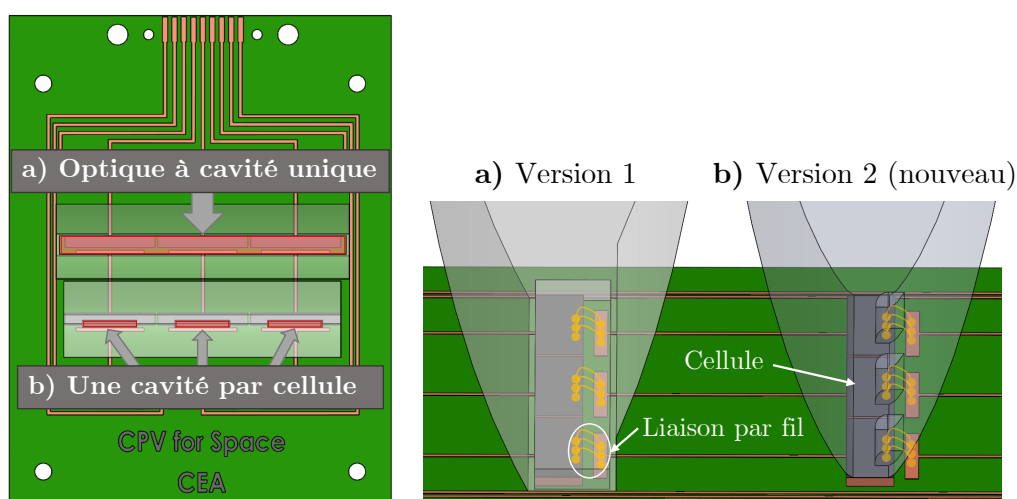


Figure B4: Modèle CAO du CPC : (a) version 1 (7.6X), et (b) version 2 (8.6X).

Pour diminuer la présence de bulles lors de l'injection du silicone, une nouvelle distribution des canaux de moulage a donc été conçue et intégrée, voir Figure B5. Cette amélioration empêche le reflux de silicone et le moulage d'arêtes vives à travers les canaux d'injection. De plus, la plaque d'injection de silicone est pourvue de quatre trous de sortie d'injection permettant une évacuation plus efficace des bulles d'air pendant l'injection du silicone et le processus de mise sous vide.

Après optimisation, une caractérisation comparative entre les efficacités théoriques du CPV, optique et électrique, et ses performances expérimentales relatives a été réalisée. L'efficacité optique théorique est augmentée de 19% par rapport à la conception précédente tout en conservant la même masse. Les mesures ont ensuite montré une augmentation expérimentale de 12% (Figure B6). Il a été déterminé que le système CPC optimisé atteint une efficacité optique mesurée d'environ 80% et un facteur de concentration de 8,6X, conduisant à une puissance spécifique d'environ 20 W/kg. Cette augmentation de performance n'est malheureusement pas suffisante car elle ne permet pas d'atteindre

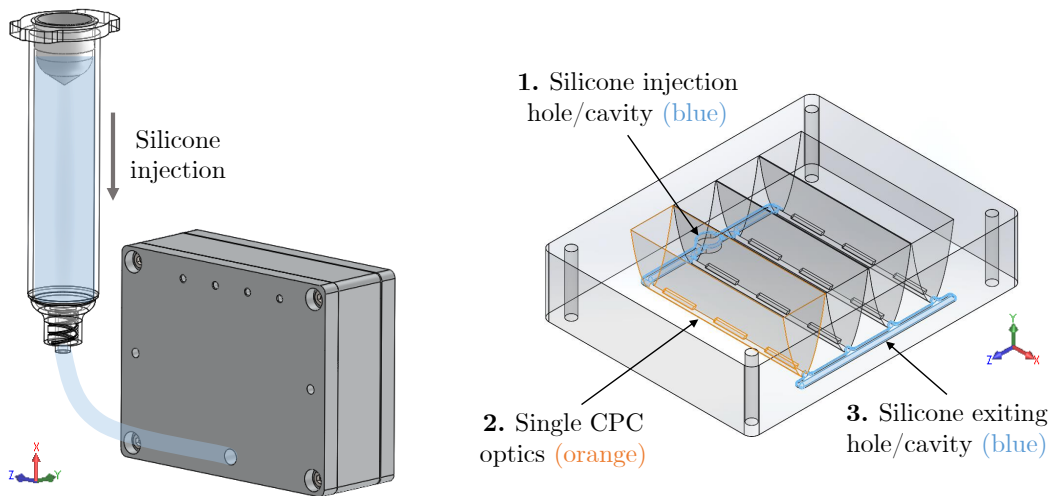
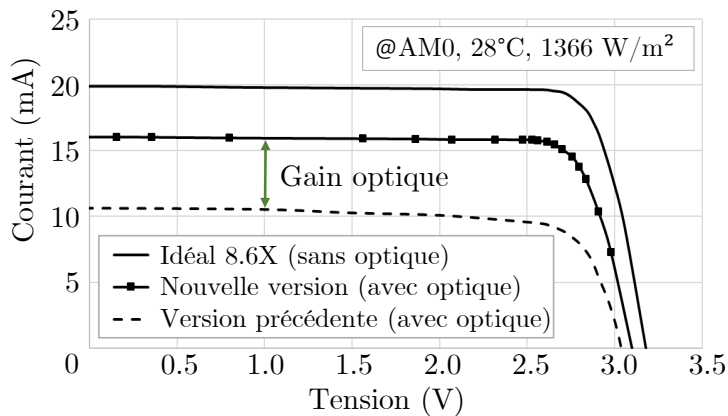


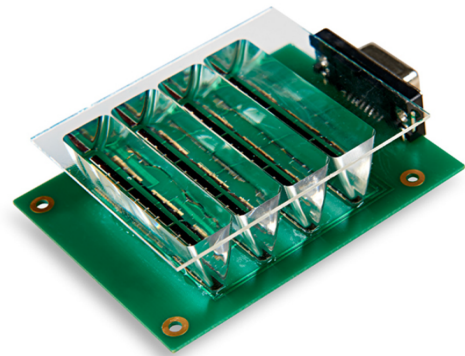
Figure B5: Schéma illustrant l'ensemble d'injection de silicone avec une seringue (à gauche) ; la cavité d'injection et la sortie de silicone (1.) et (3.), respectivement (en bleu), ainsi qu'une seule optique CPC (3.) en orange.

les standards actuelle exigé pour les générateurs solaires pour le spatiale, à savoir une puissance supérieure à 100 W/kg. Cette excès de masse est principalement due aux optiques qui représente près de 90% de la masse totale du module.

Caractéristiques IV : une comparaison entre les versions utilisant une cellule



(a)



(b)

Figure B6: (a) Comparaison des performances entre les versions utilisant une cellule et les caractéristiques IV idéales sans intégration optique; et (b) photographie du prototype du CPC de nouvelle génération.

Comme discuté également dans le Chapitre 1, la microconcentration peut être une solution pour alimenter en énergie les engins spatiaux. Le chapitre suivant présente la conception optique et la validation d'un nouveau concept d'intégration de micro-CPV qui vise à augmenter la puissance spécifique du réseau à > 100 W/kg en utilisant un réseau de paraboles réfléchissantes à l'échelle micrométrique.

Chapitre 4 : Conception optique d'un réflecteur ultra intégré pour micro-CPV

Dans ce chapitre, la conception optique d'un nouveau concept de micro-CPV est présentée. Il s'agit plus précisément d'un miroir parabolique miniaturisé intégré dans un nid d'abeille. L'objectif est de :

i.) Réduire significativement le coût du panneau solaire CIC standard en utilisant des cellules micrométriques (< 1 mm), tout en préservant une rigidité spécifique élevée.

ii.) Augmenter la puissance spécifique jusqu'à 150 W/kg à AM0 incident, par rapport à une technologie CIC standard existante, actuellement entre 50-80 W/kg.

iii.) Fournir une architecture compacte entre 4 - 15 mm d'épaisseur, comparé aux 20-30 mm du système standard, et ainsi augmenter la puissance volumétrique (W/m^3).

iv.) Réduire le nombre d'étapes de fabrication de l'optique en moulant un assemblage complet en une seule étape. *v.)* Inclure une structure monolithique qui évite le déploiement dans l'espace, entre le réseau optique et les cellules où le nid d'abeille fournit la rigidité et maintient l'optique et les cellules solaires ensemble.

Cette idée nouvelle, qui a fait l'objet d'un brevet [346], concerne un CPV comprenant des éléments optiques et une structure en nid d'abeille, chaque élément optique étant disposé dans l'une des cellules du cœur en nid d'abeille. L'invention comprend une structure monolithique qui fonctionnalise les éléments constitutifs, d'une part en utilisant l'optique comme partie du support mécanique, et d'autre part, le nid d'abeille est utilisé pour rigidifier l'ensemble et maintenir l'alignement entre l'optique et les cellules solaires.

Pour cela, l'utilisation d'une âme en nid d'abeille constituée d'un mince panneau d'aluminium sous forme de cellules hexagonales (quasi-régulières) perpendiculaires aux faces est proposée. Cette âme est rigidifiée à la base par un CFRP, tandis qu'au sommet se trouve un verre de couverture intégrant les micro-cellules PV et les interconnexions. Enfin, à l'intérieur des alvéoles du nid d'abeille sont intégrés les éléments optiques réfléchissants qui vont concentrer la lumière du soleil vers le haut sur le réseau de cellules interconnectées. De plus, la densité de remplissage est maximisée en utilisant des cellules unitaires hexagonales. La Figure 4.2 illustre le concept, en montrant la conception CAD d'un mini-module, composé d'un ensemble de 30 optiques et cellules unitaires. Ce mini-module correspond à une surface de demi-cellule d'un 3J standard pour les applications spatiales (soit 40×40 mm²) [8]. D'autre part, la rigidité requise par une matrice dépend de la taille des ailes des panneaux et de l'architecture du cadre utilisé pour la supporter. Dans certains cas, un seul étage en matériaux composites tel que décrit ci-dessus n'est pas suffisant pour fournir la rigidité requise. C'est pourquoi un deuxième étage en matériaux composites peut être envisagé, comme le montre la Figure B7 (c).

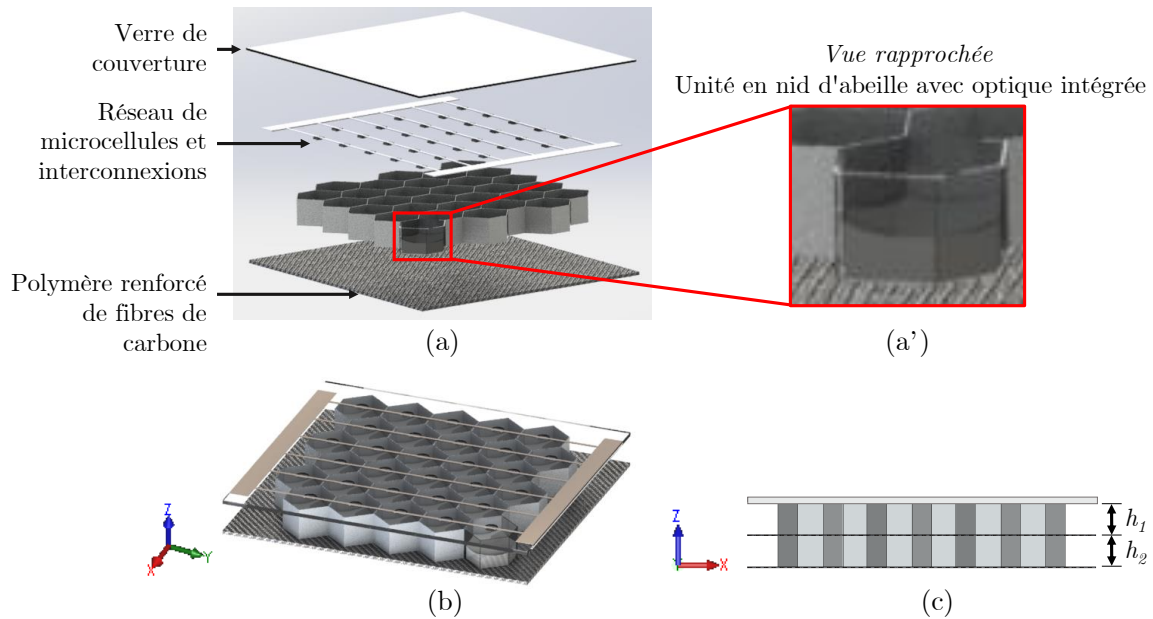


Figure B7: Schéma du mini-module micro-CPV étudié, qui intègre 30 micro-cellules interconnectées. (a) Vue éclatée des éléments qui composent le mini-module dont la surface est d'environ 40x40 mm², (a') vue rapprochée d'une unité intégrée, (b) vue isométrique montrant et (c) une architecture à double couche renforcée, où h_1 et h_2 sont les hauteurs des couches.

La première partie de ce chapitre est consacrée à la description du concept de micro-CPV hautement intégré, ainsi qu'à sa structure mécanique et à ses avantages potentiels; voir Section 4.1. Ensuite, une étude a été menée pour comparer deux systèmes de réflecteurs idéaux : un système parabolique et un système optimisé de forme libre; voir la Section 4.2. À cet égard, nous avons cherché la distribution de flux la plus homogène possible sur la cellule, qui puisse garantir une tolérance angulaire donnée. Puis, la modélisation et la simulation optique du réflecteur intégré dans une cellule hexagonale en nid d'abeille ont été réalisées (voir Section 4.3). La chaîne de perte optique a été étudiée, ainsi que la distribution du flux concentré et la tolérance angulaire. Enfin, une estimation de la densité de courant de court-circuit basée sur les mesures EQE a été réalisée.

Afin d'établir un système de réflecteur adapté au micro-CPV dans l'espace (utilisant des cellules d'environ 0,6 μm²), des critères de conception ont été établis, tels que : un angle d'acceptance uni-axial et bi-axial de $> 4^\circ$ et $> 2,5^\circ$, respectivement, une concentration entre 25X et 30X, une tolérance de désalignement > 50 μm, et la meilleure uniformité de flux possible. Pour cela, une étude comparative de deux systèmes idéalisés a été réalisée, en utilisant une parabole avec différents plans de défocalisation et une forme libre optimisée. Tous deux avec un flux distribué dans 60% de la cellule.

On en a conclu que pour le système parabolique considéré, le plan de réception qui garantit la tolérance angulaire désirée avec la distribution de flux la plus homogène (PAR = 4.4) est $z = -0.225$ mm, voir Figure B8, avec un $AA_y = 4^\circ$ et $AA_{xy} = 3^\circ$.

Par la suite, un réflecteur de forme libre a été optimisé pour améliorer la tolérance angulaire et l'uniformité du flux d'un spot de taille équivalente à celle de la parabole pour le plan $z = -0.225$ mm. Il a été observé que la forme libre optimisée du réflecteur a un angle d'acceptance qui ne correspond pas aux spécifications de conception, avec $AA_y = 3^\circ$ et $AA_{xy} = 2^\circ$. Ainsi, des SOE ont été utilisés pour améliorer la tolérance angulaire et l'uniformité du réseau, en utilisant un hémisphère et une forme libre radiale optimisée. Ces derniers ont considérablement amélioré la tolérance angulaire, en particulier le SOE de forme libre, pour $AA_y = 8,2^\circ$ et $AA_{xy} = 5,7^\circ$. Ce dernier a également entraîné une amélioration de 20% de l'homogénéité du flux, réduisant le PAR de 6,7 à 5,6 par rapport à celui sans SOE (voir Figure B8).

Bien que le réflecteur à forme libre puisse largement garantir les critères de tolérance angulaire minimale établis lors de l'utilisation d'un SOE, il présente un spot avec un PAR environ 21% plus élevé que la parabole (voir Figure B8), et surtout il implique une plus grande complexité de fabrication. Le réflecteur parabolique s'est donc avéré être une solution efficace en termes d'homogénéité du flux, ainsi qu'en termes de simplicité de fabrication. Pour cette raison, cette dernière conception a été choisie pour valider le concept d'un réflecteur hautement intégré dans un nid d'abeille.

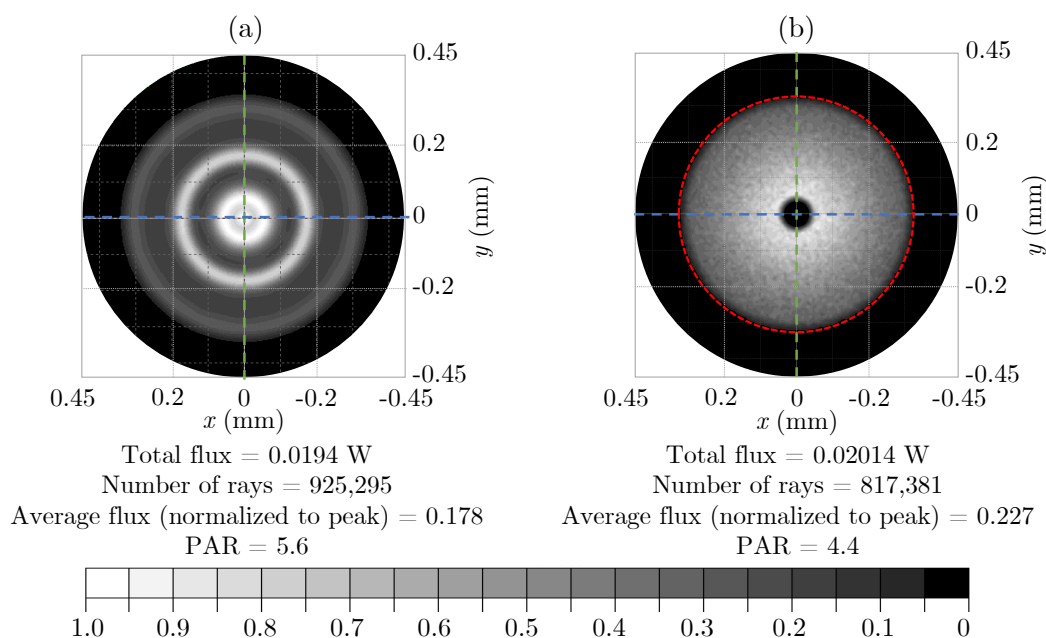


Figure B8: Cartes d'irradiance normalisées au pic de : (a) un réflecteur de forme libre avec un SOE de forme libre et (b) une parabole avec un détecteur à $z = -0,225$ mm du foyer. Montrant le flux total et le nombre de rayons perçus, ainsi que le flux moyen normalisé au pic et le PAR relatif.

Puis nous sommes passés de l'étude de systèmes idéalisés pour proposer une simulation optique d'un réflecteur parabolique intégré dans un nid d'abeille. Dans un premier temps, nous avons décrit le système optique tronqué et chacun des éléments et matériaux considérés. Puis nous avons étudié la convergence du flux incident sur l'ouverture optique hexagonale d'une source solaire AM0 (circulaire).

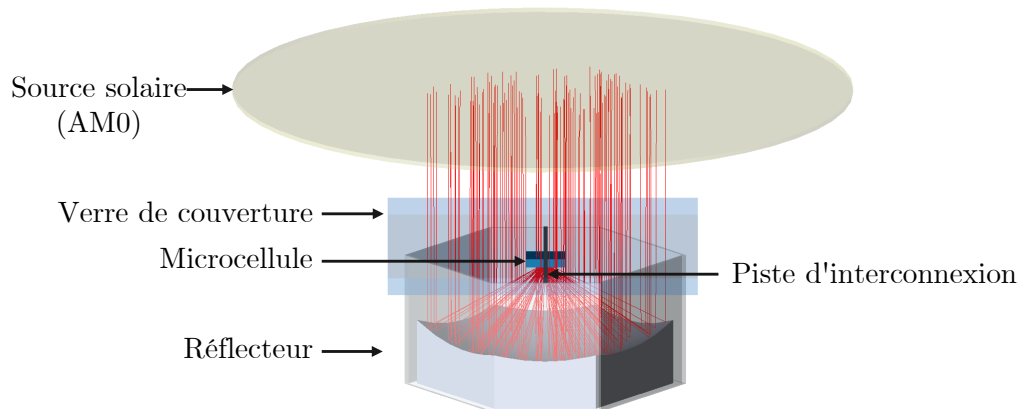


Figure B9: Modèle de conception optique utilisant TracePro®, représentant les principaux éléments impliqués et pris en compte lors de l'analyse par tracé de rayons.

Ensuite, les pertes optiques prédominantes du micro-CPV en cours de développement ont été étudiées, en considérant les pertes par réflexion, absorption et diffusion; voir Figure B10. Cela a permis d'obtenir une efficacité optique estimée à environ 82%, qui, en considérant un ARC des deux côtés du verre de couverture, pourrait être augmentée jusqu'à 86%, tandis que l'optimisation de la largeur d'interconnexion pourrait l'améliorer jusqu'à 88%.

En outre, les premiers revêtements argentés (c'est-à-dire non optimisés) ont été réalisés sur du silicone DC 93-500, qui ont été comparés à des échantillons réalisés sur du verre. Ensuite, la réflectance spéculaire et totale des échantillons ont été mesurées. Nous avons ainsi observé une réflexion spéculaire d'environ 97% pour les revêtements sur un substrats en verre, tandis que ceux fabriqués sur du silicone étaient d'environ 70%. Ces mesures sont des données d'entrée pour notre modèle optique.

Ensuite, des simulations de tracé de rayons ont été réalisées pour évaluer les performances du système. Nous avons commencé par évaluer la tolérance angulaire du réflecteur parabolique intégré. Pour avoir une tolérance angulaire minimale avec une déviation uni-axiale $> 4^\circ$, la cellule doit se situer à -0.225 mm et -0.15 mm du point focal (selon z), pour les axes y et x , respectivement. Alors que la plage qui garantit une $AA_{xy} > 2,5^\circ$ est comprise entre le foyer et la position $z = -0,2$ mm. Ainsi, en termes de tolérance angulaire, l'axe limite est x , pour un plan de détection à $-0,15$ mm, qui a lui-même un $PAR = 7,1$. La Figure B11 montre les cartes d'irradiance du système intégré pour un détecteur à $z = -0.15$ mm du plan focal : (a) pour une irradiance normale à l'ouverture

optique; ainsi que les angles d'acceptance : (b) autour de l'axe y ($5,5^\circ$), (c) autour de l'axe x (4°) et (d) pour une déviation bi-axiale xy ($3,4^\circ$).

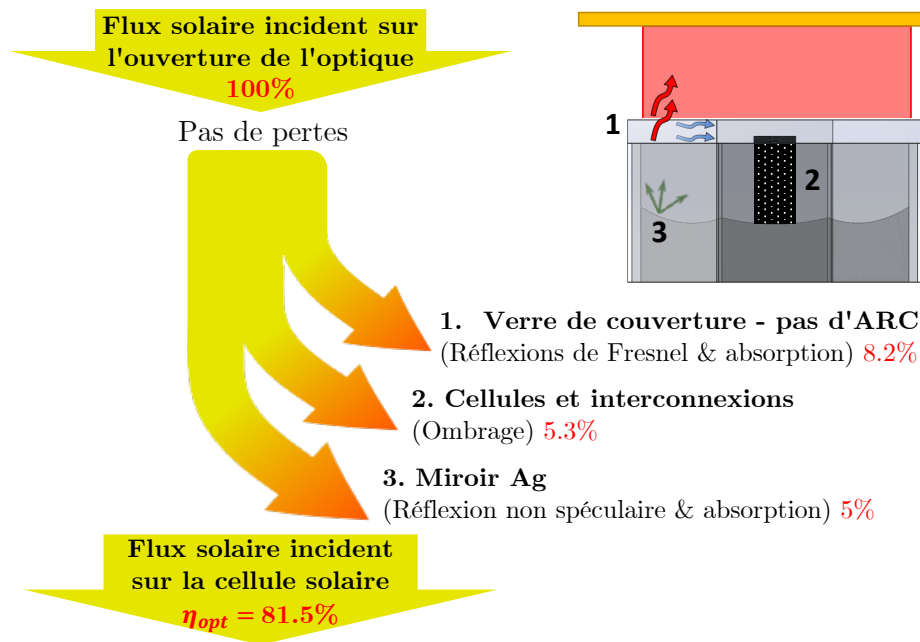


Figure B10: Représentation des principales pertes de puissance optique le long des éléments constitutifs.

En outre, si nous comparons la distance au plan de réception (selon z) qui garantit la tolérance angulaire souhaitée avec la distribution de flux la plus homogène, il a diminué de 1,5 fois, passant de $z = -0,225$ mm à $z = -0,15$ mm d'un système parabolique (idéal) à un système intégré. En lien avec cela, le PAR associé a augmenté de 38%, passant de 4,4 à 7,1 pour un système parabolique avant et après intégration, respectivement. Des estimations qui impliquent une augmentation due aux pertes de résistance en série ($> 2\%$), qui devront être étudiées plus en détail en utilisant des systèmes réels.

Ensuite, concernant l'analyse du désalignement, une tolérance d'environ ± 0.4 mm et ± 0.3 mm a été trouvée, autour de l'axe x et y respectivement. En revanche, autour de l'axe z , on observe une réponse non symétrique variant entre $-0,25$ et $0,35$ mm. Les tolérances mécaniques sont également conformes aux spécifications minimales initiales ($50 \mu\text{m}$).

Enfin, nous avons estimé la densité de courant de court-circuit (J_{SC}) de chaque jonction, sur la base des mesures EQE. La sous-cellule centrale est la plus limitante avec un courant d'environ 2,26 mA, voir Figure B12. De plus, un $\text{SMR}(\text{TOP}/\text{MID}) = 1.15$ a été trouvé. Le chapitre suivant détaille les étapes de fabrication des premiers prototypes.

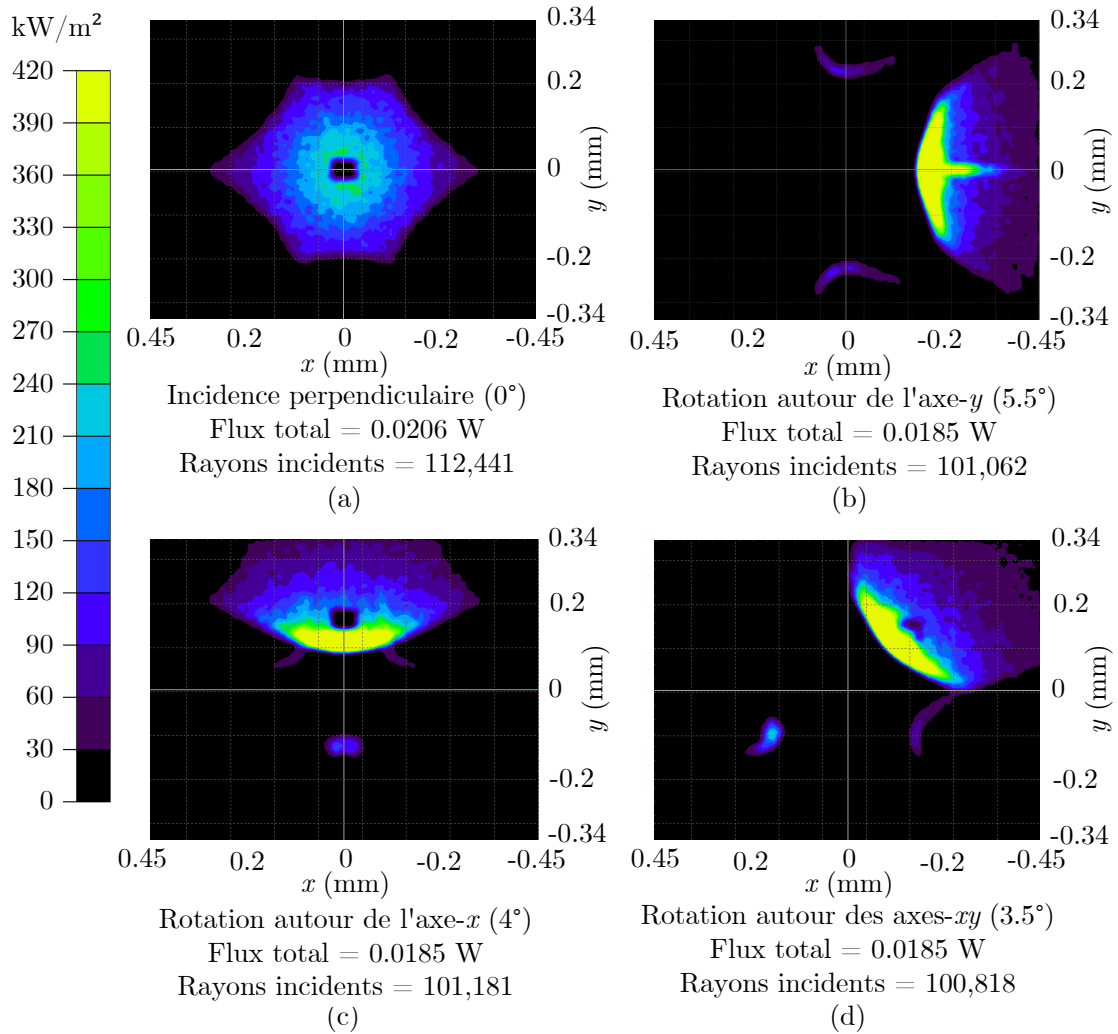


Figure B11: Carte d'irradiance pour un détecteur placé à $z = -0.15$ mm du point focal, utilisant une parabole intégrée.

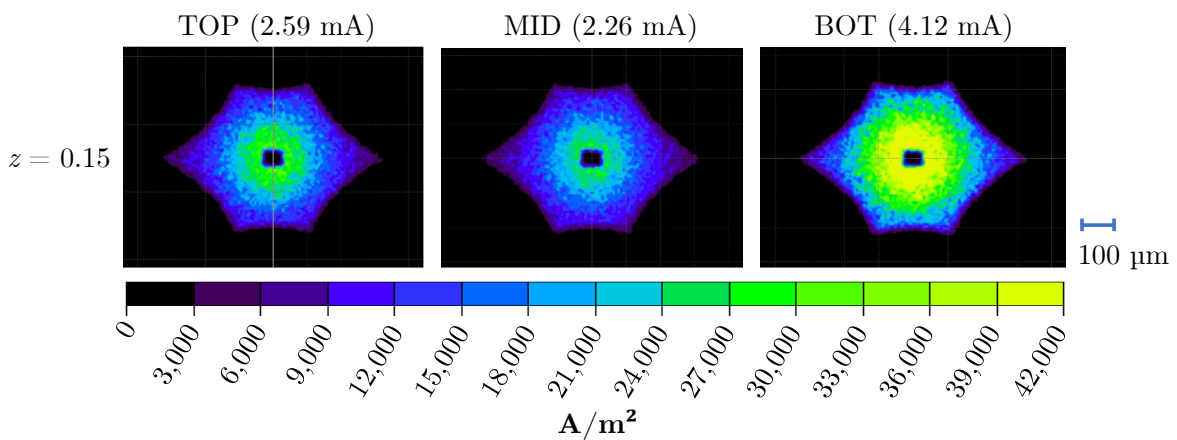


Figure B12: Cartographie photocourant de chaque sous-jonction, TOP (GaInP), MID (GaAs) and BOT (Ge), en utilisant la réponse spectrale EQE et un spectre AM0.

Chapitre 5 : Validation expérimentale d'un réflecteur parabolique hautement intégré

La fabrication de la matrice micro-CPV proposée peut être divisée en deux sous-ensembles: d'une part, la fabrication de la structure composite et de l'optique formée à l'intérieur, et d'autre part, les cellules interconnectées sur le verre de couverture. Ensuite, ces deux parties doivent être soigneusement assemblées en respectant les tolérances mécaniques décrites ci-dessus afin de garantir des performances nominales minimales.

Dans ce chapitre, nous nous concentrons plus particulièrement sur les réflecteurs intégrés dans la structure en nid d'abeille. Plus spécifiquement, une technique de moulage est privilégiée, afin de passer d'un concept théorique à un prototype à potentiel industriel. Cette technique a été choisie principalement parce qu'il s'agit d'une technologie prometteuse à faible coût qui permet la fabrication d'un assemblage optique complet, dans notre cas, le réseau de paraboles en un seul moulage par injection. De plus, il s'agit d'une technique disponible au laboratoire. Le processus de prototypage des miroirs peut être divisé en trois étapes :

(1.) Fabrication de la structure composite;

(2.) Formation de l'optique;

(3.) Métallisation de la surface réfléchissante. Dans la phase de prototypage, notre objectif est de valider le concept avec des mini-modules d'environ $40 \times 40 \text{ mm}^2$, formés par 6 strings (connectés en série), chacun d'eux étant constitué par 5 cellules (connectées en parallèle), pour former finalement un module de 30 unités (cellules/réflecteurs).

A cet égard, la méthode de lamination du composite en deux étapes a été améliorée pour maximiser la surface utilisable, jusqu'à sa totalité, en évitant les déformations de forme de l'empilement. D'autre part, la réticulation du silicone polymère a été étudiée dans le moulage d'optiques afin d'établir le rapport température et temps nécessaire pour obtenir une réticulation complète au moyen d'une analyse DSC. Il a été observé qu'à 90°C le silicone a une enthalpie de réaction élevée, ce qui correspond à un optimum (maximum) de réticulation près de cette température.

Pour concevoir un moule permettant la formation de surfaces paraboliques à l'intérieur d'un réseau en nid d'abeille, il était nécessaire de concevoir des cavités dans le moule ayant la même forme que le réseau pour permettre à la forme parabolique de s'y insérer, en tenant compte d'une tolérance mécanique pour obtenir une insertion en douceur, et de considérer d'éventuelles petites variations dans la forme du noyau en nid d'abeille.

Ensuite, pour assurer l'herméticité du système pendant l'injection du polymère, une plaque de serrage inférieure a été conçue pour permettre à la structure composite d'être fixée au moule à l'aide de quatre vis, comme le montre la Figure B13. En outre, le moule possède une cavité rectangulaire qui abrite le polymère pendant le moulage. Cette cavité a

une hauteur de 8 mm pour contenir le matériau lorsqu'il est soumis au vide, afin d'éliminer les bulles potentielles. La Figure B13 (à droite) montre (en bleu), en haut une des cavités d'injection et en bas le silicone injecté dans le nid d'abeille. D'autre part, 8 trous répartis autour du réseau de cavités d'injection ont été conçus pour démouler le prototype, ceux-ci doivent être fermés à l'aide de 8 vis étanches lors du moulage.

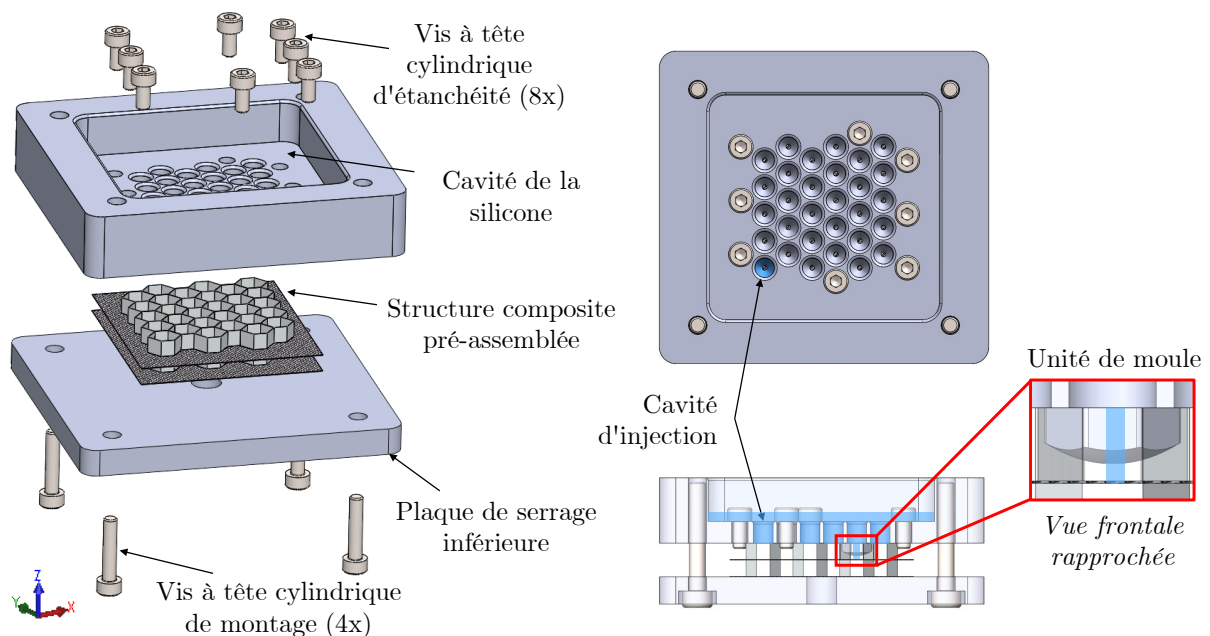


Figure B13: Mono-module stratifié assemblé dans le moule, montrant : une vue éclatée de chaque élément utilisé (à gauche), la face supérieure montrant les canaux d'injection de silicone (en haut à droite), et une vue rapprochée d'une unité de moule injectée en silicone.

Enfin, une fois fabriqué, le moule a été ensuite caractérisé., en commençant par la rugosité et l'analyse dimensionnelle. En identifiant et en mesurant les défauts de surface permanents et non-permanents de chaque unité, il a été observé que les défauts de surface maximums représente environ 4% de la surface d'une unité, respectivement 1,7% et 2% (voir Figure B15).

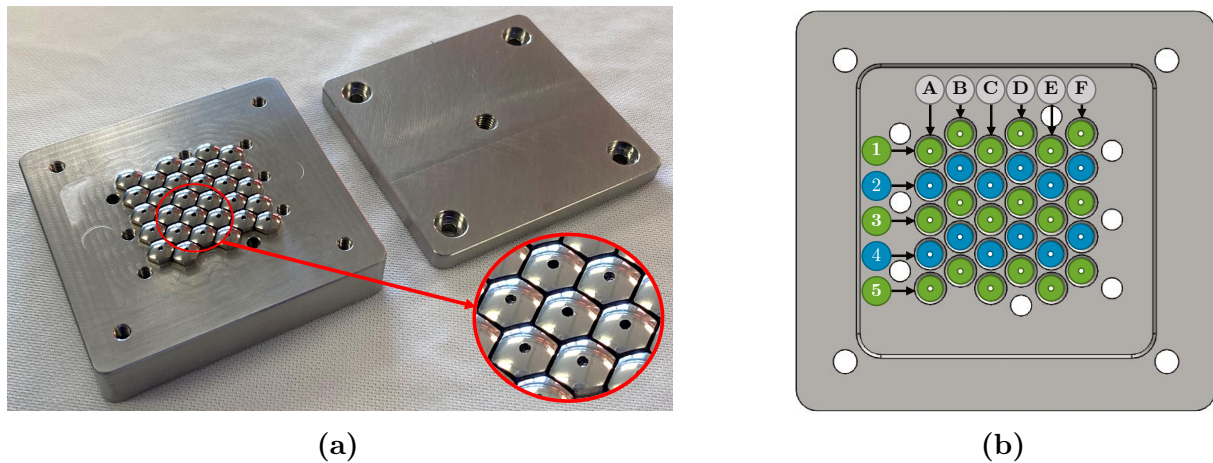


Figure B14: (a) Photographie du moule final fabriqué, montrant une vue rapprochée de 7 unités; et (b) nomenclature des unités de moulage.

Défauts permanents (Éraflures mécaniques + Corrosion)								Pollution par des composés chimiques détachables							
	A	B	C	D	E	F	Unités		A	B	C	D	E	F	Unités
1	0.01	0.03	0.02	0.05	0.02	0.22	mm ²	1	0.19	0.11	0.06	0	0.1	0	mm ²
	0.03	0.18	0.09	0.29	0.11	1.27	%		1.13	0.63	0.37	0	0.60	0	%
2	0.17	0.06	0.23	0.19	0	0.10	mm ²	2	0	0.07	0.18	0.07	0.06	0.08	mm ²
	0.99	0.34	1.33	1.12	0	0.60	%		0	0.40	1.02	0.41	0.35	0.48	%
3	0.15	0.26	0.17	0.11	0.09	0.11	mm ²	3	0	0.35	0.27	0.05	0	0.08	mm ²
	0.87	1.49	0.99	0.61	0.52	0.62	%		0	2.04	1.57	0.28	0	0.46	%
4	0	0.01	0.13	0.30	0.08	0	mm ²	4	0.03	0.03	0.12	0	0.08	0.15	mm ²
	0	0.05	0.76	1.71	0.44	0	%		0.16	0.15	0.69	0	0.49	0.86	%
5	0.29	0.15	0.02	0.01	0.10	0.17	mm ²	5	0	0	0.1	0	0.14	0.06	mm ²
	1.70	0.84	0.13	0.07	0.59	0.99	%		0	0	0	0	0.83	0.38	%

Figure B15: Cartes de mesure par défaut des moules.

Une fois caractérisé, le moule a été utilisé, comme le montre la Figure B16, pour le prototypage de la structure et de l'optique d'un module de 30 unités.

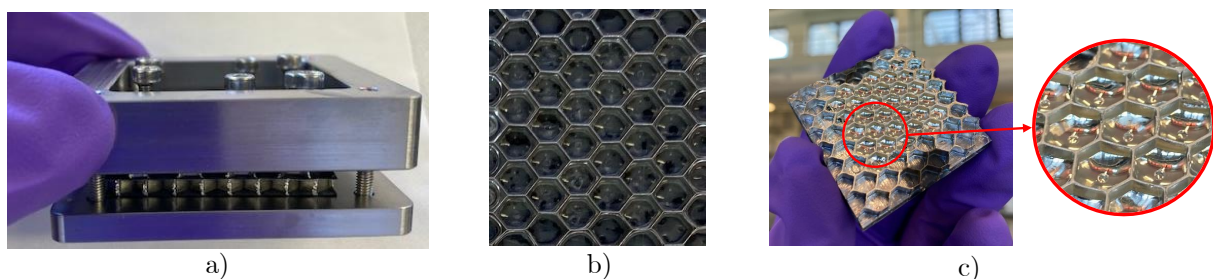


Figure B16: Prototypage d'un module de 30 unités (40x40 mm²) : a) Procédé de moulage, b) Optique moulée, c) Module avec revêtement argenté réfléchissant.

En complément de cette validation expérimentale, le chapitre suivant présente une méthode de caractérisation de la topographie de la surface parabolique du moule et des

optiques afin d'estimer les performances.

Chapitre 6 : Estimation de l'efficacité optique via la caractérisation topographique par microscopie optique et tracé de rayons

La qualité optique des surfaces réfléchissantes est une question de grande importance dans les systèmes CPV, tant pour les applications terrestres que spatiales. Les déviations des formes optiques par rapport à leur géométrie nominale, théoriquement parfaite, ainsi que les irrégularités des interfaces optiques, peuvent entraîner des pertes d'énergie substantielles sous forme de fuites de rayonnement.

Pour valider le système micro-CPV proposé, fortement intégré dans un nid d'abeille, nous cherchons à quantifier les défauts de forme de fabrication des optiques, c'est-à-dire l'erreur de forme, par rapport aux surfaces idéales issues de la conception optique. Dans ce chapitre, nous présentons une méthode de caractérisation développée pour estimer l'efficacité optique d'un réflecteur moulé en évaluant sa forme topographique par des mesures de microscopie optique combinées à des simulations de tracé de rayons. Nous commencerons par exposer la caractérisation de la méthode proposée qui utilise un revêtement matifiant auto-évaporant pour améliorer le contraste des surfaces mesurées. Nous nous intéressons ensuite à la caractérisation de la forme du moule et de l'optique fabriquée, qui se divise en deux parties principales. Premièrement, une reconnaissance de la forme quadratique décrite par le nuage de points mesurés sera faite en utilisant un ajustement par la méthode des moindres carrés. Ensuite, nous avons effectué une reconstruction de la forme, qui a ensuite été utilisée dans l'estimation de l'efficacité optique en utilisant TracePro. Enfin, une analyse de corrélation entre la reconnaissance et la reconstruction de la forme est présentée.

Dans cette étude, nous nous intéressons à la mesure de la topographie des réflecteurs à l'échelle micrométrique en utilisant un microscope optique. Cette technique sans contact a été choisie, compte tenu de la petite taille des optiques, alors que d'autres techniques comme les profilomètres mécanique de surface (c'est-à-dire de type contact) ne sont pas adaptées car les surfaces sont trop courbes et de trop petite tailles.

Après avoir vu que la microscopie optique n'est pas adaptée à la mesure de surfaces spéculairement réfléchissantes et transparentes, nous nous sommes intéressés à la recherche d'alternatives pour rendre les surfaces diffuses pour que les mesures puissent être effectuées. Dans ce cas, la difficulté réside dans la recherche de matériaux appropriés pour réaliser ce dépôt. Pour cela, nous avons considéré les critères suivants :

- i)* Le matériau doit être facile à déposer et former une couche qui s'adapte à la surface.
- ii)* La couche formée doit être uniforme sur la surface, et la rugosité doit être négligeable par rapport à la forme.
- iii)* Le matériau doit être facile à enlever et ne doit laisser aucun résidu.

Nous proposons l'utilisation d'un spray de matifiant bleu AESUB® [368], un revêtement auto-effaçant destiné à s'évaporer en quelques heures sans laisser de résidus. Bien que la

composition exacte du revêtement ne soit pas communiquée, il contient 67,36% de solvant, 0% de solides et 32,64% de gaz propulseur. Selon la fiche technique, le revêtement est appliqué "humide", à une distance de 15 à 20 cm et la température ambiante recommandée est de 21°C. En outre, le fabricant affirme que l'épaisseur d'une couche opaque est de 8-15 μm , selon l'application spécifique de l'utilisateur. Par conséquent, avant d'utiliser le revêtement, quelques mesures préliminaires ont été effectuées pour qualifier et valider la méthode en termes de précision par rapport à la surface parabolique à mesurer, et pour trouver les conditions de travail adéquates.

Qualification des paramètres d'application d'un revêtement matifiant pour les mesures de surface

Pour qualifier l'utilisation d'un spray de matifiant auto-évaporant afin d'améliorer le contraste des mesures de microscopie optique, plusieurs analyses ont été réalisées. Nous présentons d'abord les mesures d'épaisseur et de surface couverte en fonction du nombre de couches déposées. Ensuite, nous présentons les mesures de rugosité, et enfin nous déterminons le temps de sublimation de la surface couverte, sous l'éclairage du microscope pendant la caractérisation de la surface. Pour ces essais, des portions d'une plaquette de silicium monocristallin polie, choisie pour sa faible rugosité, ont été utilisées comme échantillon de référence.

La Figure B17 présente les résultats de la série de tests effectués sur la plaque de silicium, en appliquant 1 à 13 couches de pulvérisation. D'une part, on constate que l'épaisseur du revêtement est d'environ 1,6 μm ($2\sigma = 0,3 \mu\text{m}$) avec une surface remplie d'environ 43% ($2\sigma = 3,1\%$) et évolue de façon continue jusqu'à une épaisseur maximale de 17 μm ($2\sigma = 0,8 \mu\text{m}$) pour une couverture quasi-totale, c'est-à-dire, 99,8% ($2\sigma = 0,1\%$). L'épaisseur moyenne de chaque cycle de pulvérisation (i.e. épaisseur/nombre de cycles) a également été calculée et il a été observé que chaque couche génère en moyenne 1,2 μm de surépaisseur avec une déviation standard moyenne entre 1 et 13 couches appliquées de $2\sigma = 0.6 \mu\text{m}$.

De plus, l'évolution de la surface couverte commence à stagner entre 7 et 9 cycles, avec une couverture de surface de 95% ($2\sigma = 1,2\%$) à 96,4% ($2\sigma = 1,5\%$), et des épaisseurs de 7,6 ($2\sigma = 0,5 \mu\text{m}$) à 9,5 μm ($2\sigma = 0,7 \mu\text{m}$), respectivement. Nous avons choisi l'utilisation de 8 cycles de pulvérisation équivalent à une surface couverte de plus de 96,5% ($2\sigma = 0,8\%$) et une épaisseur de 8,8 μm ($2\sigma = 0,25 \mu\text{m}$).

Le revêtement appliqué induit une augmentation de la rugosité, qui tend à s'atténuer lorsque le nombre de couches augmente. Sur la base des 8 couches appliquées, la rugosité moyenne quadratique mesurée (ou Rq) est de 1100 nm avec une rugosité pic à pic maximale (ou Rz) de 1700 nm. Nous pourrions donc détecter des défauts de taille de l'ordre de 4-5 μm . De plus, il a été démontré que le temps maximal pour effectuer la mesure et garantir les

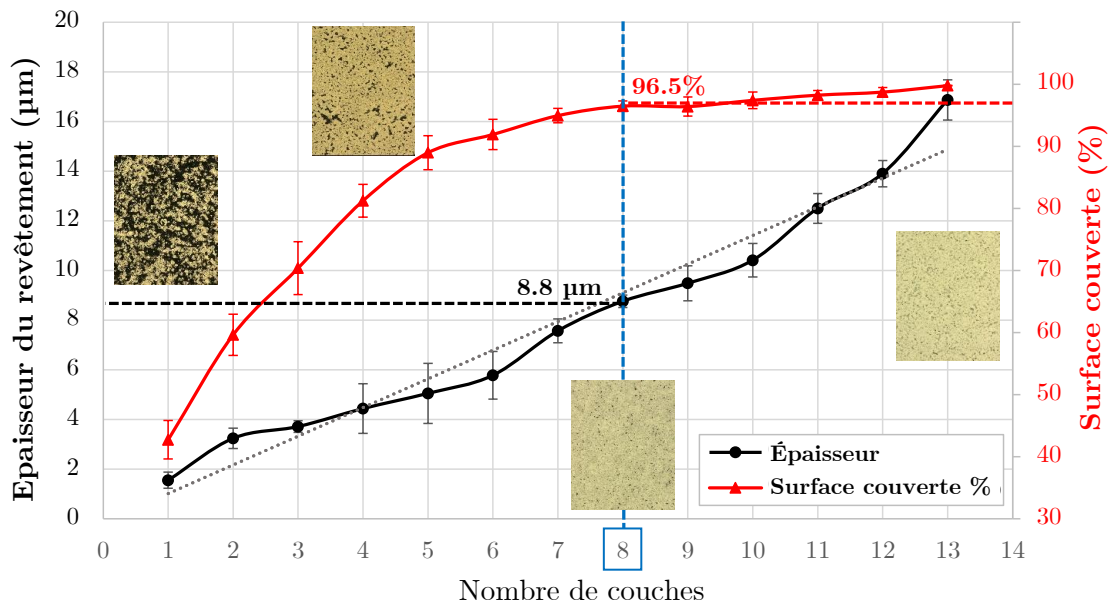


Figure B17: Évolution de l'épaisseur des couches et de la surface couverte pour différents nombres de couches.

90% de la surface couverte dépend à la fois des matériaux utilisés et de leur structure. Dans notre cas, en considérant des structures plates et 8 couches de pulvérisation, un temps de mesure maximal de moins de 15 minutes a été observé pour un substrat constitué uniquement de silicone, alors que si l'on considère un substrat en silicium, ou un substrat en silicone sur CFRP, ce temps augmente à près de 30 minutes.

Reconnaissance, reconstruction et analyse des surfaces mesurées

Une fois qualifié la méthode de caractérisation, nous l'utilisons pour extraire l'image de la surface réfléchissante et pour reconstruire la surface sous forme d'un nuage de points. Cette méthode, de la préparation de l'échantillon au traitement des données, est illustrée sous la forme d'un diagramme dans la Figure B18.

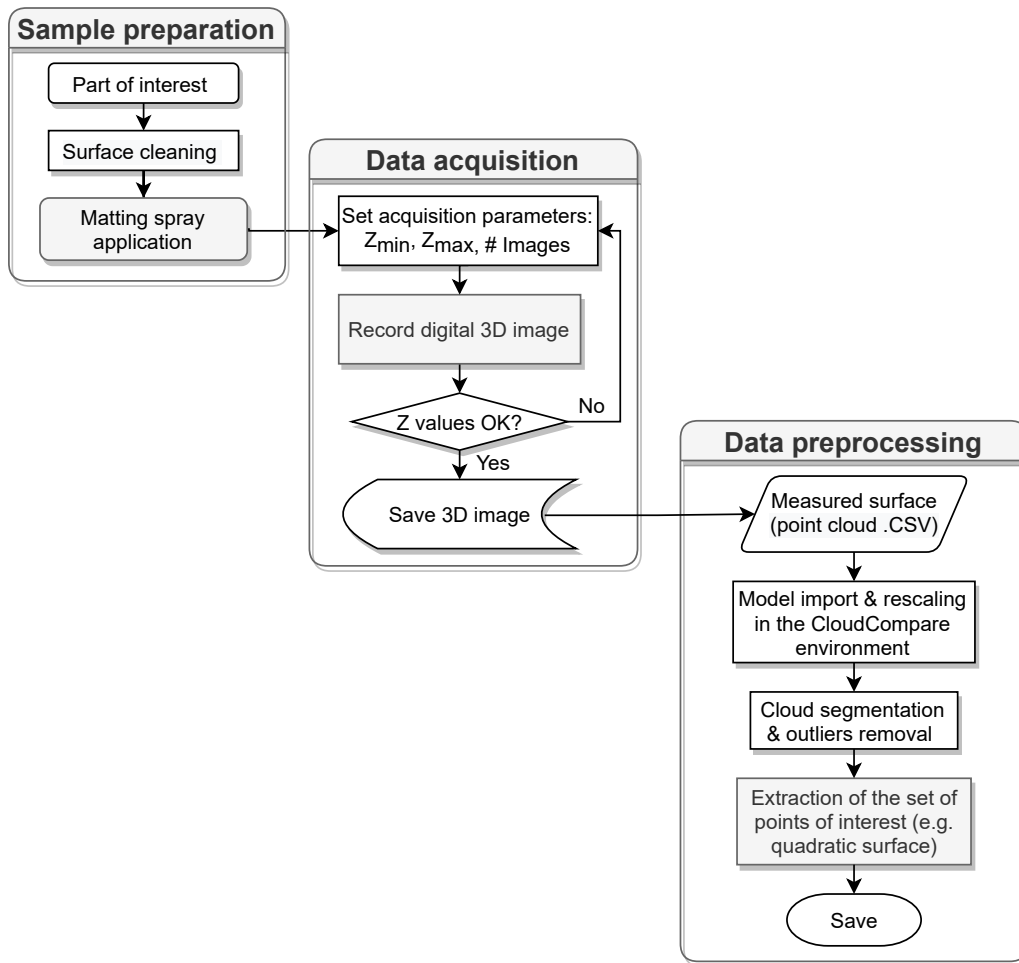


Figure B18: Diagramme du processus global de la préparation de l'échantillon au traitement des données.

Premièrement, nous nous sommes intéressés par la reconnaissance de la forme quadratique décrite par le nuage de points mesurés au moyen d'un ajustement par la méthode des moindres carrés, dans le but d'identifier les déviations potentielles de la surface évaluée, voir Figure B19 (a).

Dans un deuxième temps, nous voulons pouvoir reconstruire à partir de ce nuage de points une surface aussi représentative que possible de la surface réelle mesurée, et estimer l'erreur de cette reconstruction. Cette reconstruction est ensuite utilisée pour l'estimation de l'efficacité optique par tracé de rayons, voir Figure B19 (b).

Enfin, une analyse de corrélation entre les écarts obtenues (reconnaissance et reconstruction) et la forme nominale conçue est proposée. Pour le traitement des données, nous utilisons le logiciel libre CloudCompare [370], dédié à l'édition et au traitement de nuages de points 3D (et de mailles triangulaires), afin de comparer les mesures à une forme nominale, d'ajuster une équation qui décrit au mieux le nuage de points, et enfin de reconstruire la surface optique par une méthode de Poisson.

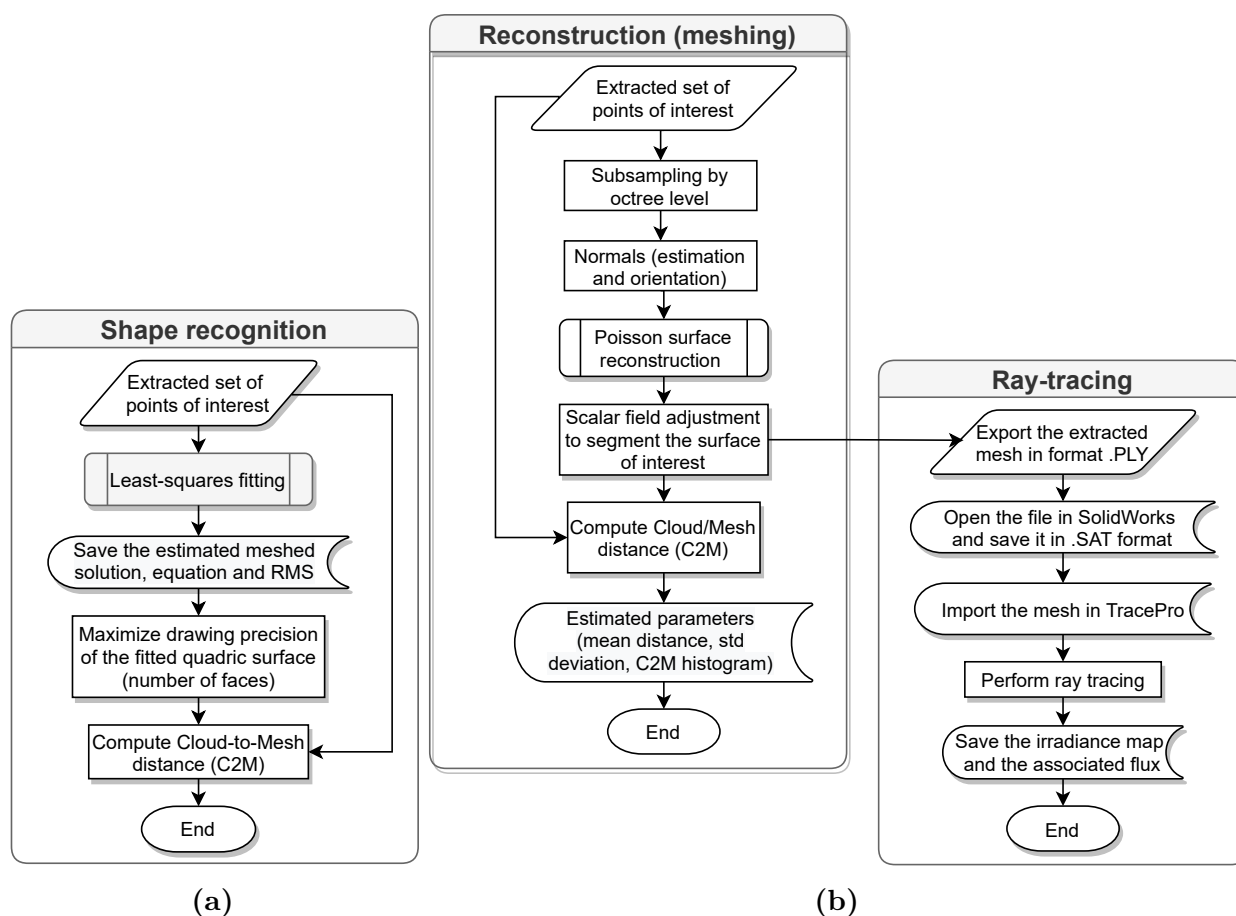


Figure B19: Diagramme du processus de: (a) reconnaissance et (b) de reconstruction et estimation de l'efficacité des surfaces optiques.

Nous avons commencé la validation de l'ajustement en utilisant des formes quadratiques idéalisées, c'est-à-dire une conception CAO virtuelle d'une unité de moulage. Pour cela, nous avons utilisé différents nombres de points décrivant la surface d'intérêt, qui après reconnaissance de forme ont présenté des écarts types évoluant de 14.6 nm pour 993,427 points à 610 nm en utilisant 2,529 points. Ceci garantit un ajustement relativement précis, inférieur de deux ordres de grandeur à la rugosité RMS du dépôt (1.1 μm).

Ensuite, pour qualifier la technique de moulage (en utilisant le silicone DC-93500 qui est utilisé pour fabriquer des optiques), et pour déterminer la précision de la reconnaissance topographique, nous avons utilisé une bille de roulement de rayon 2,5 mm comme référence, voir Figure B20.

Grâce à l'analyse de reconnaissance de forme, nous avons constaté qu'il y avait une déviation de forme significative au sommet de la sphère de 49 μm qui est 25 fois plus grande que la déviation maximale attendue du revêtement. Ceci a été attribué à une surépaisseur de silicone sur la sphère. Ainsi, cette surépaisseur a induit une sous-estimation du rayon (par la méthode des moindres carrés) d'environ 10,2 μm .

Cette approche s'est avérée sensible aux valeurs atypiques qui étaient concentrées à une

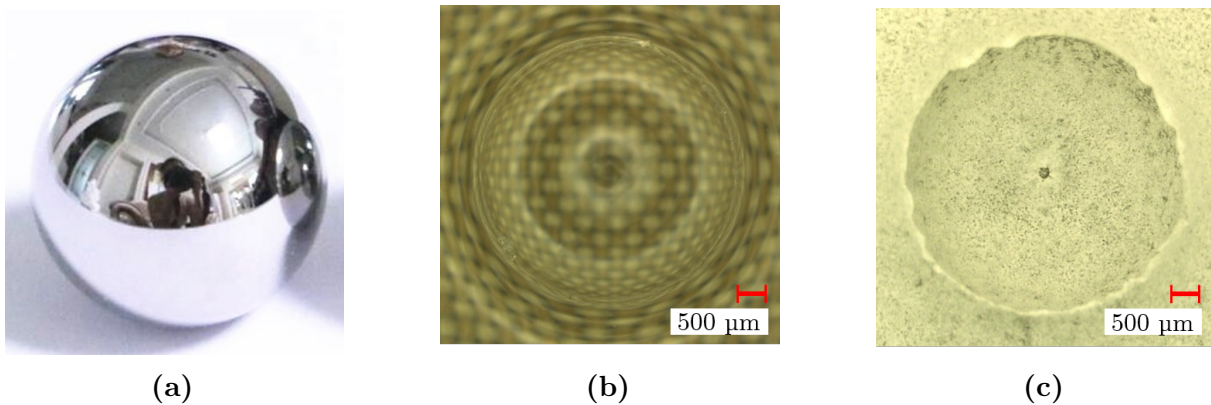


Figure B20: (a) Bille de roulement (diamètre 2.5 µm) ; Forme moulée en utilisant du silicone DC 93-500 : (b) avant le revêtement, (c) après le revêtement en utilisant 8 couches.

hauteur d'environ 0,3 mm ($< 10\%$ du nombre total de points), voir Figure B21. Cependant, nous avons profité de ce défaut apparent pour filtrer les points aberrants et estimer à partir de quel pourcentage du nuage de points mesurés correspond la forme nominale de la bille. Nous avons observé qu'une fois le nuage de points segmenté, le diamètre de la sphère moulée pouvait être estimé avec une précision de 0,4% (soit 4,486 mm).

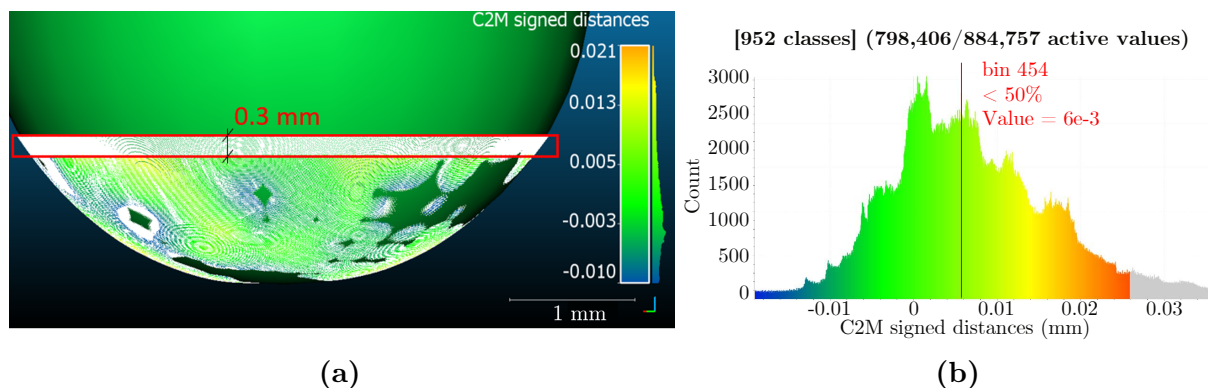


Figure B21: (a) C2M distance pour la bille de roulement utilisant un nuage de points segmenté (un million de points); (b) Histogramme de distance C2M.

Ensuite, nous avons utilisé la méthode pour caractériser une unité du moule fabriqué. Nous avons vu que les écarts maximaux d'environ 0,1 mm se produisent sur les bords de la forme hexagonale. Ces écarts de forme sont liés en partie aux défauts de fabrication du moule : surfaces mal polies ou rayures. À cet égard, nous avons considéré les bords, qui sont la principale composante de l'erreur, comme des valeurs aberrantes, et la segmentation ultérieure de celles-ci comme un filtre passe-bas, voir Figure B22. En ce sens, nous avons constaté à partir des mesures du moule que la forme idéale peut être reconnue à partir de 90% (projection supérieure) et une erreur maximale associée de 1,3%. Alors que celle-ci atteint 0,3% lorsque 85% de la surface totale est utilisée.

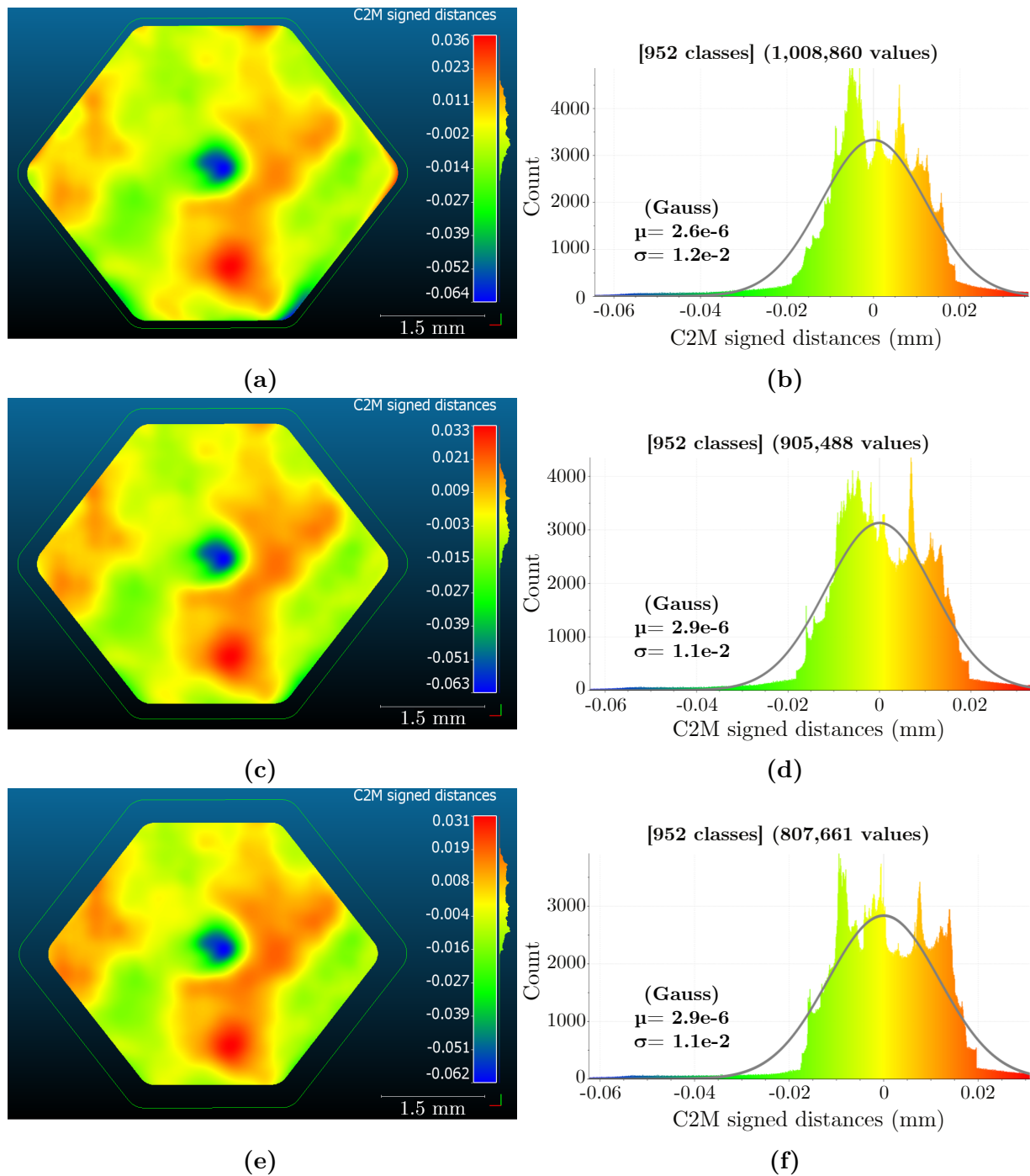


Figure B22: Comparaison C2M entre le nuage de points mesuré sur l'unité d'un moule (position B2) et le quadratique ajusté, pour différentes surfaces segmentées au niveau des bords pour éviter toute distorsion, en considérant : 95% (a), 90% (c) y 85% (e) de la surface ; et Histogramme de comparaison C2M avec un ajustement de la distribution gaussienne pour 95% (b), 90% (d) y 85% (f) du modèle de nuage de points.

La même procédure de reconnaissance de forme a été réalisée pour une optique moulée utilisant la même unité de moulage. Dans ce cas, en considérant la surface totale mesurée,

une déviation maximale de 0,18 mm a été obtenue sur les bords et une erreur maximale des coefficients estimés de 7,5%, qui diminue à 2,2% et 1,6% en considérant 90% et 85% de la surface totale, respectivement. Cette différence dans les écarts entre l'unité de moulage et l'optique est le résultat d'une combinaison d'artefacts de mesure et d'erreurs associées au moulage. Ayant terminé la reconnaissance des formes par la méthode des moindres carrés, nous allons maintenant procéder à la reconstruction de ces formes, des moules et des unités optiques, afin d'estimer leur efficacité optique par tracé de rayons.

Dans ce travail, nous avons reconstruit les surfaces mesurées à partir d'un ensemble de points en utilisant une méthode de reconstruction par maillage de Poisson. Cette méthode permet d'ajuster les données numérisées et de remplir les trous de surface pour un ensemble de points d'une densité d'échantillonnage donnée ; elle est incorporée dans le logiciel CloudCompare [374].

Pour estimer l'efficacité optique de cette surface, nous avons d'abord déterminé la position du plan de mesure optimal par rapport au foyer (le long de l'axe z) pour étudier la distribution du spot. Sachant que la distance optimale d'intérêt doit maximiser le flux perçu ainsi que la taille du spot pour obtenir le plus de détails possible sur la forme et la distribution du flux. Pour cela, nous avons considéré un modèle paramétrique et l'avons comparé à des modèles maillés en utilisant différents nombres de facettes considérés, entre 1,000 et 20,000. Nous avons observé que ce plan est situé à -0,19 mm du foyer et qu'en utilisant entre 10,000 et 20,000 facettes, et 500,000 rayons tracés, il est possible d'obtenir à la fois la distribution du flux et le flux total plus proches de ceux obtenus avec le modèle paramétrique idéal, avec des erreurs inférieurs à 0,1% (voir Figure B23). Alors que l'utilisation d'un nombre inférieur de facettes impliquerait à la fois des pertes de flux et de distribution de l'irradiance de, par exemple, 6,8% et 0,5% du flux perçu, pour 1,000 et 5,000 facettes, respectivement.

Nous avons ensuite procédé à la reconstruction du maillage en utilisant l'ensemble des points mesurés (préalablement segmentés), à partir d'une unité de moulage et d'une optique fabriquée, via la technique de Poisson. Dans la reconstruction du moule, il a été observé que le maillage généré est précis par rapport au nuage de points, avec une déviation de la distance moyenne entre ces entités de $5e-4$ mm, soit trois fois moins que la précision de la méthode de recouvrement. Alors que pour le moule, cette distance était de $9e-4$ mm, soit 1,6 fois moins.

Ensuite, un tracé de rayons des mailles reconstruites a été effectué en utilisant une source solaire AM0 et 500,000 rayons. Les irrégularités observées sur les bords, à partir de la reconstruction, des deux surfaces, présentent des difficultés de focalisation. Nous avons ensuite estimé l'efficacité optique par rapport au tracé de rayons d'un modèle paramétrique idéal avec la même source solaire. Le moule a une efficacité optique de 87,4%, alors que pour l'optique moulée, l'efficacité était de 81,2% (soit environ 7% de moins), voir

Figure B24. Cette différence d'estimation de l'efficacité, entre la même unité de moulage et l'optique fabriquée, est sûrement liée à des erreurs de moulage comme le retrait du silicone.

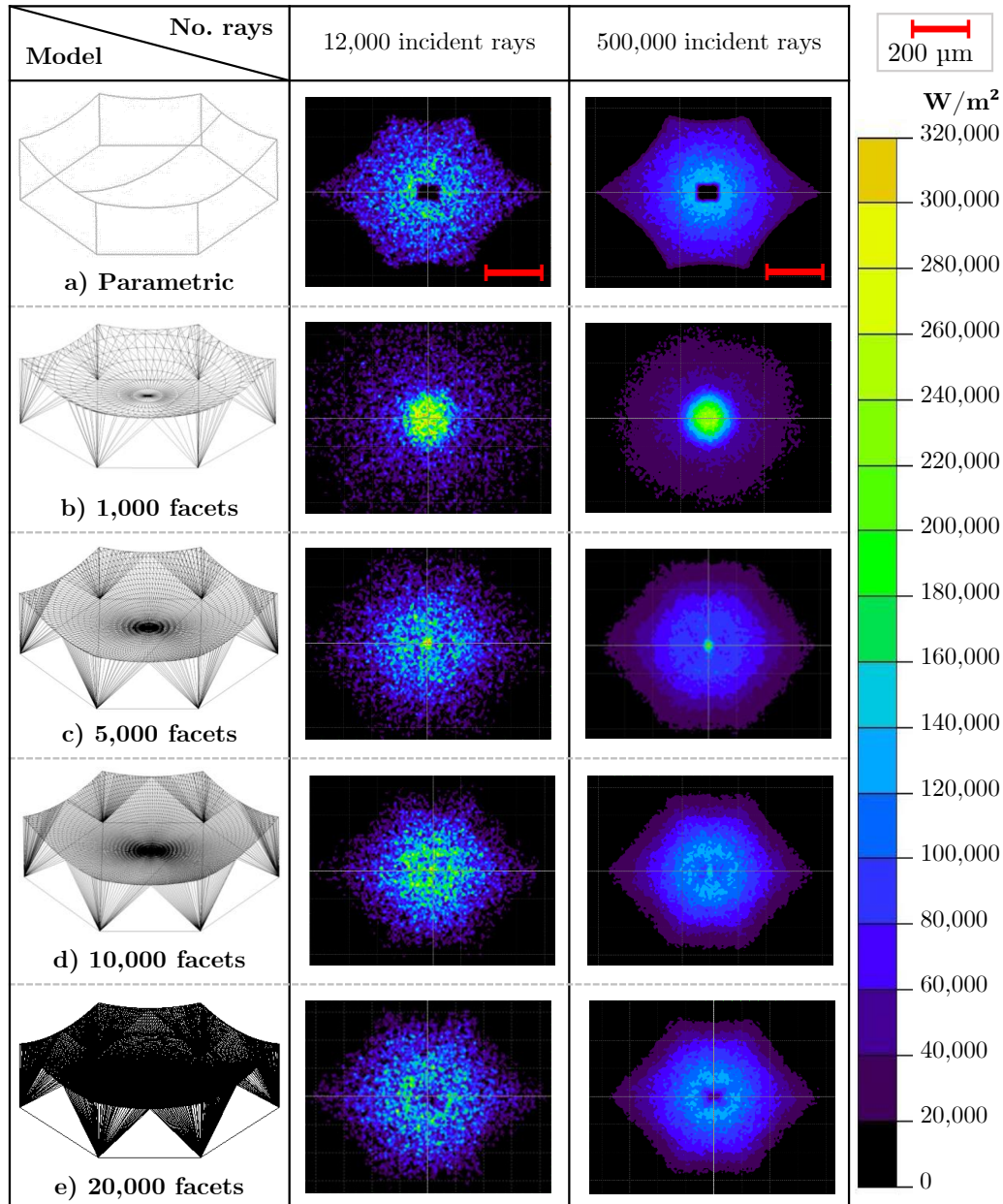


Figure B23: Analysis of the number of mesh facets and traced rays (for a plane $z = -0.19$ mm), considering: a) a parametric model, and a mesh composed of b) 1,000 facets; c) 5,000 facets, d) 10,000 facets and e) 20,000 facets.

Ainsi, la méthode de Poisson permet d'obtenir des maillages fiables pour estimer l'efficacité optique via un logiciel de tracé de rayons. Des écarts de 12.6% et 18.8% sont relevés, pour le moule et l'optique, respectivement. D'autre part, la méthode proposée, qui utilise un revêtement mat pour améliorer le contraste, induit à la fois une sur-épaisseur de 8,8 μm et une rugosité Rq mesurée jusqu'à 1,4 μm (soit pour 8 couches appliquées), sur la

surface étudiée, ce qui induit des biais dans la topographie mesurée par microscopie optique.

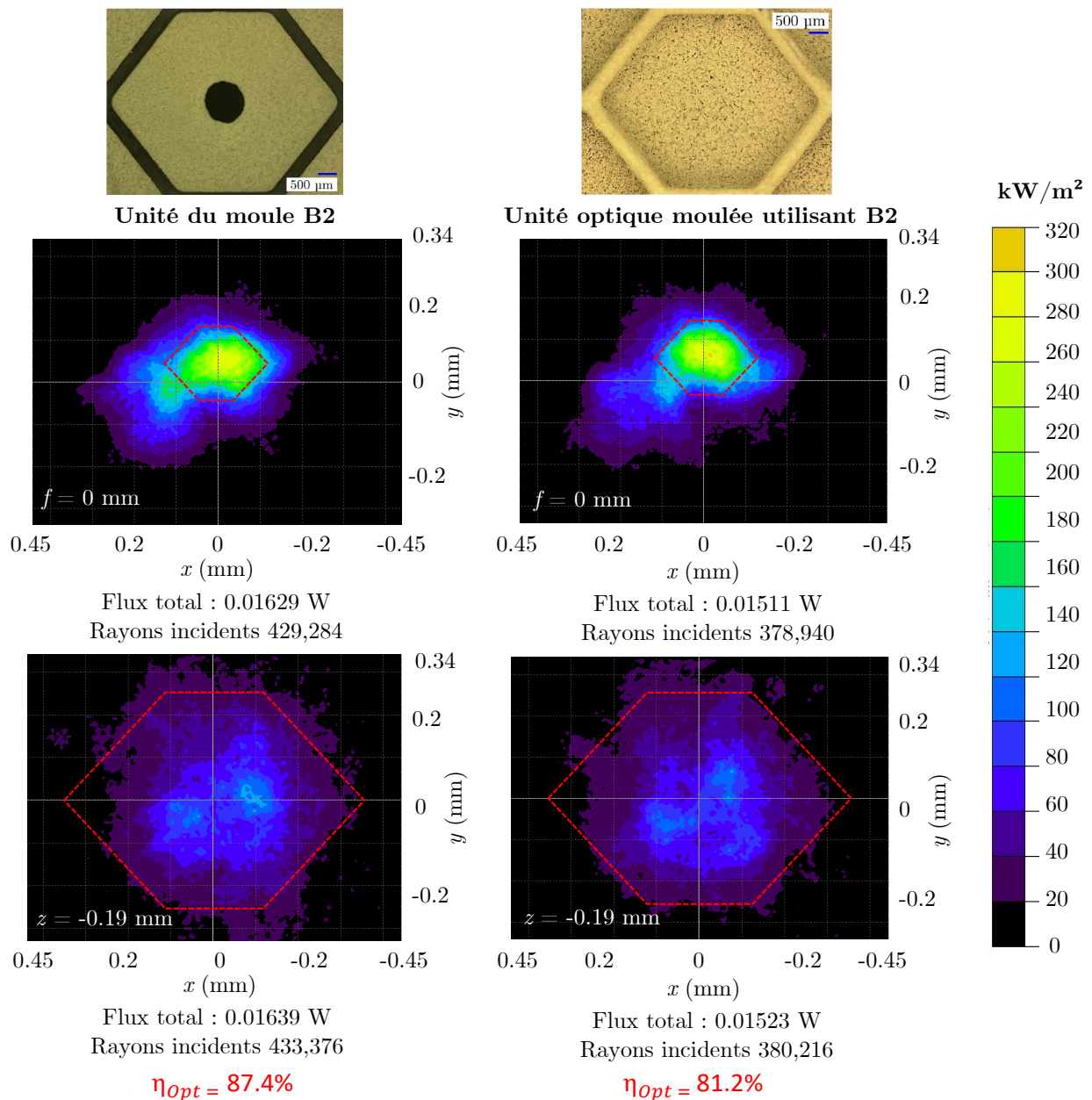


Figure B24: Comparaison de l'efficacité optique estimée entre une unité de moulage (B2) et son unité optique moulée relative.

Ensuite, il a pu être mis en évidence que le moule présente des erreurs de fabrication, de polissage et de rayures, notamment localisées sur les bords de l'unité optique. Ce dernier, à son tour, transmet les défauts de surface à l'optique moulée, comme on peut le voir sur la Figure B24, dans laquelle les spots générés par les deux surfaces optiques, moule et optique, tendent à avoir une forme similaire, aussi bien pour le plan focal $f = 0 \text{ mm}$ que pour le plan situé à $z = -0.19 \text{ mm}$.

Ainsi, la méthode développée permet de caractériser les erreurs de forme des optiques, ainsi que les défauts de surface $>10\ \mu\text{m}$, cependant elle n'est pas utile pour la mesure de défauts plus petits, tels que la rugosité des surfaces optiques, puisque le revêtement utilisé les recouvre.

Par conséquent, la caractérisation de la performance optique ne peut être faite que sur le module complet avec des mesures sous irradiation, en utilisant les cellules interconnectées sur le verre de couverture, ce qui n'a pas pu être fait dans cette thèse par manque de temps. Cela fait donc partie des travaux futurs à réaliser.

Conclusions et perspectives

Dans cette thèse, nous avons étudié la pertinence et la faisabilité de nouveaux concepts photovoltaïques à microconcentration, pour les applications spatiales, afin d'étudier les avantages en termes de performance pour atteindre des rendements optiques élevés et des densités de puissance spécifiques et volumétriques élevées. Un certain nombre de questions scientifiques ont été soulevées, concernant l'optique, les matériaux et leur compatibilité et stabilité par rapport à l'environnement, ainsi que l'intégration des optiques dans un module photovoltaïque efficace et léger.

Pour répondre à ces questions, un examen de l'état de l'art des systèmes CPV a d'abord été effectué, mettant en évidence certaines méthodes permettant d'obtenir des technologies photovoltaïques plus efficaces, en intégrant non seulement de nouvelles géométries, mais aussi des matériaux et des structures sur mesure. Il a été constaté que, par rapport aux précédents systèmes CPV destinés aux applications spatiales avec des cellules solaires $> 1\ \text{cm}^2$, les systèmes micro-CPV (cellules $< 1\ \text{mm}^2$) ont le potentiel de réduire la masse, en assurant une gestion thermique passive avec des niveaux de concentration moyens ($< 100X$).

Nous avons ensuite évalué les missions et environnements spécifiques adaptés au déploiement du CPV dans l'espace. Ainsi, il a été constaté que ces systèmes offrent une protection inhérente aux cellules photovoltaïques actives contre les flux élevés de particules chargées à haute énergie que l'on trouve sur les orbites terrestres et autour des systèmes jovien et kronien, ce qui rend le CPV bien adapté pour fournir de l'énergie à ces missions. À de grandes distances, jusqu'à cinq unités astronomiques, les effets de la faible irradiation et de la dégradation à basse température (LILT) peuvent être atténués par les systèmes CPV en augmentant l'irradiation effective et en fonctionnant comme s'ils étaient plus proches du Soleil.

Ensuite, nous sommes passés à l'étude de deux concepts différents de CPV. Une première approche a consisté à optimiser un système CPV. À cette fin, une optimisation à plusieurs niveaux a été réalisée, depuis la reconception du système optique par tracé de rayons pour maximiser le flux de lumière solaire sur les récepteurs, en passant par le

processus de moulage de fabrication, jusqu'à l'intégration de cellules solaires à base de silicium (III-V/Si) à faible coût. Après avoir été optimisée, une efficacité optique de 80% a été mesurée, conduisant à une puissance spécifique d'environ 20 W/kg. Cependant, ce dernier n'est pas en ligne avec les métriques actuelles attendues pour les panneaux solaires recherchant des puissances spécifiques > 100 W/kg.

Ensuite, un nouveau concept basé sur un miroir miniaturisé hautement intégré dans un panneau sandwich à âme en nid d'abeille a été proposé, avec pour objectif d'augmenter la puissance spécifique et volumétrique. Tout en fournissant une structure monolithique qui évite le déploiement dans l'espace, entre les optiques et les cellules, le nid d'abeille fournit la rigidité et maintient l'optique et les cellules solaires séparés et alliés. Les pertes optiques prédominantes du réflecteur parabolique choisi ont été étudiées, en tenant compte des pertes par réflexion, absorption et diffusion. Il en ressort une efficacité optique estimée à environ 82%, qui, en tenant compte d'un ARC des deux côtés du verre de couverture et de lignes d'interconnexion optimisées, pourrait être augmentée jusqu'à 88%. Ainsi, en termes de tolérance angulaire, il a été constaté que le plan de détection optimal pour localiser la cellule et garantir les critères de tolérance angulaire minimum (uniaxial $> 4^\circ$, et bi-axial $> 2.5^\circ$), est situé à -0.15 mm le long de l'axe z , qui à son tour a un PAR estimé d'environ 7. Enfin, la densité de courant de court-circuit de chaque jonction a été estimée à partir des mesures EQE.

Pour passer d'un concept théorique à un prototype validé ayant un potentiel industriel (dans le PDMS), nous avons proposé une méthode de moulage pour fabriquer des optiques intégrées directement dans un nid d'abeille. Pour caractériser les défauts de surface et de forme d'une surface optique (à l'échelle micrométrique) et ainsi estimer son efficacité optique, une méthode de caractérisation a été développée, basée sur des mesures topographiques par microscopie optique combinées à des simulations de tracé de rayons. La méthode proposée utilise un revêtement matifiant auto-évaporant pour améliorer le contraste des surfaces mesurées.

Ensuite, nous avons étudié la forme du moule et de l'optique associée. Tout d'abord, une reconnaissance de la topographie (forme quadratique) décrite par le nuage de points mesurés a été effectuée au moyen d'un ajustement par les moindres carrés. En outre, une reconstruction de la forme optique a été effectuée à l'aide d'un algorithme de Poisson, qui est ensuite utilisé dans l'estimation de l'efficacité optique par tracé de rayons. La corrélation entre la reconnaissance de forme et la reconstruction de forme a montré que dans les deux cas, les bords de l'unité optique (entre 5% et 15% de la surface totale) présentent des déviations par rapport à la forme idéale, ce qui correspond en grande partie à des erreurs de fabrication du moule (par exemple, polissage et rayures). Ces écarts peuvent également être associés dans une certaine mesure à la surépaisseur, à la rugosité et à l'homogénéité du revêtement appliqué. Leurs contributions restent à être dissociées.

Enfin, un tracé de rayons des mailles reconstruites a été effectué à l'aide d'une source solaire AM0. La qualité d'intégration du moule de 87,4% par rapport à l'idéal, alors que pour l'optique moulée elle était de 81,2%, soit 7% de moins. Cette différence d'estimation de la qualité, entre la même unité de moule et l'optique fabriquée, est liée à des erreurs de moulage et doit être améliorée.

Le travail de thèse laisse certaines questions ouvertes qui pourraient être abordées dans des travaux futurs, telles que :

(i.) Pour la finition de la pièce optique, les paramètres et la méthode de dépôt du revêtement réfléchissant utilisés pourraient être optimisés pour obtenir des performances optiques élevées, c'est-à-dire une réflectivité $> 90\%$, aussi leur durabilité par rapport aux contraintes spatiales (stabilité chimique, résistance mécanique liée à la dilatation différentielle lors des cycles thermiques, sensibilité aux rayonnements, etc.)

(ii.) Par ailleurs, une autre façon d'améliorer l'efficacité optique de ce système est d'optimiser les lignes d'interconnexion utilisées afin de réduire l'ombrage qu'elles génèrent.

(iii.) La suite directe du travail effectué consiste en l'intégration de cellules interconnectées pour la réalisation d'un module complet pour caractériser son efficacité. Ce résultat n'a pu être atteint par manque de temps durant la thèse, mais il permettra de compléter l'étude de cette solution en termes de performances.

(iv.) Puisque l'application cible de la technologie micro-CPV proposée est l'espace, une série de qualifications doit être réalisée pour étudier les différents phénomènes de dégradation des matériaux utilisés, par rapport aux conditions environnementales étudiées dans le chapitre 2, comme le dégazage, le cycle thermique, les vibrations, entre autres études de vieillissement en fonction des facteurs de stress rencontrés dans l'environnement spatial. Enfin, l'étude de ce type de système dans un environnement spatial permettra de valider la conception et les choix technologiques.

*The first kind of intellectual and artistic personality
belongs to the hedgehogs, the second to the foxes ...*

— Sir Isaiah Berlin

References

- [1] M.R. Patel. *Spacecraft Power Systems*. Taylor & Francis, 2004.
- [2] R. Ambrosi et al. “Radioisotope Power Systems for the European Space Nuclear Power Program”. In: *2019 IEEE Aerospace Conference*. ISSN: 1095-323X. Mar. 2019, pp. 1–10.
- [3] Stephen Dawson et al. “JUNO Photovoltaic Power at Jupiter”. In: *10th International Energy Conversion Engineering Conference*. 2012. URL: <https://arc.aiaa.org/doi/abs/10.2514/6.2012-3833>.
- [4] A. De Vos. “Detailed balance limit of the efficiency of tandem solar cells”. In: *Journal of Physics D: Applied Physics* 13.5 (May 1980). Publisher: IOP Publishing, pp. 839–846. URL: <https://doi.org/10.1088%2F0022-3727%2F13%2F5%2F018>.
- [5] The National Renewable Energy Laborator (NREL). *Best Research-Cell Efficiency Chart*. English (US). Tech. rep. 2021. URL: <https://www.nrel.gov/pv/cell-efficiency.html>.
- [6] Myles A. Steiner et al. “High Efficiency Inverted GaAs and GaInP/GaAs Solar Cells With Strain-Balanced GaInAs/GaAsP Quantum Wells”. In: *Advanced Energy Materials* 11.4 (2021). _eprint: <https://onlinelibrary.wiley.com/doi/pdf/10.1002/aenm.202002874>, p. 2002874. URL: <https://onlinelibrary.wiley.com/doi/abs/10.1002/aenm.202002874>.
- [7] Robert W. Francis, Charles. Sve, and Timothy S. “Thermal Cycling Techniques for Solar Panels”. In: (2005), Vol. 6.
- [8] AZUR SPACE Solar Power GmbH. “Space state-of-the-art solar cells products”. 74072 Heilbronn Germany. URL: <http://www.azurspace.com/>.
- [9] Jet Propulsion Laboratory (NASA). *Solar Power Technologies for Future Planetary Science Missions*. Tech. rep. Pasadena, CA 91109, Dec. 2017.
- [10] Matthew K. Chamberlain et al. “On-orbit flight testing of the Roll-Out Solar Array”. In: *Acta Astronautica* 179 (2021), pp. 407–414. URL: <https://www.sciencedirect.com/science/article/pii/S0094576520306196>.
- [11] Brian R. Spence et al. “International Space Station (ISS) Roll-Out Solar Array (ROSA) Spaceflight Experiment Mission and Results”. In: *2018 IEEE 7th World Conference on Photovoltaic Energy Conversion (WCPEC) (A Joint Conference of 45th IEEE PVSC, 28th PVSEC 34th EU PVSEC)*. 2018, pp. 3522–3529.

- [12] Dominique Vergnet et al. “Advanced Lightweight Flexible Array with Mechanical Architecture”. In: *2019 IEEE 46th Photovoltaic Specialists Conference (PVSC)*. 2019, pp. 2808–2810.
- [13] IEC 62108. “Concentrator photovoltaic (CPV) modules and assemblies - Design qualification and type approval”. Sept. 2016.
- [14] Peng Wang et al. “Chapter 3 - Metal-energy nexus in the global energy transition calls for cooperative actions”. In: *The Material Basis of Energy Transitions*. Ed. by Alena Bleicher and Alexandra Pehlken. Academic Press, 2020, pp. 27–47. URL: <https://www.sciencedirect.com/science/article/pii/B9780128195345000039>.
- [15] Arnaud Ritou, Philippe Voarino, and Olivier Raccurt. “Does micro-scaling of CPV modules improve efficiency? A cell-to-module performance analysis”. In: *Solar Energy* 173 (2018), pp. 789–803. URL: <http://www.sciencedirect.com/science/article/pii/S0038092X18307382>.
- [16] Murphy, David M. *The Scarlet Solar Array: Technology Validation and Flight Results*. Tech. rep. Pasadena, CA 91109: AEC-Able Engineering Co., Inc, 2000. URL: www.aec-able.com.
- [17] Mark Perry et al. “Earth Observing-1 Spacecraft Bus”. In: 2001.
- [18] Brian R. Clapp et al. “GOES-R active vibration damping controller design, implementation, and on-orbit performance”. In: *CEAS Space Journal* 10.4 (Dec. 2018), pp. 501–517. URL: <https://doi.org/10.1007/s12567-017-0190-4>.
- [19] Daniel Chemisana and Tapas Mallick. “Building integrated concentrating solar systems”. In: Jan. 2014, pp. 545–788.
- [20] Katie Shanks, S. Senthilarasu, and Tapas K. Mallick. “Optics for concentrating photovoltaics: Trends, limits and opportunities for materials and design”. In: *Renewable and Sustainable Energy Reviews* 60 (2016), pp. 394–407. URL: <http://www.sciencedirect.com/science/article/pii/S1364032116001192>.
- [21] Roland Winston, Juan C. Miñano, and Pablo Benítez. “1 - Nonimaging optical systems and their uses”. In: *Nonimaging Optics*. Ed. by Roland Winston, Juan C. Miñano, and Pablo Benítez. Burlington: Academic Press, 2005, pp. 1–6. URL: <https://www.sciencedirect.com/science/article/pii/B9780127597515500014>.
- [22] W. T. Xie et al. “Concentrated solar energy applications using Fresnel lenses: A review”. In: *Renewable and Sustainable Energy Reviews* 15.6 (2011), pp. 2588–2606. URL: <https://www.sciencedirect.com/science/article/pii/S1364032111001341>.
- [23] Marta Victoria et al. “Assessment of the optical efficiency of a primary lens to be used in a CPV system”. In: *Solar Energy* 134 (2016), pp. 406–415. URL: <https://www.sciencedirect.com/science/article/pii/S0038092X16301104>.

- [24] Maike Wiesenfarth et al. "Investigation of different Fresnel lens designs and methods to determine the optical efficiency". In: vol. 1616. Sept. 2014, pp. 97–101.
- [25] Joe T. Howell, John C. Fikes, and Mark J. O'Neill. "Novel Space-Based Solar Power Technologies and Architectures for Earth and Beyond". In: *56th International Astronautical Congress*. Fukuoka, Japan, Jan. 2005. URL: <https://ntrs.nasa.gov/citations/20050245136>.
- [26] Z. Mathys and P.J. Burchill. "Influence of location on the weathering of acrylic sheet materials". In: *Polymer Degradation and Stability* 55.1 (1997), pp. 45–54. URL: <https://www.scopus.com/inward/record.uri?eid=2-s2.0-0030736617&doi=10.1016%2fS0141-3910%2896%2900131-0&partnerID=40&md5=88406d6d6bdcb368d62ccad7b8da1065>.
- [27] D.C. Miller et al. "Analysis of transmitted optical spectrum enabling accelerated testing of multijunction concentrating photovoltaic designs". In: *Optical Engineering* 50.1 (2011). URL: <https://www.scopus.com/inward/record.uri?eid=2-s2.0-81755184798&doi=10.1117%2f1.3530092&partnerID=40&md5=37bd3387e7f219d6c9bf5ccf60c1b364>.
- [28] A.L. Andradý. "Wavelength sensitivity in polymer degradation". In: *Adv. Polym. Sci.* 128.128 (1997), pp. 47–94.
- [29] A.L. Andradý et al. "Effects of increased solar ultraviolet radiation on materials". In: *Journal of Photochemistry and Photobiology B: Biology* 46.1-3 (1998), pp. 96–103. URL: <https://www.scopus.com/inward/record.uri?eid=2-s2.0-0032445361&doi=10.1016%2fS1011-1344%2898%2900188-2&partnerID=40&md5=608c5eafd2ec194976f2551971a8484c>.
- [30] John E Greivenkamp. *Field guide to geometrical optics*. Vol. 1. SPIE press Bellingham, WA, 2004.
- [31] S.N. Kasarova et al. "Analysis of the dispersion of optical plastic materials". In: *Optical Materials* 29.11 (2007), pp. 1481–1490. URL: <https://www.scopus.com/inward/record.uri?eid=2-s2.0-34249051054&doi=10.1016%2fj.optmat.2006.07.010&partnerID=40&md5=a54cec66002af6165ad3454abdf79b9d>.
- [32] E. Lorenzo and G. Sala. "Hybrid silicone-glass fresnel lens as concentrator for photovoltaic applications." In: *Electric Power Research Institute (Report) EPRI EA* (1979), pp. 536–539. URL: <https://www.scopus.com/inward/record.uri?eid=2-s2.0-0018587643&partnerID=40&md5=73e5a116723d6e579d656bd72cf6930f>.
- [33] JR Egger. "Manufacturing fresnel lens master tooling for solar photovoltaic concentrators". In: (1979). Publisher: SAND.

- [34] Ralf Leutz, Ling Fu, and Hans Philipp Annen. “Stress in large-area optics for solar concentrators”. In: *Reliability of Photovoltaic Cells, Modules, Components, and Systems II*. Ed. by Neelkanth G. Dhere, John H. Wohlgemuth, and Dan T. Ton. Vol. 7412. Backup Publisher: International Society for Optics and Photonics. SPIE, 2009, pp. 39–45. URL: <https://doi.org/10.1117/12.827357>.
- [35] Marc Steiner et al. “FLATCON® CPV module with 36.7% efficiency equipped with four-junction solar cells”. In: *Progress in Photovoltaics: Research and Applications* 23.10 (2015). _eprint: <https://onlinelibrary.wiley.com/doi/pdf/10.1002/pip.2568>, pp. 1323–1329. URL: <https://onlinelibrary.wiley.com/doi/abs/10.1002/pip.2568>.
- [36] Maria Brogren et al. “Optical properties, durability, and system aspects of a new aluminium-polymer-laminated steel reflector for solar concentrators”. In: *Solar Energy Materials and Solar Cells* 82.3 (2004), pp. 387–412. URL: <https://www.sciencedirect.com/science/article/pii/S0927024804000522>.
- [37] Lee A. Weinstein et al. “Concentrating Solar Power”. In: *Chemical Reviews* 115.23 (Dec. 2015). Publisher: American Chemical Society, pp. 12797–12838. URL: <https://doi.org/10.1021/acs.chemrev.5b00397>.
- [38] Stefan Braendle. “Benefits of Metal Reflective Surfaces for Concentrating Solar Applications”. In: (Aug. 2010).
- [39] U.S. Department of Energy. *SunShot Vision Study: February 2012 (Book)*. English. Tech. rep. United States, Feb. 2012.
- [40] Cheryl E. Kennedy and Kent M. Terwilliger. “Optical Durability of Candidate Solar Reflectors”. In: *Journal of Solar Energy Engineering-transactions of The Asme* 127 (2005), pp. 262–269.
- [41] J. Deubener et al. “Glasses for solar energy conversion systems”. In: *Journal of the European Ceramic Society* 29.7 (2009), pp. 1203–1210. URL: <https://www.sciencedirect.com/science/article/pii/S0955221908004408>.
- [42] C. E. Kennedy et al. “Optical performance and durability of solar reflectors protected by an alumina coating”. In: *Thin Solid Films* 304.1 (1997), pp. 303–309. URL: <https://www.sciencedirect.com/science/article/pii/S0040609097001983>.
- [43] Paul Schissel et al. “Silvered-PMMA reflectors”. In: *Solar Energy Materials and Solar Cells* 33.2 (1994), pp. 183–197. URL: <https://www.sciencedirect.com/science/article/pii/0927024894902070>.
- [44] Michael J. DiGrazia and Gary J. Jorgensen. “ReflecTech Mirror Film: Design Flexibility and Durability in Reflecting Solar Applications”. In: 2010.
- [45] H. Curtis et al. “Early results from the PASP Plus flight experiment”. In: *Proceedings of 1994 IEEE 1st World Conference on Photovoltaic Energy Conversion - WCPEC (A Joint Conference of PVSC, PVSEC and PSEC)*. Vol. 2. Dec. 1994, 2169–2172 vol.2.

- [46] Michael F. Piszczor et al. “The mini-dome Fresnel lens photovoltaic concentrator array: current status of components and prototype panel testing”. In: *IEEE Conference on Photovoltaic Specialists* (1990), 1271–1276 vol.2.
- [47] Henry B. Curtis and Dean C. Marvin. “Final results from the PASP Plus flight experiment”. In: *Conference Record of the Twenty Fifth IEEE Photovoltaic Specialists Conference - 1996* (1996), pp. 195–198.
- [48] D. M. Murphy and D. M. Allen. “SCARLET development, fabrication, and testing for the Deep Space 1 spacecraft”. In: *IECEC-97 Proceedings of the Thirty-Second Intersociety Energy Conversion Engineering Conference (Cat. No.97CH6203)*. Vol. 4. July 1997, 2237–2245 vol.4.
- [49] D. M. Allen et al. “The SCARLET light concentrating solar array”. In: *Conference Record of the Twenty Fifth IEEE Photovoltaic Specialists Conference - 1996*. 1996, pp. 353–356.
- [50] J.J. Wachholz and D.M. Murphy. “SCARLET I: Mechanization solutions for deployable concentrator optics integrated with rigid array technology”. In: (May 1996).
- [51] O’Neil Mark Joseph. “Stretched Fresnel lens solar concentrator for space power.” 6,075,200. 2000.
- [52] H Brandhorst, J Rodiek, and Mark O’Neill. “The Stretched Lens Array’s Testing and Mission Success in Harsh Environments”. In: *European Space Agency, (Special Publication) ESA SP* (Jan. 2008).
- [53] P. P. Jenkins et al. “Initial results from the TacSat-4 solar cell experiment”. In: *2013 IEEE 39th Photovoltaic Specialists Conference (PVSC)*. ISSN: 0160-8371. June 2013, pp. 3108–3111.
- [54] M. O’Neill et al. “Recent space PV concentrator advances: More robust, lighter, and easier to track”. In: *2015 IEEE 42nd Photovoltaic Specialist Conference (PVSC)*. June 2015, pp. 1–6.
- [55] B. Spence and M. Eskenazi. “The CellSaver Concentrator Solar Array System and Qualification Program”. In: *Space Power*. Ed. by A. Wilson. Vol. 502. ESA Special Publication. May 2002, p. 451.
- [56] C. J. Gelderloos et al. “Characterization testing of Hughes 702 solar array”. In: *Conference Record of the Twenty-Eighth IEEE Photovoltaic Specialists Conference - 2000 (Cat. No.00CH37036)*. ISSN: 0160-8371. Sept. 2000, pp. 972–975.
- [57] Stephen S. Gates, Stephen M. Koss, and Michael F. Zedd. “Advanced Tether Experiment Deployment Failure”. In: *Journal of Spacecraft and Rockets* 38.1 (2001). [eprint: https://doi.org/10.2514/2.3655](https://doi.org/10.2514/2.3655), pp. 60–68. URL: <https://doi.org/10.2514/2.3655>.

- [58] R. K. Jain et al. “New concentrator technology experiment on a geosynchronous satellite”. In: *3rd World Conference on Photovoltaic Energy Conversion, 2003. Proceedings of*. Vol. 1. ISSN: null. May 2003, 865–868 Vol.1.
- [59] M. Eskenazi. “Design, analysis testing of the CellSaver concentrator for spacecraft solar arrays”. In: *Conference Record of the Twenty-Ninth IEEE Photovoltaic Specialists Conference, 2002*. ISSN: 1060-8371. May 2002, pp. 935–938.
- [60] M. Eskenazi et al. “Preliminary test results for the CellSaver concentrator in geosynchronous earth orbit”. In: *Conference Record of the Thirty-first IEEE Photovoltaic Specialists Conference, 2005*. ISSN: 0160-8371. Jan. 2005, pp. 622–625.
- [61] M. Bodeau. *Root-Cause of the 702 Concentrator Array Anomaly*. Redondo Beach, Apr. 2003.
- [62] C. J. Ruud et al. “Lightweight Monolithic Microcell CPV for Space”. In: *2018 IEEE 7th World Conference on Photovoltaic Energy Conversion (WCPEC) (A Joint Conference of 45th IEEE PVSC, 28th PVSEC 34th EU PVSEC)*. ISSN: 0160-8371. June 2018, pp. 3535–3538.
- [63] M. P. Lumb et al. “Six-junction (6J) microscale concentrating photovoltaics (CPV) for space applications”. In: *2016 IEEE 43rd Photovoltaic Specialists Conference (PVSC)*. June 2016, pp. 3415–3420.
- [64] ARPA-E. *Micro-scale Optimized Solar-cell Arrays with Integrated Concentration (MOSAIC) Program*. Aug. 2015. URL: <https://arpa-e.energy.gov/technologies/programs/mosaic>.
- [65] B. Furman et al. “A high concentration photovoltaic module utilizing micro-transfer printing and surface mount technology”. In: *2010 35th IEEE Photovoltaic Specialists Conference*. ISSN: 0160-8371. June 2010, pp. 000475–000480.
- [66] K. Ghosal et al. “Semprius module and system results”. In: *2014 IEEE 40th Photovoltaic Specialist Conference (PVSC)*. ISSN: 0160-8371. June 2014, pp. 3287–3292.
- [67] A. J. Grede et al. “Fixed-tilt $660 \times$ Concentrating Photovoltaic System with 30% Efficiency”. In: *2017 IEEE 44th Photovoltaic Specialist Conference (PVSC)*. June 2017, pp. 1469–1472.
- [68] H. Arase et al. “A Novel Thin Concentrator Photovoltaic With Microsolar Cells Directly Attached to a Lens Array”. In: *IEEE Journal of Photovoltaics* 4.2 (Mar. 2014), pp. 709–712.
- [69] Etienne Menard et al. “Optics development for micro-cell based CPV modules”. In: *Proceedings of SPIE - The International Society for Optical Engineering* (Sept. 2011).

- [70] Tohru Nakagawa et al. “High-efficiency Thin and Compact Concentrator Photovoltaics with Micro-solar Cells Directly Attached to Lens Array”. In: *Light, Energy and the Environment*. Journal Abbreviation: Light, Energy and the Environment. Optical Society of America, 2014, RF4B.5. URL: <http://www.osapublishing.org/abstract.cfm?URI=OSE-2014-RF4B.5>.
- [71] N. Hayashi et al. “Nonuniformity Sunlight-Irradiation Effect on Photovoltaic Performance of Concentrating Photovoltaic Using Microsolar Cells Without Secondary Optics”. In: *IEEE Journal of Photovoltaics* 6.1 (Jan. 2016), pp. 350–357.
- [72] Nobuhiko Hayashi et al. “Thin concentrator photovoltaic module with micro-solar cells which are mounted by self-align method using surface tension of melted solder”. In: *AIP Conference Proceedings* 1881.1 (2017). _eprint: <https://aip.scitation.org/doi/pdf/10.1063/1.5001443>, p. 080005. URL: <https://aip.scitation.org/doi/abs/10.1063/1.5001443>.
- [73] M. Takase et al. “Light plastic integrated micro CPV module: PIC with three-junction PV cells”. In: *2018 18th International Workshop on Junction Technology (IWJT)*. Mar. 2018, pp. 1–3.
- [74] Gregory N. Nielson et al. “216 cell microconcentrator module with moderate concentration, $\pm 4^\circ$ acceptance angle, and 13.3 mm focal length”. In: *2013 IEEE 39th Photovoltaic Specialists Conference (PVSC)*. 2013, pp. 0465–0469.
- [75] Jose Luis Cruz-Campa et al. “Ultrathin and Flexible Single Crystal Silicon Mini-Modules”. In: 2012.
- [76] Gregory Nielson et al. “Microsystem Enabled Photovoltaics.” In: (Feb. 2016). URL: <https://www.osti.gov/biblio/1344846>.
- [77] Bradley H. Jared et al. “Micro-Concentrators for a Microsystems-Enabled Photovoltaic System”. In: *Renewable Energy and the Environment*. Journal Abbreviation: Renewable Energy and the Environment. Optical Society of America, 2013, RT3D.5. URL: <http://www.osapublishing.org/abstract.cfm?URI=OSE-2013-RT3D.5>.
- [78] L. Li et al. “Highly-integrated Hybrid Micro-Concentrating Photovoltaics”. In: *2018 IEEE 7th World Conference on Photovoltaic Energy Conversion (WCPEC) (A Joint Conference of 45th IEEE PVSC, 28th PVSEC 34th EU PVSEC)*. ISSN: 0160-8371. June 2018, pp. 1655–1657.
- [79] Xing Sheng et al. “Printing-based assembly of quadruple-junction four-terminal microscale solar cells and their use in high-efficiency modules”. In: *Nature Materials* 13.6 (June 2014), pp. 593–598. URL: <https://doi.org/10.1038/nmat3946>.
- [80] Arnaud Ritou et al. “Micro-concentrator with a self-assembly process”. In: *AIP Conference Proceedings* 1766.1 (2016). _eprint: <https://aip.scitation.org/doi/pdf/10.1063/1.4962103>, p. 080005. URL: <https://aip.scitation.org/doi/abs/10.1063/1.4962103>.

- [81] E. Chinello et al. “A comparative performance analysis of stand-alone, off-grid solar-powered sodium hypochlorite generators”. In: *RSC Adv.* 9.25 (2019). Publisher: The Royal Society of Chemistry, pp. 14432–14442. URL: <http://dx.doi.org/10.1039/C9RA02221J>.
- [82] K. Ghosal et al. “Ultrahigh Efficiency HCPV Modules and Systems”. In: *IEEE Journal of Photovoltaics* 6.5 (Sept. 2016), pp. 1360–1365.
- [83] Jared S. Price et al. “High-concentration planar microtracking photovoltaic system exceeding 30% efficiency”. In: *Nature Energy* 2.8 (July 2017), p. 17113. URL: <https://doi.org/10.1038/nenergy.2017.113>.
- [84] Arnaud Ritou et al. “Mechanical tolerances study through simulations and experimental characterization for a 1000X micro-concentrator CPV module”. In: *AIP Conference Proceedings* 1881.1 (2017). _eprint: <https://aip.scitation.org/doi/pdf/10.1063/1.5001418>, p. 030007. URL: <https://aip.scitation.org/doi/abs/10.1063/1.5001418>.
- [85] Christian J. Ruud et al. “Design and demonstration of ultra-compact microcell concentrating photovoltaics for space”. In: *Opt. Express* 27.20 (Sept. 2019). Publisher: OSA, A1467–A1480. URL: <http://www.opticsexpress.org/abstract.cfm?URI=oe-27-20-A1467>.
- [86] Anderson Bermudez-Garcia, Philippe Voarino, and Olivier Raccurt. “Environments, needs and opportunities for future space photovoltaic power generation: A review”. In: *Applied Energy* 290 (2021), p. 116757. URL: <https://www.sciencedirect.com/science/article/pii/S030626192100266X>.
- [87] Christian A. Gueymard. “Revised composite extraterrestrial spectrum based on recent solar irradiance observations”. In: *Solar Energy* 169 (2018), pp. 434–440. URL: <http://www.sciencedirect.com/science/article/pii/S0038092X1830433X>.
- [88] Christian A. Gueymard. “Reference solar spectra: Their evolution, standardization issues, and comparison to recent measurements”. In: *Advances in Space Research* 37.2 (2006), pp. 323–340. URL: <http://www.sciencedirect.com/science/article/pii/S0273117705003649>.
- [89] Christoph Wehrli. “Extraterrestrial solar spectrum”. In: *World Radiation Center (WRC), Davos-Dorf, Switzerland, WRC Publication* 615.1 (1985), pp. 10–17.
- [90] H. Neckel and D. Labs. “Improved data of solar spectral irradiance from 0.33 to 1.25 μ ”. In: *Solar Physics* 74.1 (1981), pp. 231–249. URL: <https://www.scopus.com/inward/record.uri?eid=2-s2.0-0000999597&doi=10.1007%2fBF00151293&partnerID=40&md5=d7d0d9e77721621f38949e6a9ac7cf6a>.
- [91] The American Society for Testing and Materials (ASTM). “Standard Solar Constant and Zero Air Mass Solar Spectral Irradiance Tables, ASTM E490-00a (2019)”. West Conshohocken, PA, 2019. URL: www.astm.org.

- [92] NREL. “Standard Reference Spectra Data Files, ASTM G-173-03 (International standard ISO 9845-1)”. US, 1992. URL: <https://www.nrel.gov/grid/solar-resource/spectra-am1.5.html>.
- [93] The American Society for Testing and Materials (ASTM). “2000 ASTM Standard Extraterrestrial Spectrum Reference E-490”. 2000. URL: <https://www.nrel.gov/grid/solar-resource/spectra-astm-e490.html>.
- [94] ASTM International. “ASTM E1559-09, Standard Test Method for Contamination Outgassing Characteristics of Spacecraft Materials”. West Conshohocken, PA, 2009. URL: www.astm.org.
- [95] ASTM International. “ASTM E595-15, Standard Test Method for Total Mass Loss and Collected Volatile Condensable Materials from Outgassing in a Vacuum Environment”. West Conshohocken, PA, 2015. URL: www.astm.org.
- [96] (ECSS) European Cooperation for Space Standardization. “ECSS-Q-ST-70-02C – Thermal vacuum outgassing test for the screening of space materials”. Nov. 2008. URL: <https://ecss.nl/>.
- [97] NASA/TP-2361. “NASA technical paper: design guidelines for assessing and controlling spacecraft charging effects”. 1984.
- [98] European Cooperation for Space Standardization (ECSS). “ECSS-E-ST-20-06C Rev.1 – Spacecraft charging”. May 2019. URL: ecss.nl.
- [99] D. N. Baker. “The occurrence of operational anomalies in spacecraft and their relationship to space weather”. In: *IEEE Transactions on Plasma Science* 28.6 (Dec. 2000), pp. 2007–2016.
- [100] N. Iucci et al. “Space weather conditions and spacecraft anomalies in different orbits”. In: *Space Weather* 3.1 (2005). _eprint: <https://agupubs.onlinelibrary.wiley.com/doi/pdf/10.1029/2003SW000056>. URL: <https://agupubs.onlinelibrary.wiley.com/doi/abs/10.1029/2003SW000056>.
- [101] Shu Lai. “Fundamentals of spacecraft charging: Spacecraft interactions with space plasmas”. In: *Fundamentals of Spacecraft Charging: Spacecraft Interactions with Space Plasmas* (Oct. 2011).
- [102] J.-C. Matéo-Vélez et al. “Spacecraft surface charging induced by severe environments at geosynchronous orbit”. In: *Space Weather* 16.1 (2018). _eprint: <https://agupubs.onlinelibrary.wiley.com/doi/pdf/10.1002/2017SW001689>, pp. 89–106. URL: <https://agupubs.onlinelibrary.wiley.com/doi/abs/10.1002/2017SW001689>.
- [103] M Berger. “Stopping-Power and Range Tables for Electrons, Protons, and Helium Ions: Physical Reference Data”. In: (1999). Publisher: NIST.
- [104] AE9/AP9 Development Team (Air Force). “AE9/AP9/SPM radiation environment model: Technical documentation”. 2014.

- [105] Daniel Engelhart et al. “Space Plasma Interactions with Spacecraft Materials”. In: Nov. 2018.
- [106] (ECSS) European Cooperation for Space Standardization. “ECSS-E-ST-10-04C – Space environment”. Nov. 2008. URL: ecss.nl.
- [107] Gail P. Anderson et al. “MODTRAN2: suitability for remote sensing”. In: *Proceedings of SPIE - The International Society for Optical Engineering*. Vol. 1968. 1993, pp. 514–525. URL: <https://www.scopus.com/inward/record.uri?eid=2-s2.0-0027843858&partnerID=40&md5=55492c0e68b21def4e7afdd41d7aeab5>.
- [108] NASA Technical Standards. “NASA-STD-4005A, Low Earth Orbit Spacecraft Charging Design Standard”. Feb. 2016. URL: standards.nasa.gov.
- [109] T. Muranaka et al. “Development of Multi-Utility Spacecraft Charging Analysis Tool (MUSCAT)”. In: *IEEE Transactions on Plasma Science* 36.5 (Oct. 2008), pp. 2336–2349.
- [110] International Organization for Standardization (ISO). “ISO 11221, Space systems – Space solar panels – Spacecraft charging induced electrostatic discharge test methods, Reference number ISO 11221:2011(E), .” 2011.
- [111] Changzi Qu et al. “Morphology and Mechanical Properties of Polyimide Films: The Effects of UV Irradiation on Microscale Surface”. In: *Materials* 10.11 (2017). URL: <https://www.mdpi.com/1996-1944/10/11/1329>.
- [112] Giovanni Marletta and Fabio Iacona. “Chemical and Physical Property Modifications Induced by Ion Irradiation in Polymers”. In: *Materials and Processes for Surface and Interface Engineering*. Ed. by Yves Pauleau. Dordrecht: Springer Netherlands, 1995, pp. 597–640. URL: https://doi.org/10.1007/978-94-011-0077-9_16.
- [113] Elena A. Plis et al. “Review of Radiation-Induced Effects in Polyimide”. In: *Applied Sciences* 9.10 (2019). URL: <https://www.mdpi.com/2076-3417/9/10/1999>.
- [114] J. R. Dennison, A. Sim, and C. D. Thomson. “Evolution of the Electron Yield Curves of Insulators as a Function of Impinging Electron Fluence and Energy”. In: *IEEE Transactions on Plasma Science* 34.5 (Oct. 2006), pp. 2204–2218.
- [115] G. Wilson and J. R. Dennison. “Approximation of Range in Materials as a Function of Incident Electron Energy”. In: *IEEE Transactions on Plasma Science* 40.2 (Feb. 2012), pp. 291–297.
- [116] J.R. Srour and J.W. Palko. “Displacement damage effects in irradiated semiconductor devices”. In: *IEEE Transactions on Nuclear Science* 60.3 (2013), pp. 1740–1766. URL: <https://www.scopus.com/inward/record.uri?eid=2-s2.0-84879242888&doi=10.1109%2fTNS.2013.2261316&partnerID=40&md5=dd351c79782905205eee6a7410d52b53>.

- [117] S. R. Messenger et al. “Modeling solar cell degradation in space: A comparison of the NRL displacement damage dose and the JPL equivalent fluence approaches†”. In: *Progress in Photovoltaics: Research and Applications* 9.2 (2001). _eprint: <https://onlinelibrary.wiley.com/doi/pdf/10.1002/pip.357>, pp. 103–121. URL: <https://onlinelibrary.wiley.com/doi/abs/10.1002/pip.357>.
- [118] HY Tada et al. “Solar cell radiation handbook”. In: (1982).
- [119] Bruce E. Anspaugh. “GaAs Solar Cell Radiation Handbook”. In: 1996.
- [120] Scott Messenger, Eric Jackson, and Jeffrey Warner. “SCREAM: A new code for solar cell degradation prediction using the displacement damage dose approach”. In: *Conference Record of the IEEE Photovoltaic Specialists Conference* (June 2010), pp. 001106–001111.
- [121] European Space Agency (ESA). *SPENVIS (SPace ENVironment Information System), ESA (European Space Agency)*. URL: <https://www.spervis.oma.be/>.
- [122] H. Klinkrad J. Bendisch et al. “An Introduction to the 1997 ESA Master Model”. In: 1997.
- [123] N. Johnson et al. “Nasa/jsc Orbital Debris Models”. In: *Second European Conference on Space Debris*. Ed. by Brigitte Kaldeich-Schuermann. Vol. 393. ESA Special Publication. Jan. 1997, p. 225.
- [124] Xin Gao, Sheng-sheng Yang, and Zhan-zu Feng. “Radiation Effects of Space Solar Cells”. In: *High-Efficiency Solar Cells: Physics, Materials, and Devices*. Ed. by Xiaodong Wang and Zhiming M. Wang. Cham: Springer International Publishing, 2014, pp. 597–622. URL: https://doi.org/10.1007/978-3-319-01988-8_20.
- [125] E. Grossman and I. Gouzman. “Space environment effects on polymers in low earth orbit”. In: *Nuclear Instruments and Methods in Physics Research Section B: Beam Interactions with Materials and Atoms* 208 (2003), pp. 48–57. URL: <http://www.sciencedirect.com/science/article/pii/S0168583X03006402>.
- [126] Bruce A Banks, Kim K Degroh, and Daniela C Smith. *Environmental Durability Issues for Solar Power Systems in Low Earth Orbit*. Tech. rep. Nov. 1994. URL: <http://ntrs.nasa.gov/search.jsp?R=19950009355> (visited on 10/23/2019).
- [127] D. R. Peplinski, G. S. Arnold, and E. N. Borson. “Introduction to simulation of upper atmosphere oxygen satellite exposed to atomic oxygen in low Earth orbit”. In: *13th Space Simulation Conf.* Jan. 1984, pp. 133–145.
- [128] Bruce Banks, Kim deGroh, and Sharon Miller. “Low Earth Orbital Atomic Oxygen Interactions With Spacecraft Materials”. In: *Materials Research Society Symposium Proceedings* 851 (Dec. 2004).
- [129] Joyce A. Dever. “Low Earth orbital atomic oxygen and ultraviolet radiation effects on polymers”. In: NASA Lewis Research Center Cleveland, OH, United States, 1991.
- [130] Lewis Richard Koller. *Ultraviolet radiation*. Vol. 2. Wiley New York, 1965.

- [131] NASA ISS Program Science Office. “Space environmental effects”. 2015.
- [132] M. Meshishnek, S. R. Gyetvay, and C. Jagers. “Long Duration Exposure Facility Experiment M0003 Deintegration/Findings and Impacts”. In: 1992.
- [133] Quasi-Zenith Satellite System (QZSS). “List of Positioning Satellites”. URL: <https://qzss.go.jp/en/technical/satellites/index.html> (visited on 09/25/2019).
- [134] G. P. Ginet et al. “AE9, AP9 and SPM: New Models for Specifying the Trapped Energetic Particle and Space Plasma Environment”. In: *The Van Allen Probes Mission*. Ed. by Nicola Fox and James L. Burch. Boston, MA: Springer US, 2014, pp. 579–615. URL: https://doi.org/10.1007/978-1-4899-7433-4_18.
- [135] I. Sandberg et al. “Data Exploitation of New Galileo Environmental Monitoring Units”. In: *IEEE Transactions on Nuclear Science* 66.7 (July 2019), pp. 1761–1769.
- [136] J. Wang et al. “Electron Environment Characteristics and Internal Charging Evaluation for MEO Satellite”. In: *IEEE Transactions on Nuclear Science* 65.8 (Aug. 2018), pp. 1685–1693.
- [137] Douglas M. Sawyer and James I. Vette. “AP-8 trapped proton environment for solar maximum and solar minimum”. In: 1976.
- [138] D. H. Brautigam et al. “Specification of the radiation belt slot region: comparison of the NASA AE8 model with TSX5/CEASE data”. In: *IEEE Transactions on Nuclear Science* 51.6 (Dec. 2004), pp. 3375–3380.
- [139] E. J. Daly et al. “Problems with models of the radiation belts”. In: *IEEE Transactions on Nuclear Science* 43.2 (Apr. 1996), pp. 403–415.
- [140] M. S. Gussenhoven, E. G. Mullen, and D. H. Brautigam. “Near-earth radiation model deficiencies as seen on CRRES”. In: *Advances in Space Research* 14.10 (1994), pp. 927–941. URL: <http://www.sciencedirect.com/science/article/pii/0273117794905592>.
- [141] T. Armstrong and B. Colborn. “Evaluation of Trapped Radiation Model Uncertainties for Spacecraft Design”. In: (Apr. 2000).
- [142] G. P. Ginet et al. “The Trapped Proton Environment in Medium Earth Orbit (MEO)”. In: *IEEE Transactions on Nuclear Science* 57.6 (Dec. 2010), pp. 3135–3142.
- [143] G. P. Ginet et al. “Correction to “The Trapped Proton Environment in Medium Earth Orbit (MEO)” [Dec 10 3135-3142]”. In: *IEEE Transactions on Nuclear Science* 59.3 (June 2012), pp. 685–685.
- [144] W. Johnston et al. “AE9/AP9/SPM: New models for radiation belt and space plasma specification”. In: *Proceedings of SPIE - The International Society for Optical Engineering*. Vol. 9085. June 2014, p. 908508.

- [145] H. D. R. Evans et al. “Results from the ESA SREM monitors and comparison with existing radiation belt models”. In: *Advances in Space Research* 42.9 (2008), pp. 1527–1537. URL: <http://www.sciencedirect.com/science/article/pii/S0273117708001737>.
- [146] D.C. Law et al. “Development of XTJ Targeted Environment (XTE) Solar Cells for Specific Space Applications”. In: *2018 IEEE 7th World Conference on Photovoltaic Energy Conversion, WCPEC 2018 - A Joint Conference of 45th IEEE PVSC, 28th PVSEC and 34th EU PVSEC*. 2018, pp. 3360–3363. URL: <https://www.scopus.com/inward/record.uri?eid=2-s2.0-85059909897&doi=10.1109%2F2fPVSC.2018.8548238&partnerID=40&md5=bb014c62505563af462cc5681623cc6e>.
- [147] Gao Xin et al. “The Effects of MEO Radiation Environment on Triple-Junction GaAs Solar Cells”. In: *Protection of Materials and Structures From the Space Environment*. Ed. by Jacob Kleiman, Masahito Tagawa, and Yugo Kimoto. Berlin, Heidelberg: Springer Berlin Heidelberg, 2013, pp. 151–158.
- [148] Roger L. Freeman. “Satellite Communications”. In: *Reference Manual for Telecommunications Engineering*. _eprint: <https://onlinelibrary.wiley.com/doi/pdf/10.1002/0471208051.fre018>. American Cancer Society, 2002. URL: <https://onlinelibrary.wiley.com/doi/abs/10.1002/0471208051.fre018>.
- [149] V. Pilipenko et al. “Statistical relationships between satellite anomalies at geostationary orbit and high-energy particles”. In: *Advances in Space Research* 37.6 (2006), pp. 1192–1205. URL: <http://www.sciencedirect.com/science/article/pii/S0273117705005867>.
- [150] Sherman E. DeForest. “Spacecraft charging at synchronous orbit”. In: *Journal of Geophysical Research (1896-1977)* 77.4 (1972). _eprint: <https://agupubs.onlinelibrary.wiley.com/doi/pdf/10.1029/JA077i004p00651>, pp. 651–659. URL: <https://agupubs.onlinelibrary.wiley.com/doi/abs/10.1029/JA077i004p00651>.
- [151] Sherman E. DeForest. “Electrostatic Potentials Developed by ATS-5”. In: *Photon and Particle Interactions with Surfaces in Space*. Ed. by R. J. L. Grard. Dordrecht: Springer Netherlands, 1973, pp. 263–267.
- [152] T. Hiriart et al. “Comparative reliability of geo, leo, and meo satellites”. In: 9 (Jan. 2009), pp. 7182–7196.
- [153] J. F. Fennell et al. “Internal charging: a preliminary environmental specification for satellites”. In: *IEEE Transactions on Plasma Science* 28.6 (Dec. 2000), pp. 2029–2036.

- [154] T. P. O'Brien et al. "Extreme electron fluxes in the outer zone". In: *Space Weather* 5.1 (2007). _eprint:
<https://agupubs.onlinelibrary.wiley.com/doi/pdf/10.1029/2006SW000240>. URL:
<https://agupubs.onlinelibrary.wiley.com/doi/abs/10.1029/2006SW000240>.
- [155] Y. Lu et al. "A Review of the Space Environment Effects on Spacecraft in Different Orbits". In: *IEEE Access* 7 (2019), pp. 93473–93488.
- [156] T. P. O'Brien et al. "Changes in AE9/AP9-IRENE Version 1.5". In: *IEEE Transactions on Nuclear Science* 65 (2018), pp. 462–466.
- [157] US National Oceanographic and Atmospheric Administration. "Space Weather Prediction Center". URL: <https://www.swpc.noaa.gov/products/ace-realtime-solar-wind>.
- [158] M. A. Xapsos et al. "Model for solar proton risk assessment". In: *IEEE Transactions on Nuclear Science* 51.6 (Dec. 2004), pp. 3394–3398.
- [159] H. Nesse Tyssøy and J. Stadsnes. "Cutoff latitude variation during solar proton events: Causes and consequences". In: *J. Geophys. Res. Space Physics* 120.1 (2015), pp. 553–563. URL: <https://doi.org/10.1002/2014JA020508>.
- [160] Barry Mauk and Nicola Fox. "Electron radiation belts of the solar system". In: *Journal of Geophysical Research* 115 (Dec. 2010).
- [161] B. H. Mauk et al. "Energetic particles and hot plasmas of Neptune." In: *Neptune and Triton*. Jan. 1995, pp. 169–232.
- [162] B. H. Mauk. "Comparative investigation of the energetic ion spectra comprising the magnetospheric ring currents of the solar system". In: *Journal of Geophysical Research: Space Physics* 119.12 (2014). _eprint:
<https://agupubs.onlinelibrary.wiley.com/doi/pdf/10.1002/2014JA020392>, pp. 9729–9746.
URL: <https://agupubs.onlinelibrary.wiley.com/doi/abs/10.1002/2014JA020392>.
- [163] Carol Paty et al. "Ice giant magnetospheres". In: *Philosophical Transactions of the Royal Society A: Mathematical, Physical and Engineering Sciences* 378.2187 (2020). _eprint:
<https://royalsocietypublishing.org/doi/pdf/10.1098/rsta.2019.0480>, p. 20190480. URL:
<https://royalsocietypublishing.org/doi/abs/10.1098/rsta.2019.0480>.
- [164] James R Gaier. "The effects of lunar dust on EVA systems during the Apollo missions". In: (2007).
- [165] M. K. Mazumder et al. "Lunar and Martian Dust Dynamics". In: *IEEE Industry Applications Magazine* 16.4 (July 2010), pp. 14–21.
- [166] Eberhard Grün, Mihaly Horanyi, and Zoltan Sternovsky. "The lunar dust environment". In: *Planetary and Space Science* 59.14 (2011), pp. 1672–1680. URL:
<http://www.sciencedirect.com/science/article/pii/S0032063311001140>.

- [167] Ashwin R. Vasavada, David A. Paige, and Stephen E. Wood. “Near-Surface Temperatures on Mercury and the Moon and the Stability of Polar Ice Deposits”. In: *Icarus* 141.2 (1999), pp. 179–193. URL: <http://www.sciencedirect.com/science/article/pii/S0019103599961754>.
- [168] Grant H. Heiken, David T. Vaniman, and Bevan M. French. *Lunar Sourcebook, A User’s Guide to the Moon*. 1991.
- [169] R. Goodwin. *Apollo 17 NASA Mission Report (1973)*. Tech. rep. 2002. URL: <https://www.hq.nasa.gov/alsj/a17/a17mr.html>.
- [170] Lawrence A. Taylor et al. “Mineralogical and chemical characterization of lunar highland soils: Insights into the space weathering of soils on airless bodies”. In: *Journal of Geophysical Research: Planets* 115.E2 (2010). _eprint: <https://agupubs.onlinelibrary.wiley.com/doi/pdf/10.1029/2009JE003427>. URL: <https://agupubs.onlinelibrary.wiley.com/doi/abs/10.1029/2009JE003427>.
- [171] R. K. Tripathi et al. “A characterization of the moon radiation environment for radiation analysis”. In: *Advances in Space Research* 37.9 (2006), pp. 1749–1758. URL: <http://www.sciencedirect.com/science/article/pii/S0273117706001384>.
- [172] Nima Afshar-Mohajer et al. “Review of dust transport and mitigation technologies in lunar and Martian atmospheres”. In: *Advances in Space Research* 56.6 (2015), pp. 1222–1241. URL: <http://www.sciencedirect.com/science/article/pii/S0273117715004111>.
- [173] W David Carrier III. “Particle size distribution of lunar soil”. In: *Journal of Geotechnical and Geoenvironmental Engineering* 129.10 (2003). Publisher: American Society of Civil Engineers, pp. 956–959.
- [174] L. P. Keller et al. “Space Weathering in the Fine Size Fractions of Lunar Soils: Soil Maturity Effects”. In: *Workshop on New Views of the Moon II: Understanding the Moon Through the Integration of Diverse Datasets*. Sept. 1999, p. 32.
- [175] Lawrence A. TAYLOR et al. “The effects of space weathering on Apollo 17 mare soils: Petrographie and chemical characterization”. In: *Meteoritics & Planetary Science* 36.2 (2001). _eprint: <https://onlinelibrary.wiley.com/doi/pdf/10.1111/j.1945-5100.2001.tb01871.x>, pp. 285–299. URL: <https://onlinelibrary.wiley.com/doi/abs/10.1111/j.1945-5100.2001.tb01871.x>.
- [176] Timothy J Stubbs, Richard R Vondrak, and William M Farrell. “A dynamic fountain model for dust in the lunar exosphere”. In: *Dust in Planetary Systems* 643 (2007). Publisher: ESA Publications, pp. 185–189.
- [177] David R. Criswell. “Lunar dust motion”. In: *Lunar and Planetary Science Conference Proceedings* 3 (Jan. 1972), p. 2671.

- [178] Otto E Berg, Henry Wolf, and John Rhee. “Lunar soil movement registered by the apollo 17 cosmic dust experiment”. In: *Interplanetary dust and zodiacal light*. Springer, 1976, pp. 233–237.
- [179] James E McCoy and David R Criswell. “Evidence for a high altitude distribution of lunar dust”. In: *Lunar and planetary science conference proceedings*. Vol. 5. 1974, pp. 2991–3005.
- [180] J. J. Rennilson and D. R. Criswell. “Surveyor observations of lunar horizon-glow”. In: *The moon* 10.2 (June 1974), pp. 121–142. URL: <https://doi.org/10.1007/BF00655715>.
- [181] Nilton O. Renno and Jasper F. Kok. “Electrical Activity and Dust Lifting on Earth, Mars, and Beyond”. In: *Planetary Atmospheric Electricity*. Ed. by F. Leblanc et al. New York, NY: Springer New York, 2008, pp. 419–434. URL: https://doi.org/10.1007/978-0-387-87664-1_26.
- [182] O. E. Berg. “A lunar terminator configuration”. In: *Earth and Planetary Science Letters* 39.3 (1978), pp. 377–381. URL: <http://www.sciencedirect.com/science/article/pii/0012821X78900250>.
- [183] O Walton. “Adhesion of Lunar Dust”. In: (Jan. 2007).
- [184] Yvonne Jean Pendleton et al. “DUST ANALYSIS AT THE MOON”. In: 2007.
- [185] W. M. Farrell et al. “Complex electric fields near the lunar terminator: The near-surface wake and accelerated dust”. In: *Geophysical Research Letters* 34.14 (2007). _eprint: <https://agupubs.onlinelibrary.wiley.com/doi/pdf/10.1029/2007GL029312>. URL: <https://agupubs.onlinelibrary.wiley.com/doi/abs/10.1029/2007GL029312>.
- [186] Stewart W Johnson, G Jeffrey Taylor, and John P Wetzell. “Environmental effects on lunar astronomical observatories”. In: *NASA CONFERENCE PUBLICATION*. NASA, 1992, pp. 329–329.
- [187] J.G. Williams, S.G. Turyshev, and D.H. Boggs. “Lunar laser ranging tests of the equivalence principle”. In: *Classical and Quantum Gravity* 29.18 (2012). URL: <https://www.scopus.com/inward/record.uri?eid=2-s2.0-84865065435&doi=10.1088%2f0264-9381%2f29%2f18%2f184004&partnerID=40&md5=7c2de8db7e3d7ee7a9001c1a6a195911>.
- [188] T. W. Murphy et al. “Long-term degradation of optical devices on the Moon”. In: *Icarus* 208.1 (2010), pp. 31–35. URL: <http://www.sciencedirect.com/science/article/pii/S0019103510000898>.
- [189] A.L. Hammond. “Mars as an active planet: The view from Mariner 9”. In: *Science* 175.4019 (1972), pp. 286–287. URL: <https://www.scopus.com/inward/record.uri?eid=2-s2.0-37049235587&doi=10.1126%2fscience.175.4019.286&partnerID=40&md5=2ce775173d818d1e392b04fe81b75af0>.

- [190] G. A. Landis. “Solar cell selection for Mars”. In: *IEEE Aerospace and Electronic Systems Magazine* 15.1 (Jan. 2000), pp. 17–21.
- [191] P. H. Smith et al. “Results from the Mars Pathfinder Camera”. In: *Science* 278.5344 (1997). Publisher: American Association for the Advancement of Science _eprint: <https://science.sciencemag.org/content/278/5344/1758.full.pdf>, pp. 1758–1765. URL: <https://science.sciencemag.org/content/278/5344/1758>.
- [192] Maureen E. Ockert-Bell et al. “Absorption and scattering properties of the Martian dust in the solar wavelengths”. In: *Journal of Geophysical Research: Planets* 102.E4 (1997). _eprint: <https://agupubs.onlinelibrary.wiley.com/doi/pdf/10.1029/96JE03991>, pp. 9039–9050. URL: <https://agupubs.onlinelibrary.wiley.com/doi/abs/10.1029/96JE03991>.
- [193] David Crisp, Asmin V. Pathare, and Richard C. Ewell. “The performance of gallium arsenide/germanium solar cells at the Martian surface”. In: *Acta Astronautica* 54 (2004), pp. 83–101.
- [194] Geoffrey A. Landis and Phillip P. Jenkins. “Measurement of the settling rate of atmospheric dust on Mars by the MAE instrument on Mars Pathfinder”. In: *Journal of Geophysical Research: Planets* 105.E1 (2000). _eprint: <https://agupubs.onlinelibrary.wiley.com/doi/pdf/10.1029/1999JE001029>, pp. 1855–1857. URL: <https://agupubs.onlinelibrary.wiley.com/doi/abs/10.1029/1999JE001029>.
- [195] Richard W. Zurek and Leonard J. Martin. “Interannual variability of planet-encircling dust storms on Mars”. In: *Journal of Geophysical Research: Planets* 98.E2 (1993). _eprint: <https://agupubs.onlinelibrary.wiley.com/doi/pdf/10.1029/92JE02936>, pp. 3247–3259. URL: <https://agupubs.onlinelibrary.wiley.com/doi/abs/10.1029/92JE02936>.
- [196] Leonard J. Martin and Richard W. Zurek. “An analysis of the history of dust activity on Mars”. In: *Journal of Geophysical Research: Planets* 98.E2 (1993). _eprint: <https://agupubs.onlinelibrary.wiley.com/doi/pdf/10.1029/92JE02937>, pp. 3221–3246. URL: <https://agupubs.onlinelibrary.wiley.com/doi/abs/10.1029/92JE02937>.
- [197] Thomas W. Kerslake and Lisa L. Kohout. “Solar Electric Power System Analyses for Mars Surface Missions”. In: *SAE Technical Paper*. SAE International, Aug. 1999. URL: <https://doi.org/10.4271/1999-01-2482>.
- [198] Geoffrey A. Landis. “Dust obscuration of Mars solar arrays”. In: *Acta Astronautica* 38.11 (1996), pp. 885–891. URL: <http://www.sciencedirect.com/science/article/pii/S0094576596000884>.
- [199] C. Flores et al. “GaAs solar cells for the Mars surface”. In: *3rd World Conference on Photovoltaic Energy Conversion, 2003. Proceedings of*. Vol. 1. May 2003, 650–653 Vol.1.

- [200] Robert O. Pepin. “Atmospheres on the terrestrial planets: Clues to origin and evolution”. In: *Earth and Planetary Science Letters* 252.1 (2006), pp. 1–14. URL: <http://www.sciencedirect.com/science/article/pii/S0012821X06006522>.
- [201] Alfonso Delgado-Bonal and F. Javier Martín-Torres. “Solar cell temperature on Mars”. In: *Solar Energy* 118 (2015), pp. 74–79. URL: <http://www.sciencedirect.com/science/article/pii/S0038092X15002418>.
- [202] George L. Hashimoto et al. “Felsic highland crust on Venus suggested by Galileo Near-Infrared Mapping Spectrometer data”. In: *Journal of Geophysical Research: Planets* 113.E5 (2008). _eprint: <https://agupubs.onlinelibrary.wiley.com/doi/pdf/10.1029/2008JE003134>. URL: <https://agupubs.onlinelibrary.wiley.com/doi/abs/10.1029/2008JE003134>.
- [203] James A. Cutts et al. “Technology Perspectives in the Future Exploration of Venus”. In: *Exploring Venus as a Terrestrial Planet*. _eprint: <https://agupubs.onlinelibrary.wiley.com/doi/pdf/10.1029/176GM13>. American Geophysical Union (AGU), 2013, pp. 207–225. URL: <https://agupubs.onlinelibrary.wiley.com/doi/abs/10.1029/176GM13>.
- [204] A. Beatty J. K; Petersen C. C.; Chakin. “The New Solar System (eds) 1999.” In: *Geological Magazine* 137.4 (2000). Edition: 2000/07/01 Publisher: Cambridge University Press, pp. 463–479. URL: <https://www.cambridge.org/>.
- [205] Fredric W. Taylor, Håkan Svedhem, and James W. Head. “Venus: The Atmosphere, Climate, Surface, Interior and Near-Space Environment of an Earth-Like Planet”. In: *Space Science Reviews* 214.1 (Jan. 2018), p. 35. URL: <https://doi.org/10.1007/s11214-018-0467-8>.
- [206] F. Taylor. *The Scientific Exploration of Venus*. Cambridge University Press. New York, 2014.
- [207] Dmitry V. Titov et al. “Radiation in the Atmosphere of Venus”. In: *Exploring Venus as a Terrestrial Planet*. _eprint: <https://agupubs.onlinelibrary.wiley.com/doi/pdf/10.1029/176GM08>. American Geophysical Union (AGU), 2013, pp. 121–138. URL: <https://agupubs.onlinelibrary.wiley.com/doi/abs/10.1029/176GM08>.
- [208] J. Grandidier et al. “Solar Cell Analysis under Venus Atmosphere Conditions”. In: *2018 IEEE 7th World Conference on Photovoltaic Energy Conversion, WCPEC 2018 - A Joint Conference of 45th IEEE PVSC, 28th PVSEC and 34th EU PVSEC*. 2018, pp. 1580–1582. URL: <https://www.scopus.com/inward/record.uri?eid=2-s2.0-85059915970&doi=10.1109%2fPVSC.2018.8548025&partnerID=40&md5=ba4aa19c234dce5ff502e8e878c0d95f>.
- [209] Geoffrey Landis and Emily Haag. “Analysis of Solar Cell Efficiency for Venus Atmosphere and Surface Missions”. In: July 2013.

- [210] Ulrich R. Christensen. “A deep dynamo generating Mercury’s magnetic field”. In: *Nature* 444.7122 (Dec. 2006), pp. 1056–1058. URL: <https://doi.org/10.1038/nature05342>.
- [211] Louise M. Prockter. “Ice in the solar system”. In: *Johns hopkins ApL TechnicAL Digest* 26 (Jan. 2005).
- [212] Park, Seonyong et al. “Origin of the Degradation of Triple Junction Solar Cells at low Temperature”. In: *E3S Web Conf.* 16 (2017), p. 04004. URL: <https://doi.org/10.1051/e3sconf/20171604004>.
- [213] A. L. Broadfoot, D. E. Shemansky, and S. Kumar. “Mariner 10: Mercury atmosphere”. In: *Geophysical Research Letters* 3.10 (1976). _eprint: <https://agupubs.onlinelibrary.wiley.com/doi/pdf/10.1029/GL003i010p00577>, pp. 577–580. URL: <https://agupubs.onlinelibrary.wiley.com/doi/abs/10.1029/GL003i010p00577>.
- [214] Shailendra Kumar. “Mercury’s atmosphere: A perspective after Mariner 10”. In: *Icarus* 28.4 (1976), pp. 579–591. URL: <http://www.sciencedirect.com/science/article/pii/0019103576901317>.
- [215] S.C. Solomon et al. “The MESSENGER mission to Mercury: Scientific objectives and implementation”. In: *Planetary and Space Science* 49.14-15 (2001), pp. 1445–1465. URL: <https://www.scopus.com/inward/record.uri?eid=2-s2.0-14344270011&doi=10.1016%2fs0032-0633%2801%2900085-X&partnerID=40&md5=de949f7fcbcc0aba6ec0886ed963a7c3>.
- [216] G. Dakermanji, J. Jenkins, and C. J. Ercol. “The Messenger Spacecraft Solar Array Design and Early Mission Performance”. In: *2006 IEEE 4th World Conference on Photovoltaic Energy Conference*. Vol. 2. ISSN: 0160-8371. May 2006, pp. 1919–1922.
- [217] G. Cremonese et al. “The surface of mercury as seen by mariner 10”. In: *Space Science Reviews* 132.2-4 (2007), pp. 291–306. URL: <https://www.scopus.com/inward/record.uri?eid=2-s2.0-37649019712&doi=10.1007%2fs11214-007-9231-1&partnerID=40&md5=f663a2b80c3be7075ed0751ad0bf1493>.
- [218] T. Shimada et al. “Durability evaluation of InGaP/GaAs/Ge triple-junction solar cells in HIHT environments for Mercury exploration mission”. In: *2010 35th IEEE Photovoltaic Specialists Conference*. ISSN: 0160-8371. June 2010, pp. 001112–001117.
- [219] R. Stall et al. “UV Degradation of Space Solar Cell Assemblies under High Temperature and Irradiance”. In: *2018 IEEE 7th World Conference on Photovoltaic Energy Conversion, WCPEC 2018 - A Joint Conference of 45th IEEE PVSC, 28th PVSEC and 34th EU PVSEC*. 2018, pp. 3339–3343. URL: <https://www.scopus.com/inward/record.uri?eid=2-s2.0-85059890133&doi=10.1109%2fPVSC.2018.8547643&partnerID=40&md5=e2bd0d181ef4dcc2cd5fe5e0da670d6f>.

- [220] Sarbani Basu and H. M. Antia. “Helioseismology and solar abundances”. In: *Physics Reports* 457.5 (2008), pp. 217–283. URL: <http://www.sciencedirect.com/science/article/pii/S0370157307004565>.
- [221] N. J. Fox et al. “The Solar Probe Plus Mission: Humanity’s First Visit to Our Star”. In: *Space Science Reviews* 204.1 (Dec. 2016), pp. 7–48. URL: <https://doi.org/10.1007/s11214-015-0211-6>.
- [222] A. Lyngvi et al. “The Solar Orbiter Thermal Design”. In: *56th International Astronautical Congress of the International Astronautical Federation, the International Academy of Astronautics, and the International Institute of Space Law*. _eprint: <https://arc.aiaa.org/doi/pdf/10.2514/6.IAC-05-C2.6.02>. URL: <https://arc.aiaa.org/doi/abs/10.2514/6.IAC-05-C2.6.02>.
- [223] Henry W. Brandhorst and Zheng Chen. “Photovoltaic Approaches for Near-Sun Missions”. In: *34th Intersociety Energy Conversion Engineering Conference*. ISSN: 0148-7191. SAE International, Aug. 1999. URL: <https://doi.org/10.4271/1999-01-2631>.
- [224] William R. Corliss. *The Interplanetary Pioneers. NASA SP-279*. Vol. 279. 1972.
- [225] G. Sandscheper. “The trip to hot space”. In: *New Scientist* (Dec. 1974), pp. 918–920. (Visited on 01/05/2019).
- [226] V. Domingo, B. Fleck, and A. I. Poland. “The SOHO mission: An overview”. In: *Solar Physics* 162.1 (Dec. 1995), pp. 1–37. URL: <https://doi.org/10.1007/BF00733425>.
- [227] P. Rumler, H. Schweitzer, and H. Evans. “SOHO Solar Array: A Performance Evaluation of 2,5 Years in Orbit and Capabilities for a Mission Extension of 5 Years”. In: *Proceedings of the Fifth European Space Power Conference (ESPC)*. Ed. by R. A. Harris. Vol. 416. ESA Special Publication. Jan. 1998, p. 621.
- [228] Pål Brekke et al. “Space Weather Effects on SOHO and its Space Weather Warning Capabilities”. In: Jan. 2006, pp. 109–122.
- [229] Robin M. Canup and William R. Ward. “Formation of the Galilean Satellites: Conditions of Accretion”. In: *The Astronomical Journal* 124.6 (Dec. 2002). Publisher: IOP Publishing, pp. 3404–3423. URL: <https://doi.org/10.1086%2F344684>.
- [230] Fran Bagenal, Timothy E Dowling, and William B McKinnon. *Jupiter: the planet, satellites and magnetosphere*. Vol. 1. Cambridge University Press, 2007.
- [231] Fredric W. Taylor. “Planetary atmospheres”. In: *Meteorological Applications* 17.4 (2010). _eprint: <https://rmets.onlinelibrary.wiley.com/doi/pdf/10.1002/met.212>, pp. 393–403. URL: <https://rmets.onlinelibrary.wiley.com/doi/abs/10.1002/met.212>.

- [232] J. Fincannon. “Radioisotope Reduction using solar power for outer planetary missions”. In: *6th International Energy Conversion Engineering Conference, IECEC*. 2008. URL: <https://www.scopus.com/inward/record.uri?eid=2-s2.0-77956844243&partnerID=40&md5=03ed1c2e3f1e6ce52463ef6800a479ab>.
- [233] S.J. Bolton et al. “The Juno Mission”. In: *Space Science Reviews* 213.1-4 (2017), pp. 5–37. URL: <https://www.scopus.com/inward/record.uri?eid=2-s2.0-85032993916&doi=10.1007%2fs11214-017-0429-6&partnerID=40&md5=e3d9575ade922ce4ede8bc5ef7d28561>.
- [234] Baur, Carsten et al. “Status of Solar Generator Related Technology Development Activities Supporting the Juice Mission”. In: *E3S Web Conf.* 16 (2017), p. 04005. URL: <https://doi.org/10.1051/e3sconf/20171604005>.
- [235] Khorenko, Victor et al. “BOL and EOL Characterization of Azur 3G Lilt Solar Cells for ESA Juice Mission”. In: *E3S Web Conf.* 16 (2017), p. 03011. URL: <https://doi.org/10.1051/e3sconf/20171603011>.
- [236] D.A. Scheiman and D.B. Snyder. “Low intensity low temperature (LILT) measurements of state-of-the-art triple junction solar cells for space missions”. In: *Conference Record of the IEEE Photovoltaic Specialists Conference*. 2008. URL: <https://www.scopus.com/inward/record.uri?eid=2-s2.0-84879733238&doi=10.1109%2fPVSC.2008.4922707&partnerID=40&md5=1a399315c021de910707a8dafad425df>.
- [237] Paul M. Stella et al. “PV technology for low intensity, low temperature (LILT) applications”. In: *Conference Record of the IEEE Photovoltaic Specialists Conference*. Vol. 2. 1994, pp. 2082–2087. URL: <https://www.scopus.com/inward/record.uri?eid=2-s2.0-0028706837&partnerID=40&md5=24860c7ed74af879cf52778be2c06b62>.
- [238] A. J. Dessler. *Physics of the Jovian Magnetosphere*. 2002.
- [239] V.G. Weizer and J.D. Broder. “On the cause of the flat-spot phenomenon observed in silicon solar cells at low temperatures and low intensities”. In: *Journal of Applied Physics* 53.8 (1982), pp. 5926–5930. URL: <https://www.scopus.com/inward/record.uri?eid=2-s2.0-0020169375&doi=10.1063%2f1.331435&partnerID=40&md5=3f3e50bdf46226f77fa1aafb6e6bad08>.
- [240] C. Baur et al. “Development status of triple-junction solar cells optimized for low intensity low temperature applications”. In: *Conference Record of the IEEE Photovoltaic Specialists Conference*. 2013, pp. 3237–3242. URL: <https://www.scopus.com/inward/record.uri?eid=2-s2.0-84896443274&doi=10.1109%2fPVSC.2013.6745142&partnerID=40&md5=67aa97a19297ba0e86ea1d9a87be71b1>.
- [241] Ulloa-Severino, Antonio et al. “Power Subsystem Approach for the Europa Mission”. In: *E3S Web Conf.* 16 (2017), p. 13004. URL: <https://doi.org/10.1051/e3sconf/20171613004>.

- [242] A. Boca et al. “A Data-Driven Evaluation of the Viability of Solar Arrays at Saturn”. In: *IEEE Journal of Photovoltaics* 7.4 (July 2017), pp. 1159–1164.
- [243] A. Boca et al. “Development of High-Performance Solar Cells for the Jupiter and Saturn Environments”. In: *2018 IEEE 7th World Conference on Photovoltaic Energy Conversion, WCPEC 2018 - A Joint Conference of 45th IEEE PVSC, 28th PVSEC and 34th EU PVSEC*. 2018, pp. 3324–3328. URL: <https://www.scopus.com/inward/record.uri?eid=2-s2.0-85059888886&doi=10.1109%2fPVSC.2018.8548171&partnerID=40&md5=38cedec7b826a668c28b8b4dbe2c5ddf>.
- [244] B. F. Burke and K. L. Franklin. “Observations of a variable radio source associated with the planet Jupiter”. In: *Journal of Geophysical Research (1896-1977)* 60.2 (1955). _eprint: <https://agupubs.onlinelibrary.wiley.com/doi/pdf/10.1029/JZ060i002p00213>, pp. 213–217. URL: <https://agupubs.onlinelibrary.wiley.com/doi/abs/10.1029/JZ060i002p00213>.
- [245] S. J. Bolton et al. “Ultra-relativistic electrons in Jupiter’s radiation belts”. English. In: *Nature* 415.6875 (2002). Publisher: Nature Publishing Group, pp. 987–91.
- [246] Imke de Pater and David E. Dunn. “VLA observations of Jupiter’s synchrotron radiation at 15 and 22 GHz”. In: *Icarus* 163.2 (2003), pp. 449–455. URL: <http://www.sciencedirect.com/science/article/pii/S001910350300068X>.
- [247] Elias Roussos et al. “The in-situ exploration of Jupiter’s radiation belts”. In: *Experimental Astronomy* (Oct. 2021). URL: <https://doi.org/10.1007/s10686-021-09801-0>.
- [248] T.J. Birmingham. *Charged particle motions in the distended magnetospheres of Jupiter and Saturn*. Tech. rep. NASA-TM–83899. United States, 1982, p. 37. URL: http://inis.iaea.org/search/search.aspx?orig_q=RN:14766401.
- [249] Jenna L. Kloosterman, Bryan J. Butler, and Imke de Pater. “VLA observations of synchrotron radiation at 15 GHz”. In: *Icarus* 193 (2008), pp. 644–648.
- [250] W. R. Dunn et al. “The independent pulsations of Jupiter’s northern and southern X-ray auroras”. In: *Nature Astronomy* 1.11 (Nov. 2017), pp. 758–764. URL: <https://doi.org/10.1038/s41550-017-0262-6>.
- [251] Q. Nénon, A. Sicard, and S. Bourdarie. “A new physical model of the electron radiation belts of Jupiter inside Europa’s orbit”. In: *Journal of Geophysical Research: Space Physics* 122.5 (2017). _eprint: <https://agupubs.onlinelibrary.wiley.com/doi/pdf/10.1002/2017JA023893>, pp. 5148–5167. URL: <https://agupubs.onlinelibrary.wiley.com/doi/abs/10.1002/2017JA023893>.

- [252] Neil Divine and H. B. Garrett. “Charged particle distributions in Jupiter’s magnetosphere”. In: *Journal of Geophysical Research: Space Physics* 88.A9 (1983). [_eprint: https://agupubs.onlinelibrary.wiley.com/doi/pdf/10.1029/JA088iA09p06889](https://agupubs.onlinelibrary.wiley.com/doi/pdf/10.1029/JA088iA09p06889), pp. 6889–6903. URL: <https://agupubs.onlinelibrary.wiley.com/doi/abs/10.1029/JA088iA09p06889>.
- [253] European Cooperation for Space Standardization (ECSS). “ECSS-E-ST-20-08C Rev. 1, Space engineering - Photovoltaic assemblies and components”. July 2012. URL: <https://ecss.nl/>.
- [254] V. Inguibert et al. “Measurements of the Flashover Expansion on a Real-Solar Panel—Preliminary Results of EMAGS3 Project”. In: *IEEE Transactions on Plasma Science* 41.12 (Dec. 2013), pp. 3370–3379.
- [255] M. F. Piszczor et al. “Advanced solar cell and array technology for NASA deep space missions”. In: *2008 33rd IEEE Photovoltaic Specialists Conference*. ISSN: 0160-8371. May 2008, pp. 1–5.
- [256] N. S. Fatemi et al. “Performance of high-efficiency advanced triple-junction solar panels for the LILT Mission Dawn”. In: *Conference Record of the Thirty-first IEEE Photovoltaic Specialists Conference, 2005*. ISSN: 0160-8371. Jan. 2005, pp. 618–621.
- [257] NASA/JPL/DLR. *Landscape Comparisons - Galilean Satellites*. Feb. 1998. URL: <http://galileo.jpl.nasa.gov>.
- [258] Rosaly M. C. Lopes et al. “Lava lakes on Io: observations of Io’s volcanic activity from Galileo NIMS during the 2001 fly-bys”. In: *Icarus* 169.1 (2004), pp. 140–174. URL: <http://www.sciencedirect.com/science/article/pii/S0019103503003774>.
- [259] A.S. McEwen et al. “Active Volcanism on Io as Seen by Galileo SSI”. In: *Icarus* 135.1 (1998), pp. 181–219. URL: <https://www.scopus.com/inward/record.uri?eid=2-s2.0-0001471362&doi=10.1006%2fincar.1998.5972&partnerID=40&md5=4bb0acd7f6a83f6ef028c0172cdf51a5>.
- [260] J.R. Spencer and N.M. Schneider. “Io on the eve of the Galileo mission”. In: *Annual Review of Earth and Planetary Sciences* 24 (1996), pp. 125–190. URL: <https://www.scopus.com/inward/record.uri?eid=2-s2.0-0030470324&doi=10.1146%2fannurev.earth.24.1.125&partnerID=40&md5=72c2339ea5476fcc026849f5ead3de50>.
- [261] Emmanuel Lellouch, Melissa A. McGrath, and Kandis Lea Jessup. “Io’s atmosphere”. In: *Io After Galileo: A New View of Jupiter’s Volcanic Moon*. Berlin, Heidelberg: Springer Berlin Heidelberg, 2007, pp. 231–264. URL: https://doi.org/10.1007/978-3-540-48841-5_10.

- [262] A.P. Ingersoll. “Io meteorology: How atmospheric pressure is controlled locally by volcanos and surface frosts”. In: *Icarus* 81.2 (1989), pp. 298–313. URL: <https://www.scopus.com/inward/record.uri?eid=2-s2.0-0001604551&doi=10.1016%2f0019-1035%2889%2990055-9&partnerID=40&md5=f2378665266406b51c54819cc2d02486>.
- [263] G. S. Orton et al. “Galileo Photopolarimeter-Radiometer Observations of Jupiter and the Galilean Satellites”. In: *Science* 274.5286 (1996). _eprint: <https://www.science.org/doi/pdf/10.1126/science.274.5286.389>, pp. 389–391. URL: <https://www.science.org/doi/abs/10.1126/science.274.5286.389>.
- [264] A. S. McEwen et al. “High-Temperature Silicate Volcanism on Jupiter’s Moon Io”. In: *Science* 281.5373 (1998). Publisher: American Association for the Advancement of Science _eprint: <https://science.sciencemag.org/content/281/5373/87.full.pdf>, pp. 87–90. URL: <https://science.sciencemag.org/content/281/5373/87>.
- [265] Gary D. Clow and Michael H. Carr. “Stability of sulfur slopes on Io”. In: *Icarus* 44.2 (1980), pp. 268–279. URL: <http://www.sciencedirect.com/science/article/pii/0019103580900226>.
- [266] Rosaly M. C. Lopes and David A. Williams. “Io afterGalileo”. In: *Reports on Progress in Physics* 68.2 (Jan. 2005). Publisher: IOP Publishing, pp. 303–340. URL: <https://doi.org/10.1088%2F0034-4885%2F68%2F2%2Fr02>.
- [267] Fritz M. Neubauer. “The sub-Alfvénic interaction of the Galilean satellites with the Jovian magnetosphere”. In: *Journal of Geophysical Research: Planets* 103.E9 (1998). _eprint: <https://agupubs.onlinelibrary.wiley.com/doi/pdf/10.1029/97JE03370>, pp. 19843–19866. URL: <https://agupubs.onlinelibrary.wiley.com/doi/abs/10.1029/97JE03370>.
- [268] John Robert. Spencer. *The surfaces of Europa, Ganymede, and Callisto: An investigation using voyager iris thermal infrared spectra (Jupiter)*. 1987. URL: <http://hdl.handle.net/10150/184098>.
- [269] Arthur L. Lane, Robert M. Nelson, and Dennis L. Matson. “Evidence for sulphur implantation in Europa’s UV absorption band”. In: *Nature* 292.5818 (July 1981), pp. 38–39. URL: <https://doi.org/10.1038/292038a0>.
- [270] Roger N. Clark. “Ganymede, Europa, Callisto, and Saturn’s rings: Compositional analysis from reflectance spectroscopy”. In: *Icarus* 44.2 (1980), pp. 388–409. URL: <https://www.sciencedirect.com/science/article/pii/0019103580900330>.
- [271] James B. Pollack et al. “Near-infrared spectra of the Galilean satellites: Observations and compositional implications”. In: *Icarus* 36.3 (1978), pp. 271–303. URL: <https://www.sciencedirect.com/science/article/pii/0019103578901100>.

- [272] M.H. Carr et al. “Evidence for a subsurface ocean on Europa”. In: *Nature* 391.6665 (1998), pp. 363–365. URL: <https://www.scopus.com/inward/record.uri?eid=2-s2.0-18144435537&doi=10.1038%2f34857&partnerID=40&md5=2aaf97fa3667bdbe8a3511f92fb8fd4b>.
- [273] David Morrison and Mildred Shapley Matthews. *Satellites of Jupiter*. English. Tucson, Ariz.: University of Arizona Press, 1982.
- [274] Adam P. Showman, Malhotra, and Renu. “The Galilean Satellites”. In: *Science* 286.5437 (1999). Publisher: American Association for the Advancement of Science _eprint: <https://science.sciencemag.org/content/286/5437/77.full.pdf>, pp. 77–84. URL: <https://science.sciencemag.org/content/286/5437/77>.
- [275] M. G. Kivelson, K. K. Khurana, and M. Volwerk. “The Permanent and Inductive Magnetic Moments of Ganymede”. In: *Icarus* 157.2 (2002), pp. 507–522. URL: <https://www.sciencedirect.com/science/article/pii/S001910350296834X>.
- [276] D. T. Hall et al. “The Far-Ultraviolet Oxygen Airglow of Europa and Ganymede”. In: 499.1 (May 1998). Publisher: American Astronomical Society, pp. 475–481. URL: <https://doi.org/10.1086%2F305604>.
- [277] NASA’s Goddard Space Flight Center. *NASA Scientists Confirm Water Vapor on Europa*. Tech. rep. Greenbelt, Md, Nov. 2019. URL: <https://www.nasa.gov/feature/goddard/2019/nasa-scientists-confirm-water-vapor-on-europa> (visited on 02/02/2020).
- [278] Jp Collette et al. “Phase change material device for spacecraft thermal control”. In: *62nd International Astronautical Congress 2011, IAC 2011* 7 (Jan. 2011), pp. 6020–6031.
- [279] John F. Cooper et al. “Energetic Ion and Electron Irradiation of the Icy Galilean Satellites”. In: *Icarus* 149.1 (2001), pp. 133–159. URL: <http://www.sciencedirect.com/science/article/pii/S0019103500964984>.
- [280] T.A. Nordheim, Kevin Hand, and C. Paranicas. “Preservation of potential biosignatures in the shallow subsurface of Europa”. In: *Nature Astronomy* 2 (Aug. 2018).
- [281] C. Paranicas, R. W. Carlson, and R. E. Johnson. “Electron bombardment of Europa”. In: *Geophysical Research Letters* 28.4 (2001). _eprint: <https://agupubs.onlinelibrary.wiley.com/doi/pdf/10.1029/2000GL012320>, pp. 673–676. URL: <https://agupubs.onlinelibrary.wiley.com/doi/abs/10.1029/2000GL012320>.
- [282] M. K. Pospieszalska and R. E. Johnson. “Magnetospheric ion bombardment profiles of satellites: Europa and Dione”. In: *Icarus* 78.1 (1989), pp. 1–13. URL: <http://www.sciencedirect.com/science/article/pii/0019103589900651>.
- [283] D. J. Williams et al. “The Galileo Energetic Particles Detector”. In: *Space Science Reviews* 60.1 (May 1992), pp. 385–412. URL: <https://doi.org/10.1007/BF00216863>.

- [284] Robert T. Pappalardo et al. “Geology of Ganymede”. In: *Jupiter. The Planet, Satellites and Magnetosphere*. Ed. by Fran Bagenal, Timothy E. Dowling, and William B. McKinnon. Vol. 1. 2004, pp. 363–396.
- [285] Tristan Guillot et al. “Saturn’s Exploration Beyond Cassini-Huygens”. In: *Saturn from Cassini-Huygens* (Dec. 2009).
- [286] Julianne I. Moses et al. “Photochemistry of Saturn’s Atmosphere: II. Effects of an Influx of External Oxygen”. In: *Icarus* 145.1 (2000), pp. 166–202. URL: <http://www.sciencedirect.com/science/article/pii/S0019103599963200>.
- [287] E. J. SMITH et al. “Saturn’s Magnetic Field and Magnetosphere”. In: *Science* 207.4429 (1980). Publisher: American Association for the Advancement of Science _eprint: <https://science.sciencemag.org/content/207/4429/407.full.pdf>, pp. 407–410. URL: <https://science.sciencemag.org/content/207/4429/407>.
- [288] H. Smith et al. “Enceladus and Its Influence on Saturn’s Magnetosphere”. In: Jan. 2018.
- [289] Ali Sulaiman et al. “Enceladus and Titan: Emerging Worlds of the Solar System (ESA Voyage 2050 White Paper)”. In: 2019.
- [290] Amanda R. Hendrix et al. “The NASA Roadmap to Ocean Worlds”. In: *Astrobiology* 19.1 (2019). _eprint: <https://doi.org/10.1089/ast.2018.1955>, pp. 1–27. URL: <https://doi.org/10.1089/ast.2018.1955>.
- [291] R.D. Lorenz et al. “Dragonfly: A rotorcraft lander concept for scientific exploration at titan”. In: *Johns Hopkins APL Technical Digest (Applied Physics Laboratory)* 34 (Oct. 2018), pp. 374–387.
- [292] John R. Spencer and Francis Nimmo. “Enceladus: An Active Ice World in the Saturn System”. In: *Annual Review of Earth and Planetary Sciences* 41.1 (2013). _eprint: <https://doi.org/10.1146/annurev-earth-050212-124025>, pp. 693–717. URL: <https://doi.org/10.1146/annurev-earth-050212-124025>.
- [293] C. J. A. Howett et al. “Thermal inertia and bolometric Bond albedo values for Mimas, Enceladus, Tethys, Dione, Rhea and Iapetus as derived from Cassini/CIRS measurements”. In: *Icarus* 206.2 (2010), pp. 573–593. URL: <http://www.sciencedirect.com/science/article/pii/S001910350900308X>.
- [294] L. Iess et al. “The Gravity Field and Interior Structure of Enceladus”. In: *Science* 344.6179 (2014). Publisher: American Association for the Advancement of Science _eprint: <https://science.sciencemag.org/content/344/6179/78.full.pdf>, pp. 78–80. URL: <https://science.sciencemag.org/content/344/6179/78>.
- [295] C. C. Porco et al. “Cassini Observes the Active South Pole of Enceladus”. In: *Science* 311.5766 (2006). Publisher: American Association for the Advancement of Science _eprint: <https://science.sciencemag.org/content/311/5766/1393.full.pdf>, pp. 1393–1401. URL: <https://science.sciencemag.org/content/311/5766/1393>.

- [296] C. J. Hansen et al. “The composition and structure of the Enceladus plume”. In: *Geophysical Research Letters* 38.11 (2011). _eprint: <https://agupubs.onlinelibrary.wiley.com/doi/pdf/10.1029/2011GL047415>. URL: <https://agupubs.onlinelibrary.wiley.com/doi/abs/10.1029/2011GL047415>.
- [297] R. E. Johnson et al. “The Enceladus and OH Tori at Saturn”. In: *Japjl* 644.2 (June 2006), pp. L137–L139.
- [298] Andrew P. Ingersoll and Shawn P. Ewald. “Total particulate mass in Enceladus plumes and mass of Saturn’s E ring inferred from Cassini ISS images”. In: *Icarus* 216.2 (2011), pp. 492–506. URL: <http://www.sciencedirect.com/science/article/pii/S0019103511003708>.
- [299] Sascha Kempf, Uwe Beckmann, and Jürgen Schmidt. “How the Enceladus dust plume feeds Saturn’s E ring”. In: *Icarus* 206.2 (2010), pp. 446–457. URL: <http://www.sciencedirect.com/science/article/pii/S0019103509004084>.
- [300] Ben S. Southworth, Sascha Kempf, and Joe Spitale. “Surface deposition of the Enceladus plume and the zenith angle of emissions”. In: *Icarus* 319 (2019), pp. 33–42. URL: <http://www.sciencedirect.com/science/article/pii/S0019103518300551>.
- [301] N. Krupp et al. “The Cassini Enceladus encounters 2005–2010 in the view of energetic electron measurements”. In: *Icarus* 218.1 (2012), pp. 433–447. URL: <http://www.sciencedirect.com/science/article/pii/S0019103511004994>.
- [302] William Farrell et al. “Modification of the plasma in the near-vicinity of Enceladus by the enveloping dust”. In: *Geophysical Research Letters - GEOPHYS RES LETT* 37 (Oct. 2010).
- [303] Christophe Sotin et al. “Titan’s Interior Structure”. In: *Titan from Cassini-Huygens*. Ed. by Robert H. Brown, Jean-Pierre Lebreton, and J. Hunter Waite. Dordrecht: Springer Netherlands, 2010, pp. 61–73. URL: https://doi.org/10.1007/978-1-4020-9215-2_4.
- [304] Ralph D. Lorenz, Michael E. Brown, and F. Michael Flasar. “Seasonal Change on Titan”. In: *Titan from Cassini-Huygens*. Ed. by Robert H. Brown, Jean-Pierre Lebreton, and J. Hunter Waite. Dordrecht: Springer Netherlands, 2010, pp. 353–372. URL: https://doi.org/10.1007/978-1-4020-9215-2_14.
- [305] C. Bertucci et al. “Titan’s interaction with the supersonic solar wind”. In: *Geophysical Research Letters* 42.2 (2015). _eprint: <https://agupubs.onlinelibrary.wiley.com/doi/pdf/10.1002/2014GL062106>, pp. 193–200. URL: <https://agupubs.onlinelibrary.wiley.com/doi/abs/10.1002/2014GL062106>.
- [306] H. Y. Wei et al. “Plasma environment at Titan’s orbit with Titan present and absent”. In: *Geophysical Research Letters* 36.23 (2009). _eprint: <https://agupubs.onlinelibrary.wiley.com/doi/pdf/10.1029/2009GL041048>. URL: <https://agupubs.onlinelibrary.wiley.com/doi/abs/10.1029/2009GL041048>.

- [307] Darrell F. Strobel et al. “Atmospheric Structure and Composition”. In: *Titan from Cassini-Huygens*. Ed. by Robert H. Brown, Jean-Pierre Lebreton, and J. Hunter Waite. Dordrecht: Springer Netherlands, 2010, pp. 235–257. URL: https://doi.org/10.1007/978-1-4020-9215-2_10.
- [308] Edward C. Sittler et al. “Energy Deposition Processes in Titan’s Upper Atmosphere and Its Induced Magnetosphere”. In: *Titan from Cassini-Huygens*. Ed. by Robert H. Brown, Jean-Pierre Lebreton, and J. Hunter Waite. Dordrecht: Springer Netherlands, 2010, pp. 393–453. URL: https://doi.org/10.1007/978-1-4020-9215-2_16.
- [309] S. A. Ledvina, T. E. Cravens, and K. Kecskeméty. “Ion distributions in Saturn’s magnetosphere near Titan”. In: *Journal of Geophysical Research: Space Physics* 110.A6 (2005). _eprint: <https://agupubs.onlinelibrary.wiley.com/doi/pdf/10.1029/2004JA010771>. URL: <https://agupubs.onlinelibrary.wiley.com/doi/abs/10.1029/2004JA010771>.
- [310] G. Tobie et al. “Science goals and mission concept for the future exploration of Titan and Enceladus”. In: *Planetary and Space Science* 104 (2014), pp. 59–77. URL: <http://www.sciencedirect.com/science/article/pii/S0032063314003158>.
- [311] J. I. Lunine et al. “Future Exploration of Enceladus and Other Saturnian Moons”. In: *Enceladus and the Icy Moons of Saturn*. Ed. by Paul M. Schenk et al. 2018, p. 453.
- [312] S. P. Tobin et al. “Advanced metallization for highly efficient solar cells”. In: *19th IEEE Photovoltaic Specialists Conference*. Jan. 1987, pp. 70–75.
- [313] M. B. Spitzer et al. “Gallium arsenide concentrator solar cells with highly stable metallization”. In: *Conference Record of the Twentieth IEEE Photovoltaic Specialists Conference*. ISSN: null. Sept. 1988, 930–933 vol.2.
- [314] Geoffrey A. Landis. “Solar power for near-sun, high-temperature missions”. In: *2008 33rd IEEE Photovoltaic Specialists Conference* (2008), pp. 1–5.
- [315] James R Gaier, Marla E Perez-Davis, and Mark Marabito. “Aeolian removal of dust from photovoltaic surfaces on Mars”. In: (1990).
- [316] James R Gaier and Marla E Perez-Davis. “Effect of particle size of Martian dust on the degradation of photovoltaic cell performance”. In: (1991).
- [317] R. Brett Williams et al. “Vibration Characterization of Self-Cleaning Solar Panels with Piezoceramic Actuation”. In: *48th AIAA/ASME/ASCE/AHS/ASC Structures, Structural Dynamics, and Materials Conference*. _eprint: <https://arc.aiaa.org/doi/pdf/10.2514/6.2007-1746>. URL: <https://arc.aiaa.org/doi/abs/10.2514/6.2007-1746>.
- [318] CI Calle et al. “Dust particle removal by electrostatic and dielectrophoretic forces with applications to NASA exploration missions”. In: *Proc. ESA Annual Meeting on Electrostatics*. Vol. 2008. ESA Minneapolis, MN, 2008.

- [319] Rajesh Sharma et al. “Experimental evaluation and analysis of electrodynamic screen as dust mitigation technology for future Mars missions”. In: *IEEE Transactions on Industry Applications* 45.2 (2009). Publisher: IEEE, pp. 591–596.
- [320] M. K. Mazumder et al. “Self-Cleaning Transparent Dust Shields for Protecting Solar Panels and Other Devices”. In: *Particulate Science and Technology* 25.1 (2007). Publisher: Taylor & Francis _eprint: <https://doi.org/10.1080/02726350601146341>, pp. 5–20. URL: <https://doi.org/10.1080/02726350601146341>.
- [321] Nima Afshar-Mohajer et al. “Design of an electrostatic lunar dust repeller for mitigating dust deposition and evaluation of its removal efficiency”. In: *Journal of Aerosol Science* 69 (2014), pp. 21–31. URL: <http://www.sciencedirect.com/science/article/pii/S0021850213002334>.
- [322] Clément Weick. “Vers un module photovoltaïque à concentration ultra-intégré : développement du concept et des moyens de caractérisations associés”. PhD Thesis. Nov. 2017.
- [323] J. Kleiman, Masahito Tagawa, and Yugo Kimoto. *Protection of Materials and Structures From the Space Environment*. Vol. 32. Jan. 2013.
- [324] Benjamin Charnay and Sébastien Lebonnois. “Two boundary layers in Titan’s lower troposphere inferred from a climate model”. In: *Nature Geoscience* 5.2 (Feb. 2012), pp. 106–109. URL: <https://doi.org/10.1038/ngeo1374>.
- [325] G. H. Jones et al. “Enceladus’ Varying Imprint on the Magnetosphere of Saturn”. In: *Science* 311.5766 (2006). Publisher: American Association for the Advancement of Science _eprint: <https://science.sciencemag.org/content/311/5766/1412.full.pdf>, pp. 1412–1415. URL: <https://science.sciencemag.org/content/311/5766/1412>.
- [326] Philippe Voarino et al. “Microconcentration for space applications: A 7.6X TIR design”. In: *AIP Conference Proceedings* 2149.1 (Aug. 2019). Publisher: American Institute of Physics, p. 050008. URL: <https://aip.scitation.org/doi/abs/10.1063/1.5124193> (visited on 11/21/2021).
- [327] Philippe Voarino et al. “A space self-integrated micro-concentrator design: the SLIT”. In: *2019 European Space Power Conference (ESPC)*. 2019, pp. 1–6.
- [328] Dow Corning 93-500. “Space-Grade Encapsulate (Datasheet)”. 2008.
- [329] J. A. Nelder and R. Mead. “A Simplex Method for Function Minimization”. In: *The Computer Journal* 7.4 (1965), pp. 308–313. URL: <https://doi.org/10.1093/comjnl/7.4.308>.
- [330] P. A. Davies. “Edge-ray principle of nonimaging optics”. In: *J. Opt. Soc. Am. A* 11.4 (Apr. 1994). Publisher: OSA, pp. 1256–1259. URL: <http://www.osapublishing.org/josaa/abstract.cfm?URI=josaa-11-4-1256>.

- [331] Harald Ries and Ari Rabl. "Edge-ray principle of nonimaging optics". In: *J. Opt. Soc. Am. A* 11.10 (Oct. 1994). Publisher: OSA, pp. 2627–2632. URL: <http://www.osapublishing.org/josaa/abstract.cfm?URI=josaa-11-10-2627>.
- [332] Kelsey A. Horowitz et al. "A Techno-Economic Analysis and Cost Reduction Roadmap for III-V Solar Cells". In: (Nov. 2018).
- [333] A. Richter, M. Hermle, and S. W. Glunz. "Reassessment of the Limiting Efficiency for Crystalline Silicon Solar Cells". In: *IEEE Journal of Photovoltaics* 3.4 (Oct. 2013), pp. 1184–1191.
- [334] Keith McIntosh et al. "An Optical Comparison of Silicone and EVA Encapsulants for Conventional Silicon PV Modules: A Ray-Tracing Study". In: *Conference Record of the IEEE Photovoltaic Specialists Conference*. June 2009, pp. 000544–000549.
- [335] G. J. Rayl. "An investigation of the adhesive bonding of Teflon solar cell covers". NASA Lewis research center, 1979. URL: www.ntrs.nasa.gov.
- [336] D. Jacobsen. *LED lighting design optimization: Theory, methods, and applications*. Oct. 2014.
- [337] Takashi Fuyuki et al. "Photographic surveying of minority carrier diffusion length in polycrystalline silicon solar cells by electroluminescence". In: *Applied Physics Letters* 86.26 (2005). _eprint: <https://doi.org/10.1063/1.1978979>, p. 262108. URL: <https://doi.org/10.1063/1.1978979>.
- [338] P. Würfel et al. "Diffusion lengths of silicon solar cells from luminescence images". In: *Journal of Applied Physics* 101.12 (2007). _eprint: <https://doi.org/10.1063/1.2749201>, p. 123110. URL: <https://doi.org/10.1063/1.2749201>.
- [339] David Hinken et al. "Series resistance imaging of solar cells by voltage dependent electroluminescence". In: *Applied Physics Letters* 91.18 (2007). _eprint: <https://doi.org/10.1063/1.2804562>, p. 182104. URL: <https://doi.org/10.1063/1.2804562>.
- [340] Pere Roca i Cabarrocas et al. "Quantitative Assessment of TCO Sheet Resistance in Thin-Film Silicon Devices from Electroluminescence Images". In: 2013.
- [341] T. Trupke et al. "Spatially resolved series resistance of silicon solar cells obtained from luminescence imaging". In: *Applied Physics Letters* 90.9 (2007). _eprint: <https://doi.org/10.1063/1.2709630>, p. 093506. URL: <https://doi.org/10.1063/1.2709630>.
- [342] Universidad Politécnica de Madrid "Instituto de energía solar. *HELIOS 3198 solar simulator for CPV modules*. URL: <https://www.ies.upm.es/>.
- [343] A. Bermudez-Garcia et al. "First space concentrator prototype using III-V/Si cells". In: *2019 European Space Power Conference (ESPC)*. ISSN: null. Sept. 2019, pp. 1–7.

- [344] A. Petras and M. P. F. Sutcliffe. “Failure mode maps for honeycomb sandwich panels”. In: *Composite Structures* 44.4 (1999), pp. 237–252. URL: <https://www.sciencedirect.com/science/article/pii/S0263822398001238>.
- [345] Jeom Kee Paik, Anil K. Thayamballi, and Gyu Sung Kim. “The strength characteristics of aluminum honeycomb sandwich panels”. In: *Thin-Walled Structures* 35.3 (1999), pp. 205–231. URL: <https://www.sciencedirect.com/science/article/pii/S0263823199000269>.
- [346] Anderson Bermudez-Garcia, Philippe Voarino, and Olivier Raccurt. “Concentrateur optique a structure alveolaire”. FR2013856 (CEA). 2020.
- [347] V. Vareilles et al. “First Mechanical Study on Lightweight Microconcentrators Systems for Space Applications”. In: 2021, pp. 1101–1105. URL: www.eupvsec-proceedings.com.
- [348] Yongha Kim et al. “Optimal Design of a High-Agility Satellite with Composite Solar Panels”. In: *International Journal of Aeronautical and Space Sciences* 17 (Dec. 2016), pp. 476–490.
- [349] Hasan Baig, Keith C. Heasman, and Tapas K. Mallick. “Non-uniform illumination in concentrating solar cells”. In: *Renewable and Sustainable Energy Reviews* 16.8 (2012), pp. 5890–5909. URL: <https://www.sciencedirect.com/science/article/pii/S1364032112004133>.
- [350] Rebeca Herrero et al. “Concentration photovoltaic optical system irradiance distribution measurements and its effect on multi-junction solar cells”. In: *Progress in Photovoltaics: Research and Applications* 20.4 (2012). _eprint: <https://onlinelibrary.wiley.com/doi/pdf/10.1002/pip.1145>, pp. 423–430. URL: <https://onlinelibrary.wiley.com/doi/abs/10.1002/pip.1145>.
- [351] Hexcel. “Composite Materials and Structures”. US. URL: <https://www.hexcel.com/>.
- [352] Rebeca Herrero et al. “Indoor Characterization of Multi-Junction Solar Cells Under Non Uniform Light Patterns”. In: *AIP Conference Proceedings*. Vol. 1277. Oct. 2010, pp. 36–38.
- [353] Lawrence W James. *Use of imaging refractive secondaries in photovoltaic concentrators*. Tech. rep. Sandia National Lab.(SNL-NM), Albuquerque, NM (United States), 1989.
- [354] Stephen Askins et al. “Hybrid dome with total internal reflector as a secondary optical element for CPV”. In: *AIP Conference Proceedings* 1766.1 (2016). _eprint: <https://aip.scitation.org/doi/pdf/10.1063/1.4962084>, p. 050002. URL: <https://aip.scitation.org/doi/abs/10.1063/1.4962084>.
- [355] Klemens Ilse et al. “Quantification of abrasion-induced ARC transmission losses from reflection spectroscopy”. In: (2019), pp. 2883–2888.
- [356] James Harvey. “Light-Scattering Characteristics Of Optical Surfaces”. In: *Proceedings of SPIE - The International Society for Optical Engineering* 107 (July 1976).

- [357] Lambda Research Corporation. *Ghost and Stray Light Analysis using TracePro®*. Webinar. Littleton, MA, Feb. 2012. URL: www.lambdaresearch.com.
- [358] John C. Stover. “Optical Scattering: Measurement and Analysis”. In: 1990.
- [359] Mark O’Neill et al. “Space photovoltaic concentrator using robust fresnel lenses, 4-junction cells, graphene radiators, and articulating receivers”. In: June 2016, pp. 1337–1342.
- [360] Habib Sidhom et al. “Effect of electro discharge machining (EDM) on the AISI316L SS white layer microstructure and corrosion resistance”. In: *The International Journal of Advanced Manufacturing Technology* 65.1 (Mar. 2013), pp. 141–153. URL: <https://doi.org/10.1007/s00170-012-4156-6>.
- [361] Halil M. Güven and Richard B. Bannerot. “Determination of error tolerances for the optical design of parabolic troughs for developing countries”. In: *Solar Energy* 36.6 (1986), pp. 535–550. URL: <https://www.sciencedirect.com/science/article/pii/0038092X86900186>.
- [362] H M Guven and R B Bannerot. “Derivation of universal error parameters for comprehensive optical analysis of parabolic troughs”. English. In: *J. Sol. Energy Eng.; (United States)* 108:4 (Nov. 1986). Place: United States. URL: <https://www.osti.gov/biblio/6953257>.
- [363] Camilo Arancibia-Bulnes et al. “A survey of methods for the evaluation of reflective solar concentrator optics”. In: *Renewable and Sustainable Energy Reviews* 69 (Mar. 2017), pp. 673–684.
- [364] H. Schwenke et al. “Optical Methods for Dimensional Metrology in Production Engineering”. In: *CIRP Annals - Manufacturing Technology* 51 (July 2007), pp. 685–699.
- [365] R. J. Hocken, N. Chakraborty, and C. Brown. “Optical Metrology of Surfaces”. In: *CIRP Annals* 54.2 (2005), pp. 169–183. URL: <https://www.sciencedirect.com/science/article/pii/S0007850607600250>.
- [366] L. De Chiffre et al. “Surfaces in Precision Engineering, Microengineering and Nanotechnology”. In: *CIRP Annals* 52.2 (2003), pp. 561–577. URL: <https://www.sciencedirect.com/science/article/pii/S0007850607602042>.
- [367] KEYENCE. *Digital Microscope VHX-series*. Tech. rep. Osaka, Japan. URL: www.keyence.com.
- [368] AESUB blue. *State of the Art Scanningspray*. Tech. rep. Recklinghausen, Germany. URL: www.aesub.com.
- [369] Wayne Rasband. *ImageJ 1.46r*. USA. URL: <https://imagej.nih.gov/ij/index.html>.
- [370] Daniel Girardeau-Montaut. *CloudCompare*. France. URL: www.cloudcompare.org.
- [371] Daniel Girardeau-Montaut. “Détection de changement sur des données géométriques tridimensionnelles”. In: (May 2006).

- [372] J. A. C. Heijmans, M. Müller, and Ronald Holzlöhner. “Combined Opto-mechanical analysis for modern optical instruments”. In: *Astronomical Telescopes + Instrumentation*. 2018.
- [373] Christian Lauterbach, Sung-eui Yoon, and Dinesh Manocha. “Ray-Strips: A Compact Mesh Representation for Interactive Ray Tracing”. In: *IEEE Symposium on Interactive Ray Tracing*. Oct. 2007, pp. 19–26.
- [374] Michael M. Kazhdan, Matthew Bolitho, and Hugues Hoppe. “Poisson surface reconstruction”. In: *SGP '06*. 2006.
- [375] Daniel Girardeau-Montaut et al. “Change detection on point cloud data acquired with a ground laser scanner”. In: *International Archives of Photogrammetry, Remote Sensing and Spatial Information Sciences* 36 (Jan. 2005).
- [376] R Cariou et al. “Development of Highly-Efficient III-V//Si Wafer-Bonded Triple-Junction Solar Cells”. In: June 2016.
- [377] Audrey Morisset et al. “Highly passivating and blister-free hole selective poly-silicon based contact for large area crystalline silicon solar cells”. In: *Solar Energy Materials and Solar Cells* 200 (2019), p. 109912. URL: <https://www.sciencedirect.com/science/article/pii/S0927024819302338>.
- [378] Laura Vauche et al. “Wafer bonding approaches for III-V on Si multi-junction solar cells”. In: *2017 IEEE 44th Photovoltaic Specialist Conference (PVSC)*. 2017, pp. 2492–2497.
- [379] Elias Veinberg-Vidal et al. “Characterization of dual-junction III-V on Si tandem solar cells with 23.7% efficiency under low concentration”. In: *Progress in Photovoltaics: Research and Applications* 27.7 (2019). _eprint: <https://onlinelibrary.wiley.com/doi/pdf/10.1002/pip.3128>, pp. 652–661. URL: <https://onlinelibrary.wiley.com/doi/abs/10.1002/pip.3128>.
- [380] HOWARD G. ALLEN. “Chapter 5 - Bending and buckling of isotropic sandwich panels with very thin identical faces”. In: *Analysis and Design of Structural Sandwich Panels*. Ed. by HOWARD G. ALLEN. The Commonwealth and International Library: Structures and Solid Body Mechanics Division. Pergamon, 1969, pp. 76–98. URL: <https://www.sciencedirect.com/science/article/pii/B9780080128702500092>.
- [381] Junlan Li and Shaoze Yan. “Thermally induced vibration of composite solar array with honeycomb panels in low earth orbit”. In: *Applied Thermal Engineering* 71 (Oct. 2014), pp. 419–432.
- [382] Donald Meagher. *Octree Encoding: A New Technique for the Representation, Manipulation and Display of Arbitrary 3-D Objects by Computer*. Oct. 1980.
- [383] Matthew Berger et al. “A Survey of Surface Reconstruction from Point Clouds”. In: *Computer Graphics Forum* 36.1 (2017). _eprint: <https://onlinelibrary.wiley.com/doi/pdf/10.1111/cgf.12802>, pp. 301–329. URL: <https://onlinelibrary.wiley.com/doi/abs/10.1111/cgf.12802>.

- [384] A. C. Öztireli, G. Guennebaud, and M. Gross. “Feature Preserving Point Set Surfaces based on Non-Linear Kernel Regression”. In: *Computer Graphics Forum* 28.2 (2009). _eprint: <https://onlinelibrary.wiley.com/doi/pdf/10.1111/j.1467-8659.2009.01388.x>, pp. 493–501. URL: <https://onlinelibrary.wiley.com/doi/abs/10.1111/j.1467-8659.2009.01388.x>.
- [385] Oliver van Kaick, Ghassan Hamarneh, and Daniel Cohen-Or. “A Survey on Shape Correspondence”. In: *Comput. Graph. Forum* 30 (Sept. 2011), pp. 1681–1707.
- [386] P.J. Besl and Neil D. McKay. “A method for registration of 3-D shapes”. In: *IEEE Transactions on Pattern Analysis and Machine Intelligence* 14.2 (1992), pp. 239–256.
- [387] P. Cignoni, C. Rocchini, and R. Scopigno. “Metro: Measuring Error on Simplified Surfaces”. In: *Computer Graphics Forum* 17.2 (1998). _eprint: <https://onlinelibrary.wiley.com/doi/pdf/10.1111/1467-8659.00236>, pp. 167–174. URL: <https://onlinelibrary.wiley.com/doi/abs/10.1111/1467-8659.00236>.
- [388] O. Monserrat and M. Crosetto. “Deformation measurement using terrestrial laser scanning data and least squares 3D surface matching”. In: *ISPRS Journal of Photogrammetry and Remote Sensing* 63.1 (2008), pp. 142–154. URL: <https://www.sciencedirect.com/science/article/pii/S0924271607000810>.
- [389] Dimitri Lague, Nicolas Brodu, and Jérôme Leroux. “Accurate 3D comparison of complex topography with terrestrial laser scanner: Application to the Rangitikei canyon (N-Z)”. In: *ISPRS Journal of Photogrammetry and Remote Sensing* 82 (2013), pp. 10–26. URL: <https://www.sciencedirect.com/science/article/pii/S0924271613001184>.
- [390] Martin A. Fischler and Robert C. Bolles. “Random sample consensus: a paradigm for model fitting with applications to image analysis and automated cartography”. In: *Commun. ACM* 24 (1981), pp. 381–395.
- [391] R. Schnabel, R. Wahl, and R. Klein. “Efficient RANSAC for point-cloud shape detection”. English. In: *Computer Graphics Forum* 26.2 (2007). Publisher: Blackwell Publishing Ltd, pp. 214–226. URL: <https://www.scopus.com/inward/record.uri?eid=2-s2.0-34248995532&doi=10.1111%2fj.1467-8659.2007.01016.x&partnerID=40&md5=d9a07fd57c30ac18d12e991d6335b530>.
- [392] Gerhard Roth and Martin D. Levine. “Extracting geometric primitives”. In: *Cvgip: Image Understanding* 58 (1993), pp. 1–22.

